

Dynamic Cellular Cartography: Mapping the Local Determinants of Oligodendrocyte Transcription Factor 2 (OLIG2) Function in Live Cells Using Massively Parallel Fluorescence Correlation Spectroscopy Integrated with Fluorescence Lifetime Imaging Microscopy (mpFCS/FLIM)

Sho Oasa,[¶] Aleksandar J. Krmpot,[¶] Stanko N. Nikolić,[¶] Andrew H. A. Clayton, Igor F. Tsigelny, Jean-Pierre Changeux, Lars Terenius, Rudolf Rigler,^{*} and Vladana Vukojević^{*}

Cite This: *Anal. Chem.* 2021, 93, 12011–12021

Read Online

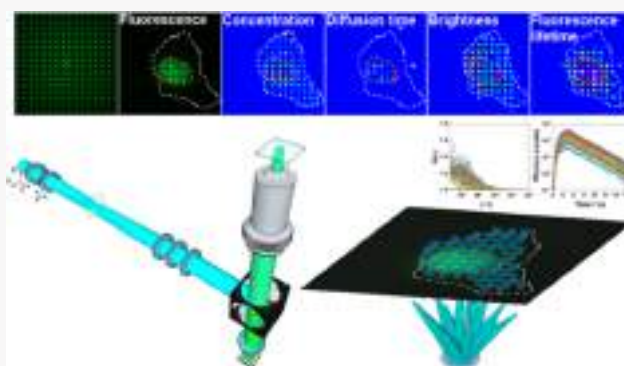
ACCESS |

Metrics & More

Article Recommendations

Supporting Information

ABSTRACT: Compartmentalization and integration of molecular processes through diffusion are basic mechanisms through which cells perform biological functions. To characterize these mechanisms in live cells, quantitative and ultrasensitive analytical methods with high spatial and temporal resolution are needed. Here, we present quantitative scanning-free confocal microscopy with single-molecule sensitivity, high temporal resolution ($\sim 10 \mu\text{s}/\text{frame}$), and fluorescence lifetime imaging capacity, developed by integrating massively parallel fluorescence correlation spectroscopy with fluorescence lifetime imaging microscopy (mpFCS/FLIM); we validate the method, use it to map in live cell location-specific variations in the concentration, diffusion, homodimerization, DNA binding, and local environment of the oligodendrocyte transcription factor 2 fused with the enhanced Green Fluorescent Protein (OLIG2-eGFP), and characterize the effects of an allosteric inhibitor of OLIG2 dimerization on these determinants of OLIG2 function. In particular, we show that cytoplasmic OLIG2-eGFP is largely monomeric and freely diffusing, with the fraction of freely diffusing OLIG2-eGFP molecules being $f_{D,\text{free}}^{\text{cyt}} = (0.75 \pm 0.10)$ and the diffusion time $\tau_{D,\text{free}}^{\text{cyt}} = (0.5 \pm 0.3)$ ms. In contrast, OLIG2-eGFP homodimers are abundant in the cell nucleus, constituting $\sim 25\%$ of the nuclear pool, some $f_{D,\text{bound}}^{\text{nuc}} = (0.65 \pm 0.10)$ of nuclear OLIG2-eGFP is bound to chromatin DNA, whereas freely moving OLIG2-eGFP molecules diffuse at the same rate as those in the cytoplasm, as evident from the lateral diffusion times $\tau_{D,\text{free}}^{\text{nuc}} = \tau_{D,\text{free}}^{\text{cyt}} = (0.5 \pm 0.3)$ ms. OLIG2-eGFP interactions with chromatin DNA, revealed through their influence on the apparent diffusion behavior of OLIG2-eGFP, $\tau_{D,\text{bound}}^{\text{nuc}}$ (850 ± 500) ms, are characterized by an apparent dissociation constant $K_{d,\text{app}}^{\text{OLIG2-DNA}} = (45 \pm 30)$ nM. The apparent dissociation constant of OLIG2-eGFP homodimers was estimated to be $K_{d,\text{app}}^{(\text{OLIG2-eGFP})_2} \approx 560$ nM. The allosteric inhibitor of OLIG2 dimerization, compound NSC 50467, neither affects OLIG2-eGFP properties in the cytoplasm nor does it alter the overall cytoplasmic environment. In contrast, it significantly impedes OLIG2-eGFP homodimerization in the cell nucleus, increasing five-fold the apparent dissociation constant, $K_{d,\text{app}}^{(\text{OLIG2-eGFP})_2} \approx 3 \mu\text{M}$, thus reducing homodimer levels to below 7% and effectively abolishing OLIG2-eGFP specific binding to chromatin DNA. The mpFCS/FLIM methodology has a myriad of applications in biomedical research and pharmaceutical industry. For example, it is indispensable for understanding how biological functions emerge through the dynamic integration of location-specific molecular processes and invaluable for drug development, as it allows us to quantitatively characterize the interactions of drugs with drug targets in live cells.



The intracellular environment is a complex and crowded, spatially heterogeneous medium the organization of which is bestow and dynamically maintained through innumerable reaction-diffusion processes.^{1,2} While strong interactions (bond dissociation energies $D_0 > 20$ kJ/mol) are important determinants of cellular physiology as they confer specificity and selectivity,³ it is well established that weak, nonspecific interactions ($D_0 < 20$ kJ/mol), such as hydrogen bonding and interactions between permanent and transient

Received: May 21, 2021
Accepted: August 9, 2021
Published: August 24, 2021



dipoles, are equally important despite being so weak that they can be broken with energies that are within the range of thermal fluctuations. At the molecular level, weak interactions define macromolecular configuration and conformation, and hence, their function.⁴ At the cellular level, they are critical determinants of the overall organization of the cellular interior and significantly contribute to compartmentalization, i.e., the formation of distinct local environments (often called membrane-less organelles), where particular interactions between relevant biomolecules are enabled to efficiently proceed.^{5–7} The evolution of mechanisms that harness weak cooperative interactions was recently shown to render living organisms more capable of robustly undergoing evolutionary changes, and it appears that such mechanisms have been repeatedly positively selected during the evolution of increasingly complex organisms.⁸ The quest to deploy weak cooperative interactions is also of relevance for designing new drugs, in particular for the development of so-called allosteric drugs.^{9–11} Allosteric drugs exploit a fundamental mechanism, initially identified in multisubunit/multimeric proteins,^{12–14} which was later observed also in monomeric, intrinsically disordered proteins.¹⁵ They bind to a distant binding site, inducing rearrangements in the network of weak cooperative interactions that propagate across comparatively long distances, eventually rendering the active site more/less amenable for orthosteric ligand/drug binding.¹⁶ Efforts to develop allosteric drugs focus on understanding the function of natural molecules that act as allosteric modulators,¹⁷ rely on the use of computational approaches to identify allosteric binding sites that can be specifically targeted,^{18,19} and are inseparable from the advancement of experimental techniques to understand detailed molecular mechanisms that underlie allostery²⁰ and to characterize the effects of prospective allosteric drug candidates.²¹ Experimental techniques designed to probe these processes in the cellular milieu need to be sensitive over a range of timescales (nanoseconds-to-seconds) and length scales (nanometers to microns).

Fluorescence correlation spectroscopy (FCS) and its dual-color variant fluorescence cross-correlation spectroscopy (FCCS) are the only presently available techniques that can nondestructively measure the concentration, diffusion, and binding of fluorescent/fluorescently labeled molecules in live cells with single-molecule sensitivity and high, sub-microsecond, temporal resolution.²² However, the same feature of FCS/FCCS that enables the ultimate, single-molecule sensitivity—the possibility to probe a minute observation volume element, thereby significantly reducing the background and improving the signal-to-background-ratio, confers also a serious limitation. Thus, conventional FCS/FCCS is of limited overview, i.e., measurements are restricted to a single-point location, probing in the cell a tiny volume of $(0.2–2) \times 10^{-15}$ l.^{23–26} To overcome this limitation, FCS was “amalgamated” with imaging-based methods, yielding new experimental techniques, such as temporal image correlation spectroscopy (TICS)²⁷ and raster image correlation spectroscopy (RICS),^{28,29} which rely on raster scanning of the laser beam to illuminate a larger area; and single-plane illumination microscopy-based FCS (SPIM-FCS)^{30–33} and massively parallel FCS (mpFCS),^{34–36} which deploy different illumination strategies to cover a larger area. While these new techniques enable location-specific mapping of molecular concentration and diffusion in cells, they also entail some limitations. For example, the temporal and spatial resolution of

TICS are inversely related and one is improved at the expense of the other—spatial resolution of TICS increases when the temporal resolution is in the millisecond range, due to long image plane acquisition time by raster scanning. This renders TICS either ill-suited for the study of fast processes or confers low spatial resolution.²⁷ Similarly, RICS sacrifices spatial resolution to determine the diffusion and the number of molecules,^{28,29,37} as averaging over a relatively large number of pixels (>64) is needed to allow an accurate spatial correlation analysis. It also has significant problems when analyzing heterogeneous samples since the presence of bright speckles significantly deforms the autocorrelation curve. SPIM-FCS, which relies on the use of light-sheet illumination and a 2D camera to examine larger areas, can achieve high temporal resolution—recently reaching 6 μ s for a reasonably short (≈ 100 s) measurement duration using the Swiss single-photon avalanche diode array (CHSPAD) camera.^{32,38} SPIM-FCS is, however, inherently hampered by the nonuniform thickness of the light sheet, which widens toward the edges, thus forming larger observation volume elements. Furthermore, scattering of the light sheet in heterogeneous environments and the presence of opaque compounds within the specimen alter the light-sheet intensity and can even completely block the incident light, which is recognized by the appearance of dark stripes in SPIM images. In SPIM-FCS, this translates to nonuniform illumination and hence a nonuniform signal-to-noise (SNR) ratio across the image. mpFCS relies on the spatial modulation of the incident laser beam by a diffractive optical element (DOE) to generate a large number of illumination spots, and a matching SPAD camera to detect in a confocal arrangement of the fluorescence intensity fluctuations from a large number (1024 in a 32×32 arrangement) of observation volume elements, providing single-molecule sensitivity and high spatial (~ 250 nm) and temporal (21 μ s) resolution.^{34,35,39,40} mpFCS was shown to be widely applicable, for the analysis of fast diffusion processes of eGFP-fused functional biomolecules in live cells³⁵ and in live tissue *ex vivo*.³⁹ The broad applicability of the mpFCS for functional fluorescence microscopy imaging (ffMI) was a motivation for us to go a step further and develop a new ffMI modality, mpFCS integrated with fluorescence lifetime imaging microscopy (mpFCS/FLIM). The fluorescence lifetime of a fluorophore or a fluorescently labeled macromolecule provides information on the environment local to the fluorophore (e.g., refractive index, polarity, pH, PO₂, Ca²⁺). It can provide complementary insights into nanoscale (1–10 nm) macromolecular interactions or conformations via Förster resonance energy transfer (FRET) and dynamic quenching on the nanosecond timescale.

Here, we present an integrated massively parallel FCS and FLIM system (mpFCS/FLIM) on the same microscope frame. This enables massively parallel measurements to quantitatively characterize the location-specific concentration, mobility and interactions (via FCS), and local properties of the immediate surrounding of biomolecules (via fluorescence lifetime). We demonstrate the capabilities of mpFCS/FLIM for quantitative live cell biochemistry and cellular pharmacology by characterizing the effect of test compound NSC 50467 on oligodendrocyte transcriptional factor 2 (OLIG2) dimerization. OLIG2, a basic helix–loop–helix transcription factor in the central nervous system, plays an important role in neuronal cell differentiation during development,⁴¹ adult neurogenesis,⁴² and glioblastoma development.⁴³ Substances that target

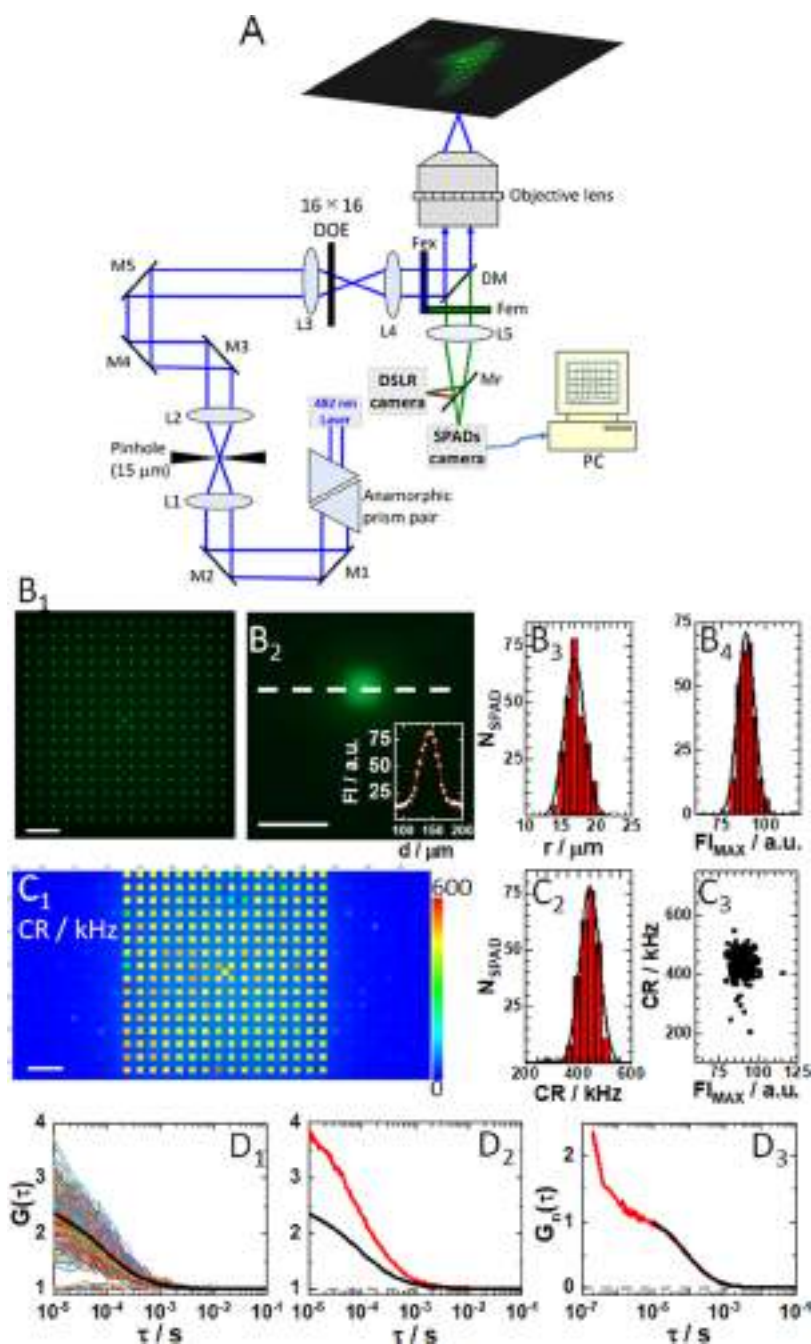


Figure 1. Optical setup for mpFCS/FLIM. (A) Schematic drawing of the mpFCS/FLIM optical setup. The 482 nm laser beam with elliptical cross-section is transformed into a circular beam using an anamorphic prism pair and expanded using a Kepler telescope setup (L1 and L2) with a pinhole in its focus. The expanded circular laser beam is focused by the focusing lens (L3) mounted on an *xyz* translation stage, which is positioned in front of the diffractive optical element (DOE) that can be translated along and rotated around the *z*-axis. The illumination matrix consisting of 16×16 (256) spots, which are generated in the image plane of the back port of the microscope, is imaged by the microscope relay optics (L4) and the objective lens to the object plane. Fluorescence is detected by a single-photon avalanche diode (SPAD) camera that can be translated along the *z*-axis and tilted at two angles (pitch and yaw) or a digital single-lens reflex (DSLR) camera. (B₁) Image of the illumination matrix visualized by the DSLR camera using a thin fluorescence layer as a specimen. (B₂) Enlarged image of a single illumination spot shown in (B₁). Inset: Fluorescence intensity (FI) distribution through the center of the spot (white dashed line) and the best-fit Gaussian curve (red solid line). Spot roundness, assessed by measuring the spot radius in different directions: horizontal (0° ; white dashed line), 45° , 90° , and 135° , showed that the ratio of spot radius over the spot radius at 0° was 1.00, 1.02, 0.96, and 1.04, respectively. (B₃) Histogram of spot radii for all 256 spots in the confocal image of the illumination matrix is shown in (B₁). The average spot radius, $r_{\text{spot}} = (17 \pm 2) \mu\text{m}$, was determined from a half of the full width at half-maximum (FWHM) of the best-fit Gaussian curve. (B₄) Histogram of peak fluorescence intensity for all spots in the confocal image of the illumination matrix is shown in (B₁). The average peak fluorescence intensity, $FI_{\text{MAX}} = (90 \pm 5) \text{ a.u.}$ (C₁) Scanning-free confocal image of the same specimen as in (B₁) acquired using the SPC³ SPAD camera. Here, each SPAD in addition to being a photodetector also acts as a 30 nm pinhole. Of note, every other SPAD in the centrally positioned 32×32 SPADs of the 64×32 SPC³ SPAD camera was used. Unilluminated SPADs (dark blue), on the sides and in-between the illuminated ones (yellow–red ones), are clearly distinguishable by fluorescence intensity. (C₂) Histogram of fluorescence intensity, i.e., photon count rates (CR) measured in all illuminated SPADs shown in (C₁). The average fluorescence intensity was

Figure 1. continued

determined, $CR = (440 \pm 35)$ kHz. (C_3) Scatter plot showing spot peak intensity measured using the SPC³ SPAD camera (C_1) as compared to the spot intensity measured using the DSLR camera (B_1). While a unimodal distribution is observed, six SPADs with disparate values were identified. (D_1) 256 single-SPAD autocorrelation curves (ACCs) recorded in an aqueous buffer solution of eGFP, $c_{\text{eGFP}} = 4$ nM, with the corresponding average ACC (black). (D_2) ACCs acquired in the same solution as in D_1 by mpFCS (black; same as in D_1) and spFCS ACC (red). The dashed gray line shows $G(\tau) = 1$. (D_3) ACCs shown in D_2 normalized to the same amplitude, $G(10 \mu\text{s}) = 1$ at $\tau = 10 \mu\text{s}$, acquired using the spFCS (red) and the mpFCS (black) systems. The dashed gray line shows $G_n(\tau) = 0$. In all images, scale bar is $10 \mu\text{m}$.

OLIG2 are attractive candidates for the development of therapeutic agents for glioblastoma.⁴⁴ However, identification of such molecules is not trivial due to the large and complex surface through which OLIG2 interacts with itself and other partners, which is uncharacteristic and with no hydrophobic pockets.^{18,19} The NSC 50467 compound was identified *in silico* using the so-called “combined pharmacophore approach” and was predicted to act as an allosteric inhibitor of OLIG2 homodimerization^{45–47} thus impeding OLIG2 homodimer binding to the enhancer box (E-box), which is the canonical bHLH transcription factor binding site.^{45–47}

EXPERIMENTAL SECTION

Optical Setup for Massively Parallel Fluorescence Correlation Spectroscopy Integrated with Fluorescence Lifetime Imaging Microscopy (mpFCS/FLIM). The optical design of the mpFCS/FLIM system and important features are shown in Figure 1A–C₃. Information about optical alignment, calibration, data acquisition, analysis, image rendering, and fitting of temporal autocorrelation curves (ACCs) using eq S1 is provided in the Supporting Information (Section S1, Figures S1–S5).

Software for mpFCS/FLIM. mpFCS/FLIM data acquisition, analysis, and graphical presentation were carried out using our own software, into which the Micro Photon Device (MPD) software for running the 2D SPAD array was integrated. The software was written in Embarcadero C++ Builder 10.2 (Embarcadero Technologies). Detailed information about data acquisition, analysis, and image rendering are given for mpFCS in Section S1b and for FLIM in Section S1c. Phasor plot analysis is presented in Section S1d.

Cell Culture and Transfection. Procedures for cell culturing and transfection for mpFCS/FLIM measurements (Section S2a), pharmacological treatment of cells (Section S2b), and cell culture for FRET-FLIM measurements (Section S2c) can be found in the indicated sections in the Supporting Information.

Dissociation Constant Assessment. Procedures for calculating the apparent dissociation constants of OLIG2-eGFP dimers (Section S3) and Olig2-eGFP–DNA complexes (Section S4) can be found in the indicated sections in the Supporting Information.

Standard Solutions for mpFCS/FLIM Calibration. Relevant information about standard solutions used for mpFCS/FLIM system calibration can be found in Section S5.

Statistical Analysis. All values are presented as mean \pm standard deviation (SD). Two-tailed Student's *t*-test was used to compare two groups. The correlation analyses were reported using the probability value (*p*-value). Differences between two groups were considered to be significant when $p < 0.05$. Pearson's sample correlation coefficient *r* was used to assess the strength of a linear association between two variables. Statistical analysis was performed using the Origin 2018 program for interactive scientific graphing and data analysis

and/or Excel. During data analysis, data from a few pixels (<5%) were disregarded due to the extremely high background in these SPADs. The results were replicated in three independent experiments, starting from cell transfection, culturing, treatment, and measurement. Similar trends were observed in all three experiments. Figures show representative data acquired in a single cell.

RESULTS

Validation of mpFCS/FLIM System Performance for FCS. The sensitivity and temporal resolution of the mpFCS/FLIM system are unprecedented, enabling us to perform measurements in a buffered aqueous solution of the enhanced Green Fluorescent Protein (eGFP; Figure 1D₁–D₃). Of note, the amplitude of the average ACC acquired by mpFCS is half the amplitude of the ACC acquired using conventional single-point FCS (spFCS), largely due to a higher background in the mpFCS system than in the spFCS system (Figure 1D₂). In contrast, normalized autocorrelation curves nicely overlap (Figure 1D₃), revealing that the observation volume elements (OVes) in the mpFCS and the spFCS systems are of similar size. We also show that the ACC can be fitted with the acceptable signal to noise using eq S1, $\alpha = 1$, $i = 1$, $T = 0$ (Figure S4A,B) and that the axial ratio is not diverging ($s = \omega_z / \omega_{xy} = 4.6$), which indicates that the assumption of a 3D-ellipsoidal Gaussian OVE is applicable. Finally, we show by *z*-stack imaging that the fluorescence intensity profile in the axial direction is Gaussian with a half width at half-maximum, $\text{HWHM} = (1.15 \pm 0.09) \mu\text{m}$ (Figure S4C).

Validation of mpFCS/FLIM System Performance for FLIM. To characterize the performance of the mpFCS/FLIM system for fluorescence lifetime (τ_f) measurements, the instrument response function (IRF) was measured and single-exponential decay fitting of FLIM curves was compared to convolution fitting with the IRF (Figure S6); effects of the gate width and the step size between gates on τ_f were examined (Figure S7); the precision with which τ_f of pure species can be determined was assessed using solutions of molecules with known fluorescence lifetimes (Figures 2 and S8); and the ability of our system to resolve two lifetimes using measurements at a single frequency was evaluated using a series of two-component solutions with different relative contributions of the two component (Figures 2 and S9). The most important results are summarized in Figure 2.

Briefly, Figure 2A₁ shows 256 simultaneously recorded fluorescence decay curves in a phosphate buffer solution of eGFP. Analysis using the single-exponential decay model (eq S2) yielded a histogram of fluorescence lifetimes from which eGFP fluorescence lifetime was determined, $\tau_{\text{f,eGFP}} = (2.5 \pm 0.02)$ ns (Figure 2A₂). This value agrees well (i.e., to within 10%) with the values obtained in other laboratories.^{48–50}

Using a 2.0 ns gate width and a 0.2 ns gate step time, τ_f was measured for several standards in solution, covering a τ_f range from 1 to 10 ns (Figure 2B₁,B₂). The agreement between

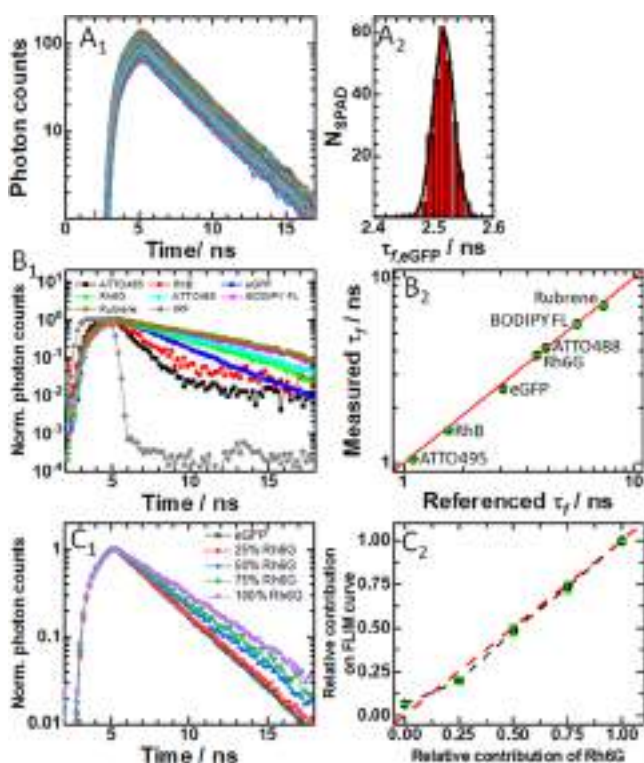


Figure 2. Fluorescence lifetime imaging microscopy (FLIM) using the integrated mpFCS/FLIM system. (A₁) 256 simultaneously recorded eGFP fluorescence decay curves in aqueous phosphate buffer. (A₂) Corresponding histogram of fluorescence lifetimes obtained using a one-component exponential decay model to fit the fluorescence decay curves. From a best-fit Gaussian curve, the fluorescence lifetime was determined, $\tau_{f,eGFP} = (2.50 \pm 0.02)$ ns. (B₁) Fluorescence decay curves recorded in aqueous solutions of different fluorescent dyes: ATTO495 (black), Rhodamine B (RhB; red), eGFP (blue), Rhodamine 6G (Rh6G; green), ATTO488 (cyan), BODIPY FL (magenta), Rubrene (dark yellow), and the Instrumental Response Function (IRF; gray), all acquired using the same SPAD in the SPC3 camera. (B₂) Comparison of fluorescence lifetimes measured using the mpFCS/FLIM system with literature values. Pearson's correlation indicated that there was a significant positive association between the measured and literature values ($r(7) = 0.999$, $p < 0.001$). The red line indicates perfect agreement. (C₁) Normalized fluorescence decay curves for Rh6G, eGFP, and their mixtures made so that a specified number of photons originates from Rh6G, e.g., 50% Rh6G indicates that 50% of photons are from Rh6G: eGFP (0% Rh6G; dark gray), 25% Rh6G (red), 50% Rh6G (blue), 75% Rh6G (green), and 100% Rh6G (violet). (C₂) Comparison of the relative contribution of Rh6G, as determined from fluorescence lifetime measurements using a two-component exponential decay fitting model with fixed fluorescence lifetimes: $\tau_{f,eGFP} = 2.5$ ns and $\tau_{f,Rh6G} = 3.8$ ns (black dots), with its actual concentration in a two-component mixture. Pearson's correlation indicated that there was a significant positive association between the measured τ_f and values found in the literature ($r(5) = 0.995$, $p < 0.01$).

expected and measured fluorescence lifetimes, which can be gleaned from Figure 2B₂, is excellent ($r = 0.999$, $p < 0.001$).

Given that τ_f can be considered a “molecular fingerprint,” allowing detection and discrimination between multiple species that emit fluorescence over the same spectral window, we tested the capability of our instrument to distinguish fluorophores that emit in the same spectral region and have discernible lifetimes, Rhodamine 6G (Rh6G), $\tau_{f,Rh6G} = (3.80 \pm 0.04)$ ns, and eGFP, $\tau_{f,eGFP} = (2.50 \pm 0.02)$ ns. To this aim, we

mixed Rh6G and eGFP solutions at different proportions (Figure 2C₁,C₂). As expected, the total τ_f increased as the proportion of the species with the longer τ_f (here Rh6G) was increased (Figure 2C₁). A fit of the data to an exponential decay function by two processes (eq S3; with τ_f for eGFP and Rh6G fixed and amplitudes floated) yielded relative amplitudes that matched well the calculated relative contribution of the components in the mixture (Figure 2C₂).

Since attempts to fit the data with a two-component-exponential decay model with free-floating τ_f and their relative contributions did not lead to extraction of the correct component lifetimes and their relative amounts (Figure S9A₁,A₂), phasor analysis^{S1–S3} was used to analyze the simultaneously acquired fluorescence decay curves, assuming that two lifetime components were common to all of the curves. By deploying phasor analysis, which uses the Fourier transform to decompose experimentally measured fluorescence decay curves into complex-valued functions of the modulus (m) and the phase angle (θ_{tot}) (eqs S4–S21), global analysis of a two-component system is reduced to algebraic calculations in the phasor space (Figure S9B₃). Following calibration experiments (Figure S8), we computed by phasor analysis τ_f and components' fractions with dramatically improved accuracy and precision (Figure S9B₁,B₂).

Spatial Mapping of Fluorescence Lifetime in a Fixed Specimen. To demonstrate spatial mapping of τ_f , a fixed plant specimen, the aridline orange stained section through the rhizome of the lily of the valley (*Convallaria majalis*) was used (Figure 3).

Fluorescence images acquired using a spot-wise, 16×16, illumination and the DSLR camera (Figure 3A,B₁) show cells in the central parenchyma made visible owing to the fluorescence signal from the cell wall. The fluorescence image of the same cell as in Figure 3B₁ acquired using the SPC³ SPAD camera is shown in Figure 3B₂. Fluorescence decay curves simultaneously recorded in 256 individual SPADs (Figure S10), exemplified in Figure 3C, when fitted using a two-component exponential decay model (Figure 3D₁), yielded a short, $\tau_{f,wall1} = (0.6 \pm 0.1)$ ns (Figure 3D₂) and a long fluorescence lifetime component, $\tau_{f,wall2} = (2.9 \pm 0.2)$ ns (Figure 3D₃). Importantly, the thus determined τ_f provided significant image contrast (Figure 3E₁,E₂), and even a “ratiometric” image could be obtained revealing the relative contribution of the component with the short fluorescence lifetime (Figure 3E₃).

Spatial Mapping of Concentration, Diffusion, and Fluorescence Lifetime in Live Cells. To demonstrate spatial mapping of the concentration, diffusion, and lifetime in live cells (Figure S11), we first performed measurements on fluorescent proteins, eGFP (Figures 4 and S12) or eGFP tetramer (eGFP_{tet}; Figures S13 and S14), as nonreactive molecular probes.

Our data show that for similar eGFP concentrations in the cell, $c_{eGFP} \approx 20$ nM, and in the aqueous buffer solution, $c_{eGFP} \approx 4$ nM, the mean diffusion time of eGFP was about 2.5 times longer in the cell than in the aqueous buffer, $\tau_{D,eGFP,cell} = (260 \pm 60)$ μ s vs $\tau_{D,eGFP,buffer} = (110 \pm 10)$ μ s, consistent with previous studies,^{S4} whereas the molecular brightness and fluorescence lifetimes were similar $CPSM_{eGFP,cell} = (1.0 \pm 0.3)$ kHz and $CPSM_{eGFP,buffer} = (1.0 \pm 0.2)$ kHz, $\tau_{f,eGFP,cell} = (2.50 \pm 0.05)$ ns and $\tau_{f,eGFP,buffer} = (2.50 \pm 0.02)$ ns. However, the relative standard deviations (RSD) of all measured variables were higher in the living cell (Figure 4B₂,C₂,D₂,E₂) than those

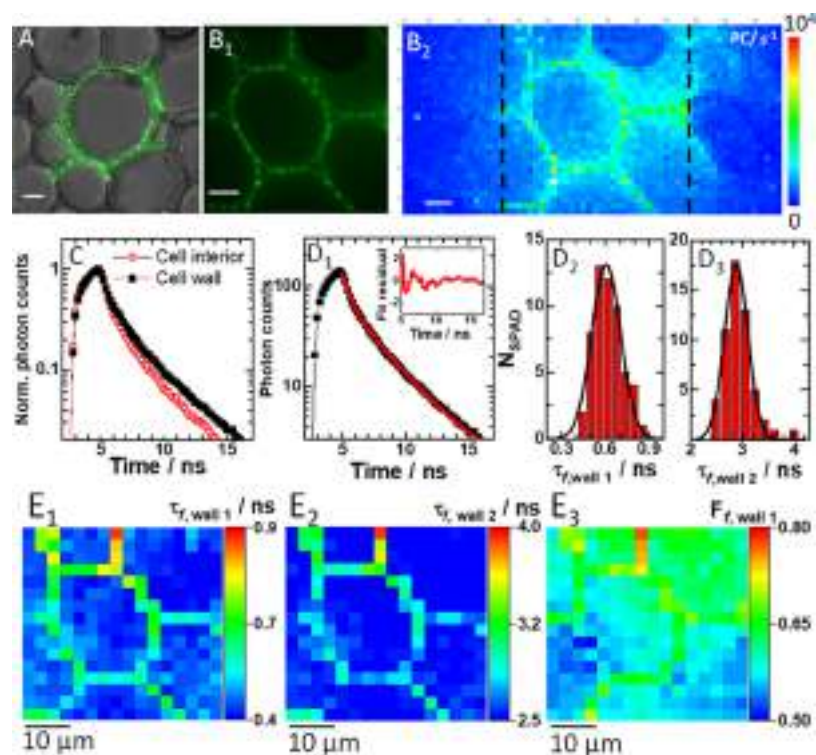


Figure 3. Spatial distribution of fluorescence lifetime in a fixed section of the rhizome of lily of the valley (*C. majalis*). (A) Fluorescence image of a spot-wise, 16×16 , illuminated cell (green) overlaid on a wide-field transmission image (gray) of a region in the central parenchyma recorded using the DSLR camera. (B₁) Zoomed fluorescence image of a spot-wise illuminated cell in the central parenchyma recorded using the DSLR camera. (B₂) Fluorescence image of the same cell as in (B₁) acquired using the SPC³ SPAD camera. Fluorescence intensity is given in photon counts (PC), exposure time 46 ms. (C) Fluorescence decay curves recorded in individual SPADs at distinct intracellular locations: cell wall (black squares) and inside the cell (red circles). All fluorescence decay curves are shown in Figure S10. (D₁) A fluorescence decay curve recorded in an individual SPAD at the cell wall (black squares) fitted using a two-component exponential decay model (eq S3, red line). Inset: Corresponding residuals. (D₂) Histogram of the short fluorescence lifetime component in the plasma membrane and the best-fit Gaussian curve yield $\tau_{f,\text{wall}1} = (0.6 \pm 0.1)$ ns. (D₃) Histogram of the long fluorescence lifetime component in the plasma membrane and the best-fit Gaussian curve yield $\tau_{f,\text{wall}2} = (2.9 \pm 0.2)$ ns. (E₁₋₃) FLIM images of the cell in (B₂) rendered visible by mapping the: short (E₁) and long (E₂) fluorescence lifetime component and the relative contribution of the short component (E₃). In all images, the scale bar is $10 \mu\text{m}$.

in the homogenous solution (Figure S3B–E), indicating that the cell environment presents a spatial variation in local concentration, local diffusion processes (Figure S15), and local excited-state decay (environment). Correlation maps (Figure S16) showed that no correlation was observed between the concentration (number of eGFP), molecular brightness, and lifetime, ruling out any spatially dependent concentration quenching in the fluorescence lifetime and absence of diffusion-influenced lifetime quenching. Taken together, these results are largely consistent with the view of eGFP being a biochemically inert, monomeric protein, able to roam largely unimpeded inside the cellular milieu. The broadened distribution functions observed here (relative to homogenous aqueous buffer) reveal that the cellular interior is not uniform and that eGFP is not totally confined to the cytosol but is also found in cytoplasmic organelles.

In contrast to eGFP, which can access the entire cell, a fluorescence image of a HEK cell-expressing eGFP_{tet} reveals distinctive fluorescence intensities in the cytoplasm and the cell nucleus (Figures S11B and S13A). Furthermore, the large RSD of the diffusion time for eGFP_{tet} in the cytoplasm is of particular note, as it is ten-fold larger than the corresponding value for the monomeric eGFP in the cytoplasm. Because the eGFP_{tet} is 4 times larger than eGFP (4 nm long axis dimension), this suggests that obstacles in the size range of 10 nm or more in the cellular environment affect eGFP_{tet}

dynamics, as revealed using the anomalous diffusion model (eq S1, $\alpha \neq 1$)^{55–57} to fit the experimentally derived ACCs and determine the anomalous diffusion exponent (α ; Figure S15B). Furthermore, and in contrast to the diffusion time, the fluorescence lifetime was homogeneous in cells expressing eGFP_{tet} (Figure S13E₁). FLIM curves in the nucleus showed lower photon counts but revealed similar decay rates (Figure S14C₁₋₃). The histogram of fluorescence lifetime quantified $\tau_{f,\text{eGFPtet}} = (2.4 \pm 0.05)$ ns in the cytoplasm and similarly in the nucleus (Figure S13E₂).

Spatial Mapping of Transcription Factor OLIG2-eGFP in Live Cells Before and After Treatment with Compound NSC 50467: an Allosteric Inhibitor of OLIG2 Dimerization. To demonstrate spatial mapping of the concentration, diffusion, and lifetime of interacting molecules in live cells, intracellular localization and dynamics of OLIG2 was characterized (Figures 5, S11C,D, and S17–S25).

OLIG2 is known to bind as a homodimer to the enhancer box (E-box), the canonical bHLH transcription factor binding site.^{45–47} It is predominantly localized in the cell nucleus (Figures SA₁ and S11C), but is known to shuttle between the nucleus and the cytoplasm (Figure S11D), with the actual localization pattern emerging from a dynamic equilibrium that is predominantly governed by the nuclear export signal.⁵⁸ Spatial mapping of the number of OLIG2-eGFP in untreated

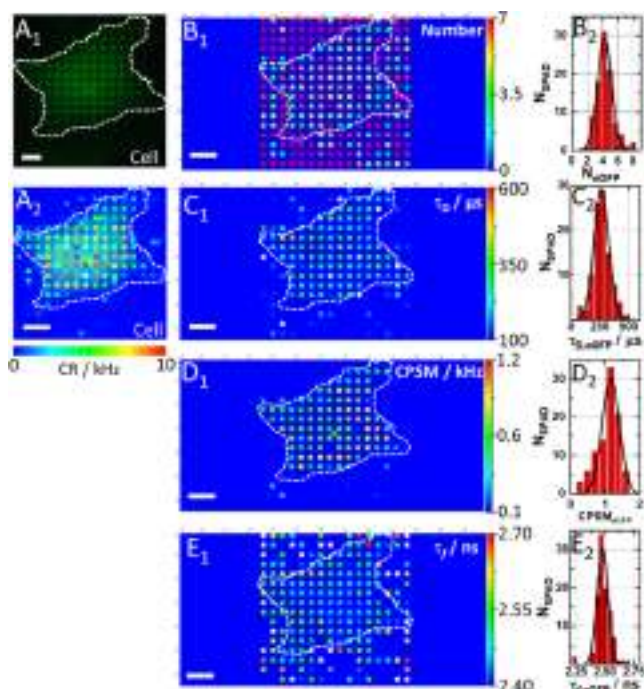


Figure 4. Spatial map of eGFP concentration, diffusion, brightness, and fluorescence lifetime in a live HEK cell. (A₁) Fluorescence image of an eGFP-expressing HEK cell acquired using a spot-wise, 16×16 , illumination and a DSLR camera. The hand-drawn dashed line highlights the cell border visualized by transmission light imaging. (A₂) Count rate map. Corresponding ACCs and FLIM curves are shown in Figure S12. (B₁) Spatial map of the average N_{eGFP} in the OVE. Of note, the apparently high average number of molecules in the cell surrounding is an artifact of the near-zero amplitude of the ACCs in the cell culture medium (see Figure S12A₂). (B₂) Histogram corresponding to B₁. The best-fit Gaussian curve yields $N_{\text{eGFP}} = (4.22 \pm 0.92)$, corresponding to $c_{\text{eGFP}} \approx 20$ nM. (C₁) Spatial map of $\tau_{\text{D,eGFP}}$. (C₂) Histogram corresponding to (C₁) yields the average eGFP diffusion time, $\tau_{\text{D,eGFP}} = (260 \pm 60)$ μs . (D₁) Spatial map of eGFP brightness as reflected by counts per second per molecule (CPSM). (D₂) Histogram corresponding to (D₁) yields average $\text{CPSM}_{\text{eGFP}} = (1.0 \pm 0.3)$ kHz. (E₁) Spatial map of eGFP fluorescence lifetimes. (E₂) Histogram corresponding to (E₁) yields the average eGFP fluorescence lifetime, $\tau_{\text{f,eGFP}} = (2.50 \pm 0.05)$ ns.

cells revealed that the concentration of OLIG2-eGFP in the cell nucleus is higher than in the cytoplasm (Figure 5A₂); the diffusion time, determined from the full width of the ACC at half maximum, is significantly longer in the cell nucleus than in the cytoplasm, $\tau_{\text{D}}^{\text{nuc}} = (250 \pm 300)$ ms vs $\tau_{\text{D}}^{\text{cyt}} = (0.9 \pm 1.5)$ ms (Figure 5A₃,E), and the fluorescence lifetime map revealed a significantly longer lifetime states in the cell nucleus, fluorescence lifetime, $\tau_{\text{f,OLIG2-eGFP}}^{\text{nuc}} = (3.0 \pm 0.3)$ ns vs $\tau_{\text{f,OLIG2-eGFP}}^{\text{cyt}} = (2.7 \pm 0.2)$ ns (Figure 5F), reflecting differences in the local environment surrounding the eGFP probe of OLIG2-eGFP in these cellular locations (Figure 5A₄). Given the unexpectedly large experimental errors for diffusion times, we further examined ACCs. This analysis revealed two characteristic decay times in both, the cytoplasm (Figures 5C₁ and S18B₁,C₁) and the cell nucleus (Figures 5C₂ and S18B₂,C₂), with the fast-decaying components being, within the experimental error, indistinguishable between these compartments, $\tau_{\text{D,free}}^{\text{cyt}} = \tau_{\text{D,free}}^{\text{nuc}} = (0.5 \pm 0.3)$ ms, while the relative amplitude and the diffusion time of the second component were larger and much longer in the cell nucleus

than in the cytoplasm, $f_{\text{D,bound}}^{\text{nuc}} = (0.65 \pm 0.10)$ vs $f_{\text{D,bound}}^{\text{cyt}} = (0.25 \pm 0.10)$ and $\tau_{\text{D,bound}}^{\text{nuc}} = (850 \pm 500)$ ms vs $\tau_{\text{D,bound}}^{\text{cyt}} = (60 \pm 30)$ ms, respectively. (Of note, fluorescence intensity time series (Figure S18A₁,A₂) show that the signal intensity is unchanged over time and is not distorted by photobleaching. Rather, the ACCs recorded in the cell nucleus do not settle at 1 because the decay time of the second component is comparable to the signal acquisition time length (20 s).) Finally, OLIG2-eGFP molecular brightness in the cytoplasm, $\text{CPSM}_{\text{OLIG2-eGFP}}^{\text{cyt}} = (1.0 \pm 0.7)$ kHz (Figure 5G), was within the experimental error indistinguishable from that of eGFP in live cells, $\text{CPSM}_{\text{eGFP}} = (1.0 \pm 0.3)$ kHz, measured under the same conditions, suggesting that OLIG2-eGFP is monomeric in the cytoplasm. In the nucleus, average molecular brightness is higher, $\text{CPSM}_{\text{OLIG2-eGFP}}^{\text{nuc}} = (1.4 \pm 0.7)$ kHz (Figure 5G and Table S1), suggesting that a dynamic equilibrium between OLIG2-eGFP monomers and dimers exists.

Treatment with the allosteric inhibitor of OLIG2 dimerization did neither change the concentration, nor the diffusion time, nor the fluorescence lifetime, and nor the molecular brightness of OLIG2-eGFP residing in the cytoplasm; $p > 0.05$ for all measurements (Figures 5C₁, D–G, S17A_{1–3} and S19A_{1–4}). However, it significantly perturbed the motions and the local environment of OLIG2-eGFP in the cell nucleus, causing, on the average, a decrease in the diffusion time by 4 times (from 850 to 200 ms; Figures 5C₂,E and S19B₂, $p = 5 \times 10^{-3}$), and reduced the fluorescence lifetime (Figure 5F, $p = 1.5 \times 10^{-8}$) and the molecular brightness (Figures 5G, S17B₃ and S19B₄, $p = 7 \times 10^{-3}$), while leaving the overall OLIG2-eGFP concentration unchanged, as reflected by the number of OLIG2-eGFP molecules (Figures 5D and S17B₁, $p > 0.05$). Moreover, the positive correlation between local OLIG2-eGFP molecular brightness and the local diffusion, which was strong in the cell nuclei of untreated cells, was significantly reduced (Figure S19B₂₋₂₃₋₂).

Finally, mpFCS measurements enabled us to assess the value of the apparent dissociation constants for OLIG2-eGFP binding to chromatin DNA before, $K_{\text{d,app}}^{\text{OLIG2-DNA}} = (45 \pm 30)$ nM, and after treatment, $K_{\text{d,NSC50467}}^{\text{OLIG2-DNA}} = (130 \pm 40)$ nM (Figure S19C_{1–3}). Also, mpFCS measurement of OLIG2-eGFP concentration and molecular brightness revealed that in untreated cells about 25% of OLIG2-eGFP molecules are homodimers and that treatment with NSC 50467 effectively reduced OLIG2-eGFP homodimer levels to below 7% (Table S1). This, in turn, enabled us also to infer apparent OLIG2-eGFP homodimer dissociation constants in untreated cells $K_{\text{d,app}}^{(\text{OLIG2-eGFP})_2} \approx 560$ nM, which upon treatment becomes $K_{\text{d,app}}^{(\text{OLIG2-eGFP})_2} \approx 3$ μM .

Taken together, the mpFCS data indicate that treatment with the allosteric modulator NSC 50467 does not significantly alter OLIG2-eGFP properties in the cytoplasm, whereas in the cell nucleus OLIG2-eGFP dimers are not efficiently formed in the presence of NSC 50467 and OLIG2-eGFP binding to the chromatin DNA is significantly abolished.

We then used Förster resonance energy transfer (FRET) via FLIM (FRET-FLIM), to further characterize NSC 50467 effects on OLIG2-eGFP dimer formation. To this aim, cells expressing OLIG2-eGFP, with eGFP acting as a FRET donor, and dark yellow fluorescent protein ShadowY tagged OLIG2 molecules (OLIG2-ShY), with ShY acting as FRET acceptor, were used. For a positive FRET control, a tandem dimer of eGFP and ShadowY (eGFP-ShY) was transfected into cells. As expected, robust FRET was observed with the positive FRET

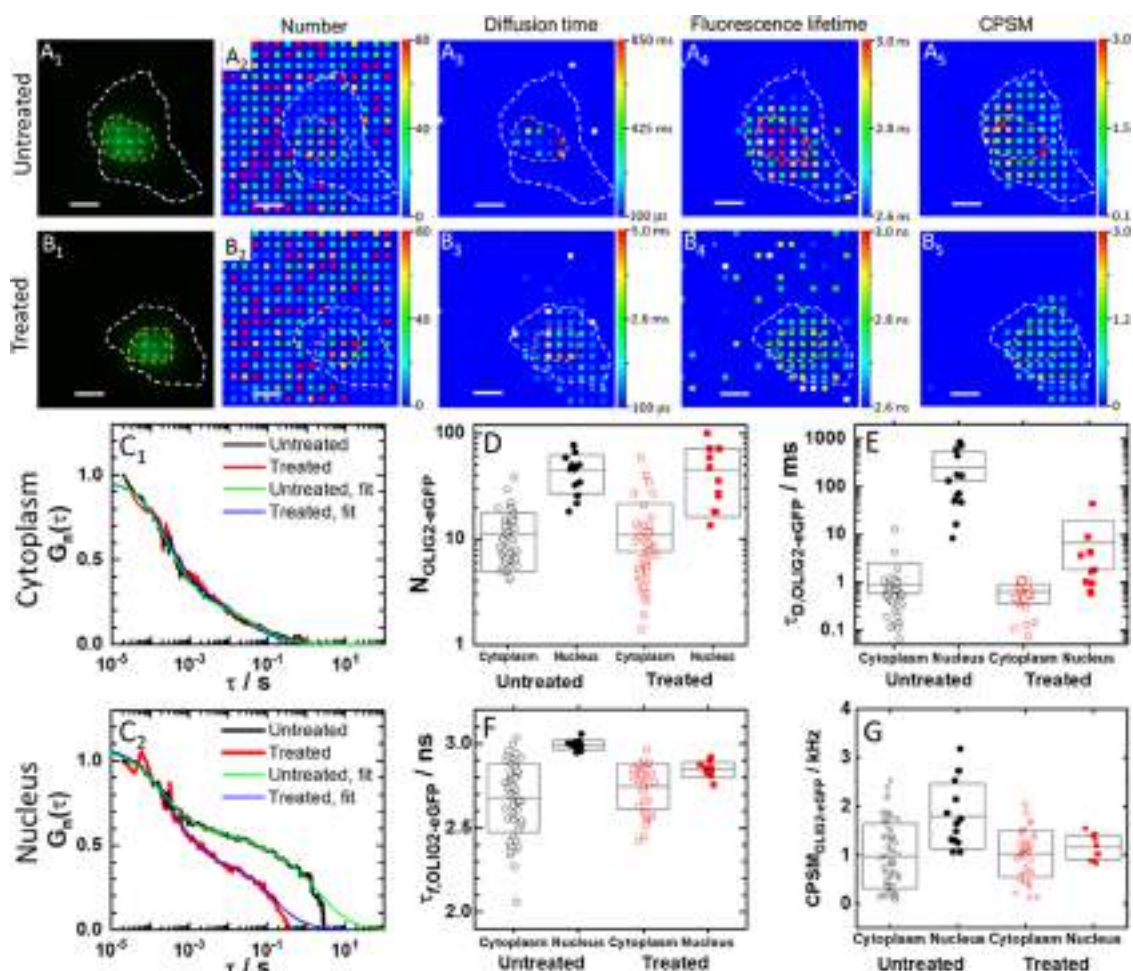


Figure 5. Spatial map of OLIG2-eGFP concentration, diffusion, brightness, and fluorescence lifetime in a live HEK cell before and after treatment with NSC 50467. (A₁, B₁) Fluorescence images of an untreated (A₁) and a treated (B₁) HEK cell-expressing OLIG2-eGFP, acquired using a spot-wise, 16 × 16, illumination and a DSLR camera. The hand-drawn dashed lines that highlight the cell border (white) and the cell nucleus (orange) were visualized by transmission light microscopy. Corresponding fluorescence intensity fluctuation time series and ACCs are shown in Figure S18. (A₂, B₂) Spatial map of the average number of OLIG2-eGFP molecules in an OVE, recorded in an untreated (A₂) and a treated (B₂) cell. (A₃, B₃) Spatial map of OLIG2-eGFP diffusion times recorded in an untreated (A₃) and a treated (B₃) cell. (A₄, B₄) Spatial map of fluorescence lifetimes recorded in an untreated (A₄) and a treated (B₄) cell. Corresponding FLIM curves are shown in Figure S18. (A₅, B₅) Spatial map of OLIG2-eGFP brightness (CPSM) recorded in an untreated (A₅) and a treated (B₅) cell. (C₁, C₂) Single-pixel ACCs normalized to the same amplitude, $G(20 \mu\text{s}) = 1$ at $\tau = 20 \mu\text{s}$, recorded in the same pixel in the cytoplasm (C₁) and the same pixel in the cell nucleus (C₂) before (black) and after (red) treatment. Two-component 3D free diffusion model fitting to the ACCs recorded in the cell nucleus and the cytoplasm in the untreated (green) and the treated (blue) cell. (D–G) Effect of treatment on the number of molecules (D), diffusion time (E), average fluorescence lifetime (F), and average molecular brightness (G).

control probe, with a FRET efficiency of 55% (as determined by phasor analysis of the FLIM data, Figure S20). Phasor plots recorded in cells expressing OLIG2-eGFP and OLIG2-ShadowY showed evidence of emission from a mixture of FRET and non-FRET states including the FRET contribution from the OLIG2 dimer (Figure S21A). In the context of a FRET/non-FRET state model (involving donor, acceptor, and FRET states), our analysis delivered an amplitude fraction of FRET to be (0.3 ± 0.1) in the absence of allosteric inhibitor, which decreased to (0.07 ± 0.06) upon treatment with the inhibitory compound, also observable at other cells (Figure S21B,E,F). As expected, the decrease in the FRET fraction was accompanied by an increase in the contribution of non-FRET states. This data provides evidence for the efficient inhibition of OLIG2 dimer formation by the inhibitory compound. Since the RSD of the amplitude of the FRET fraction of OLIG2 without compound is larger than that of the tandem dimer of

fluorescent proteins (eGFP-ShY), we can conclude that OLIG2 dimerization in the nucleus was in addition to OLIG2 dimerization inhibition also affected by the nuclear environment (e.g., genome DNA structure).

DISCUSSION

In this work, we present two important achievements, the development of a new functional fluorescence microscopy imaging (ffMI) modality attained by integrating massively parallel fluorescence correlation spectroscopy with fluorescence lifetime imaging microscopy (mpFCS/FLIM) and demonstrate its use to characterize the action of a compound with potential therapeutic effects that target OLIG2.

Our instrument is a quantitative scanning-free confocal fluorescence microscope with single-molecule sensitivity; it has similar confocal volume elements with single-point FCS and 10 μs /frame temporal resolution and can map fluorescence

lifetimes from 1 to 10 ns. The instrument builds on our previous work,³⁵ but we have now improved to longer signal acquisition duration, ~ 10 s from previous 2.7 s, with a higher temporal resolution, ~ 10 μ s/frame from previous ~ 21 μ s/frame, toward tracking faster dynamic processes. In addition, the SNR was dramatically improved. In particular, the number of particles ratio against spFCS reduced 10 times, from 50 to 5 for fluorospheres ($d = 100$ nm). Also, single-pixel autocorrelation curves in eGFP and QD525 in water agree to within 10% with spFCS. Importantly, the system integrated with FLIM enabled us to perform mpFCS and FLIM at the same position in the cell. This is a significant improvement compared to current practice, where considerable time lags are introduced when moving the specimen from one microscope to the other. At the same time, the time needed for finding the same cell after moving the specimen from one microscope to the other is entirely abolished. Our dedicated software provides mono- and two-component exponential decay fitting for all 256 SPADs nearly instantly, rendering a fluorescence lifetime image in a few seconds. Implementation of phasor analysis makes multicomponent analysis in FLIM easily achieved without the need to fit multicomponent exponential decay curves.

In comparison with other presently available 2D FCS instruments, such as FCS based on total internal reflection (TIR-FCS^{59–62}) and single plane illumination microscopy (SPIM-FCS^{30–33}), our approach is more versatile. The main limitation of TIR-FCS is its restriction to an investigation of processes at the basal plasma membrane. SPIM-FCS, on the other hand, enables us to visualize the inside of cells and perform measurements there, but it is hampered by an inhomogeneous illumination and is characterized by a relatively larger observation volume ($\sim 1 \times 10^{-15}$ l). Advantages of our approach are optical sectioning, homogeneous illumination and detection, and small confocal volume elements ($\sim 0.35 \times 10^{-15}$ l), which is particularly important since larger observation volume elements average local differences in concentration, mobility, and intermediate surrounding of molecules in a live cell. Thus, the integrated mpFCS/FLIM system uniquely enables us to map with great precision the molecular numbers and mobility via mpFCS and characterize the local environment immediately surrounding fluorescent/fluorescently labeled molecules via FLIM. Instrument performance was stringently assessed in a series of validation experiments using well-characterized samples. Most notably, we have demonstrated that we could measure the concentration and diffusion of eGFP in a dilute aqueous solution ($c_{\text{eGFP}} = 4$ nM, Figure 1D₁–D₃) and showed that it is uniform (Figures S3 and S15). We have also shown that noninteracting molecules smaller than 5 nm, e.g., eGFP, diffuse without significant hindrance through the entire cell (Figures 4 and S15), while molecules/molecular complexes that are larger than 10 nm, such as eGFP_{tet}, largely reside in the cytoplasm where their diffusion is hindered by internal membranes in the cytoplasm (Figures S13 and S15). These findings are in line with experimental findings reported in the literature and with theoretical findings showing that the cytoplasm behaves to a very large extent as a liquid phase for length scales shorter than 100 nm and as a dynamically structured macromolecular matrix for longer length scales.⁶³ They are also important for the validation of our instrument performance.

Importantly, the integrated mpFCS/FLIM system enabled us to characterize in live cells the heterogeneous reaction-

diffusion landscape of transcription factor OLIG2-eGFP and provided important new insights into its intracellular organization. It also enabled us to characterize in great detail the effects of the allosteric inhibitor NSC 50467 on OLIG2-eGFP homodimerization and interactions with chromatin DNA. The possibility to quantitatively characterize in live cells location-specific differences in transcription factor concentration, homodimerization, and DNA binding and the effect of pharmacological agents on these determinants of transcription factor function opens transcription factors to experimental therapeutics. Here, we have shown that the therapeutic compound NSC 50467 targeting OLIG2 homodimerization efficiently abolishes OLIG2-eGFP binding to chromatin DNA. We have also shown that this compound does not affect OLIG2-eGFP levels in the cytoplasm and its distribution in cytoplasmic organelles/membrane-less microdomains. The possibility to perform such detailed, previously intractable measurements may significantly facilitate new therapeutic discoveries.

In conclusion, the methodology presented here is a versatile tool with myriads of applications in biomedical research. In its current realization with 256 (16×16) OVEs, simultaneous sampling in cellular organelles is limited to a handful of locations. This, however, can be improved using another DOE (e.g., (32×32)), as we have previously shown^{35,39}). Also, while we have demonstrated the application of our method for studies in live tissue *ex vivo*,^{35,39} our approach is better suited for studies in cell cultures, where the background from scattered fluorescence is lower than in tissues/small organisms. Despite these limitations, the strength of our approach lies in the user-friendly instrument design and the capacity of our methods to characterize both, compartmentalization of molecular processes, by measuring local excited-state decay via FLIM, and their dynamic integration, by measuring diffusion/active transport using mpFCS. Compartmentalization and dynamic integration of molecular processes are opposed yet coexisting and intertwined principles essential for normal cellular physiology as they enable location-specific processing of information and integral whole-cell response. Our methodology is thus paving the way to better understanding how biological functions emerge from underlying spatially confined chemical processes.

■ ASSOCIATED CONTENT

Supporting Information

The Supporting Information is available free of charge at <https://pubs.acs.org/doi/10.1021/acs.analchem.1c02144>.

S1: Optical setup for mpFCS/FLIM, data analysis, and image rendering; S2: Cell culture and transfection procedures; S3: Determining the apparent dissociation constant of OLIG2-eGFP homodimers; S4: Determining the apparent dissociation constant for OLIG2-eGFP binding to chromatin DNA by FCS; and S5: Standard solutions for mpFCS/FLIM system calibration (PDF)

■ AUTHOR INFORMATION

Corresponding Authors

Rudolf Rigler – Department of Medical Biochemistry and Biophysics (MBB), Karolinska Institutet, 17177 Stockholm, Sweden; Department of Clinical Neuroscience (CNS), Center for Molecular Medicine (CMM), Karolinska Institutet, 17176 Stockholm, Sweden; Email: Rudolf.Rigler@ki.se

Vladana Vukojević – Department of Clinical Neuroscience (CNS), Center for Molecular Medicine (CMM), Karolinska Institutet, 17176 Stockholm, Sweden; orcid.org/0000-0003-0873-5653; Email: Vladana.Vukojevic@ki.se

Authors

Sho Oasa – Department of Clinical Neuroscience (CNS), Center for Molecular Medicine (CMM), Karolinska Institutet, 17176 Stockholm, Sweden; orcid.org/0000-0003-3800-590X

Aleksandar J. Krmpot – Institute of Physics Belgrade, University of Belgrade, 11080 Belgrade, Serbia; Department of Clinical Neuroscience (CNS), Center for Molecular Medicine (CMM), Karolinska Institutet, 17176 Stockholm, Sweden

Stanko N. Nikolić – Institute of Physics Belgrade, University of Belgrade, 11080 Belgrade, Serbia; Department of Clinical Neuroscience (CNS), Center for Molecular Medicine (CMM), Karolinska Institutet, 17176 Stockholm, Sweden

Andrew H. A. Clayton – Optical Sciences Centre, Department of Physics and Astronomy, School of Science, Swinburne University of Technology, Melbourne, Victoria 3122, Australia; orcid.org/0000-0002-6182-3049

Igor F. Tsigelny – Department of Neurosciences, University of California San Diego, La Jolla, California 92093-0819, United States

Jean-Pierre Changeux – Department of Neuroscience, Unité Neurobiologie Intégrative des Systèmes Cholinergiques, Institut Pasteur, F-75724 Paris 15, France

Lars Terenius – Department of Clinical Neuroscience (CNS), Center for Molecular Medicine (CMM), Karolinska Institutet, 17176 Stockholm, Sweden

Complete contact information is available at:

<https://pubs.acs.org/10.1021/acs.analchem.1c02144>

Author Contributions

[†]S.O., A.J.K., and S.N.N. contributed equally. The manuscript was written through the contributions of all authors. All authors have given approval to the final version of the manuscript.

Notes

The authors declare no competing financial interest. Research reported in this publication was supported by the National Institute on Alcohol Abuse and Alcoholism of the National Institutes of Health under Award Number R01AA028549. The content is solely the responsibility of the authors and does not necessarily represent the official views of the National Institutes of Health. The funding agencies had no influence on the study design, methods, data collection, analyses, or the manuscript writing. The authors declare no competing financial interest. All data are available in the main text or the supporting materials.

ACKNOWLEDGMENTS

The authors thank Dr. Hideji Murakoshi, Supportive Center for Brain Research, National Institute for Physiological Sciences, Aichi, Japan, for providing the ShadowY and eGFP-ShadowY expression plasmids. Test compounds were obtained through the National Cancer Institute Chemotherapeutic Agents Repository, Bethesda, MD. Financial support by the Swedish Research Council (2018-05337); Olle Engkvists Foundation (199-0480); Magnus Bergvall Foundation (2019-

03381, 2020-04043); Karolinska Institutet's Research Foundation Grants (2020-02325); Swedish Foundation for Strategic Research (SBE13-0115); NIH/NIAAA (R01AA028549); Nakatani Foundation for Advancement of Measuring Technologies in Biomedical Engineering; Strategic Research Program in Neuroscience (StratNeuro); Yoshida Foundation for Science and Technology; ERASMUS+: European Union Programme for Education, Training, Youth, and Sport; Qatar National Research Foundation (PPM 04-0131-200019); and Science Fund of the Republic of Serbia (call PROMIS, Grant no. 6066079) is gratefully acknowledged.

REFERENCES

- (1) Rivas, G.; Minton, A. P. *Trends Biochem. Sci.* **2016**, *41*, 970–981.
- (2) Baum, M.; Erdel, F.; Wachsmuth, M.; Rippe, K. *Nat. Commun.* **2014**, *5*, No. 4494.
- (3) Helm, C. A.; Knoll, W.; Israelachvili, J. N. *Proc. Natl. Acad. Sci. U.S.A.* **1991**, *88*, 8169–8173.
- (4) Johnson, E. R.; Keinan, S.; Mori-Sánchez, P.; Contreras-García, J.; Cohen, A. J.; Yang, W. *J. Am. Chem. Soc.* **2010**, *132*, 6498–6506.
- (5) Alberti, S.; Gladfelter, A.; Mittag, T. *Cell* **2019**, *176*, 419–434.
- (6) Wheeler, R. J.; Hyman, A. A. *Philos. Trans. R. Soc. B* **2018**, *373*, No. 20170193.
- (7) Hyman, A. A.; Weber, C. A.; Jülicher, F. *Annu. Rev. Cell Dev. Biol.* **2014**, *30*, 39–58.
- (8) Gao, A.; Shrinivas, K.; Lepeudry, P.; Suzuki, H. I.; Sharp, P. A.; Chakraborty, A. K. *Proc. Natl. Acad. Sci. U.S.A.* **2018**, *115*, E11053–E11060.
- (9) Nussinov, R.; Tsai, C. J. *Curr. Pharm. Des.* **2012**, *18*, 1311–1316.
- (10) Amor, B. R.; Schaub, M. T.; Yaliraki, S. N.; Barahona, M. *Nat. Commun.* **2016**, *7*, No. 12477.
- (11) Huang, W.; Nussinov, R.; Zhang, J. *Methods Mol. Biol.* **2017**, *1529*, 439–446.
- (12) Monod, J.; Wyman, J.; Changeux, J. P. *J. Mol. Biol.* **1965**, *12*, 88–118.
- (13) Koshland, D. E., Jr.; Némethy, G.; Filmer, D. *Biochemistry* **1966**, *5*, 365–385.
- (14) Kirschner, K.; Eigen, M.; Bittman, R.; Voigt, B. *Proc. Natl. Acad. Sci. U.S.A.* **1966**, *56*, 1661–1667.
- (15) Gunasekaran, K.; Ma, B.; Nussinov, R. *Proteins* **2004**, *57*, 433–443.
- (16) Cui, Q.; Karplus, M. *Protein Sci.* **2008**, *17*, 1295–1307.
- (17) Bruder, M.; Polo, G.; Trivella, D. B. *Nat. Prod. Rep.* **2020**, *37*, 488–514.
- (18) Tsigelny, I. F.; Mukthavaram, R.; Kouznetsova, V. L.; Chao, Y.; Babic, I.; Nurmammedov, E.; Pastorino, S.; Jiang, P.; Calligaris, D.; Agar, N.; Scadeng, M.; Pingle, S. C.; Wrasidlo, W.; Makale, M. T.; Kesari, S. *Oncotarget* **2017**, *8*, 22370–22384.
- (19) Wodak, S. J.; Paci, E.; Dokholyan, N. V.; Berezovsky, I. N.; Horovitz, A.; Li, J.; Hilser, V. J.; Bahar, I.; Karanicolas, J.; Stock, G.; Hamm, P.; Stote, R. H.; Eberhardt, J.; Chebaro, Y.; Dejaegere, A.; Cecchini, M.; Changeux, J. P.; Bolhuis, P. G.; Vreede, J.; Faccioli, P.; Orioli, S.; Ravasio, R.; Yan, L.; Brito, C.; Wyart, M.; Gkeka, P.; Rivalta, I.; Palermo, G.; McCammon, J. A.; Panecka-Hofman, J.; Wade, R. C.; Di Pizio, A.; Niv, M. Y.; Nussinov, R.; Tsai, C. J.; Jang, H.; Padhorny, D.; Kozakov, D.; McLeish, T. *Structure* **2019**, *27*, 566–578.
- (20) Motlagh, H. N.; Wrabl, J. O.; Li, J.; Hilser, V. J. *Nature* **2014**, *508*, 331–339.
- (21) Oasa, S.; Vukojević, V.; Rigler, R.; Tsigelny, I. F.; Changeux, J. P.; Terenius, L. *Proc. Natl. Acad. Sci. U.S.A.* **2020**, *117*, 2683–2686.
- (22) Rigler, R.; Elson, E. S. *Fluorescence Correlation Spectroscopy. In Theory and Applications*; Springer: Berlin, 2001; Vol. 65.
- (23) Vukojević, V.; Papadopoulos, D. K.; Terenius, L.; Gehring, W. J.; Rigler, R. *Proc. Natl. Acad. Sci. U.S.A.* **2010**, *107*, 4093–4098.
- (24) Mikuni, S.; Pack, C.; Tamura, M.; Kinjo, M. *Exp. Mol. Pathol.* **2007**, *82*, 163–168.
- (25) Ries, J.; Schwille, P. *BioEssays* **2012**, *34*, 361–368.

- (26) Tiwari, M.; Oasa, S.; Yamamoto, J.; Mikuni, S.; Kinjo, M. *Sci. Rep.* **2017**, *7*, No. 4336.
- (27) Kolin, D. L.; Costantino, S.; Wiseman, P. W. *Biophys. J.* **2006**, *90*, 628–639.
- (28) Hendrix, J.; Dekens, T.; Schrimpf, W.; Lamb, D. C. *Biophys. J.* **2016**, *111*, 1785–1796.
- (29) Brown, C. M.; Dalal, R. B.; Hebert, B.; Digman, M. A.; Horwitz, A. R.; Gratton, E. *J. Microsc.* **2008**, *229*, 78–91.
- (30) Wohland, T.; Shi, X.; Sankaran, J.; Stelzer, E. H. *Opt. Express* **2010**, *18*, 10627–10641.
- (31) Ng, X. W.; Teh, C.; Korzh, V.; Wohland, T. *Biophys. J.* **2016**, *111*, 418–429.
- (32) Buchholz, J.; Krieger, J.; Bruschini, C.; Burri, S.; Ardelean, A.; Charbon, E.; Langowski, J. *Biophys. J.* **2018**, *114*, 2455–2464.
- (33) Singh, A. P.; Galland, R.; Finch-Edmondson, M. L.; Greci, G.; Sibarita, J. B.; Studer, V.; Viasnoff, V.; Saunders, T. E. *Biophys. J.* **2017**, *112*, 133–142.
- (34) Vitali, M.; Bronzi, D.; Krmpot, A. J.; Nikolić, S. N.; Schmitt, F.; Junghans, C.; Tisa, S.; Friedrich, T.; Vukojević, V.; Terenius, L.; Zappa, F.; Rigler, R. *IEEE J. Sel. Top. Quantum Electron.* **2014**, *20*, 344–353.
- (35) Krmpot, A. J.; Nikolić, S. N.; Oasa, S.; Papadopoulos, D. K.; Vitali, M.; Oura, M.; Mikuni, S.; Thyberg, P.; Tisa, S.; Kinjo, M.; Nilsson, L.; Terenius, L.; Rigler, R.; Vukojević, V. *Anal. Chem.* **2019**, *91*, 11129–11137.
- (36) Gösch, M.; Serov, A.; Anhut, T.; Lasser, T.; Rochas, A.; Besse, P. A.; Popovic, R. S.; Blom, H.; Rigler, R. *J. Biomed. Opt.* **2004**, *9*, 913–921.
- (37) Scipioni, L.; Di Bona, M.; Vicidomini, G.; Diaspro, A.; Lanzanò, L. *Commun. Biol.* **2018**, *1*, No. 10.
- (38) Buchholz, J. Evaluation of Single Photon Avalanche Diode Arrays for Imaging Fluorescence Correlation Spectroscopy: FPGA-Based Data Readout and Fast Correlation Analysis on CPUs, GPUs and FPGAs. Dissertation, Heidelberg University, 2015.
- (39) Papadopoulos, D. K.; Krmpot, A. J.; Nikolić, S. N.; Krautz, R.; Terenius, L.; Tomancak, P.; Rigler, R.; Gehring, W. J.; Vukojević, V. *Mech. Dev.* **2015**, *138*, 218–225.
- (40) Krmpot, A. J.; Nikolic, S. N.; Vitali, M.; Papadopoulos, D. K.; Oasa, S.; Thyberg, P.; Tisa, S.; Kinjo, M.; Nilsson, L.; Gehring, W. J.; Terenius, L.; Rigler, R.; Vukojevic, V. In *Quantitative Confocal Fluorescence Microscopy of Dynamic Processes by Multifocal Fluorescence Correlation Spectroscopy*, Advanced Microscopy Techniques IV; and Neurophotonics II SPIE Proceedings, Optical Society of America, 2015; p 953600.
- (41) Dennis, D. J.; Han, S.; Schuurmans, C. *Brain Res.* **2019**, *1705*, 48–65.
- (42) Buffo, A.; Vosko, M. R.; Ertürk, D.; Hamann, G. F.; Jucker, M.; Rowitch, D.; Götz, M. *Proc. Natl. Acad. Sci. U.S.A.* **2005**, *102*, 18183–18188.
- (43) Franceschi, E.; Minichillo, S.; Brandes, A. A. *CNS Drugs* **2017**, *31*, 675–684.
- (44) Kosty, J.; Lu, F.; Kupp, R.; Mehta, S.; Lu, Q. R. *Cell Cycle* **2017**, *16*, 1654–1660.
- (45) Edwards, A. L.; Meijer, D. H.; Guerra, R. M.; Molenaar, R. J.; Alberta, J. A.; Bernal, F.; Bird, G. H.; Stiles, C. D.; Walensky, L. D. *ACS Chem. Biol.* **2016**, *11*, 3146–3153.
- (46) Meijer, D. H.; Kane, M. F.; Mehta, S.; Liu, H.; Harrington, E.; Taylor, C. M.; Stiles, C. D.; Rowitch, D. H. *Nat. Rev. Neurosci.* **2012**, *13*, 819–831.
- (47) Sagner, A.; Gaber, Z. B.; Delile, J.; Kong, J. H.; Rousso, D. L.; Pearson, C. A.; Weicksel, S. E.; Melchionda, M.; Mousavy Gharavy, S. N.; Briscoe, J.; Novitch, B. G. *PLoS Biol.* **2018**, *16*, No. e2003127.
- (48) Pepperkok, R.; Squire, A.; Geley, S.; Bastiaens, P. I. *Curr. Biol.* **1999**, *9*, 269–272.
- (49) Sarkisyan, K. S.; Goryashchenko, A. S.; Lidsky, P. V.; Gorbachev, D. A.; Bozhanova, N. G.; Gorokhovatsky, A. Y.; Pereverzeva, A. R.; Ryumina, A. P.; Zherdeva, V. V.; Savitsky, A. P.; Solntsev, K. M.; Bommaris, A. S.; Sharonov, G. V.; Lindquist, J. R.; Drobizhev, M.; Hughes, T. E.; Rebane, A.; Lukyanov, K. A.; Mishin, A. S. *Biophys. J.* **2015**, *109*, 380–389.
- (50) Boens, N.; Qin, W.; Basaric, N.; Hofkens, J.; Ameloot, M.; Pouget, J.; Lefevre, J. P.; Valeur, B.; Gratton, E.; vandeVen, M.; Silva, N. D., Jr.; Engelborghs, Y.; Willaert, K.; Sillen, A.; Rumbles, G.; Phillips, D.; Visser, A. J.; van Hoek, A.; Lakowicz, J. R.; Malak, H.; Gryczynski, I.; Szabo, A. G.; Krajcarski, D. T.; Tamai, N.; Miura, A. *Anal. Chem.* **2007**, *79*, 2137–2149.
- (51) Vallmitjana, A.; Dvornikov, A.; Torrado, B.; Jameson, D. M.; Ranjit, S.; Gratton, E. *Methods Appl. Fluoresc.* **2020**, *8*, No. 035001.
- (52) Clayton, A. H.; Hanley, Q. S.; Verveer, P. J. *J. Microsc.* **2004**, *213*, 1–5.
- (53) Weber, G. *J. Phys. Chem. A* **1981**, *85*, 949–953.
- (54) Dauty, E.; Verkman, A. S. *J. Mol. Recognit.* **2004**, *17*, 441–447.
- (55) Feder, T. J.; Brust-Mascher, I.; Slattery, J. P.; Baird, B.; Webb, W. W. *Biophys. J.* **1996**, *70*, 2767–2773.
- (56) Weiss, M.; Hashimoto, H.; Nilsson, T. *Biophys. J.* **2003**, *84*, 4043–4052.
- (57) Schwille, P.; Hausteiner, E. Fluorescence Correlation Spectroscopy: An Introduction to its Concepts and Applications. <https://pages.jh.edu/~iic/resources/ewExternalFiles/FCS-Schwille.pdf> (accessed May 17, 2019).
- (58) Setoguchi, T.; Kondo, T. *J. Cell Biol.* **2004**, *166*, 963–968.
- (59) Thompson, N. L.; Burghardt, T. P.; Axelrod, D. *Biophys. J.* **1981**, *33*, 435–454.
- (60) Ohsugi, Y.; Kinjo, M. *J. Biomed. Opt.* **2009**, *14*, No. 014030.
- (61) Hassler, K.; Leutenegger, M.; Rigler, P.; Rao, R.; Rigler, R.; Gösch, M.; Lasser, T. *Opt. Express* **2005**, *13*, 7415–7423.
- (62) Veerapathiran, S.; Wohland, T. *Methods* **2018**, *140–141*, 140–150.
- (63) Kwapiszewska, K.; Szczepański, K.; Kalwarczyk, T.; Michalska, B.; Patalas-Krawczyk, P.; Szymański, J.; Andryszewski, T.; Iwan, M.; Duszyński, J.; Hołyst, R. *J. Phys. Chem. Lett.* **2020**, *11*, 6914–6920.



One-step preparation of gold nanoparticles - exfoliated graphene composite by gamma irradiation at low doses for photothermal therapy applications

D.P. Kević^{a,*}, D.N. Kleut^a, Z.M. Marković^a, D.V. Bajuk-Bogdanović^b, V.B. Pavlović^c, A. J. Krmpot^d, M.M. Lekić^d, D.J. Jovanović^a, B.M. Todorović-Marković^a

^a Vinča Institute of Nuclear Sciences - National Institute of the Republic of Serbia, University of Belgrade, P.O.B. 522, 11001 Belgrade, Serbia

^b Faculty of Physical Chemistry, University of Belgrade, Studentski trg 12-16, 11158 Belgrade 118, P.O.B. 47, Serbia

^c Faculty of Agriculture, Department of Agricultural Engineering, University of Belgrade, Nemanjina 6, 11080 Belgrade, Serbia

^d Institute of Physics Belgrade, University of Belgrade, Pregrevica 118, 11080 Belgrade, Serbia

ARTICLE INFO

Keywords:

Electrochemically exfoliated graphene
Gold nanoparticles
Composite nanomaterials
Gamma irradiation
Photothermal therapy
Cancer treatment

ABSTRACT

Graphene is an excellent material to anchor metal nanoparticles due to its large surface area. In this paper, we report the use of electrochemically exfoliated graphene as support to anchor gold nanoparticles (Au NPs). Au NPs are synthesized via the reduction of chloroauric acid under gamma irradiation at low doses of 1, 5, and 10 kGy and directly deposited onto the graphene surface, making this procedure simple and fast. Good water dispersibility of exfoliated graphene, due to the presence of oxygen-containing functional groups in the structure of graphene, provides long-term stability of Au NPs - graphene composite dispersions. The majority of the Au NPs obtained by this method have sizes of up to 40 nm, while the increase in the applied dose leads to an increase in the amount of smaller nanoparticles. The increase of temperature of the prepared composite material upon irradiation with an 808 nm continuous wave laser was monitored. All samples show a temperature increase between 21.5 and 25.6 °C for 10 min of the laser exposure, which indicates that Au NPs - graphene composite can effectively be used in photothermal treatment for cancer therapy.

1. Introduction

The unique structure of graphene put this material in the focus of scientific interest in the past years. Its fascinating electrical, mechanical, thermal, and optical properties are thoroughly investigated for the potential application in electronics as the new-generation electronic devices [1,2], sensors [3,4], and energy storage devices [5,6], as well as in biomedicine for bioimaging [7], drug delivery [8,9], and photothermal therapy [10], to name some. However, a major challenge in the processing of graphene lies in its poor dispersibility in water and other commonly used solvents. This issue can be solved by covalently modifying graphene's chemical structure by strong oxidants to introduce polar functional groups and make it water dispersible. The procedure generally involves the use of strong oxidants in acidic environments and elevated temperatures. As obtained material, denoted as graphene oxide (GO), is rich in oxygen-containing functional groups, but graphene sp² honeycomb structure becomes highly disrupted which negatively affects its performance. An additional step is required to reduce graphene oxide, but the structure becomes only partially restored leaving a large

number of structural defects. A good alternative is electrochemical exfoliation of graphite [11,12], which reduces the oxidation degree of graphene and preserves its structural and electronic properties. Briefly, hydroxyl ions created from the reduction of water during electrochemical process bind to graphene edges and weaken van der Waals forces in graphite allowing the intercalation of electrolyte ions between graphene layers. In the next step, the reduction of intercalated ions and expansion of gas bubbles occur and graphene layers become detached. Since hydroxyl ions covalently bond graphene sheet only in the initial stage of the exfoliation, graphene structure is well preserved but with a sufficient number of attached polar groups to make graphene water dispersible. Following this approach, it is possible to obtain a high-yield of single- and few-layer graphene with large flake size. Compared to well-established methods for the production of graphene oxide, electrochemical exfoliation of graphite does not require harsh chemicals, making the procedure cost-efficient and environmentally friendly.

The large surface area of graphene could be easily used for the adsorption of various molecules and nanoparticles (NPs), creating graphene-based composites and hybrid materials [13,14]. Of particular

* Corresponding author.

E-mail address: d.kepic@vin.bg.ac.rs (D.P. Kević).

<https://doi.org/10.1016/j.matchar.2021.110944>

Received 4 December 2020; Received in revised form 1 February 2021; Accepted 1 February 2021

Available online 4 February 2021

1044-5803/© 2021 Elsevier Inc. All rights reserved.

interest are metal nanoparticles, which have mechanical, thermal, optical, and magnetic properties different from their bulk counterparts due to the effects that emerge from their size. Currently, various synthetic strategies are being developed for their production and a majority of them imply the reduction of metal ions to their zero-valent state. To prevent agglomeration and overgrowth of a freshly formed NPs, a stabilizing agent is introduced to the reaction mixture during synthesis. The role of the agent usually has sodium citrate, which deactivates the surface of formed nanoparticles, and polymers such as polyvinyl pyrrolidone (PVP) [15,16] or cetyltrimethylammonium bromide (CTAB) [17,18], which acts as a capping agent and anchors metal nanoparticles on its surface. Graphene oxide was used as a support for the synthesis of Ir NPs [19], as well as Pt–Ru NPs for the electro-oxidation of methanol and ethanol [20] and Au NPs for glucose biosensor [21,22] and for the development of surface-enhanced Raman spectroscopy (SERS) platforms [23]. Additionally, metal NPs have great potential to be applied in photothermal therapy for cancer treatment [24–26]. Photothermal therapy has emerged as a promising strategy for cancer treatment due to the selective hyperthermia of tumor tissue. The strategy involves selective delivery of various nanoparticles into tumor tissue and the irradiation of the tissue with wavelengths that correspond to the near-infrared or therapeutic window. The electrons in the conduction band tend to oscillate under the irradiation and the absorbed light is converted into heat, which further leads to the irreversible damage of the tumor tissue. Among different nanoparticles that can be implemented in this strategy, gold nanoparticles are of particular interest because they absorb light in the near-infrared region and their optical properties can be easily tuned by varying their dimensions and structure [27,28].

Compared to classical chemical approach, gamma irradiation provides fast and clean route to perform reduction reactions at room temperature. To date, various metal nanoparticles were synthesized following this method. Wang et al. prepared Ag NPs - reduced graphene oxide (RGO) hybrids at doses of 50 and 160 kGy [29]. RGO was used as a support for Pt–Au nanocomposite prepared a dose of 150 kGy [30], and Ag–Au alloy nanoparticles at doses in a range from 29 to 115 kGy [31]. Ag NPs - GO nanocomposite was prepared by Zhao et al. at a dose of 150 kGy [32]. Beside GO and RGO, there is no report in the literature of the use of electrochemically exfoliated graphene as a support for the synthesis of metal nanoparticles under gamma irradiation.

In this work, for the first time electrochemically exfoliated graphene was used as a support to anchor Au nanoparticles. Au NPs were synthesized in one step by means of gamma irradiation at low doses (1–10 kGy) from chloroauric acid as a precursor in graphene dispersion in the absence of any stabilizing agents. The absence of reductants and polymers as stabilizing molecules preserves the chemical environment of metal NPs and consequently their performance, which makes this procedure simple and fast. The morphology of the obtained composite material was thoroughly investigated and the size distribution of the synthesized Au NPs was determined. The temperature elevation under an 808 nm laser irradiation of the Au NPs - exfoliated graphene was measured and the potential of this composite material for photothermal therapy is demonstrated.

2. Experimental procedure

2.1. Sample preparation

Electrochemical exfoliation of highly oriented pyrolytic graphite (HOPG, Vinča Institute of Nuclear Sciences, Serbia) was performed in a two-electrode system using graphite rods as both the counter and the working electrode, with the constant distance of 4 cm between the electrodes. The electrolyte solution was prepared by dissolving ammonium persulfate (Alfa Aesar) in water to obtain a concentration of 0.1 M. Direct current (DC) voltage of +12 V was applied, and the voltage was kept constant until the exfoliation process was completed (indicated by the total consumption of the working electrode). Exfoliated product was

collected by vacuum filtration and washed with a copious amount of deionized water to remove any residual salt. After washing, the product was dispersed in water using an ultrasound bath. To remove graphitic residuals, the dispersion was centrifuged at $2575 \times g$, and supernatant was used for further procedure. Gravimetrically determined graphene concentration in the dispersion was 1 mg/ml. In a certain volume of graphene dispersion was added chloroauric acid (Sigma Aldrich) to obtain final concentration of 1.25×10^{-4} M and isopropyl alcohol (1:10 volume ratio), and the mixture was purged with argon for 15 min to remove dissolved oxygen. After that, the vials are hermetically sealed and irradiated. Irradiations were carried out by gamma-ray flux from ^{60}Co nuclide at a radiation dose rate of 10.5 kGy/h. Samples were exposed to the gamma irradiation source absorbing the doses of 1, 5, and 10 kGy. Irradiation treatment was followed by filtration (0.2 μm pore size, Isopore Membrane Filters), after which the samples were washed with deionized water, and dried at 60 °C.

2.2. Sample characterization

Transmission electron microscopy (TEM) analyses were performed on TEM-JEOL JEM-1400 microscope operated at accelerating voltage of 120 kV. All samples for TEM were dispersed in ethanol and a drop of dispersion was deposited on lacey carbon copper grids (200 mesh). The particle size distribution was determined using Gwyddion software (version 2.44).

Atomic force microscopy (AFM) measurements were performed on Quesant microscope operating in tapping mode in air at room temperature. 50 μl of sample was dispersed in 300 μl of water and well homogenized on an ultrasound bath. A drop of dispersion was drop-casted on Si substrate and imaged after drying. Silicon tips (purchased from Nano and More) with constant force of 40 N/m were used. AFM images were analyzed using Gwyddion software (version 2.44).

The UV–vis absorption spectra were measured using Avantes UV–vis spectrophotometer (Apeldoorn, The Netherlands). Samples were recorded in quartz cuvettes at room temperature.

Raman spectra were recorded by confocal Raman microscope (alpha 300 R+, WiTec, Ulm, Germany). The excitation laser of the 532 nm wavelength and 76 μW power was focused using $100 \times$ (NA = 0.9) objective onto the sample surface. The confocal pinhole diameter was 50 μm and the accumulation time for a single Raman spectrum was set to 40 s. Constant background was subtracted from all measured Raman spectra.

Fourier transform infrared spectroscopy (FTIR) spectra were acquired on Avatar 370 Thermo Nicolet spectrometer. The spectral resolution was 4 cm^{-1} . Samples were recorded in a form of KBr pellets.

XPS was performed using a Thermo Scientific K-Alpha XPS system (Thermo Fisher Scientific, UK) equipped with a micro-focused, monochromatic Al K α X-ray source (1486.6 eV). An X-ray beam of 400 μm in size was used at 6 mA \times 12 kV. The spectra were acquired in the constant analyzer energy mode with pass energy of 200 eV for the survey. Narrow regions were collected with pass energy of 50 eV. Charge compensation was achieved with the system flood gun that provides low energy electrons (~ 0 eV) and low energy argon ions (20 eV) from a single source. Thermo Scientific Advantage software, version 5.952 (Thermo Fisher Scientific), was used for the digital acquisition and data processing. Spectral calibration was determined by using the automated calibration routine and the internal Au, Ag and Cu standards supplied with the K-Alpha system.

For the photothermal efficiency measurements, stable dispersions of the samples in water with concentration of 1 mg/ml were prepared. Irradiation was conducted in quartz cuvettes at room temperature (20.3 °C). The samples were exposed to 808 nm continuous wave laser radiation with TEM00 mode radial distribution, slightly elliptical, with major and minor axes of 7.14 mm and 6.35 mm, respectively. The total laser irradiance was 2.16 W/cm^2 . The temperature was monitored by a thermocouple (accuracy 0.1 °C) every 30 s. After 10 min of laser

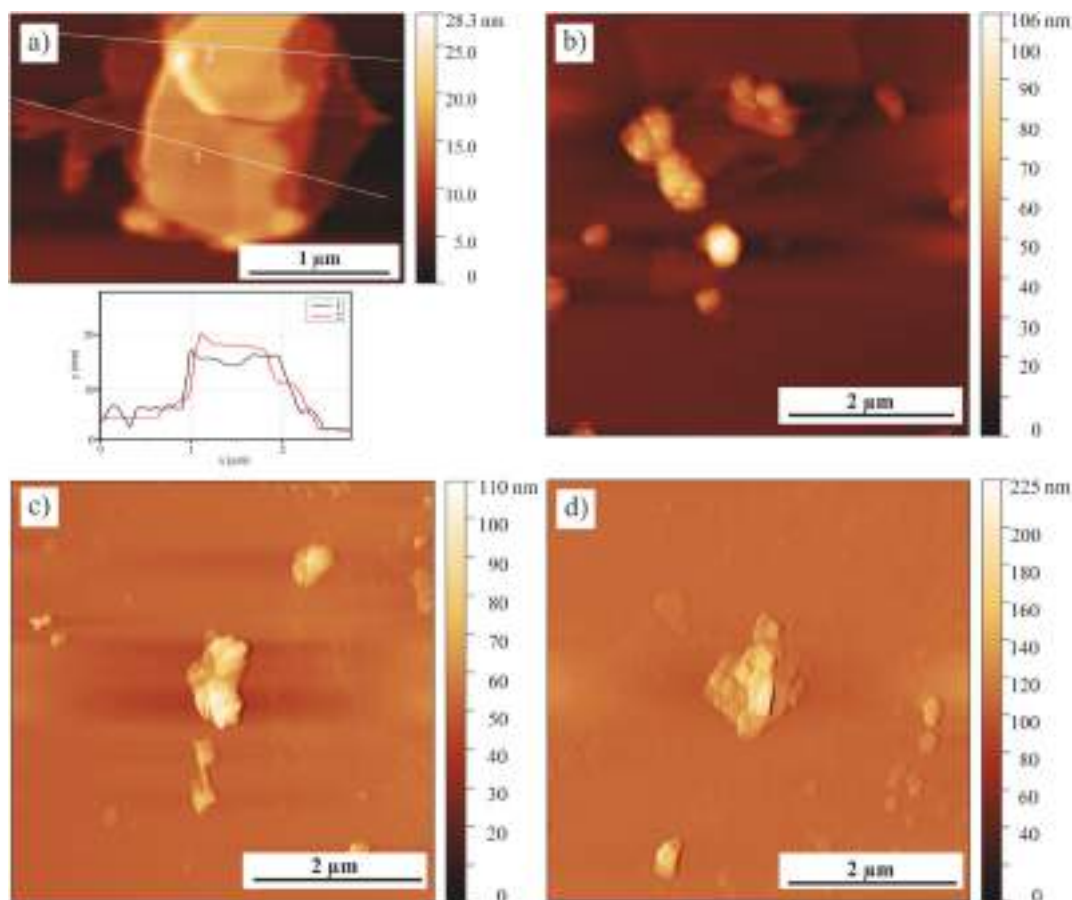


Fig. 1. Top view AFM images of (a) Au NPs - exfoliated graphene irradiated at 1 kGy and the corresponding height profiles (1 and 2) as indicated in the AFM image, (b) Au NPs - exfoliated graphene irradiated at 1 kGy, (c) Au NPs - exfoliated graphene irradiated at 5 kGy and (d) Au NPs - exfoliated graphene irradiated at 10 kGy.

irradiation laser was switched off and the temperature was monitored for the next 15 min. The photothermal efficiency (η) of the samples was calculated using Roper's method [33,34] according to the equation:

$$\eta = \frac{hS(T_{max} - T_{amb}) - Q_{loss}}{I(1 - 10^{-A_{808}})} \quad (1)$$

where h is the heat transfer coefficient, S the surface area of the cuvette, and T_{max} and T_{amb} are the maximum and the ambient temperature, respectively. I represents the laser power, A_{808} the absorbance of the samples at 808 nm, and Q_{loss} is the heat dissipated from the light absorbed by the solvent and the cuvette. The value hS was calculated according to the equation:

$$hS = \frac{\sum_i m_i C_{pi}}{\tau_s} \quad (2)$$

where m_i and C_{pi} are the mass and the specific heat capacity of each component of the system, respectively. τ_s is the time constant that was calculated from Fig. 8b using the equations:

$$\theta = \frac{T - T_{amb}}{T_{max} - T_{amb}} \quad (3)$$

and

$$t = -\tau_s \ln(\theta) \quad (4)$$

3. Results and discussion

3.1. Au NPs synthesis

Radiolysis of water induced by gamma irradiation generates both reductive and oxidative species [35]. In the presence of oxidation species scavenger, such as isopropyl alcohol, reactive species produced by water radiolysis generate isopropyl radical that is, among other generated reducing species, capable of reducing metal ions to metal in zero-valent state. The reduction of $[\text{AuCl}_4]^-$ forms Au^0 which combination further creates particle nuclei and leads to particle growth. The presence of a stabilizing agent such as polymers or surfactants plays an important role in the overall formation of nanoparticles. Functional groups from those molecules serve as anchoring sites for NPs nuclei. After the synthesis, it is often necessary to remove the stabilizing agent for the maximum performance of obtained NPs. Exfoliated graphene has a large surface area and a large number of functional groups that can anchor Au NPs nuclei and influence particle formation. The unique 2D structure of graphene can be effectively decorated with Au NPs to create novel composite material with good water dispersibility, making the removing step of the stabilizing agent redundant.

3.2. Morphology analyses

Morphology analyses were conducted by AFM and TEM. Fig. 1 shows representative AFM images of Au NPs - exfoliated graphene composite indicating that exfoliated graphene is mainly presented in a form of few-layer graphene. Statistical analysis based on AFM images shows that lateral sizes of exfoliated graphene flakes are in the range of several hundreds of nanometers up to several micrometers, without any

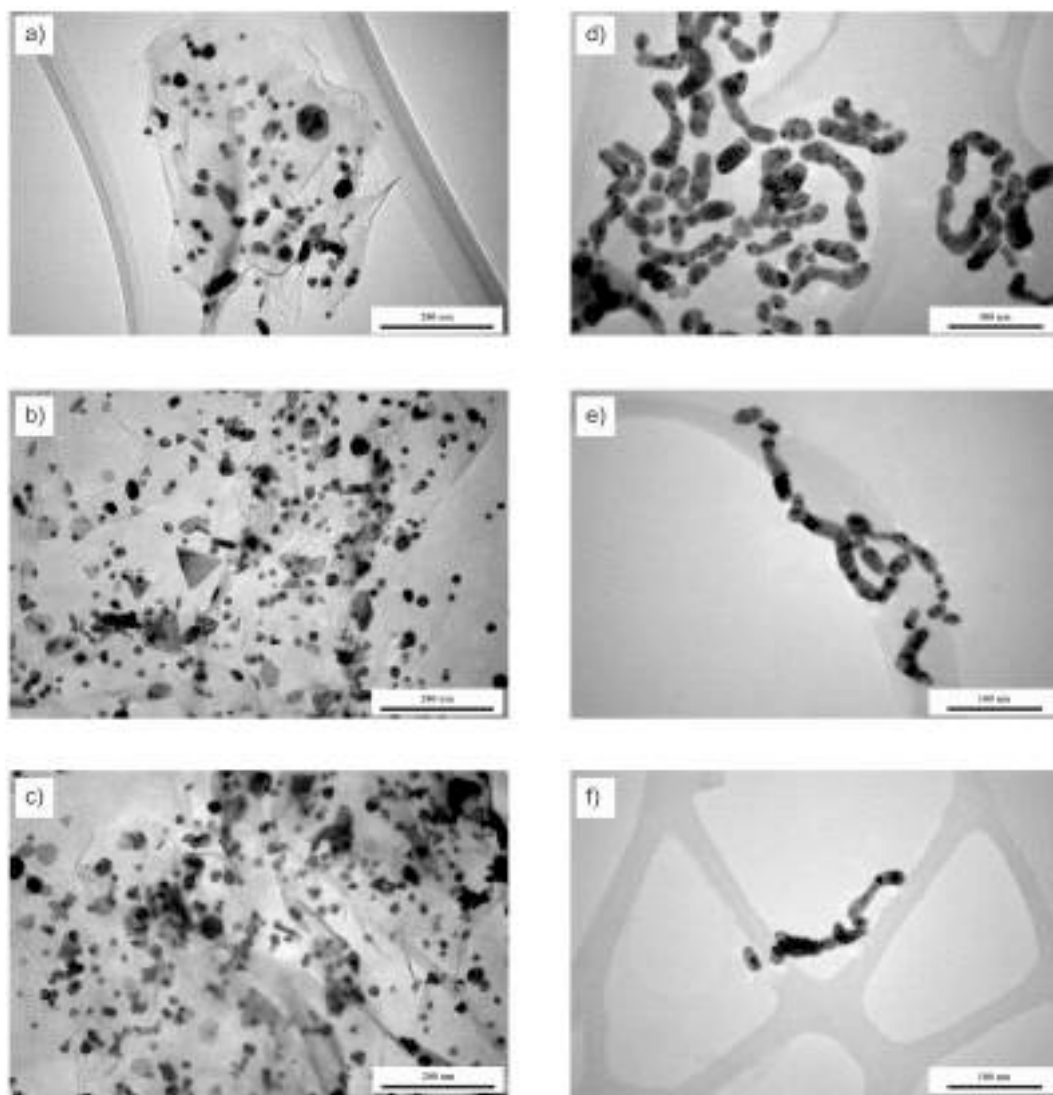


Fig. 2. TEM images of (a) Au NPs - exfoliated graphene irradiated at 1 kGy, (b) Au NPs - exfoliated graphene irradiated at 5 kGy, (c) Au NPs - exfoliated graphene irradiated at 10 kGy (d) Au NPs irradiated at 1 kGy, (e) Au NPs irradiated at 5 kGy and (f) Au NPs irradiated at 10 kGy.

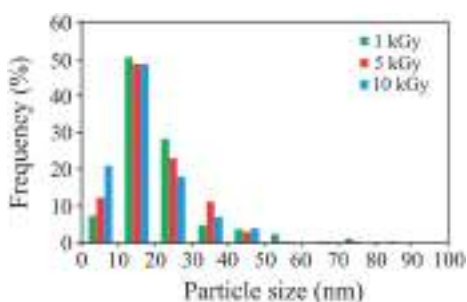


Fig. 3. Particle size distribution of Au NPs irradiated in the presence of graphene.

significant deviation caused by gamma irradiation at the applied doses.

TEM images of Au NPs - exfoliated graphene composites are presented in Fig. 2. As can be seen from the images, for the applied doses of 1, 5, and 10 kGy Au NPs are well distributed on the graphene surface. Also, for all the aforementioned doses gold nanoparticles of spherical, triangular, hexagonal, trapezoidal, and rod-shaped morphology are observed. A variety of Au NPs morphologies attached to the graphene

sheet was previously reported and is related to the presence and the abundance of functional groups and defects on graphene layers [36]. To investigate this issue, we irradiated chloroauric acid at the same conditions in the absence of graphene and analyzed the morphology of obtained NPs. The reduction of chloroauric acid under gamma irradiation takes place, but the final result are irregularly shaped gold nanowires and, to a smaller extent, irregularly shaped gold nanospheres. Interestingly, similar Au formations were found as a product of quenched citrate reduction of chloroauric acid [37].

Gamma irradiation is found to be an efficient synthetic route for metal NPs because of the possibility to control the nanoparticles' sizes and size distribution by controlling the radiation dose [38]. According to the statistical analysis, nearly half of the prepared Au NPs have sizes in the 11–20 nm range for all the applied doses (Fig. 3). It is worth noting that the increase in the applied dose leads to the increase in the amount of smaller nanoparticles (up to 10 nm in size). The formation of Au NPs is composed of two consecutive steps - nucleation and aggregation. At low doses the concentration of formed nuclei is smaller than the concentration of the Au ions that participate in the growth step, therefore the synthesized Au NPs are larger in size. On the other hand, at the higher applied doses most of the Au precursor is consumed to form nuclei which concentration becomes larger than the concentration of

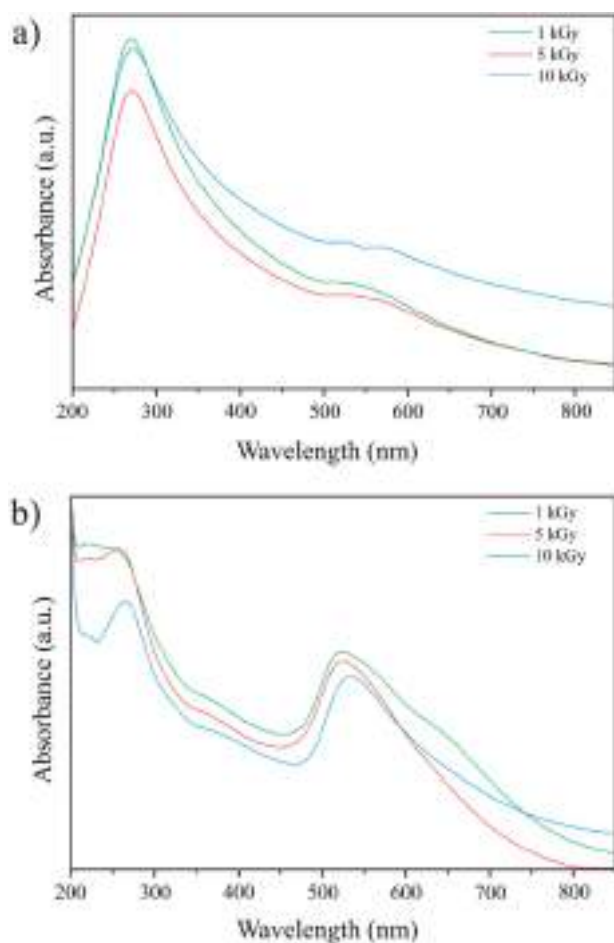


Fig. 4. UV-vis spectra of (a) Au NPs - exfoliated graphene and (b) Au NPs irradiated at different doses.

unreduced Au ions, which consequently leads to the growth of smaller NPs [39].

3.3. Spectroscopy analyses

While UV-vis spectrum of graphene oxide is dominated by the peak at 230 nm, originating from $\pi-\pi^*$ transition of aromatic C=C bonds, and a shoulder at ~ 300 nm attributed to $n-\pi^*$ transition of C=O bonds [40], exfoliated graphene displays only one broad peak at 270 nm [41]. The red shift of $\pi-\pi^*$ transition peak to the values of 270 nm is already documented and it is attributed to the restoration of graphene's electronic conjugation upon hydrazine reduction [42]. The peak at 270 nm for exfoliated graphene, along with the absence of a 300 nm shoulder peak, indicates that in the exfoliated graphene the graphene's structure is well preserved. UV-vis spectra of Au NPs - exfoliated graphene composite (Fig. 4a) show one large intensity peak at 270 nm and a smaller broad peak at 530 nm. The peak at 530 nm originates from the localized surface plasmon resonance of Au NPs. In the UV-vis spectra of Au NPs synthesized without graphene (Fig. 4b) this peak shows a slight red shift with the increase of the radiation dose. Interestingly, the same spectra show a peak at 261 nm from the electron transition from the occupied d-level states to empty states in the conducting band above the Fermi level [36] and is more prominent for the higher applied doses. In the spectra of Au NPs - exfoliated graphene composites this peak overlaps $\pi-\pi^*$ transition peak from graphene.

Reactive species produced by water radiolysis induce also the reduction of graphene materials [43]. Prepared exfoliated graphene dispersion in a concentration of 1 mg/ml shows long-term stability in

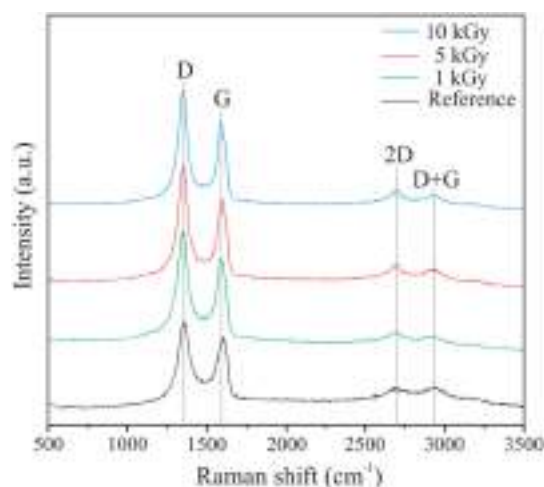


Fig. 5. Raman spectra of exfoliated graphene (reference) and Au NPs - exfoliated graphene irradiated at different doses.

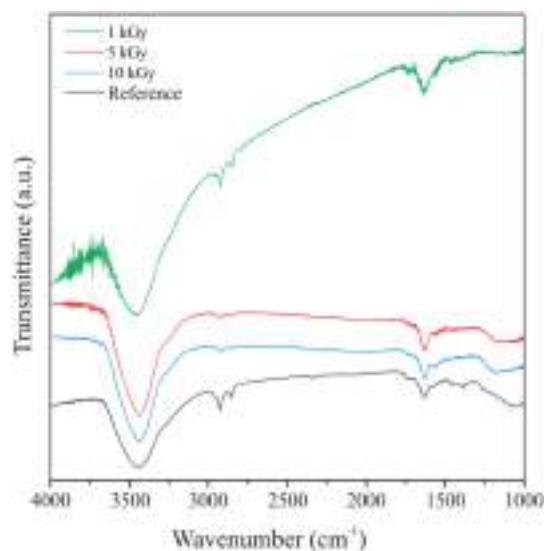


Fig. 6. FTIR spectra of exfoliated graphene (reference) and Au NPs - exfoliated graphene irradiated at different doses.

water. Good graphene dispersibility in a polar solvent is due to the presence of polar oxygen-containing functional groups attached to the graphene surface, such as hydroxyl, carboxyl, epoxy, and carbonyl. The changes in graphene structure upon irradiation were investigated by means of FTIR, XPS, and Raman spectroscopy. Two dominant peaks in Raman spectra of Au NPs - graphene composite are located at 1351 cm^{-1} and 1591 cm^{-1} and are attributed to D and G band respectively (Fig. 5). The D band is attributed to disordered sp^3 -hybridized carbon material from defects and functionalities, while the G band is related to well-ordered sp^2 graphite-type structures [44]. Besides, peaks at 2695 cm^{-1} and 2938 cm^{-1} are also observable and can be attributed to 2D band and (D + G) combination mode. For all the applied doses Raman peaks do not show any shift. The intensity ratio of D and G bands (I_D/I_G) gradually increases with the increase of the irradiation dose from 1.14 for non-irradiated graphene to 1.30 for Au NPs - graphene composite irradiated at 10 kGy. This could be the consequence of Au NPs bonding to the graphene sheets.

To get a better insight into the type of functional groups attached to the graphene structure, FTIR spectroscopy was performed (Fig. 6). The most prominent bands in FTIR spectra correspond to the stretching and

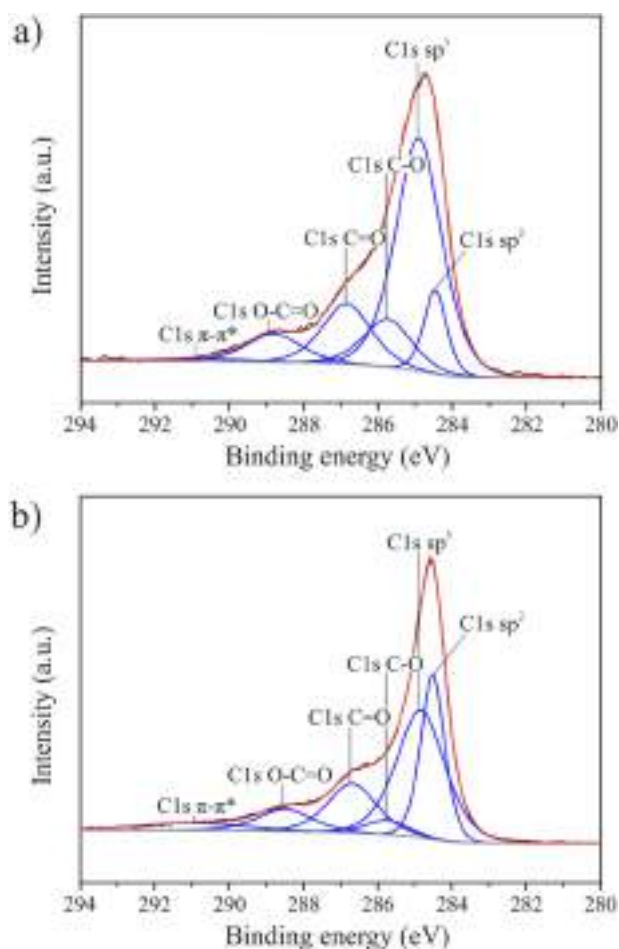


Fig. 7. XPS spectra of (a) non-irradiated graphene and (b) graphene irradiated at 10 kGy.

Table 1

XPS data of the characteristic bonds from deconvoluted C1s peak.

Name	Binding energy (eV)	Exfoliated graphene (at. %)	Graphene irradiated at 10 kGy (at.%)
C1s sp ²	284.5	9.7	26.0
C1s sp ³	284.9	54.4	41.1
C1s C-O	258.7	11.8	4.0
C1s C=O	286.8	14.9	16.0
C1s O-C=O	288.6	7.8	7.9
C1s π-π*	291.0	1.4	5.0

bending mode of hydroxyl groups (3400–3500 cm⁻¹ and ~ 1633 cm⁻¹, respectively) [45]. Bands at 2930 and 2850 cm⁻¹ indicate the presence of CH₂ groups. In addition, in the FTIR spectra of exfoliated graphene bands at ~1734 cm⁻¹ (C=O groups), ~1574 cm⁻¹ (C=C groups) and ~1177 cm⁻¹ (C-O groups) can also be observed. As the irradiation dose increases, the band at ~1574 cm⁻¹ becomes more prominent, while the bands in the range 2930–2850 cm⁻¹ show a decrease, which implies the partial restoration of graphene structure.

The restoration of the graphene structure is further confirmed by means of XPS. Deconvoluted high-resolution XPS spectra of C1s peak of as-prepared exfoliated graphene and graphene irradiated at the dose of 10 kGy are shown in Fig. 7 and the data for the characteristic bonds are listed in Table 1. The deconvolution of C1s XPS spectra gives features at 284.5, 284.9, 258.7, 286.8, 288.6, and 291.0 eV which reveal the presence of sp² and sp³ carbon, hydroxyl/epoxy groups, carbonyl, and carboxyl groups, and π-π* shake up band [46,47]. From the XPS data, it

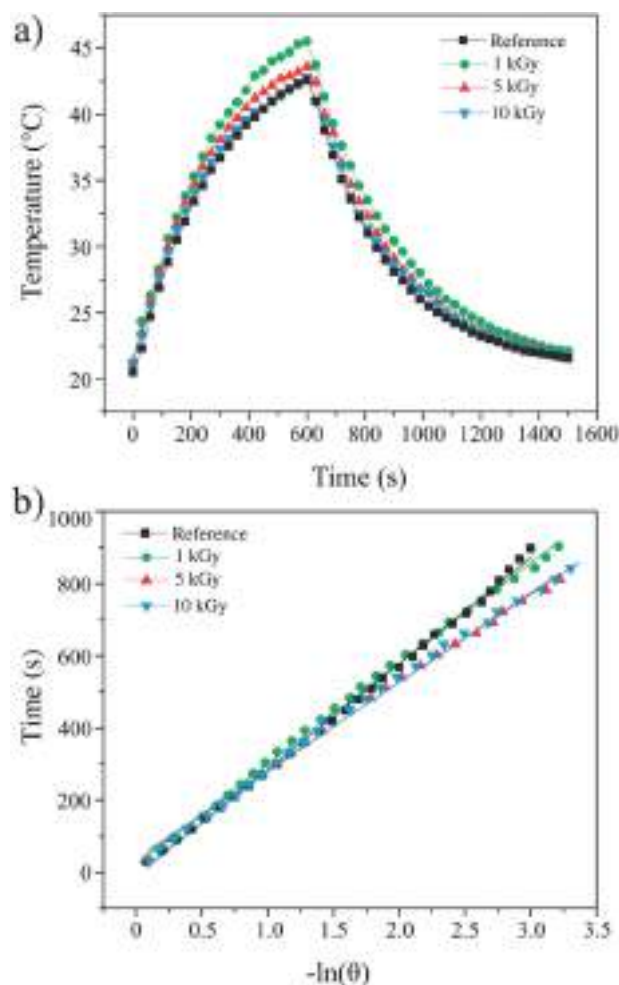


Fig. 8. (a) Temperature profiles of exfoliated graphene (reference) and Au NPs - exfoliated graphene composites under 808 nm continuous wave laser excitation and (b) linear fitting of time data versus $-\ln(\theta)$ acquired from the cooling period.

is evident the increase of the carbon sp² content after the irradiation. Simultaneously, the carbon sp³ content decreases, along with the content of C-O bonds. The irradiation induces the change in C/O ratio from 1.8 for non-irradiated graphene to 3.5 for graphene irradiated at 10 kGy.

3.4. Photothermal efficiency measurements

For the photothermal efficiency measurements, the prepared Au NPs - exfoliated graphene composites were irradiated with an 808 nm continuous wave laser and the temperature elevation was monitored for 10 min. After that time the laser was switched off and the temperature was monitored during the cooling period (15 min). The results of these measurements are presented in Fig. 8a.

For successful photothermal therapy, it is important to heat the tumor tissue at a minimum of 41 °C, which corresponds to the 4 °C temperature increase in the body [48]. Nanomaterials that are able to convert the absorbed light into heat and cause a temperature increase of a minimum of 4 degrees are considered suitable for photothermal therapy. As expected, the irradiation of pure medium (water) does not induce the temperature increase. On the other hand, the irradiation of exfoliated graphene, as well as Au NPs - exfoliated graphene composites, induce the temperature increase. The highest temperature elevation of 25.6 °C is observed for Au NPs - graphene irradiated at 1 kGy. With the increase of the irradiation dose, a slight decrease in the temperature elevation could be observed. To determine the photothermal efficiency

Table 2

Calculated photothermal efficiency of exfoliated graphene (reference) and Au NPs - exfoliated graphene composites irradiated at different doses.

Sample	Time constant τ_s	Absorbance at 808 nm	Photothermal efficiency (η)
Reference	293.77	0.13	58.26%
1 kGy	246.99	0.13	73.55%
5 kGy	278.66	0.12	72.16%
10 kGy	243.70	0.12	70.96%

of the samples, the temperature decrease was monitored with the laser switched off. The values of τ_s were calculated from Fig. 8b using eqs. (3) and (4). Taking into account the values of hS obtained from the eq. (2), laser incident power of 0.77 W, and the absorbances at 808 nm, photothermal efficiency (η) was calculated from the eq. (1) and listed in Table 2. As expected, the highest value of photothermal efficiency of 73.55% has Au NPs - graphene composite irradiated at 1 kGy, while the increase in the irradiation dose slightly decreases the photothermal efficiency of the material. These measurements demonstrate the efficient photothermal conversion of the incident laser light of Au NPs - graphene composites that have the potential to be used in photothermal treatment in cancer therapy.

4. Conclusion

In this paper, one-step synthesis of graphene supported Au NPs via gamma irradiation at low doses is demonstrated. Graphene, prepared by the electrochemical exfoliation of highly ordered pyrolytic graphite, is presented as few-layer graphene with lateral sizes that range from several hundred nanometers up to several micrometers. Au NPs were synthesized from chloroauric acid as a precursor in graphene dispersion in the absence of any stabilizing agents at doses of 1, 5, and 10 kGy. Polar oxygen-containing functional groups at the graphene surface provide good water dispersibility of Au NPs - graphene composites. Nearly half of the prepared Au NPs have sizes in the range from 11 to 20 nm, and the increase in the applied dose leads to an increase in the amount of smaller nanoparticles (up to 10 nm in size). For all the applied doses particles of spherical, triangular, hexagonal, trapezoidal, and rod-shaped morphology are observed. The prepared composite material shows the increase of temperature upon irradiation with an 808 nm continuous wave laser, which is the most prominent for Au NPs - graphene irradiated at 1 kGy. Consequently, the same sample shows the highest photothermal efficiency. Observed temperature elevation under laser irradiation can effectively be used in photothermal treatment for cancer therapy.

Declaration of Competing Interest

The authors declare that they have no known competing financial interests or personal relationships that could have appeared to influence the work reported in this paper.

Acknowledgements

The research was supported by the Ministry of Education, Science and Technological Development of the Republic of Serbia [451-03-2/2020-14/20] and by the Science Fund of the Republic of Serbia, PROMIS, [Grant No. 6066079, HEMMAGINERO]. D. Kepić acknowledges the COST Action CA15107 Multicomp, supported by the COST Association (European Cooperation in Science and Technology). A. Krmpot and M. Lekić acknowledge funding provided by the Institute of Physics Belgrade, through the grant by the Ministry of Education, Science and Technological Development of the Republic of Serbia.

References

- [1] J. Yang, P. Hu, G. Yu, Perspective of graphene-based electronic devices: Graphene synthesis and diverse applications, *APL Mater.* 7 (2019), 020901.
- [2] T.-H. Han, H. Kim, S.-J. Kwon, T.-W. Lee, Graphene-based flexible electronic devices, *Mater. Sci. Eng. R. Rep.* 118 (2017) 1–43.
- [3] T. Yang, X. Zhao, Y. He, H. Zhu, 6 - graphene-based sensors, in: H. Zhu, Z. Xu, D. Xie, Y. Fang (Eds.), *Graphene*, Academic Press, 2018, pp. 157–174.
- [4] J. Peña-Bahamonde, H.N. Nguyen, S.K. Fanourakis, D.F. Rodrigues, Recent advances in graphene-based biosensor technology with applications in life sciences, *J. Nanobiotechnol.* 16 (2018) 75.
- [5] L. Bai, Y. Zhang, W. Tong, L. Sun, H. Huang, Q. An, N. Tian, P.K. Chu, Graphene for energy storage and conversion: synthesis and interdisciplinary applications, *Electrochem. Energy Rev.* 3 (2019) 395–430.
- [6] M. Pumera, Graphene-based nanomaterials for energy storage, *Energy Environ. Sci.* 4 (2011) 668–674.
- [7] C. Wang, J. Li, C. Amatore, Y. Chen, H. Jiang, X.-M. Wang, Gold nanoclusters and graphene nanocomposites for drug delivery and imaging of cancer cells, *Angew. Chem. Int. Ed.* 50 (2011) 11644–11648.
- [8] L. Zhang, J. Xia, Q. Zhao, L. Liu, Z. Zhang, Functional graphene oxide as a nanocarrier for controlled loading and targeted delivery of mixed anticancer drugs, *Small* 6 (2010) 537–544.
- [9] Z. Liu, J.T. Robinson, X. Sun, H. Dai, PEGylated nanographene oxide for delivery of water-insoluble cancer drugs, *J. Am. Chem. Soc.* 130 (2008) 10876–10877.
- [10] K. Yang, S. Zhang, G. Zhang, X. Sun, S.-T. Lee, Z. Liu, Graphene in mice: ultrahigh in vivo tumor uptake and efficient photothermal therapy, *Nano Lett.* 10 (2010) 3318–3323.
- [11] K. Parvez, Z.-S. Wu, R. Li, X. Liu, R. Graf, X. Feng, K. Müllen, Exfoliation of graphite into graphene in aqueous solutions of inorganic salts, *J. Am. Chem. Soc.* 136 (2014) 6083–6091.
- [12] K. Parvez, R. Li, S.R. Puniredd, Y. Hernandez, F. Hinkel, S. Wang, X. Feng, K. Müllen, Electrochemically exfoliated graphene as solution-processable, highly conductive electrodes for organic electronics, *ACS Nano* 7 (2013) 3598–3606.
- [13] V.B. Mohan, K.-t. Lau, D. Hui, D. Bhattacharyya, Graphene-based materials and their composites: a review on production, applications and product limitations, *Compos. Part B* 142 (2018) 200–220.
- [14] Y. Ioni, E. Buslaeva, S. Gubin, Synthesis of graphene with noble metals nanoparticles on its surface, *Mater. Today: Proc.* 3 (2016) S209–S213.
- [15] M.M. Chilli, V.S.R.R. Pullabhotla, N. Revaprasadu, Synthesis of PVP capped gold nanoparticles by the UV-irradiation technique, *Mater. Lett.* 65 (2011) 2844–2847.
- [16] S.K. Seol, D. Kim, S. Jung, W.S. Chang, Y.M. Bae, K.H. Lee, Y. Hwu, Effect of citrate on poly(vinyl pyrrolidone)-stabilized gold nanoparticles formed by PVP reduction in microwave (MW) synthesis, *Mater. Chem. Phys.* 137 (2012) 135–139.
- [17] K. Okitsu, Y. Nunota, One-pot synthesis of gold nanorods via autocatalytic growth of sonochemically formed gold seeds: the effect of irradiation time on the formation of seeds and nanorods, *Ultrason. Sonochem.* 21 (2014) 1928–1932.
- [18] J. Lai, L. Zhang, W. Niu, W. Qi, J. Zhao, Z. Liu, W. Zhang, G. Xu, One-pot synthesis of gold nanorods using binary surfactant systems with improved monodispersity, dimensional tunability and plasmon resonance scattering properties, *Nanotechnology* 25 (2014) 125601.
- [19] J.V. Rojas, M.C. Molina Higgins, M. Toro Gonzalez, C.E. Castano, Single step radiolytic synthesis of iridium nanoparticles onto graphene oxide, *Appl. Surf. Sci.* 357 (2015) 2087–2093.
- [20] L. Dong, R.R.S. Gari, Z. Li, M.M. Craig, S. Hou, Graphene-supported platinum and platinum-ruthenium nanoparticles with high electrocatalytic activity for methanol and ethanol oxidation, *Carbon* 48 (2010) 781–787.
- [21] L. Cao, P. Wang, L. Chen, Y. Wu, J. Di, A photoelectrochemical glucose sensor based on gold nanoparticles as a mimic enzyme of glucose oxidase, *RSC Adv.* 9 (2019) 15307–15313.
- [22] S.-K. Kim, C. Jeon, G.-H. Lee, J. Koo, S.H. Cho, S. Han, M.-H. Shin, J.-Y. Sim, S. K. Hahn, Hyaluronate-gold nanoparticle/glucose oxidase complex for highly sensitive wireless noninvasive glucose sensors, *ACS Appl. Mater. Interfaces* 11 (2019) 37347–37356.
- [23] R. Britto Hurtado, M. Cortez-Valadez, L.P. Ramírez-Rodríguez, E. Larios-Rodríguez, R.A.B. Alvarez, O. Rocha-Rocha, Y. Delgado-Belano, C.E. Martínez-Núñez, H. Arizpe-Chávez, A.R. Hernández-Martínez, M. Flores-Acosta, Instant synthesis of gold nanoparticles at room temperature and SERS applications, *Phys. Lett. A* 380 (2016) 2658–2663.
- [24] Y. Liu, B.M. Crawford, T. Vo-Dinh, Gold nanoparticles-mediated photothermal therapy and immunotherapy, *Immunotherapy* 10 (2018) 1175–1188.
- [25] J.B. Vines, J.-H. Yoon, N.-E. Ryu, D.-J. Lim, H. Park, Gold nanoparticles for photothermal cancer therapy, *Front. Chem.* (2019) 7.
- [26] A. Samadi, H. Klingberg, L. Jauffred, A. Kjaer, P.M. Bendix, L.B. Oddershede, Platinum nanoparticles: a non-toxic, effective and thermally stable alternative plasmonic material for cancer therapy and bioengineering, *Nanoscale* 10 (2018) 9097–9107.
- [27] H. Moustouji, J. Saber, I. Djeddi, Q. Liu, A.T. Diallo, J. Spadavecchia, M. Lamy de la Chapelle, N. Djaker, Shape and size effect on Photothermal heat elevation of gold nanoparticles: absorption coefficient experimental measurement of spherical and urchin-shaped gold nanoparticles, *J. Phys. Chem. C* 123 (2019) 17548–17554.
- [28] W. Yang, H. Liang, S. Ma, D. Wang, J. Huang, Gold nanoparticle based photothermal therapy: development and application for effective cancer treatment, *Sustain. Mater. Technol.* 22 (2019), e00109.
- [29] S. Wang, Y. Zhang, H.-L. Ma, Q. Zhang, W. Xu, J. Peng, J. Li, Z.-Z. Yu, M. Zhai, Ionic-liquid-assisted facile synthesis of silver nanoparticle-reduced graphene oxide hybrids by gamma irradiation, *Carbon* 55 (2013) 245–252.

- [30] X. Li, L. Liu, Z. Xu, W. Wang, J. Shi, L. Liu, M. Jing, F. Li, X. Zhang, Gamma irradiation and microemulsion assisted synthesis of monodisperse flower-like platinum-gold nanoparticles/reduced graphene oxide nanocomposites for ultrasensitive detection of carcinoembryonic antigen, *Sensors Actuators B Chem.* 287 (2019) 267–277.
- [31] K. Hareesh, R.P. Joshi, D.V. Sunitha, V.N. Bhoraskar, S.D. Dhole, Anchoring of Ag-Au alloy nanoparticles on reduced graphene oxide sheets for the reduction of 4-nitrophenol, *Appl. Surf. Sci.* 389 (2016) 1050–1055.
- [32] X. Zhao, N. Li, M. Jing, Y. Zhang, W. Wang, L. Liu, Z. Xu, L. Liu, F. Li, N. Wu, Monodispersed and spherical silver nanoparticles/graphene nanocomposites from gamma-ray assisted in-situ synthesis for nitrite electrochemical sensing, *Electrochim. Acta* 295 (2019) 434–443.
- [33] D.K. Roper, W. Ahn, M. Hoepfner, Microscale heat transfer transduced by surface Plasmon resonant gold nanoparticles, *J. Phys. Chem. C* 111 (2007) 3636–3641.
- [34] Z. Qi, J. Shi, Z. Zhang, Y. Cao, J. Li, S. Cao, PEGylated graphene oxide-capped gold nanorods/silica nanoparticles as multifunctional drug delivery platform with enhanced near-infrared responsiveness, *Mater. Sci. Eng. C* 104 (2019) 109889.
- [35] A. Appleby, H.A. Schwarz, Radical and molecular yields in water irradiated by gamma-rays and heavy ions, *J. Phys. Chem.* 73 (1969) 1937–1941.
- [36] D. Hernández-Sánchez, G. Villabona-Leal, I. Saucedo-Orozco, V. Bracamonte, E. Pérez, C. Bittencourt, M. Quintana, Stable graphene oxide-gold nanoparticle platforms for biosensing applications, *Phys. Chem. Chem. Phys.* 20 (2018) 1685–1692.
- [37] B.-K. Pong, H.I. Elim, J.-X. Chong, W. Ji, B.L. Trout, J.-Y. Lee, New insights on the nanoparticle growth mechanism in the citrate reduction of gold(III) salt: formation of the Au nanowire intermediate and its nonlinear optical properties, *J. Phys. Chem. C* 111 (2007) 6281–6287.
- [38] N. Misra, J. Biswal, A. Gupta, J.K. Sainis, S. Sabharwal, Gamma radiation induced synthesis of gold nanoparticles in aqueous polyvinyl pyrrolidone solution and its application for hydrogen peroxide estimation, *Radiat. Phys. Chem.* 81 (2012) 195–200.
- [39] A. Abedini, A.R. Daud, M.A. Abdul Hamid, N. Kamil Othman, E. Saion, A review on radiation-induced nucleation and growth of colloidal metallic nanoparticles, *Nanoscale Res. Lett.* 8 (2013) 474.
- [40] J. Li, C.-y. Liu, Ag/graphene heterostructures: synthesis, characterization and optical properties, *Eur. J. Inorg. Chem.* 2010 (2010) 1244–1248.
- [41] Z.M. Marković, D.P. Kepić, D.M. Matijašević, V.B. Pavlović, S.P. Jovanović, N. K. Stanković, D.D. Milivojević, Z. Spitalsky, I.D. Holclajtner-Antunović, D.V. Bajuk-Bogdanović, M.P. Nikšić, B.M. Todorović Marković, Ambient light induced antibacterial action of curcumin/graphene nanomesh hybrids, *RSC Adv.* 7 (2017) 36081–36092.
- [42] D. Li, M.B. Müller, S. Gilje, R.B. Kaner, G.G. Wallace, Processable aqueous dispersions of graphene nanosheets, *Nat. Nanotechnol.* 3 (2008) 101–105.
- [43] A. Ansón-Casas, J.A. Puértolas, F.J. Pascual, J. Hernández-Ferrer, P. Castell, A. M. Benito, W.K. Maser, M.T. Martínez, The effect of gamma-irradiation on few-layered graphene materials, *Appl. Surf. Sci.* 301 (2014) 264–272.
- [44] L.M. Malard, M.A. Pimenta, G. Dresselhaus, M.S. Dresselhaus, Raman spectroscopy in graphene, *Phys. Rep.* 473 (2009) 51–87.
- [45] V. Tũcureanu, A. Matei, A.M. Avram, FTIR spectroscopy for carbon family study, *Crit. Rev. Anal. Chem.* 46 (2016) 502–520.
- [46] D. Yang, A. Velamakanni, G. Bozoklu, S. Park, M. Stoller, R.D. Piner, S. Stankovich, I. Jung, D.A. Field, C.A. Ventrice, R.S. Ruoff, Chemical analysis of graphene oxide films after heat and chemical treatments by X-ray photoelectron and micro-Raman spectroscopy, *Carbon* 47 (2009) 145–152.
- [47] A. Ganguly, S. Sharma, P. Papakonstantinou, J. Hamilton, Probing the thermal Deoxygenation of Graphene oxide using high-resolution in situ X-ray-based spectroscopies, *J. Phys. Chem. C* 115 (2011) 17009–17019.
- [48] D. Jaque, L. Martínez Maestro, B. del Rosal, P. Haro-Gonzalez, A. Benayas, J. L. Plaza, E. Martín Rodríguez, J. García Solé, Nanoparticles for photothermal therapies, *Nanoscale* 6 (2014) 9494–9530.



Full length article

Micromechanical imaging of dentin with Brillouin microscopy

Tijana Lainović^a, Jérémie Margueritat^b, Quentin Martinet^b, Xavier Dagany^b, Larisa Blažič^{a,c}, Dejan Pantelić^d, Mihailo D. Rabasović^d, Aleksandar J. Krmpot^d, Thomas Dehoux^{b,*}



^a Faculty of Medicine, School of Dental Medicine, University of Novi Sad, Hajduk Veljkova 3, 21000 Novi Sad, Serbia

^b Univ Lyon, Univ Claude Bernard Lyon 1, CNRS, Institut Lumière Matière, F-69622, Villeurbanne, France

^c Dental Clinic of Vojvodina, Hajduk Veljkova 12, 21000 Novi Sad, Serbia

^d Institute of Physics Belgrade, University of Belgrade, Pregrevica 118, 11080 Belgrade, Serbia

ARTICLE INFO

Article history:

Received 26 July 2019

Revised 20 January 2020

Accepted 21 January 2020

Available online 24 January 2020

Keywords:

Mechanical characterization

Dentin

Brillouin microscopy

Hybrid layer

ABSTRACT

The structure of teeth can be altered by diet, age or diseases such as caries and sclerosis. It is very important to characterize their mechanical properties to predict and understand tooth decay, design restorative dental procedures, and investigate their tribological behavior. However, existing imaging techniques are not well suited to investigating the micromechanics of teeth, in particular at tissue interfaces. Here, we describe a microscope based on Brillouin light scattering (BLS) developed to probe the spectrum of the light scattered from tooth tissues, from which the mechanical properties (sound velocity, viscosity) can be inferred with *a priori* knowledge of the refractive index. BLS is an inelastic process that uses the scattering of light by acoustic waves in the GHz range. Our microscope thus reveals the mechanical properties at the micrometer scale without contact with the sample. BLS signals show significant differences between sound tissues and pathological lesions, and can be used to precisely delineate carious dentin. We also show maps of the sagittal and transversal planes of sound tubular dentin that reveal its anisotropic microstructure at 1 μm resolution. Our observations indicate that the collagen-based matrix of dentine is the main load-bearing structure, which can be considered as a fiber-reinforced composite. In the vicinity of polymeric tooth-filling materials, we observed the infiltration of the adhesive complex into the opened tubules of sound dentine. The ability to probe the quality of this interfacial layer could lead to innovative designs of biomaterials used for dental restorations in contemporary adhesive dentistry, with possible direct repercussions on decision-making during clinical work.

Statement of Significance

Mechanical properties of teeth can be altered by diet, age or diseases. Yet existing imaging modalities cannot reveal the micromechanics of the tooth. Here we developed a new type of microscope that uses the scattering of a laser light by naturally-occurring acoustic waves to probe mechanical changes in tooth tissues at a sub-micrometer scale without contact to the sample. We observe significant mechanical differences between healthy tissues and pathological lesions. The contrast in mechanical properties also reveals the microstructure of the polymer-dentin interfaces. We believe that this new development of laser spectroscopy is very important because it should lead to innovative designs of biomaterials used for dental restoration, and allow delineating precisely destructed dentin for minimally-invasive strategies.

© 2020 Acta Materialia Inc. Published by Elsevier Ltd. All rights reserved.

1. Introduction

Human dentin is an organized, hard, mineralized tissue of the tooth, composed of 70 wt% calcified tissue (hydroxyapatite), 20 wt% organic phase (mostly composed of collagen type I as well as other fibrils), and 10 wt% water [1]. It is perfused with microtubules that allow sensory communication with the underlying

pulp and nerves [2]. This fiber-composite-like structure provides an anisotropic distribution of mechanical properties that support masticatory stress concentrated in the surrounding enamel [3],[45–47]. Tooth mechanical strength can be altered by diet, age or diseases such as caries or sclerosis [44]. It is essential to characterize the mechanical properties of teeth to predict and understand tooth decay, design restorative dental procedures, and investigate their tribological behavior.

Most of the methods used for characterization have been inherited from material science, and involve destructive testing such as

* Corresponding author.

E-mail address: thomas.dehoux@univ-lyon1.fr (T. Dehoux).

compression tests [57], or nanoindentation with AFM tips or normalized indenters [3,47]. These techniques have notably allowed demonstrating the loss of hardness in caries-affected dentin [58]. Using dynamic mechanical analysis, the storage and loss moduli of intertubular and peritubular dentin have been obtained with frequencies up to 100 Hz [59]. Fatigue tests can also be deployed to analyze the fracture behavior of teeth [60]. Recently, recording the deformation of dentin in the vicinity of holes milled by a focused ion beam has revealed the existence of residual stresses [61]. In restorative dentistry, shear bond tests and 3-points bend tests have allowed assessing the efficacy and durability of bonding procedures [62,63]. Due to the variety of techniques and the complexity of the dentin microstructure, there is a lack of quantified consensus regarding the mechanical properties of dentin [38]. Moreover, such approaches are clearly difficult to implement *in vivo*. Dentinal pathological changes can be detected by visuotactile and radiographic methods to help clinicians establish relevant diagnostics, and propose adequate therapies [4]. However, such approaches cannot give precise information on the microstructure, nor precisely delineate caries margins [5], and are highly dependent on the clinician [6].

Acoustic techniques have long been used to probe the mechanics of dentin, initially analyzing the reflection or transmission of ultrasonic pulses emitted from a piezoelectric transducer in the MHz range [39]. Later implementations in tooth tissues in various sound and pathological states used resonant ultrasonic spectroscopy, Kinney et al. [38] acoustic microscopy, Maev et al. [7,9] surface waves [10] and laser ultrasonics [11,12]. The implementation of surface acoustic waves in acoustic microscopy has allowed probing dentin at frequencies up to 1 GHz [8]. In these procedures, however, the acoustic lens has to be defocused, resulting in measurements averaged over a 1 mm-diameter area. Thus, they are not suited to investigating the micromechanics of the tooth, in particular at tissue interfaces. Acoustic microscopy has also been used to measure the reflection of bulk waves and produce images of the acoustic impedance in dentin at a resolution of 23 μm [8]. With this technique, images at 1.2 GHz have also been obtained in bone at a resolution of 1 μm , suggesting potential for micro-imaging in dentin [55].

State-of-the-art microscopies, such as multiphotonic and nonlinear technologies [41] can offer optical resolution but cannot provide any information on the mechanics of the sample. Laser spectroscopies have recently come into vogue, offering quantitative imaging of the chemical structure of tooth tissues and restorative materials [13–16]. In this paper we propose a new approach to probe acoustic waves in the GHz range by laser spectroscopy, thus offering quantitative microscopy with a contrast based on the mechanical properties of tooth tissues.

We have developed a microscope based on Brillouin light scattering (BLS) to probe mechanical changes in tooth tissues, by measuring the characteristics of the scattered light. BLS is an inelastic process similar to Raman scattering. Raman-based techniques rely on the scattering of light by optical phonons, and operate at THz frequencies. They provide information on the molecular structure of the sample. By contrast, Brillouin scattering uses the scattering of light by acoustic phonons [18]. Since acoustic phonons have lower energies than optical phonons, Brillouin scattering produces frequency shifts in the GHz range that reveal the mechanical properties of the sample. Developed in the 1960s for solid-state physics, BLS has only recently emerged as a key technology in life sciences due to its ability to produce non-contact, label-free microscopic images of the mechanical properties of cells and tissues [19]. It has notably been applied for the analysis of biological fibers, connective tissues and muscles [17,20,21], eye tissues [22,23], bone [24,26] and tumors [35].

We prepared thick slices of teeth extracted in accordance with the ethical requirements for ex-vivo studies. We obtained maps of Brillouin frequency shift and linewidth that can be interpreted as maps of sound velocity and viscosity. In order to illustrate the potential of our approach in different areas of dentistry, we analyzed carious lesions, the mechanical anisotropy of sound dentin, and the structure of the dentin-resin interface. Our results first show significant changes between sound tissues and pathological lesions. Such results allow precisely delineating deteriorated dentin, paving the way for minimally invasive strategies. We also provide maps of the sagittal and transversal planes of sound tubular dentin that reveal its anisotropic microstructure with a 1 μm resolution, several orders of magnitude below previous reports [38]. Our observations indicate that the collagen-based matrix of dentin is the main load-bearing structure, which can be considered as a fiber-reinforced composite. In the vicinity of polymeric tooth-filling materials, we observed the infiltration of the adhesive complex into the opened tubules of sound dentin. We confirmed our observations with two-photon excitation fluorescence (2PEF) and second harmonic generation (SHG) microscopies that reveal teeth microstructure due to two-photon excited autofluorescence and collagen-specific second-order nonlinear optical susceptibility [27]. The ability to probe the quality of this interfacial layer could lead to innovative designs of biomaterials used for dental restorations in contemporary adhesive dentistry, with possible direct repercussions on decision-making during clinical work.

2. Materials and methods

2.1. Sample preparation and staining

Teeth were collected at the Faculty of Medicine, School of Dental Medicine, at the Department of Oral Surgery of the Dental Clinic of Vojvodina, Serbia. They were extracted for medical reasons and donated voluntarily by patients after they read and signed the informed written consent. This study was approved by the Ethical Board of the Dental Clinic of Vojvodina, Serbia. All types of permanent teeth were analyzed, including incisors, canines, premolars, and molars. Since extracted human teeth are difficult to collect, different groups of teeth were included in the study. Having previously confirmed that there were no statistically significant differences in variances for the dentinal tissue among the various tooth groups, we pooled together different groups in order to increase the significance of statistical tests. The teeth were classified in the following groups: sound teeth with intact hard tissues (two subgroups – teeth cut perpendicularly to their longitudinal axis, teeth cut longitudinally), teeth with carious lesions in dentin [score 5 on the International Caries Detection and Assessment System (ICDAS) scale; distinct cavity with visible dentin], restored teeth with composite resin.

Freshly extracted teeth were kept in 0.5% chloramine solution until cutting. They were then sectioned across the sagittal and transversal tooth axes in 0.5+/-0.05 mm thick slices by a water-cooled, low-speed diamond saw using a hard tissue microtome. Samples were wet-polished with abrasive sandpaper sheets of silicone-carbide of increasing grit numbers (400–2000). This was followed by polishing with a diamond paste on a soft fabric, in order to eliminate surface corrugations. The smear layer produced by polishing was removed by 10% polyacrylic acid used for 5 s, after which the samples were rinsed, slightly dry-aired and disinfected in a 0.5% chloramine solution. After preparation, each slice was kept in a plastic bag with 100 mL distilled water. In these conditions, the samples kept their natural moisture until examination. However, during the measurements, the samples were tested in dry conditions in air.

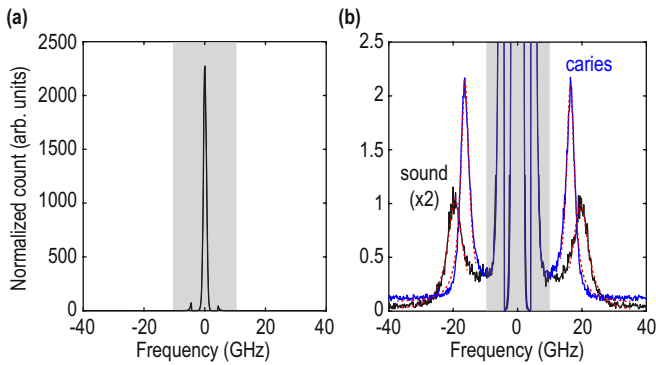


Fig. 1. Typical spectrum. (a) Raw spectrum where the contribution of Rayleigh scattering is indicated by the gray box. (b) Zoom on the Stokes (negative frequencies) and anti-Stokes (positive frequencies) peaks for sound tissue (black, intensity multiplied by 2 for clarity) and a caries lesion (blue line). Fits by Lorentzian functions are superimposed (red dashed lines). (For interpretation of the references to colour in this figure legend, the reader is referred to the web version of this article.)

Teeth restored with composite used for the imaging of the dentin-adhesive interface were prepared according to the standard dental adhesive placement procedure, after the etching procedure by using 37% ortho-phosphoric acid for 15 s, rinsing, and placing a single bond universal adhesive (3 M Deutschland GmbH, LOT 663414), before restoration with the Filtek Ultimate Body composite. For 2PEF imaging of the dentin-adhesive interface, a water solution containing 0.5% eosin-Y was added in small quantities into the adhesive in order to distinguish the adhesive from the surrounding dentinal tissue.

2.2. Nonlinear laser scanning microscopy

Teeth specimens were observed by a nonlinear optical microscopy setup at the Institute of Physics in Belgrade. The homemade nonlinear laser-scanning microscope used in this study has been described in detail elsewhere [42,43]. Briefly, a Ti:Sapphire femtosecond laser (Coherent, Mira 900-F) tunable in the 700–1000 nm range and a Yb:KGW (Time-Bandwidth Products AG, Yb GLX) femtosecond laser at 1040 nm were used as laser light sources. The samples were imaged using a Carl Zeiss, EC Plan-NEOFLUAR, 40×1.3 oil immersion objective or a Plan-APOCHROMAT 20×0.8 air objective for laser focusing and signal collection. A visible interference filter (415 nm–685 nm) positioned in front of the detector was used to remove scattered laser light in the fluorescence images. Thus, the whole visible range was detected in two-photon fluorescence images. Tooth auto-fluorescence was excited by the Ti:Sapphire laser at 730 nm. Eosin-Y fluorescence was excited by the Ti:Sapphire laser at 820 nm. Narrowband interference filters (10 nm FWHM) were used for second-harmonic generation imaging. The SHG filter central wavelength was 520 nm (FB520-10, Thorlabs) for the Yb:KGW laser. The SHG filter central wavelength was 420 nm (FB420-10, Thorlabs) for the Ti:Sapphire laser when tuned at 840 nm. The SHG excitation wavelength and filter were selected so that fluorescence leakage to the SHG channel was minimal.

2.3. Brillouin spectroscopy

BLS uses the scattering of light by phonons. Thermal phonons (incoherent vibrations) produce a broad peak at low frequencies due to Rayleigh scattering, while acoustic phonons (coherent vibration) with wavenumbers that fulfill the Bragg condition produce well-defined peaks (Fig. 1). Using a monochromatic light beam of wavelength λ in a normal incidence backscattering geometry, forward propagating phonons produce a positive shift at a frequency $f = 2n\nu/\lambda$ (anti-Stokes peak) with a width $\Gamma = \omega f\nu/V^2$, where

V is the sound velocity, ν is the kinematic viscosity and n is the refractive index. Backward propagating phonons create a negative Stokes peak at $-f$.

For comparison with the literature, it can be useful to express the loss and storage moduli. Assuming that the sample is homogeneous over the scattering volume, the BLS spectra can be interpreted as the response of a damped harmonic oscillator with frequency position f and full width at half maximum Γ . In this approximation, the storage modulus is $' = \rho(f\lambda/2n)^2$, where ρ is the mass density. The linewidth Γ is ascribed to the loss modulus $M'' = \rho\Gamma f(\lambda/2n)^2$. It is however not mandatory to evaluate M' and M'' , and the mechanical properties can be assessed using only V and ν .

From these equations it is clear that BLS probes the sound velocity and viscosity of the sample, but f and Γ both depend linearly on n . The mechanical properties V and ν and the refractive index n both contribute to the frequency shift and linewidth, but with our measurement alone, we cannot distinguish their respective influences. Interestingly, we can also determine the loss tangent [59] $\tan \varphi = \frac{M''}{M'} = \frac{\Gamma}{f}$ that does not depend on the refractive index. More importantly, in situations where Γ (resp. f) does not vary, i.e. both n and ν are constant as in Fig. 3, variations of f can be attributed to changes in the sound velocity (resp. viscosity). Note that at the high magnifications we used, Γ can increase artificially due to the finite solid angle of collection of the backscattered light.

The size of the laser spot, estimated using the Rayleigh criterion, corresponds to an ellipsoid of $\sim 1 \mu\text{m}$ in the lateral direction and $\sim 10 \mu\text{m}$ in the axial direction. Although this is an overestimation, since the penetration inside the tooth at 647.1 nm is not known, we consider that the volume of the laser spot defines a scattering volume of $\sim 40 \mu\text{m}^3$.

2.4. Brillouin microscope

The Brillouin spectrometer is based on a tandem Fabry-Pérot interferometer (JRS Scientific Instruments) [35]. In order to reduce phototoxicity, we used a $\lambda = 647.1 \text{ nm}$ continuous-wave laser as a light source (instead of classical designs based on a frequency-doubled YAG laser at 532 nm) which gives a $\frac{\lambda}{2n} \approx 200 \text{ nm}$ acoustic resolution, where $n = 1.6$ is the typical refractive index of dentin. The spectrometer offers a 40 GHz free spectral range sampled with a 30 MHz sampling rate. Appropriate signal analysis allows obtaining an accuracy of 6 MHz at a -10 dB noise level. It is equipped with two sets of mirrors with 95% reflectivity, and an avalanche photodiode (Count[®] Blue, Laser Components) with a dark count lower than 10 counts/s (typically 2 counts/s) and a quantum efficiency of 65% at this wavelength. The spectrometer is coupled with an inverted life science microscope (Eclipse Ti-U, Nikon) equipped with a micro-positioning stage (Mad City Labs). The collimated linearly-polarized laser light is focused onto the sample using a $100 \times$ objective (NA 0.9), providing a resolution of $\sim 1 \mu\text{m}$. The typical power used at the focus was 5 mW, resulting in a power density over the scattering volume a hundred times smaller than that previously reported in tissues and cells, again to ensure low phototoxicity. The backscattered light is collected by the same objective lens and collected outside the microscope using a telescope. Particular attention was paid to comply with the f -number ($f/18$) of the spectrometer to maximize photon collection on the photodiode. Spectra were acquired by averaging over ~ 100 acquisitions.

2.5. Dentinal positions examined

The middle crown sections were probed by the BLS microscope. In this area, the tubules form an "S" curve and diverge in the tooth

crown. We selected intertubular regions manually for BLS measurements. Note that these regions might also contain the signature of the peritubular wall, but not that of the tubular lumen which does not produce any BLS signal.

For the study of caries, the tooth was cut longitudinally to show the dentinal carious zones, including caries-infected and caries-affected dentin. The data were collected in the sagittal plane in the middle-dentinal crown portion. The BLS scanning passed from the sound dentin over the histopathological carious layers to the carious decay.

The dentin-adhesive interfaces were tested, passing over the composite restoration, the adhesive layer, the hybrid layer, the etched dentin, and to the completely untreated dentinal core.

2.6. Data analysis

Raw spectra sampled at 30 MHz were recorded by the proprietary software of the spectrometer (Ghost software, Table Stable Ltd., Switzerland). When only one peak was observed on each side of the Rayleigh line (see Fig. 1b for instance), we fitted the anti-Stokes and Stokes peaks separately to a Lorentzian function using Matlab and extracted amplitude A , frequency shift f and linewidth Γ . We chose the Lorentzian function since it is that best suited for analyzing solid samples [50]. Values for each peak were then averaged. When two closely-spaced peaks were observed, we sequentially windowed around each peak and fitted the windows individually with a single Lorentzian function. This procedure may slightly underestimate the true spacing between the two peaks, but it reduces the error of the fit and hence allows automating the fitting procedure to analyze large images.

In Figs. 3, 6 and 7, we plot point distributions where jitter has been added to the data points to avoid overlap. This type of plot, called plot spread plot, allows visualizing the distribution of points within a distribution, and identify possible outliers. The data collected from the different groups of samples were statistically analyzed using Matlab software (version R2017a). The level of significance (p -value) was evaluated according to an unpaired two-tailed t -test.

3. Results

3.1. Mechanical signature of carious lesions

Brillouin spectra were recorded for sound tissues ($n = 34$ in 5 different teeth) and carious lesions ($n = 39$ in 5 different teeth). These data were acquired in the sagittal plane in the middle-dentinal crown portion (see Material and Methods). By way of illustration, we plot a typical spectrum in Fig. 1. Fig. 1a shows that the raw spectrum is dominated by Rayleigh scattering (grey box). Fig. 1b shows a zoom on the Stokes (negative frequencies) and anti-Stokes (positive frequencies) peaks for the sound tissue and caries lesion. We fit these peaks with Lorentzian functions (dashed lines) to extract the frequency shift f and linewidth Γ (Methods). The distributions of frequency and linewidth values are plotted in Fig. 2a and b, respectively. Note that the spreading of the data is larger in the case of caries because BLS features depend on the position within the highly heterogeneous lesion, as discussed below. The frequency shift is clearly different between sound and carious conditions. We do not, however, observe any significant variation in the linewidth. This observation suggests that BLS features could be used to delineate lesions.

To investigate this, we scanned the laser along a line across the frontier between sound tissue and a caries lesion. Fig. 3 shows the frequency shift f and linewidth Γ measured from the sound region (left) to the core of the lesion (right). We can see that Γ does not

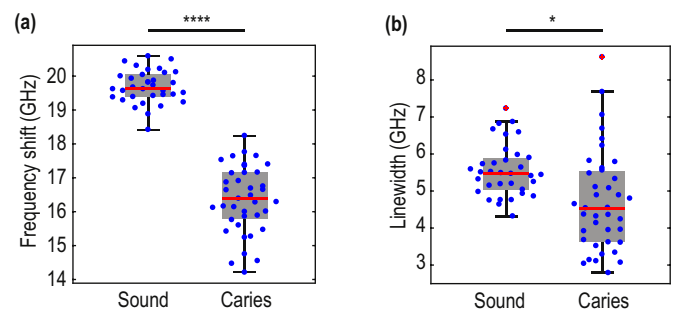


Fig. 2. Comparison between sound tissues ($n = 34$) and carious lesions ($n = 39$). Distributions of (a) frequency shift and (b) linewidth (**** $p < 0.0001$, * $p < 0.05$, unpaired two-tailed t -test). The bottom and top edges of each gray box indicate the 25th and 75th percentiles, respectively. The red central line indicates the median. The whiskers extend to the most extreme data points, not considering outliers ('+' symbol). (For interpretation of the references to colour in this figure legend, the reader is referred to the web version of this article.)

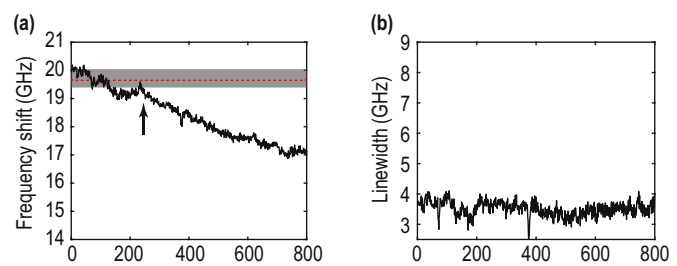


Fig. 3. Scan across a caries lesion. (a) frequency shift and (b) linewidth. The gray box and red dashed line indicate the 25th and 75th percentiles and median identified in Fig. 2a. The upward arrow indicates the position where the frequency shift falls below the 25th percentile. (For interpretation of the references to colour in this figure legend, the reader is referred to the web version of this article.)

vary, as already observed in Fig. 2b, meaning that the refractive index does not change across the probed region (see Methods). On the other hand, f decreases slowly. In this situation, we can ascertain that the sound velocity is the main contributor to the change observed in f .

The slow decrease in f makes the precise delineation difficult. As a reference, we indicate the median (red dashed line) and the 25th and 75th percentiles (grey box) measured in Fig. 2a. The upward arrow indicates where f falls below the 25th percentile. This criterion can be used to define the limit of the sound tissue. In this example, f decreases almost linearly by ~ 0.01 GHz/ μm within the lesion. Given the spreading of the data for sound dentin measured in Fig. 2a, ~ 0.2 GHz between the mean and the 25th percentile, such a decrease would lead to a precision of 20 μm in the identification of the lesion margins.

3.2. Mechanical anisotropy of the dentin

Sound dentin is composed of a mineralized collagen matrix (intertubular dentin) perfused by microtubules called tubules surrounded by peritubular mineralized dentinal tissue (peritubular dentin). This structure leads to an anisotropic distribution of mechanical properties, largely documented in the literature on the macroscale [38]. To investigate the anisotropy of the sound tubular dentin on the microscopic scale, sound teeth were cut longitudinally and transversally (Methods). The microstructure of the sound dentin in the sagittal and transversal planes is clearly revealed by the combination of the 2PEF image obtained with the Ti:Sapphire tuned at 730 nm and the SHG image obtained with the Ti:Sapphire tuned at 840 nm (Figs. 4 and 5). The typical tubular structure of

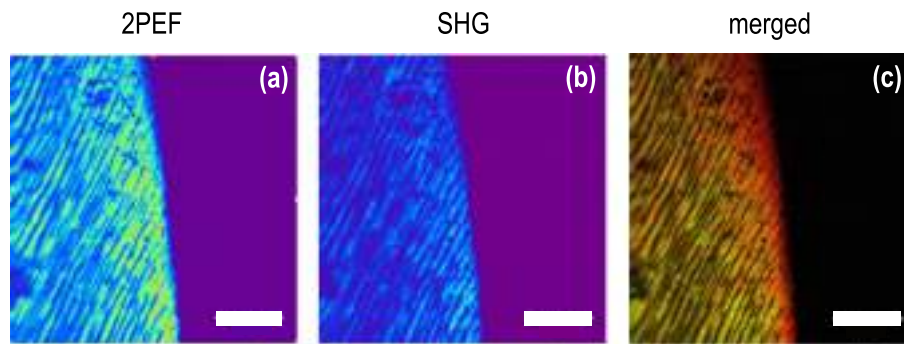


Fig. 4. 2PEF and SHG images of sound dentin in the sagittal plane. (a) The 2PEF image reveals the tubular structure of dentin; (b) the SHG image reveals the presence of collagen type I, (c) merged. Scale bars: 20 μm .

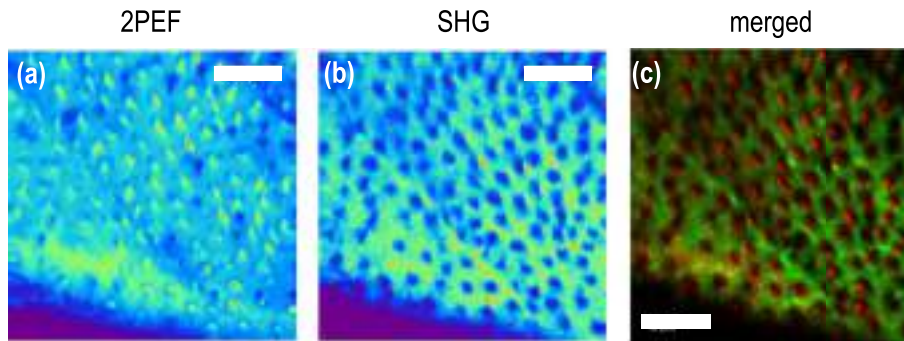


Fig. 5. 2PEF and SHG images of sound dentin in the transversal plane. (a) The 2PEF image reveals the tubular structure of dentin; (b) the SHG image reveals the presence of collagen type I, (c) merged. Scale bars: 20 μm .

dentin appears clearly on the 2PEF image. Collagen type I, a triple-helical molecule, the organic component on which the dentin is mostly built, is aligned in a non-centrosymmetric manner, and is responsible for the contrast in the SHG images. The SHG images of dentin thus reveal the intertubular dentin, which is less mineralized than the peritubular dentin [28].

The exposed surfaces in the sagittal and transversal planes were mapped with BLS. The laser was scanned in a raster pattern at a resolution of 1 μm and spectra were recorded at each pixel. The resulting images obtained in the sagittal (along the tubules) and transversal planes (perpendicular to the tubules) of the tooth are shown in Figs. 6 and 7, respectively. In the sagittal plane, the tubules are clearly visible on the optical image (Fig. 6a), and are characterized by a lower amplitude (Fig. 6b) and a lower f (Fig. 6c). We define an amplitude threshold of $A_{th} = 0.5A_m$, where A_m is the maximum amplitude that separates the tubular region (containing tubules and peritubular dentin) from the surrounding intertubular dentin. Pixels in the f and Γ images that correspond to an amplitude $A < A_{th}$ are ascribed to the tubular region, and the remaining pixels to the intertubular dentin. The distribution of pixels for f and Γ are shown in Figs. 6e and 6f. While the linewidth does not allow distinguishing the two components (as observed in Fig. 6d), f -values are slightly higher for the tubules.

In the transverse plane, the tubules appear as disks on the optical image (Fig. 7a). They are also clearly visible on the BLS images, characterized here too by a low amplitude (Fig. 7b). In this case, however, the low amplitude of the Brillouin peaks does not allow identifying f or Γ -values in the tubular regions, and only the peritubular and intertubular dentin appear in the f and Γ images, Figs. 7d and 7f. This is because the tubules cause a depression in the transverse plane that defocuses the laser beam. Considering pixels where $A < A_{th}$ therefore reveals only the distributions of values for the intertubular dentin, plotted in Figs. 7c and 7e, respectively. The f and Γ values differ significantly ($p < 0.0001$) in

the sagittal and transverse planes, suggesting that the matrix itself is anisotropic.

3.3. Characterization of the dentin-resin interface

In this section, we examine the adhesive interface between sound dentin and tooth-filling resin. Fig. 8a shows a typical sample with an adhesive interface indicated by the arrow. A merged 2PEF image obtained with the Ti:Sapphire tuned at 820 nm and an SHG image obtained with the Yb:KGW (Fig. 8b) reveals the typical structure of the interface between dentin (SHG, blue pseudocolor) and adhesive (labeled by eosin in 2PEF, red pseudocolor). This image reveals that the low-viscous monomer adhesive protrudes in-between the exposed dentinal collagen fibers of intertubular dentin, or in the tubules themselves, forming the so-called hybrid layer. Extensions of monomer entering a few individual dentinal tubules, i.e. resin tags, are also observable (a typical extension is indicated by a white arrow).

We probed the interface between sound dentin and resin with BLS. Fig. 9a shows a typical spectrum where we recognize the signature of sound dentin at around 20 GHz (blue area). In addition, we also observe a second peak at around 13 GHz (pink area), revealing the presence of the adhesive. This result demonstrates that BLS is able to detect the presence of the two components mixed in the hybrid layer. To investigate this, we recorded BLS images in a typical hybrid layer. The frequency shift (Fig. 9b) and linewidth (Fig. 9c) both allow us to observe the adhesive, hybrid layer and dentin. The adhesive is recessed in the vicinity of the hybrid layer (left part of Figs. 9b and 9c), causing the laser to defocus and the signal to fall below detectable levels. Such pixels with an amplitude lower than 0.1 are shown in white. These images clearly highlight the ability of BLS to quantify adhesive interfaces and reveal the infiltration of the adhesive in the hybrid layer.

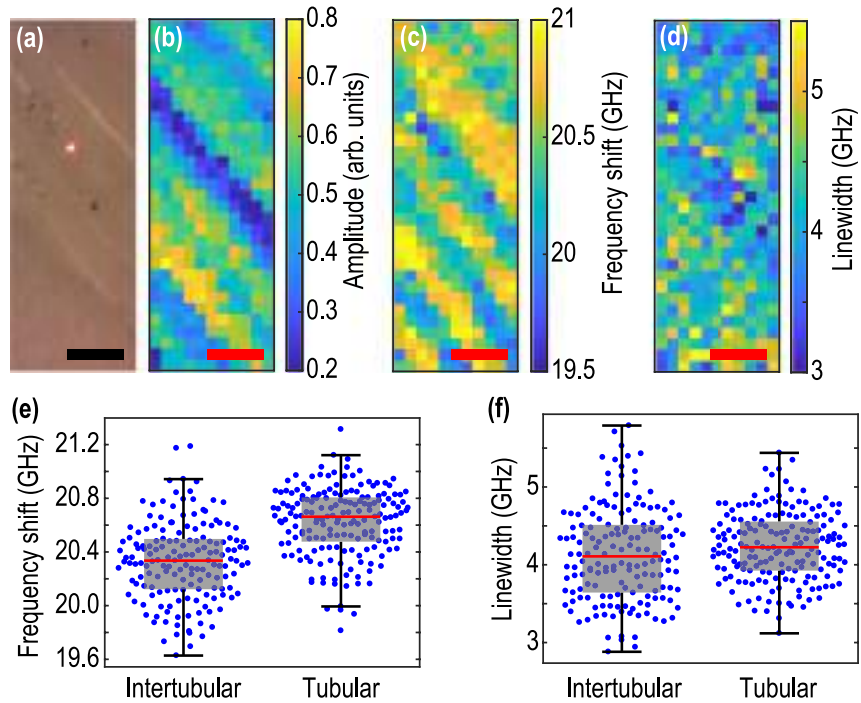


Fig. 6. Images of sound dentin in the sagittal plane. (a) Optical image, (b) amplitude of the Brillouin peaks, (c) frequency shift and (d) linewidth. Panels (e) and (f) show the distribution of f and Γ -values measured in panels (c) and (d), respectively. The tubular region is identified in panel (b) by amplitude values lower than 50% of the maximum amplitude, and the intertubular dentin corresponds to the remaining pixels. Scale bars: 5 μ m.

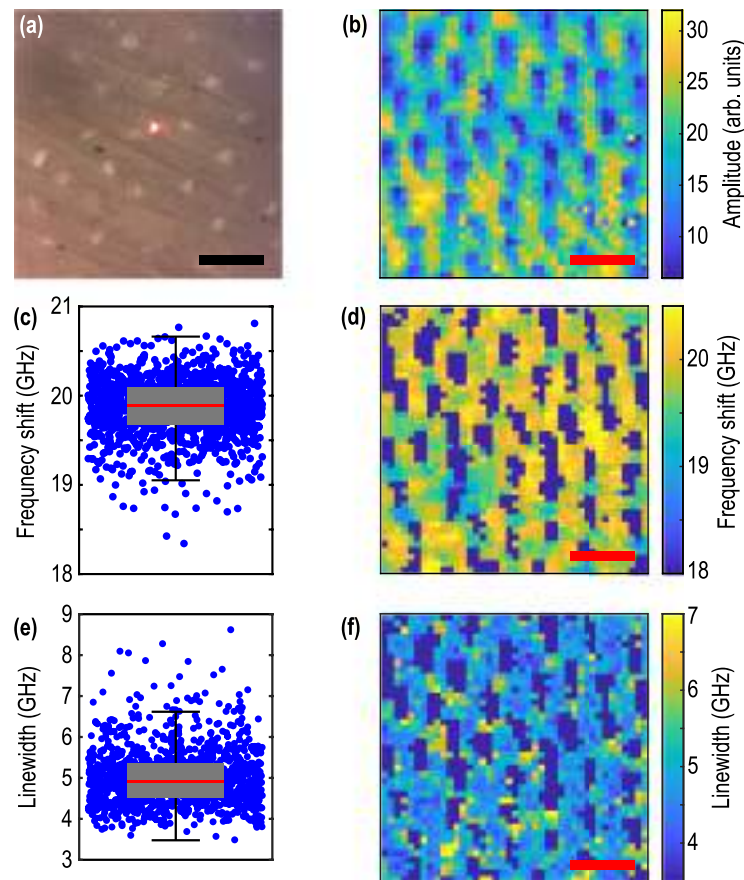


Fig. 7. Images of sound dentin in the transversal plane. (a) Optical image, (b) amplitude of the Brillouin peaks, (d) frequency shift, and (f) linewidth. Panels (c) and (e) show the distribution of f and Γ -values measured in panels (d) and (f), respectively. Scale bars: 10 μ m.

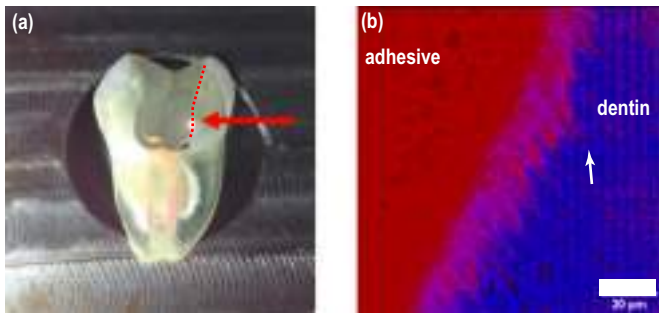


Fig. 8. Structure of a typical dentin adhesive interface. (a) photograph of an dentin-resin adhesive interface shown by a dashed line and arrow. (b) Merged 2PEF and SHG images of a dentin-adhesive interface. A 2PEF micrograph reveals the adhesive colored by eosin Y (red pseudocolor) and a SHG micrograph reveals dentin (blue pseudocolor). The arrow points to a typical resin tag. Scale bar: 20 μm . (For interpretation of the references to colour in this figure legend, the reader is referred to the web version of this article.)

4. Discussion

We demonstrated the potential of BLS to examine non-destructively and with high resolution the mechanical properties of different sound, diseased and restored dental tissues. The BLS maps in the sagittal and transverse planes clearly reveal the tubular structure of dentin. We segmented the images to separate the tubular region from the surrounding intertubular dentin. With this approach the peritubular dentin might contribute to segmented intertubular dentin, depending on the threshold value. However, we found that the intertubular dentin was stiffer compared to the peritubular dentin, in line with previous publications [47]. This suggests peritubular dentin contributes marginally to the stiffness of segmented-intertubular dentin. Our results showed $f_s \sim 20.4$ GHz in the sagittal plane, and $f_t \sim 19.8$ GHz in the transverse plane for the matrix alone. These values correspond to sound velocities $V_s = \frac{f_s \lambda}{2n_s} \approx 4100$ m/s and $V_t = \frac{f_t \lambda}{2n_t} \approx 4300$ m/s, assuming refractive indices $n_s = 1.6$ and $n_t = 1.5$ in the sagittal and transverse planes, respectively [37]. These sound velocity values are comparable with the values measured by acoustic interferometry (from 3900 to 4100 m/s, see [40]) and acoustic microscopy (from 4100 to 4200 m/s, see [56]). Ref. [8] gives lower values (3800–3900 m/s) but it is important to note that these are surface wave velocities, not bulk waves as in the other works, and that the algorithm they use greatly depends on the assumed sym-

metry of the sample. For further comparisons, we can also estimate the storage moduli $M'_s = \rho V_s^2 \sim 36$ GPa and $M'_t = \rho V_t^2 \sim 38$ GPa, assuming a mass density $\rho \sim 2100$ kg/m³ (see **Materials and Methods, “Brillouin spectroscopy”**) [36]. Our values, ~ 36 – 38 GPa, are comparable with previous results obtained by resonant ultrasound spectroscopy (36.5 GPa, see [48]) and with simulated values [45]. Variations between these different values can come from uncertainties in n , ρ , the assumed symmetry, the type of acoustic wave (bulk or surface wave) or the sample itself. In particular, water content can also play a role. Note that, while the samples were stored in a hydrated environment, the BLS measurements were performed in ambient conditions (see **Material and Methods, “Sample preparation and staining”**). Future studies should consider a possible hydration-dependent Brillouin frequency shift in dentin, since more anisotropic dentinal values have been observed in hydrated environments [48]. In addition, simultaneous measurements of the refractive indices should make it possible to perform a quantitative determination of the sound velocity.

The difference between the frequencies of sound dentin and those of carious lesions is very clear ($p < 0.0001$). The transition from sound dentin to caries allowed delineation at a precision of 20 μm for the samples we probed. The linewidth $\Gamma = 2\pi\eta(2n/\lambda)^2$ was constant across this region, meaning that both n and kinematic viscosity η are constant. The change in f can thus be ascribed to a reduction in the sound velocity of the tooth in the lesion. This observation demonstrates the high specificity of BLS, and its ability to produce quantitative indicators of tooth decay. In the future, it will be necessary to repeat such measurements on a larger population of samples to obtain a robust delineation threshold. In contemporary clinical practice, the visuotactile method is the dominant approach for caries delineation, but it is obviously less resolved than BLS, and operator-dependent. To avoid inter-examiner variations, visual examination can be aided by dyes, light-fluorescence based methods, and fiber-optic transillumination. In this context, BLS has unique potential for providing quantitative information at the microscale in a label-free, non-invasive, non-ionizing manner. Further comparison with histological sections of lesions with different scores should reveal the sensitivity of BLS, and grant new minimally invasive strategies in dentistry. As has been done for cancer therapy [35], ophthalmology [30] and orthopedic treatments [25], BLS could be used as a platform for the early diagnosis of tooth decay, micrometric precision caries detection during clinical work, and for monitoring the efficacy of therapeutic techniques [31,34].

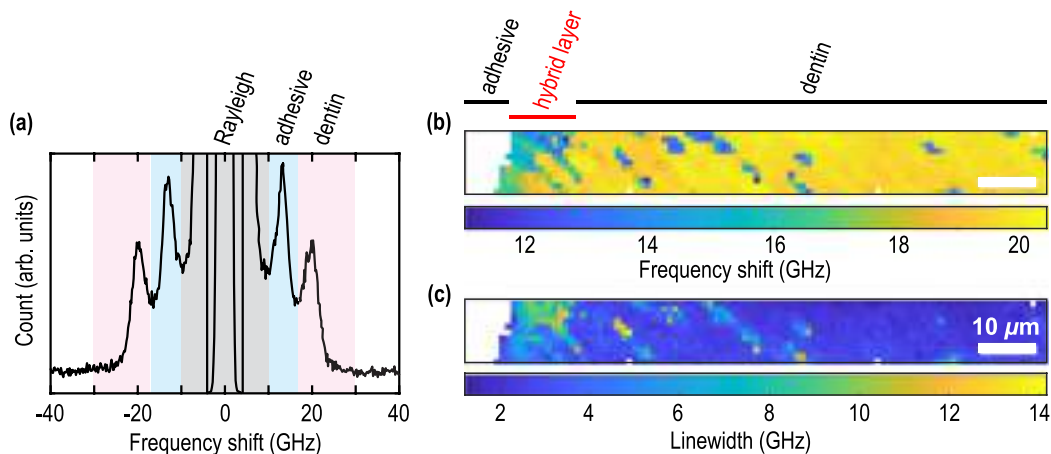


Fig. 9. Imaging the hybrid layer. (a) Typical spectrum at the dentin-adhesive interface. The peaks arising from dentin and adhesive are shown in blue and pink, respectively. (b) Frequency shift and (c) linewidth maps of the hybrid layer. Scale bars: 10 μm . (For interpretation of the references to colour in this figure legend, the reader is referred to the web version of this article.)

BLS images of the hybrid layer provide new information on the spatial distribution of mechanical properties at the adhesive junction. This interface is of great interest in modern adhesive dentistry [51] since it is suspected to be the main reason for restoration failure [52]. It has indeed been demonstrated that the effectiveness of hybrid layer remineralization processes (for instance after treatment with ion-releasing materials and therapeutic phosphoproteins [34], or after collagen cross-linking treatment [53]) is associated with increased stiffness [54]. In the future, in combination with fatigue tests and refractive index measurements, as well as other techniques such as acoustic microscopy [49] and Raman spectroscopy [13], BLS could be used to test the stiffness and viscosity of different types of adhesives under preclinical investigation and the weakening of the hybrid layer by enzyme-based degradation of collagen, adhesive, mineral-depleted dentin [31,32] and caries lesions [33]. Our results also show a reduction of the frequency shift near the interface. To explain this, it can be postulated that etching at the interface is responsible for reduced stiffness, as observed by SAM [49]. If such an effect could be detected by BLS, it would be another advantage for investigations in adhesive dentistry. To investigate this in the future we will compare dentin prepared by different total-etch and self-etch dental adhesive protocols, as well as specific treatments for hybrid layer reinforcement. Moreover, the hybrid layer is subjected to multiaxial stresses during functional use, and it has been predicted that stress concentration in the underlying hard dental tissues depends on the stiffness of this interface [29]. In the future, BLS could also help studying the impact of wear on this interface at the microscale.

Clinically, it should be possible to develop a BLS fiber-optic tool for dental applications. Similar developments are being implemented for other applications, such as cancer diagnostics. The development of a fiber optic probe would require the area of interest to be directly accessible from the surface (not buried under other tissues), in the depth of the laser light penetration. For example, exposed carious lesions could be probed with microscopic precision, and carious-sound dentin thresholds could be defined based on the features of the BLS spectra. The adhesive interface between dentin and adhesive is rarely directly exposed, though BLS could be used during preclinical investigations in adhesive dentistry. Moreover, BLS could be used to probe dentin-adhesive interfaces directly in non-carious cervical lesions in the case where the overlying enamel has worn away. Beyond dentistry, BLS could also provide new tools for investigating the link between microwear, stiffness, and diet, offering important information in the field of paleobiology.

Declaration of Competing Interest

We declare no conflict of interest.

Acknowledgements

The work was partly supported by the COST Action CA16124 “Brillouin Light Scattering Microspectroscopy for Biological and Biomedical Research and Applications”, the Agence Nationale de la Recherche (Grant No. ANR-17-CE11-0010-01), and the Ministry of Education, Science and Technological Development of Serbia (projects TR35020, III 45016, ON 171038). The authors thank Tatjana Maravić and the team of professor Bojan Petrović (Faculty of Medicine, School of Dental Medicine, University of Novi Sad), especially Aleksandar Jović, for their support in samples preparation. This work was also partially supported by the bilateral Serbian-Chinese project I-2.

References

- [1] M. Goldberg, A.B. Kulkarni, M. Young, A. Boskey, Dentin: structure, composition and mineralization, *Front. Biosci. (Elite Ed)* 3 (2011) 711.
- [2] S.R. Stock, A.C. Deymier-Black, A. Veis, A. Telser, E. Lux, Z. Cai, Bovine and equine peritubular and intertubular dentin, *Acta Biomater.* 10 (2014) 3969.
- [3] J.H. Kinney, M. Balooch, S.J. Marshall, G.W. Marshall JR, T.P. Weihs, Hardness and Young's modulus of human peritubular and intertubular dentine, *Arch. Oral Biol.* 41 (1) (1996) 9–13.
- [4] S.K. Makhijaa, M.E. Robinson, J.D. Bader, D.A. Shugars, M.S. Litaker, H.R. Im, D.B. Rindal, D.J. Pihlstrom, C. Meyerowitz, V.V. Gordan, M.H. Buckberg, G.H. Gilbert, Dentists' decision strategies for suspicious occlusal caries lesions in a national dental PBRN study, *J. Dent.* 69 (2018) 83.
- [5] F. Schwendicke, S. Paris, Y.-K. Tu, Effects of using different criteria for caries removal: a systematic review and network meta-analysis, *J. Dent.* 43 (1) (2015) 1–15.
- [6] G.J. Joves, G. Inoue, A. Sadr, T. Nikaido, J. Tagami, Nanoindentation hardness of intertubular dentin in sound, demineralized and natural caries-affected dentin, *J. Mech. Behav. Biomed. Mater.* 32 (2014) 39–45.
- [7] R. Maev, L. Denisova, E. Maeva, D. AA, New data on histology and physico-mechanical properties of human tooth tissue obtained with acoustic microscopy, *Ultrasound Med. Biol.*, 28 (2002) 131–136.
- [8] K. Raum, K. Kempf, H.J. Hein, J. Schubert, P. Maurer, Preservation of microelastic properties of dentin and tooth enamel in vitro—A scanning acoustic microscopy study, *Dent. Mater.* 2 (3) (2007) 1221–1228.
- [9] A. Shelke, M. Blume, M. Mularczyk, C. Landes, R. Sader, J. Bereiter-Hahn, Visualisation of localized elastic properties in human tooth and jawbone as revealed by scanning acoustic microscopy, *Ultrasound Med. Biol.* 39 (5) (2013) 853–859.
- [10] S. Toda, T. Fujita, H. Arakawa, K. Toda, Nondestructive testing in human teeth using a leaky Lamb wave device, *Ultrasonics* 44 (2006) e1151–e1155.
- [11] K. Sun, L. Yuan, Z. Shen, Q. Zhu, J. Lu, X. Ni, Experimental and numerical studies for nondestructive evaluation of human enamel using laser ultrasonic technique, *Appl. Opt.* 52 (28) (2013) 6896–6905.
- [12] H.-C. Wang, S. Fleming, Y.-C. Lee, M. Swain, S. Law, J. Xue, Laser ultrasonic evaluation of human dental enamel during remineralization treatment, *Biomed. Opt. Express* 2 (2) (2011) 345–355.
- [13] H. Salehi, E. Terrer, I. Panayotov, B. Levallois, B. Jacquot, H. Tassery, F. Cuisinier, Functional mapping of human sound and carious enamel and dentin with Raman spectroscopy, *J. Biophotonics* 6 (2013) 765–774.
- [14] R. Ramakrishnaiah, G. ur Rehman, S. Basavarajappa, A.A. Al Khuraif, B.H. Durgesh, A.S. Khan, I. ur Rehman, Applications of Raman spectroscopy in dentistry: analysis of tooth structure, *Appl. Spectrosc. Rev.* 50 (4) (2015) 332–350.
- [15] C. de, C.A. Lopes, P.H.J.O. Limirio, V.R. Novais, P. Dechichi, Fourier transform infrared spectroscopy (FTIR) application chemical characterization of enamel, dentin and bone, *Appl. Spectrosc. Rev.* 53 (9) (2018) 747–769.
- [16] Z.A. Steelman, D.S. Ho, K.K. Chu, A. Wax, Light-scattering methods for tissue diagnosis, *Optica* 6 (2019) 479–489.
- [17] R. Harley, D. James, A. Miller, J.W. White, Phonons and the elastic moduli of collagen and muscle, *Nature* 267 (1977) 285–287.
- [18] L. Brillouin, Diffusion de la lumière et des rayonnés X par un corps transparent homogène; influence de l'agitation thermique, *Ann. Phys.* 17 (1922) 88–122.
- [19] F. Palombo, D. Fioretto, Brillouin light scattering: applications in biomedical sciences, *Chem. Rev.* 119 (2019) 7833–7847.
- [20] J. Randall, J.M. Vaughan, S. Cusak, Brillouin scattering in systems of biological significance, *Philos. Trans. R. Soc. A* 293 (1979) 341–348.
- [21] F. Palombo, C.P. Winlove, R.S. Edginton, E. Green, N. Stone, S. Caponi, M. Madami, D. Fioretto, Biomechanics of fibrous proteins of the extracellular matrix studied by Brillouin scattering, *J. R. Soc. Interface* 11 (2014) 20140739.
- [22] J.M. Vaughan, J.T. Randall, Brillouin scattering, density and elastic properties of the lens and cornea of the eye, *Nature* 284 (5755) (1980) 489–491.
- [23] G. Scarcelli, S.H. Yun, Confocal Brillouin microscopy for three-dimensional mechanical imaging, *Nat. Photonics* 2 (1) (2008) 39.
- [24] S. Lees, N.J. Tao, S.M. Lindsay, Studies of compact hard tissues and collagen by means of Brillouin light scattering, *Connect. Tissue Res.* 24 (3–4) (1990) 187–205.
- [25] R. Tsubota, K. Fukui, and M. Matsukawa, “Local ultrasonic wave velocities in trabeculae measured by micro-Brillouin scattering,” *J. Acoust. Soc. Am.*, vol. 2, pp. EL109–EL114, 135AD.
- [26] V. Mathieu, K. Fukui, M. Matsukawa, M. Kawabe, R. Vayron, E. Soffer, F. Anagnostou, G. Haiat, Micro-Brillouin scattering measurements in mature and newly formed bone tissue surrounding an implant, *J. Biomech. Eng.* 133 (February) (2011) 021006-1-021006-6.
- [27] M. Oheim, D. Michael, M. Geisbauer, M. Dorte, R. Chow, Principles of two-photon excitation fluorescence microscopy and other nonlinear imaging approaches, *Adv. Drug Deliv. Rev.* 58 (2006) 788–808.
- [28] R. Elbaum, E. Tal, A.I. Perets, D. Oron, D. Ziskind, Y. Silberberg, H.D. Wagner, Dentin micro-architecture using harmonic generation microscopy, *J. Dent.* 35 (2) (2007) 150–155.
- [29] A. Misra, V. Singh, R. Parthasarathy, Material-tissue Interfacial phenomena: Challenges in Mathematical Modeling, Elsevier Ltd, 2016.
- [30] S.H. Yun, D. Chernyak, Brillouin microscopy: assessing ocular tissue biomechanics, *Curr. Opin. Ophthalmol.* 29 (4) (2018) 299–305.

- [31] S. Sauro, V.P. Feitosa, T.F. Watson, D.H. Pashley, Therapeutic bonding approaches to remineralize dentin-bonded interfaces, *Dent. Mater.* 32 (Supplement 1) (2016) e3–e4.
- [32] M. Hashimoto, H. Ohno, H. Sano, M. Kaga, H. Oguchi, In vitro degradation of resin–dentin bonds analyzed by microtensile bond test, scanning and transmission electron microscopy, *Biomaterials* 24 (2003) 3795–3803.
- [33] M. Oliveir, F. Chasqueira, S. Arantes-Oliveira, S. Pessanha, The use of micro-Raman spectroscopy for the analysis of caries-affected dentin adhesive interfaces, *Int. J. Adhesion Adhesives* 87 (2020) 216–222.
- [34] S. Sauro, R. Osorio, T.F. Watson, M. Toledano, Influence of phosphoproteins ' biomimetic analogs on remineralization of mineral-depleted resin – dentin interfaces created with ion-releasing resin-based systems, *Dent. Mater.* 31 (7) (2015) 759–777.
- [35] J. Margueritat, A. Virgone-Carlotta, S. Monnier, H. Delanoë-Ayari, H.C. Mertani, A. Berthelot, Q. Martinet, X. Dagany, C. Rivière, J.-P. Rieu, T. Dehoux, High-frequency mechanical properties of tumors measured by Brillouin light scattering, *Phys. Rev. Lett.* 122 (2019) 018101.
- [36] Regine Gradl, Irene Zanette, Maite Ruiz-Yaniz, Martin Dierolf, Alexander Rack, Paul Zaslansky, Franz Pfeiffer, Mass density measurement of mineralized tissue with grating-based X-Ray phase tomography, *PLoS One* 11 (2016) e0167797.
- [37] I. Hariiri, A. Sadr, Y. Shimada, J. Tagami, Y. Sumi, Effects of structural orientation of enamel and dentine on light attenuation and local refractive index: an optical coherence tomography study, *J. Dentistry* 40 (2012).
- [38] J.H. Kinney, S.J. Marshall, G.W. Marshall, The mechanical properties of human dentin: a critical review and re-evaluation of the dental literature, *Crit. Rev. Oral. Biol. Med.* 14 (2003) 13–29.
- [39] G. Kossoff, C.J. Sharpe, Examination of the contents of the pulp cavity in teeth, *Ultrasonics* 4 (1966) 77–83.
- [40] S. Lees, F.R. Rollins, Anisotropy in hard dental tissues, *J. Biomech.* 5 (1972) 557–566.
- [41] T. Cloitre, I.V. Panayotov, H. Tassery, C. Gergely, B. Levallois, F.J. Cuisinier, Multiphoton imaging of the dentine-enamel junction, *J. Biophotonics* 6 (2013) 330–337.
- [42] M. Rabasović, D. Pantelić, B. Jelenković, S. Čurčić, M. Rabasović, M. Vrbica, et al., Nonlinear microscopy of chitin and chitinous structures: a case study of two cave-dwelling insects, *J. Biomed. Opt.* 20 (2015) 016010.
- [43] K. Bukara, S.Z. Jovanić, I.T. Drvenica, A. Stančić, V. Ilić, M.D. Rabasović, D.V. Pantelić, B.M. Jelenković, B. Bugarski, A.J. Krmpot, Mapping of hemoglobin in erythrocytes and erythrocyte ghosts using two photon excitation fluorescence microscopy, *J. Biomed. Opt.* 22 (2017) 026003.
- [44] D. Zaytsev, S. Grigoriev, P. Panfilov, Deformation behavior of root dentin under Sjogren's syndrome, *Mater. Lett.* 65 (2011) 2435–2438.
- [45] Y. Yoon, Estimation of the elastic constants of dentin, *Int. J. Precision Eng. Manufact.* 14 (2013) 317–322.
- [46] S. Seyedkavoosi, I. Sevostianov, Multiscale micromechanical modeling of the elastic properties of dentin, *J. Mech. Behav. Biomed. Mater.* 100 (2019) 103397.
- [47] Y.-R. Zhang, W. Du, X.-D. Zhou, H.-Y. Yu, Review of research on the mechanical properties of the human tooth, *Int. J. Oral Sci.* 6 (2014) 61–69.
- [48] J.H. Kinney, J.R. Gladden, G.W. Marshall, S.J. Marshall, J.H. So, J.D. Maynard, Resonant ultrasound spectroscopy measurements of the elastic constants of human dentin, *J. Biomech.* 37 (2004) 437–441.
- [49] O. Marangos, A. Misra, P. Spencer, B. Bohaty, J.L. Katz, Physico-mechanical properties determination using microscale homotopic measurements: application to sound and caries-affected primary tooth dentin, *Acta Biomater.* 5 (2009) 1338–1348.
- [50] C.J. Montrose, V.A. Solov'yev, T.A. Litovitz, Brillouin scattering and relaxation in liquids, *J. Acoust. Soc. Am.* 43 (1968) 117.
- [51] L. Breschi, T. Maravic, S.R. Cunha, A. Comba, M. Cadenaro, L. Tjäderhane, D.H. Pashley, F.R. Tay, A. Mazzoni, Dentin bonding systems: from dentin collagen structure to bond preservation and clinical applications, *Dent. Mater.* 34 (2018) 78–96.
- [52] P. Spencer, Q. Ye, J. Park, E.M. Topp, A. Misra, Y. Wang, B.S. Bohaty, V. Singh, F. Sene, J. Eslick, J.L. Katz, Adhesive/dentin interface: the weak link in the composite restoration, *Ann. Biomed. Eng.* 38 (6) (2011) 1989–2003.
- [53] T. Maravić, L. Breschi, A. Comba, S.R. Cunha, V. Angeloni, C. Nuccia, J. Hebling, D. Pashley, F. Tay, A. Mazzoni, Experimental use of an acrolein-based primer as collagen cross-linker for dentine bonding, *J. Dent.* 68 (2018) 85–90.
- [54] Z. Zhang, M. Mutlay, A. Tezvergil-Mutlay, F.R. Tay, D.H. Pashley, D. Arola, Effects of EDC crosslinking on the stiffness of dentin hybrid layers evaluated by nanoDMA over time, *Dent. Mater.* 33 (2017) 904–914.
- [55] K. Raum, Microelastic imaging of bone, *IEEE Trans. Ultrason. Ferroelec. Freq. Control* 55 (2008) 1418–1431.
- [56] J. Kushibiki, K.L. Ha, H. Kato, N. Chubachi, F. Dunn, Application of acoustic microscopy to dental material characterization, in: *Proceedings of the Ultrasonics Symposium*, 1987.
- [57] R. Wang, L. Niu, Q. Li, Q. Liu, H. Zuo, The peritubular reinforcement effect of porous dentine microstructure, *PLoS One* 12 (2017) 1–15.
- [58] G.J. Joves, G. Inoue, A. Sadr, T. Nikaido, J. Tagami, Nanoindentation hardness of intertubular dentin in sound, demineralized and natural caries-affected dentin, *J. Mech. Behav. Biomed. Mater.* 32 (2014) 39–45.
- [59] H. Ryou, E. Romberg, D.H. Pashley, F.R. Tay, D. Arola, Nanoscopic dynamic mechanical properties of intertubular and peritubular dentin, *J. Mech. Behavior Biomed. Mater.* 7 (2012) 3–16.
- [60] M. Yahyazadehfar, D. Zhang, D. Arola, On the importance of aging to the crack growth resistance of human enamel, *Acta Biomater.* 32 (2016) 264–274.
- [61] T. Sui, A.J.G. Lunt, N. Baimpas, M.A. Sandholzer, T. Li, K. Zeng, G. Landini, A.M. Korsunsky, Understanding nature's residual strain engineering at the human dentine–enamel junction interface, *Acta Biomater.* 32 (2016) 256–263.
- [62] S. Liaqat, A. Aljabo, M. Khan, H. Ben Nuba, L. Bozec, P. Ashley, A. Young, Characterization of dentine to assess bond strength of dental composites, *Materials* 8 (2015) 2110–2126.
- [63] M. Özcan, M. Jonasch, Effect of cyclic fatigue tests on aging and their translational implications for survival of all-ceramic tooth-borne single crowns and fixed dental prostheses, *J. Prosthodont.* 27 (2018) 364–375.

Functional Fluorescence Microscopy Imaging: Quantitative Scanning-Free Confocal Fluorescence Microscopy for the Characterization of Fast Dynamic Processes in Live Cells

Aleksandar J. Krmpot,^{◆,‡,§} Stanko N. Nikolić,^{◆,‡} Sho Oasa,^{◆,§} Dimitrios K. Papadopoulos,^{§,†,§} Marco Vitali,^{||} Makoto Oura,[⊥] Shintaro Mikuni,[⊥] Per Thyberg,[#] Simone Tisa,[¶] Masataka Kinjo,[⊥] Lennart Nilsson,^{∇,§} Lars Terenius,^{◆,§} Rudolf Rigler,^{*,◆,○,§} and Vladana Vukojević^{*,◆,§}

[◆]Department of Clinical Neuroscience (CNS), Center for Molecular Medicine (CMM), Karolinska Institutet, Stockholm 17176, Sweden

[‡]Institute of Physics Belgrade, University of Belgrade, Belgrade 11080, Serbia

[§]Max-Planck Institute for Molecular Cell Biology and Genetics, Dresden 01307, Germany

^{||}Sicoya GmbH, Berlin 12489, Germany

[⊥]Laboratory of Molecular Cell Dynamics, Faculty of Advanced Life Science, Hokkaido University, Sapporo, Hokkaido 001-0021, Japan

[#]Department of Applied Physics, AlbaNova University Center, Royal Institute of Technology, Stockholm 10691, Sweden

[¶]Micro Photon Devices (MPD), Bolzano 39100, Italy

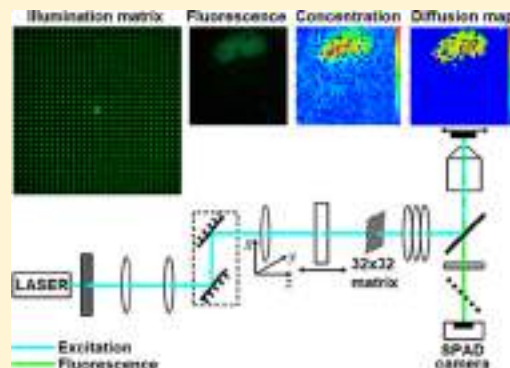
[∇]Department of Biosciences and Nutrition, Karolinska Institutet, Huddinge 14183, Sweden

[○]Department of Medical Biochemistry and Biophysics (MBB), Karolinska Institutet, Stockholm 17177, Sweden

Supporting Information

ABSTRACT: Functional fluorescence microscopy imaging (fFMI), a time-resolved (21 μ s/frame) confocal fluorescence microscopy imaging technique without scanning, is developed for quantitative characterization of fast reaction-transport processes in solution and in live cells. The method is based on massively parallel fluorescence correlation spectroscopy (FCS). Simultaneous excitation of fluorescent molecules in multiple spots in the focal plane is achieved using a diffractive optical element (DOE). Fluorescence from the DOE-generated 1024 illuminated spots is detected in a confocal arrangement by a matching matrix detector comprising 32×32 single-photon avalanche photodiodes (SPADs). Software for data acquisition and fast auto- and cross-correlation analysis by parallel signal processing using a graphic processing unit (GPU) allows temporal autocorrelation across all pixels in the image frame in 4 s and cross-correlation between first- and second-order neighbor pixels in 45 s. We

present here this quantitative, time-resolved imaging method with single-molecule sensitivity and demonstrate its usefulness for mapping in live cell location-specific differences in the concentration and translational diffusion of molecules in different subcellular compartments. In particular, we show that molecules without a specific biological function, e.g., the enhanced green fluorescent protein (eGFP), exhibit uniform diffusion. In contrast, molecules that perform specialized biological functions and bind specifically to their molecular targets show location-specific differences in their concentration and diffusion, exemplified here for two transcription factor molecules, the glucocorticoid receptor (GR) before and after nuclear translocation and the Sex combs reduced (Scr) transcription factor in the salivary gland of *Drosophila* ex vivo.



The living cell is a complex dynamic system where local concentrations and spatial distribution of molecules are perpetually changing. Living cells control the concentration and spatial distribution of biological molecules through molecular interactions and transport processes. Through reaction-transport processes, biomolecules are integrated over space and time into dynamical self-regulatory networks and perform complex, life-sustaining functions, such as gene transcription and signal

transduction. To understand how these complex biological functions emerge through random motion and molecular collisions, the concentration and mobility of biological molecules need to be quantitatively characterized in live cells.^{1,2}

Received: April 13, 2019

Accepted: July 31, 2019

Published: July 31, 2019

So far, fluorescence microscopy techniques, confocal laser scanning microscopy (CLSM)^{3–10} and fluorescence correlation spectroscopy (FCS)^{11–16} in particular, have proven to be indispensable for such studies. However, despite their great versatility, CLSM and FCS also have limitations. Most notably, CLSM imaging is not directly quantitative; while fluorescence is inherently quantitative and fluorescence intensity is proportional to the number of molecules, involved calibration experiments are needed to relate the signal intensity measured using a CLSM system to the number of molecules.¹⁷ Moreover, because of the heterogeneous chemical composition inside different subcellular compartments or because of different conditions in different cells (e.g., pH, oxidative stress, crowding), fluorescent molecules are not necessarily in the same local environment. Hence, their brightness may be different.¹⁸ Under such circumstances, the difference in fluorescence intensity need not necessarily reflect differences in molecular numbers but may rather reflect differences in molecular brightness due to local differences in environmental conditions.

In addition, the temporal resolution of CLSM is low. In CLSM, the acquisition at the level of individual pixels is fast, in the order of microseconds, but the acquisition of an image frame is slow, lasting more than a quarter of a second for a 512×512 pixels image. On top of this, the signals in a CLSM image are not acquired at the same point in time, and there is always a time lag between the signals acquired in individual pixels. The temporal resolution of CLSM can be improved by scaling down the number of pixels, i.e., by reducing the area from which the signal is acquired. This, however, results in loss of overview. Classical single-point FCS (spFCS) is also hampered by limited overview, providing quantitative information in a minute observation volume element (OVE) that is typically $0.2\text{--}2.0$ fl (μm^3). Hence, to acquire quantitative information from several locations in a cell using the conventional spFCS setup, spFCS measurements need to be performed successively, which is not suitable for the study of fast dynamical processes.

To overcome these limitations, specific illumination techniques are used to irradiate a larger area in the sample and the signal is simultaneously recorded from different locations using array detectors. Following the pioneering work at the beginning of this millennium,^{19–22} several different experimental realizations of multiplexed FCS have been reported.^{23–36} These inventions have significantly advanced our capacity to characterize the spatiotemporal dynamics of complex biological transformations and approach challenging biological problems from the holistic point of view.^{24,26,28,33,35,37–48} However, further improvements are needed in order to develop instrumentation with better temporal resolution and with data acquisition and analysis software that are sufficiently robust for reliable routine application in biomedical research.

We present here a setup for quantitative, time-resolved confocal fluorescence microscopy imaging without scanning that is based on massively parallel FCS (mpFCS) measurements, where a diffractive optical element (DOE) and a matching matrix single-photon avalanche photodiode (SPAD) camera are used to achieve massively parallel confocal arrangement.^{32,34,38} We show that this approach can map the local concentration and translational diffusion coefficients of molecules in live cells. Since these properties are tightly linked to biomolecular activity at functional sites and are crucial for understanding their mechanisms of action, we call this method functional fluorescence microscopy imaging (fFMI).

MATERIALS AND METHODS

fFMI Instrumental Setup. The fFMI system consists of an inverted epi-fluorescence microscope Axio Observer D1 equipped with a C-Apochromat $63\times/1.2$ W Corr objective and a high efficiency filter set (Filter Set 38 HE) for enhanced green fluorescent protein (eGFP) consisting of an excitation bandpass filter EX BP 470/40 nm (central wavelength/bandwidth), long pass dichroic mirror with a cutoff wavelength of 495 nm, and an emission band pass filter EM BP 525/50 (all from Carl Zeiss, Germany); a continuous wave (CW) 488 nm frequency-doubled diode laser Excelsior 488 (Spectra-Physics, France); a telescopic laser beam expander; a double filter wheel with 10 (5 + 5) uniform neutral density filters of different optical density (OD) to enable a wide range of attenuation (OD 0.2–8.0) in discrete steps (Thorlabs Inc., USA); a diffractive optical element (DOE) specially designed to split the single laser beam into 32×32 beams (Holoeye, Germany); a Single Photon Counting Camera SPC² that enables parallel single photon counting by means of a monolithic 32×32 array (Micro Photon Devices MPD, Italy).³² These elements were assembled on an optical table with active vibration damping (Technical Manufacturing Corporation TMC, USA) using standard optomechanical components (Newport Corporation, USA, and Thorlabs Inc., USA). To enable fast sample localization, an 18.0 megapixel digital single-lens reflex (DSLR) camera Canon EOS 600D (Canon Inc., Japan) with a pixel size of $18.5 \mu\text{m}^2$ and a pixel pitch of $4.3 \mu\text{m}$ (http://snapsort.com/compare/Canon-600d-vs-Canon_EOS_550D/specs) was coupled to the side port opposite to the SPAD camera, and the light path between the two camera ports was manually switched.

Raw data, i.e., photon counts, acquired by the SPAD camera were transferred to a Dell Precision Fixed Workstation T5600-Xeon E5-2620 2 GHz equipped with an NVIDIA GeForce GTX 780 graphic card containing 2304 compute unified device architecture (CUDA) cores that were used for fast data analysis by auto- and cross-correlation.

LSM 510 ConfoCor 3 System. An individually modified ConfoCor 3 instrument (Carl Zeiss, Germany) for laser scanning fluorescence microscopy imaging and for spFCS was used as a reference.⁴⁶ spFCS data were analyzed using the program for data analysis in the running software package and the scientific graphing and data analysis software Origin (OriginLab).

Software for fFMI. The software for data acquisition and analysis was written in Embarcadero C++ Builder XE7 (Embarcadero Technologies, USA).

RESULTS

Instrumental Design. Key elements of the instrumental design, highlighted in Figure 1a and insets a₁–a₃, describe the underlying working principle. Briefly, collimated light from the single-beam CW laser is expanded and led to an achromatic doublet lens (focal length $f = 150$ mm) mounted on a precise x – y – z translation stage (Figure 1a, focusing lens), which focuses the expanded and collimated laser beam on the DOE mounted on a single-axis precise translation stage (Figure 1a, DOE). By filling the aperture of the DOE, the diffraction pattern consisting of 32×32 well-separated illumination spots and the zeroth-order diffraction maximum in the center is formed in the focal plane of the focusing lens that coincides with the image plane of the rear port of the inverted epi-fluorescence microscope (Figure 1a, rear port image plane). Formation of the spot-wise

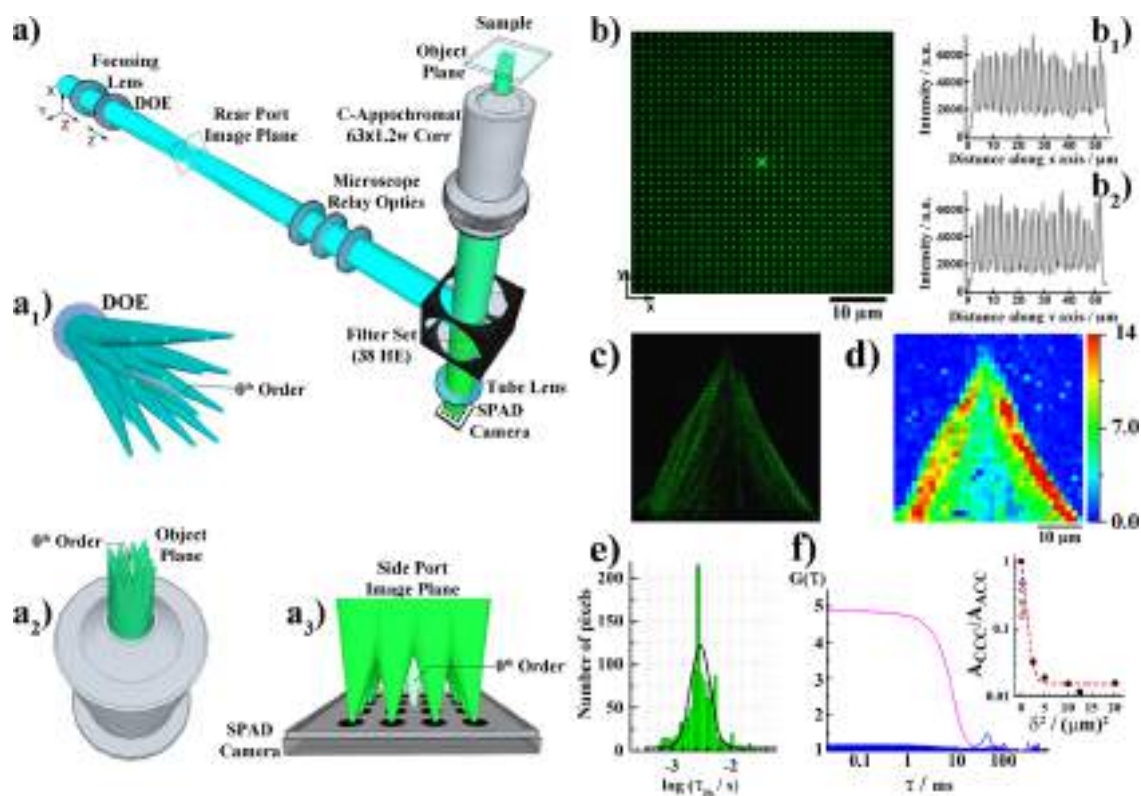


Figure 1. Instrumental setup for functional fluorescence microscopy imaging (fFMI). (a) Schematic presentation of the optical arrangement in the fFMI instrument. The expanded single laser beam is focused by the focusing lens on the diffractive optical element (DOE). The illumination matrix of 32×32 laser beam spots (here depicted as a 4×4 matrix for simplicity) is formed at the image plane of the rear port of the microscope. Inset: Formation of the ordered spotty pattern at three characteristic planes: (a_1) in the rear port image plane, (a_2) in the object plane, and (a_3) in the side port image plane. Of note, the zeroth-order diffraction peak falls exactly between 4 central pixels of the SPAD camera when the fFMI system is fully aligned and is therefore not detected by the SPAD camera. (b) Image of the illumination matrix generated in the focal plane of the microscope objective. A thin layer formed by drying of a concentrated Rhodamine 6G (Rh6G) solution was used as the sample, and the image was acquired by the 18.0 megapixel digital single-lens reflex (DSLR) camera. The zeroth-order diffraction peak is readily visible when using the pixel-dense DSLR camera. Inset: Fluorescence intensity profiles along (b_1) the x -axis and (b_2) the y -axis show that the sample is illuminated in a distinct pattern of 32×32 spots. The pitch (the shortest distance between two adjacent spots) of the illumination matrix in the sample plane is $1.587 \mu\text{m}$. (c) Image of filamentous actin in fixed muntjac skin fibroblast cells acquired under spot-wise illumination using the 18.0 megapixel DSLR camera. (d) Image of the sample described in (c) acquired by the SPAD camera. Signal acquisition time = 1 ms. Fluorescence intensities ranged from 0 (dark blue) to $\geq 13\,700$ photons per second (red). The scale bar is $10 \mu\text{m}$. (e) Distribution of diffusion times in a dilute aqueous suspension of fluospheres, $d = 100 \text{ nm}$, recorded by the fFMI system. The average diffusion time was determined to be $\tau_D = (3 \pm 2) \text{ ms}$. (f) ACC recorded in an individual pixel, i.e., by an individual SPAD in the SPAD matrix detector (magenta). Cross-correlation curves (CCCs) derived by cross-correlating the signals recorded in this particular SPAD and its first- and second-order neighbors (blue). Inset: (f_1) Amplitude of the CCCs (blue) normalized to the amplitude of the ACC (magenta), $A_{\text{CCC}}/A_{\text{ACC}}$, as a function of the squared distance between neighboring OVEs (δ). As expected, the amplitudes of the CCCs decay exponentially with the distance between neighboring OVEs squared,⁴⁷ and the data from this study (black dots) agree well with results reported in the literature: Buchholz, PhD Thesis (CCC1 and CCC2, Figure 6.4; red circles),⁴⁸ Dertinger et al. (Figure 6; blue triangle),⁴⁷ Ries and Schwille (Figure 4; green inverted triangle),⁴⁹ and Ries et al. (Figure 2d; lilac diamond).⁵⁰ The relative amplitude $A_{\text{CCC}}/A_{\text{ACC}} = 1$ at OVE distance $\delta = 0$ corresponds to cross-correlation of fluorescence intensity fluctuations in the reference pixel to itself. The fitted single-exponential decay curve (red, dashed) shows that the amplitude of the CCC decays exponentially with δ^2 .⁴⁷

illumination pattern is schematically depicted in Figure 1, inset a_1 , featuring for the sake of clarity an array of 4×4 spots with the clearly indicated zeroth-order diffraction maximum. The relay optics of the rear port of the microscope (Figure 1a, microscope relay optics), the dichroic mirror (integrated in the Filter Set 38 HE), and the objective lens project the illumination matrix from the rear port into the focal plane of the objective (Figure 1a, object plane; Figure 1, inset a_2). A uniform thin layer of dried Rh6G was used to visualize the illumination matrix. The image acquired using the pixel-dense DSLR camera shows that the sample is illuminated in a distinct spot-wise array of 32×32 well-separated points of similar intensity, except for the zeroth-order diffraction spot visible in the center (Figure 1b). Corresponding fluorescence intensity distribution profiles

along the x and y axes are shown in Figure 1, insets b_1 and b_2 , respectively.

After passing through the dichroic mirror and the emission filter integrated in the Filter Set 38 HE, the spot-wise fluorescence matrix is imaged by the objective and the tube lenses onto the SPAD camera (Figure 1a and inset a_3). The SPAD camera is attached to one of the two side ports of the microscope, with the DSLR camera being attached to the other side and used for fast sample localization using standard wide-field imaging. The SPAD camera contains a photosensitive chip and a 16-bit photon counter based on a field programmable gate array (FPGA). The photosensitive area of the chip consists of 32×32 circular SPADs that are $20 \mu\text{m}$ in diameter. The distance between adjacent diodes along a row/column, i.e., the pitch of

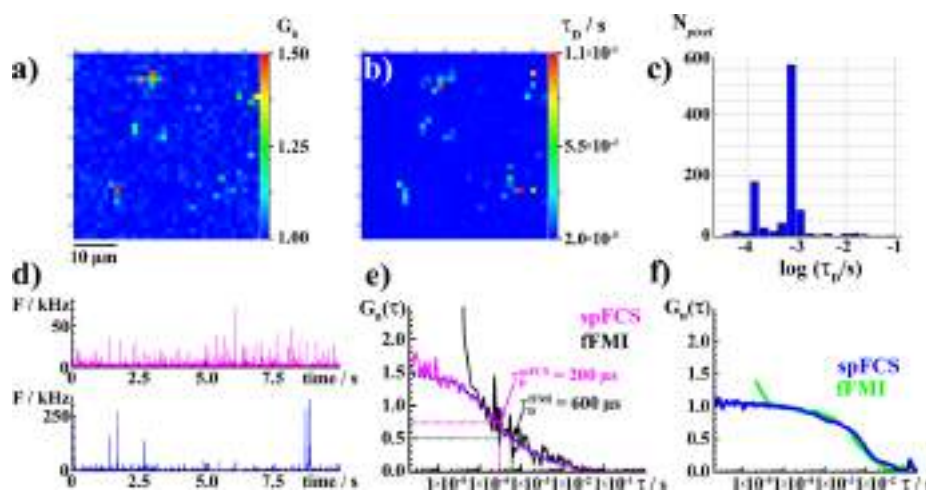


Figure 2. fFMI instrument calibration and performance characterization using a dilute aqueous suspension of quantum dots. (a) Spatial map of amplitudes (G_0) of individual ACCs at the lag time $\tau = 103.7 \mu\text{s}$, acquired by fFMI. Fluorescence intensity fluctuations were recorded in a single measurement lasting 2.7 s. (b) Corresponding spatial map of translational diffusion times (τ_D). (c) Diffusion time distribution histogram corresponding to the data shown in (b). (d) Fluorescence intensity fluctuations recorded in the same sample as in (a–c) acquired using a conventional spFCS system. Fluorescence intensity bursts of different intensities (note the different scales on the ordinates) reveal that the dilute quantum dot suspension is polydisperse, containing single quantum dots (magenta) and a significantly lower amount of very bright quantum dot agglomerates that were sporadically observed (blue trace). (e) ACCs normalized to the same amplitude, $G_n(\tau) = 1$ at lag time $\tau = 103.7 \mu\text{s}$, obtained by temporal autocorrelation analysis of fluorescence intensity fluctuations reflecting diffusion of single quantum dots. The ACCs were acquired by fFMI (black) and spFCS (magenta). The black ACC is an average ACC acquired from 10 consecutive fFMI recordings of fluorescence intensity fluctuations in a single SPAD, i.e., in a single OVE/single pixel, each measurement lasting 2.7 s. The magenta ACC is acquired from the fluorescence intensity fluctuation time series of 10 s. The dotted blue line shows fitting of the magenta ACC. (f) ACCs normalized to the same amplitude, $G_n(\tau) = 1$ at lag time $\tau = 103.7 \mu\text{s}$, reflecting diffusion of sparse quantum dot agglomerates, acquired by fFMI in a single pixel and in a 2.7 s measurement (blue) and by spFCS (green).

the camera, is $100 \mu\text{m}$. Further details on the SPAD camera design and performance can be found in refs 32 and 51–53. Since the aperture of every SPAD is a pinhole positioned in the conjugate focal plane with respect to the illumination matrix, confocal configuration is achieved for all 32×32 foci.

By imaging the complex spatial distribution of filamentous actin in fixed muntjac skin fibroblast cells, we could verify that there is no significant loss of information due to interspaced sampling (Figure 1c,d). Images acquired by the pixel-dense DSLR camera (Figure 1c) and the SPAD camera (Figure 1d) clearly show that the SPAD camera veritably reflects the spatial distribution of actin filaments over long distances.

In a well-aligned fFMI system, similar values for the translational diffusion time are obtained in the majority of pixels, and the distribution of diffusion times across the whole matrix is narrow, exemplified here for a measurement performed in a dilute aqueous suspension of 100 nm fluospheres (Figure 1e). The measured diffusion time, $\tau_D = (3 \pm 2) \text{ms}$ (Figure 1e), is in good agreement with the value obtained using the reference spFCS system, $\tau_D = (2.5 \pm 0.5) \text{ms}$ (see fFMI Instrument Calibration and Performance Characterization for details on instrument calibration).

Finally, cross-correlation of signals recorded in a reference pixel with the signal recorded in its first- and second-order neighbors showed that there is virtually no cross-talk between neighboring SPADs, as is evident from the relatively small amplitude of the CCCs (Figure 1f, blue) that is less than 4% of the amplitude of the ACC (Figure 1f, magenta). The Supporting Information contains details of the software for data analysis, the calculation of auto- and cross-correlation curves, and image rendering (Section S1), cell culture (Section S2), instrument alignment (Section S3, Figure S1), OVE size determination

(Section S4, Figure S2), and accuracy, precision, and sensitivity (Section S5, Figure S3).

fFMI Instrument Calibration and Performance Characterization. A dilute aqueous suspension of carboxylate functionalized quantum dots (2 nM) was used to compare the fFMI instrument performance with respect to the conventional spFCS system used as a reference. For this purpose, fFMI and conventional spFCS measurements were performed on the same sample (Figure 2a–f). To have similar conditions in both experiments, the illumination intensity in the conventional spFCS instrument was set to $14.8 \mu\text{W}$ at the microscope objective lens, in order to match the intensity in individual foci of the fFMI instrument, which was estimated to be $1/1024$ of the intensity measured at the microscope objective (18.9mW) reduced by 20% to account for the intensity of the zeroth-order diffraction peak.

Both fFMI and spFCS revealed that, despite prolonged sonication, the quantum dots suspension is polydisperse, being made up of individual quantum dots present in large excess (Figure 2a,b (blue pixels), Figure 2d (top), and corresponding ACCs in Figure 2e) but also containing a small amount of very bright quantum dot agglomerates of different sizes (Figure 2a,b (green-red pixels), Figure 2d (bottom), and corresponding ACCs in Figure 2f). In measurements using the conventional spFCS instrument, the presence of sparse agglomerates could be readily revealed in some but not all recordings (Figure 2d, the magenta time series exemplifies a measurement where quantum dot agglomerates were not observed), whereas fFMI revealed in a single shot that the quantum dot suspension is polydisperse and provided the spatial localization of agglomerates at the moment of measurement, as is evident from the map of ACC amplitudes, G_0 , (Figure 2a, green-red pixels), the translational

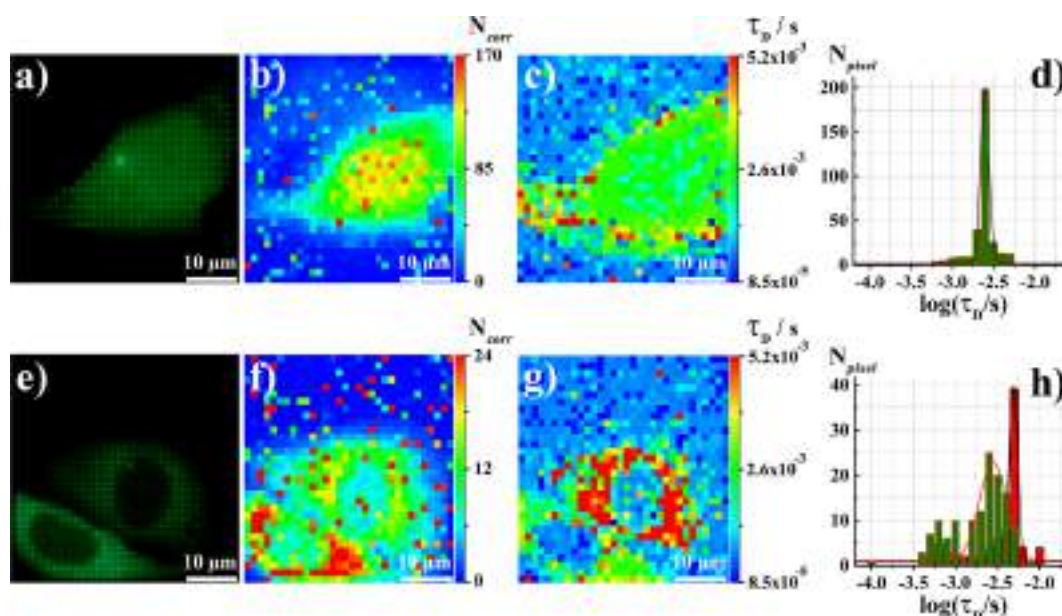


Figure 3. Spatial distribution of molecular numbers and diffusion time maps in live U-2 OS cells expressing monomeric or tetrameric eGFP. (a) 18.0 megapixel DSLR image of a spot-wise illuminated U-2 OS cell expressing monomeric eGFP. (b) Spatial distribution of molecular numbers (N_{corr}) across an optical section in the cell, with slight eGFP accumulation in the nucleus. (c) eGFP diffusion times (τ_D) across the same section as in (b). (d) The corresponding τ_D distribution histogram shows that eGFP mobility inside the cell is rather uniform, $\tau_D = (2.5 \pm 0.5)$ ms. (e) DSLR image of two cells expressing eGFP₄, acquired as described in (a). (f) Molecular numbers (N_{corr}) map reveals eGFP₄ prevalence in the cytoplasm. (g) eGFP₄ diffusion time map in two adjacent cells. In the upper cell, the average diffusion time, $\tau_D = (5.0 \pm 0.8)$ ms, is two times longer than the diffusion time measured for eGFP in (d). This is in agreement, within the experimental error, with the expected theoretical difference of 1.6 times. In the lower cell, where eGFP₄ degradation was observed, the average nuclear concentration was higher than in the upper cell, $N_{\text{corr}}^{\text{cell}} \approx 12$ versus $N_{\text{corr}}^{\text{cell}} \approx 6$; τ_D was the same as in cells expressing monomeric eGFP, and a wider distribution of diffusion times ((h), green histogram, versus (d)) was observed. (h) Diffusion time distribution histograms in the upper (red) and the lower (green) cell shown in (g).

diffusion time, τ_D , map (Figure 2b, green-red pixels), and the distribution of diffusion times (Figure 2c).

Both, the conventional spFCS and the fFMI system, showed marked differences in diffusion times between single quantum dots, $\tau_{D,\text{sqd}}^{\text{spFCS}} = (200 \pm 50)$ μs (Figure 2e), and quantum dot agglomerates, $\tau_{D,\text{sqda}}^{\text{spFCS}} = (7 \pm 2)$ ms (Figure 2f). Importantly, the characteristic decay times of ACC obtained using the fFMI instrument and the conventional spFCS setup concurred, as is evident from the overlap of the ACCs normalized to the same amplitude, $G_n(\tau) = 1$ at $\tau = 103.7$ μs , for individual quantum dots (Figure 2e) and for quantum dot agglomerates (Figure 2f). This observation is in line with calibration measurements showing that the OVEs in the fFMI system are similar in size to that in the conventional spFCS instrument.

Of note, the average diffusion time for single quantum dots estimated from the diffusion time histogram, $\tau_{D,\text{sqd}}^{\text{hist}} = (600 \pm 100)$ μs (Figure 2c), is evidently longer than the value determined by fitting spFCS data, $\tau_{D,\text{sqd}}^{\text{spFCS}} = (200 \pm 50)$ μs (Figure 2e, magenta). This discrepancy, which is particularly pronounced for molecules/particles with short diffusion times, arises because of the comparatively low temporal resolution of the matrix SPAD detector, due to which plateauing of the ACC cannot be observed (Figure 2e). Consequently, the translational diffusion time, estimated from the full width of the ACC at its half-maximum (Figure 2e, black), will appear to be somewhat longer than what it really is (Figure 2e, magenta). Using fluorospheres of different size, we could demonstrate that, the longer the translational diffusion time, the less pronounced will be this difference, and the diffusion coefficient could be correctly determined (as shown in Section S5, Figure S2).

Small Differences in Translational Diffusion Time between eGFP Monomers and Tetramers Could Be Measured in Live Cells by fFMI. In order to assess the precision of the fFMI system, its capacity to measure small differences in translational diffusion time was probed using live U-2 OS cells expressing monomeric or tetrameric eGFP, eGFP, or eGFP₄, respectively (Figure 3).

fFMI could also measure subtle differences in the translational diffusion between eGFP (Figure 3c,d) and eGFP₄ (Figure 3g,h, red pixels and bars). It showed that translational diffusion of eGFP monomers in U-2 OS cells is rather uniform across the cell, with an average diffusion time $\tau_{D,\text{eGFP}} = (2.5 \pm 0.5)$ ms (Figure 3c,d), whereas the translational diffusion time of eGFP₄ is about two times longer, $\tau_{D,\text{eGFP}_4} = (5.0 \pm 0.8)$ ms (Figure 3g, upper cell; Figure 3h, red histogram). This difference, derived from measurements in 10 cells in each group, is in agreement with the theoretically expected value of 1.6 times.

fFMI also indicated cells where oligomeric forms containing less than four eGFP molecules prevail. Such cells (Figure 3g, lower cell) are identifiable through the shorter translational diffusion time (Figure 3h, green histogram (lower cell) versus the red histogram (upper cell)), higher average nuclear concentration of fluorescent molecules, $N_{\text{corr}}^{\text{cell}} \approx 12$ versus $N_{\text{corr}}^{\text{cell}} \approx 6$ (Figure 3f), and wider distribution of diffusion times (Figure 3h, green histogram, versus Figure 3d). Lower size oligomers can occur due to degradation processes. While eGFP is not efficiently degraded by proteinases, the flexible linker is, due to the specific construction of the plasmid where each eGFP sequence is preceded by an ATG start codon.

Mapping the Heterogeneous Distribution and Dynamics of Molecules in Live Cells by fFMI. Having

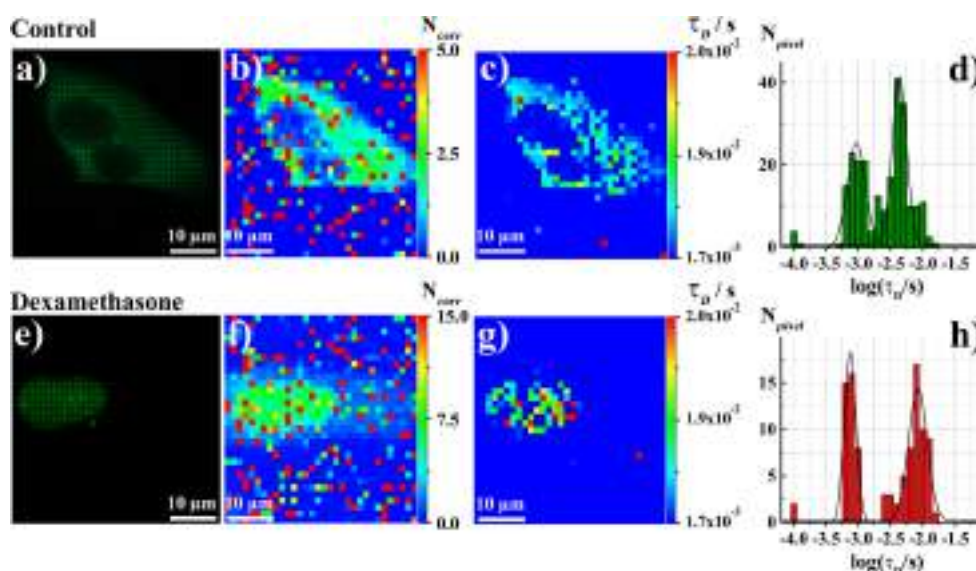


Figure 4. Spatial distribution of molecular numbers and diffusion time maps of glucocorticoid receptors (GR) before and upon ligand-induced nuclear translocation in live U-2 OS cells. (a) DSLR image of a spot-wise illuminated unstimulated U-2 OS cell expressing eGFP-GR_{wt}. (b) fFMI reveals the spatial distribution of eGFP-GR_{wt} numbers (N_{corr}) across an optical section in the cell with their accumulation in the cytoplasm. (c) Spatial distribution of translational diffusion times (τ_D) across the same section as in (b). (d) Diffusion time distribution histogram in the cytoplasm of cells shown in (c). (e) DSLR image showing eGFP-GR_{wt} translocation to the cell nucleus after stimulation with dexamethasone. (f) Spatial distribution of molecular numbers (N_{corr}) reveals eGFP-GR_{wt} translocation from the cytoplasm to the cell nucleus. (g) fFMI map of eGFP-GR_{wt} diffusion times (τ_D), reflecting a patchy distribution due to differences in eGFP-GR_{wt} interactions with the surrounding molecules. (h) Diffusion time distribution histogram in the cell nucleus shown in (g).

established that fFMI can measure small differences in translational diffusion between cells that express uniformly diffusing molecules of different size, we assessed its capacity to map the heterogeneous distribution and nonuniform dynamic behavior of a molecule in the same cell (Figure 4). We have therefore chosen the glucocorticoid receptor (GR), a transcription factor for which the heterogeneous distribution and complex intracellular dynamics are well established and characterized by conventional spFCS.^{54–56}

fFMI readily revealed the nonuniform distribution and uneven diffusion of fluorescently tagged wild type glucocorticoid receptors (eGFP-GR_{wt}) in the cytoplasm of untreated U-2 OS cells (Figure 4a–d), showing that eGFP-GR_{wt} concentration in the periphery is lower, $N_{\text{avg}}^{\text{pr}} \approx 1.25$, and its diffusion time is shorter, $\tau_D^{\text{pr}} = (0.8 \pm 0.2)$ ms, than in the perinuclear region that is enriched in intracellular membranes, $N_{\text{avg}}^{\text{pr}} \approx 2.5$ and $\tau_D^{\text{pr}} = (4.0 \pm 0.5)$ ms.

As expected, treatment of U-2 OS cells with the GR agonist dexamethasone (100 nM Dex) induced eGFP-GR_{wt} translocation from the cytoplasm to the cell nucleus (Figure 4). In the nucleus (Figure 4e–h), eGFP-GR_{wt} partitioned into different domains, showing both an uneven distribution of molecular numbers (Figure 4f) and “patchy” diffusion behavior (Figure 4g), revealing domains where eGFP-GR_{wt} motility is fast and interactions with other molecules are scarce and/or nonspecific, characterized by short diffusion times, as opposed to regions where binding with higher affinities is observed; eGFP-GR_{wt} motion is therefore stalled, and diffusion times are longer.

Mapping Dynamic Processes in the Plasma Membrane of Live Cells by fFMI. The capacity of the fFMI system was tested for quantitative characterization of dynamic processes in the plasma membrane. For this purpose, PC12 cells stably transformed to express a G protein-coupled receptor (GPCR), the wild type μ -opioid receptor fused at the N-terminal end with eGFP (eGFP-MOP), were used to map in live cells its spatial

surface density and lateral diffusion in the plasma membrane (Figure 5). As can be seen, the plasma membrane and the perinuclear region, enriched with membranous structures of the endoplasmic reticulum and the Golgi complex, could be easily distinguished from the remaining cellular compartments and the surroundings by fluorescence intensity imaging using the DSLR camera under spot-wise illumination (Figure 5a). While the map of the average number of molecules in the OVE (N_{corr}) was noisy due to low expression levels of eGFP-MOP (Figure 5b), the translational diffusion time maps could be readily acquired, rendering the plasma membrane and the membranous structures in the perinuclear region clearly visible (Figure 5c). fFMI revealed that the eGFP-MOP diffusion in the plasma membrane (Figure 5d, red) and in membranous structures in the perinuclear region (Figure 5d, blue) is complex, and two principal decay times were identified: $\tau_{D1} = (1.0 \pm 0.5)$ ms and $\tau_{D2} = (100 \pm 20)$ ms (Figure 5d).

Mapping ex Vivo the Heterogeneous Distribution and Dynamics of Molecules in Thick Tissue Specimen by fFMI. While we have established that crosstalk between pixels is not an issue for quantitative characterization of concentration and diffusion in dilute solutions/suspensions (Figure 1f), it is well-known that the main challenge for quantitative fluorescence microscopy imaging of a thick specimen using multifocal optical arrangement arises because out-of-focus light that originates from bright structures in remote focal planes above/below the sample plane can pass through adjacent pinholes. This increases the background signal, i.e., reduces the SNR, and gives rise to hazy images where the details that are normally observed in confocal laser scanning microscopy are obscured in spinning disk confocal microscopy.⁵⁷ In order to probe the capacity of the fFMI system to characterize dynamical processes in thick samples, the concentration and nuclear dynamics of the mCitrine-tagged Sex combs reduced (Scr) dimeric transcription factor (mCitrine-(Scr)₂) were investigated in salivary glands

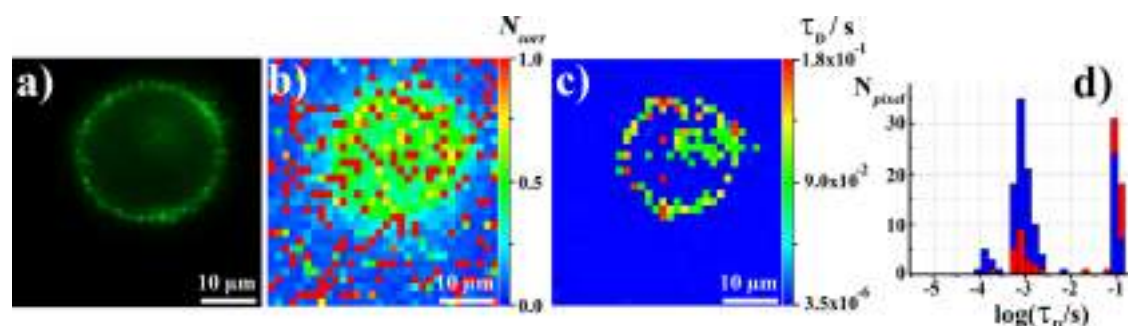


Figure 5. Dynamic lateral organization of mu-opioid receptor in the plasma membrane. (a) DSLR image of a spot-wise illuminated PC12 cell expressing eGFP-MOP. (b) Spatial distribution of eGFP-MOP numbers (N_{corr}) across an optical section in the cell. (c) Spatial distribution of diffusion times (τ_D) across the same section as in (b). (d) Corresponding diffusion time distribution histograms inside the cell (blue) and in the plasma membrane (red).

from *Drosophila* third instar larvae bearing in the genome a multimeric specific binding site of Scr (*fkh250^{con}*; see Section S2 and ref 38 for details). The results are presented in Section S6 and Figure S4.

DISCUSSION

Spatial filtering of fluorescence, which is at the heart of CLSM, is achieved by conjugate focal plane arrangement of optical elements and obstruction of out-of-focus light by detection through a pinhole. This significantly improves the SNR of fluorescence microscopy, enabling optical sectioning and fluorescence imaging with high spatiotemporal resolution and single-molecule sensitivity. Advantages for biomedical research and diagnostics brought about by confocal imaging are so numerous that it has been stated that "...confocal technology is proving to be one of the most important advances ever achieved in optical microscopy."⁵⁸ Confocal configuration was also shown to be critical for FCS;^{59,60} by reducing the size of the OVE, a significantly smaller number of solvent molecules was observed, which efficiently reduced the background and enhanced the signal-to-noise ratio. This, in turn, has enabled single-molecule detection and short measurement time. The possibility to have multiplexed confocal arrangements of excitation and detection pathways is therefore essential for quantitative studies of fast dynamic processes in live cells that require high spatiotemporal resolution and single-molecule sensitivity.

Presently available state-of-the-art instruments for massively parallel FCS measurements, such as the systems described in refs 29 and 31, rely on the use of light sheet illumination and point-wise detection via an electron multiplying charge coupled device (EMCCD) camera²⁹ or a SPAD matrix detector.^{31,36} In these arrangements, a selected plane in the sample is illuminated at a defined z-position by a micrometer-thin light sheet that is perpendicular to the optical axis of the detection objective lens. The advantage of light sheet illumination over a confocal arrangement comes from the specific illumination of an area that is significantly larger than the cross sectional area of the confocal volume element. The disadvantage of light sheet illumination as compared to multiplexed confocal arrangement comes from the nonuniformity of the light sheet over longer distances, which means that the area over which OVEs of the same size are obtained is restricted. In addition, structures in the specimen that absorb/scatter the excitation light distort the light sheet, and the size of the OVEs is not uniform across heterogeneous samples.^{29,31} To circumvent these problems in light sheet based microscopy imaging, the sample needs to be repositioned and

precisely rotated, which is a limiting factor for the study of fast dynamical processes. It also complicates sample preparation and mounting, and sample preparation procedures are considerably more complex for light sheet microscopy than for confocal imaging.⁶¹ Such restrictions do not exist for fFMI. Here, the limit in number of focal spots is set by the intensity of the single-beam laser and the dark count of individual SPADs that comprise the matrix detector.

The advantage of the SPAD matrix detectors over EMCCD cameras primarily lies in the temporal resolution, which is inherently low in EMCCD cameras because of the slow readout and frame-transfer processes. At present, the temporal resolution of EMCCDs is in the millisecond range, at best, whereas the temporal resolution of SPADs is easily in the microsecond and even submicrosecond range. Thus, SPAD matrices hold the promise to significantly improve the temporal resolution of fluorescence microscopy imaging, allowing a 100- to 1000-times better temporal resolution. Furthermore, no analogue measurement of voltage or current is needed for SPADs, so no additional noise is added by the readout process. Finally, the SPAD detector is typically less sensitive than EMCCD to electromagnetic interference due to electromagnetic radiation generated by other equipment.

The disadvantage of SPAD matrix detectors over an EMCCD stems mainly from the variability in dark count rates between individual detectors, which gives a nonuniform SNR over an image frame (Figure 1f). This, however, is not too big a problem for fFMI; while differences in dark count rates affect the signal intensity, the outcome of temporal autocorrelation analysis is not significantly affected and the average number of molecules in the OVE and the diffusion time could still be accurately determined by autocorrelation analysis even though the SNR is not exactly the same in all foci. Of course, this is only possible when the SNR is sufficiently high in all foci. If this is not the case, the amplitude of the autocorrelation curve becomes unreliable.

Another well-known limitation associated with SPADs is related to afterpulsing.^{32,62,63} In the present camera, afterpulsing is observed in the ACCs as a prominent and fast-decaying peak at lag times, $\tau < 100 \mu\text{s}$ (Figure 2e, black; Figure 2f, green; Section S6, Figure S4g, blue). Afterpulsing is more prominently observed in measurements where low signal intensities were measured, e.g., individual quantum dots (Figure 2e, black) versus bright quantum dot agglomerates (Figure 2f, green). However, afterpulsing-related distortion of ACCs may be circumvented by cross-correlating the signals between two detectors,^{32,62} by subtracting the contribution of afterpulsing from the ACCs,⁶³ and by SPAD design.⁶⁴

Despite the limitations of currently available technologies for massive production of SPADs, which restrain the temporal resolution and affect quantitative characterization in live cells as discussed above, the data presented here compellingly show that it is possible to achieve a massively parallel confocal arrangement and quantitative confocal imaging with single-molecule sensitivity without scanning via massively parallel FCS. This yields quantitative confocal imaging with an unprecedented temporal resolution, which in the present setup is 21 $\mu\text{s}/\text{frame}$. We have demonstrated that massively parallel analysis of fluorescence intensity fluctuations by temporal autocorrelation and spatiotemporal cross-correlation analyses can be achieved, yielding 1024 ACCs in about 4 s and about 24 000 CCCs in 45 s. The use of the graphic processing unit (GPU) is a major advantage for the calculation of CCCs, since the number of CCCs is much larger than the number of ACCs. The FPGA approach described in ref 30 calculates ACCs in real time, but the memory constraints would not allow the calculation of CCCs as well. Hence, a combination of these two approaches will likely be the best for future applications.

CONCLUDING REMARKS

The quantitative, time-resolved confocal fluorescence microscopy imaging approach developed here retains the capacity to perform optical sectioning and is empowered by the abolishment of scanning, thus allowing simultaneous data acquisition in all points in an image frame with a submillisecond temporal resolution (here 21 $\mu\text{s}/\text{frame}$). It provides, with diffraction limited spatial resolution, quantitative information about location-specific differences in the concentration and mobility of the molecules, which cannot be otherwise deduced. The possibility to characterize the fast cellular dynamics of molecules: quantitatively, nondestructively, with the ultimate sensitivity and with unprecedented temporal resolution, enables us to address how biomolecules are integrated via chemical reactions and transport processes into dynamical self-regulated networks through which emergent properties, such as gene transcription and signal transduction, arise at the higher level of organization and at longer spatio-temporal scales.

ASSOCIATED CONTENT

Supporting Information

The Supporting Information is available free of charge on the ACS Publications website at DOI: 10.1021/acs.analchem.9b01813.

Details of software for data analysis and calculation of auto- and cross-correlation curves, image rendering, cell culture, and instrument alignment along with imaging in a thick tissue specimen (PDF)

AUTHOR INFORMATION

Corresponding Authors

*E-mail: Vladana.Vukojevic@ki.se.

*E-mail: Rudolf.Rigler@ki.se.

ORCID

Aleksandar J. Krmpot: 0000-0003-2751-7395

Sho Oasa: 0000-0003-3800-590X

Dimitrios K. Papadopoulos: 0000-0003-0914-3051

Lennart Nilsson: 0000-0002-5067-6397

Lars Terenius: 0000-0003-2880-9576

Rudolf Rigler: 0000-0003-4742-0857

Vladana Vukojević: 0000-0003-0873-5653

Present Address

[†]D.K.P.: MRC Human Genetics Unit, Institute of Genetics and Molecular Medicine, University of Edinburgh, Edinburgh EH4 2XU, UK.

Author Contributions

The manuscript was written through contributions of all authors. All authors have given approval to the final version of the manuscript.

Notes

The funding agencies had no influence on the study design, methods, data collection, analyses, or the manuscript writing. The authors declare no competing financial interest.

ACKNOWLEDGMENTS

Financial support from The Knut and Alice Wallenberg Foundation (KAW 2011.0218), the Swedish Research Council (VR 2016-01922; 2018-05337), the Swedish Foundation for Strategic Research (SBE13-0115), FP7-Health-2013-Innovation-IGLORIA-602919 Project, and the Magnus Bergvall's Foundation (2016-01615; 2018-02642) is gratefully acknowledged. A.J.K. and S.N.N. gratefully acknowledge financial support from the Rajko and Maj Đermanović Fund, ERASMUS+ European Union Programme for Education, Training, Youth and Sport, and the Ministry of Education and Science of the Republic of Serbia (Grant Nos. III45016 and OI171038). S.O. gratefully acknowledges a postdoctoral fellowship by The Nakatani Foundation for Advancement of Measuring Technologies in Biomedical Engineering and a travel grant by Yoshida Foundation for Science and Technology. D.K.P. was supported by a Federation of European Biochemical Societies (FEBS) postdoctoral fellowship. We thank Milan Radosavljević, M.Sc. (Eng) for his help with hardware assembly.

REFERENCES

- (1) Qian, H. *J. Stat. Phys.* **2010**, *141* (6), 990–1013.
- (2) Qian, H.; Ge, H. *Mol. Cell. Biomech.* **2012**, *9* (1), 1–30.
- (3) Claridge, S. A.; Schwartz, J. J.; Weiss, P. S. *ACS Nano* **2011**, *5* (2), 693–729.
- (4) Diekmann, S.; Hoischen, C. *Physics of life reviews* **2014**, *11* (1), 1–30.
- (5) Lock, J. G.; Stromblad, S. *Exp. Cell Res.* **2010**, *316* (8), 1438–44.
- (6) Mavrikakis, M.; Pourquie, O.; Lecuit, T. *Development* **2010**, *137* (3), 373–87.
- (7) Owen, D. M.; Williamson, D.; Rentero, C.; Gaus, K. *Traffic* **2009**, *10* (8), 962–71.
- (8) Petibois, C. *Anal. Bioanal. Chem.* **2010**, *397* (6), 2051–65.
- (9) Requejo-Isidro, J. *Journal of chemical biology* **2013**, *6* (3), 97–120.
- (10) Weigert, R.; Porat-Shliom, N.; Amornphimoltham, P. *J. Cell Biol.* **2013**, *201* (7), 969–79.
- (11) Ries, J.; Schwill, P. *BioEssays* **2012**, *34* (5), 361–8.
- (12) Elson, E. L. *Biophys. J.* **2011**, *101* (12), 2855–70.
- (13) Fitzpatrick, J. A.; Lillemeier, B. F. *Curr. Opin. Struct. Biol.* **2011**, *21* (5), 650–60.
- (14) Digman, M. A.; Gratton, E. *Annu. Rev. Phys. Chem.* **2011**, *62*, 645–68.
- (15) Tian, Y.; Martinez, M. M.; Pappas, D. *Appl. Spectrosc.* **2011**, *65* (4), 115A–124A.
- (16) Elson, E. L. *Methods* **2018**, *140–141*, 3–9.
- (17) Kedziora, K. M.; Prehn, J. H.; Dobrucki, J.; Bernas, T. *J. Microsc.* **2011**, *244* (1), 101–11.
- (18) Morikawa, T. J.; Fujita, H.; Kitamura, A.; Horio, T.; Yamamoto, J.; Kinjo, M.; Sasaki, A.; Machiyama, H.; Yoshizawa, K.; Ichimura, T.; Imada, K.; Nagai, T.; Watanabe, T. *M. Sci. Rep.* **2016**, *6*, 22342.

- (19) Blom, H.; Johansson, M.; Hedman, A. S.; Lundberg, L.; Hanning, A.; Hard, S.; Rigler, R. *Appl. Opt.* **2002**, *41* (16), 3336–42.
- (20) Blom, H.; Johansson, M.; Gosch, M.; Sigmundsson, T.; Holm, J.; Hard, S.; Rigler, R. *Appl. Opt.* **2002**, *41* (31), 6614–20.
- (21) Gosch, M.; Serov, A.; Anhut, T.; Lasser, T.; Rochas, A.; Besse, P. A.; Popovic, R. S.; Blom, H.; Rigler, R. *J. Biomed. Opt.* **2004**, *9* (5), 913–21.
- (22) Gosch, M.; Blom, H.; Anderegg, S.; Korn, K.; Thyberg, P.; Wells, M.; Lasser, T.; Rigler, R.; Magnusson, A.; Hard, S. *J. Biomed. Opt.* **2005**, *10* (5), 054008.
- (23) Michalet, X.; Colyer, R. A.; Antelman, J.; Siegmund, O. H.; Tremsin, A.; Vallerga, J. V.; Weiss, S. *Curr. Pharm. Biotechnol.* **2009**, *10* (5), 543–58.
- (24) Needleman, D. J.; Xu, Y.; Mitchison, T. J. *Biophys. J.* **2009**, *96* (12), 5050–9.
- (25) Colyer, R. A.; Scalia, G.; Rech, I.; Gulinatti, A.; Ghioni, M.; Cova, S.; Weiss, S.; Michalet, X. *Biomed. Opt. Express* **2010**, *1* (5), 1408–1431.
- (26) Capoulade, J.; Wachsmuth, M.; Hufnagel, L.; Knop, M. *Nat. Biotechnol.* **2011**, *29* (9), 835–9.
- (27) Colyer, R. A.; Scalia, G.; Villa, F. A.; Guerrieri, F.; Tisa, S.; Zappa, F.; Cova, S.; Weiss, S.; Michalet, X. *Proc. SPIE* **2011**, *7905*, 790503.
- (28) Oh, D.; Zidovska, A.; Xu, Y.; Needleman, D. J. *Biophys. J.* **2011**, *101* (6), 1546–54.
- (29) Bag, N.; Sankaran, J.; Paul, A.; Kraut, R. S.; Wohland, T. *ChemPhysChem* **2012**, *13* (11), 2784–94.
- (30) Buchholz, J.; Krieger, J. W.; Mocsar, G.; Kreith, B.; Charbon, E.; Vamosi, G.; Kobschull, U.; Langowski, J. *Opt. Express* **2012**, *20* (16), 17767–82.
- (31) Singh, A. P.; Krieger, J. W.; Buchholz, J.; Charbon, E.; Langowski, J.; Wohland, T. *Opt. Express* **2013**, *21* (7), 8652–68.
- (32) Vitali, M.; Bronzi, D.; Krmpot, A. J.; Nikolic, S. N.; Schmitt, F. J.; Junghans, C.; Tisa, S.; Friedrich, T.; Vukojevic, V.; Terenius, L.; Zappa, F.; Rigler, R. *IEEE J. Sel. Top. Quantum Electron.* **2014**, *20* (6), 344.
- (33) Krieger, J. W.; Singh, A. P.; Bag, N.; Garbe, C. S.; Saunders, T. E.; Langowski, J.; Wohland, T. *Nat. Protoc.* **2015**, *10* (12), 1948–74.
- (34) Krmpot, A. J.; Nikolic, S. N.; Vitali, M.; Papadopoulos, D. K.; Oasa, S.; Thyberg, P.; Tisa, S.; Kinjo, M.; Nilsson, L.; Gehring, W. J.; Terenius, L.; Rigler, R.; Vukojevic, V. *SPIE Proc.* **2015**, *9536*, 95360O.
- (35) Singh, A. P.; Galland, R.; Finch-Edmondson, M. L.; Grecni, G.; Sibarita, J. B.; Studer, V.; Viasnoff, V.; Saunders, T. E. *Biophys. J.* **2017**, *112* (1), 133–142.
- (36) Buchholz, J.; Krieger, J.; Bruschini, C.; Burri, S.; Ardelean, A.; Charbon, E.; Langowski, J. *Biophys. J.* **2018**, *114* (10), 2455–2464.
- (37) Bruges, J.; Needleman, D. *Proc. Natl. Acad. Sci. U. S. A.* **2014**, *111* (52), 18496–500.
- (38) Papadopoulos, D. K.; Krmpot, A. J.; Nikolic, S. N.; Krautz, R.; Terenius, L.; Tomancak, P.; Rigler, R.; Gehring, W. J.; Vukojevic, V. *Mech. Dev.* **2015**, *138*, 218.
- (39) Bag, N.; Ng, X. W.; Sankaran, J.; Wohland, T. *Methods Appl. Fluoresc.* **2016**, *4* (3), 034003.
- (40) Sezgin, E.; Azbazar, Y.; Ng, X. W.; Teh, C.; Simons, K.; Weidinger, G.; Wohland, T.; Eggeling, C.; Ozhan, G. *FEBS J.* **2017**, *284* (15), 2513–2526.
- (41) Huang, S.; Lim, S. Y.; Gupta, A.; Bag, N.; Wohland, T. *Biochim. Biophys. Acta, Biomembr.* **2017**, *1859* (9 Pt A), 1483–1492.
- (42) Hanley, M. L.; Yoo, T. Y.; Sonnett, M.; Needleman, D. J.; Mitchison, T. J. *Mol. Biol. Cell* **2017**, *28* (11), 1444–1456.
- (43) Ng, X. W.; Teh, C.; Korzh, V.; Wohland, T. *Biophys. J.* **2016**, *111* (2), 418–429.
- (44) Oh, D.; Yu, C. H.; Needleman, D. J. *Proc. Natl. Acad. Sci. U. S. A.* **2016**, *113* (31), 8729–34.
- (45) Langowski, J. *Methods* **2017**, *123*, 3–10.
- (46) Vukojevic, V.; Heidkamp, M.; Ming, Y.; Johansson, B.; Terenius, L.; Rigler, R. *Proc. Natl. Acad. Sci. U. S. A.* **2008**, *105* (47), 18176–81.
- (47) Dertinger, T.; Pacheco, V.; von der Hocht, I.; Hartmann, R.; Gregor, I.; Enderlein, J. *ChemPhysChem* **2007**, *8* (3), 433–443.
- (48) Buchholz, J. *Evaluation of single photon avalanche diode arrays for imaging fluorescence correlation spectroscopy: FPGA-based data readout and fast correlation analysis on CPUs, GPUs and FPGAs*; German Cancer Research Center (DKFZ), Helmholtz Association of National Research Centers: Heidelberg, Germany, 2015.
- (49) Ries, J.; Schwille, P. *Biophys. J.* **2006**, *91* (5), 1915–1924.
- (50) Ries, J.; Petrásek, Z.; García-Sáez, A. J.; Schwille, P. *New J. Phys.* **2010**, *12*, 113009.
- (51) Michalet, X.; Siegmund, O. H.; Vallerga, J. V.; Jelinsky, P.; Millaud, J. E.; Weiss, S. *J. Mod. Opt.* **2007**, *54* (2–3), 239.
- (52) Michalet, X.; Colyer, R. A.; Scalia, G.; Weiss, S.; Siegmund, O. H.; Tremsin, A. S.; Vallerga, J. V.; Villa, F.; Guerrieri, F.; Rech, I.; Gulinatti, A.; Tisa, S.; Zappa, F.; Ghioni, M.; Cova, S. *Proc. SPIE* **2011**, *8033*, 803316.
- (53) Michalet, X.; Colyer, R. A.; Scalia, G.; Ingargiola, A.; Lin, R.; Millaud, J. E.; Weiss, S.; Siegmund, O. H.; Tremsin, A. S.; Vallerga, J. V.; Cheng, A.; Levi, M.; Aharoni, D.; Arisaka, K.; Villa, F.; Guerrieri, F.; Panzeri, F.; Rech, I.; Gulinatti, A.; Zappa, F.; Ghioni, M.; Cova, S. *Philos. Trans. R. Soc., B* **2013**, *368* (1611), 20120035.
- (54) Mikuni, S.; Pack, C.; Tamura, M.; Kinjo, M. *Exp. Mol. Pathol.* **2007**, *82* (2), 163–8.
- (55) Stortz, M.; Presman, D. M.; Bruno, L.; Annibale, P.; Dansey, M. V.; Burton, G.; Gratton, E.; Pecci, A.; Levi, V. *Sci. Rep.* **2017**, *7* (1), 6219.
- (56) Mikuni, S.; Tamura, M.; Kinjo, M. *FEBS Lett.* **2007**, *581* (3), 389–93.
- (57) Shimosawa, T.; Yamagata, K.; Kondo, T.; Hayashi, S.; Shitamukai, A.; Konno, D.; Matsuzaki, F.; Takayama, J.; Onami, S.; Nakayama, H.; Kosugi, Y.; Watanabe, T. M.; Fujita, K.; Mimori-Kiyosue, Y. *Proc. Natl. Acad. Sci. U. S. A.* **2013**, *110* (9), 3399–404.
- (58) Claxton, N. S.; Fellers, T. J.; Davidson, M. W. *Microscopy, confocal*. In *Encyclopedia of medical devices and instrumentation*, Webster, J. G., Ed. John Wiley & Sons: Hoboken, NJ; 2006, 449–477.
- (59) Rigler, R.; Mets, U.; Widengren, J.; Kask, P. *Eur. Biophys. J.* **1993**, *22* (3), 169–175.
- (60) Eigen, M.; Rigler, R. *Proc. Natl. Acad. Sci. U. S. A.* **1994**, *91* (13), 5740–5747.
- (61) Reynaud, E. G.; Krzic, U.; Greger, K.; Stelzer, E. H. K. *HFSP J.* **2008**, *2* (5), 266–275.
- (62) Overbeck, E.; Sinn, C.; Flammer, I.; Ricka, J. *Rev. Sci. Instrum.* **1998**, *69* (10), 3515–3523.
- (63) Zhao, M.; Jin, L.; Chen, B.; Ding, Y.; Ma, H.; Chen, D. Y. *Appl. Opt.* **2003**, *42* (19), 4031–4036.
- (64) Ziarkash, A. W.; Joshi, S. K.; Stipcevic, M.; Ursin, R. *Sci. Rep.* **2018**, *8* (1), 5076.

The genus *Pheggomisetes* Knirsch, 1923 (Coleoptera: Carabidae: Trechinae) in Serbia: taxonomy, morphology and molecular phylogeny

Maja Vrbica¹, Andjeljko Petrović¹, Dejan Pantelić², Aleksandar J. Krmpot², Mihailo D. Rabasović², Danica Pavlović², Svetlana Jovanić², Borislav Guéorguiev³, Stoyan Goranov³, Nikola Vesović¹, Dragan Antić¹, Đorđe Marković¹, Matija Petković¹, Ljubiša Stanisavljević¹ and Srećko Ćurčić^{1*}

¹Institute of Zoology, University of Belgrade – Faculty of Biology, Studentski Trg 16, 11000 Belgrade, Serbia

²Institute of Physics, University of Belgrade, Pregrevica 118, 11080 Belgrade, Serbia

³National Museum of Natural History – Bulgarian Academy of Sciences, 1 Tsar Osvoboditel Blvd., 1000 Sofia, Bulgaria

Received 17 June 2016; revised 9 September 2017; accepted for publication 27 September 2017

The genus *Pheggomisetes* Knirsch, 1923 consists of stenoendemic troglobitic ground beetles restricted to underground habitats in both Western Bulgaria and Southeast Serbia. A review of the genus in Serbia is given in this article. The following new taxa are described from three caves and pits on slopes of the Stara Planina Mountains in Southeast Serbia: *Pheggomisetes serbicus* sp. nov., *P. serbicus belensis* subsp. nov. and *P. globiceps ciniglavensis* subsp. nov. Also, *Pheggomisetes ninae* S. Ćurčić, Schönmann, Brajković, B. Ćurčić & Tomić, 2004, originally described as an independent species, is downgraded to a subspecies of *P. globiceps* Buresch, 1925 – *P. globiceps ninae* S. Ćurčić, Schönmann, Brajković, B. Ćurčić & Tomić, 2004 **comb. & stat. nov.** All the important morphological features of the taxa are listed in the article. The diagnoses of taxa are based on the characters ascertained by bright-field microscopy and nonlinear microscopy (NLM). The use of NLM in investigating *Pheggomisetes* anatomy is explained, and it is shown to be superior to classical microscopy in observing minute details of different structures (e.g. genitalia) on cross and longitudinal sections. A key to the species of *Pheggomisetes* (including the Serbian taxa) is given. In addition, we have included morphometric and molecular analyses of all Serbian *Pheggomisetes* taxa.

ADDITIONAL KEYWORDS: ground beetles – molecular systematics – morphometrics – new species – new subspecies – Trechini – troglobites.

INTRODUCTION

The genus *Pheggomisetes* Knirsch, 1923 includes four species and 12 subspecies of supposedly archaic troglobitic ground beetles, which have been highly modified during their evolution (Beron, 1994; Moravec, Uéno & Belousov, 2003; Ćurčić *et al.*, 2004). The genus occupies an isolated position in the tribe Trechini, alone forming

a distinct phyletic series (Jeannel, 1928; Casale & Laneyrie, 1982; Casale, Vigna Taglianti & Juberthie, 1998). It is considered to be related to the Caucasian aphaenopoid genus *Taniatrechus* Belousov & Dolzhansky, 1994 based on the supernumerary supraorbital and submentum setae, two widened male protarsomeres and male genital structure (Belousov & Dolzhansky, 1994; Belousov & Koval, 2009). All representatives of *Pheggomisetes* are stenoendemics and restricted to certain caves and pits in Western Bulgaria and Southeast Serbia. The currently known species of the genus are *Pheggomisetes buresi* (Knirsch, 1923); *Pheggomisetes globiceps* Buresch, 1925; *Pheggomisetes*

*Corresponding author. E-mail: srecko@bio.bg.ac.rs
[Version of Record, published online 13 December 2017;
<http://zoobank.org/urn:lsid:zoobank.org:pub:85900D92-A76D-4781-8829-CBED73A49334>]

radevi Knirsch, 1924; and *Pheggomisetes ninae* S. Ćurčić, Schönmann, Brajković, B. Ćurčić & Tomić, 2004 (Casale & Laneyrie, 1982; Moravec *et al.*, 2003; Ćurčić *et al.*, 2004). One species (*P. ninae*) and one subspecies (*P. globiceps ilandjievi* V. Guéorguiev, 1964 according to Pretner, 1970) have been recorded in Serbia so far (Guéorguiev, 1964; Ćurčić *et al.*, 2004; Ćurčić, Brajković & Ćurčić, 2007; Nešić *et al.*, 2010).

The morphology and anatomy of *Pheggomisetes* taxa have been investigated by several authors (Jeannel, 1928; Decou & Botosaneanu, 1964; Juberthie & Decu, 1968). Jeannel (1928) was the first to investigate features of the mouthparts, the dorsal habitus and male genital structures. Other aspects of the nervous, digestive, genital and pygidial gland systems were analysed in *P. buresi* (Decou & Botosaneanu, 1964; Juberthie & Decu, 1968). Most recently, thanks to two-photon excitation autofluorescence (auto-TPEF) of the chitin, certain features of the mouthparts and male genitalia were presented for *P. ninae* (Rabasović *et al.*, 2015).

Troglobitic insects are depigmented or transparent, with a thin cuticle consisting mostly of homogeneous chitin (Christiansen, 2012). The use of TPEF microscopy seems to be a highly promising way to study troglobitic taxa like *Pheggomisetes* since it enables the investigator to avoid the fluorescence of pigments and other cuticle components. The fluorescent signal of chitin is dominant here, in contrast to the situation with strongly coloured insects.

Troglobitic beetles, including trechine ground beetles, are regarded as good models for deliberations about both biogeography and evolution since the reduced dispersal out of subterranean environments produces phylogenetic patterns of area distribution that largely match the geological history of mountain ranges and underground habitats (Ribera *et al.*, 2010; Faille *et al.*, 2014). The molecular phylogeny of trechine ground beetles (especially the troglobites) is largely unknown in spite of the fact that these are among the best-studied and widespread groups of beetles (Faille *et al.*, 2013). Within the Trechinae, the molecular phylogeny of *Trechus* species from Spain and subterranean Pyrenean taxa (Faille, Casale & Ribera, 2010a; Faille *et al.*, 2010b) and that of Alpine taxa (Faille *et al.*, 2013) have been more or less thoroughly treated in recently published articles (Contreras-Díaz *et al.*, 2007; Faille, Bourdeau & Fresneda, 2012; Faille *et al.*, 2014). Among other groups of ground beetles, representatives of the Carabinae and Harpalinae have been somewhat better studied with respect to molecular biology (Ober, 2002; Osawa, Su & Imura, 2004; Ober & Maddison, 2008; Ruiz, Jordal & Serrano, 2009; Ober & Heider, 2010; Andújar *et al.*, 2012; Deuve *et al.*, 2012; Šerić Jelaska *et al.*, 2014).

Phylogenetic relationships of the highly diverse trechine fauna of the Balkan Peninsula are almost

unknown. One study only concluded that the genera *Neotrechus* Müller, 1913 and *Adriaphaenops* Noeske, 1928 are related to certain Alpine or Pyrenean taxa (Faille *et al.*, 2013). Sparse molecular data on the genus *Pheggomisetes* are mentioned solely by Faille *et al.* (2013).

Organized by the Institute of Zoology, University of Belgrade – Faculty of Biology, several field trips were carried out in Southeast Serbia from 2012 until 2014. They resulted in the discovery of one new species and two new subspecies of *Pheggomisetes*. The aims of this article were as follows: (1) to describe and diagnose the new trechine taxa; (2) to review the taxonomic status of *Pheggomisetes* taxa from Serbia; (3) to show the benefits of nonlinear microscopy (NLM) in investigating morphology of the beetles' internal chitinous structures (genitalia and some sclerites); (4) to conduct a morphometric study of all the investigated *Pheggomisetes* taxa; and (5) to perform a phylogenetic analysis of all the Serbian taxa using molecular data.

MATERIAL AND METHODS

SAMPLING INFORMATION

Ground beetle specimens were collected by hand or by pitfall trapping (the traps contained salt-saturated water/alcoholic vinegar and rotten meat as bait) (Faille *et al.*, 2012) in a number of underground habitats from Southeast Serbia and Western Bulgaria belonging to the Stara Planina (Balkan) Mountain system. The traps were placed on both the floor and walls in dark parts of the explored caves and pits, where the level of humidity was high. All the analysed *Pheggomisetes* taxa are troglobitic and live in underground habitats (caves and pits) in the Stara Planina (Balkan) Mountains of Southeast Serbia and Western Bulgaria. Collected specimens were transferred to 70% ethanol at room temperature, except in the case of specimens designated for molecular analysis, which were transferred to 96% ethanol at -20°C . They were analysed in laboratories of the Institute of Zoology, University of Belgrade – Faculty of Biology, Belgrade, Serbia; the Department of Crop Science, University of Belgrade – Faculty of Agriculture, Belgrade, Serbia; and the Photonics Centre, Institute of Physics, University of Belgrade, Belgrade, Serbia.

MEASUREMENTS

AL – maximum length of antennae including the scape
AL/TL – ratio of maximum length of antennae including the scape to total body length (from the anterior margin of the clypeus to the elytral apex)

BW/PW – ratio of the elytral base width to maximum pronotum width as the greatest transverse distance

EL – elytral length (as the linear distance along the suture from the elytral base to the apex)

EL/EW – ratio of elytral length (as the linear distance along the suture from the elytral base to the apex) to maximum elytral width

EL/TL – ratio of elytral length (as the linear distance along the suture from the elytral base to the apex) to total body length (from the anterior margin of the clypeus to the elytral apex)

EW – maximum elytral width

EWP – position of maximum elytral width (percentage of length)

FL – length of frontal furrows

FL/HL – ratio of frontal furrow length to head length

HL – head length

HL/AL – ratio of head length to maximum length of antennae including the scape

HL/HW – ratio of head length to maximum head width

HL/PL – ratio of head length to pronotum length (along the median line)

HL/TL – ratio of head length to total body length (from the anterior margin of the clypeus to the elytral apex)

HW – maximum head width

HW/EW – ratio of maximum head width to maximum elytral width

HW/NW – ratio of maximum head width to maximum neck width

HW/PW – ratio of maximum head width to maximum pronotum width as the greatest transverse distance

HWP – position of maximum head width (percentage of length)

M – mean value for certain measurements

NW – maximum neck width

PaW – width of pronotal apex between tips of the anterior angles

PaW/PbW – ratio of pronotal apex width between tips of the anterior angles to pronotal base width between tips of the posterior angles

PaW/PW – ratio of pronotal apex width between tips of the anterior angles to maximum pronotum width as the greatest transverse distance

PbW – pronotal base width between tips of the posterior angles

PbW/PW – ratio of pronotal base width between tips of the posterior angles to maximum pronotum width as the greatest transverse distance

PL – pronotum length (along the median line)

PL/PW – ratio of pronotum length (along the median line) to maximum pronotum width as the greatest transverse distance

PL/TL – ratio of pronotum length (along the median line) to total body length (from the anterior margin of the clypeus to the elytral apex)

PW – maximum pronotum width as the greatest transverse distance

PW/EW – ratio of maximum pronotum width as the greatest transverse distance to maximum elytral width

PWP – position of maximum pronotum width (percentage of length)

R – range of total measurements performed

TL – total body length (from the anterior margin of the clypeus to the elytral apex)

COLLECTIONS

HT – holotype

IZFB – collection of the Institute of Zoology, University of Belgrade – Faculty of Biology, Belgrade, Serbia

NMNH – collection of the National Museum of Natural History, Sofia, Bulgaria

OTHER EXAMINED TAXA

Pheggomisetes buresi (Knirsch, 1923): one topotype male, Bulgaria, Balkan Mts., Ledenika Cave, 830 m a.s.l., near Vratsa, 19.VII.1963, leg. E. Pretner (IZFB).

Pheggomisetes globiceps globiceps Buresch, 1925: syntype male, Bulgaria, West Balkan range, Mt. Ponor Planina, Sofia district, a cave near Iskrets (= Dushnika Cave), village of Iskrets, 580 m a.s.l., 10.XII.1924, leg. D. Ilchev (NMNH); two topotype females, *idem*, 08.VII.1925, leg. N. Radev (NMNH); one topotype female, *idem*, 17.IX.1943, collector unknown (NMNH); one topotype male, *idem*, 15.II.1992, leg. I. Pandurski (NMNH); two topotype males and one topotype female, *idem*, 16.X–04.XI.2016, from pitfall traps, leg. B. Guéorguiev & S. Goranov (IZFB); one female, Bulgaria, West Balkan range, Mt. Ponor Planina, Sofia district, Otechestvo Cave, village of Iskrets, 720 m a.s.l., 24.V.1959, leg. A. Popov (NMNH); two males, *idem*, 16.X.2016, leg. B. Guéorguiev & S. Goranov (NMNH).

Pheggomisetes globiceps ilandjievi V. Guéorguiev, 1964: two topotype males and three topotype females, Bulgaria, Balkan Mts., Golyama Balabanova Dupka Cave, 1100 m a.s.l., village of Komshtitsa, near Godech, 12.X.1995, leg. B. Guéorguiev & V. Beshkov (IZFB); two topotype males and three topotype females, *idem*, 30.V.2015, leg. S. Goranov (IZFB).

TAXONOMIC AND MORPHOLOGICAL ANALYSES

The traditional method of studying insect morphology by bright-field microscopy was mainly used in the study. Apart from this, 3D images and clips obtained by NLM provided additional details that were used for descriptions of the genital structures and diagnoses of the studied taxa.

Bright-field microscopy

The genitalia were removed from the bodies, preserved in clove oil for a few days and subsequently fixed on microscope slides in Canada balsam. The beetles were then glued onto rectangular paper labels and analysed as dry specimens. Stemi 2000 and Stereo Discovery.V8 binocular stereomicroscopes (Carl Zeiss, Jena, Germany) with AxioCam MRc and Axio Cam ICc 1 digital cameras (Carl Zeiss, Jena, Germany) attached were used to photograph whole specimens, while a DMLS light microscope (Leica, Wetzlar, Germany) with a DC 300 camera (Leica, Wetzlar, Germany) attached was used to photograph the genitalia.

Nonlinear microscopy

Bright-field microscopy is most often used to study insect morphology, but recently a few articles have appeared treating the use of confocal fluorescence microscopy to observe certain structures of insects and crustaceans (Klaus, Kulasekera & Schawaroch, 2003; Michels, 2007; de Campos Vidal, 2011). NLM has also been introduced as a method offering unique insight into a variety of biological structures. This technique is similar to confocal microscopy (in employing localized laser excitation and scanning), but is characterized by higher penetration depth, reduced photodamage and photobleaching, and no need for specimen staining in most cases (Denk, Strickler & Webb, 1990; Williams, Zipfel & Webb, 2001; Mertz, 2004; Masters & So, 2008). Tissues and individual cells can be observed with high resolution of volume details. Up until now, NLM has been used extensively in biomedical research, but only marginally in entomology (Lin *et al.*, 2008; Chien *et al.*, 2011). It was recently confirmed that NLM can be used for deep imaging of chitinous structures (both chemically purified chitin and chitin originating from insect integument) (Rabasović *et al.*, 2015; Reinhardt, Breunig & König, 2017). On the basis of the autofluorescence properties of chitin, the TPEF modality of NLM was mainly used in the latter study. In addition, even a second harmonic generation signal originating from chitinous structures was detected, but this signal is unsuitable for imaging since it is weak and hindered by the much stronger auto-TPEF.

Before analysis, specimens were stored in 70% ethanol at room temperature. The genitalia were removed from the bodies and preserved in clove oil for 2 weeks. Genital structures were placed on double-sided adhesive tape on microscope slides in glycerin as the medium, with or without a cover slip, depending on the microscope objective used.

STATISTICAL ANALYSIS

All variables that entered the statistical analysis were tested for normality using the Shapiro-Wilk test. A multivariate test of significance (one-way MANOVA) of normally distributed data, followed by a univariate test of significance (one-way ANOVA) for each variable, was used to identify which data sets (between groups) differ significantly. Non-normally distributed variables were compared between taxon samples using the Mann-Whitney *U* test ($P \leq 0.05$). MANOVA allows comparison of population means of all variables of interest at the same time (multivariate response) rather than considering multiple responses as a suite of univariate responses (Zar, 1999). The statistical test most often used in biology, Wilks' lambda, was applied (Zar, 1999). One-way MANOVA was used to examine the differences in morphological variation among Serbian *Pheggomisetes* taxa (species and subspecies). To describe and interpret effects from MANOVA, multivariate discriminant analysis (DA) was used only on normally distributed variables to determine the relative importance of characters as discriminators between a priori groups and the relative positions of centroids of the groups (Manly, 1986).

The distance matrix for subspecies was calculated based on the squared Mahalanobis distance between subspecies centroids, and a dendrogram was generated using UPGMA (unweighted pair group method with arithmetic mean) clustering. This was used to evaluate the phenetic relationships between subspecies. Statistical analyses were conducted using the Statistica 6 software package (StatSoft, Inc., 2001).

MOLECULAR ANALYSIS

DNA extraction, PCR amplification and sequencing

We used nine *Pheggomisetes* specimens (belonging to all Serbian taxa) for molecular analyses (Table 1). DNA was extracted from one hind leg of each specimen using the KAPA Express Extract Kit (Kapa Biosystems Inc., Boston, MA, USA) and following the manufacturer's instructions. The primers used to amplify the barcoding region of cytochrome *c* oxidase subunit I (*COI*) gene were Jerry [(CI-J-2183)5'-CAACATTTATTTTGATTTTGG-3'] and Pat [(TL2-N-3014)5'-TCCAAAGCACTAATCTGCCATATTA-3'] (Simon *et al.*, 1994). Each PCR was carried out in a volume of 25 µL containing 1 µL of extracted DNA, 9 µL of H₂O, 1.25 µL of each primer and 12.5 µL of KAPA2GtmHotStart ReadyMix. All PCRs were conducted in an Eppendorf Mastercycler (Hamburg, Germany) using the following

Table 1. Trechine specimens used for molecular analyses with GenBank accession numbers

Code	Locality	Taxon	Accession number
S3	Hodžina Dupka Pit	<i>Pheggomisetes globiceps ninae</i> comb. & stat. nov.	KY351544
S12	Tmna Dupka Cave	<i>P. globiceps ninae</i> comb. & stat. nov.	KY351545
S28	Petrlaška Pećina Cave	<i>P. globiceps ninae</i> comb. & stat. nov.	KY351546
S19	Propas Pit	<i>P. globiceps ciniglavcensis</i> subsp. nov.	KY351547
S21	Pež Dupka Cave	<i>P. serbicus serbicus</i> subsp. nov.	KY351548
S26	Suva Dupka Cave	<i>P. serbicus belensis</i> subsp. nov.	KY351549
S27	A cave in the vicinity of the Suva Dupka Cave	<i>P. serbicus belensis</i> subsp. nov.	KY351542
S41	Golyama Balabanova Dupka Cave	<i>P. globiceps ilandjjevi</i>	KY351543
S66	Otechestvo Cave	<i>P. globiceps globiceps</i>	KY351550
S1	Zlotska (= Lazareva) Pećina Cave	<i>Duvalius (Paraduvalius) stankovitchi georgevitchi</i> *	KY351551

*Outgroup.

thermal profile: initial denaturation (95 °C for 5 min); amplification (35 cycles consisting of 60 s at 95 °C, 60 s at 51 °C and 120 s at 72 °C); and final extension (72 °C for 7 min).

The PCR products were purified using the QIAquick Purification Kit (QIAGEN Inc., Valencia, CA, USA) according to the manufacturer's instructions.

DNA sequencing was performed using automated equipment (Macrogen Inc., Seoul, South Korea).

Sequences were manually edited in FinchTV (Geospiza Inc., Seattle, WA, USA) and aligned using the ClustalW program integrated in MEGA5 (Tamura *et al.*, 2011).

Genetic divergence was estimated using Kimura's two-parameter (K2P) method of base substitution (Kimura, 1980).

Phylogenetic reconstruction was performed using maximum parsimony (MP), maximum likelihood (ML) and neighbor-joining (NJ) incorporated in the MEGA5 software package. One thousand bootstrap replicates were performed in every analysis to assess robustness of the trees. Tamura's three-parameter model (T92 + G) was identified as the best-fitting model of sequence evolution based on the Bayesian information criterion and corrected Akaike information criterion (Nei & Kumar, 2000) for the ML method of phylogenetic reconstruction. The subspecies *Duvalius (Paraduvalius) stankovitchi georgevitchi* (Jeannel, 1924) was used as an outgroup. The nucleotide sequence data were deposited in the GenBank database under accession numbers KY351542–KY351551 (Table 1). K2P model was used to estimate genetic divergence of the analysed taxa.

RESULTS AND DISCUSSION

TAXONOMY

FAMILY CARABIDAE LATREILLE, 1802

SUBFAMILY TRECHINAE BONELLI, 1810

TRIBE TRECHINI BONELLI, 1810

GENUS *PHEGGOMISETES* KNIRSCH, 1923

***PHEGGOMISETES SERBICUS* ČURČIĆ, VRBICA & B. GUÉORGUIEV SP. NOV.**

(FIGS 1 AND 2A–H)

Material examined: Holotype male labelled as follows: 'Southeast Serbia, Stara Planina Mts., Pež Dupka Cave, 43°13'17.77"N 22°47'17.08"E, village of Dojkinci, 869 m a.s.l., near Pirot, 11.VII–10.X.2013, from pitfall traps, leg. D. Antić & M. Petković' (white label, printed)/'Holotypus *Pheggomisetes serbicus* sp. nov. Čurčić, Vrbica & Guéorguiev det. 2016' (red label, printed) (IZFB). Paratypes: six males and eight females, same data as for holotype (IZFB); three males and four females labelled as follows: 'Southeast Serbia, Stara Planina Mts., Pež Dupka Cave, village of Dojkinci, 869 m a.s.l., near Pirot, 11.VII.2013, leg. D. Antić & M. Petković' (IZFB). All paratypes are labelled with white printed locality labels and with red printed labels 'Paratypus *Pheggomisetes serbicus* sp. nov. Čurčić, Vrbica & Guéorguiev det. 2016'.

Description: TL R 5.55–6.675 mm (M 6.11 mm) (HT 6.30 mm). Head oval, HL/HW R 1.18–1.34 (M 1.26) (HT 1.27), widest somewhat before its middle, scarcely wider than pronotum (Fig. 1). Frontal furrows long, slightly exceeding mid head level, deeply impressed



Figure 1. *Pheggomisetes serbicus* sp. nov. from the Pež Dupka Cave, village of Dojkinci (near Pirot), Stara Planina Mts., Southeast Serbia. Holotype male, habitus (dorsal view). Scale = 5.0 mm.

anteriorly and sigmoidally curved. Neck narrow, HW/NW R 1.97–2.75 (M 2.50) (HT 2.19). Antennae long, around the same length as TL in males, while shorter than TL in females.

Pronotum widest somewhat after the anterior third, almost as long as wide (Fig. 1). Anterior pronotal margin concave, shorter than pronotal base. Lateral pronotal margins rounded anteriorly and slightly concave posteriorly. Pronotal base somewhat concave in the middle. Fore pronotal angles obtuse, rounded. Hind pronotal angles acute, almost right.

Elytra relatively long, oval, convex, with the lateral sides rounded anteriorly, widest slightly after the mid level, EL/EW R 1.61–1.83 (M 1.725) (HT 1.81). Elytral base slightly narrower than pronotum (Fig. 1). Humeral angles obtuse, rounded and quite elevated. Elytral apex rounded.

Legs and claws long and thin (Fig. 1).

Median lobe of the aedeagus in lateral view curved, with a rounded somewhat elevated apex (Fig. 2A, E). Basal bulb small, rounded. Parameres with three apical setae each. Median lobe in dorsal view straight, with a rounded apex, narrowing towards basal bulb (Fig. 1B). Gutter-shaped copulatory piece covered with numerous spines (Fig. 2B, F), wide at its basal three fifths and markedly narrowed at its apical two fifths.

Male abdominal sternite IX (urite) subtriangular, slightly elongate, slightly longer than aedeagus (Fig. 2C, G). Apophysis narrow, constricted proximally.

Both gonocoxites IX and gonosubcoxites IX as presented in Figure 2D, H. Gonocoxites IX of moderate length, slightly curved, apically rounded, basally completely jointed with massive gonosubcoxites IX (Fig. 2D, H).

Chaetotaxy. Frons with six to seven (HT – 7) setae on each side. Pronotum with normal chaetotaxy (two pairs of setae). Five to seven setae on third interstria (HT – 7) on each elytron (Fig. 1).

Elytral umbilicate series: First three humeral setae close to marginal gutter, fourth being somewhat farther from the gutter, distance between umbilicate pores 2 and 3 shortest, while between pores 3 and 4 longest; median series at around the middle of the elytra, two setae being somewhat distanced from marginal gutter, distance between pores 5 and 6 about as long as distance between pores 2 and 3; apical series: setae 7 and 8 being somewhat distanced from marginal gutter, distance between pores 7 and 8 longer than distance between pores 3 and 4 (Fig. 1).

Differential diagnosis: The new species is compared here with the other known *Pheggomisetes* species (Casale & Laneyrie, 1982; Moravec et al., 2003). A comparison of the new species with *P. ninae* is not provided here since the latter taxon is regarded as a subspecies of *P. globiceps* (see below).

The new species differs from *P. globiceps* in having a smaller value of TL M (6.11 vs. ≥ 6.295 mm), a smaller value of HL M (1.39 vs. ≥ 1.40 mm), smaller values of AL M (5.91, males 6.01, females 5.70 vs. ≥ 6.525 mm, males ≥ 6.56 mm, females ≥ 6.30 mm), smaller values of AL/TL M (0.97, males 0.99, females 0.92 vs. ≥ 1.01 , males ≥ 1.05 , females ≥ 0.97), a greater value of HL/AL M (0.235 vs. ≤ 0.225), a greater value of FL M (0.75 vs. ≤ 0.68 mm), a greater value of FL/HL M (0.54 vs. ≤ 0.48), different shape of the humeral angles (more rounded, quite elevated vs. more obtuse, less elevated), a greater value of EL/TL M (0.55 vs. ≤ 0.54) and different shape of the copulatory piece in dorsal aspect (more markedly narrowed apically vs. gradually narrowed apically) (Tables 2 and 3; Figs 1–13; Supporting Information, Table S1) (Jeannel, 1928; Guéorguiev, 1964; this study). Even though the differences

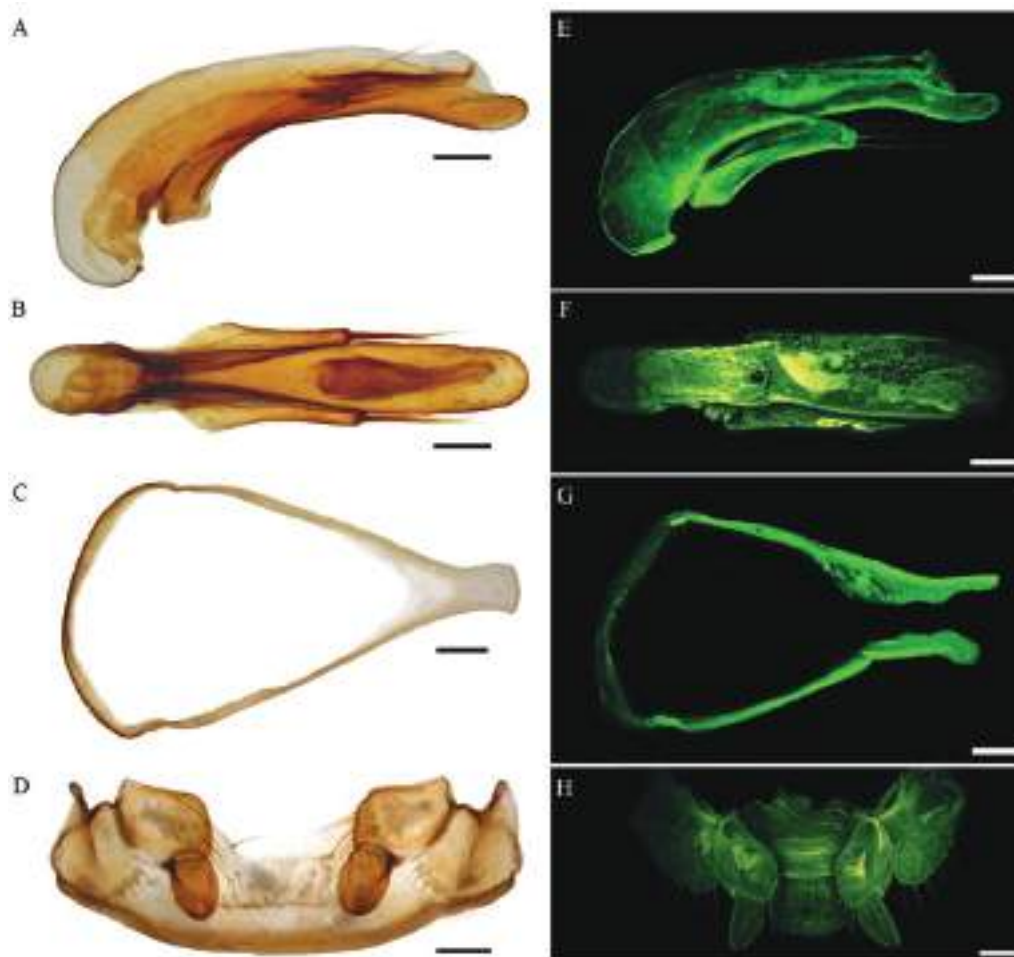


Figure 2. *Pheggomisetes serbicus* sp. nov. from the Pež Dupka Cave, village of Dojkinci (near Pirot), Stara Planina Mts., Southeast Serbia. Bright-field (A–D) and TPEF (E–H) microscopy images. A, E, holotype male, aedeagus (lateral view). B, F, holotype male, aedeagus (dorsal view). C, G, holotype male, abdominal sternite IX (urite). D, H, paratype female, gonocoxites IX and gonosubcoxites IX. Scales = 0.1 mm.

obtained between the mean values of certain measurements (HL) and ratios (HL/AL, EL/TL) are very small (Supporting Information, Table S1), the distributions of ranges in the two species show statistically significant differences (Table 3).

The new species differs from *P. radevi* in having a smaller value of TL R (5.55–6.675 vs. 7–8 mm), a greater value of HL/HW M (1.26 vs. 1.00), different shape of the head (widest slightly before its mid part, posteriorly somewhat convex vs. widest around its mid part, posteriorly very convex), a smaller value of HW/NW M (2.50 vs. c. 3.00), different shape of the pronotum (weakly narrowed basally, strongly rounded anteriorly, well sinuate in back vs. strongly narrowed basally, weakly rounded anteriorly, strongly sinuate in back), a different value of PaW/PbW (pronotal apex between tips of the anterior angles narrower than pronotal base between tips of the posterior angles vs. pronotal apex

between tips of the anterior angles wider than pronotal base between tips of the posterior angles), different shape of the hind pronotal angles (almost right, not prominent vs. acute, protruding backwards and outwards), different form of the elytra (less elongate, with more prominent shoulders vs. more elongate, with less prominent shoulders), different shape of the median lobe (less bent vs. more bent) and different shape of the basal bulb (relatively small, rounded vs. medium-sized, relatively elongate) (Jeannel, 1928; Guéorguiev, 1964; this study).

The new species differs from *P. buresi* in having a smaller value of TL R (5.55–6.675 vs. 7.20–9.00 mm), different shape of the head (less elongate, posteriorly more convex, abruptly narrowing towards the neck vs. more elongate, posteriorly less convex, gradually narrowing towards the neck), a different position of maximum head width (slightly in front of the

Table 2. Results of ANOVA for each variable between *P. serbicus* sp. nov. and *P. globiceps* (exact significance level $P \leq 0.05$, marked in bold)

Variable	<i>F</i>	<i>P</i> -value
HL	4.760	0.033
HW	0.273	0.603
FL	11.519	0.001
HL/HW	1.346	0.251
HL/AL	54.485	< 0.001
HL/PL	0.559	0.458
HL/TL	22.596	< 0.001
HW/NW	1.875	0.176
HW/PW	0.040	0.843
AL/TL	17.269	< 0.001
PW	1.092	0.300
PL/PW	3.788	0.056
PaW	5.207	0.026
PbW	0.287	0.594
PaW/PW	3.582	0.063
PbW/PW	0.047	0.829
PaW/PbW	3.744	0.058
EW	11.428	0.001
EWP	0.673	0.415
BW/PW	0.643	0.426

Table 3. Results of Mann–Whitney *U* test between *P. serbicus* sp. nov. ($n = 24$) and *P. globiceps* ($n = 44$) (exact significance level $P \leq 0.05$, marked in bold)

Variable	<i>U</i>	<i>P</i> -value
TL	116.5	< 0.001
HWP	447.5	0.305
AL	1.5	< 0.001
FL/HL	250.0	< 0.001
HW/EW	320.0	0.014
PL	345.5	0.026
PWP	233.5	< 0.001
PL/TL	224.5	< 0.001
PW/EW	245.0	0.001
EL	431.0	0.325
EL/EW	351.5	0.042
EL/TL	206.0	< 0.001

middle vs. anteriorly), a greater value of HW/NW M (2.50 vs. *c.* 2.00), different form of the lateral pronotal margins (a little rounded anteriorly, slightly sinuate posteriorly vs. somewhat arcuate), different shape of the hind pronotal angles (almost right, not prominent vs. acute, protruding backwards and outwards), different shape of the elytra (less elongate, with more pronounced shoulders vs. more elongate, with less pronounced shoulders), different shape of

the median lobe (less elongate, less bent vs. more elongate, more bent) and different shape of the basal bulb (relatively small, rounded vs. relatively massive, elongate) (Jeannel, 1928; Guéorguiev, 1964; this study).

Among the three known species of the genus, *P. globiceps* is the smallest one and the only species that has right hind angles of the pronotum (Jeannel, 1928; Guéorguiev, 1964). It has a pronotum that is weakly narrowed basally, with lateral margins moderately rounded anteriorly and weakly sinuate posteriorly, in addition to a relatively narrow elytral base (Jeannel, 1928; Guéorguiev, 1964). Thus, it is quite clear that *P. serbicus* sp. nov. shares the same character states and is closely related to it. In addition, *P. buresi* differs from all other congeners in having a rather thick neck. No significant differences within the genus are evident in the male genitalia (especially in regard to shape of the median lobe), even at the species level (Jeannel, 1928; Guéorguiev, 1964; this article).

Variability: The number of setae on both frons (six to seven on each side) and elytra can vary (five to seven on each side).

Etymology: The new species is named after Serbia, its terra typica.

Distribution: The type locality is the Pež Dupka Cave in the village of Dojkinci (near Pirot) in the Stara Planina Mountains of Southeast Serbia. The new species inhabits a few caves in the villages of Dojkinci and Bela in the Stara Planina Mountains of Southeast Serbia; *P. buresi* and *P. radevi* live in caves near the town of Vratsa and villages of Chiren, Eliseyna, Chelopek, Druzhevo and Milanovo in the West Stara Planina Mountains of Western Bulgaria; and *P. globiceps* inhabits numerous caves in the West Stara Planina Mountains and Pre-Balkan region of Western Bulgaria, as well as a few caves in the villages of Petrlaš and Činiglavci in the Stara Planina Mountains of Southeast Serbia (Guéorguiev & Guéorguiev, 1995; this study).

***PHEGGOMISETES SERBICUS BELENSIS* ČURČIĆ,
VRBICA & B. GUÉORGUIEV SUBSP. NOV.**

(FIGS 4 AND 5A–H)

Material examined: Holotype male labelled as follows: ‘Southeast Serbia, Stara Planina Mts., Suva Dupka Cave, 43°14′40.9″N 22°44′16.5″E, village of Bela, 801 m a.s.l., near Pirot, 25.V.2014, leg. S. Čurčić, D. Antić & I. Petrović’ (white label, printed)/‘Holotypus *Pheggomisetes serbicus belensis* subsp. nov. Čurčić, Vrbica & Guéorguiev det. 2016’ (red label, printed) (IZFB). Paratypes: three males

and two females, same data as for holotype (IZFB); four males and eight females labelled as follows: 'Southeast Serbia, Stara Planina Mts., Suva Dupka Cave, village of Bela, 801 m a.s.l., near Pirot, 25.V-05.VII.2014, from pitfall traps, leg. D. Antić' (IZFB); one female labelled as follows: 'Southeast Serbia, Stara Planina Mts., a cave in the vicinity of the Suva Dupka Cave, 43°14'30.84"N 22°44'9.40"E, village of Bela, 793 m a.s.l., near Pirot, 25.V-05.VII.2014, from pitfall traps, leg. D. Antić' (IZFB). All paratypes are labelled with white printed locality labels and with red printed labels '*Paratypus Pheggomisetes serbicus belensis* subsp. nov. Ćurčić, Vrbica & Guéorguiev det. 2016'.

Description: TL R 5.70–6.60 mm (M 6.045 mm) (HT 5.925 mm). HL/HW R 1.23–1.33 (M 1.27) (HT 1.24) (Fig. 4). Frontal furrows reaching mid head level. HW/NW R 2.09–2.50 (M 2.24) (HT 2.25).

Anterior pronotal margin clearly (in males) or slightly (in females) concave, shorter than pronotal base (Fig. 3). Lateral pronotal margins very slightly concave posteriorly.

Elytra with lateral sides almost straight in the anterior half, EL/EW R 1.62–1.92 (M 1.77) (HT 1.71) (Fig. 4).

Median lobe of the aedeagus in lateral view slightly convex dorsally at around the level of two fifths, having an almost straight apex (Fig. 5A, E). Median lobe

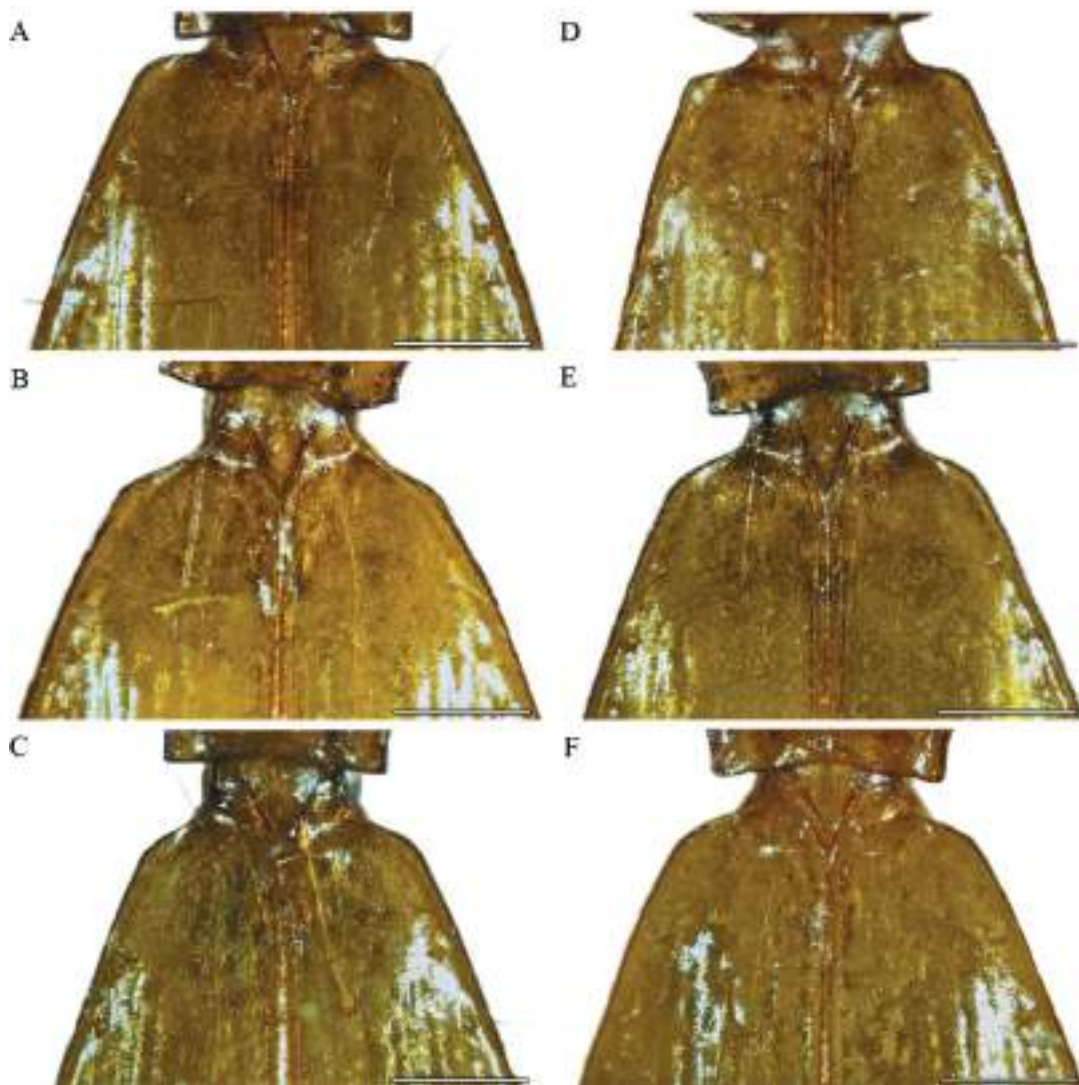


Figure 3. Shape of the shoulders in the *Pheggomisetes* subspecies analysed. A, *P. serbicus serbicus* subsp. nov. B, *P. globiceps ciniglavcensis* subsp. nov. C, *P. globiceps ilandjjevi*. D, *P. serbicus belensis* subsp. nov. E, *P. globiceps ninae* comb. & stat. nov. F, *P. globiceps globiceps*. Scales = 0.5 mm.



Figure 4. *Pheggomisetes serbicus belensis* subsp. nov. from the Suva Dupka Cave, village of Bela (near Pirot), Stara Planina Mts., Southeast Serbia. Holotype male, habitus (dorsal view). Scale = 5.0 mm.

in dorsal view as presented in [Figure 5B, F](#) and inner sac as presented in [Figure 5A, B, E, F](#).

Male abdominal sternite IX (urite) as presented in [Figure 5C, G](#), subtriangular, slightly elongate, slightly longer than aedeagus. Apophysis narrow, constricted proximally.

Both gonocoxites IX and gonosubcoxites IX as presented in [Figure 5D, H](#).

Chaetotaxy. Frons with six to eight (HT – 6) setae on each side. Pronotum with normal chaetotaxy (two pairs of setae). Five to seven setae on third interstria (HT – 6–7) on each elytron ([Fig. 4](#)).

Elytral umbilicate series: First three humeral setae close to marginal gutter, fourth being somewhat farther from the gutter, distance between umbilicate pores 2 and 3 shortest, distance between pores 1 and 2 approximately the same as between pores 3 and 4; median series at around the middle of the elytra, two setae being somewhat distanced from the gutter, distance between pores 5 and 6 somewhat shorter than distance between pores 2 and 3; apical series: setae 7 and 8 being somewhat distanced from marginal gutter, distance between pores 7 and 8 longer than distance between pores 3 and 4 ([Fig. 4](#)).

Differential diagnosis: The new subspecies is compared with the nominal subspecies, *P. serbicus serbicus* subsp. nov.

The new subspecies clearly differs from *P. serbicus serbicus* subsp. nov. in having a smaller value of TL M (6.045 vs. 6.11 mm), a different value of FL/HL M (frontal furrows reaching mid head level vs. frontal furrows somewhat exceeding mid head level), a smaller value of HW/NW M (2.24 vs. 2.50), a smaller value of FL M (0.68 vs. 0.75 mm), a greater value of AL M (5.99 vs. 5.91 mm), different shape of the anterior pronotal margin in females (less concave vs. more concave), different shape of the pronotal base in the middle (less concave vs. more concave), different shape of the lateral margins of the elytra anteriorly (more straight vs. rounded), a greater value of PaW/PbW M (0.78 vs. 0.74), a greater value of EL/EW M (1.77 vs. 1.725), a different position of certain humeral and median setae (distance between pores 2 and 3 shortest, distance between pores 1 and 2 approximately the same as between pores 3 and 4, distance between pores 5 and 6 somewhat shorter than distance between pores 2 and 3 vs. distance between pores 2 and 3 shortest, distance between pores 3 and 4 longest, distance between pores 5 and 6 about as long as distance between pores 2 and 3) belonging to the elytral umbilicate series, different shape of the median lobe apex in lateral aspect (almost straight vs. somewhat elevated) and different shape of the median lobe's basal bulb in lateral aspect (more curved vs. less curved) (Supporting Information, Table S1) (this study).

Variability: The number of setae on both frons (six to eight on each side) and elytra can vary (five to seven on each side).

Etymology: The new subspecies is named after the village of Bela, in which the type locality is situated.

Distribution: It inhabits two caves in the village of Bela (near Pirot) in the Stara Planina Mountains of Southeast Serbia – the Suva Dupka Cave and a cave in its vicinity.

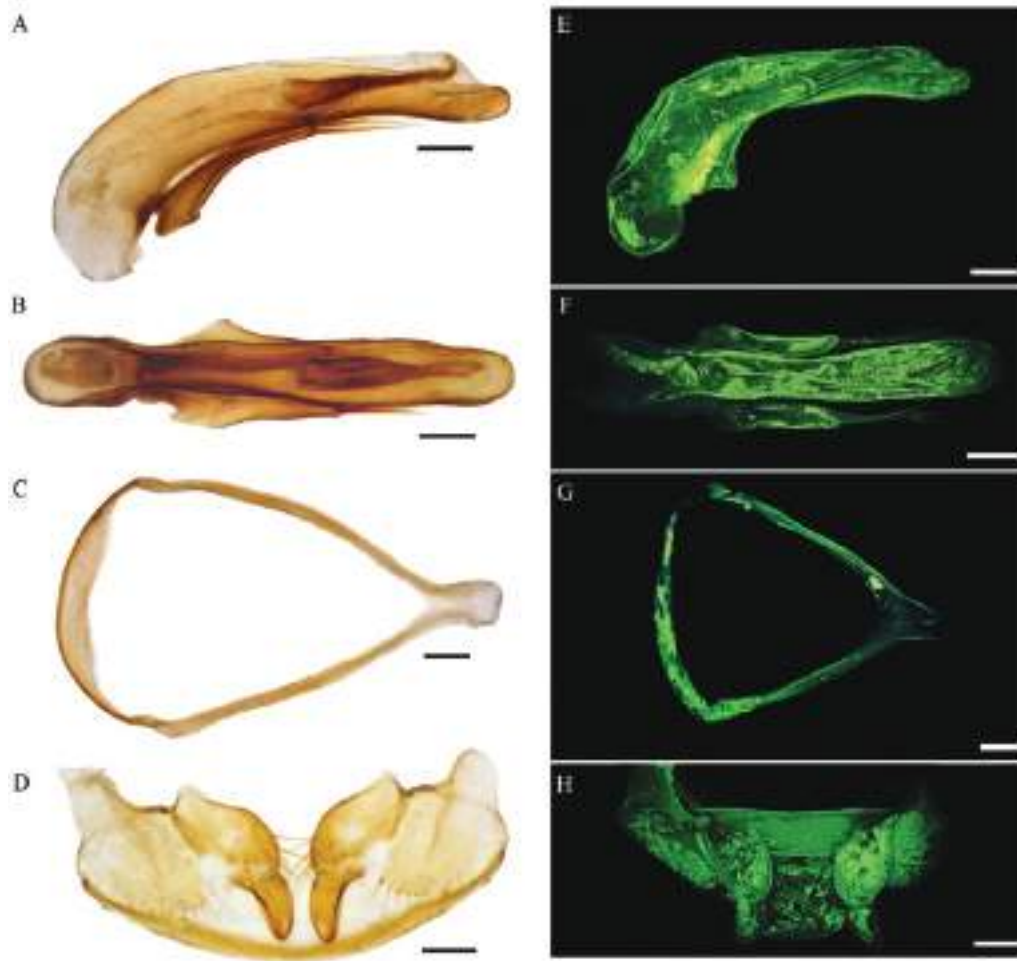


Figure 5. *Pheggomisetes serbicus belensis* subsp. nov. from the Suva Dupka Cave, village of Bela (near Pirot), Stara Planina Mts., Southeast Serbia. Bright-field (A–D) and TPEF (E–H) microscopy images. A, E, holotype male, aedeagus (lateral view). B, F, holotype male, aedeagus (dorsal view). C, G, holotype male, abdominal sternite IX (urite). D, H, paratype female, gonocoxites IX and gonosubcoxites IX. Scales = 0.1 mm.

PHEGGOMISETES GLOBICEPS BURESCH, 1925

PHEGGOMISETES GLOBICEPS CINIGLAVCENSIS
 ČURČIĆ & VRBICA, SUBSP. NOV.

(FIGS 6 AND 7A–H)

Pheggomisetes globiceps ilandjivi: Gajović *et al.* (2011: 80).

Material examined: Holotype male labelled as follows: ‘Southeast Serbia, Stara Planina Mts., Propas Pit, 43°04′05.7″N 22°44′18.5″E, village of Činiglavci, 714 m a.s.l., near Pirot, 29.V-08.VII.2013, from pitfall traps, leg. Đ. Marković & M. Petković’ (white label, printed)/‘Holotypus *Pheggomisetes globiceps ciniglavcensis* subsp. nov. Čurčić, Vrbica & Guéorguiev det. 2016’ (red label, printed) (IZFB). Paratypes: 29 males and 20 females, same data as for holotype (IZFB). All paratypes are labelled with white printed locality labels and with red printed labels ‘Paratypus

Pheggomisetes globiceps ciniglavcensis subsp. nov. Čurčić, Vrbica & Guéorguiev det. 2016’.

Description: TL R 6.15–6.825 mm (M 6.46 mm) (HT 6.525 mm). Head oval, HL/HW R 1.19–1.355 (M 1.275) (HT 1.19), widest somewhat before its mid part, scarcely wider than pronotum (Fig. 6). Frontal furrows almost reaching mid head level, deeply impressed anteriorly and sigmoidally curved. Neck narrow, HW/NW R 2.17–2.61 (M 2.405) (HT 2.50). Antennae long, longer (in males) or slightly shorter (in females) than TL.

Pronotum widest somewhat after the anterior third, almost as long as wide (Fig. 6). Anterior pronotal margin slightly concave, shorter than pronotal base. Lateral pronotal margins rounded anteriorly and slightly concave posteriorly. Pronotal base very slightly concave in the middle. Fore pronotal angles obtuse, rounded. Hind pronotal angles acute, almost right.



Figure 6. *Pheggomisetes globiceps ciniglavcensis* subsp. nov. from the Propas Pit, village of Činiglavci (near Pirot), Stara Planina Mts., Southeast Serbia. Holotype male, habitus (dorsal view). Scale = 5.0 mm.

Elytra relatively long, oval, convex, widest somewhat after the mid level, EL/EW R 1.53–1.73 (M 1.64) (HT 1.68). Elytral base slightly wider than pronotum (BW/PW R 0.85–1.10, M 1.03, HT 1.00) (Fig. 6). Humeral angles obtuse, rounded and relatively elevated. Elytral apex rounded.

Legs and claws long and thin (Fig. 6).

Median lobe of the aedeagus curved, slightly convex dorsally around the basal fourth, with a rounded apex (Fig. 7A, B, E, F). Basal bulb small, rounded. Parameres with three setae each, of which two are apically positioned. Triangular gutter-shaped copulatory piece covered with numerous thorns (Fig. 7B, F), gradually narrowed apically in dorsal aspect.

Male abdominal sternite IX (urite) subtriangular, slightly elongate, somewhat longer than aedeagus (Fig. 7C, G). Apophysis narrow, gradually narrowing distally.

Both gonocoxites IX and gonosubcoxites IX as presented in Figure 7D, H. Gonocoxites IX slightly elongate, somewhat curved, apically rounded, basally completely jointed with massive gonosubcoxites IX (Fig. 7D, H).

Chaetotaxy. Frons with five to seven setae (HT – 6–7) on each side. Pronotum with normal chaetotaxy (two pairs of setae). Six to eight setae on third interstria (HT – 6–7) on each elytron (Fig. 6).

Elytral umbilicate series: First three humeral setae close to marginal gutter, fourth being somewhat farther from the gutter, distance between umbilicate pores 2 and 3 shortest, distance between pores 1 and 2 is approximately the same as between pores 3 and 4; median series at around the middle of the elytra, two setae being somewhat distanced from marginal gutter, distance between pores 5 and 6 about as long as distance between pores 2 and 3; apical series: setae 7 and 8 being somewhat distanced from marginal gutter, distance between pores 7 and 8 longer than distance between pores 3 and 4 (Fig. 6).

Differential diagnosis: The known subspecies of *P. globiceps* differ in shape of the head, length and depth of the frontal furrows, shape of the hind pronotal angles, lateral margins of the head and pronotum, the HL/PL and shape of the humeral angles (Guéorguiev, 1964). Some new characters should also be taken into account in separating *Pheggomisetes* taxa (e.g. TL, HL, HL/HW, HL/AL, HL/TL, HW/NW, HW/PW, HW/EW, AL, AL/TL, PL, PL/PW, PL/TL, PaW, PbW, PW, PW/EW, PWP, EW, EL/EW, BW/PW, elytral umbilicate series position, and aedeagus and copulatory piece shapes) (Tables 2 and 3; Supporting Information, Table S1). The new subspecies is compared here with the morphologically and geographically closest subspecies of *P. globiceps* and the nominotypical subspecies. The former are *P. globiceps ilandjievi* (Figs 10, 11A–D) and *P. globiceps ninae* comb. & stat. nov. (with the head elongately ovoid, lateral margins of the head moderately rounded, head slightly rounded both anteriorly and posteriorly as well, acute/right posterior pronotal angles, pronotum basally constricted, head slightly broader than pronotum and humeral angles slightly elevated) (Guéorguiev, 1964; Ćurčić et al., 2004; this article).

Pheggomisetes globiceps ciniglavcensis subsp. nov. differs from *P. globiceps ilandjievi* in having a smaller value of TL M (6.46 vs. 6.60 mm), different shape of the head (widest at 2/5 of its length vs. widest slightly before the middle), a smaller value of HL/HW M (1.275

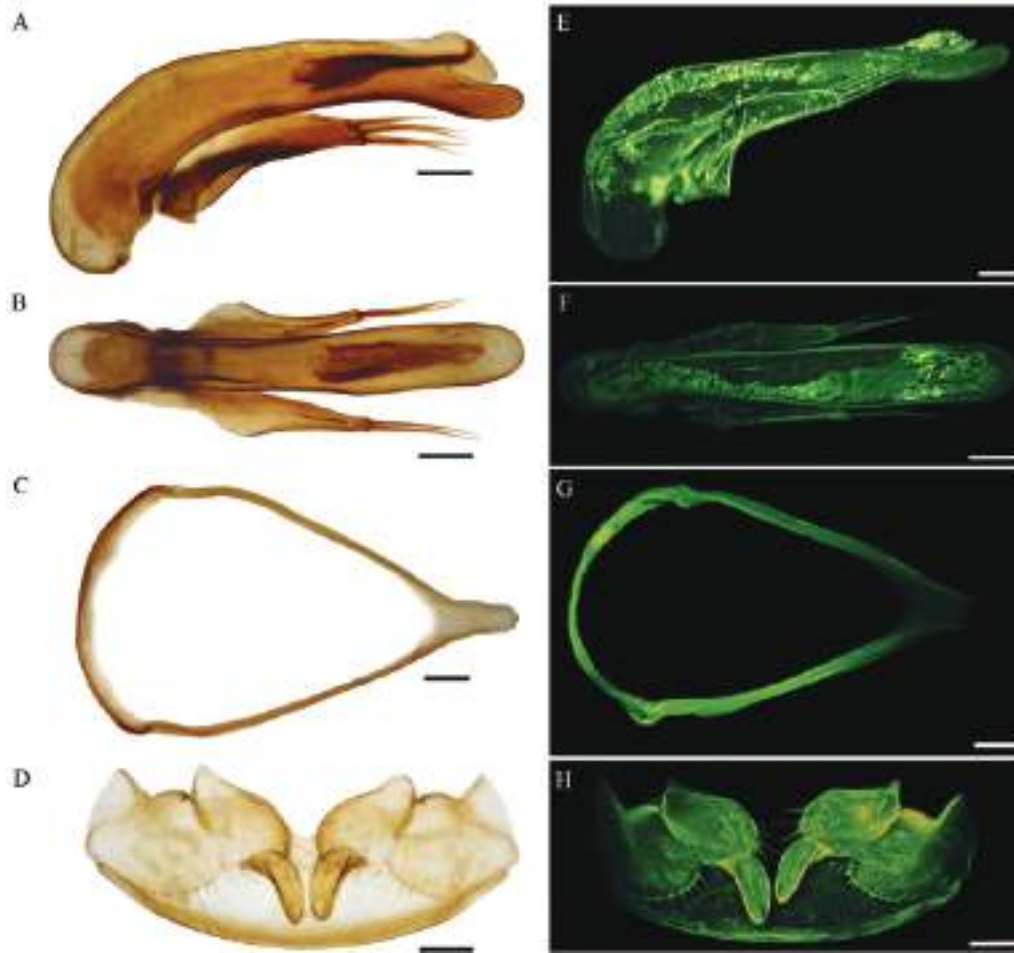


Figure 7. *Pheggomisetes globiceps ciniglavcensis* subsp. nov. from the Propas Pit, village of Činiglavci (near Piroć, Stara Planina Mts., Southeast Serbia. Bright-field (A–D) and TPEF (E–H) microscopy images. A, E, holotype male, aedeagus (lateral view). B, F, holotype male, aedeagus (dorsal view). C, G, holotype male, abdominal sternite IX (urite). D, H, paratype female, gonocoxites IX and gonosubcoxites IX. Scales = 0.1 mm.

vs. 1.32), a greater value of AL M (6.775 vs. 6.64 mm), a greater value of AL/TL M (1.05 vs. 1.01), different shape of the lateral pronotal margins (less rounded anteriorly, more concave posteriorly vs. more rounded anteriorly, less concave posteriorly), greater values of PaW (R 0.63–0.68, M 0.66 vs. R 0.53–0.595 mm, M 0.57 mm), a greater value of PbW M (0.83 vs. 0.75 mm), a greater value of PaW/PW M (0.64 vs. 0.57), different shape of the humeral angles (less rounded and less elevated vs. more rounded and more elevated), a smaller value of EL/EW M (1.64 vs. 1.83), a greater value of BW/PW M (1.03 vs. 0.95), different shape of the median lobe (slightly convex dorsally around the basal fourth, with a narrower apex in dorsal view vs. not convex dorsally around the basal fourth, with a wider apex in dorsal view) and different size of the basal bulb (smaller vs. bigger) (Supporting Information, Table S1) (Guéorguiev, 1964; this study).

Pheggomisetes globiceps ciniglavcensis subsp. nov. differs from *P. globiceps niniae* comb. & stat. nov. in having a greater value of TL M (6.46 vs. 6.295 mm), a smaller value of HL/HW M (1.275 vs. 1.30), a greater value of FL M (0.68 vs. 0.63 mm), greater values of AL M (6.775, males 6.84, females 6.50 vs. 6.525 mm, males 6.56 mm, females 6.30 mm), a greater value of HW/NW M (2.405 vs. 2.26), a greater value of EL M (3.50 vs. 3.36 mm), a greater value of EW M (2.135 vs. 1.99 mm), a smaller value of EL/EW M (1.64 vs. 1.69), a greater value of BW/PW M (1.03 vs. 0.91), different shape of the median lobe (narrower, somewhat more curved basally, then regularly curved, slightly convex dorsally around the basal fourth, with a narrow anterior part in dorsal view vs. thicker, regularly curved, somewhat convex dorsally in the middle, with a wide anterior part in dorsal view) and a different number of parameral

setae (three, two of them apical vs. five, three of them apical) (Supporting Information, Table S1) (Ćurčić *et al.*, 2004; this study).

Pheggomisetes globiceps ciniglavcensis subsp. nov. differs from *P. globiceps globiceps* (Figs 12, 13A–D) in having different shape of the head (widest at the anterior 2/5 of its length vs. widest somewhat after the middle), a greater value of HW/NW M (2.405 vs. 2.24), greater values of AL M (6.775, males 6.84, females 6.50 vs. 6.585 mm, males 6.775 mm, females 6.30 mm), a smaller value of HL/PL M (1.51 vs. 1.63), a greater value of PL/PW M (0.91 vs. 0.88), a greater value of EW M (2.135 vs. 2.02 mm), a smaller value of EL/EW M (1.64 vs. 1.725), a greater value of BW/PW M (1.03 vs. 0.885), different shape of the median lobe (narrower, elongate, with more elongate basal bulb vs. wider, stout, especially basally, with a short stout basal bulb) and different shape of the copulatory piece in dorsal aspect (gradually narrowing towards the apex vs. wide at the basal 3/5 and markedly narrowed at the apical 2/5) (Supporting Information, Table S1) (Guéorguiev, 1964; this study).

Variability: The number of setae on both frons (five to seven on each side) and elytra can vary (six to eight on each side).

Etymology: The subspecies is named after the village of Činiglavci, in which the type locality is situated.

Distribution: It lives solely in the Propas Pit in the village of Činiglavci (near Pirot) in the Stara Planina Mountains of Southeast Serbia.

Remarks: The new subspecies was originally treated as *P. globiceps ilandjjevi* by Gajović *et al.* (2011), who collected a sample several years ago.

***PHEGGOMISETES GLOBICEPS NINAE* S. ĆURČIĆ,
SCHÖNMANN, BRAJKOVIĆ, B. ĆURČIĆ & TOMIĆ, 2004
COMB. & STAT. NOV.**

(FIGS 8 AND 9A–H)

Material examined: Sixty topotype males and 75 topotype females, Southeast Serbia, Stara Planina Mts., Hodžina Dupka Pit, 43°04'27.9"N 22°47'48.5"E, 692 m a.s.l., village of Petrlaš, near Dimitrovgrad, 26.VI–24.IX.2012, from pitfall traps, leg. Đ. Marković & D. Dragulović (IZFB); nine males and 25 females, Southeast Serbia, Mt. Stara Planina Mts., Petrlaška (= Velika) Pećina Cave, 43°04'27.81"N 22°47'46.50"E, 701 m a.s.l., village of Petrlaš, near Dimitrovgrad, 26.VI–24.IX.2012, both collected by hand and from pitfall traps, leg. D. Antić & S. Ćurčić (IZFB); one male and one female, *idem*, 03.XII.2012, leg. D. Antić &



Figure 8. *Pheggomisetes globiceps ninae* comb. & stat. nov. from the Hodžina Dupka Pit, village of Petrlaš (near Dimitrovgrad), Stara Planina Mts., Southeast Serbia. Topotype male, habitus (dorsal view). Scale = 5.0 mm.

S. Ćurčić (IZFB); one female, *idem*, 19.IX.2013, leg. P. Beron (IZFB); two females, Southeast Serbia, Stara Planina Mts., Džemanska Propast Pit, 43°07'44.2"N 22°79'15.9"E, 738 m a.s.l., village of Petrlaš, near Dimitrovgrad, 24.IX.2012, leg. M. Petković & D. Dragulović (IZFB); one male, Southeast Serbia, Stara Planina Mts., Tmna Dupka Cave, 43°04'42.0"N 22°47'24.5"E, 720 m a.s.l., village of Petrlaš, near



Figure 9. *Pheggomisetes globiceps ninae* comb. & stat. nov. from the Hodžina Dupka Pit, village of Petrlaš (near Dimitrovgrad), Stara Planina Mts., Southeast Serbia. Bright-field (A–D) and TPEF (E–H) microscopy images. A, E, topotype male, aedeagus (lateral view). B, F, topotype male, aedeagus (dorsal view). C, G, topotype male, abdominal sternite IX (urite). D, H, topotype female, gonocoxites IX and gonosubcoxites IX. Scales = 0.1 mm.

Dimitrovgrad, 24.IX.2012, leg. S. Ćurčić (IZFB); two males and ten females, *idem*, 24.IX-03.XII.2012, from pitfall traps, leg. D. Antić & S. Ćurčić (IZFB).

Description: The description has been already presented by Ćurčić *et al.* (2004).

Elytral umbilicate series: First three humeral setae close to marginal gutter, fourth being somewhat farther from the gutter, distance between umbilicate pores 2 and 3 shortest, distance between pores 3 and 4 longest; median series at around the middle of the elytra, two setae being somewhat distanced from marginal gutter, distance between pores 5 and 6 somewhat shorter than distance between pores 2 and 3; apical series: setae 7 and 8 being somewhat distanced from marginal gutter, distance between pores 7 and 8 shorter than distance between pores 3 and 4 (Fig. 8).

Differential diagnosis: The subspecies is compared here with both the morphologically and geographically closest subspecies of *P. globiceps* and the nominotypical subspecies. The former are *P. globiceps ilandjievi* and *P. globiceps ciniglavcensis* subsp. nov. (Guéorguiev, 1964; this study).

Pheggomisetes globiceps ninae comb. & stat. nov. differs clearly from *P. globiceps ilandjievi* in having a smaller value of TL M (6.295 vs. 6.60 mm), smaller values of AL M (6.525, males 6.56, females 6.30 vs. 6.64 mm, males 6.675 mm, females 6.60 mm), a smaller value of HW/NW M (2.26 vs. 2.35), a greater value of PaW M (0.61 vs. 0.57 mm), a greater value of PbW M (0.79 vs. 0.75 mm), different shape of the pronotal base in males (straight vs. concave), different shape of the hind pronotal angles (almost right vs. acute, rarely right), a smaller value of EL M (3.36 vs. 3.555 mm), a



Figure 10. *Pheggomisetes globiceps ilandjjevi* from the Golyama Balabanova Dupka Cave, village of Komshtitsa (near Sofia), Stara Planina Mts., Western Bulgaria. Topotype male, habitus (dorsal view). Scale = 5.0 mm.

greater value of EW M (1.99 vs. 1.905 mm), a smaller value of EL/EW M (1.69 vs. 1.83), different shape of the median lobe (thicker, with a wider anterior part in dorsal view vs. more elongate, with a narrower anterior part in dorsal view) and a different number of parameral setae (five vs. three to four) (Supporting Information, Table S1) (Guéorguiev, 1964; Ćurčić *et al.*, 2004; this study).

All morphological differences between *P. globiceps ninae* comb. & stat. nov. and *P. globiceps ciniglavcensis* subsp. nov. are mentioned above (see the Differential diagnosis of *P. globiceps ciniglavcensis*

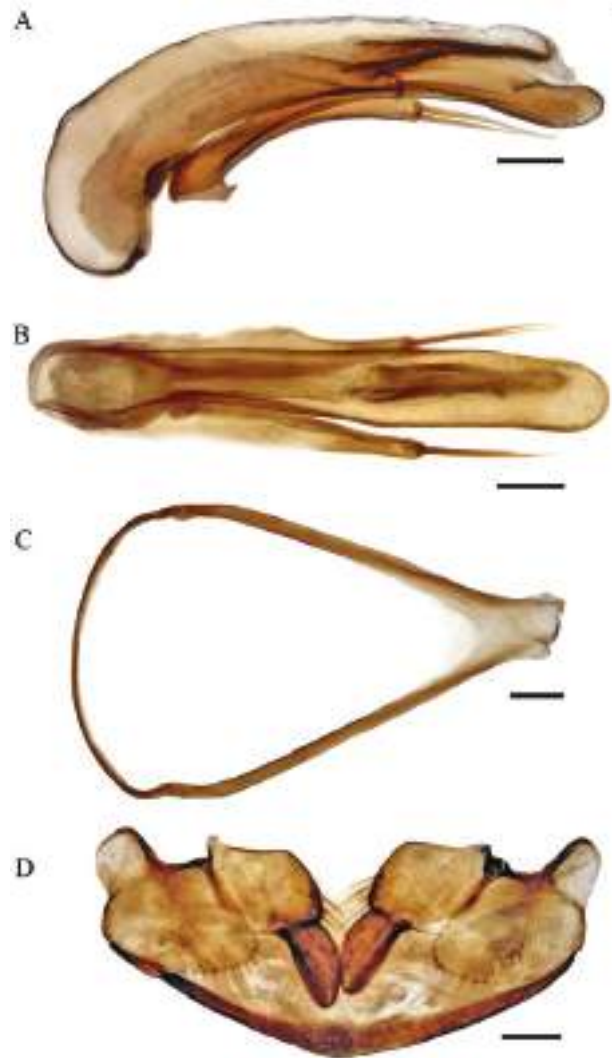


Figure 11. *Pheggomisetes globiceps ilandjjevi* from the Golyama Balabanova Dupka Cave, village of Komshtitsa (near Sofia), Stara Planina Mts., Western Bulgaria. A, topotype male, aedeagus (lateral view). B, topotype male, aedeagus (dorsal view). C, topotype male, abdominal sternite IX (urite). D, topotype female, gonocoxites IX and gonosubcoxites IX. Scales = 0.1 mm.

subsp. nov.) (Figs 6, 7A–H, 8, 9A–H; Supporting Information, Table S1) (Ćurčić *et al.*, 2004; this study).

P. globiceps ninae comb. & stat. nov. can be easily distinguished from *P. globiceps globiceps* on the basis of having a smaller value of TL M (6.295 vs. 6.405 mm), a smaller value of HL M (1.40 vs. 1.47 mm), a smaller value of HW M (1.08 vs. 1.17 mm), a greater value of HL/HW M (1.30 vs. 1.26), different shape of the head (widest at around the anterior 2/5 of its length vs. widest somewhat after the middle), a smaller value of HL/PL M (1.52 vs. 1.63), a smaller value of



Figure 12. *Pheggomisetes globiceps globiceps* from the Dushnika Cave, village of Iskrets (near Sofia), Mt. Ponor Planina, Western Bulgaria. Topotype male, habitus (dorsal view). Scale = 5.0 mm.

HW/PW M (1.07 vs. 1.14), a greater value of PL/PW M (0.92 vs. 0.88), a smaller value of EL M (3.36 vs. 3.47 mm), a different number of parameral setae (five vs. three to four) and different shape of the median lobe (somewhat convex dorsally around the middle, with a somewhat elongate basal bulb vs. somewhat convex dorsally around the basal third, with a stout, relatively small basal bulb) (Supporting Information, Table S1) (Guéorguiev, 1964; Ćurčić *et al.*, 2004; this study).

Distribution: It lives in a few caves and pits on the western border of the Odorovačko Polje (692–738 m a.s.l.) in the village of Petrlaš (near Dimitrovgrad) in the Stara Planina Mountains of Southeast Serbia.

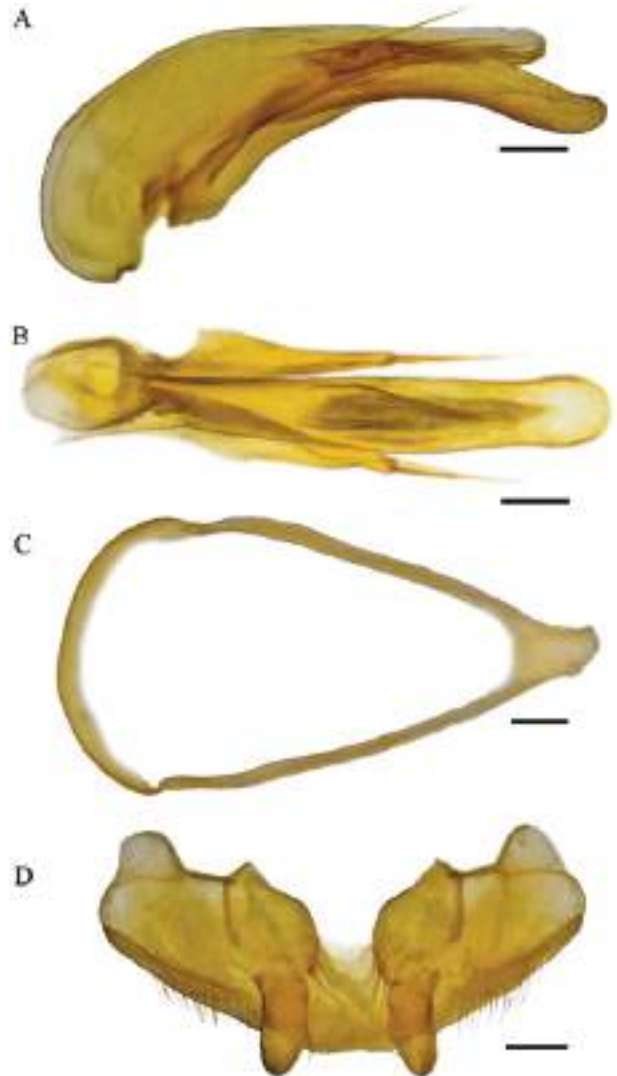


Figure 13. *Pheggomisetes globiceps globiceps* from the Dushnika Cave, village of Iskrets (near Sofia), Mt. Ponor Planina, Western Bulgaria. A, topotype male, aedeagus (lateral view). B, topotype male, aedeagus (dorsal view). C, topotype male, abdominal sternite IX (urite). D, topotype female, gonocoxites IX and gonosubcoxites IX. Scales = 0.1 mm.

Remarks: Interestingly, the taxon was originally treated as *P. globiceps ilandjievi* by Pretner (1970), who collected the first specimens from the Hodžina Dupka Pit with P. R. Deeleman. A similar opinion was expressed by Nešić *et al.* (2010) in a recent contribution. After the performed morphological and molecular analyses, we found that there is no difference between *Pheggomisetes* specimens from the Hodžina Dupka Pit, the Petrlaška (= Velika) Pečina Cave, the Džemanska Propast Pit and the Tmna Dupka Cave, all situated in the village of Petrlaš near Dimitrovgrad in the Stara Planina Mountains

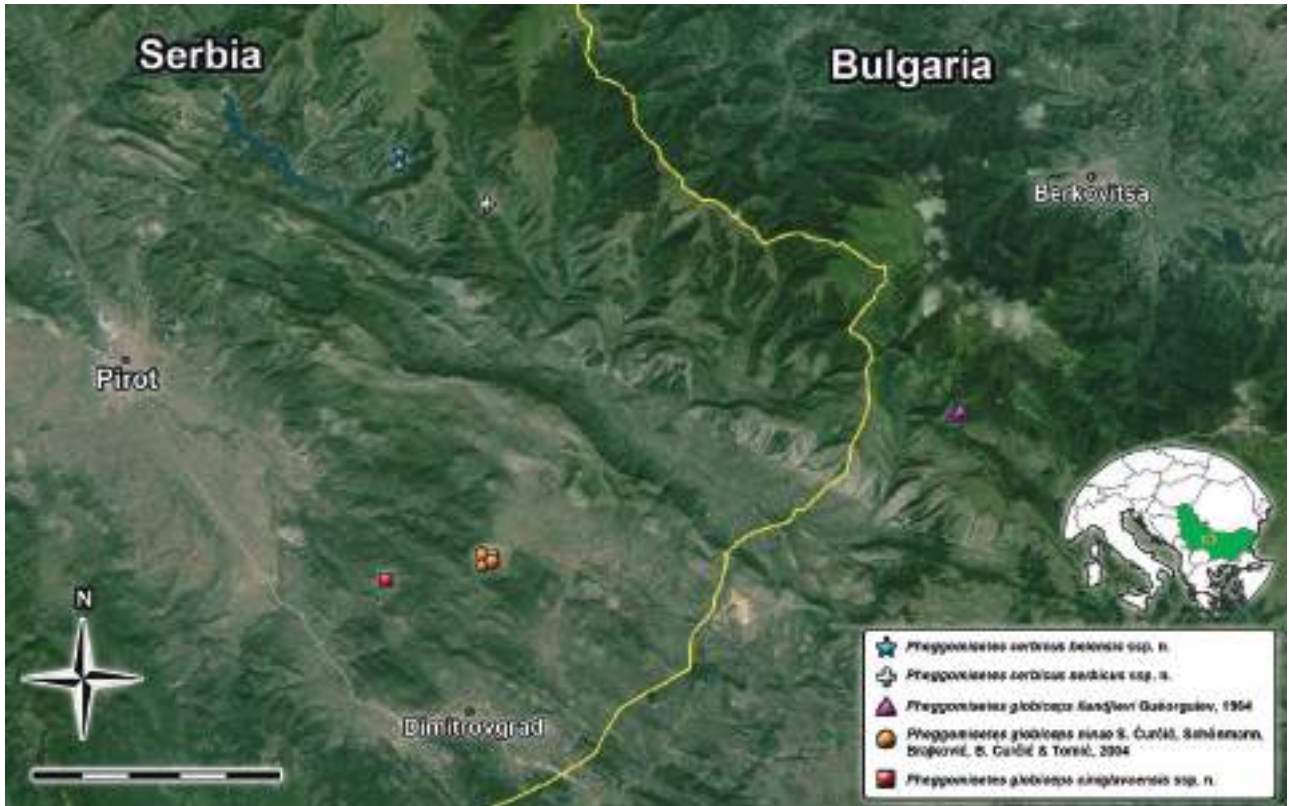


Figure 14. Distribution of *Pheggomisetes* taxa in Serbia and the immediate surroundings. Scale = 10 km.

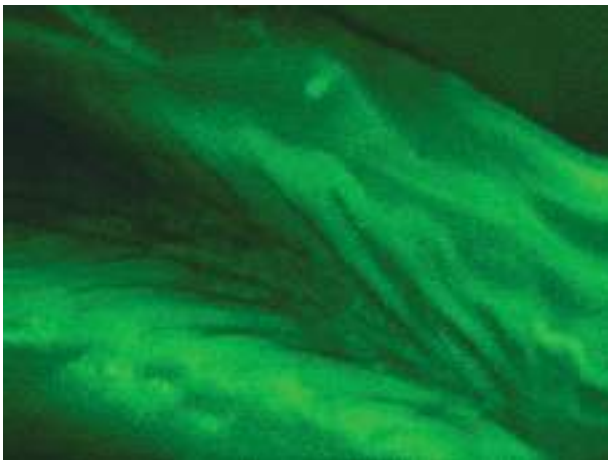


Figure 15. TPEF microscopy image of part of the tooth-like copulatory piece of *P. globiceps ninae* comb. & stat. nov., showing fine details of the structure.

of Southeast Serbia. They all belong to the same taxon, which was previously described under the name *P. ninae*.

After a thorough morphological analysis supported by molecular data, we established that the

existing differences between *P. ninae* and other *Pheggomisetes* species are not great enough to treat it as a distinct species. The taxon in question deserves a subspecies rank within *P. globiceps* since certain smaller differences (both morphological and phylogenetical) were proved to exist between it and the geographically nearest subspecies of *P. globiceps*, but these were not significant enough to convince us of the need to separate it as a species. To be specific, certain morphological differences were observed in regard to TL, AL, HW/NW, FL, FL/HL, PaW, PbW, PaW/PW, shape of the lateral pronotal margins, pronotal base shape, EL, EW, EL/EW, BW/PW, shape of the humeral angles and position of the elytral umbilicate series (Supporting Information, Table S1), but shapes of the aedeagi and copulatory pieces are quite similar, indicating that the above-mentioned differences are in reality interpopulational, not interspecific (an assertion supported by small genetic differences recorded between the given taxon and its closest relatives, 0.5 and 1.3%, respectively). We therefore suggest that the taxonomic status of *P. ninae* be changed to *P. globiceps ninae* comb. & stat. nov.

KEY TO SPECIES OF THE GENUS *PHEGGOMISETES* KNIRSCH, 1923 (FIG. 14)

- 1 Neck constriction very broad and not abrupt in dorsal view, while flat in lateral view. Head elliptical, cheeks less rounded (Northwest Bulgaria) *P. buresi* (Knirsch, 1923)
- Neck constriction narrow and abrupt in dorsal view, while deeper in lateral view. Head circular or ovoid, cheeks more rounded 2
- 2 Pronotum clearly narrowed in front of base. Head very broad in posterior third, with frontal furrows very deep (Northwest Bulgaria) *P. radevi* Knirsch, 1924
- Pronotum not narrowed in front of base, sometimes with lateral margins more or less sinuate in posterior third. Head narrower in posterior third, with frontal furrows less deep 3
- 3 Longer TL M (≥ 6.295 mm), antennae longer (M ≥ 6.525 mm), longer than body, frontal furrows not reaching middle of the head, humeral angles more obtuse, less elevated, copulatory piece gradually narrowed apically (Western Bulgaria and Southeast Serbia) [*P. globiceps* Buresch, 1925] 4
- Smaller TL M (≤ 6.11 mm), antennae shorter (M ≤ 5.99 mm), slightly shorter than body, frontal furrows exceeding/reaching middle of the head, humeral angles more rounded, quite elevated, copulatory piece more markedly narrowed apically (Southeast Serbia) [*P. serbicus* Ćurčić, Vrbica & B. Guéorguiev, sp. nov.] 5
- 4 TL M 6.295 mm, antennae shorter (M 6.525 mm), humeral angles more elevated, HW/NW M 2.26, EL M 3.36 mm, EW M 1.99 mm, elytra at the base narrower than pronotum, median lobe thicker, regularly curved, somewhat convex dorsally in the middle, with a wide anterior part in dorsal view (Southeast Serbia) *P. globiceps ninae* S. Ćurčić, Schönmann, Brajković, B. Ćurčić & Tomić, 2004 comb. & stat. nov.
- TL M 6.46 mm, antennae longer (M 6.775 mm), humeral angles less elevated, HW/NW M 2.405, EL M 3.50 mm, EW M 2.135 mm, elytra at the base slightly wider than pronotum, median lobe narrower, somewhat more curved basally, then regularly curved, slightly convex dorsally around the basal fourth, with a narrow anterior part in dorsal view (Southeast Serbia) *P. globiceps ciniglavcensis* Ćurčić & Vrbica, subsp. nov.
- 5 TL M 6.11 mm, frontal furrows somewhat exceeding mid head level, HW/NW M 2.50, FL M 0.75 mm, AL M 5.91 mm, anterior pronotal margin more concave in females, pronotal base more concave in the middle, PaW/PbW M 0.74, EL/EW M 1.725, lateral margins of elytra rounded anteriorly, median lobe apex somewhat elevated, basal bulb and basal part of median lobe narrower (Southeast Serbia) *P. serbicus serbicus* Ćurčić, Vrbica & B. Guéorguiev, subsp. nov.
- TL M 6.045 mm, frontal furrows reaching mid head level, HW/NW M 2.24, FL M 0.68 mm, AL M 5.99 mm, anterior pronotal margin less concave in females, pronotal base less concave in the middle, PaW/PbW M 0.78, EL/EW M 1.77, lateral margins of elytra more straight anteriorly, median lobe apex almost straight, basal bulb and basal part of median lobe wider (Southeast Serbia) *P. serbicus belensis* Ćurčić, Vrbica & B. Guéorguiev, subsp. nov.

TPEF MICROSCOPY OF THE INTERNAL STRUCTURES OF *PHEGGOMISETES*

Certain well-chitinized internal morphological structures of *Pheggomisetes* ssp. were observed by two-photon excited autofluorescence microscopy. The samples were not fluorescently labelled, so autofluorescence was detected and used for imaging. For the study, we used a 25 \times numerical aperture 0.8 water/glycerin immersion objective and 930-nm excitation wavelength. This somewhat longer wavelength was utilized to avoid the autofluorescence of residual tissues remaining after beetle dissection. In addition, it was possible to penetrate deeper (up to 200 μ m for the studied sample) through the chitinous cuticle due to the reduced two-photon absorption of chitin (Rabasović *et al.*, 2015).

We present TPEF 3D images of the male (aedeagus) and female (gonocoxites IX and gonosubcoxites IX) genitalia and the male abdominal sternite IX (urite) of all *Pheggomisetes* taxa from Serbia. The images revealed

morphological details similar to those observed using classical bright-field microscopy (Figs 2E–H, 5E–H, 7E–H, 9E–H). In addition, selected 3D video clips of the three morphological structures are included, showing them in rotation around the longitudinal, lateral and vertical axes (Supporting Information, Appendices S1–S6). This makes it possible for the structures to be observed in every direction, which provides better insight into the shape and spatial relations of internal structures.

The aedeagus is observed both laterally and dorsally (Figs 2E, F, 5E, F, 7E, F, 9E, F). The structure of both the surface (the fine relief) and the inner part (the copulatory piece composed of numerous tooth-like structures and the inner sac) of the median lobe (Fig. 15) is clearly distinguished. Both strongly (e.g. the copulatory piece) and weakly (e.g. the inner sac) chitinized parts of the aedeagus are visible (Figs 2E, F, 5E, F, 7E, F, 9E, F). All parts of the aedeagus (median

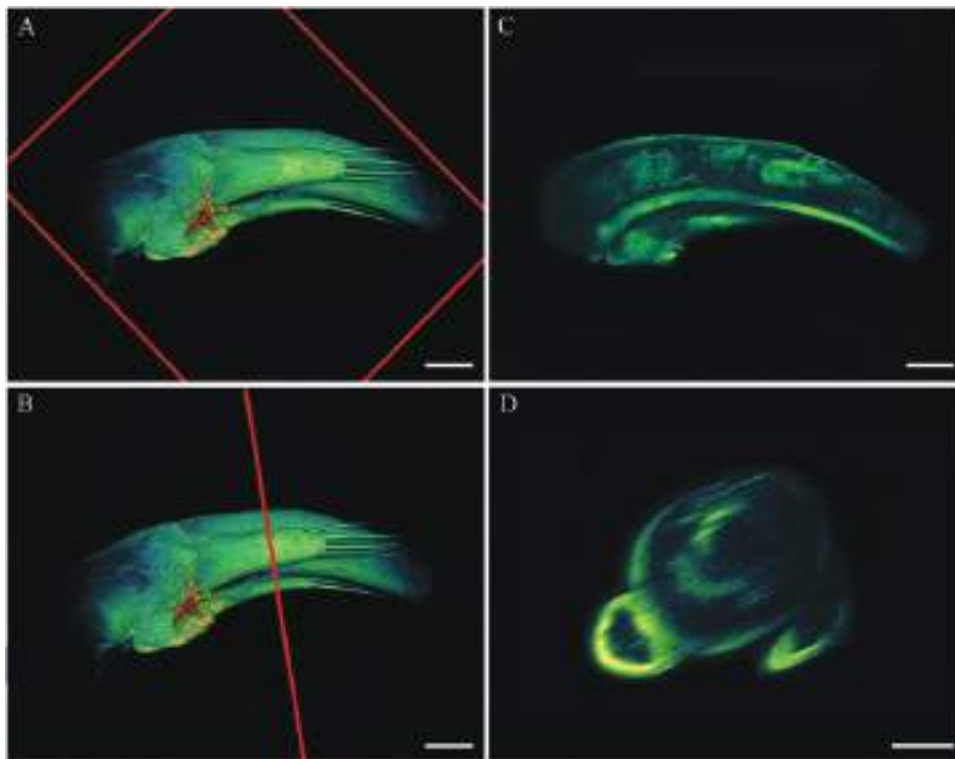


Figure 16. TPEF microscopy images of the aedeagus of *P. globiceps ninae* comb. & stat. nov. A, lateral view with longitudinal section plane (red square). B, lateral view with cross-sectional plane (red line). C, a corresponding longitudinal section. D, a corresponding cross section. Scales = 0.10 mm (A–C) and 0.05 mm (D).

lobe, basal bulb, parameres and their setae, copulatory piece and inner sac) are sharply delimited from each other (Figs 2E, F, 5E, F, 7E, F, 9E, F), as in the case of the images recorded earlier by bright-field microscopy (Figs 2A, B, 5A, B, 7A, B, 9A, B).

One of the male internal sclerites, abdominal sternite IX (urite), is clearly visible and can be imaged by TPEF microscopy since it is well chitinized (Figs 2G, 5G, 7G, 9G). The shape and thickness of the structure are as visible as in the photographs obtained by bright-field microscopy (Figs 2C, 5C, 7C, 9C).

Similarly, the parts of the female genitalia, which are highly sclerotized (gonocoxites IX and gonosubcoxites IX), were also observed. Sharply delimited parts of the aforementioned female genital structures are visible. The setation and fine relief are distinctly discernible on the surface, while the internal structure can also be observed (Figs 2H, 5H, 7H, 9H).

The images of both cross and longitudinal sections of *Pheggomisetes* male genitalia (Fig. 16C, D) show the clear advantage of NLM vs. traditional classical microscopy in investigating anatomical features. To be specific, all features of the internal structures (e.g. shape and position of copulatory piece) are discernible on any section of the genitalia using this

method (Fig. 16A–D). Apart from internal characteristics of the structures, their thickness can be ascertained and measured as well. One more benefit of using TPEF is that it provides additional data on the shapes of certain structures (e.g. median lobe, parameres, parameral setae) on cross sections (any level) (Fig. 16D), which cannot be detected by classical light microscopy. The images can be further used to calculate data on the structure's surface, shape and volume. The female genitalia can be observed in a similar manner as well.

STATISTICAL MORPHOMETRIC ANALYSIS

Only 20 variables (eight commonly used morphological trait measurements and 12 ratio variables) passed the Shapiro-Wilk normality test (HL, HW, FL, PW, PaW, PbW, EW, EWP, HL/HW, HL/AL, HL/PL, HL/TL, HW/NW, HW/PW, AL/TL, PL/PW, PaW/PW, PbW/PW, PaW/PbW and BW/PW) and were further used for parametric analyses. Normality tests were also performed on log-transformed data, but they resulted in the same 20 variables.

Descriptive statistics of the quantitative traits and ratio variables of *P. globiceps* and *P. serbicus* sp.

nov. subspecies from Serbia are given in Supporting Information, Table S1.

One-way MANOVA of samples of the two *Pheggomisetes* species revealed significant differences between the species [Wilks' $\Lambda = 0.095$, $F(20, 40) = 19$, $P < 0.001$]. Post hoc pairwise comparison using Scheffe's test indicated that seven variables are statistically significant (Table 2). The HL/AL and HL/TL variables have the most distinct discriminative power. AL/TL, FL, EW, PaW and HL are statistically less important for distinguishing the two species.

Table 3 presents the results of non-parametric comparisons between samples of the two species (for non-normally distributed variables) using the Mann–Whitney U test. Ten variables are recognized as statistically significant, but AL and TL are most important, while EL/TL and PL/TL are somewhat less important, followed by PWP, PW/EW, FL/HL, HW/EW, PL and EL/EW.

One-way MANOVA of *Pheggomisetes* taxa (populations belonging to two species and six subspecies)

revealed significant differences in the variation of eight commonly used morphological trait measurements and 12 ratios [Wilks' $\Lambda = 0.095$, $F(20, 40) = 18.941$, $P < 0.001$ and Wilks' $\Lambda = 0.003$, $F(90, 222) = 5.890$, $P < 0.001$, respectively].

The results of linear DA of 20 variables showed that the total correct percentage of the classification matrix of all six *Pheggomisetes* subspecies was very high (95.59%). Only one specimen from the *P. serbicus belensis* group is classified into the *P. serbicus serbicus* group, and one specimen from the *P. globiceps ciniglavensis* group is classified into the *P. globiceps ninae* group.

All pairwise squared Mahalanobis distances between the taxa were significant at a level of 99%. UPGMA cluster analysis of the squared Mahalanobis distances clustered both *P. serbicus* sp. nov. subspecies in the same branch and all the analysed subspecies of *P. globiceps* together in another branch, indicating that the two species are clearly separate (Fig. 17).

On the basis of morphometric study, it can be asserted that the phenetically closest subspecies

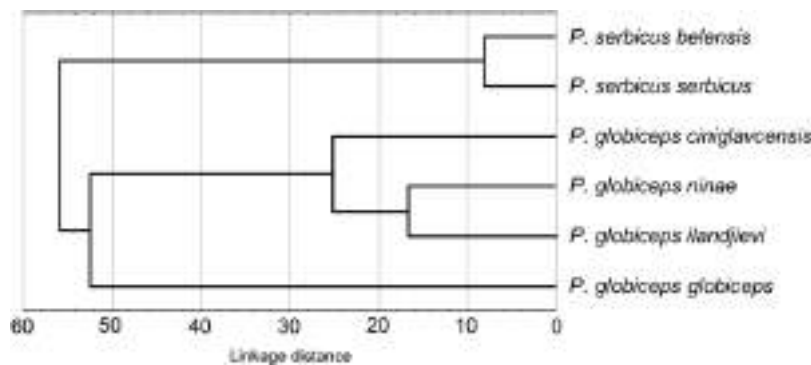


Figure 17. UPGMA tree diagram of two *Pheggomisetes* species and six subspecies based on squared Mahalanobis distances (scale shown) obtained from eight analysed morphological trait measurements and 12 ratio variables.

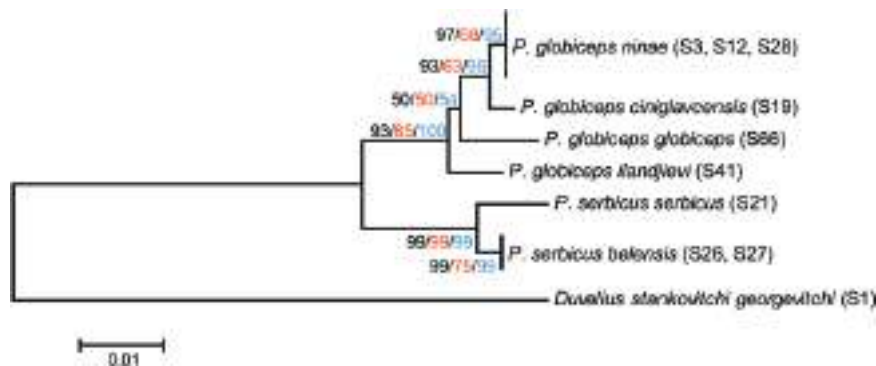


Figure 18. Phylogenetic tree of *Pheggomisetes* taxa based on *COI* sequences obtained using the neighbor-joining (NJ), maximum parsimony (MP) and maximum likelihood (ML) methods. Bootstrap values are indicated above/below branches in the following order: NJ (black)/MP (red)/ML (blue). *Duvalius stankovitchi georgevitchi* was used as the outgroup taxon. Specimen codes are listed in parentheses.

within *P. globiceps* are *P. globiceps ninae* comb. & stat. nov., *P. globiceps ilandjievi* and *P. globiceps ciniglavcensis* subsp. nov., while *P. globiceps globiceps* is morphologically somewhat separate (Fig. 17).

Unquestionably, there is a need for a comprehensive morphometric analysis within the genus, including all currently existing taxa and more numerous samples of specimens, to obtain the most precise results possible.

MOLECULAR AND PHYLOGENETIC ANALYSES

Since the taxonomy of *Pheggomisetes* is not well settled (Guéorguiev, 1964; Ćurčić et al., 2004), a substantial molecular analysis performed on the taxa could help us to solve some taxonomic problems. An appreciable interspecific, intraspecific and individual variability of characters (number of supraorbital, elytral and parameral setae; dorsal outlines of the head, pronotum and elytra) is evident (Guéorguiev, 1964; Nešić et al., 2010) within this morphologically isolated genus (Jeannel, 1928; Guéorguiev, 1977). For these reasons, we performed a molecular analysis of the Serbian taxa and their closest Bulgarian relatives that were available to us.

Phylogenetic reconstruction of *Pheggomisetes* taxa was performed using three different methods, and all of them resulted in trees with the same topology (Fig. 18). Specimens were grouped into two distinct, well-supported clades. The mean genetic distance between clades was 3.6%.

The taxa grouped within the first clade belong to *P. globiceps*. Four recognized subspecies are clustered separately with high bootstrap support. *Pheggomisetes globiceps globiceps* and *P. globiceps ilandjievi* are separate from the subclade consisting of *P. globiceps ciniglavcensis* subsp. nov. and *P. globiceps ninae* comb. & stat. nov. The genetic distances between subspecies range from 0.5% between *P. globiceps ciniglavcensis* subsp. nov. and *P. globiceps ninae* comb. & stat. nov. up to 1.8% between *P. globiceps globiceps* and *P. globiceps ilandjievi*. The distance between *P. globiceps ilandjievi* and *P. globiceps ciniglavcensis* subsp. nov. was 1.5%, while distance between *P. globiceps ilandjievi* and *P. globiceps ninae* comb. & stat. nov. was 1.3%. Conversely, the distance between *P. globiceps globiceps* and *P. globiceps ciniglavcensis* subsp. nov. was 1.5%, while distance between *P. globiceps globiceps* and *P. globiceps ninae* comb. & stat. nov. was 1.3%.

The taxa grouped within the second clade belong to the newly described *P. serbicus* sp. nov., which clearly differentiates into two subspecies, viz., *P. serbicus serbicus* subsp. nov. and *P. serbicus belensis* subsp. nov., with a mean genetic distance of 1.1% between them.

The obtained levels of sequence divergence between the species (> 3.5%) and subspecies (0.5–1.8%) are

significant at species/subspecies levels (Hebert, Ratnasingham & de Waard, 2003), as was recently shown for the trechine genus *Paraphaenops* Jeannel, 1916 (Ortuño et al., 2016), as well as for other animal models (Hebert et al., 2003).

The recorded molecular data are in agreement with the results achieved by classical taxonomic analysis (based on morphological characters and their variations) of Serbian *Pheggomisetes* taxa, thus confirming the correctness of erecting three taxa new to science (a species and two subspecies) and assigning a new status (subspecific within *P. globiceps*) to a taxon previously treated as a species.

On the basis of two analysed *Pheggomisetes* taxa (*P. globiceps globiceps* Buresch, 1925 and *P. globiceps ninae* comb. & stat. nov., the latter being treated as *P. globiceps ilandjievi*), Faille et al. (2013) hypothesized that the genus is most likely an adelphotaxon of a clade containing isotopic species of the largely paraphyletic *Duvalius* Delarouzeé, 1859 and five other subterranean genera. More genera inhabiting both Dinaric and Balkan mountain ranges need to be included in a comprehensive phylogenetic analysis to establish the true relationships of subterranean trechines in the region and disclose the origin and paths of colonization of different lineages on the Balkan Peninsula (Faille et al., 2013).

CONCLUSIONS

On the basis of the results of taxonomic, morphological and molecular analyses, we were able to identify one new trechine ground beetle species (*P. serbicus* sp. nov.) and two new subspecies (*P. serbicus belensis* subsp. nov. and *P. globiceps ciniglavcensis* subsp. nov.), in addition to which we propose a change in the status of one taxon (*P. globiceps ninae* comb. & stat. nov.). The new trechine taxa belong to an isolated and probably ancient phyletic lineage that most likely originated in the Oligocene (Guéorguiev, 1977; Ćurčić et al., 2004; Faille et al., 2013). The aforementioned new taxa are all relicts whose current distribution is limited to confined underground localities in Southeast Serbia.

The use of TPEF microscopy in this study has provided better knowledge and additional information about the morphology and anatomy of *Pheggomisetes* taxa. It is one more tool that taxonomists can use to define more easily the taxonomic status of lower taxa, especially ones whose morphology is difficult to examine using classical light microscopy. NLM images and 3D models enable investigators to achieve deeper penetration into chitinized tissues, thereby revealing in-volume details that represent additional information useful in the determination of taxa.

In analysing partial sequences of the *COI* gene, we confirmed our taxonomic findings. In this study, we show that the *COI* gene can be used for molecular identification of *Pheggomisetes* taxa.

It would be of importance in the future to arrange a comprehensive morphological and molecular analysis of *Pheggomisetes* specimens from all known sites in both Bulgaria and Serbia to find out whether they belong to the taxa and species groups already known or whether a new classification would be more appropriate. In addition, a detailed molecular study of all *Pheggomisetes* subspecies (especially those subordinate to *P. globiceps*) with analysis of various morphological characteristics is needed to define their true taxonomic position.

ACKNOWLEDGEMENTS

This study was financially supported by the Serbian Ministry of Education, Science, and Technological Development (Grants Nos. ON173038, III43001, ON171038 and III45016). We are grateful for the support of the EU Commission Project AREA (Grant No. 316004). In addition, we owe many thanks to Prof. Dr Zora Dajić-Stevanović and Mr Radenko Radošević (University of Belgrade – Faculty of Agriculture, Belgrade, Serbia) for helping us with imaging. Finally, we also thank Mr Darko Dragulović (Podgorac Timok, Serbia), Mr Ivo Petrović (Pirót, Serbia) and Prof. Dr Petar Beron (Sofia, Bulgaria), who helped us in collecting some of the beetle specimens analysed in this article.

REFERENCES

- Andújar C, Gómez-Zurita J, Rasplus JY, Serrano J. 2012.** Molecular systematic and evolution of the subgenus *Mesocarabus* Thomson, 1875 (Coleoptera: Carabidae: *Carabus*), based on mitochondrial and nuclear DNA. *Zoological Journal of the Linnean Society* **166**: 787–804.
- Belousov IA, Dolzhansky VY. 1994.** A new aphaenopsoid genus of the tribe Trechini from the Caucasus. *Mitteilungen der Münchner Entomologischen Gesellschaft* **84**: 59–63.
- Belousov IA, Koval AG. 2009.** To the knowledge on the aphaenopsoid trechine beetles (Coleoptera: Carabidae: Trechini) of the Caucasus. *Caucasian Entomological Bulletin* **5**: 163–173.
- Beron P. 1994.** Résultats des recherches biospéléologiques en Bulgarie de 1971 à 1994 et liste des animaux cavernicoles Bulgares. *Tranteeva* **1**: 1–137.
- Casale A, Laneyrie R. 1982.** Trechodinae et Trechinae du Monde. Tableau des sous-familles, tribus, séries phylétiques, genres, et catalogue général des espèces. *Mémoires de Biospéologie* **9**: 1–226.
- Casale A, Vigna Taglianti A, Juberthie C. 1998.** Coleoptera Carabidae. In: Juberthie C, Decu V, eds. *Encyclopaedia biospéologica. Tome II*. Moulis-Bucharest: Société de Biospéologie & Académie Roumaine, 1047–1081.
- Chien CH, Chen WW, Wu JT, Chang TC. 2011.** Label-free imaging of *Drosophila* in vivo by coherent anti-Stokes Raman scattering and two-photon excitation autofluorescence microscopy. *Journal of Biomedical Optics* **16**: 016012.
- Christiansen K. 2012.** Morphological adaptations. In: White WB, Culver DC, eds. *Encyclopedia of caves, 2nd edn*. Amsterdam: Elsevier, 517–528.
- Contreras-Díaz HG, Moya O, Oromí P, Juan C. 2007.** Evolution and diversification of the forest and hypogean ground-beetle genus *Trechus* in the Canary Islands. *Molecular Phylogenetics and Evolution* **42**: 687–699.
- Ćurčić SB, Brajković MM, Ćurčić BPM. 2007.** *The carabids of Serbia*. Belgrade–Vienna: Institute of Zoology, Faculty of Biology, University of Belgrade, Committee for Karst and Speleology, Serbian Academy of Sciences and Arts, Department of Conservation Biology, Vegetation- and Landscape Ecology, Faculty of Life Sciences, University of Vienna & UNESCO MAB Committee of Serbia.
- Ćurčić SB, Schönmann H, Brajković MM, Ćurčić BPM, Tomić VT. 2004.** On a new cave-dwelling beetle (Trechinae, Carabidae) from Serbia. *Archives of Biological Sciences, Belgrade* **56**: 109–113.
- de Campos Vidal B. 2011.** Butterfly scale form birefringence related to photonics. *Micron* **42**: 801–807.
- Decou V, Botosaneanu L. 1964.** Quelques données relatives à l'anatomie de *Pheggomisetes bureschi* Knirsch (Coleoptera, Trechinae). *Annales de Spéléologie* **19**: 759–768.
- Denk W, Strickler JH, Webb WW. 1990.** Two-photon laser scanning fluorescence microscopy. *Science* **248**: 73–76.
- Deuve T, Cruaud A, Genson G, Rasplus JY. 2012.** Molecular systematics and evolutionary history of the genus *Carabus* (Col. Carabidae). *Molecular Phylogenetics and Evolution* **65**: 259–275.
- Faille A, Andújar C, Fadrique F, Ribera I. 2014.** Late Miocene origin of a Ibero-Maghrebian clade of ground beetles with multiple colonisations of the subterranean environment. *Journal of Biogeography* **41**: 1979–1990.
- Faille A, Bourdeau C, Fresneda J. 2012.** Molecular phylogeny of the *Trechus brucki* group, with description of two new species from the Pyreneo-Cantabrian area (France, Spain) (Coleoptera, Carabidae, Trechinae). *ZooKeys* **217**: 11–51.
- Faille A, Casale A, Balke M, Ribera I. 2013.** A molecular phylogeny of Alpine subterranean Trechini (Coleoptera: Carabidae). *BMC Evolutionary Biology* **13**: 248.
- Faille A, Casale A, Ribera I. 2010a.** Phylogenetic relationships of Western Mediterranean subterranean Trechini groundbeetles (Coleoptera: Carabidae). *Zoologica Scripta* **40**: 282–295.
- Faille A, Ribera I, Deharveng L, Bourdeau C, Garnery L, Quéinnec E, Deuve T. 2010b.** A molecular phylogeny shows the single origin of the Pyrenean subterranean Trechini ground beetles (Coleoptera: Carabidae). *Molecular Phylogenetics and Evolution* **54**: 97–106.
- Gajović V, Mandić M, Njunjić I, Pavićević D. 2011.** Kompleksna speleološka istraživanja jame Propas' u Činiglavcima. In: Čalić

- J, ed. *Conference Proceedings of the 7th Symposium on Karst Protection*, 21–22 May 2011, Bela Palanka, Serbia. Belgrade: Academic Speleological Alpinistic Club, 71–81.
- Guéorguiev VB. 1964.** Révision du genre *Pheggomisetes* Knirsch (Coleoptera, Carabidae). *Časopis Československé Společnosti Entomologické* **61**: 265–278.
- Guéorguiev VB. 1977.** *La faune troglobie terrestre de la péninsule Balkanique. Origine, formation et zoogéographie, special edn.* Sofia: Bulgarian Academy of Sciences.
- Guéorguiev VB, Guéorguiev BV. 1995.** *Catalogue of the ground-beetles of Bulgaria (Coleoptera: Carabidae)*. Sofia-Moscow: Pensoft Publishers.
- Hebert PDN, Ratnasingham S, de Waard JR. 2003.** Barcoding animal life: cytochrome *c* oxidase subunit 1 divergences among closely related species. *Proceedings of the Royal Society of London B: Biological Sciences* **270**: 596–599.
- Jeannel R. 1928.** Monographie des Trechinae. Morphologie comparée et distribution géographique d'un groupe de Coléoptères (Troisième Livraison). Les Trechini cavernicoles. *L'Abeille* **35**: 1–808.
- Juberthie C, Decu V. 1968.** Les glandes pygidiales de quelques Trechitae cavernicoles. *Annales de Spéléologie* **23**: 195–210.
- Kimura M. 1980.** A simple method for estimating evolutionary rates of base substitutions through comparative studies of nucleotide sequences. *Journal of Molecular Evolution* **16**: 111–120.
- Klaus AV, Kulasekera VL, Schawaroch V. 2003.** Three-dimensional visualization of insect morphology using confocal laser scanning microscopy. *Journal of Microscopy* **212**: 107–121.
- Lin CY, Hovhannisyan V, Wu JT, Lin CW, Chen JH, Lin SJ, Dong CY. 2008.** Label-free imaging of *Drosophila* larva by multiphoton autofluorescence and second harmonic generation microscopy. *Journal of Biomedical Optics* **13**: 050502.
- Manly FJB. 1986.** *Multivariate statistical methods – a primer*. New York: Chapman and Hall.
- Masters BR, So PTC. 2008.** *Handbook of biomedical nonlinear optical microscopy*. Oxford: Oxford University Press.
- Mertz J. 2004.** Nonlinear microscopy: new techniques and applications. *Current Opinion in Neurobiology* **14**: 610–616.
- Michels J. 2007.** Confocal laser scanning microscopy: using cuticular autofluorescence for high resolution morphological imaging in small crustaceans. *Journal of Microscopy* **227**: 1–7.
- Moravec P, Uéno S-I, Belousov IA. 2003.** Tribe Trechini. In: Löbl I, Smetana A, eds. *Catalogue of Palaearctic Coleoptera. Vol. 1. Archostemata – Myxophaga – Adephaga*. Stenstrup: Apollo Books, 288–346.
- Nei M, Kumar S. 2000.** *Molecular evolution and phylogenetics*. Oxford: Oxford University Press.
- Nešić D, Kličković M, Pavićević D, Mijatović M, Ognjenović S. 2010.** Rezultati novijih istraživanja Petrlaških pećina. *Zaštita prirode* **61**: 117–142.
- Ober KA. 2002.** Phylogenetic relationships of the carabid subfamily Harpalinae (Coleoptera) based on molecular sequence data. *Molecular Phylogenetics and Evolution* **24**: 228–248.
- Ober KA, Heider TN. 2010.** Phylogenetic diversification patterns and divergence times in ground beetles (Coleoptera: Carabidae: Harpalinae). *BMC Evolutionary Biology* **10**: 262.
- Ober KA, Maddison DR. 2008.** Phylogenetic relationships of tribes within Harpalinae (Coleoptera: Carabidae) as inferred from 28S ribosomal DNA and the *wingless* gene. *Journal of Insect Science* **8**: 63.
- Ortuño VM, Sendra A, Reboleira ASPS, Fadrique F, Faille A. 2016.** The Iberian genus *Paraphaenops* Jeannel, 1916 (Coleoptera: Carabidae: Trechini): morphology, phylogeny and geographical distribution. *Zoologischer Anzeiger* **266**: 71–88.
- Osawa S, Su Z-H, Imura Y. 2004.** *Molecular phylogeny and evolution of carabid ground beetles*. Tokyo: Springer Verlag.
- Pretner E. 1970.** *Antrosedes longicollis* sp. n. iz Bosne, razprostranjenost vrste *Blattodromus herculeus* Reitter in rod *Pheggomisetes* v Srbiji (Coleoptera: Bathysciinae in Trechinae). *Razprave IV razreda SAZU* **13**: 153–164.
- Rabasović MD, Pantelić DV, Jelenković BM, Čurčić SB, Rabasović MS, Vrbica MD, Lazović VM, Čurčić BPM, Krmpot AJ. 2015.** Nonlinear microscopy of chitin and chitinous structures: a case study of two cave-dwelling insects. *Journal of Biomedical Optics* **20**: 016010.
- Reinhardt K, Breunig HG, König K. 2017.** Autofluorescence lifetime variation in the cuticle of the bedbug *Cimex lectularius*. *Arthropod Structure & Development* **46**: 56–62.
- Ribera I, Fresneda J, Bucur R, Izquierdo A, Vogler AP, Salgado JM, Cieslak A. 2010.** Ancient origin of a Western Mediterranean radiation of subterranean beetles. *BMC Evolutionary Biology* **10**: 29.
- Ruiz C, Jordal B, Serrano J. 2009.** Molecular phylogeny of the tribe Sphodrini (Coleoptera: Carabidae) based on mitochondrial and nuclear markers. *Molecular Phylogenetics and Evolution* **50**: 44–58.
- Simon C, Frati F, Beckenbach A, Crespi B, Liu H, Flook P. 1994.** Evolution, weighting and phylogenetic utility of mitochondrial gene sequences and a compilation of conserved polymerase chain reaction primers. *Annals of the Entomological Society of America* **87**: 651–701.
- StatSoft, Inc. 2001.** *STATISTICA (data analysis software system), version 6*. Available at: www.statsoft.com
- Šerić Jelaska L, Jambrošić Vladić Ž, Radovanović H, Franjević D. 2014.** Comparison of molecular and morphological systematics of *Carabus* species (Coleoptera: Carabidae) with special emphasis on species from Dinaric karst. *Periodicum Biologorum* **116**: 249–257.
- Tamura K, Peterson D, Peterson N, Stecher G, Nei M, Kumar S. 2011.** MEGA5: molecular evolutionary genetics analysis using maximum likelihood, evolutionary distance, and maximum parsimony methods. *Molecular Biology and Evolution* **28**: 2731–2739.
- Williams RM, Zipfel WR, Webb WW. 2001.** Multiphoton microscopy in biological research. *Current Opinion in Chemical Biology* **5**: 603–608.
- Zar J. 1999.** *Biostatistical analysis, 4th edn*. New Jersey: Prentice Hall.

SUPPORTING INFORMATION

Additional Supporting Information can be found in the online version of this article at the publisher's web-site:

Table S1. Measurements, morphometric ratios, and qualitative characteristics of *Pheggomisetes* taxa analysed in the current paper. Numerical unbolded values out of parentheses represent mean values, the bold ones are standard deviations (SD), while the ones in parentheses are ranges. The most important characters for distinction of taxa are underlined (* - values in mm).

Appendix S1. TPEF microscopy video clip showing rotation of the aedeagus of *P. globiceps ninae* **comb. & stat. nov.** around the vertical axis.

Appendix S2. TPEF microscopy video clip showing rotation of the aedeagus of *P. globiceps ninae* **comb. & stat. nov.** around the lateral axis.

Appendix S3. TPEF microscopy video clip showing rotation of the male abdominal sternite IX (urite) of *P. globiceps ninae* **comb. & stat. nov.** around the longitudinal axis.


Appendix S4. TPEF microscopy video clip showing rotation of the male abdominal sternite IX (urite) of *P. globiceps ninae* **comb. & stat. nov.** around the lateral axis.

Appendix S5. TPEF microscopy video clip showing rotation of gonocoxites IX and gonosubcoxites IX of *P. globiceps ciniglavcensis* **subsp. nov.** around the longitudinal axis.

Appendix S6. TPEF microscopy video clip showing rotation of gonocoxites IX and gonosubcoxites IX of *P. globiceps ciniglavcensis* **subsp. nov.** around the lateral axis.

FULL ARTICLE

Polarization-resolved SHG imaging as a fast screening method for collagen alterations during aging: Comparison with light and electron microscopy

Irena Miler¹ | Mihailo D. Rabasovic² | Marija Aleksic³ |
Aleksandar J. Krmpot² | Andjelika Kalezic⁴ | Aleksandra Jankovic⁴ |
Bato Korac^{3,4} | Aleksandra Korac^{3*} 

¹Institute for Application of Nuclear Energy-INEP, University of Belgrade, Belgrade-Zemun, Serbia

²Institute of Physics, University of Belgrade, Belgrade, Serbia

³Faculty of Biology, Center for Electron Microscopy, University of Belgrade, Belgrade, Serbia

⁴Institute for Biological Research "Sinisa Stankovic", National Institute of Republic of Serbia, University of Belgrade, Belgrade, Serbia

*Correspondence

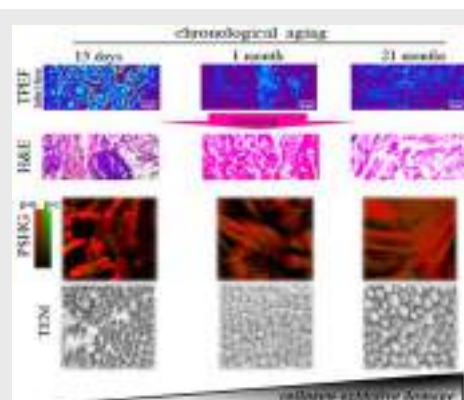
Dr. Aleksandra Korac, Full Professor, University of Belgrade-Faculty of Biology, Chair for Cell & Tissue Biology, Center for Electron Microscopy, Studentski trg 16, 11000 Belgrade, Serbia.
Email: aleksandra.korac@bio.bg.ac.rs

Funding information

Ministarstvo Prosvete, Nauke i Tehnološkog Razvoja

Abstract

Our previous study on rat skin showed that cumulative oxidative pressure induces profound structural and ultrastructural alterations in both rat skin epidermis and dermis during aging. Here, we aimed to investigate the biophotonic properties of collagen as a main dermal component in the function of chronological aging. We used second harmonic generation (SHG) and two-photon excited fluorescence (TPEF) on 5 μm thick skin paraffin sections from 15-day-, 1-month- and 21-month-old rats, respectively, to analyze collagen alterations, in comparison to conventional light and electron microscopy methods. Obtained results show that polarization-resolved SHG (PSHG) images can detect collagen fiber alterations in line with chronological aging and that this method is consistent with light and electron microscopy. Moreover, the β coefficient calculated from PSHG images points out that delicate alterations lead to a more ordered structure of collagen molecules due to oxidative damage. The results of this study also open the possibility of successfully applying this fast and label-free method to previously fixed samples.



KEYWORDS

chronological aging, collagen, electron microscopy, light microscopy, polarization-resolved SHG imaging, second-harmonic generation microscopy, two-photon excited fluorescence microscopy

1 | INTRODUCTION

Skin aging is a complex phenomenon that includes chronological and photoaging, which are both oxidative

damage-related processes. Our previous study on rat skin showed that cumulative oxidative pressure during aging induces profound structural and ultrastructural alterations in rat skin epidermis and dermis.^[1] Here, we focus

on underlying structural alterations of the dermis components during chronological aging.

The dermis has an essential role in determining the morphology and providing mechanical support of the skin. The main dermal component—collagen, is a chiral molecule that consists of three polypeptide α -chains organized in a highly crystalline triple-helix structure and is mainly produced by fibroblasts in the form of procollagen.^[2] Detailed analysis of collagen morphology is critical for assessing structural modifications of the fibrillar matrix since they are often associated with various physiological and pathological processes, for example, wound healing,^[3] cancer,^[4] diabetes and aging.^[5]

The commonly used methods for collagen visualization are conventional histological staining (hematoxylin-eosin staining), histochemistry (van Gieson staining, picosirius red), immunohistochemistry and electron microscopy. These methods are often costly, time-consuming, and have the disadvantage of affecting the sample structure. Namely, chemical alterations to the native molecular structure can occur during the sample preparation procedures. The application of improved and advantageous methods based on nonlinear multiphoton microscopy is showing promising results in overcoming this problem.

Nonlinear laser scanning microscopy utilizing ultrashort laser pulses is an imaging technique with two modalities: two-photon excited fluorescence (TPEF) providing significantly reduced phototoxicity and photobleaching when compared with, for example, confocal or epifluorescent microscopy, whereas second harmonic generation (SHG) is absolutely photobleaching and phototoxicity free.^[6–8] These characteristics come mostly because of the near-infrared light used in TPEF and SHG imaging and the interaction-free pathway of the laser beam through the sample, except in the tiny focal volume where the power is high enough. All of these aforementioned properties provide increased penetration depth for nonlinear imaging, which makes it superior for in vivo imaging nowadays.^[9,10] Moreover, TPEF and SHG have been used in multimodal imaging studies simultaneously with the third harmonic generation (THG), as one more modality of label-free nonlinear imaging, revealing, even more, mutually complementary information of the specimen.^[11–13]

Numerous studies showed that SHG microscopy is the best currently available choice for examining collagen fibers and their structural alterations in tissues. The molecular structure of collagen, a non-centro-symmetric structure, satisfies the criteria for generating the second harmonic signal.^[3,14,15] Type I collagen produces the strongest SHG signal since it has the most ordered structure out of 28 types of collagens that have been identified so far in vertebrates.^[3,16]

For all of these reasons, the number of studies using advantageous TPEF and SHG techniques, both ex vivo and in vivo, has increased significantly in recent years. However, these methods still have limited application due to the lack of protocol standardization, especially in terms of the number of examined samples and correlation of the results with conventional microscopy methods.

To resolve this, we used advantageous TPEF and SHG methods to analyze the biophotonic properties of rat dermis and collagen alterations during chronological aging, in comparison to the conventional light and electron microscopy methods. To avoid potential degradation during the sample preparation procedures, which is of particular concern with native tissues, and standardize the procedure concerning tissue thickness, we used 5 μm thick skin paraffin sections from 15-day-, 1-month- and 21-month-old rats, respectively.

2 | EXPERIMENTAL

2.1 | Sample preparation for light and transmission electron microscopy

Previously prepared paraffin and Araldite embedded skin samples from three animals per examined group were used for light and electron microscopy analyses.^[1] Paraffin blocks were serially cut in 5 μm thick sections, mounted on glass slides, routinely deparaffinized, and used unstained for TPEF and SHG or conventional hematoxylin & eosin (H&E) staining. Namely, for correlative imaging, after TPEF and SHG examination sections along with their serial pairs were stained with H&E, dehydrated, and mounted for light microscopy (Leica DMLB microscope, Leica Microsystems). Thus, using two sets of serial pairs sections, both stained with H&E, we were able to compare and correlate overall tissue morphology and collagen structure and organization.

Araldite blocks of skin samples from the same region used for light microscopy were cut in 1 μm or 80 nm thick sections using a Leica UC6 ultramicrotome (Leica Microsystems, Wetzlar, Germany), mounted on glass slides or copper grids, and stained with basic fuchsin and methylene blue (BF&MB), or contrasted using Leica EM STAIN (Leica Microsystems), respectively. Sections were examined on an optical light microscope or a Philips CM12 transmission electron microscope (Philips/FEI, Eindhoven, Netherlands) equipped with a digital camera (SIS MegaView III, Olympus Soft Imaging Solutions, Münster, Germany). The diameter of collagen fibers was measured in triplicate; 70/230/218 per 15-day/1-month/21-month group were randomly selected. All measurements and analyses were performed using iTEM software (Olympus Soft Imaging Solutions).

2.2 | Experimental setup for TPEF and SHG microscopy

A homemade experimental setup for TPEF and SHG imaging was described in detail by Rabasović et al.^[17] The brief description is as follows: The beam from mode-locked Ti:Sa laser (MIRA 900, Coherent Inc) was tuned to 730 nm for TPEF and 840 nm for SHG imaging. Neutral density filters attenuate the laser beam making it linearly polarized, which enables PSHG measurement only. Further, the laser beam is scanned by two galvo-scanning mirrors (Cambridge technology), passed through the beam expander, and reflected by the short pass dichroic mirror (700 nm cut off) toward the objective lens Zeiss EC Plan-Neofluar 40x NA = 1.3. The signal, either the TPEF or SHG, is collected by the same objective lens in back reflection. It passes through the dichroic mirror and is filtered out by broadband transmission filter (400-700 nm) for TPEF or narrow band (420 nm center, 10 nm bandwidth) for SHG imaging and detected by a photomultiplier tube (PMT). All images throughout the study were taken using pulse energies in the range 40 to 60 pJ for TPEF and 80 to 100 pJ for SHG in the object plane. Corresponding power densities in the focus are estimated to 4 to 6 MW/cm² and 8 to 10 MW/cm², respectively, assuming diffraction-limited spot.

For PSHG measurements, an additional polarizer, that is, an analyzer in the rotation stage, was inserted into the detection arm. The laser beam's polarization state at the focal plane of the objective lens was determined by means of polarization optics. The ellipticity of the polarization was negligible. The slight rotation (cca. 4 °) was measured, and the analyzer in the transmission arm was set accordingly.

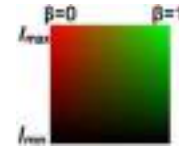
2.3 | Image acquisition and analysis

The first hyperpolarizability or β coefficient was calculated from PSHG images^[11] defined as:

$$\beta = \frac{I_{\parallel} - I_{\perp}}{I_{\parallel} + 2I_{\perp}}$$

where I_{\parallel} and I_{\perp} represent SHG intensity in a pixel of an image detected through the analyzer oriented parallel and perpendicularly to the incident laser polarization, respectively. The incident laser polarization was kept constant throughout the measurements, and it was parallel to the horizontal axis of all images. The values for the β coefficient were calculated according to the given formula in each pixel from the values I_{\parallel} and I_{\perp} in the given pixel from the corresponding images. The

map of β values was displayed according to the following scheme:



Here, β is the color-coded, and I is the SHG signal intensity in a given pixel according to an average value of two images taken through the analyzer oriented parallel and perpendicularly to the incident laser polarization. The results are corresponding to β values map.

According to Chen et al.,^[18] the borderline case when $\beta = 1$ corresponds to the complete alignment of fibrillar collagen. In this case, the SHG intensities are the maximal in the image taken through the analyzer oriented parallel to the incident laser polarization, while SHG intensities are 0 for the image when the analyzer is perpendicular.

β coefficient was calculated at standard PC using our own script for Math Lab. The calculation time for 1024 × 1024 image is 5 to 10 seconds on average. The program was not optimized; thus, the calculating time could be even faster.

There are numerous methods for detailed collagen fibers analysis based on PSHG developed for both biological^[19,20] and nonbiological samples^[21] where predominant axes are easy to predict or even to control. The measurement of the angular dependence of SHG signal, from which the details on SHG emitters (e.g., collagen fibers) alignment are extracted, is common for all aforementioned methods. The signal analysis requires a sophisticated approach and expert experience.

Hence, the simple procedure described by Chen et al.^[18] and applied here is easy to implement yet sufficient to obtain necessary information on a large number of samples (e.g., screening). This makes the procedure user-friendly even for non-experts or easy to be automated.

2.4 | Immunohistochemistry

Semi-fine (2 μ m thick) skin sections from Araldite blocks were used for 4-hydroxynonenal (4-HNE) and 3-nitrotyrosine (N-Tyr) detection with primary antibodies anti-4-HNE (1:400, ab48506, Abcam, Cambridge, UK), and anti-N-Tyr (1:100, MAB5404, Chemicon, Houston) for routine immunohistochemistry previously described in detail by Janković et al.^[1] All sections were counterstained with hematoxylin, dehydrated and mounted for light microscopy analysis.

2.5 | Statistical analysis

Statistical analysis using GraphPad Prism software (GraphPad Prism, Version 5.03) was performed by the analysis of variance (ANOVA) considering P values $\leq .05$ as the level of significance.

3 | RESULTS AND DISCUSSION

3.1 | Comparison of light, TPEF and SHG microscopy

To compare the commonly used histological method, H&E staining, for conventional light microscopy with advanced TPEF and SHG methods, we analyzed the same

region of interest (ROI) in parallel on serial 5 μm thick paraffin sections.

Light microscopy analysis (Figure 1, H&E) of the skin from 15-day-old rats revealed the process of extracellular matrix organization in the dermis, numerous fibroblasts with the intensive synthesis of procollagen, and the small number of collagen fibers found in their vicinity. Although less numerous, collagen bundles already showed specific packaging and a tendency to organize in bundles, suggesting that this pattern is predetermined. The dermis of 1-month-old rats showed a well-structured extracellular matrix with a compact and well-organized collagen bundle orientation. Among collagen bundles, numerous fibroblasts were still observed. At this stage of aging, our results showed consistency in synthesis, packing and orientation of collagen bundles in rat dermis. In

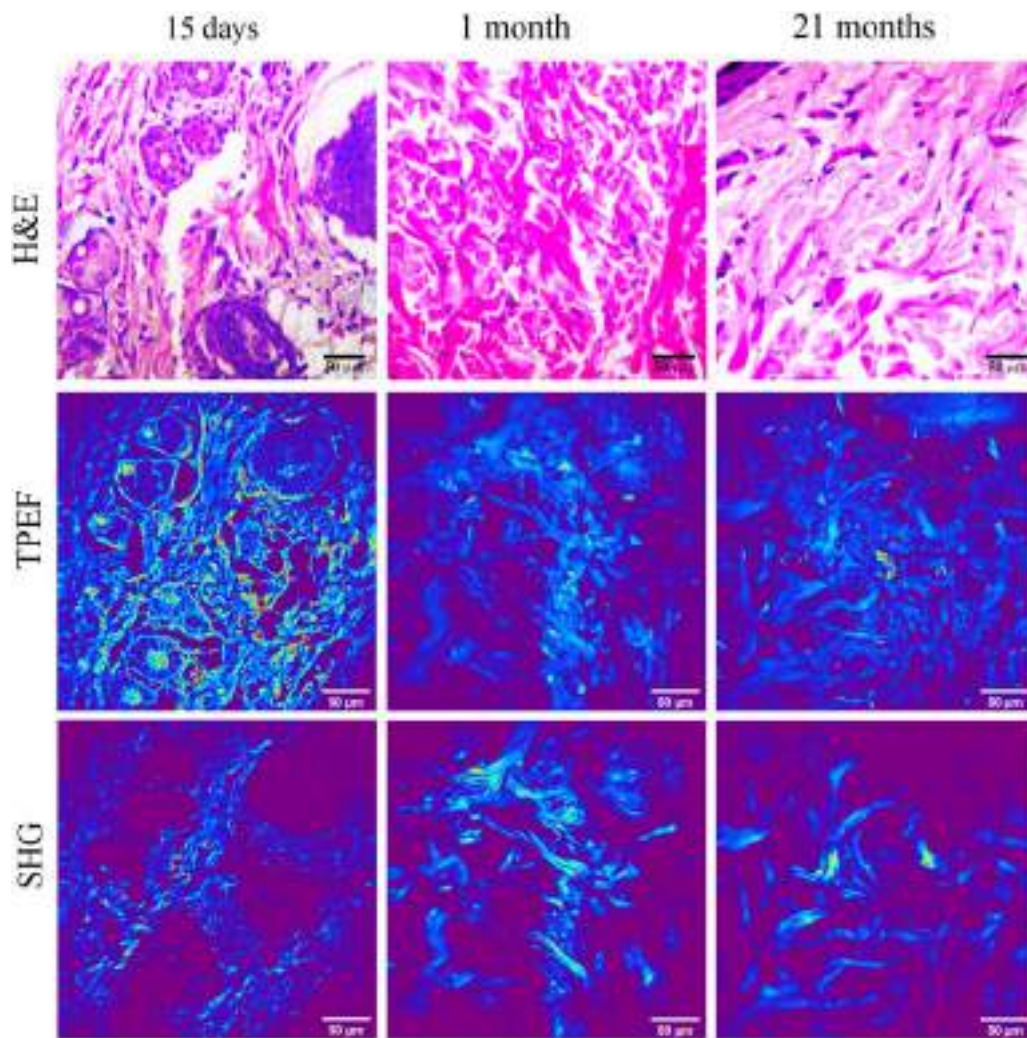


FIGURE 1 H&E staining in parallel with TPEF and SHG showing dermal collagen structure and organization in the skin of 15-day-, 1-month- and 21-month-old rats. Less numerous collagen bundles (15 days) become compact with well-organized orientation through skin maturation (1 month), suggesting a predetermined specific packaging pattern. In aged skin (21 months) vast quantity of tightly packed, large collagen bundles is present. TPEF and SHG-signal correspond to light microscopy without losing information about collagen fiber position, density and orientation. Five-micrometer thick sections; H&E staining; area analyzed with TPEF or SHG microscopy, Bars: 50 μm

aged skin (21-month-old), we found a vast quantity of tightly packed, large collagen bundles, while the number of fibroblasts was significantly reduced. Comparative analysis also showed that collagen from rat dermis in all examined groups produced strong TPEF and SHG signals corresponding to light microscopy without the loss of information about the position, density and orientation of collagen fibers.

Over the last years, among nonlinear imaging techniques, TPEF emerged as a powerful tool for skin imaging.^[8,22] Like other tissue, the skin could be easily studied with multiphoton microscopy without the use of any fluorescent dyes or agents due to the presence of endogenous fluorophores. Autofluorescence properties of the skin originate either from cells (reduced pyridine and oxidized flavin nucleotides), or extracellular components (collagen and elastin).^[23] Thanks to significant advantages—fast screening and label-free procedures, this technique has already been widely used for morphological characterization on ex vivo tissue samples.^[24,25]

Another nonlinear imaging technique, SHG, has mainly been used to visualize unstained collagenous tissues.^[15,26] Because of its non-centro-symmetrical structure, fibrillar collagen is the primary source of the SHG signals in the skin dermis.^[3,18,27] Lately, besides skin (dermis), SHG has also been used for investigation of collagen fiber orientation and structural changes in scars and keloid,^[3,28,29] tendon and ligaments,^[30,31] cardiovascular system,^[32,33] cornea^[34] and tumor microenvironment.^[35–37]

The combination of TPEF and SHG is also very useful for capturing both components of the dermis (collagen and elastin) and generating high-resolution three-dimensional images.^[22] Second-harmonic to Autofluorescence Aging Index of Dermis (SAAID method), introduced by Lin et al.,^[38] is a simple scoring method applied when TPEF and SHG are used simultaneously for the imaging of connective tissue. SAAID provides a measure of the relative abundance of collagen against elastic fibers within the skin dermis. In this particular case, we were not able to use this method since in rat skin, in contrast to human skin, collagen fibers are highly dominant over rare elastin fibers. Nonetheless, in general, the TPEF-SHG combination is a promising, reliable and powerful tool for studying skin physiology and pathology.

3.2 | β Coefficient calculation from PSHG images

To analyze structural alterations of collagen fibers and packing patterns caused by aging, which are unobservable by light microscopy, we calculated the β coefficient from PSHG images (Figure 2) obtained from

the same serial paraffin sections. Namely, the SHG images in Figure 1 are the raw SHG images that correspond to the same field of view as in β maps shown in Figure 2A. The two orthogonal components of the SHG signal recorded at the same field of view are used for the calculation of the β coefficient (Figure 2B).

We had three sections (one/animal) for each examined group (15-days-, 1-month and 21-month-old). Three different ROIs from each section were randomly selected for imaging. The β coefficient was calculated by the given formula for each pixel in the ROI. The average β coefficient was calculated for each ROI (the whole image in Figure 2A). Results were analyzed upon β coefficient calculation and arbitrarily categorized as either less, more, or highly ordered until ultrastructural examination.

The lowest β values were found in the skin of young, 15-day-old rats with an average value of 0.13. This is expected since young skin is in the phase of development characterized by intensive collagen synthesis. More ordered fibers were found in the skin of 1-month-old rats, going through maturation, with the average value of 0.20, while aged skin (21-month-old) showed the highest β coefficient, with the average value of 0.25, suggesting highly ordered organization of collagen fibers, great density and tight packing in collagen bundles. All of this data was consistent with TPEF, light and electron microscopy findings.

β Coefficient calculation from PSHG images has been frequently used in studies to establish differences between normal and malignant tissues.^[39,40] In tumors, variations in diameter and cross-sectional profile of the collagen fibrils are evident. In some cases, this is a consequence of abnormal collagen fibril aggregation,^[41] while in others, extracellular matrix remodeling occurs through the degradation of collagen fibers.^[42] Moreover, this method enables the characterization and tracking of various experimental treatments in different tissues.^[41] Thus, SHG and PSHG imaging of fibrillar collagen type I have been applied on various samples so far, but collagen samples of tendon and skin remain the most commonly analyzed.^[3]

Ericson et al.^[41] concluded that qualitative evaluation of angular dependence of the SHG signal varies in a manner related to the structural order of collagen fibrils and that data points generated from less ordered fibril structures could be useful in determining the distribution of the fiber segments orientation. They suggested that this finding could be valuable for the characterization of the fibril structure and possible structure alterations.

Bearing in mind that only ordered structures produce strong SHG signal and that immature fibrils can be distinguished from mature fibrils in the backward direction,^[27] the β coefficient calculation seems to be the

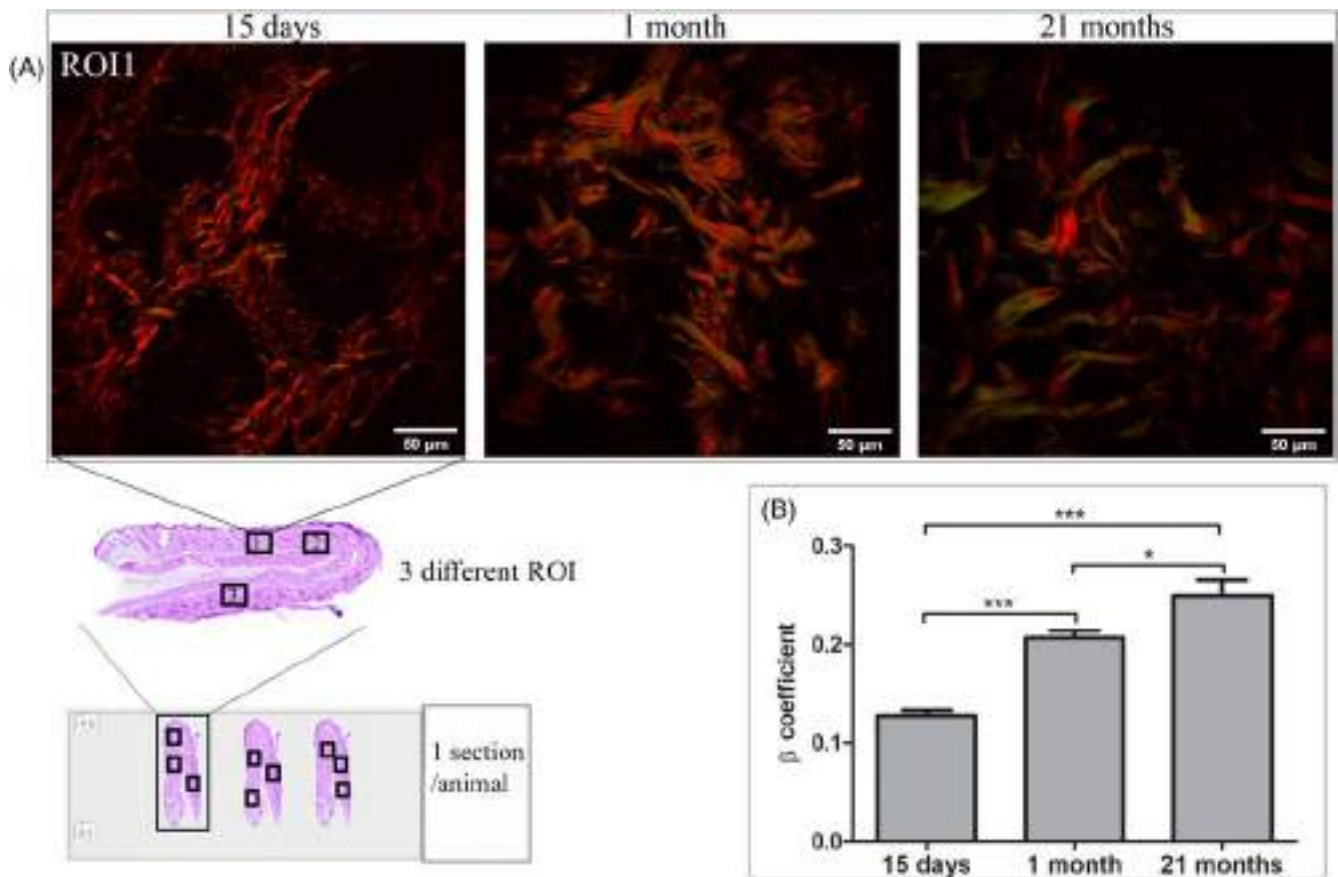


FIGURE 2 Representative ROI (A) for each tissue sample used for β coefficient calculation from PSHG images during chronological aging (15-days-, 1-month- and 21-months-old). B, Young skin (15 days) has the lowest β value (the average β value of 0.13) due to intensive collagen synthesis, while maturation and aging induced a significant increase in β value. Through maturation (1 month), skin shows more ordered collagen fiber structures with an average β value of 0.20. Aged skin (21 month) has the highest β coefficient with an average value of 0.25, suggesting highly ordered organization of collagen fibers, high density and tight packing in collagen bundles. The values represent the means of nine β values per group, 27 ROI in total (3 ROI randomly chosen from each of three different paraffin rat skin sections per slide \pm SEM). * $P < .05$ and *** $P < .001$. Bars: 50 μm

perfect tool for the study of extracellular matrix structure, as we did in our experiment.

Comparison of the β coefficient and collagen ultrastructure confirmed their correlation regarding tightness degree in the bundle as less, more, or highly ordered. The interaction of cells with the extracellular matrix is essential to cell positioning, growth and differentiation in order to form and maintain complex tissue structure and function. The mechanical properties (rigidity/stiffness) of the extracellular matrix could be evaluated through matrix density and organization. Since β values represent molecular order, the given type of anisotropy directly reflects dense packing and orientation of collagen in fibrils, for example, rigidity.

Although SHG is well known as a fixation- and label-free method, we performed it on fixed and paraffin-embedded, 5 μm thick samples to avoid differences, problems and doubts regarding the use of native, unfixed and unlabeled tissue samples. We prepared all samples in the same way, and the fixation procedure was strictly

followed to preserve the tissue structure as near, to the natural state, as possible.

Our results provide significant proof that this method is convenient for use on previously fixed samples, opening the possibility for the re-examination of archived paraffin-embedded tissue samples. Thus, new insights into the dermal structure and comparison could lead to potentially entirely new findings regarding skin aging or conditions.

3.3 | Transmission electron microscopy (TEM) analysis

To confirm that the sample preparation procedure for light and electron microscopy does not affect overall tissue structure and ultrastructure, we compared the analyses of semi-fine sections stained with BF&MB with H&E and ultrastructure of the dermis (Figure 3).

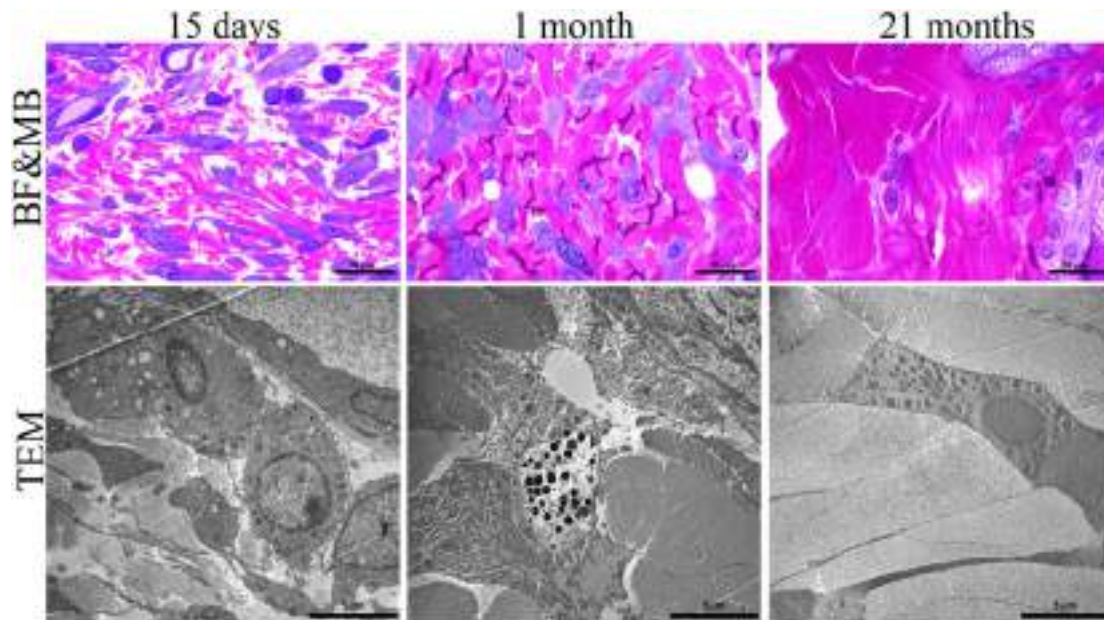


FIGURE 3 BF&MB staining shows the area analyzed with TEM. Semi-fine sections; Bars: BF&MB-20 μm , TEM-5 μm

Results confirmed the consistency in tissue and collagen structure, bundle density and quantity of ground substance, and were in line with our previous findings.^[1] We further measured the diameter of collagen fibrils in randomly selected cross-sections and compared their distribution between all examined groups (Figure 4).

Obtained results showed a striking difference between young (15-day-old), maturing (1-month-old) and aged (21-month-old) rat skin. Namely, the majority of cross-sectioned collagen fibers in 15-day-old dermis had average diameters of 50 to 60 nm, along with a similar number of diameters ranging from 40 to 50 and 60 to 80 nm. This is in line with ongoing collagen synthesis in young skin^[1] and ultrastructural findings of small quantities of loosely packed collagen fibers embedded in ground substances (Figure 3, TEM).

In contrast, maturing and aged dermis had an average value of cross-sectioned collagen fibers of 80 to 90 nm (1-month-old) and 90 to 100 nm (21-month-old). Besides the fact that the observed increase in the average collagen fiber diameter is a consequence of natural skin maturation, it is important to point out the absence of collagen with the diameter of 50 to 60 nm and the shift toward higher values (>120 nm). On the ultrastructural level, although collagen bundles in the aged dermis were large and tightly packed like in the mature skin, they presented as thicker, more turgid and electron-lucent, suggesting damage and swelling, all of which can lead to the tight packing of collagen molecules.

Knowing that collagen damage is a significant factor in age-related dermal alterations, at this level of observation,

we could not detect alterations on the molecular level. Thus, comparing these results with the β coefficient calculated from PSHG images, we observed consistency in the alignment of collagen fibers. Collagen microstructure and index of alignment were in line, however, was it a consequence of collagen degradation remained unclear. In a highly ordered collagen bundle, microfracture may induce an observed shift in diameter and rigidity, in contrast to the loose connective tissue. To clarify this, we used immunohistochemistry to analyze the expression of matrix metalloproteinases (MMP). We used two different antibodies but did not find the presence of either MMP2 or MMP9 in all examined samples (data not shown). These findings may not be surprising, bearing in mind strict and well-ordered synthesis and packing of collagen bundles in the rat dermis.

Since degradation is clearly not taking part in causing collagen alterations observed by TPEF and SHG/PSHG or differences in individual collagen fibers and collagen diameter observed by electron microscopy, we further analyzed the oxidative damage of collagen fibers on serial paraffin skin sections, in particular, per- and nitro-oxidative damage.

3.4 | Immunohistochemical detection of 4-hydroxynonenal (4-HNE) & 3-nitrotyrosine (N-Tyr)

A large body of evidence indicates that reactive oxygen species (ROS) accumulation and damage caused by ROS is one of the most important mechanisms involved in cellular aging.^[1,43] However, such evidence for the extracellular

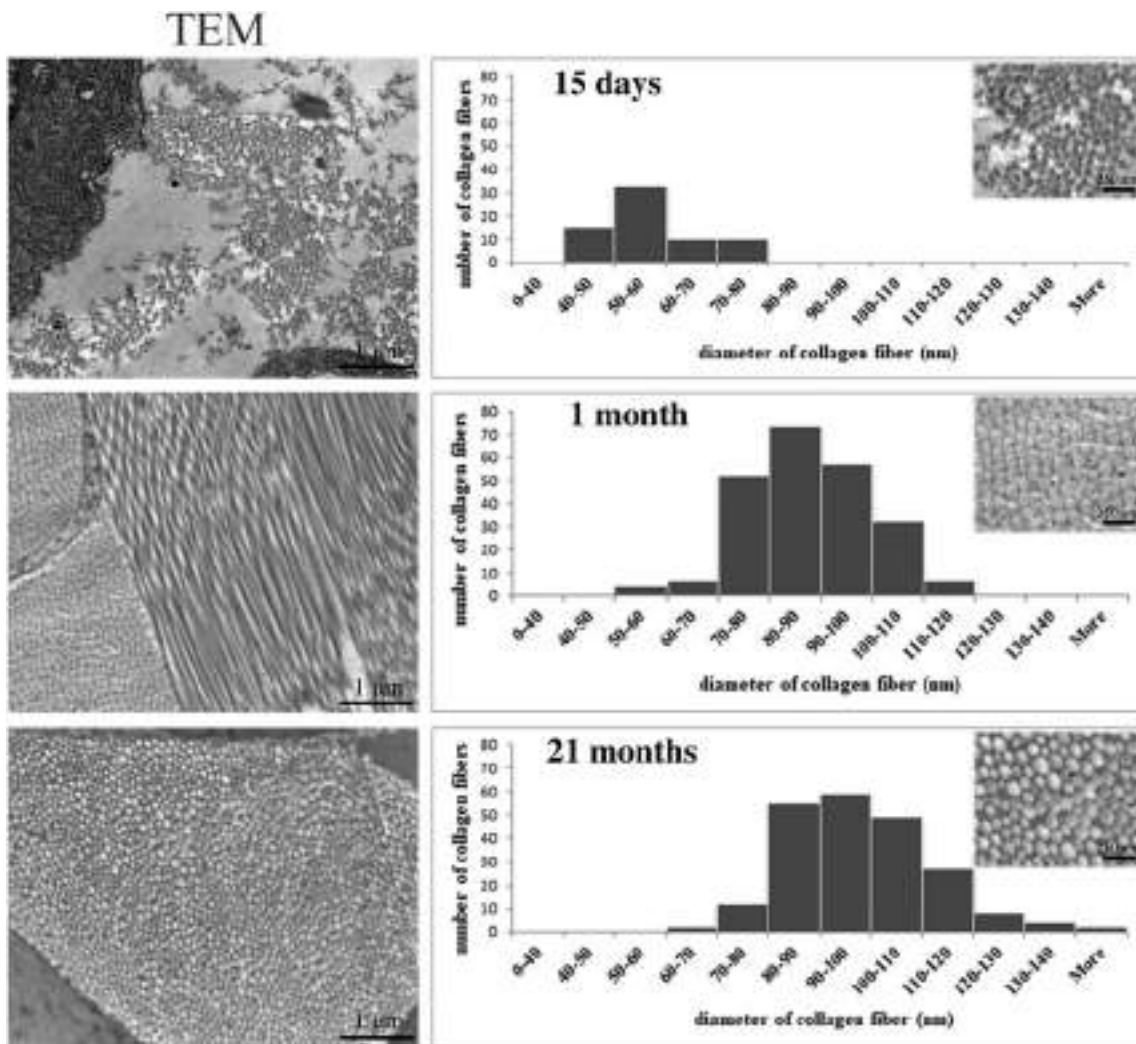


FIGURE 4 Structural alteration and collagen fiber diameter distribution in the dermis of 15-day-, 1-month- and 21-month-old rats. Aging induces a shift in collagen fiber diameter and tight packing of collagen molecules that leads to collagen organization in bundles and dermal rigidity. Bars: TEM-1 μ m, insets-250 nm

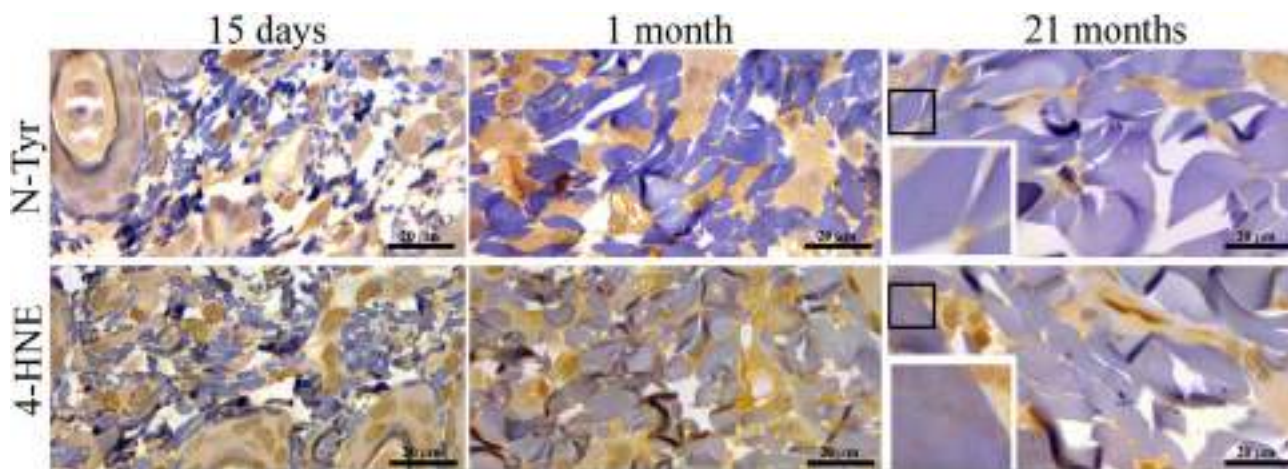


FIGURE 5 Immunohistochemical detection of 4-hydroxynonenal (4-HNE) & 3-nitrotyrosine (N-Tyr)—biomarkers of oxidative tissue damage. Insets represent the enlarged area (black square): Collagen (blue) showed immunopositivity for 4-HNE and N-Tyr only in the aged dermis (21-month-old rats). Bars: 20 μ m

matrix is still sparse. It was recently shown that increased ROS might affect collagen density directly by damaging fibers and indirectly by interfering with collagen synthesis,^[44] fibroblast proliferation and senescence.^[45]

In general, biomarkers of oxidative stress have been considered as biomarkers of aging.^[46] N-Tyr is a marker of oxidative damage caused by nitration of the free amino acid form of tyrosine or tyrosine residues in proteins, while 4-HNE is a reactive aldehyde, formed as a product of lipid peroxidation, which binds to macromolecules, proteins in particular. Thus, 4-HNE is also a propagator of lipid and protein oxidation (Figure 5).

Our results revealed the presence of 4-HNE and N-Tyr modifications on collagen fibers in 21-month-old rat dermis. Extracellular matrix molecules, such as collagens, are good targets for oxygen-free radicals. Collagen is susceptible to fragmentation by superoxide anion, as demonstrated by the liberation of small 4-hydroxyproline-containing-peptides,^[47] but the absence of MMP2 and MMP9 in our study suggests that this damage leads to more significant aggregation rather than collagen degradation. Amino acids susceptible to oxidative damage^[48] are highly present in collagen molecules, and as a result of amino acid residue oxidation, protein fragmentation, aggregation and proteolytic digestion can occur.

To the best of our knowledge, this is the first report of collagen positivity for 4-HNE and N-Tyr. This could be the underlying reason for the observed alterations in the biophotonic properties, rigidity (higher β coefficient) and ultrastructural damage of collagen during chronological aging that overwrites genetic and structural stability of collagen molecules in the rat skin.

4 | CONCLUSIONS

Our results clearly show that analysis of TPEF and SHG images of rat dermis is consistent with histological one; rat dermis is a good model not only due to collagen photonic features but bundles stability. The β coefficient calculated from PSHG is consistent with transmission electron microscopy analysis and should be used widely. Moreover, the β coefficient reflects fine collagen fiber alterations due to oxidative damage observable only by immunohistochemistry and on the ultrastructural level.

These advantageous methods work nicely on previously fixed samples and could be used along with or for further conventional analysis. In this way, degradation of samples would be avoided, and reproducibility and standardization of protocols would be fully achieved.

Hence, PSHG imaging is a fast and reliable screening method for studying collagen alteration during chronological aging linked to oxidative stress; it may be used in any

further analysis that concerns collagen structure alteration, for example, photoaging, drug delivery, cancer, and opens the opportunity for investigation of the archived samples. Our future research is directed toward it.

ACKNOWLEDGMENT

Authors acknowledge funding through the grants of the Ministry of Education, Science and Technological Development of the Republic of Serbia.

CONFLICT OF INTEREST

The authors declare no financial or commercial conflict of interest.

DATA AVAILABILITY

The data that support the findings of this study are available from the corresponding author upon request.

AUTHOR CONTRIBUTIONS

Conception and design: All authors. Acquisition of data: Irena Miler, Mihailo D. Rabasovic, Marija Aleksic, Aleksandar J. Krmpot. Analysis and interpretation of data: All authors. Drafting the manuscript: Irena Miler and Aleksandra Korac, with the contribution of all the authors. Critically revising the manuscript: All authors. Final approval of the manuscript: All authors.

AUTHOR BIOGRAPHIES

Please see Supporting Information online.

ORCID

Aleksandra Korac  <https://orcid.org/0000-0002-3044-9963>

REFERENCES

- [1] A. Jankovic, L. Saso, A. Korac, B. Korac, *Oxid. Med. Cell. Longev.* **2019**, 2019, 2471312.
- [2] M. D. Shoulders, R. T. Raines, *Annu. Rev. Biochem.* **2009**, 78, 929.
- [3] L. Mostaco-Guidolin, N. L. Rosin, T. L. Hackett, *Int. J. Mol. Sci.* **2017**, 18, 1772.
- [4] S. Xu, H. Xu, W. Wang, S. Li, H. Li, T. Li, W. Zhang, X. Yu, L. Liu, *J. Transl. Med.* **2019**, 17, 309.
- [5] J. G. Snedeker, A. Gautieri, *Muscles Ligaments Tendons J.* **2014**, 4, 303.
- [6] V. V. Dudenkova, M. V. Shirmanova, M. M. Lukina, F. I. Feldshtein, A. Virkin, E. V. Zagainova, *Biochemistry (Mosc.)* **2019**, 84, S89.
- [7] R. Cicchi, S. Sestini, V. De Giorgi, D. Massi, T. Lotti, F. S. Pavone, *J. Biophotonics* **2008**, 1, 62.
- [8] R. Cicchi, D. Kapsokalyvas, V. De Giorgi, V. Maio, A. Van Wiechen, D. Massi, T. Lotti, F. S. Pavone, *J. Biophotonics* **2010**, 3, 34.
- [9] B. R. Masters, P. T. So, E. Gratton, *Biophys. J.* **1997**, 72, 2405.
- [10] N. G. Horton, K. Wang, D. Kobat, C. G. Clark, F. W. Wise, C. B. Schaffer, C. Xu, *Nat. Photonics* **2013**, 7, 205.

- [11] E. Gavgiotaki, G. Filippidis, V. Tsafas, S. Bovasianos, G. Kenanakis, V. Georgoulis, M. Tzardi, S. Agelaki, I. Athanassakis, *Sci. Rep.* **2020**, *10*, 11055.
- [12] S. You, H. Tu, E. J. Chaney, Y. Sun, Y. Zhao, A. J. Bower, Y. Z. Liu, M. Marjanovic, S. Sinha, Y. Pu, S. A. Boppart, *Nat. Commun.* **2018**, *9*, 2125.
- [13] D. Tokarz, R. Cisek, M. N. Wein, R. Turcotte, C. Haase, S. C. A. Yeh, S. Bharadwaj, A. P. Raphael, H. Paudel, C. Alt, T. M. Liu, H. M. Kronenberg, C. P. Lin, *PLoS One* **2017**, *12*, e0186846.
- [14] P. J. Campagnola, in *Second Harmonic Generation Imaging* (Eds: F. S. Pavone, P. J. Campagnola), Taylor & Francis, Boca Raton **2014** Series in Cellular and Clinical Imaging; Chap. III.
- [15] R. Cicchi, N. Vogler, D. Kapsokalyvas, B. Dietzek, J. Popp, F. S. Pavone, *J. Biophotonics* **2013**, *6*, 129.
- [16] C. A. Couture, S. Bancelin, J. Van der Kolk, K. Popov, M. Rivard, K. Legare, G. Martel, H. Richard, C. Brown, S. Laverty, L. Ramunno, F. Legare, *Biophys. J.* **2015**, *109*, 2501.
- [17] M. D. Rabasovic, D. V. Pantelic, B. M. Jelenkovic, S. B. Curcic, M. S. Rabasovic, M. D. Vrbica, V. M. Lazovic, B. P. Curcic, A. J. Krmpot, *J. Biomed. Opt.* **2015**, *20*, 16010.
- [18] X. Chen, O. Nadiarynk, S. Plotnikov, P. J. Campagnola, *Nat. Protoc.* **2012**, *7*, 654.
- [19] G. L. Gusachenko, M. C. Schanne-Klein, *Opt. Express* **2010**, *18*, 19339.
- [20] G. Latour, I. Gusachenko, L. Kowalczyk, I. Lamarre, M. C. Schanne-Klein, *Biomed. Opt. Express* **2012**, *3*, 1.
- [21] S. Psilodimitrakopoulos, L. Mouchliadis, I. Paradisanos, G. Kourmoulakis, A. Lemonis, G. Kioseoglou, E. Stratakis, *Sci. Rep.* **2019**, *9*, 14285.
- [22] R. Cicchi, D. Kapsokalyvas, F. S. Pavone, *Biomed. Res. Int.* **2014**, *2014*, 903589.
- [23] E. Yew, C. Rowlands, P. T. So, *J. Innov. Opt. Health Sci.* **2014**, *7*, 1330010.
- [24] J. Paoli, M. Smedh, M. B. Ericson, *Semin. Cutan. Med. Surg.* **2009**, *28*, 190.
- [25] E. Baria, G. Nesi, R. Santi, V. Maio, D. Massi, C. Pratesi, R. Cicchi, F. S. Pavone, *J. Biophotonics* **2018**, *11*, e201800106.
- [26] R. Cicchi, F. S. Pavone, *Methods Mol. Biol.* **2017**, *1627*, 409.
- [27] R. M. Williams, W. R. Zipfel, W. W. Webb, *Biophys. J.* **2005**, *88*, 1377.
- [28] P. J. Su, W. L. Chen, J. B. Hong, T. H. Li, R. J. Wu, C. K. Chou, S. J. Chen, C. Hu, S. J. Lin, C. Y. Dong, *Opt. Express* **2009**, *17*, 11161.
- [29] H. B. Yu, S. Chen, X. Q. Zhu, H. Q. Yang, J. X. Chen, *J. Phys. Conf. Ser.* **2011**, *277*, 012046.
- [30] I. Gusachenko, V. Tran, Y. Goulam Houssen, J. M. Allain, M. C. Schanne-Klein, *Biophys. J.* **2012**, *102*, 2220.
- [31] J. C. Mansfield, C. P. Winlove, J. Moger, S. J. Matcher, *J. Biomed. Opt.* **2008**, *13*, 044020.
- [32] C. Doras, G. Taupier, A. Barsella, L. Mager, A. Boeglin, H. Bulou, P. Bousquet, K. D. Dorkenoo, *Opt. Express* **2011**, *19*, 15062.
- [33] A. L. Lopez, I. V. Larina, *Biomed. Opt. Express* **2019**, *10*, 2898.
- [34] P. Matteini, F. Ratto, F. Rossi, R. Cicchi, C. Stringari, D. Kapsokalyvas, F. S. Pavone, R. Pini, *Opt. Express* **2009**, *17*, 4868.
- [35] A. Keikhosravi, J. S. Bredfeldt, A. K. Sagar, K. W. Eliceiri, *Methods Cell Biol.* **2014**, *123*, 531.
- [36] K. Tilbury, P. J. Campagnola, *Perspect. Med. Chem.* **2015**, *7*, 21.
- [37] R. A. Natal, J. Vassallo, G. R. Paiva, V. B. Pelegati, G. O. Barbosa, G. R. Mendonca, C. Bondarik, S. F. Derchain, H. F. Carvalho, C. S. Lima, C. L. Cesar, L. O. Sarian, *Tumour Biol.* **2018**, *40*, 1010428318770953.
- [38] S. J. Lin, R. J. Wu, H. Y. Tan, W. Lo, W. C. Lin, T. H. Young, C. J. Hsu, J. S. Chen, S. H. Jee, C. Y. Dong, *Opt. Lett.* **2005**, *30*, 2275.
- [39] R. Hristu, S. G. Stanciu, D. E. Tranca, G. A. Stanciu, *J. Biophotonics* **2017**, *10*, 1171.
- [40] V. Tsafas, E. Gavgiotaki, M. Tzardi, E. Tsafa, C. Fotakis, I. Athanassakis, G. Filippidis, *J. Biophotonics* **2020**, *13*, e202000180.
- [41] A. Erikson, J. Ortegren, T. Hompland, C. de Lange Davies, M. Lindgren, *J. Biomed. Opt.* **2007**, *12*, 044002.
- [42] R. Mercatelli, T. Triulzi, F. S. Pavone, R. Orlandi, R. Cicchi, *J. Biophotonics* **2020**, *13*, e202000159.
- [43] V. Lobo, A. Patil, A. Phatak, N. Chandra, *Pharmacogn. Rev.* **2010**, *4*, 118.
- [44] J. P. Borel, J. C. Monboisse, G. Bellon, *Med. Sci. (Paris)* **1988**, *4*, 304.
- [45] G. Gunin, N. K. Kornilova, V. V. Petrov, O. V. Vasilyeva, *Adv. Gerontol.* **2012**, *1*, 299.
- [46] M. Rinnerthaler, J. Bischof, M. K. Streubel, A. Trost, K. Richter, *Biomolecules* **2015**, *5*, 545.
- [47] C. L. Hawkins, M. J. Davies, *Biochim. Biophys. Acta* **1997**, *1360*, 84.
- [48] S. Silva, B. Michniak-Kohn, G. R. Leonardi, *An. Bras. Dermatol.* **2017**, *92*, 367.

AUTHOR BIOGRAPHIES

Irena Miler received her MSc degree in biology from the Faculty of Biology, University of Belgrade, Serbia. Currently, she is a Ph.D. student in the Biophotonics group at the University of Belgrade, Serbia. Her research focuses on biophotonics; Light interactions with cells and tissues.

Dr. Mihailo D. Rabasovic received his MSc degree from the Physics department, University of Belgrade, Belgrade, Serbia in 2004. He received his Ph.D. in physics from the University of Belgrade, Belgrade, Serbia in 2007. His research focuses on photo-acoustics, microscopy and correlation spectroscopy. He has published over 60 articles.

Marija Aleksic received her MSc degree in molecular biology and physiology from the University of Belgrade, Belgrade, Serbia. Currently, she is a Ph.D. student in cell and tissue biology at the University of Belgrade, Serbia. Her research focuses on organelle biogenesis and remodeling in physiology and pathology.

Dr. Aleksandar J. Krmpot is an Associate Research Professor at the Institute of Physics Belgrade (IPB), University of Belgrade. He completed his master's and

Ph.D. in physics/quantum optics at the University of Belgrade, Serbia, and acquired the experience in microscopy at Institute for Electronic Structure and Lasers, Foundation for research and technology Hellas (IESL-FORTH), Heraklion, Greece. His research focuses on developing and applications of novel optical microscopic techniques, for example, nonlinear laser scanning microscopy (multiphoton, second and third harmonic generation) and fluorescent correlation spectroscopy for biomedical research and applications. He is the head of the Laboratory for biophysics at IPB and a visiting researcher at Karolinska Institute, Stockholm, Sweden. Aleksandar is a professor at Ph.D. studies in Biophotonics at the University of Belgrade.

Andjelika Kalezic received her MSc degree in molecular biology and physiology from the University of Belgrade, Belgrade, Serbia. Currently, she is a Ph.D. student in cell and tissue biology at the University of Belgrade, Serbia. Her research focuses on the tumor microenvironment.

Dr. Aleksandra Jankovic received her Ph.D. from the Faculty of Biology, University of Belgrade, Belgrade, Republic of Serbia in 2010. Her research focuses on redox regulation in physiological and pathophysiological states and processes including aging. She has published over 50 articles.

Prof. Bato Korac is a Professor of Physiology, Pathophysiology and Redox Biology at the University of Belgrade-Faculty of Biology. His research group focuses on developing new approaches in redox biology for biomedical research and applications. He has published over 70 articles and is a board member of several established journals. He is a president of the Serbian Society for Mitochondrial and Free Radical Physiology and a council member of Society for Free Radical Research—Europe.

Prof. Aleksandra Korac is a Professor of Cell and Tissue Biology at the University of Belgrade-Faculty of Biology. She is the head of Chair of Cell & Tissue Biology, head of Center for Electron Microscopy and a recognized authority in microscopy. Her research group focuses on cell and tissue ultrastructure, application and development of innovative methods for biomarker molecules visualization and bioimaging. She has published over 77 articles.

How to cite this article: Miler I, Rabasovic MD, Aleksic M, et al. Polarization-resolved SHG imaging as a fast screening method for collagen alterations during aging: Comparison with light and electron microscopy. *J. Biophotonics*. 2021;14:e202000362. <https://doi.org/10.1002/jbio.202000362>

OPEN

Altered organization of collagen fibers in the uninvolved human colon mucosa 10 cm and 20 cm away from the malignant tumor

Sanja Z. Despotović^{1*}, Đorđe N. Milićević², Aleksandar J. Krmpot³, Aleksandra M. Pavlović⁴, Vladimir D. Živanović⁴, Zoran Krivokapić⁵, Vladimir B. Pavlović⁶, Steva Lević⁶, Gorana Nikolić⁷ & Mihailo D. Rabasović³

Remodelling of collagen fibers has been described during every phase of cancer genesis and progression. Changes in morphology and organization of collagen fibers contribute to the formation of microenvironment that favors cancer progression and development of metastasis. However, there are only few data about remodelling of collagen fibers in healthy looking mucosa distant from the cancer. Using SHG imaging, electron microscopy and specialized softwares (CT-FIRE, CurveAlign and FiberFit), we objectively visualized and quantified changes in morphology and organization of collagen fibers and investigated possible causes of collagen remodelling (change in syntheses, degradation and collagen cross-linking) in the colon mucosa 10 cm and 20 cm away from the cancer in comparison with healthy mucosa. We showed that in the lamina propria this far from the colon cancer, there were changes in collagen architecture (width, straightness, alignment of collagen fibers and collagen molecules inside fibers), increased representation of myofibroblasts and increase expression of collagen-remodelling enzymes (LOX and MMP2). Thus, the changes in organization of collagen fibers, which were already described in the cancer microenvironment, also exist in the mucosa far from the cancer, but smaller in magnitude.

Extracellular matrix (ECM) is no longer considered as an inert substrate, a three-dimensional network which only “fills the spaces” between cells and provide mechanical support^{1,2}. Today, ECM is known to be a complex and dynamic structure, whose chemical and biophysical properties affect cell adhesion³, proliferation⁴ morphology⁵, migration⁶, regulate tissue morphogenesis^{7,8} and fluid volume in tissues⁹. The most abundant component of ECM in the lamina propria of the colon mucosa is type I collagen.

Remodelling of collagen fibers has been described in almost every solid cancer, including colorectal cancer. During tumor formation and progression, collagen remodelling is constantly carried out: degradation, synthesis, cross-linking of fibers, change of fiber orientation, and interaction of cells of the innate and acquired immune system with collagen fibers^{10,11}. Changes in morphology, representation, and organization of collagen fibers contribute to the formation of the microenvironment that favors tumor progression, primarily through its effect on cell migration and polarization¹². Also, remodelling of collagen fibers on premetastatic sites is of great importance in determination of survival and growth of disseminated cancer cells, and thus, formation of metastasis^{13,14}.

Remodelling of collagen fibers may be a result of changes in synthesis, degradation or cross-linking. Main cells responsible for synthesis of collagen in colon mucosa are fibroblasts and myofibroblasts. The most important enzymes for degradation of collagen fibers are matrix metalloproteinases (MMPs). It has been shown that expression of MMP2 and MMP9 is increased in colorectal cancer and influences its progression and

¹University of Belgrade, Faculty of Medicine, Institute of Histology and embryology, Belgrade, Serbia. ²Saarland University, Department of Internal Medicine V- Pulmonology, Allergology, Intensive Care Medicine, Homburg/Saar, Germany. ³University of Belgrade, Institute of Physics Belgrade, Belgrade, Serbia. ⁴University Hospital Center “Dr Dragiša-Mišović-Dedinje”, Belgrade, Serbia. ⁵Clinic for Abdominal Surgery- First surgical clinic, Clinical Center of Serbia, Belgrade, Serbia. ⁶University of Belgrade, Faculty of Agriculture, Belgrade, Serbia. ⁷University of Belgrade, Faculty of Medicine, Institute of Pathology, Belgrade, Serbia. *email: sanjadesp@gmail.com

metastatic potential^{15,16}. Covalent cross-linking of collagen fibrils is catalyzed by enzyme lysyl oxidase (LOX). LOX-dependent collagen crosslinking enhances proliferation of cancer cells and metastatic capacity^{17,18}.

The quantification of changes of collagen within the primary tumor and metastatic niches has been the subject of numerous studies and it is recognized to play an important role in both cancer development and progression^{19–21}. However, much less is known about remodelling of collagen fibers in healthy looking colon mucosa distant from the cancer. In the previous study of uninvolved colon mucosa²², we described changes in the representation and organization of collagen fibers as far as 10 cm and 20 cm away from the colon cancer. Because remodelling of collagen fibers is an important process, crucial for creating specific microenvironmental milieu, we felt that further studies were necessary to investigate the finer aspects of this phenomenon. Thus, the aim of our study was to quantify morphological parameters and organization of collagen fibers and to investigate possible causes of collagen remodelling (change in syntheses, degradation and collagen cross-linking) in the colon mucosa 10 cm and 20 cm away from the cancer in comparison with healthy mucosa. Indeed, we showed that this far from the colon cancer there are changes in collagen architecture, increased representation of myofibroblasts and increase expression of collagen-remodelling enzymes.

Results

Changes in morphology and organization of collagen fibers in the uninvolved colon lamina propria visualized using SHG imaging. On SHG images, in the lamina propria of healthy patients, collagen fibers were wavy, orderly organized throughout lamina propria and around the crypts (Fig. 1a). At the distance 10 cm (Fig. 1b,c) and 20 cm (Fig. 1d) away from the cancer, proper arrangement of collagen fibers appeared partly disturbed. It was possible to observe regions with parallel collagen fibers (Fig. 1b), thick collagen fibers (Fig. 1c), regions with edema of lamina propria where collagen fibers were separated with large pores (Fig. 1d) and regions with fibers organized as in healthy subjects.

By analyzing whole SHG images using CT-FIRE software (Fig. 2a,b; 23–25), we have shown that there was a statistically significant increase in the width of collagen fibers in the lamina propria of the colon mucosa at a distance 10 cm ($p = 0.032$) and 20 cm from the tumor ($p = 0.021$), compared with healthy subjects (Fig. 2e). Collagen fibers in the lamina propria 10 cm and 20 cm away from the cancer were significantly more straight ($p = 0.004$ and $p < 0.0001$, Fig. 2f) compared with collagen fibers in lamina propria of healthy colon. Using CurveAlign software (Fig. 2c,d)^{23–25}, based on curvelet transform, it was shown that collagen fibers in colon lamina propria 10 cm and 20 cm away from the cancer were significantly more aligned compared with collagen fibers in healthy lamina propria ($p = 0.022$ and $p = 0.041$; Fig. 2g).

Because of the heterogeneity in morphology and organization of collagen fibers in the lamina propria of colon mucosa and according to the studies which showed that the remodelling of collagen fibers within the tumor primarily could be observed in the immediate vicinity of epithelial cells^{25,26}, we also performed computational analyses of collagen fibers within 3 regions of interest per each SHG image (Fig. 3a–d). The regions of interest included lamina propria of colon mucosa in the immediate vicinity of Liberkin's crypts. The observed differences in morphology and organization of collagen fibers, detected by analyzing whole images, were even more pronounced when analysis were conducted inside the regions of interest: At a distance of 10 cm and 20 cm from the tumor, there was a statistically significant increase in width and straightness of collagen fibers compared to lamina propria of colon mucosa of healthy subjects ($p < 0.0001$, Fig. 3e,f). Also, collagen fibers in colon lamina propria both 10 cm and 20 cm away from the cancer were significantly more aligned compared with collagen fibers in healthy lamina propria ($p < 0.0001$ and $p = 0.035$, Fig. 3g).

We also quantified alignment of collagen fibers using another approach. With FiberFit software, based on FFT, we obtained the dispersion parameter k ²⁷. The dispersion parameter k was significantly increased 10 cm and 20 cm away from cancer (indicating more aligned collagen fibers), compared with healthy lamina propria ($p = 0.031$ and $p = 0.0013$; Table 1).

Changes in SHG polarization anisotropy in the uninvolved colon lamina propria. In the lamina propria of colon mucosa at distance 10 cm and 20 cm away from cancer, anisotropy coefficient β ^{28,29} was significantly higher (indicating more orderly organized collagen molecules inside fibrils), compared with lamina propria of healthy patients ($p < 0.0001$; Table 1).

Electron microscopy analysis of collagen fibers in the uninvolved colon lamina propria. On SEM collagen fibers in healthy patients were thin, curvy, and the network they were forming was relatively dense, with small pores between bundles (Fig. 4a). At the distance 10 cm and 20 cm away from the tumor the thick collagen fibers were more frequently observed (4b). Also, regions with more aligned collagen fibers were alternating with regular, network-like distribution of collagen fibers (Fig. 4c).

Changes in synthesis, cross-linking and degradation of collagen fibers in the uninvolved colon lamina propria. Next, we wanted to find out if the changes in morphology and organization of collagen fibers are due to changes in synthesis, cross-linking or degradation of collagen. The main cells involved in collagen synthesis are fibroblast and myofibroblast. We detected myofibroblasts in colon lamina propria, immunohistochemically, using α SMA-antibody. In the lamina propria of healthy patients, myofibroblasts formed continuous layer around crypts, with few α SMA-positive cells throughout lamina propria (elongated, spindle-shaped, most probably also myofibroblasts) and around blood vessels (smooth muscle cells) (Fig. 5a). At the distance 10 cm and 20 cm away from the cancer, pericryptal myofibroblast were readily identifiable, forming thicker-appearing layer. More α SMA positive cells were visible throughout lamina propria (Fig. 5a). Quantitative analysis, using Color Picker Threshold plugin, showed significantly higher representation of α SMA-positive cells 10 cm away from cancer,

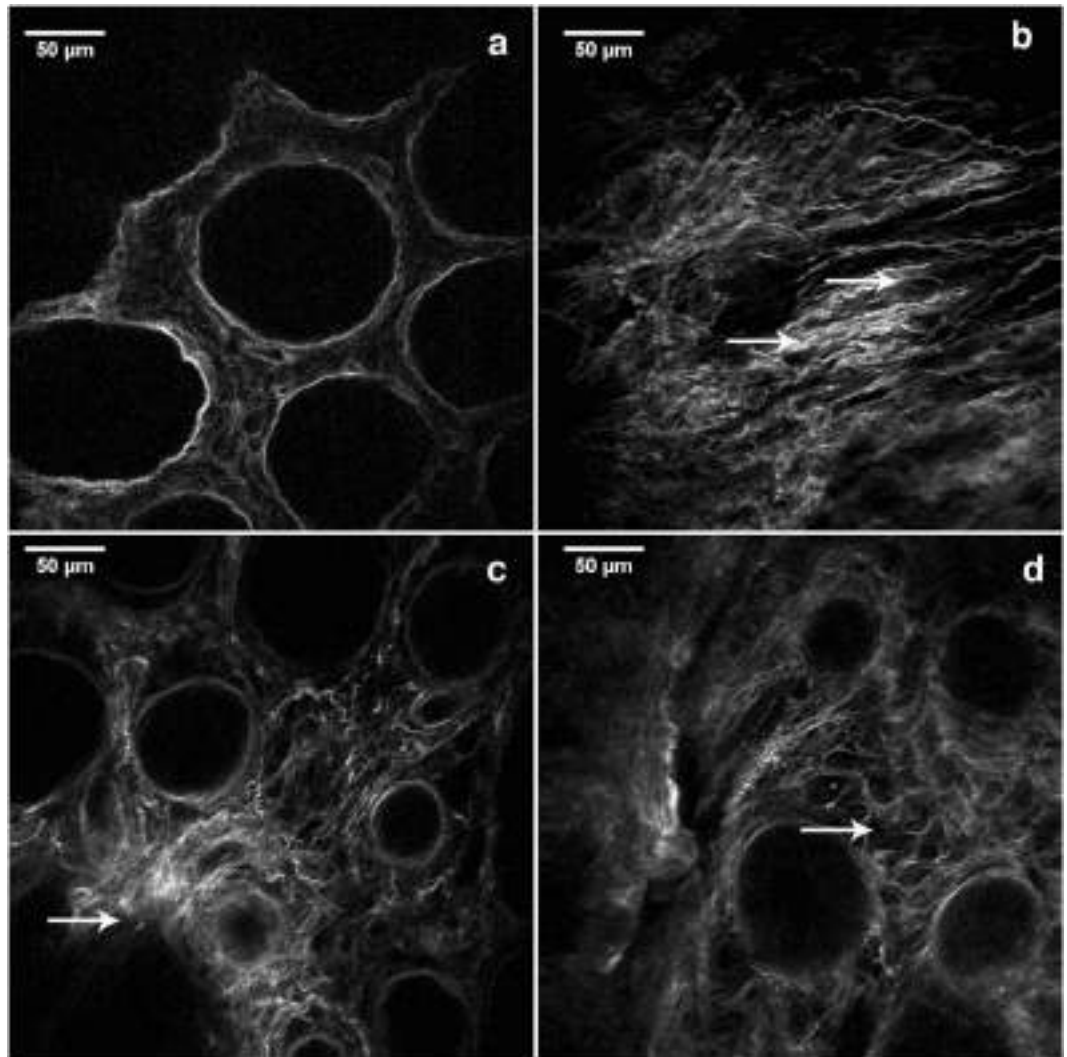


Figure 1. SHG images showing patterns of collagen fibers organization in the lamina propria of colon mucosa in the healthy patients and 10 cm and 20 cm away from the malignant tumor. Collagen fibers were wavy, orderly organized throughout lamina propria and around the crypts in the mucosa of healthy patients (a); In the lamina propria at the distance 10 cm (b,c) and 20 cm away from the cancer (d), proper arrangement of collagen fibers was partly lost: regions with parallel collagen fibers (b, arrows), thick and dense collagen fibers (c, arrow), regions with edema of lamina propria where collagen fibers were separated with large pores (d, arrow showing pore) were frequently observed.

compared with healthy lamina propria and lamina propria at the distance 20 cm away from the cancer ($p = 0.018$ and $p = 0.037$) (Fig. 5b).

Lysyl Oxidase (LOX) catalyzes crosslinking of collagen molecules during collagen fibrils assembly. We detected LOX expression in epithelial cells (both surface epithelium and epithelium of Lieberkühn glands) and in lamina propria of colon mucosa (Fig. 6a). In the colon epithelial cells, LOX mainly showed perinuclear expression pattern. LOX expression was significantly higher in epithelial cells of colon mucosa 10 cm and 20 cm away from the cancer, compared with healthy mucosa ($p < 0.0001$; Fig. 6b). In colon lamina propria, LOX was predominantly expressed by fibroblasts and myofibroblasts and subepithelial macrophages (Fig. 6a). LOX expression was significantly higher in lamina propria of colon mucosa 10 cm and 20 cm away from the cancer, compared with healthy controls ($p < 0.0001$ and $p = 0.013$; Fig. 6b).

Matrix metalloproteinases play an important role in degradation of ECM including collagen fibers. Their expression is changed in colon cancer¹⁵. We wanted to find out if MMPs were involved in remodelling of collagen fibers this far from the colon cancer. MMP2 in the colon epithelial cells showed supranuclear expression. Some intraepithelial lymphocytes were also MMP2-positive (Fig. 6a). MMP2 expression was significantly higher in epithelial cells of colon mucosa 10 cm and 20 cm away from the cancer, compared with healthy mucosa ($p = 0.037$ and $p = 0.034$; Fig. 6c). MMP2 was expressed by mononuclear cells in colon lamina propria (Fig. 6a). MMP2 expression was significantly higher in lamina propria of colon mucosa 10 cm away from the cancer, compared with healthy controls ($p < 0.0001$; Fig. 6c).

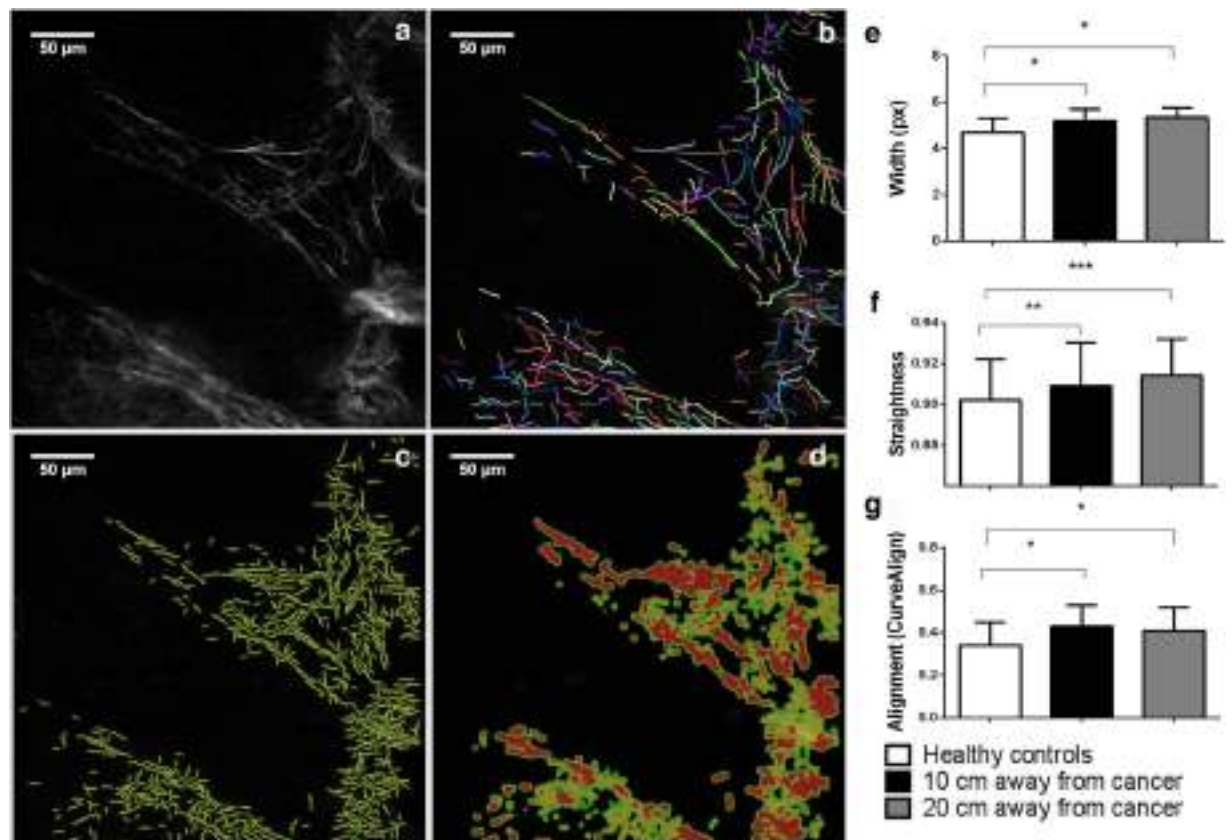


Figure 2. CT FIRE and CURVE Align in analyzing whole SHG images of collagen fiber in the lamina propria of colon mucosa in the healthy patients and 10 cm and 20 cm away from the malignant tumor. Original SHG image of lamina propria of healthy patient. (a) Graphical output from CT FIRE showing automatic extraction of collagen fibers, same patient. (b) Graphical outputs from CURVE Align for calculating alignment of collagen fibers. (c,d) Graphs are showing increased width (e), straightness (f) and alignment (g) of collagen fibers in the lamina propria 10 cm and 20 cm away from the cancer, calculated using CT FIRE and CURVE Align. * $p < 0.05$, ** $p < 0.001$, *** $p < 0.0001$ ($n = 32$ healthy patients/96 images and $n = 35$ cancer patients/105 images; Values are express as mean \pm sd; ANOVA).

MMP9 was barely detectable both in healthy colon mucosa and 10 cm and 20 cm away from the cancer: only few scattered cells through lamina propria, most likely macrophages, were MMP9 positive (Supplementary Fig S1).

Discussion

Our work demonstrated the changes in morphology and organization of collagen fibers in the colon mucosa 10 cm and 20 cm away from the cancer and provided a brief insight into the possible causes of the collagen remodelling.

Intriguingly, these changes were already described in the cancer microenvironment but larger in magnitude^{15,23,25,30,31}.

Change in deposition, alignment and cross-linking of collagen fibers, influence cell polarity and cell-cell interactions, increases growth factor signaling and stimulate migration of cancer cells^{2,32}. Cells are able to sense and respond to changes of both biochemical and biomechanical properties of the local microenvironment. Some of the main parameters determining biomechanical properties of collagen network are thickness of the fibers, alignment, stiffness and porosity. Increase of collagen fibers thickness was shown to correlate with formation of invadopodia, change in cancer cells shape and increase migratory capacity^{2,33}. Increased alignment of collagen fibers has significant impact on gene expression, differentiation, proliferation and especially migration of cancer cell, with align collagen fibers acting as “highways” for cancer cell migration². Stiffness is strongly related to LOX-induced cross-linking of collagen fibers, which as a consequence favors cell adhesion and MMPs secretion^{2,34,35}.

More recently, the importance of tissue away from the cancer is being recognized, and the number of papers investigating changes in the uninvolved tissue, on genetic, epigenetic, biochemical and structural level, is increasing^{36–38}. The most studied was the uninvolved mucosa immediately around the colon cancer, commonly up to 2 cm away from the cancer, so called transitional mucosa³⁹. Recent studies showed that there are localized densification and increased alignment of collagen fibers in the transitional mucosa immediately around the cancer⁴⁰. Rare groups of authors also analyzed healthy looking mucosa further from the cancer: Roy and

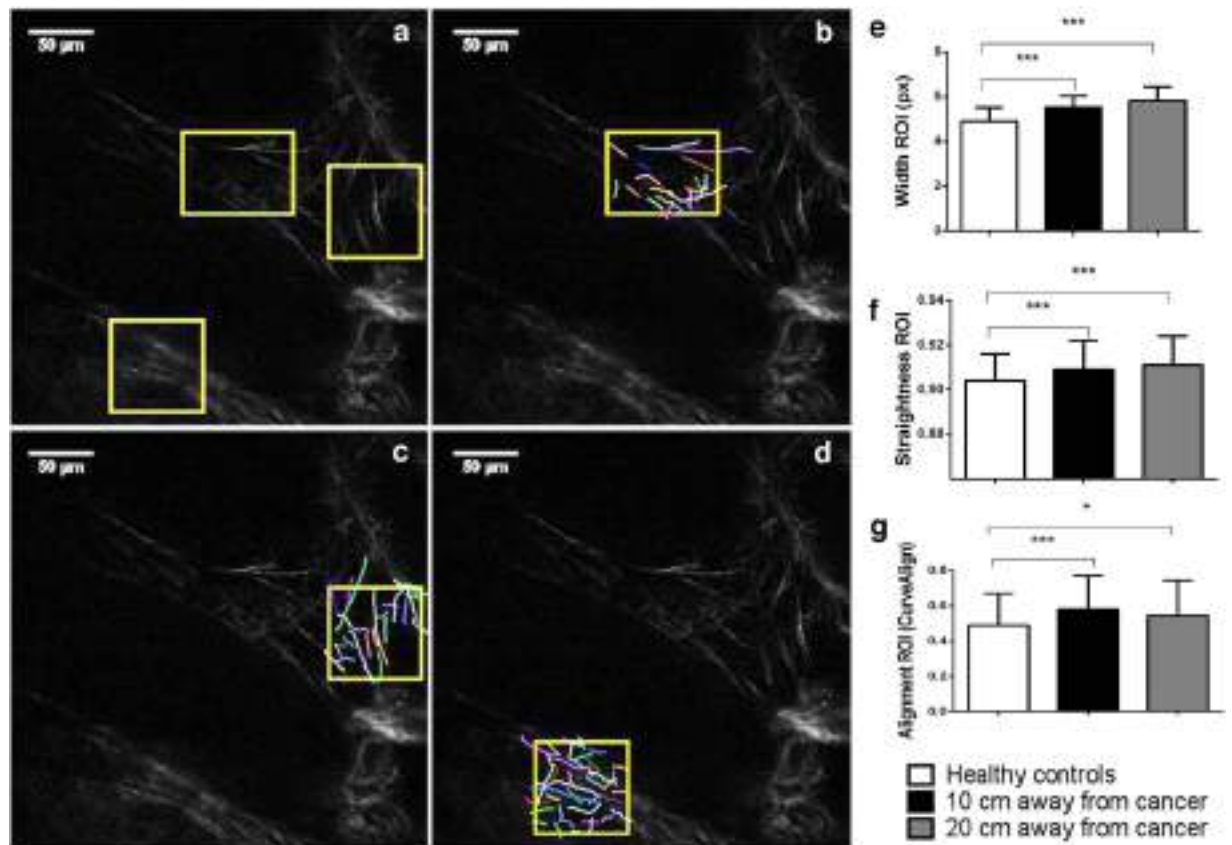


Figure 3. CT FIRE and CURVE Align in analyzing regions of interest (ROIs) on SHG images of collagen fiber in the lamina propria of colon mucosa in the healthy patients and 10 cm and 20 cm away from the malignant tumor. Original SHG image of lamina propria of healthy patient, with labeled rectangular ROIs which include collagen fibers near the Liberkün's crypts (a) and example of CT FIRE collagen fiber extraction within ROIs (b–d). Graphs are showing increased width (e), straightness (f) and alignment (g) of collagen fibers in the lamina propria 10 cm and 20 cm away from the cancer, calculated using CT FIRE and CURVE Align. * $p < 0.05$, ** $p < 0.001$, *** $p < 0.0001$ ($n = 32$ healthy patients and $n = 35$ cancer patients; Values are express as mean \pm sd, ANOVA).

	Healthy controls ($n = 32$)	10 cm away from cancer ($n = 35$)	20 cm away from cancer ($n = 35$)
k dispersion parameter	0.51 ± 0.22	$0.91 \pm 0.53^*$	$1.11 \pm 0.67^{**}$
β coefficient	0.26 ± 0.03	$0.31 \pm 0.04^{***}$	$0.32 \pm 0.05^{***}$

Table 1. Dispersion parameter k and anisotropy coefficient β in the lamina propria of colon mucosa in healthy patients and 10 cm and 20 cm away from the cancer. * $p < 0.05$, ** $p < 0.01$, *** $p < 0.001$.

colleagues have described changes in the rectal mucosa of patients bearing advanced adenomas elsewhere in the colon: metabolic reprogramming, including evidence of Warburg effect, early increase in microvascular blood supply and also, increased cross-linking and local alignment of collagen fibers^{36,38}. They have also shown that increased cross-linking of collagen in the uninvolved colon mucosa fibers was due to increased expression of LOX enzyme³⁶. Using microarray, qRT-PCR and immunohistochemistry Trujillo *et al.* have demonstrated changed gene expression signature in the tissue 1 cm and 5 cm away from the breast cancer: differentially expressed genes were involved in extracellular matrix remodelling, including genes for MMPs, wound healing, fibrosis and epithelial to mesenchymal transition⁴¹. Sanz-Pamplona *et al.* revealed number of genes that were preferentially activated in adjacent mucosa from colorectal cancer, compared with mucosa of healthy patients: among other, these were genes involved in TGF-beta signaling pathway which is associated with fibrosis, genes for MMPs, cell adhesion molecules, cell-ECM integrin signaling pathways and BMP2 signaling pathways³⁷.

So, our results are consistent with and complement the works cited: Genes involved in ECM remodelling are differentially express in the mucosa around the cancer⁴¹, and, by analyzing morphology, organization and cellular composition in the colon mucosa far from the cancer, we showed the consequences of these altered gene expression.

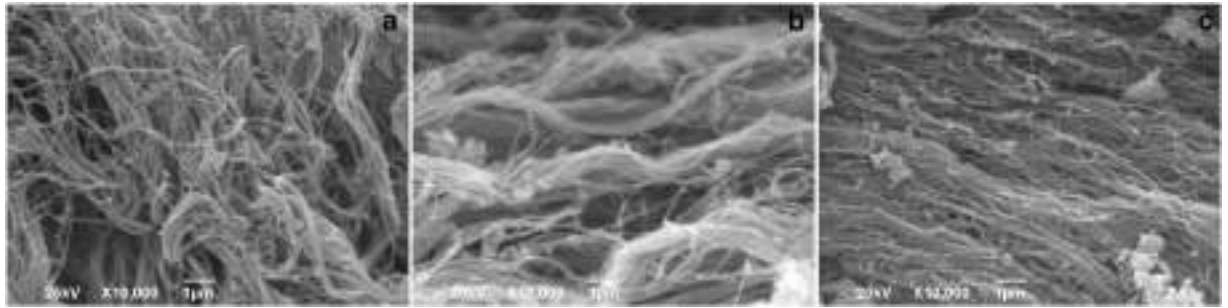


Figure 4. Representative SEM images of collagen fibers in the lamina propria of colon mucosa in the healthy patients (a) and 10 cm (c) and 20 (b) cm away from the malignant tumor. In the lamina propria of healthy patients (a) thin collagen fibers were forming relatively dense network. At the distance 10 cm and 20 cm away from the tumor, regions with thick (b, 20 cm away from tumor) and aligned collagen fibers (c, 10 cm away from tumor) were more frequently observed. Magnification x10 000.

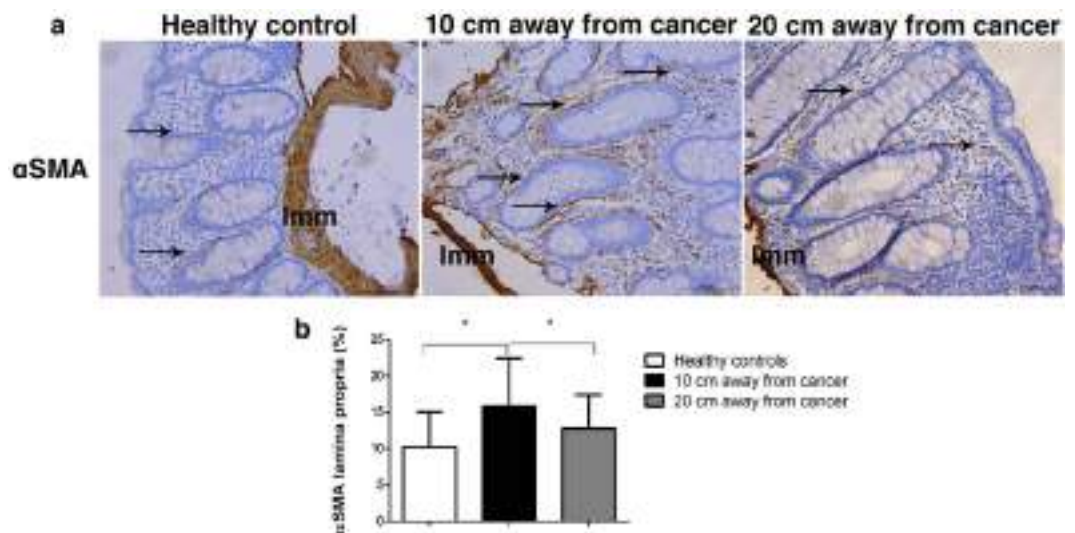


Figure 5. Representative images of α SMA-positive cells in the lamina propria of colon mucosa in healthy patients and at the distance 10 cm and 20 cm away from the tumor. Arrows are showing α SMA-positive myofibroblasts (a); Graph is showing increased representation (in %) of α SMA-positive cells in the lamina propria 10 cm and 20 cm away from the cancer, compared with healthy patients. * $p < 0.05$, ** $p < 0.001$, *** $p < 0.0001$ ($n = 27$ healthy patients and $n = 30$ cancer patients; Values are express as mean \pm sd; ANOVA).

We have analyzed uninvolved colon mucosa quite far from the colon cancer, 10 cm and 20 cm away, respectively. Most authors still consider tissue located more than 5 cm away from the colon cancer completely healthy and use it as a control in their research⁴². We had at least two reasons to believe that, although distant, this tissue could also bear changes: the systemic effects of tumors and, so-called, field carcinogenesis effect^{36,43,44}.

More recently, very interesting concept has emerged, according to which tumor initiation and progression are shaped by body's systemic response to tumor, which implied involvement of distant, uninvolved tissues and organs. Tumor produce a vast number of cytokines (for example, VEGF-A, TGF- β , TNF- α) and extrude different microvesicles, which act in a systemic fashion, modulating the behavior of host cells in distant tissues, most notably bone marrow, spleen and pre-metastatic niches. So, by secreting cytokines, tumor induce changes in distant tissues, which lead to the formation of local microenvironment that makes that particular tissue more permissive for seeding and survival of metastatic cancer cells⁴³. Remodelling of extracellular matrix play particularly important role in creating microenvironment permissive for metastatic cancer cells: activation of fibroblasts/myofibroblasts, reorganization of collagen fibers, and change in expression of ECM-remodelling enzymes such as MMP2, MMP9 and LOX^{43,45}.

On the other hand, according to the field carcinogenesis concept, environmental carcinogens and genetic risk factors act on the entire organ (in our case, entire colon mucosa) leading to the emergence of an altered field, so called "field of injury". On this altered field, additional stochastic genetic and epigenetic events within the enabling microenvironment could give rise to focal cancers^{36,44}. ECM, especially collagen and myofibroblasts, is recognized to play an important role in the field carcinogenesis concept by participating in the formation of enabling microenvironment. It is believed that altered epithelial cells induce change in the surrounding microenvironment

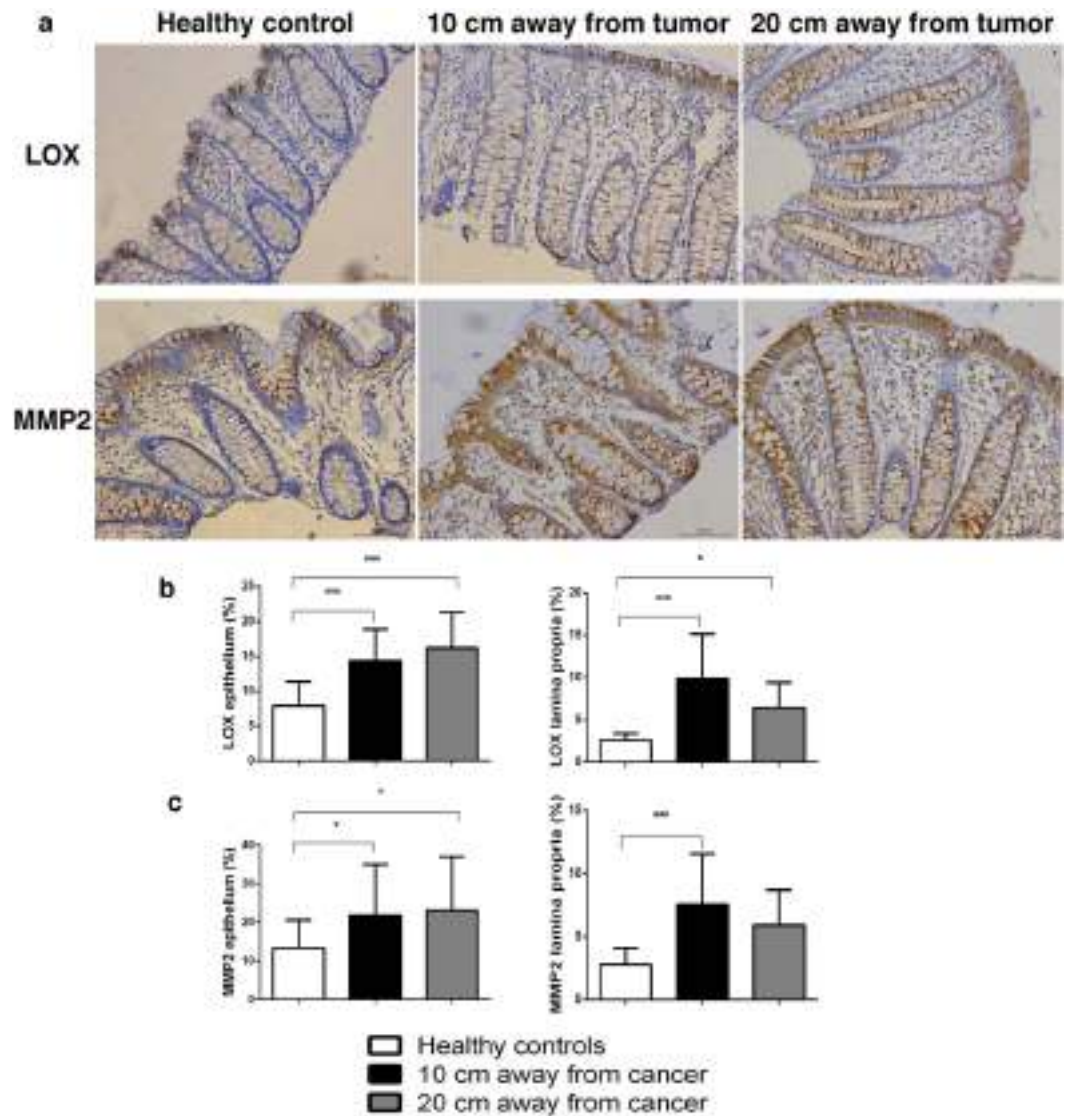


Figure 6. Representative images of LOX and MMP2 staining in the epithelium and lamina propria of colon mucosa in healthy patients and at the distance 10 cm and 20 cm away from the tumor (a); Graphs are showing increased representation (in%) of LOX (b) and MMP2-positive cells (c) in the lamina propria 10 cm and 20 cm away from the cancer, compared with healthy patients; * $p < 0.05$, ** $p < 0.001$, *** $p < 0.0001$ ($n = 27/28$ healthy patients and $n = 30$ cancer patients; Values are express as mean \pm sd; ANOVA).

that, in turn, promote or modify expansion of altered cells, or, there are even evidence indicating that ECM changes could play a primary role in both cancer initiation and progression⁴⁶.

Whether the changes in morphology and organization of collagen fibers 10 cm and 20 cm away from the cancer, represent a consequence of a growing tumor or a field effect, or a combination, we have no answer. Further analyses of mucosa more distant from the cancer are needed. Subsequently, detailed analyses of changes in the epithelium (genetic, epigenetic, biochemical and morphological) this far from the cancer and analysis of epithelial-stromal interactions on molecular level would be the next step in more thorough understanding of complex ways in which cancer interact with surroundings, distant parts of the same organ and systemically, with distant tissues and organs. Also, it would be important to conduct described analyses on the larger number of patient- to explore their potential in colon cancer screening or stratification of patients for colonoscopy.

Materials and methods

Tissue samples. Tissue samples were obtained during colonoscopy at the Department of gastrointestinal endoscopy, University Hospital Center “Dr Dragiša Mišović-Dedinje”, Belgrade, Serbia, from patients suspected to suffer from colon cancer based on clinical symptoms. When the experienced gastroenterologist noticed a suspected change during colonoscopy, they took samples of unaffected colon mucosa 10 cm and 20 cm away in caudal direction. The samples of unaffected colon mucosa were obtained from 41 patients older than 50 years (24 males and 17 females; Table 2). Only tissue samples for which pathologist confirmed that the suspected change

Patients	Number	Age (years)	Gender	
			Male	Female
Cancer	41	74.3	24	17
Healthy	39	71.9	20	19

Table 2. Demographic characteristics of patients included in the study.

was colorectal adenocarcinoma, were included in the study. For all patients, it was newly discovered cancer, so they haven't been on any kind of treatment for the malignant disease before.

As a control, the samples of colon mucosa were collected in the same institution, from 39 patients (20 males and 19 females; Table 2) who were indicated colonoscopy because of rectal bleeding, anemia or weight loss, and were without any pathological finding or diagnosed only with uncomplicated hemorrhoids (Haemorrhoides non specificatae sine complicationibus). Patients with inflammatory bowel disease, infectious colitis or diverticular disease of colon were excluded from the study. Our study was approved by the Ethics Committee of University Hospital Center "Dr Dragiša-Mišović-Dedinje", Belgrade, Serbia (18/10/2017). All methods were carried out in the accordance with relevant guidelines and regulations.

Second harmonic generation imaging of colon tissue samples. The images of collagen fibers in the label-free human colon tissue samples were obtained using an original lab frame nonlinear laser-scanning microscope^{47,48}. For second harmonic generation (SHG) imaging of collagen fibers following experimental setup for nonlinear laser scanning microscope (NLM) was used²². The tunable mode-locked Ti:sapphire laser (Coherent, Mira 900) has been source of the infrared femtosecond pulses. The laser light was directed onto the sample by a short-pass dichroic mirror (cut-off at 700 nm) through the Zeiss EC Plan-Neofluar 40×/1.3 NA Oil objective. The laser wavelength was 840 nm. The SHG was detected in back-reflection arm. The narrow bandpass filter at 420 nm (Thorlabs FB420-10, FWHM 10 nm) blocks the scattered laser light and auto-fluorescence, and passes second harmonic at 420 nm. The average laser power on the sample was 30 mW. According to the pulse duration (160 fs) and repetition rate (76 MHz), we estimate the peak laser power to be 2.5 kW.

Quantitative analysis of collagen fibers in colon lamina propria. To analyze morphology and organization of collagen fibers in colon lamina propria, on SHG images, we used two complementary morphology based and one morphology-independent approach. For morphological assessment of collagen fibers we used methods based on curvelet transform and Fourier transform. As a morphology-independent approach, we measured SHG polarization anisotropy.

Computational collagen fiber quantification. CT-FIRE, an open-source software package, was used for calculation of width and straightness of collagen fibers. CT-FIRE was developed to automatically extract and analyze individual collagen fibers from SHG images^{23–25}. Widths of collagen fibers are expressed in pixels. Straightness is represented on a scale 0–1, where 1 corresponds to perfectly straight fibers. CURVE Align software was used to calculate alignment of collagen fibers. Alignment was represented on a scale from 0–1, where 1 indicates all fibers orientated at the same angle^{23–25}. CT-FIRE and CURVE Align measurements were applied both on whole images (from 32 healthy patients and 35 cancer patients, 3 SHG images per patient) and on 3 regions of interest (300 × 300 px²) per image, located in the close vicinity to Liberkün glands.

An additional software, FiberFit, which is based on fast Fourier transforms (FFT) was used to quantify orientation of collagen fibers in colon tissue samples (from 32 healthy patients and 35 cancer patients, 3 SHG images per patient). Using FiberFit, we obtained the dispersion parameter k , used to quantify collagen fiber alignment (low k values indicates disordered networks, large k values indicates aligned networks²⁷).

SHG polarization anisotropy. The SHG anisotropy could be used to quantify alignment of collagen molecules inside fibers. The anisotropy parameter β was calculated by:

$$\beta = (I_{\text{par}} - I_{\text{orth}}) / (I_{\text{par}} + 2 \cdot I_{\text{orth}})$$

where I_{par} and I_{orth} represented SHG intensity detected when the analyzing polarizer is oriented parallel (I_{par}) and orthogonal (I_{ort}) to the laser polarization^{28,29}. Values of β range from 0 to 1, where 0 represents completely random and 1 completely aligned collagen molecules inside fibers.

We analyzed 32 samples from healthy patients and 35 from cancer patients. From each tissue sample 3 randomly chosen regions on magnification x400 were measured.

SEM analysis of collagen fibers in colon lamina propria. The surface morphology of collagen fibers (for 7 healthy patients and 6 cancer patients) has been examined using a JEOL JSM-6390LV SEM (JEOL, Japan) at an accelerating voltage of 10 kV. After fixation in 3% glutaraldehyde in cacodulte buffer, dehydration in graded alcohols (50%, 70%, 96%, 100%, 100%) the colon tissue samples were immediately dried using Critical Point Dryer K850 (Quorum Technologies, Laughton, UK). Prior to visualization, the dry samples were sputtered with gold using a Bal-Tec SCD 005 Cool putter Coater.

Immunohistochemistry. Immunohistochemical analysis was performed on formalin-fixed, paraffin-embedded sections using following antibodies and dilution ratios: anti-alphaSMA (Dako, M0851 1:500), anti-MMP9

	Number of analyzed healthy patients	Number of analyzed cancer patients (tissue away from the cancer)	
		10 cm away	20 cm away
αSMA (Dako, M0851)	27	30	30
LOX (Abcam, ab174316)	27	30	30
MMP2 (Abcam, ab37150)	28	30	30
MMP9 (Abcam, ab38898)	12	15	13

Table 3. The number of patients analyzed and the list of antibodies used for immunohistochemical analysis of myofibroblast, MMPs and LOX in the healthy lamina propria, 10 cm and 20 cm away from the cancer.

(Abcam, ab38898, 1:500), anti-MMP2 (Abcam, ab37150, 1:500), anti-LOX (Abcam, ab174316, 1:500) (Table 3). After heat-induced antigen retrieval using citrate buffer (pH = 6) and subsequent washing in PBS, primary antibodies were incubated for 60 minutes. The sections were treated with commercial Ultra Vision/3,3'-diaminobenzidine (DAB) staining kit (Thermo Scientific Lab Vision TL-060-HD, Rockford, IL, USA). The reactions were developed using DAB substrate.

For quantification of immunohistochemically stained sections, Color Picker Threshold plugin within open community platform for bioimage informatics Icy was used, as previously described²². On images stained with anti-alphaSMA antibody, the representation of myofibroblast in colon lamina propria was determined as a relative percentage of the area occupied by myofibroblast divided by the area of the lamina propria selected with an imaging processor. For slides stained with anti-MMP2 and anti-LOX antibody, the percentage of MMP2/LOX-positive area was determined separately in lamina propria and epithelial region. The number of analyzed patients for each antibody is in the Table 3. For one patient, one slide was stained with each antibody and a random selection of 10 fields per slide on magnification x200 was analyzed.

Statistical analysis. Data were presented as means and standard deviations. The statistical package SPSS for Windows 12.0 (SPSS inc., Chicago, IL, USA) was used to indicate significant differences (two-way ANOVA followed by Tukey's multiple comparison test). Statistical significance was determined by $p < 0.05$.

Data availability

The dataset generated during and/or analyzed during the current study are available from the corresponding author on reasonable request.

Received: 19 October 2019; Accepted: 30 March 2020;

<https://doi.org/10.1038/s41598-020-63368-y>

References

- Vannucci, L. Stroma as an active player in the development of the tumor microenvironment. *Cancer Microenviron* **8**, 159–66 (2015).
- Fang, M., Yuan, J., Peng, C. & Li, Y. Collagen as a double-edged sword in tumor progression. *Tumor Biol.* **35**, 2871–2882 (2014).
- Gopal, S., Malthaupt, H., Pockock, R. & Couchman, J. R. Cell-extracellular matrix and cell-cell adhesion are linked by syndecan-4. *Matrix Biol.* **60–61**, 57–69 (2017).
- Schrader, J. *et al.* Matrix stiffness modulates proliferation, chemotherapeutic response and dormancy in hepatocellular carcinoma cells. *Hepatology* **53**, 1192–205 (2011).
- Rozario, T. & DeSimone, D. W. The extracellular matrix in development and morphogenesis: A dynamic view. *Dev. Biol.* **341**, 126–140 (2010).
- Zaman, M. H. *et al.* Migration of tumor cells in 3D matrices is governed by matrix stiffness along with cell-matrix adhesion and proteolysis. *Proc. Natl. Acad. Sci.* **103**, 10889–94 (2006).
- Handorf, A. M., Zhou, Y., Halanski, M. A. & Li, W. J. Tissue stiffness dictates development, homeostasis, and disease progression. *Organogenesis* **11**, 1–15 (2015).
- Taufalele, P. V., VanderBurgh, J. A., Muñoz, A., Zanotelli, M. R. & Reinhart-King, C. A. Fiber alignment drives changes in architectural and mechanical features in collagen matrices. *Plos one.* **14**, 20216537 (2019).
- Voutouri, C., Polydorou, C., Papageorgis, P., Gkretsi, V. & Stylianopoulos, T. Hyaluronan-derived swelling of solid tumors, the contribution of collagen and cancer cells, and implications for cancer therapy. *Neoplasia* **18**, 732–741 (2016).
- Giussani, M., Triulzi, T., Sozzi, G. & Tagliabue, E. Tumor extracellular matrix remodelling: New perspectives as a circulating tool in the diagnosis and prognosis of solid tumors. *Cells.* **8**, 81 (2019).
- Crotti, S. *et al.* Extracellular Matrix and colorectal cancer: How surrounding microenvironment affects cancer cell behavior? *J. Cell. Physiol.* **232**, 967–975 (2017).
- Fischer, T., Wilharm, N., Hayn, A. & Mierke, C. T. Matrix and cellular mechanical properties are driving factors for facilitating human cancer cell motility into 3D engineered matrices. *Converg. Sci. Phys. Oncol* **3**, 044004 (2017).
- Massague, J. New concepts in tissue-specific metastases. *Clin. Adv. Hematol. Oncol.* **1**, 576–7 (2003).
- Dogliani, G., Parik, S. & Fendt, S. M. Interactions in the (pre)metastatic niche support metastasis formation. *Front. Oncol* **9**, 219 (2019).
- Siad, A. H., Raufman, J. P. & Xie, G. The role of matrix metalloproteinases in colorectal cancer. *Cancer (Basel.)* **6**, 366–375 (2014).
- Brown, G. T. & Murray, G. I. Current mechanistic insights into the roles of matrix metalloproteinases in tumor invasion and metastasis. *J. Pathol.* **237**, 273–281 (2015).
- Wei, B. *et al.* Human colorectal cancer progression correlates with LOX-induced ECM stiffening. *Int. J. Biol. Sci.* **13**, 1450–1457 (2017).
- Murdocca, M. *et al.* Targeting LOX-1 inhibits colorectal cancer metastasis in an animal model. *Front. Oncol.* **9**, <https://doi.org/10.3389/fonc.2019.00927> (2019).
- Paidi, S. K. *et al.* Label-free Raman spectroscopy detects stromal adaptations in pre-metastatic lungs primed by breast cancer. *Cancer Res.* **77**, 247–256 (2017).

20. Whatcott, C. J. *et al.* Desmoplasia in primary tumors and metastatic lesions of pancreatic cancer. *Clin. Cancer Res.* **21**, 3561–3568 (2015).
21. Zhou, Z. H. *et al.* Reorganized collagen in the tumor microenvironment of gastric cancer and its association with prognosis. *J. Cancer* **8**, 1466–1476 (2017).
22. Despotović, S. Z. *et al.* Remodelling of extracellular matrix of the lamina propria in the uninvolved human rectal mucosa 10 cm and 20 cm away from the malignant tumor. *Tumour Biol.* **39**, <https://doi.org/10.1177/1010428317711654> (2017).
23. Bredfeldt, J. S. *et al.* Computational segmentation of collagen fibers from second-harmonic generation images of breast cancer. *J. Biomed. Opt.* **19**, 016007 (2014).
24. Capella, H. *et al.* Methods for quantifying fibrillar collagen alignment in *Methods In molecular biology* (ed. Rittié, L.) 1627, 429–449 (Springer Science, 2017).
25. Driřka, C. R. *et al.* Periductal stromal collagen topology of pancreatic ductal adenocarcinoma differs from that of normal and chronic pancreatitis. *Mod. Pathol.* **28**, 1470–1480 (2015).
26. Mo, A. *et al.* Distinct transcriptional changes and epithelial-stromal interactions are altered in early stage colon cancer development. *Mol. Cancer Res.* **14**, 795–804 (2016).
27. Morrill, E. E. *et al.* A validated software application to measure fiber organization in soft tissue. *Biomech. Model. Mechanobiol.* **15**, 1467–1478 (2016).
28. Chen, X., Nadiarynkh, O., Plotnikov, S. & Campagnola, P. J. Second harmonic generation microscopy for quantitative analysis of collagen fibrillar structure. *Nat. Protoc.* **7**, 654–669 (2012).
29. Nadiarynkh, O., Lacombe, R. B., Brewer, M. A. & Campagnola, P. J. Alterations of the extracellular matrix in the ovarian cancer studied by Second Harmonic Generation imaging microscopy. *BMC Cancer.* **10**, 94 (2010).
30. Bissell, M. J. & LaBarge, M. A. Context, tissue plasticity, and cancer: Are tumor stem cells also regulated by the microenvironment? *Cancer Cell.* **7**, 17–23 (2005).
31. Wei, B. *et al.* Human colorectal cancer progression correlates with LOX-induced ECM stiffening. *Int. J. Biol. Sci.* **13**, 1450–1457 (2017).
32. Paszek, M. J. *et al.* Tensional homeostasis and the malignant phenotype. *Cancer Cell.* **8**, 241–54 (2005).
33. Artym, V. V. *et al.* Dense fibrillar collagen is a potent inducer of invadopodia via specific signaling network. *J. Cell Biol.* **208**, 331–350 (2015).
34. Yu, H., Mouw, J. K. & Weaver, V. M. Forcing form and function: Biomechanical regulation of tumor evolution. *Trends Cell Biol.* **21**, 47–56 (2011).
35. Sheieh, A. C. Biomechanical forces shape the tumor microenvironment. *Ann Biomed. Eng.* **39**, 1379–89 (2011).
36. Backman, V. & Roy, H. K. Advances in biophotonics detection of field carcinogenesis for colon cancer risk stratification. *J. Cancer* **4**, 251–261 (2013).
37. Sanz-Pamplona, R. *et al.* Aberrant gene expression in mucosa adjacent to tumor reveals a molecular crosstalk in colon cancer. *Mol. Cancer.* **13**, 1–19 (2014).
38. Dela Cruz, M. *et al.* Metabolic reprogramming of the premalignant colonic mucosa is an early event in carcinogenesis. *Oncotarget* **8**, 20543–20557 (2017).
39. Boland, C. R. & Kim, Y. S. Transitional mucosa of the colon and tumor growth factors. *Med. Hypotheses.* **22**, 237–243 (1987).
40. Ferruzzi, J. *et al.* Compressive remodelling alters fluid transport properties of collagen networks- implications for tumor growth. *Sci Rep.* **9**, 17151 (2019).
41. Trujillo, K. A. *et al.* Markers of fibrosis and epithelial to mesenchymal transition demonstrate field cancerization in histologically normal tissue adjacent to breast tumors. *Int. J. Cancer.* **129**, 1310–1321 (2011).
42. Genovese, L. *et al.* Cellular localisation, invasion, and turnover are differently influenced by healthy and tumor-derived extracellular matrix. *Tissue Eng. Part A.* **20**, 2005–18 (2014).
43. McAllister, S. S. & Weinberg, R. A. The tumour-induced systemic environment as a critical regulator of cancer progression and metastasis. *Nat. Cell Biol.* **16**, 717–727 (2014).
44. Curtius, K., Wright, N. A. & Graham, T. A. An evolutionary perspective on field cancerization. *Cancer.* **28**, 19–32 (2018).
45. Hiratsuka, S. *et al.* MMP9 induction by vascular endothelial growth factor receptor-1 is involved in lung-specific metastasis. *Cancer Cell* **2**, 289–300 (2002).
46. Dotto, P. G. Multifocal epithelial tumors and field cancerization: stroma as a primary determinant. *J. Clin. Invest.* **124**, 1446–1453 (2014).
47. Rabasović, M. D. *et al.* Nonlinear microscopy of chitin and chitinous structures: a case study of two cave-dwelling insects. *J. Biomed. Opt.* **20**, 016010 (2015).
48. Bukara, K. *et al.* Mapping of hemoglobin in erythrocyte ghosts using two photon excitation fluorescence microscopy. *J. Biomed. Opt.* **22**, 26003 (2017).

Acknowledgements

The authors are grateful to Novica Milicevic and Živana Milicevic for critically reading the manuscript and supporting each phase of development of the present work; Miloš Kiš and Dragan Beška, for excellent technical assistance. This work was supported by grant from the Ministry for Education, Science and Technological Development of Republic of Serbia (nos. 175005, OI 171038 and III45016).

Author contributions

S.D., Đ.M., V.Ž., M.R., A.K., A.P. designed the work, S.D., Đ.M., A.P., M.R. A.K., G.N., V.Ž., V.P., Z.K., S.L. conducted the experiment; S.D., Đ.M., M.R., A.P., Z.K. analyzed and interpreted the data.

Competing interests

The authors declare no competing interests.

Additional information

Supplementary information is available for this paper at <https://doi.org/10.1038/s41598-020-63368-y>.

Correspondence and requests for materials should be addressed to S.Z.D.

Reprints and permissions information is available at www.nature.com/reprints.

Publisher's note Springer Nature remains neutral with regard to jurisdictional claims in published maps and institutional affiliations.



Open Access This article is licensed under a Creative Commons Attribution 4.0 International License, which permits use, sharing, adaptation, distribution and reproduction in any medium or format, as long as you give appropriate credit to the original author(s) and the source, provide a link to the Creative Commons license, and indicate if changes were made. The images or other third party material in this article are included in the article's Creative Commons license, unless indicated otherwise in a credit line to the material. If material is not included in the article's Creative Commons license and your intended use is not permitted by statutory regulation or exceeds the permitted use, you will need to obtain permission directly from the copyright holder. To view a copy of this license, visit <http://creativecommons.org/licenses/by/4.0/>.

© The Author(s) 2020



Observation of second harmonic generation in doped polymeric carbon monoxide

Michael G. Pravica^{a,*}, Mihailo D. Rabasovic^b, Aleksandar J. Krmpot^b, Petrika Cifligu^a, Blake Harris^a, Egor Evlyukhin^a, Marko G. Nikolic^b

^a Department of Physics and Astronomy, University of Nevada Las Vegas (UNLV), Las Vegas, NV 89154-4002, USA

^b Photonics Center, Institute of Physics Belgrade, University of Belgrade, Pregrevica 118, 11080 Belgrade, Serbia

ARTICLE INFO

Article history:

Received 23 July 2019

Received in revised form 31 August 2019

Accepted 4 September 2019

Available online 7 September 2019

Keywords:

X-rays

High pressure

Second harmonic generation

SrC₂O₄

Optical sensor

ABSTRACT

Second harmonic generation (SHG) experiments were conducted on samples of a novel material: doped polymeric CO (dp-CO) that were synthesized via synchrotron X-ray irradiation of SrC₂O₄ and high pressure. The goal of the study was to ascertain if the novel material is rugged enough to handle high levels of radiation to enable its possible use as future sensors or optoelectronic devices. Three samples were tested. Two of the smaller samples that were synthesized in a diamond anvil cell (DAC) and recovered at ambient conditions rapidly decomposed/degraded in the presence of the strong 3.6×10^9 mW/cm² intensity optical beam. The larger sample that was synthesized in a Paris-Edinburgh cell at 3 GPa after 1.5 h of hard X-ray white beam irradiation and also recovered to ambient conditions was not damaged by a 6.1×10^9 mW/cm² strength optical beam and exhibited second harmonic generation. This lends credence that this novel material (when synthesized under select conditions) may offer utility as a rugged radiation hardened and easy to manufacture nonlinear optical device.

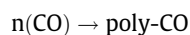
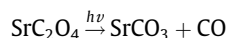
© 2019 Elsevier B.V. All rights reserved.

1. Introduction

In the quest to synthesize novel and industrially-useful materials, highly ionizing and highly penetrating hard X-rays (>7keV) in conjunction with high pressure offer a unique and relatively unexplored means to create rugged and radiation-hardened materials that may not be synthesizable by conventional means. High energy X-rays (>7keV) can overcome large thermodynamic activation barriers to ionize atoms, forcing atomic and molecular fluidity, which, coupled with high pressure (to force these radicals and ions closer together to interact), may create unique compounds. We have been developing useful hard X-ray photochemistry for a variety of applications for chemical synthesis and decomposition [1]. From the initial observation of O₂ production from synchrotron X-ray irradiated chlorate salts [2,3]: (e.g. KClO₄ $\xrightarrow{h\nu}$ 2O₂ + KCl), we have been able to successfully release O₂ [2,3], Cl₂ [4], H₂ [5], N₂ [6], NO₂ [7], and F₂ [8] inside a diamond anvil cell (DAC) or other sealed and/or pressurized chamber *in situ* to create unique metastable states of matter and observe molecular diffusion and reactions of these relatively mobile reactants (e.g. O₂ + 2F₂ $\xrightarrow{h\nu}$ 2OF₂) [5,9] at extreme conditions. By exploiting our methods to release fluorine

in situ inside a DAC, we have strong evidence of the synthesis of HgF₄ by irradiating a pressurized mixture of HgF₂ and XeF₂ (the latter compound releasing F₂ [1]). The fluorine then reacted with HgF₂ via: HgF₂ + F₂ $\xrightarrow{h\nu}$ HgF₄ as predicted [10]. We have also demonstrated that novel structures of known compounds (such as CsO₂) can be created using our irradiation methods [11].

One interesting compound that we have synthesized using our methods is a variant of polymeric CO (poly-CO) which is conventionally produced by pressurizing CO to >5 GPa [12,13] or >3 GPa with optical assistance [14]. By irradiating strontium oxalate powder at various pressures (including ambient), a novel yellowish-red amorphous compound was formed that was recoverable at ambient conditions [15,16]. Infrared spectroscopy of the recovered irradiated samples indicated the presence of trapped CO₂, SrCO₃, and characteristic spectral lines that were detected in poly-CO [16,17]. Based on this evidence and X-ray absorption studies [16], the following primary reactions were suspected [17]:



Conventional poly-CO is an unstable solid that decomposes into graphite and CO₂ in a matter of days and is very light sensitive [12–14]. Our synthesized material, however, is very stable (lasting for

* Corresponding author.

E-mail address: pravica@physics.unlv.edu (M.G. Pravica).

periods of at least 3 years) and traps CO_2 inside it for at least as long as the compound lasts suggesting the possibility of a CO_2 -storage medium [16,18]. We suspect that the presence of SrCO_3 as a dopant stabilizes the compound. There is a strong pressure dependence of the synthesis [17]. This novel compound exhibits wide bandgap semiconductor properties suggesting its potential use as a solar material or other optoelectronic device/sensor [18]. Due to the IR spectral similarity to conventionally synthesized poly-CO, we termed the compound doped solid [16] or doped polymeric [15] CO. We wish to emphasize, however, that this material is not the same as pure poly-CO as it traps CO_2 , is produced via irradiation of an oxalate salt (as opposed to pressurization of CO), and has been found to be very stable, unlike conventionally-synthesized poly-CO. Rather, it is a novel material that has yet-to-be-uncovered properties.

Related to this discovery, a natural question arises when considering what kind of light fields this compound may sustain before being damaged. And, given the strongly coupled (even if amorphous) nature of this unique extended solid, could it possibly serve as an radiation-hardened optical mixer? After all, HMX, an organic explosive, has a strong second harmonic mixing coefficient [19]. Thus, we sought to determine the effect of high intensity laser fields on our synthesized samples with the aim of determining their survivability under these extreme conditions and, to ascertain if we could produce frequency doubled light.

2. Experimental

2.1. Sample preparation

Preparation and irradiation of our samples was performed at the High Pressure Collaborative Access Team's 16 BM-B beamline at the Advanced Photon Source. We used two different means to pressurize our samples: a Paris-Edinburgh Cell (PEC) for larger samples and diamond anvil cell (DAC) for smaller samples (<3 nl). For the PEC preparation, white strontium oxalate powder (SrC_2O_4 – Alfa Aesar 97% purity) was manually loaded into a prepared composite gasket chamber which surrounded a 1 mm diameter by 1 mm deep MgO cup. The sample was pressurized by applying mechanical load to two WC anvils, bringing them towards

one another with the gasket squeezed in between via a high pressure oil hydraulic apparatus. The MgO cup also served as the pressure calibrant. This setup has been described elsewhere [20].

For samples loaded in the DAC, we employed a symmetric-style DAC with 300 μm culet-opposed diamonds. A 0.01" thick stainless steel gasket was preindented (by the opposed anvils) to a 70 μm initial thickness and then drilled in the center of the indentation via electric discharge machining to create a 120 μm diameter sample hole. Strontium oxalate powder was then manually loaded into the sample chamber along with a ~ 10 μm diameter ruby for pressure measurement.

After pressurization (as verified by the respective calibrants), each of the samples were irradiated with "white" X-rays for approximately 1.5 h. The beam was chosen to be typically defocused (PEC) or slightly defocused (DAC) to completely irradiate the samples. After irradiation, samples were recovered after depressurization to ambient conditions. For the PEC sample, the surrounding/confining composite gasket material was manually removed. For the DAC samples, the gaskets were removed from the DAC and the samples remained intact in the gasket hole.

2.2. Nonlinear optical measurements

Our optical studies were undertaken at the home made nonlinear optical facility located at the Institute of Physics in Belgrade, Serbia. For more detailed description of the experimental setup and scheme, please refer to ref. [21]. In this study the laser light from mode locked Ti:Sa laser (MIRA 900, Coherent Inc.) tuned to 840 nm was focused onto the sample by 20×0.8 air objective (Zeiss plan-Apochromat[®]). The second harmonic generation (SHG) signal passed through a narrow band filter of central wavelength 420 nm and bandwidth of 10 nm and was detected by photo multiplier tube (PMT). Due to the thickness of the samples, our measurements were performed in reflection.

3. Results

The samples under study were placed under the nonlinear microscope with a 20x objective (NA = 0.8) and a controllable translation stage. A video monitoring system was used to align

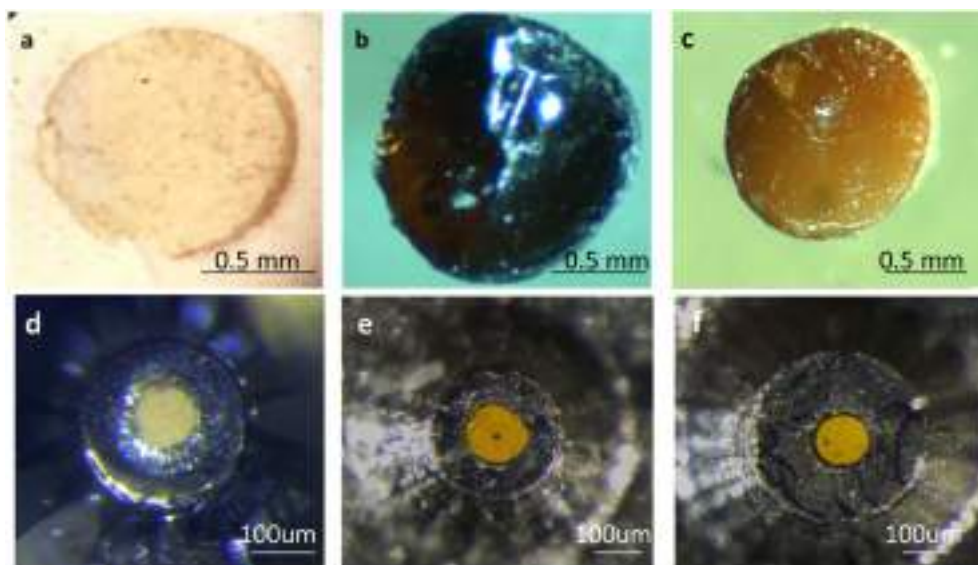


Fig. 1. Pictures of the recovered (to ambient conditions) products synthesized via X-ray irradiation at different pressure points in PEC cells (top photos) and DAC (bottom photos). a) PEC sample at ambient pressure. b) PEC sample produced at 4 GPa. c) PEC sample at 10 GPa. d) DAC sample at ambient. e) DAC sample produced at 4 GPa. f) DAC sample at 10 GPa. From reference [18].

the samples into the visual field of the microscope. The focused beam size was diffraction limited (diameter of approximately $0.5\ \mu\text{m}$). Three samples were studied. The first two were poly-CO samples that were created in a DAC (see e and f of Fig. 1). They had a yellowish waxlike consistency. The third sample was synthesized in a PEC at 3 GPa and had a similar look and consistency to reddish-brown beer bottle glass (see Fig. 1b).

When the samples produced inside a DAC were respectively irradiated with the high powered laser light (7mW), they rapidly decomposed in the beam (seconds to minutes) and no second harmonic light was generated. The third PEC-made sample, on the other hand (Fig. 1b), produced a second harmonic signal at 420 nm when placed in the path of the laser beam (see Fig. 2). The SHG signal appeared to be stable with time and no visual damage on this sample was immediately evident. For comparison purposes, a slide of virgin, unirradiated strontium oxalate powder was analyzed for SHG using the sample experimental conditions that were used in above-described measurements and no SHG light was observed (see Fig 3) demonstrating that irradiation of the oxalate salt is critical for SHG signal. Accurate determination of the SHG absolute efficiency is affected by a number of various experimental conditions (pulse duration, pulse energy, pulse-to-pulse stability, repetition rate etc) that are not easily and precisely controllable. It is a nontrivial task that is rarely performed in practice for this kind of experiment. Thus, we have compared efficiencies of the SHG in our samples and starch, since starch is the most common test sample in nonlinear microscopy. PEC generates second harmonic 30–100 times weaker than the starch grains.

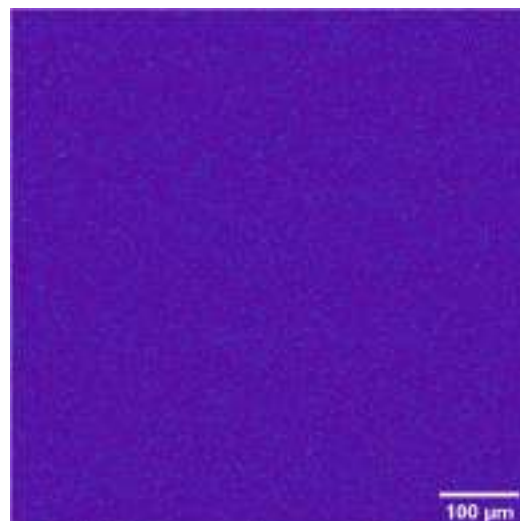


Fig. 3. Imaging scans of a slide consisting of virgin powdered SrC_2O_4 that had not been irradiated by X-rays demonstrating no SHG signal at a similar intensity level and thus that the SHG signal observed in Fig. 2 was due to the novel material (dp poly-CO).

4. Discussion

The samples made in a DAC did not survive the intense focused laser beam. Yet the PEC-made sample did. This may be due to to

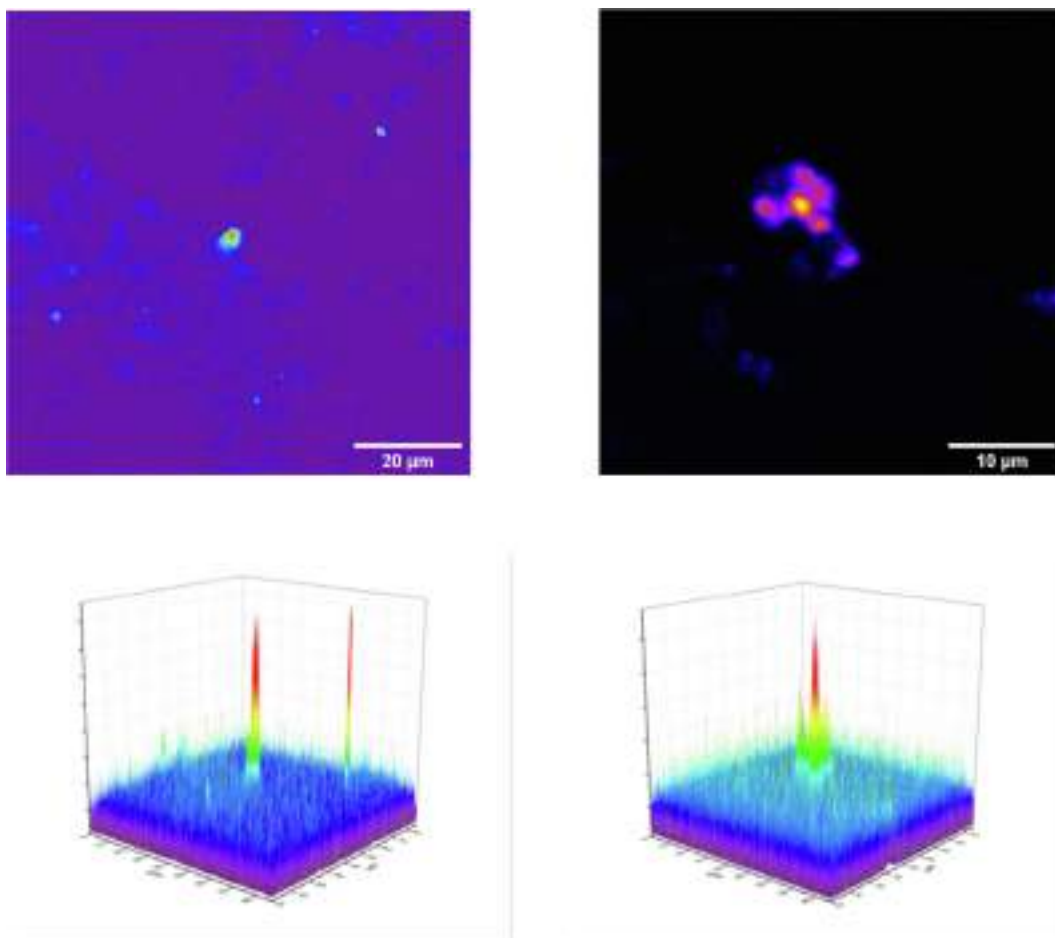


Fig. 2. SHG in the third sample that was made in a PEC taken from two different regions of the sample.

differing flux density conditions of the X-ray beam when the different samples were irradiated leading to somewhat different synthetic or incomplete pathways. As the third sample was far larger, it may be able to handle more heat and not thermally decompose under any heating caused by the laser beams. Further studies are planned to ascertain why our DAC samples decomposed in the presence of the laser beam.

Every indication suggests that our synthesized samples (both those made in the DAC and PEC) are largely amorphous. The high SHG intensity spots that were observed in Fig. 2 suggest that there may submicron crystals present in our sample which cause large SHG when oriented properly relative to the incident laser polarization. This may also imply that the synthetic process is incomplete which may also have resulted in less resilient DAC-made samples. Conventionally produced poly-CO, on the other hand is a waxy, amorphous material which is unable to survive the intense laser fields required for SHG. Thus, though the mixing efficiency of light may be lower than when using an oriented single crystal, this novel material may have utility as a relatively easy to synthesize radiation-hardened sensor/nonlinear mixer that appears to be chemically stable (or at least metastable) and may also yield more insights on the synthetic process/crystallization of our samples with extended irradiation and/or pressure.

5. Conclusion

We have conducted further studies of a novel material that we call doped polymeric or solid CO to interrogate its ability to behave as a nonlinear mixer and withstand high radiation flux. We have found that one of our larger glass-like samples exhibited second harmonic generation and was not damaged by the laser beam. Further work will seek to better understand and optimize synthetic and crystallization parameters in the hopes of creating a useful sensor and/or optical mixer for use at extreme or ambient conditions.

Declaration of Competing Interest

The authors declare that they have no known competing financial interests or personal relationships that could have appeared to influence the work reported in this paper.

Acknowledgements

We gratefully acknowledge past support from the Department of Energy National Nuclear Security Administration (DOE-NNSA)


under Award Number DE-NA0002912. We also acknowledge prior support from the DOE Cooperative Agreement No. DE-FC08-01NV14049 with the University of Nevada, Las Vegas. Portions of this work were performed at HPCAT (Sector 16), Advanced Photon Source (APS), Argonne National Laboratory. HPCAT operation is supported by DOE-NNSA's Office of Basic Sciences. The Advanced Photon Source is a U.S. Department of Energy (DOE) Office of Science User Facility operated for the DOE Office of Science by Argonne National Laboratory under Contract No. DE-AC02-06CH11357. We acknowledge the Ministry of Education, Science and Technological Development of the Republic of Serbia, grant numbers III45016 and OI171038.

References

- [1] M. Pravica, S. Schyck, B. Harris, P. Cifligu, B. Billingham, *Pap. Phys.* 11 (2019), 110001-1-6.
- [2] M. Pravica, L. Bai, C. Park, Y. Liu, M. Galley, J. Robinson, N. Bhattacharya, *Rev. Sci. Instr.* 82 (2011), 106102-1-3.
- [3] M. Pravica, B. Hulseley, L. Bai, D. Sneed, Q. Smith, G. Guardala, *J. Phys.: Conf. Series* 500 (2) (2014), 022009.
- [4] M. Pravica, D. Sneed, Q. Smith, L. Bai, *Chem. Phys. Lett.* 530 (2013) 74-76.
- [5] M. Pravica, D. Sneed, M. White, Y. Wang, *J. Chem. Phys.* 141 (2014) 091101.
- [6] M. Pravica, Y. Liu, L. Bai, *Chem. Phys. Lett.* 555 (2013) 113-115.
- [7] D. Goldberger, C. Park, E. Evlyukhin, P. Cifligu, M. Pravica, *J. Phys. Chem. A* 22 (44) (2018) 8722-8728.
- [8] M. Pravica, D. Sneed, M. White, Y. Wang, *R. Sci. Instr.* 85 (2014), 086110.
- [9] M. Pravica, M. White, Y. Wang, Y. Xiao, P. Chow, *Chim. Oggi* 36 (4) (2018) 50-52.
- [10] M. Miao, J. Botana, M. Pravica, D. Sneed, C. Park, *Jpn. J. Appl. Phys.* 56 (2017), 05FA10.
- [11] E. Evlyukhin, E. Kim, D. Goldberger, P. Cifligu, S. Schyck, P. Weck, M. Pravica, *Phys. Chem. Chem. Phys.* 20 (2018) 18949-18956.
- [12] W.J. Evans, M. Lipp, C.-S. Yoo, H. Cynn, J.L. Herberg, R.S. Maxwell, M. Nicol, *Chem. Materials* 18 (2006) 2520.
- [13] M. Lipp, W. Evans, B. Baer, C.-S. Yoo, *Nat. Materials* 4 (2005) 21.
- [14] M. Ceppatelli, A. Serdyukov, R. Bini, H.J. Jodl, *J. Phys. Chem. B* 113 (2009) 6652.
- [15] M. Pravica, D. Sneed, Q. Smith, B. Billingham, T. May, M. White, K. Dziubek, *Cogent Phys.* 3 (2016), 1169880:1-8.
- [16] M. Pravica, E. Evlyukhin, P. Cifligu, B. Harris, N. Chen, Y. Wang, *Chem. Phys. Lett.* 686 (2017) 183-188.
- [17] D. Goldberger, E. Evlyukhin, P. Cifligu, Y. Wang, M. Pravica, *J. Phys. Chem. A* 121 (2017) 7108-7113.
- [18] E. Evlyukhin, E. Kim, P. Cifligu, D. Goldberger, S. Schyck, B. Harris, S. Torre, G. Rossman, M. Pravica, *J. Mater. Chem. C* 6 (2018) 12473-12478.
- [19] B.F. Henson, B.W. Asay, R.K. Sander, S.F. Son, J.M. Robinson, P.M. Dickson, *Phys. Rev. Lett.* 82 (6) (1999) 1213-1216.
- [20] Y. Kono, C. Park, C. Kenney-Benson, G. Shen, Y. Wang, *Phys. Earth Planet. Inter.* 228 (2014) 269-280.
- [21] M.D. Rabasović, D.V. Pantelić, B.M. Jelenković, S.B. Ćurčić, M.S. Rabasović, M.D. Vrbica, V.M. Lazović, B.P.M. Ćurčić, A.J. Krmpot, *J. Biomed. Opt.* 20 (2015), 016010.

FULL ARTICLE

Naturally safe: Cellular noise for document security

Danica Pavlović¹ | Mihailo D. Rabasović¹ | Aleksandar J. Krmpot¹ | Vladimir Lazović¹ | Srećko Čurčić² | Dejan V. Stojanović³ | Branislav Jelenković¹ | Wang Zhang⁴ | Di Zhang⁴ | Nenad Vukmirović¹ | Dimitrije Stepanenko¹ | Branko Kolarić^{1,5}  | Dejan V. Pantelić^{1*}

¹Institute of Physics, University of Belgrade, Belgrade, Serbia

²Institute of Zoology, University of Belgrade—Faculty of Biology, Belgrade, Serbia

³Institute of Lowland Forestry and Environment, University of Novi Sad, Novi Sad, Serbia

⁴State Key Lab of Metal Matrix Composite, Shanghai Jiao Tong University, Shanghai, China

⁵MNM Group, Department of Physics, UMONS, Mons, Belgium

***Correspondence**

Dejan V. Pantelić, Institute of Physics, University of Belgrade, Photonics Center, Pregrevica 118, 11080 Zemun, Belgrade, Serbia.

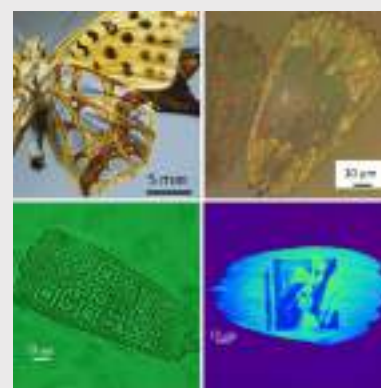
Email: pantelic@ipb.ac.rs

Funding information

Joint Funding of Development and Research Projects of the Republic of Serbia 407 and the People's Republic of China; Ministry of Education, Science and Technological 404 Development of the Republic of Serbia, Grant/Award Numbers: III45016, III43002, ON171038, ON173038, ON171017, ON171032; Institute of Physics; Innovation Fund; German Academic Exchange Service; Ministry of Education, Science and Technological Development of the Republic of Serbia

Abstract

Modern document protection relies on the simultaneous combination of many optical features with micron and submicron structures, whose complexity is the main obstacle for unauthorized copying. In that sense, documents are best protected by the diffractive optical elements generated lithographically and mass-produced by embossing. The problem is that the resulting security elements are identical, facilitating mass-production of both original and counterfeited documents. Here, we prove that each butterfly wing-scale is structurally and optically unique and can be used as an inimitable optical memory tag and applied for document security. Wing-scales, exhibiting angular variability of their color, were laser-cut and bleached to imprint cryptographic information of an authorized issuer. The resulting optical memory tag is extremely durable, as verified by several century-old insect specimens still retaining their coloration. The described technique is simple, amenable to mass-production, low cost and easy to integrate within the existing security infrastructure.

**KEYWORDS**

biophotonics, complexity, iridescence, optical document security, variability

1 | INTRODUCTION

Insects have been used more than any other living creatures as a blueprint for design of novel devices. Butterflies and moths (order: Lepidoptera) are particularly inspiring, due to vast number of species (nearly 180 000) [1] and peculiar

optical properties of their wings covered with large number (500–1000/mm²) of tiny, overlapping scales [2] (see section 1 of Appendix S1 for a short description of their properties). Some of them are structurally colored [3] that is, produce colors by interference, diffraction and scattering, rather than pigments. This is due to complex, regular or

irregular, micro/nanostructures, which can be classified in several groups according to their morphology [4]. Most frequently, iridescence (characterized by directionally dependent coloration [3]) can be observed.

Back into the XVIII century, Benjamin Franklin came up with an idea to reproduce the complexity of natural structures for document protection. He printed venation patterns of plant leaves on dollar bills to prevent counterfeiting [5]. Nowadays, his method was superseded by artificial security components, such as optically variable devices (OVDs) [6]. Diffractive optical elements (DOEs) are commonly exploited for the purpose, due to their, inherently complex microstructures, recognizable optical pattern and capability for mass-production by embossing. There is a significant drawback: for the specific type of document, all embossed copies of DOEs are identical. If a fake DOE is manufactured, counterfeited document can be made in large quantities, too. For that reason, an important goal is to invent a device which will provide unique and individual protection for each document. Protective elements should be highly complex, unique, difficult to reverse engineer and imitate. In the relevant literature, such objects are called physical one-way functions and can be realized by embedding randomly dispersed plastic, micron-sized spheres in a transparent medium and observing mesoscopic light scattering [7]. As another example, we mention using a randomized pattern of scattering from paper-based substrates [8].

Imprints of naturally occurring structures were proposed as security elements by Hamm-Dubischar [9], Biermann and Rauhe [10], and Rauhe [11], who presented the idea of document protection using biomineralized shells of radiolarians and diatoms. The protection is based on the structural complexity of their shells. The main problem is that optical effects are not particularly conspicuous, and the complexity can be assessed only at the morphological level, using scanning electron microscopy (SEM). Another problem is that structural variations among individuals of the same species seem to be small.

Whichever security element is used, it must be integrated in a security system relying on three inspection lines [6]: the first line is overt and can be visually inspected by anyone; the second is semi-covert and uses machine inspection; while the third one is covert and relies on forensic inspection with highly specialized equipment.

Here, we analyze the structural complexity, randomness, variability and uniqueness of the optical pattern of iridescent butterfly wing scales. We aim to establish their usefulness as inimitable OVDs for individualized, covert and overt, optical document security. Additionally, we investigate wing-scales as a memory medium for inscription of additional cryptographic information.

2 | STRUCTURE AND IRIDESCENCE OF *ISSORIA LATHONIA* BUTTERFLY WING-SCALES

In this section, we analyze morphological and optical features of scales belonging to the underside silver wing-patches of the Queen of Spain Fritillary, *Issoria lathonia* (Linnaeus, 1758), (see Figure 1A and section 2 of Appendix S1 for a short description of the butterfly's life history). This particular species was studied for the characteristic coloration of individual wing-scales, consisting of red, green and bluish spots randomly dispersed along a grating-like structure (see reflection microscope image in Figure 1B,C). The resulting silver color is produced by the local, additive spectral mixing [12].

Field-emission gun scanning electron microscope (FEGSEM) images reveal detailed structure of the scale's upper lamina (UL in Figure 1D). It consists of lamellar longitudinal ridges (R) regularly separated by a distance of 1.5 μm . There is, also, a fish-bone-shaped sub-wavelength grating (SW) with period of 150 nm, radiating from ridges. The interior of the scale is hollow, filled only with nano-pillars, separating UL and lower lamina (LL).

Nonlinear optical microscopy was used to analyze three-dimensional (3D) structure of wing-scales using two-photon excited fluorescence (TPEF) of chitin. Nonlinear microscope was constructed in-house [13] (see Appendix S1 for details) and used to reveal that the wing scales have irregular, wavy shape (see Figure 1E). This significantly contributes to variability of the resulting optical pattern, together with variation of the thicknesses of upper and lower laminae and their mutual distance.

We have found that the individual wing scales are iridescent, that is, the color pattern strongly depends on illumination and observation directions. The pattern has maximum brightness and sharpness for orthogonal illumination, directly through the microscope objective (resulting in an image like in Figure 1C).

3 | VARIABILITY OF OPTICAL PATTERN AND UNIQUENESS OF BUTTERFLY WING-SCALES

In this section, we will establish a connection between the wing scale morphology and the resulting reflection spectrum. To do that, we have to make a numerical model, enabling us to calculate the reflection spectrum of a single wing scale, removed from the wing and attached to a transparent substrate (as in Figure 1C). For simplicity, each scale is represented by two, wavy thin plates, separated by the layer of air. To approximate waviness each scale is divided into a number of vertical sections with different positions

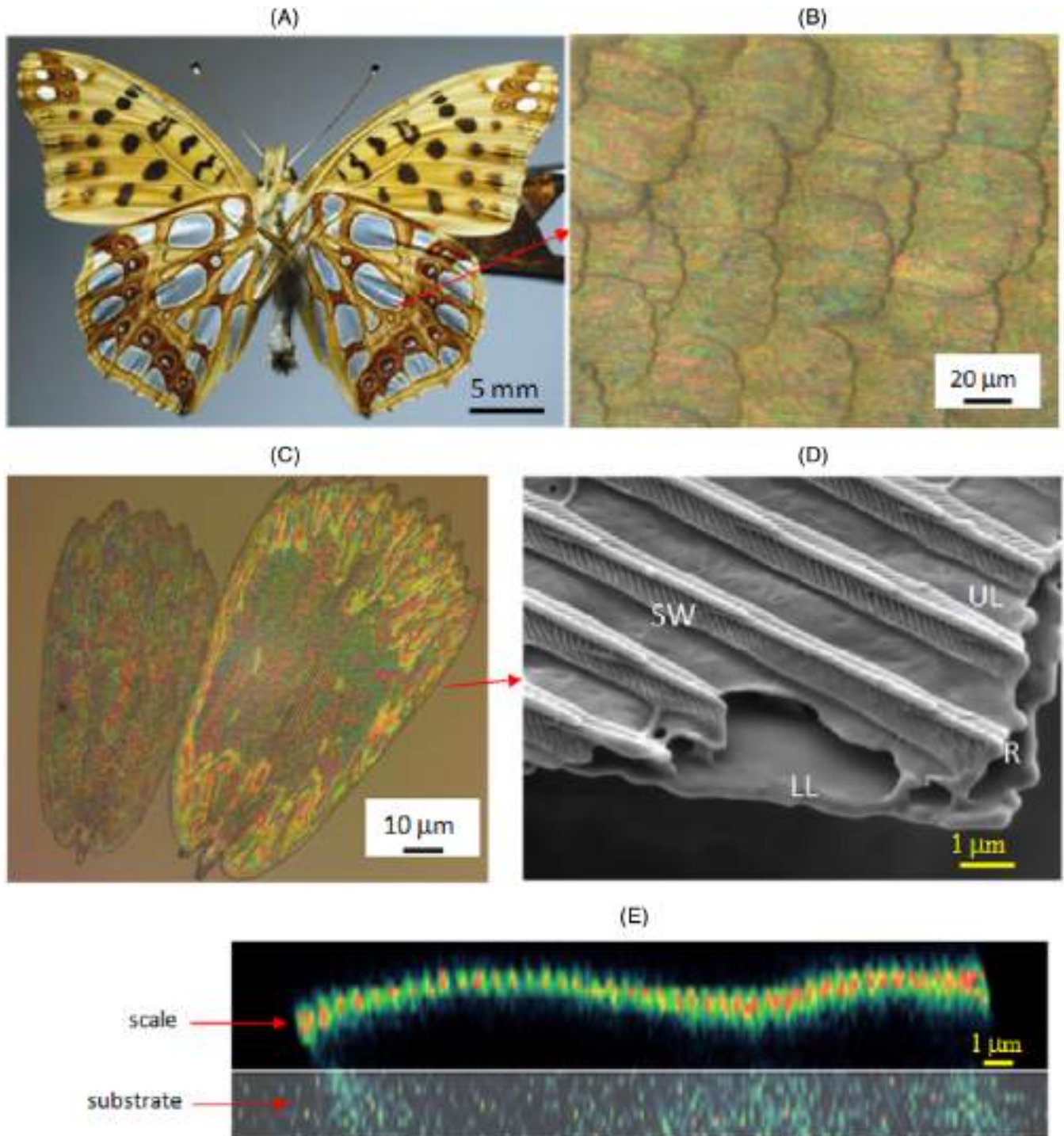


FIGURE 1 A, Ventral side of *Issoria lathonia* butterfly. B, Reflection microscope (10 \times , 0.25 NA) image of wing scales from the silver patch. C, Reflection microscope image (20 \times , 0.4 NA) image of two isolated wing-scales, removed from the wing of *I. lathonia*. D Scanning electron microscope image of the *I. lathonia* wing scale. LL and UL are lower and upper lamina, respectively, R is a ridge, while SW is a, fishbone-shaped, sub-wavelength grating. E, Wavy cross-section of butterfly wing scale (as recorded on a nonlinear optical scanning microscope)

and thicknesses of layers (Figure 2A). Each section contains two layers of chitin, the first of which was regarded as a sub-wavelength scattering surface, due to its irregularity and presence of the subwavelength grating (Figure 1D). Both

layers are separated from the glass substrate by an additional air layer.

Reflection spectrum of each section was calculated using a transfer matrix method, modified to include the effects of

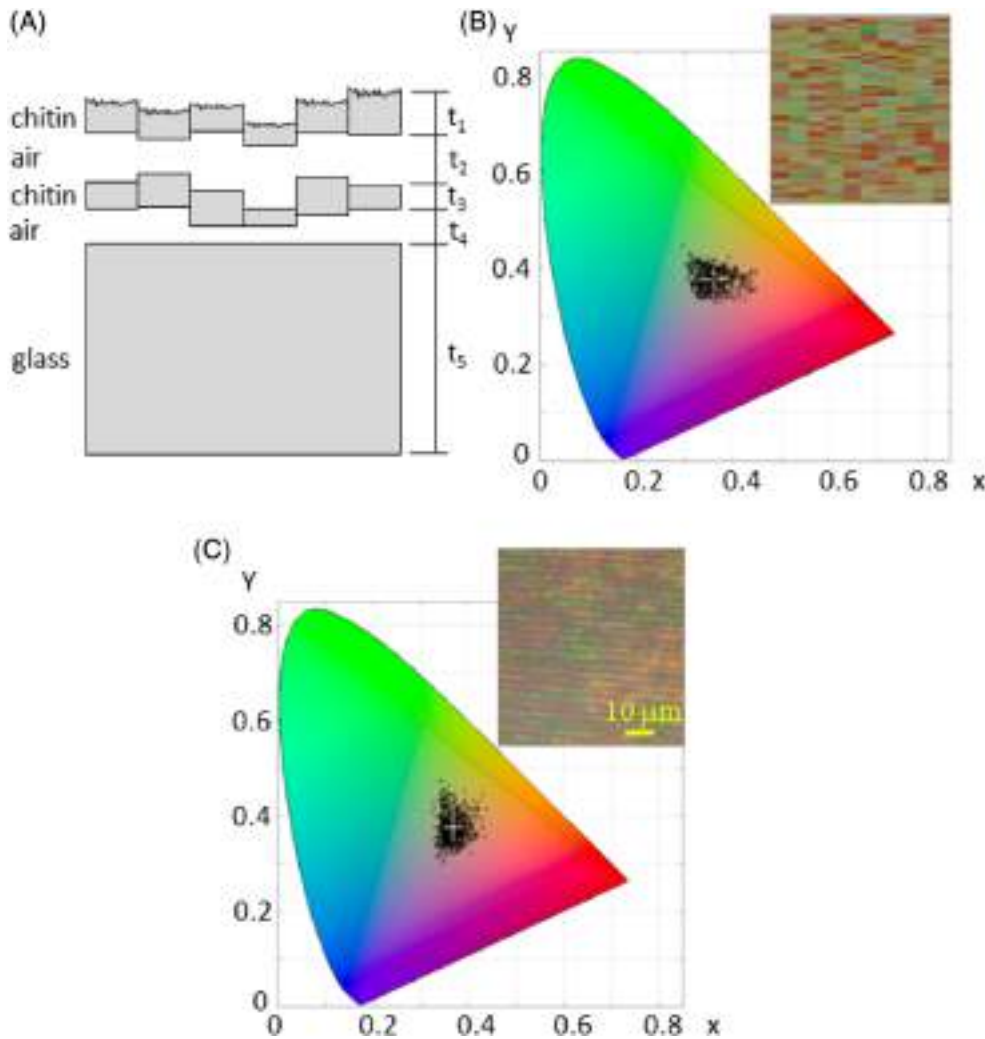


FIGURE 2 A, A theoretical model of a wing scale on the glass substrate. B, Color coordinates of a modeled pattern are presented in a CIE 1931 diagram, together with the color pattern in the inset. C, Color coordinates of *Issoria lathonia* pattern are presented in a CIE 1931 diagram. A section of a *I. lathonia* wing scale pattern, used to calculate color coordinates, is presented in the inset. Crosses in B and C represent average color value and their lengths indicate SDs in x - and y -directions

scattering [14]. Layer thicknesses (t_1, t_2, \dots, t_5 in Figure 2A) and their corresponding refractive indices were the parameters of the model, as well as the root mean square roughness (RMS) of the surfaces.

To simulate the wing scale as a whole, the same calculation was performed for each section. The starting point of our simulation was the layer thicknesses estimated from Figures 1D,E (~ 100 nm chitin, ~ 1000 nm air layer thickness—see section 3 of Appendix S1 for the complete list of parameter values). Layer thicknesses were stochastically varied (according to normal distribution) with pre-defined SD $\sigma = 15$ nm. Following the calculation of spectrum for each section, xyY color coordinates were calculated. They were presented in a CIE 1931 diagram (black dots in Figure 2B), which was designed to closely match human color perception (through three color-matching functions) [15]. It is, also, a useful tool to represent RGB values of color-camera images recorded through this research.

Calculated colors are, also, represented as a pattern of rectangular colored patches (see inset in Figure 2B). For

comparison, color coordinates of experimentally recorded pattern (inset in Figure 2C) were also computed and presented in CIE 1931 diagram (Figure 2C).

We were not able to obtain perfect match in CIE diagrams (Figures 2B,C), for the same reason which prevents a counterfeiter to forge a wing scale—complexity of the problem. However, we were able to match the position of the mean color coordinate (small white crosses in CIE diagrams) of theoretical and experimental image. The shape of the color scattering distribution is different, but the SDs are similar.

The most important result is that the variation of layer thicknesses by only ± 15 nm leads to experimentally recorded variability of coloration. This means that one trying to copy the exact coloration pattern of the wing scale, has to maintain an extreme precision of manufacturing—at least one-tenth of the layer thickness variability (~ 1.5 nm). The task is well beyond practical limits of modern technology, and cellular noise precludes replication of identical wing-scales by natural means.

Wing-scales described above have a sufficient number of degrees of freedom (in terms of layer thicknesses and waviness) to enable significant variability. Here, we want to find how difficult would be to find two identical scales.

We first analyze the statistical properties of the wing-scales color patterns by decomposing an image into its RGB components and calculating two-dimensional (2D) autocorrelation function for each color channel separately—see details in section 4 of Appendix S1. It can be seen (Figure S1) that autocorrelation peak is asymmetrical, that is, its width along the wing-scale grating was estimated at 30 μm , while in the orthogonal direction it is 1.5 μm .

By taking into account that average dimensions of the scales are 50 \times 100 μm , we can easily calculate that there are $[50/1.5] \times [100/30] = 33 \times 3 = 99$ (numbers were rounded to the nearest integer) statistically independent, colored patches. We can discriminate intensity of a single color channel in, at least, 10 discrete levels—easily achievable for any low-cost or mobile phone camera. In that case, we may estimate that there are, at least theoretically, 10^{99} wing-scales with different patterns per every channel. Thus, finding a scale exactly the same as another, previously chosen, one is impossible from any practical point of view.

Each wing-scale is a dead remnant of an individual cell and thus reflects intrinsic randomness of cellular development. This is a natural consequence of cellular noise [16], which is a well-established fact in biology, resulting in non-deterministic relation between genotype and phenotype. The important thing about butterfly wing scales is that they “freeze” the cellular noise, by leaving it in a state just before the cell died. Cellular noise cannot be switched-off and it is expected to be similar in all other butterfly species. In that sense, the similar level of randomness is expected on all wing-scales of all butterflies [17] including those of the *Issoria lathonia* species.

4 | OPTICAL DOCUMENT PROTECTION WITH WING SCALES

The main idea of this research is to use butterfly wing-scales as a natural, hologram-like, OVDs, permanently attached to a document (eg, a plastic credit card). In contrast to artificial OVDs, natural ones are unique (guaranteed by the cellular noise) and difficult to copy (due to their layered, micro- and nano-scale patterns).

We decided to use a near-field color pattern as a security feature of a document protection system and read it under the optical microscope. Practical inability to place a document at exactly the same position and orientation within the reading system requires shift- and rotation-invariant pattern recognition algorithm. We decided to use algorithm based

on Fourier-Mellin transform (FMT) [18] which fulfills the above requirements.

Nine *I. lathonia* wing-scales were attached to a glass substrate and their reflection microscope images were recorded at several positions and orientations (55 images in all). The recorded images were first decomposed into RGB components and the green one (G) was transformed using FMT. Correlations between corresponding FMT pairs were calculated and the corresponding statistical distribution is shown in Figure 3. The correlation coefficient, corresponding to the same wing-scale at displaced positions, had typical values around 0.4, while it never had values below 0.1. The most frequent values of correlation coefficient for two different wing-scales were around 0.02, and were never larger than 0.06. By placing validity threshold at 0.08, correct discrimination between wing scales is guaranteed.

To correct for accidental tilt or defocusing of the wing scale image, we have recorded images at 3 to 4, closely spaced, focal positions. Consequently, focus stacking algorithm was used (using Picolay free software) to extract well-focused parts in each recorded image and combine them in a single, sharp image.

In order to build a strong security system, malicious party has to be prevented from picking any butterfly wing-scale and attaching it to a document. This can be performed by making a document self-verifying by using a digital signature of the document issuer, within the public key infrastructure (PKI) system [19]. Here, we show that the necessary authentication information can be written on the wing-scale itself.

We used femtosecond laser-processing to additionally modify butterfly wing scales and exploit them as a write-

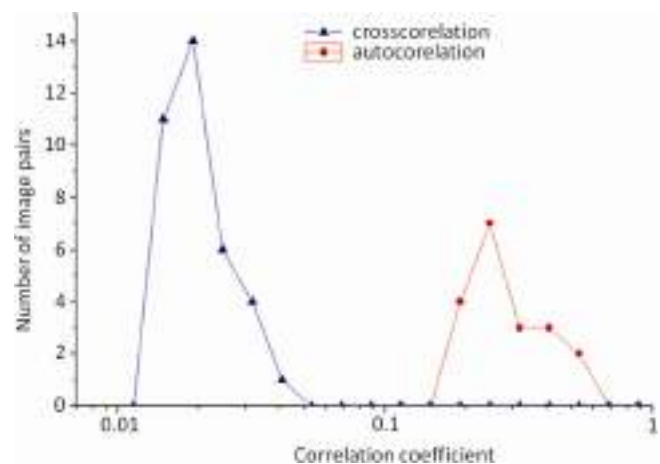
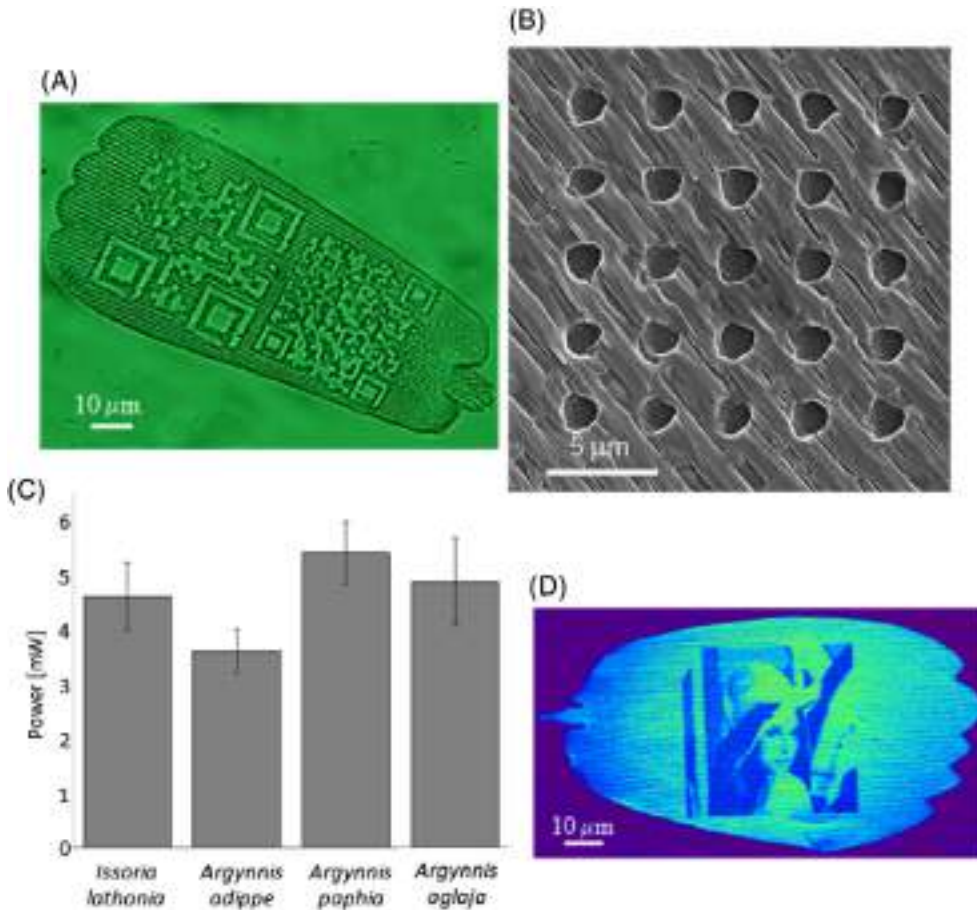


FIGURE 3 Cross- and auto-correlations of ensemble of 55 pairs of wing-scale images. Graph shows a number of image pairs vs the corresponding correlation coefficient. Maximum cross-correlation coefficient is at 0.02, while autocorrelation coefficient is always above 0.2

**FIGURE 4**

(A) Transmission microscope image of a femtosecond-laser-cut wing scale (QR-codes). (B) Array of holes on a *Issoria lathonia* wing-scale showing the minimum achievable diameter of a laser cut. (C) Thresholds for laser cutting of four butterfly species used throughout this research. (D) Selectively bleached wing scale with a Lena image observed by fluorescence modality of a nonlinear microscope

only memory. The software of a home-made nonlinear-microscope [13] was modified to enable vector and raster drawing of an arbitrary image (see section 5 of Appendix S1 for additional details). Depending on the average laser power, repetition rate and dwell time, wing scale can be cut (as in Figure 4A)). Minimal diameter of a laser cut achieved throughout this research is 1.7 μm, as shown in Figure 4B. Damage threshold is 4.5 mW (using 40 × 1.3 NA microscope objective) and 8.0 mW (with 20 × 0.8 NA microscope objective). Three more butterfly species were analyzed in that respect, with similar damage thresholds (Figure 4C). In practice, we operated above threshold to enable reliable and repeatable laser-drawing. That is why we achieved the minimum cut width which is considerably above the lateral resolution of our femtosecond system [13]. Based on that and the average size of the wing-scale (~50 × 100 μm²), we estimated the information capacity of a single scale at about 3000 bits, providing that the damaged spot is treated as binary 1, and undamaged as binary 0.

Here, we point out that each bit, written on the wing-scale, reduces the number of statistically independent patches. We will assume that one half of the wing-scale surface is laser processed (reducing the original wing-scale area of 50 × 100 = 5000 μm² to approximately 35 × 70 = 2450 μm²). That leaves approximately $\lceil 35/1.5 \rceil \times \lceil 70/30 \rceil = 23 \times 2 = 46$ colored patches

(numbers are, again, rounded to the nearest integer). Thus, as in the previous section, we may estimate the number of different wing scales at 10⁴⁶ (per every RGB channel), each one being protected by 1500 bits of additional information.

By reducing the laser power below the damage threshold, we were able to bleach the autofluorescence of the wing-scale and use it to inscribe covert information (Figures 4D) as a gray level image.

5 | DISCUSSION AND CONCLUSIONS

While speaking of document protection, an important question immediately comes to mind: how difficult it is to counterfeit wing-scale? Forgeries can be produced by either (a) imitating the structure or (b) imitating the corresponding optical effect with another, possibly simpler, structure. The first approach is based on “reverse-engineering” and manufacturing of identical protective element structure, while the second one is based on imitating the optical effect.

Reverse engineering of butterfly wing-scales implies analysis of the 3D morphology and material properties (refractive index and absorption) followed by some-kind of lithographic copying of both the morphology and material properties. Even with the most advanced technologies

(microtomography, electron or X-ray holography), this approach will be extremely limited in terms of available resolution of 3D analytic and lithographic methods (of the order of 10 nm), duration and cost [20].

Imitating the optical effect requires careful analysis of iridescence across the whole visible spectrum and angular range, followed by finding a method to faithfully reproduce the optical wavefront. This also poses a fundamental question: is it possible to have identical wave-fields generated by different structures? The question goes into scattering theory, with a plethora of papers dealing with the uniqueness of the direct and inverse problems. There is no general answer to the question, because it depends on the nature of the scatterer (penetrable or non-penetrable), boundary conditions (conductive, dielectric, amplifying), wavelength and angular range of probing radiation [21]. There are more or less exotic situations where uniqueness is not guaranteed, such as amplifying medium or medium with optical cloaks [22]. But, for the range of problems relevant to this work, the answer is no—there are no two different scatterers producing the same scattered field (far or near) [23].

The wing-scales are best protected by their uniqueness implying necessity to counterfeit every single document time and again. Another point is that, both the material composition and morphology are unique, producing a plethora of optical effects: overall shape, iridescence, absorption, polarization, fluorescence, moiré, defects, far and near-field diffraction pattern, local spectra, etc. In addition, scales possess different optical properties on their upper and under side, which may be used to produce security features which can be read from both sides in perfect alignment (so-called see-through register). Simultaneous use of all or some of the mentioned effects vastly increases the capabilities of wing scale as a protective element.

An important question is whether wing scales can be copied by some of holographic methods. Up to now, volume and surface relief holograms have been copied using contact [24], non-contact [25] or scanning [26] methods. However, these techniques are not useful for copying step-index, layered structure of wing scales, because of the sinusoidal nature of holographic gratings. Additionally, subwavelength gratings of wing-scales (S in Figure 3) cannot be copied, due to evanescent fields obtained by diffraction. These tiny structures are essential for the final coloration of the wing scale, because they produce uniformly scattered radiation in the blue part of the spectrum (see blue component of the wing scale pattern in Figure 8A).

It should be emphasized that Lepidoptera species are not equally suitable for document protection. As already mentioned, these structures must have complex nanometer to micron-size features, with significant variability and must be difficult to analyze and reverse engineer. We preferred

nymphalid species, possessing silver patches on their wings. Other Lepidoptera species, with structurally colored scales have been tested. However, the scales of these species were not so easy to process and manipulate, with the equipment at our disposal.

There is a number of ways how insect scales can be manipulated and attached to documents, as described in the following patent applications [27–29]. Generally speaking, they have to be, either embedded within the transparent medium with large refractive index difference (compared to that of the scale), or placed in a recess with a transparent, protective, covering. The procedure can be performed by micromanipulation or by standard printing techniques (silk-screen, flexo-printing).

Once embedded, scale contents have to be read by some means, which depends on the insect species, type of the scales and the optical effect sought for. In addition to iridescence pattern detection described above, there are other choices: overall shape of the scale, near field color pattern, far-field diffraction pattern, moiré pattern, or pattern of defects (looking like minutia in a fingerprint), with many variations (such as phase and amplitude) and combinations (by recording simultaneously several effects). Reading devices can be based on far- or near-field detection, holography or scanning techniques using CD/DVD readout heads. In the context of document protection, strong variability of patterns with angular position of illumination and observation, as well as the polarization sensitivity are very important. This is what prevents malicious attacks by simple color laser-printing.

The document protection described here is limited to machine reading level. It can be extended to the forensic level, by reading electron microscope image (Figure 1D)), with, for example, cross-rib distances serving as a random feature. If visual protection is desired, a large number of scales can be transferred to another substrate, so to cover large area, visible with the naked eye. One of the scales can be chosen for machine and forensic protection, as described in Reference [28].

Practical implications of the proposed document protection method are numerous. There are thousands of wing scales on a single butterfly specimen suitable for document protection (we have estimated 40 000 iridescent wing scales on *I. lathonia* silver spots). With appropriate choice of butterfly species (eg, *Morpho* spp.) this number can be much larger. If commercially available dry butterfly specimens are used, we have estimated the cost of a single wing scale at $85 \cdot 10^{-6}$ \$. Alternatively, butterfly species can be reared using well-established techniques of sericulture (silkworm raising). Wing-scales can be collected cheaply and applied using any of standard printing techniques (silk-screen, offset, ink-jet). Range of applications is huge: banknotes, credit-

cards, CD/DVDs, bonds, valuable goods. It is not even hard to imagine using wing-scales as a hardware lock for digital information security.

The base material of wing-scales is chitin, which is extremely and verifiably durable. Natural history museums have century-old butterfly specimens retaining their structural coloration and we have more than 30 years old specimens of *I. lathonia* with silver patches as shiny as in live insects. Even more, fossilized insects retain their iridescence after petrification and last for millions of years [30]. This should be compared to, recently described, five-dimensional optical memory [31], claiming “seemingly unlimited lifetime.”

Wing scales may reversibly change their dimensions in response to temperature variation [32], humidity and vapors [33]. As a consequence, there is a slight spectral shift, but it is too small to affect application of wing scales in document security, under normal atmospheric conditions. Systematic changes during extended periods of time are not expected due to hydrophobicity, insolubility and biological inertness of wing-scales [34]. However, we have not measured the long-term stability of wing scale patterns, we plan to perform accelerated aging tests in the near future and reveal details regarding the effect of aging on pattern stability.

Anyway, the validity period of most documents is less than 10 years, a period during which wing scales are expected to remain unaffected. Furthermore, taking into account the chemical and physical stability of chitin and the fact that optical response of the insects a hundred and more centuries-old (from museum) and from fossil samples exhibit extraordinary similarity with visual response measured from “the fresh” samples, suggest that corresponding patterns are very stable and could have long-term cryptographic applications.

ACKNOWLEDGMENTS

We express our gratitude to the Ministry of Education, Science and Technological Development of the Republic of Serbia for supporting this research through the projects Nos. III45016, III43002, ON171038, ON173038, ON171017, ON171032 and by the Science and Technology Development Programme—Joint Funding of Development and Research Projects of the Republic of Serbia and the People's Republic of China: Mimetics of insects for sensing and security, No. I-2. This work was also partially supported by the projects: No 451-03-01038/2015-09/1 of bilateral collaboration program between Ministry of Education, Science and Technological Development of the Republic of Serbia and German Academic Exchange Service (DAAD); by the project: “Upscaling Teslagram technology based on variable and complex biological structures for security printing,” funded by the Innovation Fund of the Republic of Serbia.

B.K. warmly acknowledges the assistance of Ms. Bojana Bokic, Institute of Physics, University of Belgrade in design of graphical abstract for this publication.

CONFLICT OF INTEREST

Institute of Physics Belgrade is the applicant and the owner of three pending patent applications given in a list of references [27–29] whose contents is partially described in this paper. Five authors (D.V.P., D.P., M.D.R., V.L. and A.J.K.) are also authors of abovementioned patent applications. Specific aspects of manuscript covered in patent applications are: laser cutting and bleaching of wing scales, as well as a partial list of butterfly species usable for this purpose.

AUTHOR CONTRIBUTIONS

D.V.P. conceived the idea; M.D.R., A.J.K. and D.V.P. have constructed the nonlinear microscope used in this research. D.P., A.J.K., M.D.R. and V.L. performed experiments and measurements. D.V.P. designed an optical model of wing-scales, while N.V. and D.S. performed the theoretical analysis of uniqueness of butterfly wing-scales. B.J. D. Z., W. Z. and B. K were included in data analysis and supervised the research. D.S., S.Ć and D.P. made adequate choice of appropriate butterfly species used in this research, while D.V.P., D.P. and M.D.R. prepared the manuscript, based on comments of other authors. This work is performed in partial fulfillment of the requirements for the PhD degree of Vladimir Lazović at the University of Belgrade, Faculty of Physics. All authors gave final approval for publication and agree to be held accountable for the work performed therein.

ETHICAL STANDARDS

Insects used in this research are NOT on the list of strictly protected and protected species defined in: By-law on proclamation and protection of strictly protected and protected wild species of plants, animals and fungi, Official gazette of the Republic of Serbia Nos. 5/2010 and 47/2011. All experiments were performed on dry specimens from the collection of Dejan Stojanović. The research did not include live insects.

ORCID

Branko Kolarić  <https://orcid.org/0000-0003-0203-7897>

REFERENCES

- [1] G. F. Robert, P. H. Adler, *Insect Biodiversity, Science and Society*, Chichester, UK: Willey-Blackwell, 2009.

- [2] X. Zhou, S. W. Applebaum, M. Coll, *Environ. Entomol.* **2000**, 29, 1289.
- [3] S. M. Doucet, M. G. Meadows, *J. R. Soc. Interface* **2009**, 6, S115.
- [4] W. Zhang, J. Gu, Q. Liu, H. Su, T. Fan, D. Zhang, *Phys. Chem. Chem. Phys.* **2014**, 16, 19767.
- [5] E. P. Newman, *Proc. Am. Philos. Soc.* **1971**, 115, 341.
- [6] R. L. Van Renesse, *Optical document security*, 3rd ed. Norwood, MA: Artech House, **2004**.
- [7] R. Pappu, B. T. J. Recht, N. Gershenfeld, *Science* **2002**, 297, 2026.
- [8] J. D. R. Buchanan et al., *Science* **2005**, 436, 475.
- [9] Hamm-Dubischar, C. Patent No. WO 2007031077 (A1), Inorganic marking particles for characterizing products for proof of authenticity method for production and use thereof (**2007**).
- [10] Biermann, N. & Rauhe, H., Method for Producing Security Markings. WO2004070667 A2 (**2004**).
- [11] Rauhe, H., Verfahren zur Herstellung von informationstragenden mikropartikelären Gemischen. Patent DE10238506 A1 (**2004**).
- [12] P. Vukusic, R. Kelly, I. Hooper, *J. Roy. Soc. Interface* **2009**, 6, S193.
- [13] D. M. Rabasović et al., *J. Biomed. Opt.* **2015**, 20(016010), 1.
- [14] D. Pantelić, S. Savić-Šević, D. V. Stojanović, S. Čurčić, A. J. Krmpot, M. Rabasović, D. Pavlović, V. Lazović, V. Milošević, *Phys. Rev. E* **2017**, 95, 032405.
- [15] J. e. Schanda, *Colorimetry: Understanding the CIE System*. Hoboken, NJ: John Wiley & Sons, **2007**.
- [16] I. G. Johnston et al., *PLoS Comput. Biol.* **2012**, 8, e1002416:1.
- [17] A. Dinwiddie, R. Null, M. Pizzano, L. Chuong, A. Leigh Krup, H. Ee Tan, N. H. Patel, *Dev. Biol.* **2014**, 392, 404.
- [18] J. Wood, *Pattern Recog.* **1996**, 29, 1.
- [19] L. O'Gorman, I. Rabinovich, *IEEE Trans. Pattern Anal. Mach. Intell.* **1998**, 20, 1097.
- [20] K. Watanabe, T. Hoshino, K. Kanda, Y. Haruyama, T. Kaito, S. Matsui, *J. Vac. Sci. Technol. B* **2005**, 23, 570.
- [21] D. Colton, R. Kress, *Inverse Acoustic and Electromagnetic Scattering Theory*, 2nd ed. New York, NY: Springer, **1998**.
- [22] F. Monticone, A. Alu, *Phys. Rev. X* **2013**, 3(041005), 1.
- [23] G. Bao, P. Li, J. Lin, F. Triki, *Inverse Probl* **2015**, 31, 093001.
- [24] S. Toxqui-López, A. Olivares-Pérez, I. Fuentes-Tapia, A. Quintero-Romo, *Opt. Mater.* **2007**, 29, 1604.
- [25] B. D. Chrysler, R. K. Kostuk, *Appl. Optics* **2018**, 57, 8887.
- [26] M. Okui, K. Wakunami, R. Oi, Y. Ichihashi, B. J. Jackin, K. Yamamoto, *Appl. Optics* **2018**, 57, 4117.
- [27] Pantelic, D., Rabasovic, M., Krmpot, A., Lazovic, V. & Pavlovic, D., Security device individualized with biological particles. PCT/EP2015/081398 (**2015**).
- [28] Pantelic, D., Rabasovic, M., Krmpot, A., Lazovic, V. & Pavlovic, D., Security tag containing a pattern of biological particles. PCT/EPO2015/081400 (**2015**).
- [29] Pantelic, D., Rabasovic, M., Krmpot, A., Lazovic, V. & Pavlovic, D., Security tag with laser-cut particles of biological origin. PCT/EP2015/081407 (**2015**).
- [30] M. E. McNamara et al., *PLoS Biol.* **2011**, 9, e1001200:1.
- [31] J. Zhang, M. Gecevičius, M. Beresna, P. G. Kazansky, *Phys. Rev. Lett.* **2014**, 112, 033901.
- [32] A. D. Pris, Y. Utturkar, C. Surman, W. G. Morris, A. Vert, S. Zalyubovskiy, T. Deng, H. T. Ghiradella, R. A. Potyrailo, *Nat Photon* **2012**, 6, 195.
- [33] R. A. Potyrailo, H. Ghiradella, A. Vertiatichikh, K. Dovidenko, J. R. Cournoyer, E. Olson, *Nat photonics* **2007**, 1, 123.
- [34] H.-M. Hu, J. A. Watson, B. W. Cribb, G. S. Watson, *Biofouling* **2011**, 27, 1125.

SUPPORTING INFORMATION

Additional supporting information may be found online in the Supporting Information section at the end of this article.

How to cite this article: Pavlović D, Rabasović MD, Krmpot AJ, et al. Naturally safe: Cellular noise for document security. *J. Biophotonics*. 2019; e201900218. <https://doi.org/10.1002/jbio.201900218>



Slowing probe and conjugate pulses in potassium vapor using four wave mixing

B. ZLATKOVIĆ,^{1,*} M. M. ĆURČIĆ,¹ I. S. RADOJIČIĆ,¹ D. ARSENOVIĆ,¹ A. J. KRMPOT,^{1,2} AND B. M. JELENKOVIĆ¹

¹*Institute of Physics Belgrade, University of Belgrade, Pregrevica 118, 11080 Belgrade, Serbia*

²*krmpot@ipb.ac.rs*

**bojan@ipb.ac.rs*

Abstract: We present an experimental study on ultraslow propagation of matched optical pulses in nondegenerate four wave mixing (FWM) in hot potassium vapor. The main figures of merit, i.e. fractional delay and fractional broadening, are determined to be 1.1 and 1.2, respectively. The latter two are approximately constant for the broad range of the two photon detuning. Input probe pulses between 20 ns and 120 ns can be delayed within broad range of the gain. The results are compared with the preceding works for Rb and Na.

© 2018 Optical Society of America under the terms of the [OSA Open Access Publishing Agreement](#)

1. Introduction

Low group velocity of light pulses i.e. slow light is of the great importance for many applications, in particular for all-optical signal processing. The applications that utilize slow light effect like optical delay lines [1,2], slow-light buffers [2], Phased Array Radar Beam Steering [2] are among many others. Since the first observation of group velocity reduction [3] a number of different techniques of slow light generation have emerged. All of these techniques are based on exploiting large dispersions which accompany narrow transparency windows. In gases, electromagnetically induced transparency (EIT) [4] has been used in hot [5,6] and cold atomic/molecular gases [1,7], as well as double absorption resonances [8,9]. EIT technique can be also applied in solids [10,11] along with coherent population oscillations [12,13], double dark states [14], and spectral hole burning [15]. In optical fibers techniques based on Brillouin scattering [16] and stimulated Raman scattering [17] were implemented. Although aforementioned techniques and methods were successful in reducing group velocity, all of them suffer from signal attenuation due to absorption.

Any technique used for optical delay lines is expected to provide arbitrary optical delay with minimum of signal distortion. In this sense light amplifying mediums are good candidates [16,18,19]. On the other hand, quantum noise accompanied with the amplifying FWM is a serious issue in quantum information applications and it is studied in details theoretically [20] and experimentally [21]. The mediums suitable for implementation of double-lambda atomic scheme are of particular interest. [22–26]. This scheme is characterized with large nonlinearities of susceptibility based on the coherence between sublevels of ground state which result in high gain of parametric FWM [23]. Obtained gain resonances are spectrally narrow which enables slowing down of optical pulses [26,27].

Since the recent observation of high-gain parametric FWM in hot potassium vapor [28], new interest has aroused for exploration of different quantum optical effects in this media [29,30]. In light of this interest, we were motivated to investigate the slowing of short light pulses in hot potassium vapor based on parametric non degenerate FWM. In particular, we find optimal pulse duration and delay-to-pulse broadening ratio.

2. Experimental realization

The double-lambda scheme was realized on D1 line of ^{39}K ($\lambda = 770 \text{ nm}$, [31]), Fig. 1(b). Pump beam couples lower hyperfine ground level $4S_{1/2}, F=1$ to the excited $4P_{1/2}$ level with one-photon detuning Δ . Due to small hyperfine splitting 55 MHz [31] the hyperfine structure of the $4P_{1/2}$ level is omitted. Probe beam couples excited $4P_{1/2}$ level to the upper hyperfine ground level $4S_{1/2}, F=2$ and it has two-photon detuning δ . Due to high intensity, pump couples $4S_{1/2}, F=2$ to the excited state having detuning $\Delta + \text{HFS}$, where HFS is ground state hyperfine splitting. The double Λ scheme is closed by the newly created conjugate beam that couples the excited state with detuning $\text{HFS} + \Delta$ and $4S_{1/2}, F=1$ level. The results for 120ns Gaussian shaped pulse duration are shown in Fig. 2. The magnitudes of probe and conjugate amplification are given by their respective gains which are defined as ratios of probe and conjugate peak intensities and reference peak intensity: $G_p = I_p/I_r$, $G_c = I_c/I_r$. The slowing of optical pulses is described by fractional delay. Fractional delay is defined as the ratio between absolute delay, which is the time difference between probe (conjugate) peak and reference peak, and reference pulse width ('Delay'/Width R' from Fig 1 (c)). Likewise, fractional broadening is defined as the ratio of probe (conjugate) pulse width to the reference pulse width ('Width P'/Width R' from Fig 1 (c) for probe). The latter parameter is informative about the broadening of the slowed light pulses and should be as close as possible to one.

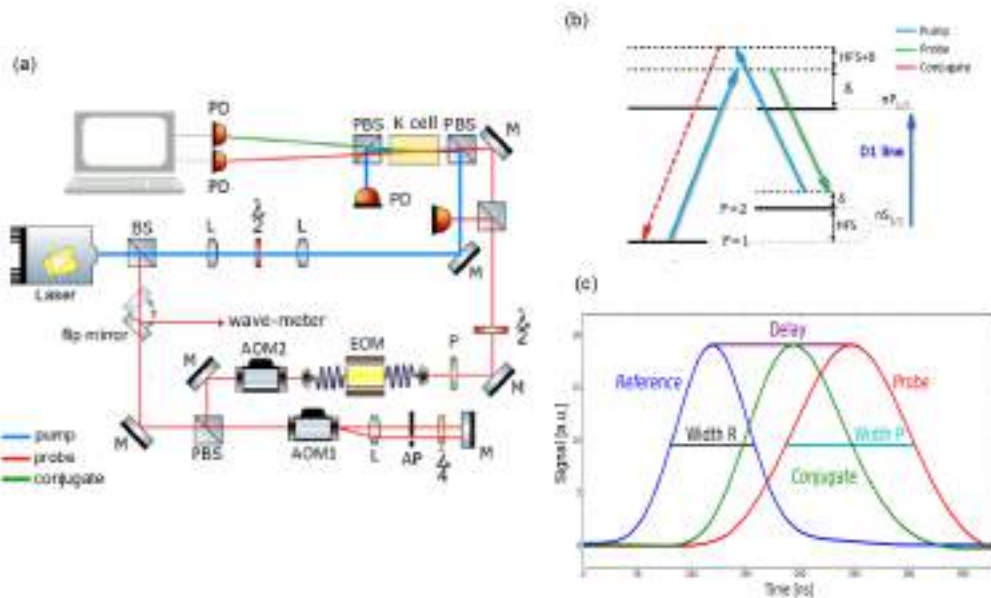


Fig. 1. (a) Experimental setup (BS - beam splitter, PBS - polarizing beam splitter, L - lens, AOM - acousto-optic modulator, EOM - fiber coupled electro optic modulator, P - linear polarizer, M - mirror, PD - photodiode, $\lambda/2$ - lambda-half wave plate, $\lambda/4$ - lambda-quarter wave plate, AP - aperture). (b) Double-lambda scheme at D1 potassium line. (c) The appearance of typical pulses order and basic definitions.

In our experiment (Fig. 1(a)) single mode Ti: Sapphire laser was stabilized to the D1 potassium line and it is used for creating pump and probe beams. A small fraction of the beam is picked by a 90:10 beam splitter and sent to the acousto-optic modulator (AOM1) in double pass configuration which operates in vicinity of 190 MHz. By scanning the RF-frequency fed to the AOM1, we were able to scan two-photon detuning δ . The AOM2 with fixed frequency of 80MHz sets

up the final frequency difference between pump and probe close to the HFS of the ^{39}K (462 MHz [31]). After the AOM2 light was fiber coupled to the LiNaO_3 amplitude electro optic modulator (EOM)(EO-SPACE, model: AZ-0K5-10-PFU-PFU-780-S) followed by a polarizer. By applying Gaussian voltage signals from the signal generator to the EOM we were able to create Gaussian polarization pulse in the plane of the polarizer. The polarizer transforms this signal to the Gaussian intensity pulse. The pulse peak power was $20\ \mu\text{W}$. For the reference pulse, a fraction of the probe pulse was picked and detected before the vapor cell. The pump (200 mW) and probe beams have mutually orthogonal polarizations set by two $\lambda/2$ plates and they are combined at a polarizing beam splitter. Pump and probe waists are 1.05 mm and 0.8 mm, respectively. These two beams intersect at the angle of 3 mrad inside 50mm long, heated, evacuated, natural-abundance potassium vapor cell. The cell temperature was 120°C . After the vapor cell another PBS deflects the pump away.

The three type of pulses; reference, amplified probe and newly generated conjugate were detected by an avalanche and two PIN photo diodes, respectively. For the reference the Si avalanche photo diode (APD) Hamamatsu S12023-10 was used. The Si APD was biased with 160 V which provides the gain of 100 and the bandwidth of 600 MHz. For both, amplified probe and conjugate, two identical Si PIN photodiodes Hamamatsu S5973-02 were used. The Si PIN photodiodes were biased with 9 V providing the bandwidth of 1.4 GHz. Due to very low intensity of the reference pulses, the Si APD had to be used because of its amplification. In all cases the photo current was fed to $50\ \Omega$ load and DC coupled to the oscilloscope. Each photodiode has enough bandwidth for detection of pulses in the duration range 20-120 ns that is used in the experiment.

3. Results and discussion

Typical results for delayed amplified probe and conjugate pulses for input pulse duration of 120 ns and 20 ns are shown in Fig. 2(a) and 2(b), respectively. The two pulse duration values are chosen from the edges of the interval in order to illustrate the fastest and the slowest signal changes in the experiment. The waveforms for the other pulses durations (40 ns and 80 ns) and/or for other parameters regardless the pulse duration are not shown, but the relevant parameters are extracted and used later on throughout the paper.

In Fig. 2(a) we present results for 120 ns long pulse with one photon detuning $\Delta = 1\ \text{GHz}$ and two photon detuning $\delta = 0\ \text{MHz}$. The curves were obtained upon 1000 averaged measurements. We have observed amplified Gaussian probe pulse of gain 16 and delay 124 ns which gives fractional delay of 1.1. The fractional broadening for this case was 1.2. Newly created conjugate pulse was also Gaussian with fractional delay of 0.56 and fractional broadening of 1.05. The emergence of conjugate pulse before the probe pulse observed in references [26,27] was confirmed for the case of potassium as well. In Fig. 2(b) the results for 20 ns long pulse are presented with one photon detuning $\Delta = 700\ \text{MHz}$ and two photon detuning $\delta = 0\ \text{MHz}$. For this set of parameters we have also observed Gaussian shape of amplified probe and conjugate signals as well as the emergence of the conjugate before the amplified probe. For amplified probe we have measured gain of 14.5, fractional delay of 3.7 and fractional broadening of 3.2. For conjugate we have measured 10, 2.7, 2.7 for gain, fractional delay and fractional broadening respectively. We would like to emphasize that separation between probe and conjugate at the exit of the cell can be tuned by choosing different parameters.

In order to obtain the results presented in this paper we scanned δ from $-4\ \text{MHz}$ to $10\ \text{MHz}$. For the values of δ out of this range, including the $-4\ \text{MHz}$ and $10\ \text{MHz}$ values, the pulse profile loses its Gaussian shape and becomes distorted, so that the relevant parameters such as pulse width, delay and broadening couldn't been extracted. The latter case is shown in Fig. 2(c) as an illustration. According to the findings in [26] waveform distortion in Fig. 2(c) could be due to complex dynamics that arises from the interplay of parametric amplification and Raman

absorption. Certain balance between losses and gains of probe beam are critical for temporal shapes of twin beams, which means that the range of δ that gives undistorted waveforms will be different at different Δ , and K density. Also, it should be noted that the gain for the amplified probe pulse in Fig. 2(c) is around 0.9, which is considered to be extremely low in potassium. All the peaks of the pulses are normalized to the same value in order to make the pulses comparable. Due to small leakage of the light through the EOM and parasitic differentiation of the signal in the detection and acquisition circuits the false undershoot at the times larger than 320 ns (Fig. 2(c)) becomes pronounced since it is magnified in the normalization procedure.

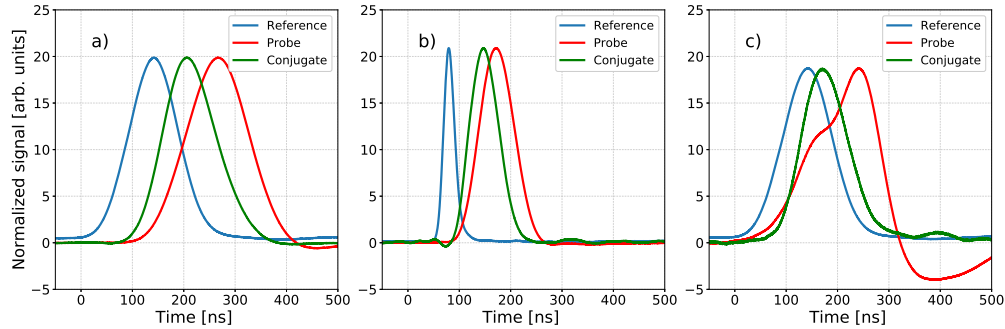


Fig. 2. Slowing the optical pulses by FWM in K vapor. The waveforms are obtained upon 1000 averaged measurements. (a) $\tau = 120$ ns, $\delta = 0$ MHz, $\Delta = 1$ GHz (b) $\tau = 20$ ns, $\delta = 0$ MHz, $\Delta = 0.7$ GHz (c) $\tau = 120$ ns, $\delta = -4$ MHz, $\Delta = 1$ GHz (Note: Gaussian shape of the probe is lost). Other parameters were kept constant throughout depicted measurements: $T=120^{\circ}\text{C}$, $\Delta=1$ GHz, $I_{\text{pump}}=200$ mW, $I_{\text{ref}}=20\mu\text{W}$, $\theta=3\text{mrad}$.

In Fig. 3 we have plotted the dependence of fractional broadening, fractional delay and gain for probe and conjugate pulse as a function of δ for $\Delta = 1$ GHz. Fractional delay and broadening of both, probe and conjugate, are either nearly flat or vary slowly with δ in the region where the gain is not negligible. The best result, in terms of the lowest broadening and largest delay, was achieved for the probe gain of 16 which is close to a half of maximum gain of 26 (achieved for $\delta = 2$ MHz). Our results are qualitatively different in comparison with results obtained in Rb [26] and Na [27]. In Rb the delay is highest near the bare state 2-photon resonance and drops down quickly as the δ is increased. Although the dependence of fractional delay and fractional broadening on pump Rabi frequency (i.e. intensity) is depicted in [27] we can conclude that the gain and the delay are in trade-off relation in Na since both gain and delay are monotonic functions of pump Rabi frequency. In other words, for sodium vapor one can say that higher the gain, smaller the delay and vice versa while in potassium we do not see such strong dependence of delay (or broadening) on gain. This difference might arise from the fact that in potassium the hyperfine splitting is less than the Doppler width and the condition, set in [26], $\Delta + HFS \gg \Delta$ is not fulfilled in this case.

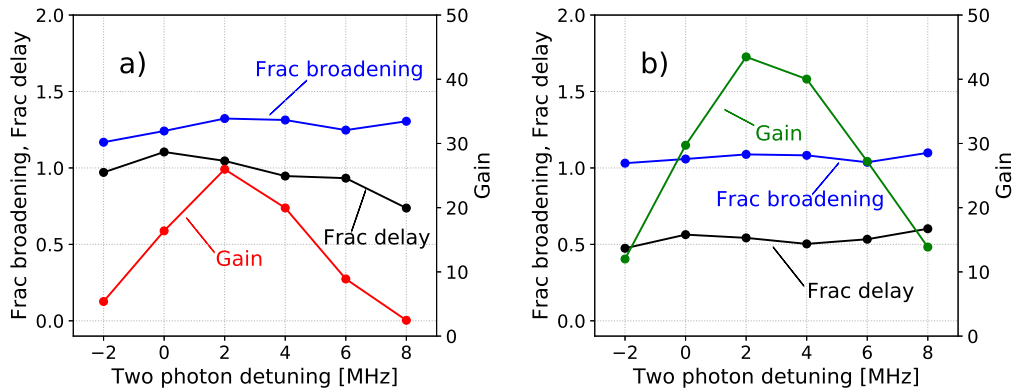


Fig. 3. Fractional delay, fractional broadening and gain dependence on δ for (a) amplified probe (b) conjugate. $T=120^\circ\text{C}$, $\Delta=1\text{ GHz}$, $I_{\text{pump}} = 200\text{mW}$, $I_{\text{ref}} = 20\mu\text{W}$, $\theta = 3\text{ mrad}$.

In Table 1 we have updated the overview of the results given in [27] with values for potassium at zero δ . The obtained (fractional) delays are somewhat larger than those in Rb [26] and comparable to those in Na [27] at the approximately same experimental conditions.

Table 1. Summary of the results for slowing of short optical pulses via FWM in Rb, Na and K.

Medium	Rb	Na	K
Reference pulsewidth [ns]	70	109	120
Gain	13	28	16
Fractional delay	0.57	1.03	1.1
Fractional broadening	-	1.12	1.2

For increasing the capacity of information carried by a train of optical pulses, the pulses have to be as short as possible. In order to find the shortest input pulse duration that will have the optimal slowing characteristics, i.e. the longest delay and minimal distortion, we have performed the measurements of fractional delay and fractional broadening with various pulse durations (Fig. 4). All the pulses had the Gaussian temporal shape. By lowering the pulse duration fractional delay and fractional broadening are increased simultaneously. As suggested by [32] the broadening of the pulse is due to the fact that a short pulse is spectrally broad and a larger number of its Fourier components gets slowed differently which manifests as broadening in time domain. An alternative explanation can be given using equations for group velocity and group delay given in [33] characterizing the slow light effect related to the EIT effect. The group delay is linearly proportional to optical depth and inversely proportional to the (EIT) control, in our case probe, intensity. Since the latter two parameters are fixed when the pulse duration is decreased, the group delay should be fixed and thus the fractional broadening will increase when decreasing input pulse duration.

In order to have optical delay lines capable of producing arbitrary delay the fractional delay should be one or higher. Comparing results from Fig. 4, we found that the 120 ns long input pulse, gives better results in terms of delay and broadening than other input pulse lengths. These results are the best suited for delay lines in potassium, since there is only about 20% of widening

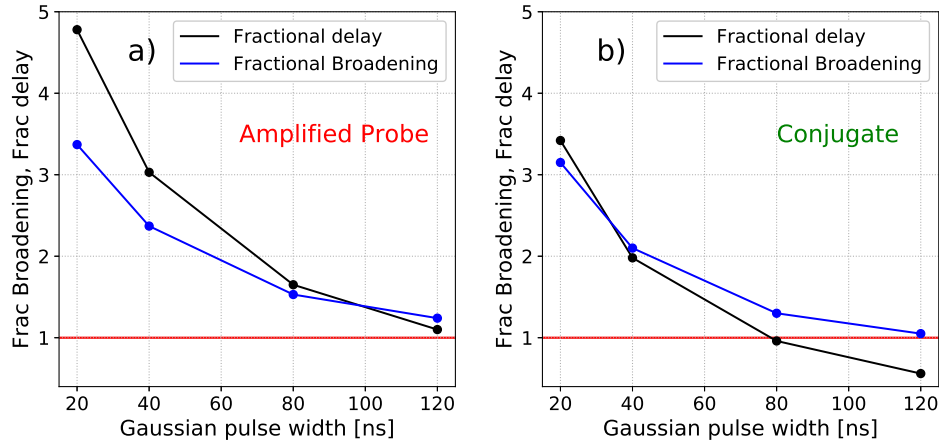


Fig. 4. Dependence of fractional broadening and fractional delay on incident pulse duration in slow light process via FWM in K vapor for (a) amplified probe (b) conjugate pulses. $\delta = 0$ MHz. $T = 120^\circ\text{C}$, $\Delta = 1$ GHz, $I_{\text{pump}} = 200$ mW, $I_{\text{ref}} = 20\mu\text{W}$, $\theta = 3$ mrad. The red line represents the value with no broadening.

while the fractional delay is above one.

In Fig 5 we show the dependence of fractional delay and fractional broadening on pump intensity. Other parameters were kept constant. One can see that unlike in sodium vapor [27] fractional delay and fractional broadening in our case don't depend strongly on the pump intensity, although they keep the same trend i.e. get lower as the pump intensity increases.

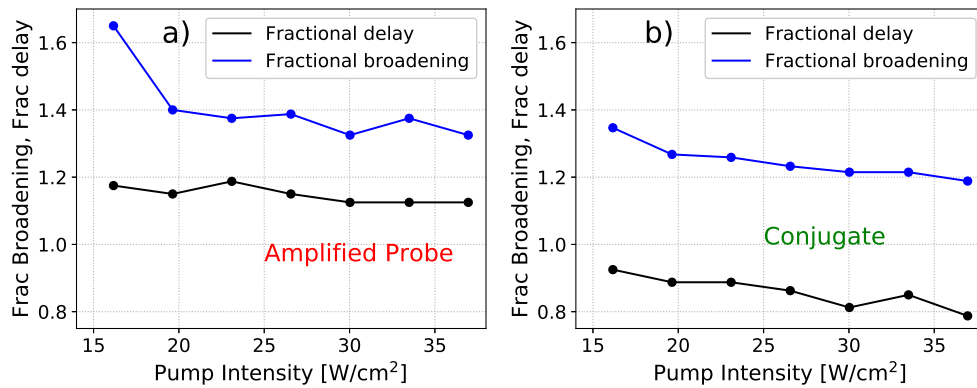


Fig. 5. Dependence of fractional broadening and fractional delay on pump intensity in slow light process via FWM in K vapor for (a) amplified probe (b) conjugate pulses. $\tau = 80$ ns, $\delta = 4$ MHz. $T = 120^\circ\text{C}$, $\Delta = 1.3$ GHz, $I_{\text{ref}} = 20\mu\text{W}$, $\theta = 3$ mrad.

Comparing the results for fractional delay and fractional broadening dependence on TPD (Fig 3) and on pump intensity (Fig 5) in potassium to the corresponding ones in Rb [26] and in Na [27] one can see that the dependence of these parameters in potassium are rather modest to almost uniform. Since the most conditions are the same (e.g. fine/hyperfine structure quantum numbers, experimental geometry) for all of the alkalis in which this kind of measurements was performed, we could conclude that ground state hyperfine splitting, which is the smallest in K, plays

important role, but possibly associated with rather large Doppler broadening (Doppler broadening in K is as twice as high compared to the ground state hyperfine splitting.). However, for the detailed description of the slow light parameters in potassium one needs to develop throughout theoretical model and to conduct simulations taking into account specific atomic properties such as ground state hyperfine splitting, Doppler broadening and dipole matrix elements. In addition, analytic approximations in the model have to be chosen with care. An approximation may be valid for some alkali atoms but not for others.

4. Conclusion

In this paper we have reported slowed propagation of short optical pulses based on parametric four wave mixing in hot potassium vapor. It is shown that within the range of δ centered around 0 the slow light's figures of merit, i.e. fractional broadening and fractional delay, are approximately constant regardless to the gain. Out of this range, the slowed pulses, amplified probe first, become distorted hindering the determination of the pulse parameters i.e. pulse width and peak. Also, we have shown that fractional delay and fractional broadening are dependent on the input pulse duration. Shortening the input pulse duration may lead to better (fractional) delay, but on the other side, to the larger broadening at the same time. This suggest the trade-off between the latter two when optimal pulse duration is required, for example in delay lines and other applications. The straight forward optical setup, that can be further simplified, doesn't require high coupling (pump) laser intensities achievable even with conventional laser diodes and enables slowing of the pulses within the broad range of gains. It turned out that light slowing systems with gains, including unity, are important in order to manipulate photonics quits [26]. Eventually, the results shown in this study suggest potassium as a medium that is worth to be considered in application of the slow light and FWM effects.

Funding

Ministry of Education, Science and Technological Development of Republic of Serbia (III45016 and OI171038).

Acknowledgments

We are thankful to Stanko Nikolić and Milan Radonjić for useful discussions and advices and to Milan Minić for the help with photodetectors design.

References

1. W. Boyd and D. J. Gauthier, *Slow and fast light*, Progress in Optics **43**, E. Wolf, ed. (Elsevier Science B.V., 2002), Chap. 6.
2. J. B. Khurgin and R. S. Tucker, *Slow Light Science and Applications*, (Chemical Rubber Company, 2009).
3. L. V. Hau, S. E. Harris, Z. Dutton, and C. H. Behroozi, "Light speed reduction to 17 metres per second in an ultracold atomic gas," Nature **397**, 594–598 (1999).
4. M. M. Kash, V. A. Sautenkov, A. S. Zibrov, L. Hollberg, G.R. Welch, M. D. Lukin, Y. Rostovtsev, E. S. Fry, and M. O.Scully, "Ultraslow group velocity and enhanced nonlinearoptical effects in a coherently driven hot atomic gas," Phys. Rev. Lett. **82**, 5229–5232 (1999).
5. M. Klein, M. Hohensee, Y. Xiao, R. Kalra, D. F. Phillips, and R. L. Walsworth, "Slow-light dynamics from electromagnetically-induced-transparency spectra," Phys.Rev. A **79**, 053833 (2009).
6. J. Zhang, G. Hernandez, and Y. Zhu, "Slow light with cavity electromagnetically induced transparency," Opt. Lett. **33**, 46–48 (2008).
7. R. M. Camacho, M. V. Pack, and J. C. Howell, "Low distortion slow light using two absorption resonances," Phys. Rev. A **73**, 063812 (2006).
8. R. M. Camacho, M. V. Pack, and J. C. Howell, "Wideband width,tunable, multiple-pulse-width optical delays usingslow light in cesium vapor," Phys. Rev. Lett. **98**, 153601 (2002).
9. J. J. Longdell, E. Fraval, M. J. Sellars, and N. B. Manson, "Stopped light with storage times greater than one second using electromagnetically induced transparency in a solid," Phys. Rev. Lett. **95**, 063601 (2005)

10. A. V. Turukhin, V. S. Sudarshanam, M. S. Shahriar, J. A. Musser, B. S. Ham, and P. R. Hemmer, "Observation of ultraslow and stored light pulses in a solid," *Phys. Rev. Lett.* **88**, 023602 (2001).
11. M. S. Bigelow, N. N. Lepeshkin, R. W. Boyd, "Superluminal and slow light propagation in a room-temperature solid," *Science* **301**, 200–202 (2003).
12. E. Baldit, K. Bencheikh, P. Monnier, J. A. Levenson, and V. Rouget, "Ultraslow light propagation in an inhomogeneously broadened rare-earth ion-doped crystal," *Phys. Rev. Lett.* **95**, 143601 (2005).
13. H. H. Wang, Y. F. Fan, R. Wang, L. Wang, D. M. Du, Z. H. Kang, Y. Jiang, J. H. Wu, and J. Y. Gao, "Slowing and storage of double light pulses in a Pr³⁺:Y₂SiO₅ crystal," *Opt. Lett.* **34**, 2596–2598 (2009).
14. B. S. Ham and J. Hahn, "Coherent dynamics of self-induced ultraslow light for all-optical switching," *Opt. Lett.* **33**, 2880–2882 (2008).
15. Y. Okawachi, M. S. Bigelow, J. E. Sharping, Z. Zhu, A. Schweinsberg, D. J. Gauthier, R. W. Boyd, and A. L. Gaeta, "Tunable all-optical delays via Brillouin slow light in an optical fiber," *Phys. Rev. Lett.* **94**, 153902 (2005).
16. J. E. Sharping, Y. Okawachi, and A. L. Gaeta, "Wide bandwidth slow light using a Raman fiber amplifier," *Opt. Express* **13**, 6092–6098 (2005).
17. J. Zhang, G. Hernandez, and Y. Zhu, "Copropagating superluminal and slow light manifested by electromagnetically assisted nonlinear optical processes," *Opt. Lett.* **31**, 2598–2600 (2006).
18. K. J. Jiang, L. Deng, M. G. Payne, "Ultraslow propagation of an optical pulse in a three-state active Raman gain medium," *Phys. Rev. A* **74**, 041803(R) (2006).
19. A. Eilam, A. D. Wilson-Gordon, and H. Friedmann, "Slow and stored light in an amplifying double- system," *Opt. Lett.* **33**, 1605–1607 (2008).
20. N. Lauk, C. O'Brien, M. Fleischhauer, "Fidelity of photon propagation in electromagnetically induced transparency in the presence of four-wave mixing," *Phys. Rev. A*, **88**, 013823 (2013).
21. Y. F. Hsiao, P. J. Tsai, C. C. Lin, Y. F. Chen, A. Y. Ite, Y. C. Chen, "Coherence properties of amplified slow light by four-wave mixing," *Opt. Lett.* **39**, 3394–3397 (2014).
22. M. D. Lukin, P. R. Hemmer, M. Löffler, and M. O. Scully, "Resonant enhancement of parametric processes via radiative interference and induced coherence," *Phys. Rev. Lett.* **81**, 2675–2678 (1998).
23. M. D. Lukin, P. R. Hemmer, M. O. Scully, "Resonant Nonlinear Optics in Phase-Coherent Media," *Adv. At. Mol. Opt. Phys.* **2**, 347–386 (2000).
24. Y. Wu, and X. Yang, "Highly efficient four-wave mixing in double- Λ system in ultraslow propagation regime," *Phys. Rev. A* **70**, 053818 (2004).
25. Y. Zhang, A. W. Brown, and M. Xiao, "Matched ultraslow propagation of highly efficient four-wave mixing in a closely cycled double-ladder system," *Phys. Rev. A* **77**, 053813 (2006).
26. V. Boyer, C. F. McCormick, E. Arimondo, and P. D. Lett, "Ultraslow propagation of matched pulses by four-wave mixing in an atomic vapor," *Phys. Rev. Lett.* **99**, 143601 (2007).
27. J. Okuma, N. Hayashi, A. Fujisawa, and M. Mitsunaga, "Ultraslow matched-pulse propagation in sodium vapor," *Opt. Lett.* **34**, 1654–1656 (2009).
28. B. Zlatković, A. J. Krmpot, N. Šibalić, M. Radonjić, and B. M. Jelenković, "Efficient parametric non-degenerate four-wave mixing in hot potassium vapor," *Laser Phys. Lett.* **13**, 015205 (2016).
29. J. D. Swaim, and R. T. Glasser, "Squeezed-twin-beam generation in strongly absorbing media," *Phys. Rev. A* **96**, 033818 (2017).
30. J. D. Swaim, and R. T. Glasser, "Causality and information transfer in simultaneously slow- and fast-light media," *Opt. Express* **25**, 24376 (2017)
31. D. A. Steck, "Potassium properties," <http://tobiastiecke.nl/archive/PotassiumProperties.pdf>
32. M. D. Lukin, and A. Imamoglu, "Controlling photons using electromagnetically induced transparency," *Nature* **413**, 273–276 (2001).
33. M. Fleischhauer, A. Imamoglu, J. P. Marangos, "Electromagnetically induced transparency: Optics in coherent media," *Rev. Mod. Phys.* **77**, 633 (2005).

Slowing 80-ns light pulses by four-wave mixing in potassium vapor

D. Arsenović, M. M. Ćurčić,* T. Khalifa, B. Zlatković, Ž. Nikitović, I. S. Radojičić, A. J. Krmpot, and B. M. Jelenković
Institute of Physics Belgrade, University of Belgrade, Pregrevica 118, 11080 Belgrade, Serbia



(Received 30 June 2018; published 14 August 2018)

We experimentally and theoretically study propagation of 80-ns Gaussian-like probe pulses in hot potassium vapor under conditions of four-wave mixing (FWM). The atomic scheme for FWM is off-resonant, double- Λ atomic scheme, with pump and probe photons, mediated in the K vapor, generating new probe and conjugate photons. We define the subset of FWM parameters, one-photon pump detuning, two-photon pump-probe Raman detuning, vapor density, the pump Rabi frequencies, when slowed pulses exit the vapor are also Gaussian-like. When Gaussian-like pulses exit the cell we are able to compare theoretical and experimental results for fractional delays and broadening for the probe and conjugate. We have obtained fractional delays above 1. Results of the model are compared with the experiment, with and without the model of Doppler averaging, when the atom velocity distribution is divided into different number of groups. We analyze possible causes for pulse broadening and distortion of slowed probe pulses and show that they are the result of quite different behavior of the probe pulse in the FWM vapor. Besides presenting the first results of slowing 80-ns probe pulses, this work is a useful test of the numerical model and values of parameters taken in the model that are not known in experiments.

DOI: [10.1103/PhysRevA.98.023829](https://doi.org/10.1103/PhysRevA.98.023829)

I. INTRODUCTION

Slow light, or reduced pulse group velocity below the speed of light, was demonstrated in different systems [1–10]. There is a strong interest for slow light because of its applications [11], in particular for all-optical signal processing. Optimizations of different slow light systems are based on results for fractional delays and broadenings of initial pulse waveforms.

There are different protocols and different physical systems for generating slow light and ultimately storage of light. A quantum phenomenon that is widely used for slow light is electromagnetically induced transparency (EIT) [12–15]. Narrow EIT resonance is accompanied by steep dispersion, effectively slowing down wave packets propagating through the medium. EIT for slowing and storing light was applied in many physical systems, very often in alkali-metal vapors [16–18].

Four-wave mixing (FWM), characterized by both quantum and strong nonlinear processes, has been used in the last decade for light slowing [19,20] and storage [21–23]. In a typical FWM scheme, in alkali vapor, pump photons and probe photons couple two sublevels of ground states to the same excited state. The second pump photon simultaneously excites the atom, allowing nonlinear conversion of pump photons into probe and conjugate photons. The process is therefore dominated by a strong photon-photon coupling mediated by the nonlinear medium, and photon conversion. Transmission and gain of twin beams strongly depend on detuning around two-photon Raman resonance. Also, the index of refraction varies strongly around the resonance. The FWM gain compensates optical losses, which is an advantage over the EIT as

a physical system, allowing much longer propagation of probe pulses.

In this work we use the off-resonant double- Λ scheme for FWM in K vapor to theoretically and experimentally investigate propagation of 80-ns probe pulses and generation and propagation of conjugate pulses. This atomic scheme was used before to investigate slow light in Rb [19] and Na [20]. However, there is a growing interest in the behavior of transitions on D lines in potassium vapor [24,25], as well as interest in potassium as an active medium for a study of strong nonlinear processes due to its characteristics [26–30]. Parameters of FWM in [26] simultaneously support two propagation regimes of light pulses, slow and fast light. In our work, we are focused on the FWM regime when this system acts as a slowing and amplifying medium, with obtained fractional delays typically larger than 1. In the model we use Maxwell-Bloch (MB) equations to calculate propagations of pump, probe, and conjugate beams through the K cell. FWM parameters in the study are one-photon detunings of the pump beam Δ , two-photon Raman detuning between pump and probe beams δ , pump and probe Rabi frequencies Ω_d and Ω_p , respectively, pump laser power P_d , and potassium vapor density N_c related to cell temperature T_c . Fixed for all measurements and calculations were phase-matching angle and probe Rabi frequency Ω_p related to the probe power P_p .

Potassium is different from other alkali metals. It has the smallest hyperfine splitting (HFS) of the ground state of all alkali metals [24], smaller than the Doppler width. Comparing theoretical and experimental results, qualitatively in terms of pulse waveforms and quantitatively in terms of fractional delays and broadening, we have tested the model and also values of dephasing and decoherence relaxation rates assumed in the calculations. We have discussed results of

*marijac@ipb.ac.rs

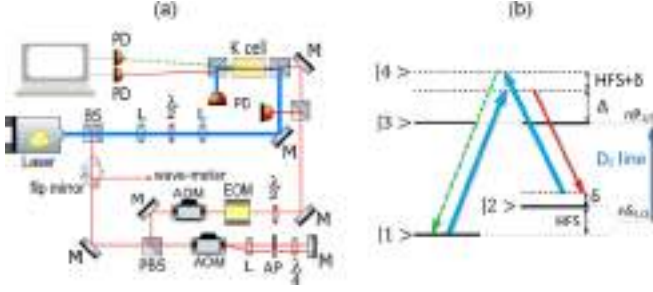


FIG. 1. (a) Experimental setup. (a) Double- Λ scheme for D_1 line in potassium. Pump beam—thick line (blue for online version), probe beam—thin line (red for online version), conjugate beam—dashed line (green for online version).

the model with and without Doppler averaging of density matrix elements. At the end, we have investigated whether there is a relation between the waveform of the outbound slowed probe pulse, which is either broadened Gaussian-like or distorted, and the pulse behavior as it propagates through the K vapor.

II. EXPERIMENT

The schematic of the experiment is shown in Fig. 1. The output from the CW laser (MBR, Coherent) locked to $4S_{1/2}-4P_{1/2}$ D_1 transition in K, at 776 nm, is used for both the pump and the probe beams. A smaller fraction of the probe is sent through two acousto-optic modulators, with the first one in double pass, in order to scan the frequency of the probe beam around Raman resonance with the pump beam frequency. We use the electro-optic modulator to form Gaussian probe pulses. The probe is combined with the pump on the nonpolarizing cube, and both beams are sent to a 4-cm-long vacuum glass cell containing the natural abundance of K vapor. The beams intersect at the center of the cell at the angle of 3 mrad. The pump and the probe beams are linearly and mutually orthogonally polarized with Gaussian radial intensity distribution $1/e^2$ at 1.08 and 0.8 mm, respectively. The K cell was heated by hot air up to 150 °C, or a K density of $1.7 \times 10^{13} \text{ cm}^{-3}$. The probe and the conjugate beams are detected with two photodiodes, and their signals are sent to the storage oscilloscope. Group velocities of the probe and conjugate beams were measured by recording the arrival times of the probe and the conjugate relative to the reference pulse.

The double- Λ scheme was realized on the D_1 line of ^{39}K ($\lambda = 770 \text{ nm}$ [24]), Fig. 1. The pump beam couples the lower hyperfine ground level $4S_{1/2}$, $F = 1$ to the excited $4P_{1/2}$ level with one-photon detuning Δ . Due to the small hyperfine splitting of 55 MHz [24], the hyperfine structure of the $4P_{1/2}$ level is omitted. The probe beam couples the excited $4P_{1/2}$ level to the upper hyperfine ground level $4S_{1/2}$, $F = 2$ and makes a lower Λ scheme with the two-photon Raman detuning δ . Pump photons and new conjugate photons couple $4S_{1/2}$, $F = 2$ to the $4S_{1/2}$, $F = 1$ via an excited state, detuned from the $4P_{1/2}$ levels by $\sim(\Delta + \text{HFS})$, in the upper Λ scheme.

III. THEORETICAL MODEL

Our model describes interaction between ^{39}K atoms in the vapor and electromagnetic (EM) field. The same as in the experiment, four levels of the double- Λ scheme, two ground states $|1\rangle$ and $|2\rangle$, and two excited states $|3\rangle$ and $|4\rangle$, are coupled to produce FWM, Fig. 1. Three components of the total electric field, pump, probe, and conjugate, are denoted by d , p , and c , respectively. The pump couples the $|1\rangle \rightarrow |3\rangle$ and $|2\rangle \rightarrow |4\rangle$ transitions and the probe couples the $|2\rangle \rightarrow |3\rangle$ transition. In the medium, the conjugate beam is generated from optical coherence between levels $|1\rangle$ and $|4\rangle$. Let the energy levels be $E_i = \hbar\omega_i$ with $\omega_3 = \omega_4$, and the angular frequencies of the EM field modes ω_d , ω_p , and ω_c for the pump, probe, and conjugate, respectively. The one-photon detuning is then $\Delta_{(13)} = \omega_d - (\omega_3 - \omega_1)$, and two-photon detuning is $\delta_{(132)} = \omega_d - \omega_p - (\omega_2 - \omega_1)$. Detuning of the conjugate beam is defined as $\Delta_{(1324)} = (2\omega_d - \omega_p) - (\omega_4 - \omega_1)$.

The total electric field

$$\vec{E} = \sum_{i=d,p,c} \vec{e}_i E_i^{(+)} e^{-i\omega_i t + i\vec{k}_i \vec{r}} + \text{c.c.} \quad (1)$$

serves as an interacting potential for ^{39}K atoms. The Hamiltonian is therefore

$$\hat{H} = \hat{H}_0 + \hat{H}_{\text{int}} = \sum_{i=1}^4 \hbar\omega_i |i\rangle\langle i| - \hat{d} \cdot \vec{E}(\vec{r}, t), \quad (2)$$

where \hat{d} is the atomic dipole operator.

To obtain the set of Bloch equations, we first start with the equation for the density matrix

$$\dot{\hat{\rho}} = -\frac{i}{\hbar} [\hat{H}, \hat{\rho}] + \widehat{SE} + \hat{R}, \quad (3)$$

with spontaneous emission \widehat{SE} and relaxation \hat{R} included. We have

$$\widehat{SE} = \sum_{i=1}^4 \Gamma_i (\hat{A}_i \hat{\rho} \hat{A}_i^\dagger - \hat{A}_i^\dagger \hat{A}_i \hat{\rho} / 2 - \hat{\rho} \hat{A}_i^\dagger \hat{A}_i / 2), \quad (4)$$

with $\hat{A}_1 = |1\rangle\langle 3|$, $\hat{A}_2 = |1\rangle\langle 4|$, $\hat{A}_3 = |2\rangle\langle 3|$, $\hat{A}_4 = |2\rangle\langle 4|$, and Γ_i all equal to half of the spontaneous emission rate. The relaxation term is

$$\hat{R} = -\gamma [\hat{\rho} - \text{diag}(\frac{1}{2}, \frac{1}{2}, 0, 0)] - \gamma_{\text{deph}} [\hat{\rho} - \text{diag}(\rho_{11}, \rho_{22}, \rho_{33}, \rho_{44})], \quad (5)$$

where γ and γ_{deph} are relaxation rates. After the substitution,

$$\tilde{\rho}_{ij} = e^{-i\omega_{(ij)}t + i\vec{k}_{(ij)}\vec{r}} \rho_{ij}, \quad (6)$$

where $\omega_{(13)} = \omega_{(24)} = \omega_d$, $\omega_{(23)} = \omega_p$, $\omega_{(14)} = \omega_c$, $\omega_{(12)} = \omega_{(13)} - \omega_{(23)}$, $\omega_{(34)} = \omega_{(14)} - \omega_{(13)}$, $\omega_{(ij)} = -\omega_{(ji)}$, $\vec{k}_{(13)} = \vec{k}_{(24)} = \vec{k}_d$, $\vec{k}_{(23)} = \vec{k}_p$, $\vec{k}_{(14)} = \vec{k}_c$, $\vec{k}_{(12)} = \vec{k}_{(13)} - \vec{k}_{(23)}$, $\vec{k}_{(34)} = \vec{k}_{(14)} - \vec{k}_{(13)}$, $\vec{k}_{(ij)} = -\vec{k}_{(ji)}$, with $\vec{k}_c = 2\vec{k}_d - \vec{k}_p - \Delta\vec{k}$, we apply the rotating wave approximation. The resulting system of differential equations does not have coefficients depending on time. Some coefficients have dependence on $e^{i\Delta k z}$, where $\Delta k = 2k_d(1 - \cos\theta)$, i.e., it is related to the angle θ between the pump and probe beam. Here we set the propagation of the pump in the z direction.

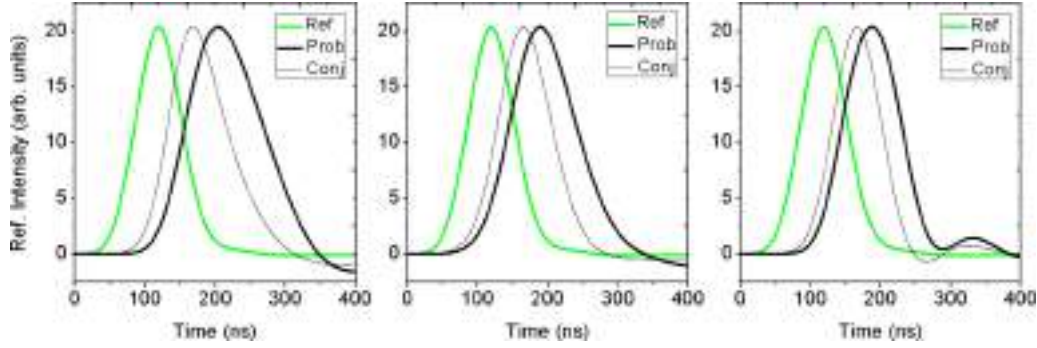


FIG. 2. Experimental observations of slow light, probe (thick black), conjugate (thin black), and reference 80-ns incoming probe beam (green) waveforms for (a) $\delta = -4$ MHz, (b) $\delta = -8$ MHz, and (c) $\delta = -12$ MHz. In all three cases (a), (b), and (c), $\Delta = 0.7$ GHz, $T = 120^\circ\text{C}$, pump power $P_d = 220$ mW, probe power $P_p = 20$ μW .

With a slowly varying envelope approximation, the propagation equations are

$$\left(\frac{\partial}{\partial z} + \frac{1}{c} \frac{\partial}{\partial t}\right) E_d^{(+)} = i \frac{k N_c}{2\epsilon_0} d(\tilde{\rho}_{42} + \tilde{\rho}_{31}), \quad (7a)$$

$$\left(\frac{\partial}{\partial z} + \frac{1}{c} \frac{\partial}{\partial t}\right) E_p^{(+)} = i \frac{k N_c}{2\epsilon_0} d\tilde{\rho}_{32}, \quad (7b)$$

$$\left(\frac{\partial}{\partial z} + \frac{1}{c} \frac{\partial}{\partial t}\right) E_c^{(+)} = i \frac{k N_c}{2\epsilon_0} d\tilde{\rho}_{41}, \quad (7c)$$

where N_c is the atom density.

In order to take into account the Doppler effect, we divide atoms into M groups, each having different z component of the velocity v_z . Due to the Doppler effect these groups differ by effective detuning. Let us denote with $\Delta_{(13)0}$, $\delta_{(132)0}$, and $\Delta_{(1324)0}$ detunings subject to atoms with velocity $v_z = 0$. For an atom with z component of the velocity v_z different than zero, the observed angular frequency ω_o is $\omega_o = \sqrt{\frac{1-\beta}{1+\beta}} \omega_s$, where ω_s is the angular frequency of the light source and $\beta = v_z/c$. The Doppler shift is $\Delta_D = \omega_o - \omega_s$. The detunings are therefore $\Delta_{(13),m} = \Delta_{(13)0} + \Delta_D$, $\delta_{(132),m} = \delta_{(132)0}$, $\Delta_{(1324),m} = \Delta_{(1324)0} + \Delta_D$, where $m = 1, \dots, M$ enumerates velocity groups of atoms. In our model, we keep track of density matrices $\rho_{ij,m}$, $m = 1, \dots, M$ for each group of atoms. There are M sets of Bloch equations. Propagation equations are slightly modified. The source term on the right-hand side of Eq. (8) is the sum of contributions of all groups of atoms:

$$\left(\frac{\partial}{\partial z} + \frac{1}{c} \frac{\partial}{\partial t}\right) E_d^{(+)} = \sum_{m=1}^M i \frac{k N_{c,m}}{2\epsilon_0} d(\tilde{\rho}_{42,m} + \tilde{\rho}_{31,m}), \quad (8a)$$

$$\left(\frac{\partial}{\partial z} + \frac{1}{c} \frac{\partial}{\partial t}\right) E_p^{(+)} = \sum_{m=1}^M i \frac{k N_{c,m}}{2\epsilon_0} d\tilde{\rho}_{32,m}, \quad (8b)$$

$$\left(\frac{\partial}{\partial z} + \frac{1}{c} \frac{\partial}{\partial t}\right) E_c^{(+)} = \sum_{m=1}^M i \frac{k N_{c,m}}{2\epsilon_0} d\tilde{\rho}_{41,m}. \quad (8c)$$

Here $N_{c,m}$ is the atom density of the k th group. We choose $v_{z,m}$ and $N_{c,m}$ to mimic Maxwell distribution $f(v_z) =$

$\sqrt{m/2\pi k_B T} e^{-mv_z^2/2k_B T}$. In the results below, with the Doppler averaging, we have chosen $M = 3$ with Doppler shifts $\Delta_1 = -0.25$ GHz, $\Delta_2 = 0$ GHz, and $\Delta_3 = +0.25$ GHz; the densities are $N_{c,2} = (1.1/3)N_c$ and $N_{c,1} = N_{c,3} = (0.95/3)N_c$.

IV. RESULTS AND DISCUSSION

The probe pulse waveform before the cell is Gaussian with a FWHM of 80 ns; behind the cell the amplified probe and conjugate pulses have different forms. For some FWM parameters they are (broadened) Gaussians, while for others they are distorted. Only when outgoing pulses are Gaussians can we get fractional delays and broadenings. We first present the experimental results, which are compared with the results of numerical simulations, with and without Doppler averaging.

A. Experimental results

We observe propagation of 80-ns probe pulses under conditions of FWM when several parameters are varied. In order to have Gaussian shapes for outgoing probe and conjugate pulses in K vapor, the FWM ought to be realized for densities between 3×10^{12} cm^{-3} and $\sim 1.75 \times 10^{13}$ cm^{-3} (cell temperature 120°C – 150°C), Δ between 700 MHz and 1.3 GHz, and δ in the range ± 10 MHz. Note that not every, or any arbitrary choice of parameter values from the above ranges will produce Gaussian-like pulses at the cell exit. In Fig. 2 we present pulses of reference, probe, and conjugate beams, with their amplitudes normalized to the reference pulse, when $\Delta = 0.7$ GHz for three values of δ , -4 , -8 , and -12 MHz. The resonant probe scatters much more than the conjugate beam, and is slowed more and amplified less than the conjugate, as shown in Fig. 3. The results presented in Fig. 3 are gains, fractional delays, and broadening versus δ obtained from waveforms of Gaussian-like outbound pulses, like the ones shown in Fig. 2. Gains of twin beams are calculated as the ratio of their outbound intensities to the probe inbound intensity. The maximum of probe gain, around 100, is at negative δ , ~ -4 MHz, a small shift from Raman resonance due to Stark shift of energy levels, induced by the blue detuned pump laser. Delays and broadening also have small maximums at these negative values of δ . Maximum values for probe and

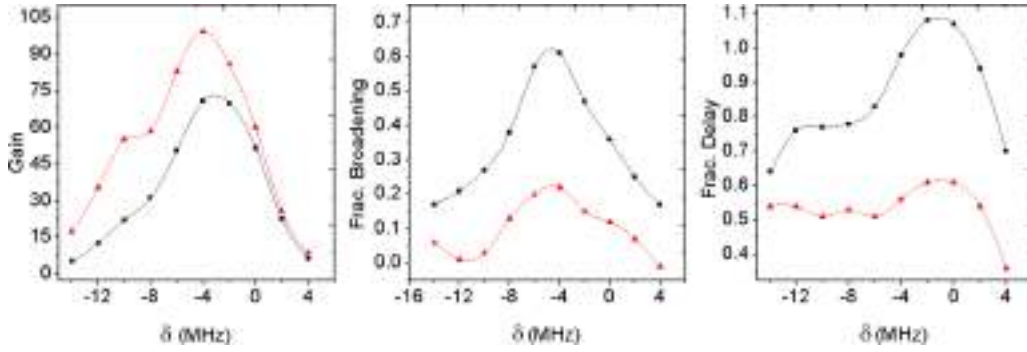


FIG. 3. Probe (solid squares, black for online version) and conjugate (solid triangles, red for online version) (a) gains, (b) fractional broadenings, and (c) fractional delays vs δ , for $\Delta = 0.7$ GHz, $T = 120^\circ\text{C}$, $P_d = 220$ mW, $P_p = 20$ μW .

conjugate fractional delays are ~ 1.08 and ~ 0.6 , while their fractional broadenings are 0.35 and 0.15, respectively.

B. Theoretical results

In the model, the probe entering the cell has a Gaussian profile with 80-ns pulse width and the pump has a constant intensity. The pump and probe detunings, and the gas density correspond to their values in the experiment. However, the model uses parameters whose values are not known in the measurements, such as relaxation coefficients. In the calculations the pump is a plane wave, and although the angle between the pump and the probe is the same as in the experiment, there is a different overlap of two beams in the model than in the experiment. Hence, to find the pump and the probe electric field amplitudes adequate to those in the experiment is not straightforward. We obtain better agreement with measurements if electric field amplitudes in the model are a little lower than those implied by the measurements. The presented results are with Doppler averaging of density matrix elements, assuming three velocity groups for atoms, resulting in three Doppler shifts $\Delta_1 = -0.25$ GHz, $\Delta_2 = 0$ GHz, $\Delta_3 = +0.25$ GHz.

Propagation of EM fields through FWM alkali vapors, when all fields are continuous waves, was discussed in [31]. When probe field is in the form of a pulse, the initial condition for

the MB equations is

$$E_p^{(+)} = E_{p0}^{(+)} \left(f_{\text{dc}} + f_{\text{pulse}} e^{-\frac{4 \ln 2 (t-t_{\text{max}})^2}{\text{FWHM}^2}} \right), \quad (9)$$

where FWHM is the pulse full width at half maximum, t_{max} is the time when the pulse reaches peak value, and $f_{\text{dc}} + f_{\text{pulse}} = 1$ and represents dc and pulse components. To improve the stability of numerical simulation, we first solve a stationary system where we set $t = 0$ in Eq. (9) and obtain dependencies of z for all unknown variables. These solutions are initial conditions for $t = 0$ in the time propagation of MB equations. Variable parameters in the numerical simulations are the pump and the probe intensities, atom density, θ , Δ , δ , propagation distance z_{max} , and relaxation coefficients. As a result, we have obtained dependencies of the probe and the conjugate beam pulses on t and z . We have found, like in the experiment, that pulse shapes may be Gaussian-like or deformed by a strong asymmetric broadening or presence of multiple peaks.

Similar to the experiment, FWM parameters giving Gaussian-like outgoing pulses in the calculations are limited to a rather small range. Both measurements and the model show more deviations from Gaussian profiles when atom densities are higher or when the gains are lower. In Fig. 4 we present calculated waveforms of the probe and the conjugate pulses at $z_{\text{max}} = 4$ cm.

If outgoing pulses have Gaussian waveforms, we can extract gains and delays of probe and conjugate pulses by fitting the

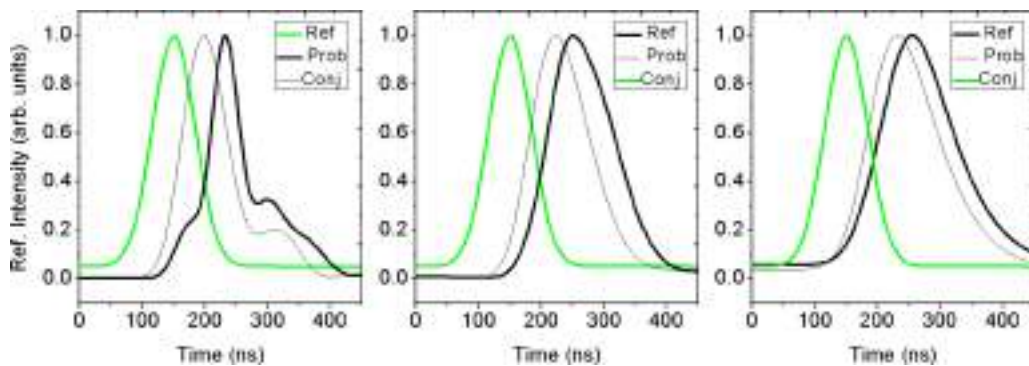


FIG. 4. Calculated waveforms of probe (thick black line) and conjugate (thin black line) for 80-ns incoming probe pulse (green line). (a) $\delta = -4$ MHz, (b) $\delta = -8$ MHz, (c) $\delta = -12$ MHz. Values of other parameters were kept constant, $\Omega_d = 1.38$ GHz, $\Omega_p = 18.9$ MHz, $\gamma = 0.5 \times 10^7$ Hz, $\gamma_{\text{deph}} = 1.5 \times 10^7$ Hz, $\Delta = 0.7$ MHz, $N_c = 3 \times 10^{12}$ cm $^{-3}$ ($T = 120^\circ\text{C}$), $\theta = 3$ mrad.

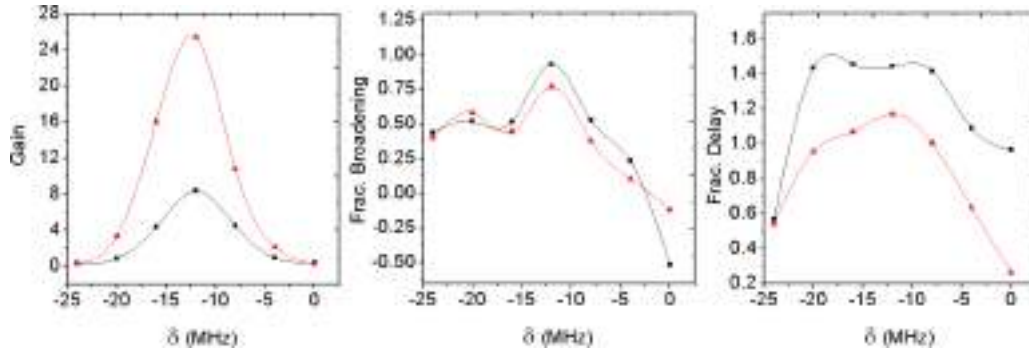


FIG. 5. Calculated probe (solid squares, black for online version) and conjugate (solid triangles, red for online version) (a) gains (note that probe gain is multiplied by 10), (b) fractional broadenings, and (c) fractional delays vs δ of 80-ns input Gaussian pulses in K vapor at $3 \times 10^{12} \text{ cm}^{-3}$ ($T = 120^\circ \text{C}$), $\Omega_d = 1.38 \text{ GHz}$, $\Omega_p = 18.9 \text{ MHz}$, $\Delta = 0.7 \text{ GHz}$.

time dependence of both fields to Gaussian profiles. The fit gives three values, $E_i^{(+)\text{out}}$, $t_{i,\text{max}\text{out}}$, and $FWHM_{i,\text{out}}$, $i = p, c$, for gains, delays, and broadening, respectively. Gains of the probe and the conjugate beams are defined as

$$G_p = \left| \frac{E_p^{(+)\text{out}}}{E_{p0}^{(+)}} \right|^2, \quad (10a)$$

$$G_c = \left| \frac{E_c^{(+)\text{out}}}{E_{c0}^{(+)}} \right|^2. \quad (10b)$$

In Fig. 5 we plot gains, fractional delays, and broadening versus δ for $\Delta = 0.7 \text{ GHz}$ and $N_c = 3 \times 10^{12} \text{ cm}^{-3}$. Gain of the conjugate beam in Fig. 5 is larger than that of the probe, but that is not the general property. At the beginning of the propagation, at $z = 0$, there is only a probe beam, $G_p = 1$ and $G_c = 0$, while at $z = z_{\text{max}}$ we have $G_c > G_p$. Therefore G_p/G_c is directly dependent on z , for other parameters fixed. The values of δ for which gains are maximal depends on the pump intensity, a property known already from the CW regime [31]. Gains have maximums at the negative δ , determined by the detuning Δ and the pump Rabi frequency Ω_d .

In the study of slowing light, we are looking for the range of values of δ where the broadening is low and fractional delay is as high as possible. Similar to the experimental results, this turns out to be the case for $\delta \sim -4 \text{ MHz}$.

Relaxation coefficients are fitting parameters in the model. For $\gamma = 0.5 \times 10^7$ and $\gamma_{\text{deph}} = 1.5 \times 10^7$, we get good agreement with the experiment.

1. Effect of Doppler averaging with different numbers of atom velocity groups

Including the Doppler effect into the model has, for most of the FWM parameters, a strong effect on probe and conjugate waveforms in and behind the vapor. Since Doppler averaging of the density matrix elements can considerably increase computing time, it is also good to know what might be the optimal number of atom velocity groups onto which the velocity distribution is divided. In Fig. 6 we plot the results of the model without taking into account the Doppler effect, top graph (a), with Doppler averaging with three velocity groups, middle graph (b), and with the Doppler averaging using five velocity groups, lower graph (c). Results are for the following parameters: $\Delta = 0.7 \text{ GHz}$ and $\delta = -12 \text{ MHz}$. Values of other parameters in simulations are: $\Omega_d = 3.08 \text{ GHz}$, $\Omega_p = 18.9 \text{ MHz}$, $N = 3 \times 10^{12} \text{ cm}^{-3}$, $\gamma = 5 \times 10^7$, $\gamma_{\text{deph}} = 1.5 \times 10^7$. Having no Doppler averaging gives very much different results than obtained in the experiment. Averaging with three velocity groups gives a more compact profile at the end of the propagating distance. It is broadened with the small secondary peaks, features that measurements have also showed. In the presented case, a further increase of the number of velocity groups does not make a big difference in

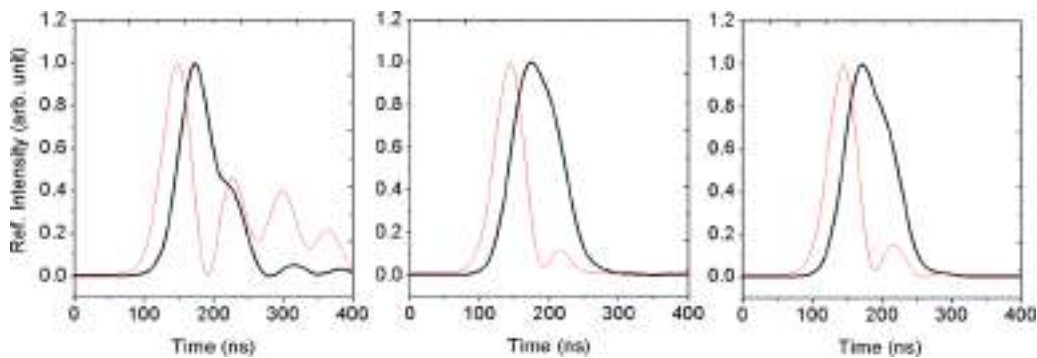


FIG. 6. Numerical simulations of probe (thick black) and conjugate (thin red) waveforms. a) without Doppler averaging, b) with Doppler averaging using 3 velocity groups, and c) using 5 velocity groups. Results are for 80 ns probe inbound pulse, $\Delta = 1 \text{ GHz}$, and $\delta = 4 \text{ MHz}$. Other parameters for simulations: $\Omega_d = 2.31 \text{ GHz}$, $\Omega_p = 18.9 \text{ MHz}$, $N_c = 3 \times 10^{12} \text{ cm}^{-3}$, $\gamma = 5 \times 10^7 \text{ Hz}$, $\gamma_{\text{deph}} = 1.5 \times 10^7 \text{ Hz}$.

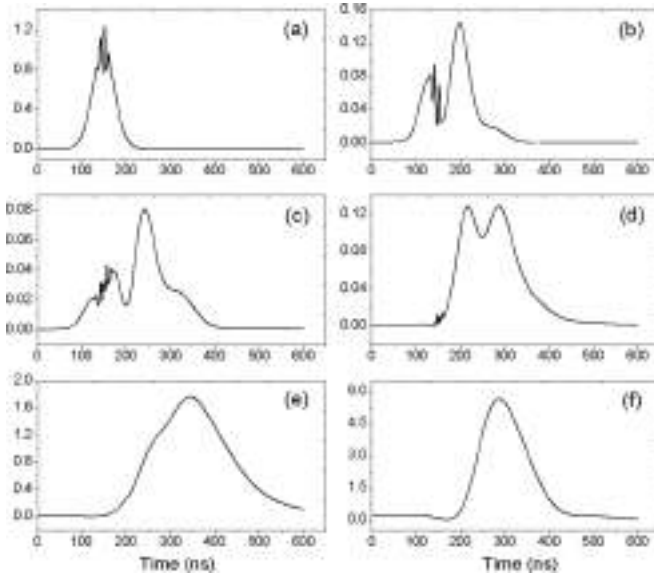


FIG. 7. Dynamics of 80-ns probe pulse propagation through K vapor cell of 4 cm, example of pulse destruction and revival. (a)–(f) Pulse waveforms at 0, 8, 16, 24, 52, and 100% of the total cell length, respectively. Small perturbations at the top of the probe pulse are followed in several figures representing pulse waveform at a later time (distance). Parameters for the simulations: $\Delta = 0.7$ GHz, $\delta = -2$ MHz, $\Omega_d = 3.08$ GHz, $\Omega_p = 18.9$ MHz, $N_c = 3 \times 10^{12}$ cm $^{-3}$, $\gamma = 0.5 \times 10^7$ Hz, $\gamma_{\text{deph}} = 1.5 \times 10^7$ Hz.

the obtained pulse’s waveforms. This is not always the case. For higher pump Rabi frequencies and higher gas temperatures, calculations with five groups of atoms give better agreement with the experiment compared to the ones with three velocity groups. Also, for larger δ , when stronger multiple peaks are observed in the pulse profile, averaging with five velocity groups is a better option. However, one has to be careful with the choice of velocity values.

2. Probe pulse behavior in the hot potassium vapor—Two case studies

Whether the outbound pulse waveform is broadened Gaussian-like or distorted with multiple pulses depends on the pulse behavior from the time it enters the vapor to the time when it exits from the vapor. We have studied probe pulse propagation, while the pulses are at different distances from the (cell) vapor entrance, for two sets of FWM parameters. Both sets of parameters give Gaussian-like outbound pulses, but as we will see below, these pulses exit the vapor after different behaviors while in the vapor. To ease comparison of different and sometimes complex behavioral studies of pulses in the K vapor, we numerically followed propagation of the marker, placed on the top of the probe input pulse, in respect to propagation of the pulse itself. This wavelet is so small that it does not generate an additional effect on the behavior of the pulse, its delay, or broadening. By following the location of the marker versus the pulse peak, we show that the Gaussian pulse at the output may not be directly connected to the input pulse by a time evolution. Instead, another pulses, behind the initial, start to appear, and with enough gain at the end of the

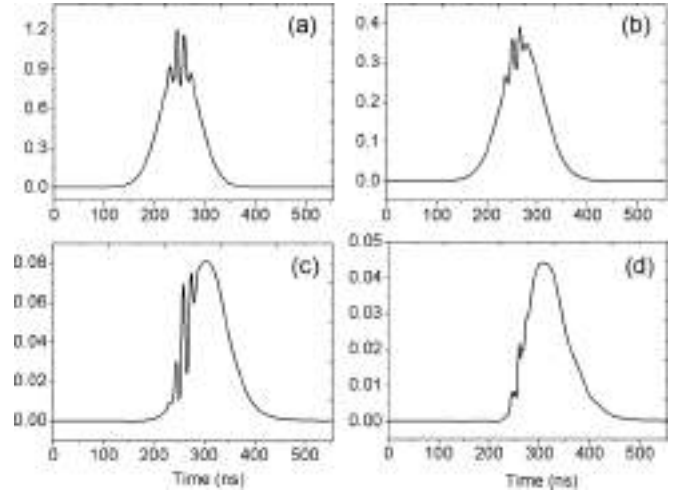


FIG. 8. Dynamics of 80-ns probe pulse propagation through K vapor cell of 4 cm, example of pulse broadening. (a)–(d) Pulse waveforms at different percentages of cell length, 0%, 20%, 60%, 100%, respectively. $\Omega_d = 1.72$ GHz, $N_c = 1 \times 10^{12}$ cm $^{-3}$ ($T = 110$ °C), $\Delta = 0.7$ GHz, and $\delta = 0$ MHz. γ and γ_{deph} are the same as in Fig. 7.

propagation distance, they dominate over the initial pulse. An example is given in Fig. 7 for the following parameters: $\Delta = 0.7$ GHz, $\delta = -2$ MHz, $\Omega_d = 3.08$ GHz, $\Omega_p = 18.9$ MHz, $N_c = 3 \times 10^{12}$ cm $^{-3}$, $\gamma = 0.5 \times 10^7$, $\gamma_{\text{deph}} = 1.5 \times 10^7$. It is clear from the location of the marker that the pulse entering the cell disappears at about $z = 0.6 \times z_{\text{max}}$ (2.5 cm from the entrance). The choice of parameters for results in Fig. 7 give a broadened and slightly distorted outbound pulse, and we see that the secondary pulses, in the high-gain regime, are responsible for the slowed light pulse and broadening.

In Fig. 8 we give an example of pulse propagation when the initial pulse is preserved, i.e., the same pulse travels from the entrance to the exit of the medium. It is only slowed and broadened, and as seen from the graphs in Fig. 8, the marker is slipping behind the pulse peak as it slowed more than the probe pulse. Observed pulse broadening is the result of the pulse front traveling faster than the back of the pulse.

The different behavior of pulses in Figs. 7 and 8 is at different gas density and pump power. This type of simulation shows that for some parameters, there will be only the primary pulse, while for others, secondary pulses may appear, in the vapor and at the exit. The additional pulses may be small, or dominate, or can completely replace the initial pulse, depending on the length of the vapor cell. For ranges of FWM parameters both theory and measurement give complex waveforms of outbound pulses, which theory describes as the result of a generation of new pulses. The secondary pulse is more delayed and less broadened than the primary, and thus offers new possibilities for slow light applications.

V. CONCLUSION

Gains, frictional delays, and broadening of probe and conjugate pulses after 80-ns probe pulses traverses the 4-cm K vapor cell have been measured and calculated when FWM is generated by the double- Λ scheme. Of the broad range of FWM parameters good for parametric gains in the

medium, only the small subrange is good for slowing Gaussian pulses. Both the experiment and the model have shown that an outbound pulse is a nondistorted Gaussian only when every FWM parameter is in a specific, small subrange: $0.7 \text{ GHz} < \Delta < 1.3 \text{ GHz}$, $-16 \text{ MHz} < \delta < 4 \text{ MHz}$, $3 \times 10^{12} \text{ cm}^{-3} < N_c < 9.96 \times 10^{12} \text{ cm}^{-3}$. Both model and experiment have shown that maximum fractional delays are at the maximum of pulse broadening, and typically at two-photon detuning when gains of the probe and conjugate have the highest values. The maximal fractional delays are 1 in the experiment and 1.4 in the model.

We have shown that without Doppler averaging the model fails to reproduce correct pulse profiles. For more complex waveforms, Doppler averaging over a larger number of atom velocity groups, a minimum of 5, might be needed. Following the time (and distance) propagation of the small wavelet, placed at the top of the probe pulse at the cell entrance, in respect to

the propagation of the probe pulse itself, we have shown that, depending on the FWM parameters, the outbound Gaussian-like pulse is the result of quite different pulse propagation dynamics in the vapor. In some cases the initial pulse will disappear and new one can be formed, and for a sufficient gain or length of the vapor, a newly generated pulse will dominate the waveform of the outbound pulse.

ACKNOWLEDGMENTS

The authors acknowledge financial help from Grants No. III45016 and No. OI131038 of the Ministry of Education, Science, and Technological Development of Serbia, MP COST 4103 NQO and IZ73Z0 152511, Joint Research Projects (SCOPEs). We are thankful to M. Minić for thoughtful discussions and help with the electronics.

-
- [1] M. M. Kash, V. A. Sautenkov, A. S. Zibrov, L. Hollberg, G. R. Welch, M. D. Lukin, Y. Rostovtsev, E. S. Fry, and M. O. Scully, *Phys. Rev. Lett.* **82**, 5229 (1999).
- [2] R. M. Camacho, M. V. Pack, and J. C. Howell, *Phys. Rev. A* **73**, 063812 (2006).
- [3] R. M. Camacho, M. V. Pack, J. C. Howell, A. Schweinsberg, and R. W. Boyd, *Phys. Rev. Lett.* **98**, 153601 (2007).
- [4] J. E. Sharping, Y. Okawachi, and A. L. Gaeta, *Opt. Express* **13**, 6092 (2005).
- [5] Y. Okawachi, M. S. Bigelow, J. E. Sharping, Z. Zhu, A. Schweinsberg, D. J. Gauthier, R. W. Boyd, and A. L. Gaeta, *Phys. Rev. Lett.* **94**, 153902 (2005).
- [6] A. V. Turukhin, V. S. Sudarshanam, M. S. Shahriar, J. A. Musser, B. S. Ham, and P. R. Hemmer, *Phys. Rev. Lett.* **88**, 023602 (2001).
- [7] E. Baldit, K. Bencheikh, P. Monnier, J. A. Levenson, and V. Rouget, *Phys. Rev. Lett.* **95**, 143601 (2005).
- [8] P.-C. Ku, F. Sedgwick, C. J. Chang-Hasnain, P. Palinginis, T. Li, H. Wang, S.-W. Chang, and S.-L. Chuang, *Opt. Lett.* **29**, 2291 (2004).
- [9] H. Su and S. L. Chuang, *Opt. Lett.* **31**, 271 (2006).
- [10] M. S. Bigelow, N. N. Lepeshkin, and R. W. Boyd, *Phys. Rev. Lett.* **90**, 113903 (2003).
- [11] J. B. Khurgin and R. S. Tucker, *Slow Light Science and Applications* (CRC Press, Boca Raton, FL, 2009).
- [12] A. Kasapi, M. Jain, G. Y. Yin, and S. E. Harris, *Phys. Rev. Lett.* **74**, 2447 (1995).
- [13] L. V. Hau, S. E. Harris, Z. Dutton, and C. H. Behroozi, *Nature (London)* **397**, 594 (1999).
- [14] J. Zhang, G. Hernandez, and Y. Zhu, *Opt. Lett.* **31**, 2598 (2006).
- [15] J. J. Longdell, E. Fraval, M. J. Sellars, and N. B. Manson, *Phys. Rev. Lett.* **95**, 063601 (2005).
- [16] L. Ma, O. Slattery, P. Kuo, and X. Tang, *Proc. SPIE* **9615**, Quantum Communications and Quantum Imaging XIII **9615**, 96150D (2015).
- [17] D. Budker, D. F. Kimball, S. M. Rochester, and V. V. Yashchuk, *Phys. Rev. Lett.* **83**, 1767 (1999).
- [18] D. F. Phillips, A. Fleischhauer, A. Mair, R. L. Walsworth, and M. D. Lukin, *Phys. Rev. Lett.* **86**, 783 (2001).
- [19] V. Boyer, C. F. McCormick, E. Arimondo, and P. D. Lett, *Phys. Rev. Lett.* **99**, 143601 (2007).
- [20] J. Okuma, N. Hayashi, A. Fujisawa, and M. Mitsunaga, *Opt. Lett.* **34**, 1654 (2009).
- [21] Y.-F. Fan, H.-H. Wang, X.-G. Wei, A.-J. Li, Z.-H. Kang, J.-H. Wu, H.-Z. Zhang, H.-L. Xu, and J.-Y. Gao, *Phys. Lett. A* **376**, 785 (2012).
- [22] R. M. Camacho, P. K. Vudiyasetu, and J. C. Howell, *Nat. Photon.* **3**, 103 (2009).
- [23] N. B. Phillips, A. V. Gorshkov, and I. Novikova, *Phys. Rev. A* **83**, 063823 (2011).
- [24] R. K. Hanley, P. D. Gregory, I. G. Hughes, and S. L. Cornish, *J. Phys. B* **48**, 195004 (2015).
- [25] A. Sargsyan, A. Tonoyan, J. Keaveney, I. G. Hughes, C. S. Adams, and D. Sarkisyan, *J. Exp. Theor. Phys.* **126**, 293 (2018).
- [26] J. D. Swaim and R. T. Glasser, *Opt. Express* **25**, 24376 (2017).
- [27] A. Lampis, R. Culver, B. Megyeri, and J. Goldwin, *Opt. Express* **24**, 15494 (2016).
- [28] B. Zlatković, A. J. Krmpot, N. Šibalić, M. Radonjić, and B. M. Jelenković, *Laser Phys. Lett.* **13**, 015205 (2016).
- [29] J. D. Swaim and R. T. Glasser, *Phys. Rev. A* **96**, 033818 (2017).
- [30] M. M. Čurčić, T. Khalifa, B. Zlatković, I. S. Radojičić, A. J. Krmpot, D. Arsenović, B. M. Jelenković, and M. Gharavipour, *Phys. Rev. A* **97**, 063851 (2018).
- [31] M. T. Turnbull, P. G. Petrov, C. S. Embrey, A. M. Marino, and V. Boyer, *Phys. Rev. A* **88**, 033845 (2013).

Four-wave mixing in potassium vapor with an off-resonant double- Λ system

M. M. Čurčić*

*Institute of Physics Belgrade, University of Belgrade, Pregrevica 118, 11080 Belgrade, Serbia
and School of Electrical Engineering, University of Belgrade, Bulevar kralja Aleksandra 73, 11120 Belgrade, Serbia*T. Khalifa, B. Zlatković, I. S. Radojičić, A. J. Krmpot, D. Arsenović, and B. M. Jelenković
Institute of Physics Belgrade, University of Belgrade, Pregrevica 118, 11080 Belgrade, Serbia

M. Gharavipour

Laboratoire Temps-Fréquence (LTF), Institut de physique, Université de Neuchâtel, Neuchâtel CH-2000, Switzerland

(Received 5 October 2017; revised manuscript received 26 March 2018; published 25 June 2018)

We investigate both theoretically and experimentally four-wave mixing (FWM) in hot potassium vapor, generated by a copropagating pump and probe in an off-resonant double- Λ system, and present conditions when this atomic system is (1) a strong phase-insensitive parametric amplifier and (2) a source of large-amplitude squeezing. Theoretically, nonperturbative numerical calculations of optical Bloch-Maxwell equations have been solved for a four-level atomic system of K in order to derive the atomic polarization and then amplitudes of propagating optical waves, pump, probe, and conjugate. For potassium, to our knowledge, there are no such comparisons of theoretical and experimental results of gains of twin beams under the large range of FWM parameters as presented here. Results have shown that one-photon detuning has to be slightly larger than the Doppler broadened transition for large gains and strong squeezing. The gain is particularly large for small red two-photon detuning ($-2-6$ MHz) and high K density ($5.5-10 \times 10^{12}$ cm $^{-3}$). Following experimentally and theoretically determined relation between gains, probe transmissions, and squeezing in Rb and Cs, we have found parameters of FWM when maximum squeezing in hot K vapor is expected.

DOI: [10.1103/PhysRevA.97.063851](https://doi.org/10.1103/PhysRevA.97.063851)**I. INTRODUCTION**

Four-wave mixing (FWM) is a nonlinear phenomenon that in alkali-metal vapors can efficiently generate entangled photon pairs, essential for probing quantum properties of light and for quantum information [1–3]. It also enables slowing and storing of light in atomic ensembles [4–9], essential elements for quantum memories.

Different schemes have been used to generate paired photons, such as on-resonant spontaneous FWM [2], the diamond [10], and double ladder scheme FWM [11]. An atomic system that is often used for generation of twin beams is off-resonant FWM in a double- Λ scheme, realized by two input fields, pump and probe, in a three (four) -level atomic system. The lower Λ is made of pump and probe photons, while the pump photon and conjugate photon close the upper Λ (see Fig. 1). This atomic scheme is similar to schemes for electromagnetically induced transparency (EIT) and becomes nonlinear FWM under certain conditions: whether the system will behave like EIT or a parametric amplifier depends on laser detunings, atomic density, and pump power [12,13]. While resonant absorption processes for EIT conditions lead to losses, FWM gains of both probe and conjugate, typically observed for high pump beam, allow for much larger propagation distances [4,14,15].

A nondegenerate, off-resonant double- Λ scheme was found to be a good source for relative amplitude squeezing [16–19] and for simultaneously generated intensity correlations and phase anticorrelations or entanglement of probe and conjugate [20,21]. Large entanglement is an important resource for quantum information [22]. A correlation between the amount of squeezing and entanglement and the gain of the twin beam is established [20].

Theoretically, FWM was studied in degenerate and counterpropagating laser beams [23], as well as in nondegenerate and copropagating beams. In the latter, nonlinear parametric processes in FWM were studied in a double- Λ configuration with either resonant (larger contribution from CPT and EIT phenomena) [24] or off-resonant pump frequency [15], in hot gas vapors or in cold atoms [25]. There are different approaches to model complex processes in FWM. They depend on the intended applications of the system, which can be parametric gain, quantum-correlations of twin beams, squeezing and entanglement, slow and stored light, i.e., whether classical or quantum properties are of interest. For work presented here, the most relevant are models that analyze the continuous wave regime and calculate gains of twin beams. Quantum mechanical theory of multiwave mixing was applied for calculating Rabi sidebands generated by FWM [26]. In most models, the treatment is based on analytical solutions, after perturbation theory and a number of approximations being applied [15]. In the seminal paper [24], pump and probe are resonant with atomic transitions with conditions for EIT, while

*marijac@ipb.ac.rs

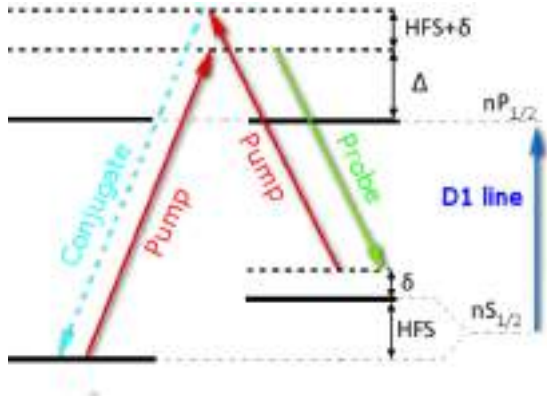


FIG. 1. Double Λ scheme at D_1 line of an alkali-metal atom. hfs = hiperfine splitting, Δ = one-photon detuning, δ = two-photon detuning. Levels: $|1\rangle$ and $|2\rangle$ = hyperfine levels of $4S_{1/2}$, $F = 1$ and $S_{1/2}$, $F = 2$ respectively, $|3\rangle = 4P_{1/2}$, $|4\rangle$ = virtual level, degenerate with $|3\rangle$, introduced by the model. Hfs of the level $|3\rangle$ is negligible in comparison with ground state hfs.

cross susceptibilities are enhanced by coherence in the ground hyperfine levels. Heisenberg-Langevin formalism was used to calculate the classical and quantum properties of probe and conjugate beams beyond the linear amplifier approximation [25,27]. A phenomenological approach when the medium is quantum mechanically described by a simple model of distributed FWM gain and probe loss was used in Ref. [16].

FWM in alkali metals has been extensively studied, particularly in Rb and Cs [4,14,16,19,25,28,31], but little work was done on potassium [32–37]. Potassium has hyperfine splitting (hfs) of the ground state of only 460 MHz, by far smaller than for any other alkali metal. For FWM based on two pump photons, small hfs means that detuning of the upper Λ scheme is not far from detuning of the lower Λ scheme. This suggests that large gains and squeezing and other FWM properties are possible at lower laser power.

With this study, we extend our previous work on FWM in K [33] with results of the theoretical model and new experimental results. The model is a semiclassical treatment of FWM processes, and atomic polarization, calculated from optical Bloch equations (written for the system presented schematically in Fig. 1), is applied in the propagation equations to obtain amplitudes of three optical fields at the exit from the K vapor. We compare calculated and measured gains for a wide range of parameters, which is important for efficiency of FWM. This includes the angle between the pump and the probe, atomic density, detuning of the pump from the D_1 transition, Δ , and two-photon detuning in respect to hfs of the ground state, δ .

Performance of FWM for high-level squeezing, quantum information protocols, and quantum cloning machines [3] strongly depends on FWM parameters: vapor density, Δ and δ . The former controls probe absorption, while two detunings control nonlinearity and gain. Measurements and models [16,18] have shown that for stronger squeezing and low noise figures, moderate gains of probe and conjugate are at a maximum, while probe absorption is minimal. We made intensive calculations of gains and probe transmissions for the large range of K density and one- and two-photon detuning,

and present parameters of FWM that we believe will generate the strongest quantum correlations and squeezing in K vapor. In the theoretical analyses for FWM parameters for strong squeezing we have included results that take into account the Doppler average of density matrix elements. These values are compared with values used in a recent experiment [38] to measure squeezing in K vapor. Since for the alkali-metal atoms with higher hyperfine splitting of the ground state, higher powers are required for efficient degree of squeezing [19,29], we believe that potassium, having the smallest hfs of the ground state, could be more convenient, compared to others, for high-level amplitude squeezing.

II. THEORETICAL MODEL

In the model, the three electric field modes, pump (drive), probe, and conjugate, with frequencies ω_d , ω_p , and ω_c , respectively, interact with four levels of the ^{39}K atom. The double- Λ scheme with modes coupling atomic levels of the D_1 transition is given in Fig. 1. Level $|3\rangle$ is $4P_{1/2}$, while levels $|1\rangle$ and $|2\rangle$ are hyperfine levels of $4S_{1/2}$, $F = 1$ and $F = 2$, respectively. The lower Λ scheme consists of the pump photon that couples the level $|1\rangle$ to the level $|3\rangle$ with the one-photon detuning $\Delta_{(13)} = \Delta$. The other “leg” of the first Λ scheme is the probe photon that stimulates the Stokes scattering from level $|3\rangle$ to the level $|2\rangle$, with two-photon detuning $\Delta_{(132)} = \delta$. The pump is sufficiently strong to drive the off-resonant transition $|2\rangle \rightarrow |4\rangle$ in the upper Λ scheme. By the way of stimulating anti-Stokes scattering the conjugate photon closes the upper scheme. The total detuning for the level $|4\rangle$ is $\Delta_{(1324)} = (2\omega_d - \omega_p) - (\omega_4 - \omega_1)$, where $\omega_4 - \omega_1$ is angular frequency of the transition $|1\rangle \rightarrow |4\rangle$. We introduce level $|4\rangle$, which is degenerate to the level $|3\rangle$, and like level $|3\rangle$ is weakly coupled to both level $|1\rangle$ and level $|2\rangle$ because of a large detuning.

Atoms are simultaneously illuminated by the pump, probe, and conjugate and experience a total electric field approximated by the sum of three monochromatic fields:

$$\mathbf{E} = \sum_{i=d,p,c} \mathbf{e}_i E_i^{(+)} e^{-i\omega t + i\mathbf{k}_i \cdot \mathbf{r}} + \text{c.c.} \quad (1)$$

Here $E^{(+)}$ is the slowly varying approximation of the fields envelope, at positive frequencies. The Hamiltonian for the atomic system is given by

$$\hat{H} = \hat{H}_0 + \widehat{H}_{\text{int}} = \sum_{i=1}^4 \hbar\omega_i |i\rangle \langle i| - \hat{\mathbf{d}} \cdot \mathbf{E}(\mathbf{r}, t), \quad (2)$$

where \hat{H}_0 is the unperturbed Hamiltonian of the system and \widehat{H}_{int} is interaction Hamiltonian, $\hbar\omega_i$ is the energy of atom level i , and $\hat{\mathbf{d}}$ is atomic dipole moment.

Atomic dynamics is described by the set of Bloch equations for density matrix elements $\hat{\rho}$:

$$\dot{\hat{\rho}} = -\frac{i}{\hbar} [\hat{H}, \hat{\rho}] + \widehat{SE} + \hat{R}, \quad (3)$$

where \widehat{SE} denotes the spontaneous emission from the excited states, and \hat{R} is the relaxation due to atom transit time-induced losses and collisional dephasing. The full set of Eq. (3) is given in the Appendix. Because of the fast oscillating laser field, as

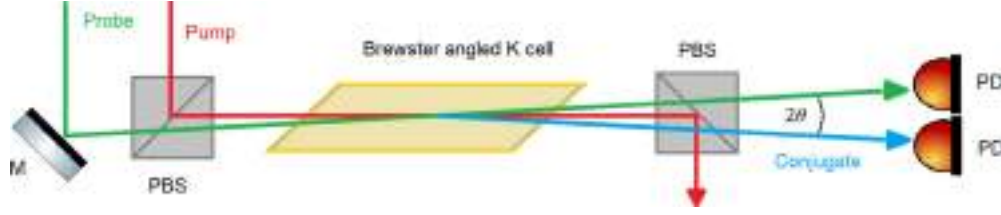


FIG. 2. Experimental setup. M = mirror, PBS = polarization beam splitter, PD = photodetector.

in Eq. (1), substituting H from Eq. (2) into Eq. (3) produces fast oscillating terms in ρ_{ij} . After substitution,

$$\tilde{\rho}_{ij} = e^{-i\omega_{(ij)}t + i\mathbf{k}_{(ij)}\mathbf{r}} \rho_{ij}, \quad (4)$$

where $\omega_{(ij)}$ are different angular frequencies: $\omega_{(13)} = \omega_{(24)} = \omega_d$, $\omega_{(23)} = \omega_p$, $\omega_{(14)} = \omega_c$, $\omega_{(12)} = \omega_{(13)} - \omega_{(23)}$, $\omega_{(34)} = \omega_{(14)} - \omega_{(13)}$, $\omega_{(ij)} = -\omega_{(ji)}$, and $\mathbf{k}_{(ij)}$ are wave vectors of sums (differences) of wave vectors: $\mathbf{k}_{(13)} = \mathbf{k}_{(24)} = \mathbf{k}_d$, $\mathbf{k}_{(23)} = \mathbf{k}_p$, $\mathbf{k}_{(14)} = \mathbf{k}_c$, $\mathbf{k}_{(12)} = \mathbf{k}_{(13)} - \mathbf{k}_{(23)}$, $\mathbf{k}_{(34)} = \mathbf{k}_{(14)} - \mathbf{k}_{(13)}$, $\mathbf{k}_{(ij)} = -\mathbf{k}_{(ji)}$ with $\mathbf{k}_c = 2\mathbf{k}_d - \mathbf{k}_p - \Delta\mathbf{k}$. Terms that oscillate with the sum of frequencies are neglected in the rotating wave approximation. Left in Eq. (3) are time-independent terms and a few spatially dependent terms with oscillating coefficients $e^{i\Delta\mathbf{k}z}$.

Propagation along the z direction and temporal evolution of pump, probe, and conjugate are described by the set of nonlinear equations for the slowly varying envelopes of the three fields:

$$\left(\frac{\partial}{\partial z} + \frac{1}{c} \frac{\partial}{\partial t} \right) E_d^{(+)} = i \frac{kN}{2\epsilon_0} d (\tilde{\rho}_{(42)} + \tilde{\rho}_{(31)}), \quad (5a)$$

$$\left(\frac{\partial}{\partial z} + \frac{1}{c} \frac{\partial}{\partial t} \right) E_p^{(+)} = i \frac{kN}{2\epsilon_0} d \tilde{\rho}_{(32)}, \quad (5b)$$

$$\left(\frac{\partial}{\partial z} + \frac{1}{c} \frac{\partial}{\partial t} \right) E_c^{(+)} = i \frac{kN}{2\epsilon_0} d \tilde{\rho}_{(41)}. \quad (5c)$$

Here N is the atom density.

Since we are also interested in probe absorption, we calculate the above equations by setting the intensity of pump beam to be zero. The probe transmission is then the quotient of the intensities of the outgoing and incoming probe beam. In a hot vapor the Doppler effect is present. The shift of the observed angular frequency is dependent on the z component of the velocity, v_z , for which the Maxwell distribution is given by

$$f(v_z) = \sqrt{\frac{m}{2\pi kT}} e^{-\frac{mv_z^2}{2kT}}, \quad (6)$$

The observed angular frequency is $\omega_0 = \sqrt{\frac{1-\beta}{1+\beta}} \omega_s$, where ω_s is angular frequency of the source and $\beta = v/c$. The frequency shift alters one photon detuning and detuning of the conjugate pulse, while two-photon detuning stays the same since the pump and probe are almost copropagating. Hence, density matrices depend on v_z . We perform Doppler averaging with the most basic approximation. We calculate the signals, gains of twin beams, and probe transmission for different v_z and then average them over the Maxwell distribution.

The gains of the probe (conjugate) are calculated from the ratio of amplitudes of probe (conjugate) at the exit from the K vapor to the probe amplitude at the entrance to the vapor. The model assumes that the pump and the probe fully overlap. The gas cell used in the experiment is 5 cm long, therefore for a typical angle between the probe and the pump ~ 3 mrad, beams are overlapped only in the part of the cell. Our theoretical results are for a 1 cm long interaction region. Parameters used in the calculations are as in the experiment, like atom density, one- and two-photon detuning, and angle between pump and probe. Rabi frequencies of the pump and probe are calculated from the laser intensity I using $\Omega = \frac{2dE_0^{(+)}}{h}$, $E = E_0 \cos(\omega t) = E_0^{(+)} e^{-i\omega t} + E_0^{(-)} e^{i\omega t}$, $E_0^{(+)} = \frac{E_0}{2} = \sqrt{(\eta I/2)}$. Here $\eta = 376.73 \Omega$ [39] is the vacuum impedance, and d is the reduced dipole matrix element, which for potassium is $d = 1.74 \times 10^{-29}$ Cm [40]. For total relaxation rates, γ (see the Appendix), we used the value $\gamma \sim 10^5$ Hz.

III. EXPERIMENT

We have measured gains of the probe and the conjugate using the setup described in Ref. [33]; see Fig. 2. Laser beam from the high-power, narrow line laser (Coherent, MBR 110) is split in two by a 90:10 beam splitter. A stronger beam is used as the pump beam, and the weaker fraction is the probe beam. The probe is sent through two AOMs, one in a double pass, for the probe frequency detuning in respect to the pump frequency, and for scanning of this detuning around the hfs of the K ground state. Thus, we vary two-photon detuning δ by changing the probe frequency and vary one-photon detuning Δ by tuning the pump frequency. Diameters of the pump and the probe beams are 1.1 mm, and 0.75 mm, respectively. Two beams are orthogonally polarized and recombined on the polarizing beam cube before entering the K cell. This is the vacuum K cell with natural abundance of isotopes, 5 cm long, 25 mm in diameter. The cell was heated by hot air up to 150 °C. Pump and probe beams enter the cell at the small angle θ . We can adjust this angle by changing the probe direction with the entrance mirror, placed before the combining cube. With the pump beam behind the cell blocked, two beams emerge: probe and the frequency up-shifted beam (conjugate). Both beams are detected with the pair of photodetectors. We get the gains of the probe and the conjugate from the ratios of measured powers of the probe and conjugate beams behind the cell to the probe beam input power. Radius and shape of beams behind the cell are monitored with a CCD beam profiler.

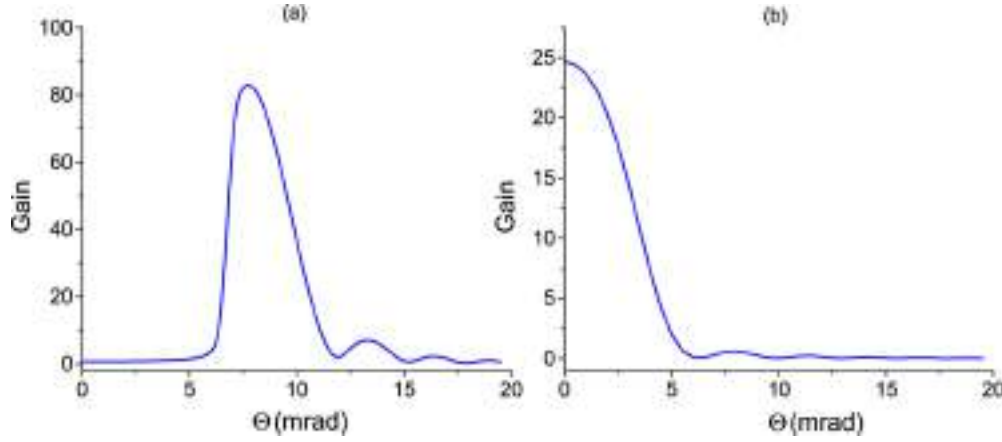


FIG. 3. Calculated gain of the conjugate beam as a function of the angle θ for two pump powers. (a) $\Omega_d = 3.25$ GHz, (b) $\Omega_d = 1.95$ GHz, for $N = 1 \times 10^{12}$ cm $^{-3}$, $\delta = -9.5$ MHz, $\Delta = 1$ GHz, and $\Omega_p = 22.5$ MHz.

IV. RESULTS AND DISCUSSION

In this section we present results of gains of twin beams as a function of FWM parameters: the angle between the pump and the probe, gas density, one- and two-photon detuning, and the probe power. But, as we will show, dependence on one of the parameters depends on values of the other parameters.

A. Measured and calculated gains of probe and conjugate

1. Dependence of gains on the angle between pump and probe

Probe and conjugate gains as a function of the angle θ between the pump and the probe are results of FWM phase matching. As we see from results in Figs. 3 and 4, the phase matching condition is satisfied at different angles θ , depending on values of other parameters. Behavior of FWM gains versus θ is influenced by the index of refraction at the probe frequency, which is influenced by values of laser powers, densities, and detunings. In Figs. 3 and 4 we present calculated conjugate beam gains as a function of θ . We decided not to show results for the probe because the model gives very similar behavior of gains of the probe and the conjugate.

Results in Fig. 3 are obtained for different pump Rabi frequencies, while results in Fig. 4 are for different density of the K vapor. Results show that FWM gains have different behavior at high and low pump Rabi frequencies Ω_d (Fig. 3)

and at high and low K densities (Fig. 4). In both figures, one- and two-photon detunings, and probe Rabi frequency Ω_p are $\Delta = 1$ GHz, $\delta = -9.5$ MHz, and $\Omega_p = 22.5$ MHz. As we can see, at high Ω_d and higher density, FWM gains are in a narrow range of angles θ and the gain maximum is away from zero values of δ . On the other hand, at lower power and density, FWM phase matching is found at smaller angles. Here gain increases as θ is decreasing. Occurrence of FWM gains at near zero angle means negligible changes of index of refraction at the probe frequency and/or its continuous change along the vapor due to strong pump absorption and therefore variation of pump power along the propagation direction. The possibility of the latter was not supported by the calculated pump absorption. On the other hand, our model shows correlation between how gain depends on angle, and the amount of the phase changes of the probe and conjugate. When the gain versus angle is a narrow peak as in Fig. 3(a), then Δk_z varies for more than 2π over the propagated distance. When gain monotonically changes as the angle increases from zero, Δk_z changes only a little, less than $\pi/4$.

Experimental results for the gains of twin beams as a function of the angle θ for K densities of 5.5×10^{12} cm $^{-3}$ (cell temperature 130 °C) and 1.75×10^{13} cm $^{-3}$ (150 °C) are given in Fig. 5. The smallest value of the angle between pump and probe we needed to separate the probe and conjugate

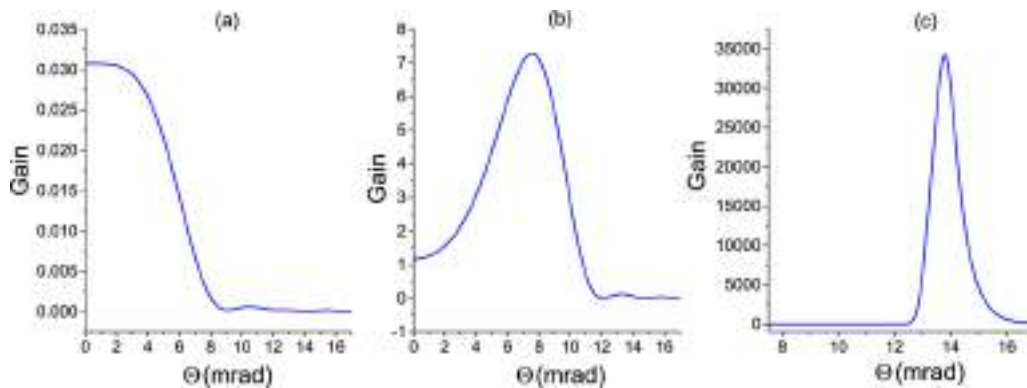


FIG. 4. Calculated gain of the conjugate beam as a function of the angle θ , for three values of the potassium density. (a) $N = 1 \times 10^{13}$ cm $^{-3}$, (b) $N = 1 \times 10^{12}$ cm $^{-3}$, and (c) $N = 1 \times 10^{11}$ cm $^{-3}$ for $\Omega_d = 1.95$ GHz, $\Omega_p = 22.5$ MHz, $\delta = -9.5$ MHz, and $\Delta = 1$ GHz.

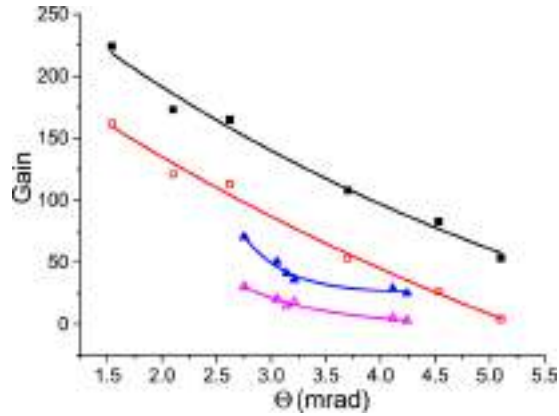


FIG. 5. Experimental results of gains of probe (open symbols) and conjugate (filled symbols) for two K density, $5.5 \times 10^{12} \text{ cm}^{-3}$ (squares) and $1.7 \times 10^{13} \text{ cm}^{-3}$ (triangles). $\Delta = 1 \text{ GHz}$ (for lower density) and 1.35 GHz (for higher density). $\delta = -3.7 \text{ MHz}$, $P_d = 370 \text{ mW}$, and $P_p = 25 \mu\text{W}$.

behind the cell was $\theta = 1.5 \text{ mrad}$. The twin beam gains at the highest vapor density that we had in the experiment are lower and were measured only at high $\Delta = 1.35 \text{ GHz}$. Experimental results of gains versus angle, as shown in Fig. 5, are typical for copropagating pump and probe with a similar diameter in a rather long gas cell, because beams do not fully overlap in parts of the cell.

2. Dependence of gains on two-photon detuning

Calculated and measured gains of the probe and the conjugate versus two-photon detuning δ , for several values of one-photon detuning, are presented in Fig. 6. Dependence is given for two Δ , 1 GHz and 1.35 GHz , and for $\theta = 5.5 \text{ mrad}$. Typical widths of calculated gains are between 1.5 and 3 MHz , and of measured gains are 6 – 13 MHz .

Maximum of gains are, at δ_m , shifted from two-photon resonance ($\delta \approx 0$). This shift is mainly due to differential Stark shift, δ_S , because of different detunings of hyperfine levels from the off-resonant pump. As shown in Fig. 6, δ_m is larger for smaller Δ . Not shown, but when Δ is 670 MHz , $\delta_m = -12 \text{ MHz}$. The maximum of the gain curve may not coincide with the FWM resonance because of Raman absorption at the resonance. We experimentally investigate how δ_m varies with certain parameters by keeping Δ fixed. For $\Delta = 1 \text{ GHz}$, $\theta = 3 \text{ mrad}$, and change of K density from $1.5 \times 10^{12} \text{ cm}^{-3}$ to $1.7 \times 10^{13} \text{ cm}^{-3}$, δ_m stayed the same, -3.7 MHz for the probe and -1.7 MHz for the conjugate. On the other hand, changing θ from 5.5 to 2.6 mrad , for the K density of $N = 5.5 \times 10^{12} \text{ cm}^{-3}$, moves δ_m from -4 MHz to -2.5 MHz . This slight shift to smaller two-photon detuning when the angle is decreasing is the same behavior of δ_m as found for Rb in Ref. [15].

It appears from Fig. 6 that typical curves representing gains versus δ , both calculated and measured, are not symmetric around the maximum. The asymmetric shape of lines might be because of inhomogeneous differential ac Stark shift, since

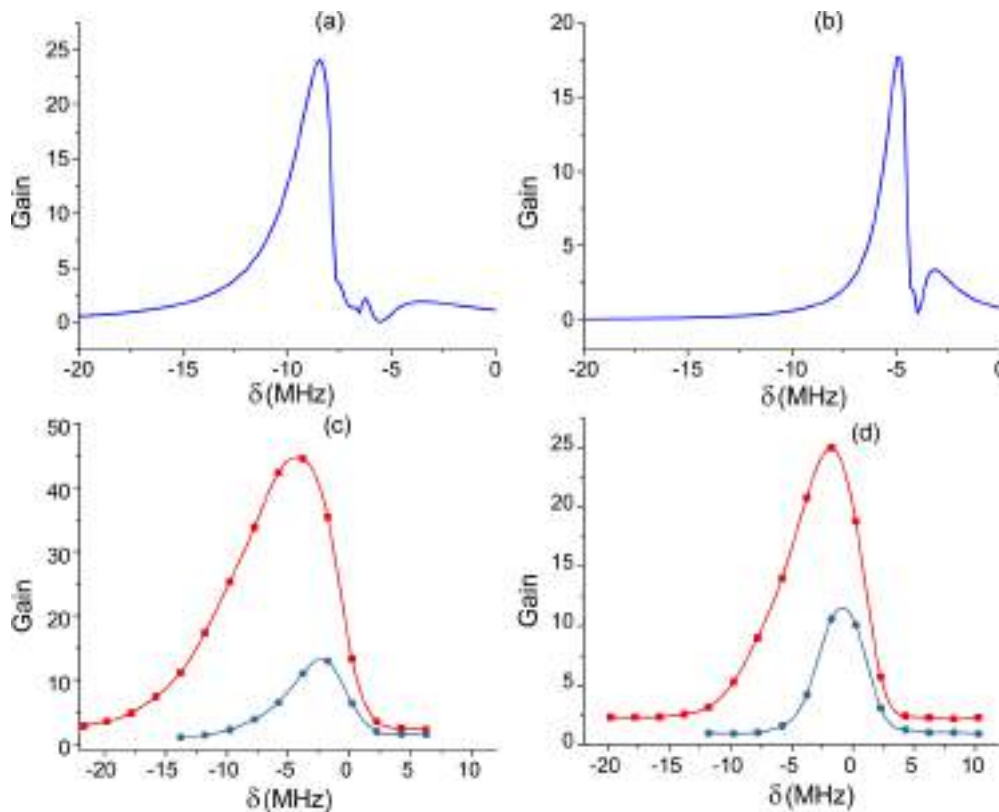


FIG. 6. Gains vs two-photon detuning. (a), (b) Calculations of the conjugate gain. The pump and probe Rabi frequencies are 1.94 GHz and 22.6 MHz , respectively. (c), (d) Experimental results of gains for the probe (solid circles, blue for online version) and the conjugate (solid squares, red for online version). Pump and probe powers are 370 mW and $25 \mu\text{W}$, respectively. (a), (c) $\Delta = 1 \text{ GHz}$, (b), (d) $\Delta = 1.35 \text{ GHz}$. Density $N = 5.5 \times 10^{12} \text{ cm}^{-3}$, $\theta = 5.5 \text{ mrad}$.

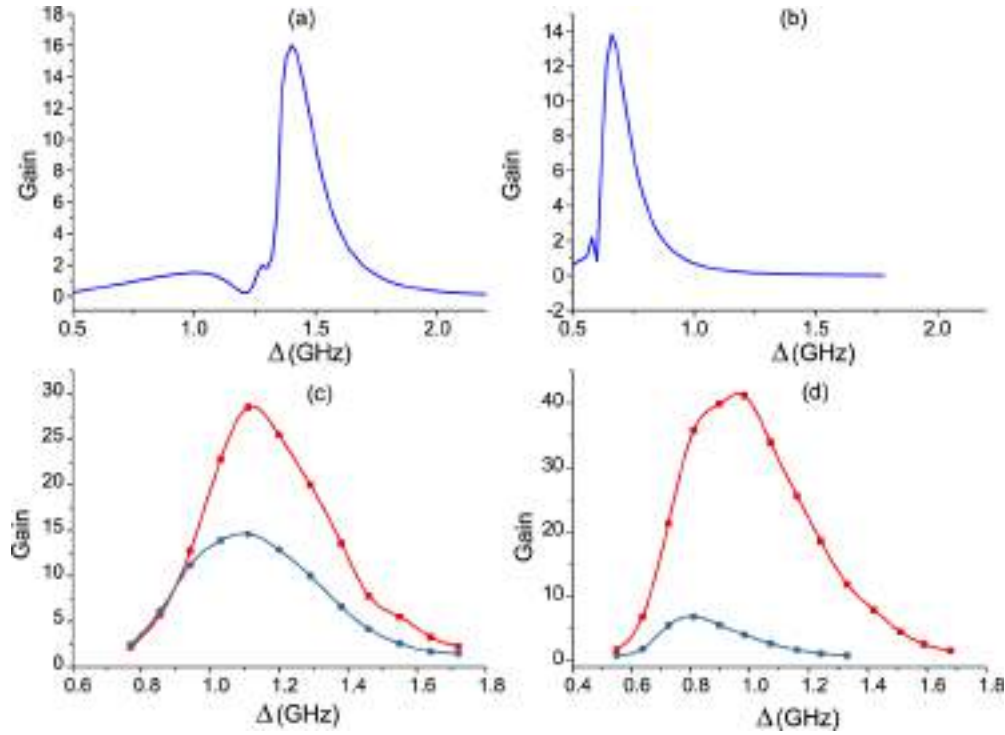


FIG. 7. Gains vs one-photon detuning. (a), (b) calculations of the conjugate gain. (c), (d) experimental results of gains of probe (solid circles, blue for online version) and conjugate (solid squares, red for online version). (a), (c) $\delta = -4$ MHz, (b), (d) $\delta = -8$ MHz. Pump and probe Rabi frequencies, as well as pump and probe powers, K vapor densities, and angle θ are the same as in Fig. 6

atoms in different areas of Gaussian beams experience different laser fields, and thus have different ac shift.

3. Dependence of gains on one-photon detuning

Potassium has larger Doppler broadening than other alkali metals, ~ 850 MHz. Width of Doppler line broadening in hot alkali metal vapors determines the range of Δ for large FWM gains. It is between 0.5 and 1 GHz for large gains and best squeezing for Rb and Cs [17,18,30,31].

We have calculated and measured gains versus Δ , with δ and θ as parameters. Presented results are for K vapor density of $N = 5.5 \times 10^{12} \text{ cm}^{-3}$ (130°C) (see Fig. 7). Parameters in the calculations are the same as for results in Fig. 6. Results

in Figs. 7(a) and 7(c) are for $\delta = -4$ MHz, while those in Figs. 7(b) and 7(d) are for $\delta = -8$ MHz. Gains versus Δ are broad, asymmetric curves whose width is 200 MHz for calculated and 400 MHz for measured results.

One-photon detuning for the maximum gain, Δ_m , is close to 1 GHz. We found that Δ_m doesn't change when θ changes if we keep δ the same. On the other hand, for the same angle θ (Fig. 7), Δ_m will have a different value when δ is changed: it is at 0.9 GHz for δ at -8 MHz and can go as far as 1.2 GHz for $\delta \sim 0$ MHz. Because of different detuning, gain of the conjugate is larger than the gain of probe. Large detuning of the probe, beyond the Doppler broadening, minimizes the effect of EIT on the probe absorption.

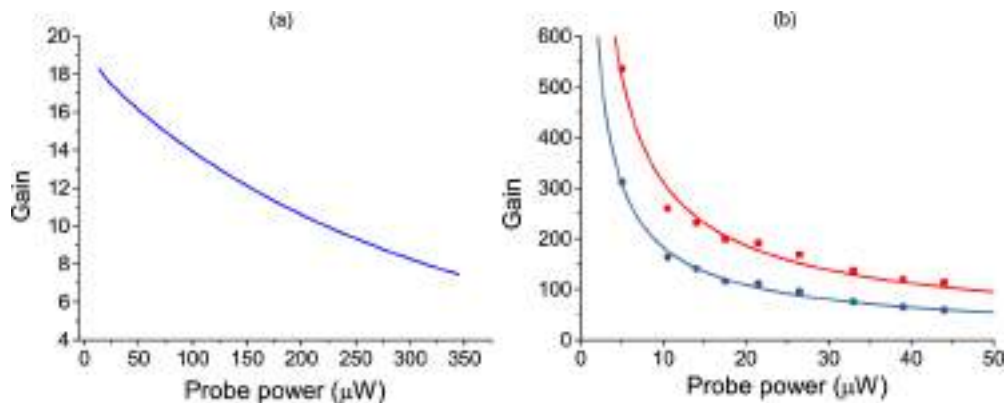


FIG. 8. (a) Calculation of conjugate gain vs probe power. (b) Measurements of probe (solid circles, blue for online version) and conjugate (solid squares, red for online version) gain vs probe power, for $\Delta = 960$ MHz, $\delta = -3.7$ MHz, and cell temperature 130°C.

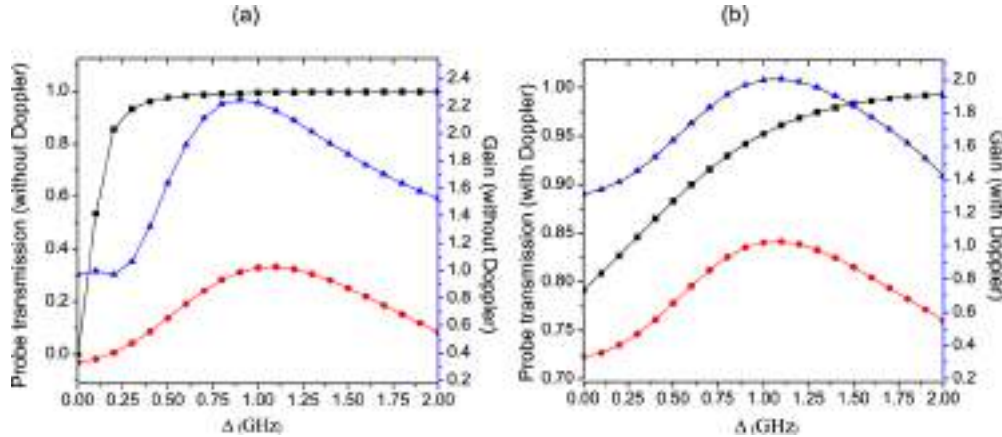


FIG. 9. Calculations of probe transmission (solid squares, black for online version) and gains for probe (solid triangles, blue for online version) and conjugate (solid circles, red for online version): (a) without Doppler averaging; (b) with Doppler averaging.

4. Gain dependence on probe power

Efficiency of FWM in alkali metals depends on the probe power, as presented in Fig. 8, for both calculated and measured values of gains. Evidently the lower the probe power, the higher the gain of both beams. The FWM gain in K vapor can thus be very large. In the experiment, we could not decrease probe below $5 \mu\text{W}$ because of limited sensitivity of photo diodes. Even without the probe beam at the entrance, with the probe initially in the vacuum state, a strong pump can generate side modes or twin photons [26].

B. Parameters of K vapor for optimum squeezing: Theoretical diagnostics

The numerical model explained above and derived in the Appendix allows us to search for the set of FWM parameters which should provide strong degrees of squeezing in K vapor. It was found, both experimentally and theoretically, in Rb and Cs [16,18,19] that in order to increase the squeezing and noise figure, it is necessary to reduce probe absorption and have modest and similar gains of both probe and conjugate. When plotted as a function of detuning, squeezing is at a maximum when gain is at a maximum. But too large gain results in probe noise that is large due to absorption and losses (fluorescence and nonlinear processes), and depending on gains, one needs FWM parameters that provide optimum probe transmission. Typically, the strongest squeezing is for Δ near the edge of Doppler broadening, when gains are at a maximum and probe transmission at about 90% [16].

We performed thorough analyses of effects of FWM parameters on gains and probe transmission in a search for those that produce maximum gains and large probe transmission at the same time. Results in Fig. 9 show dependence of gains and transmissions on Δ , for K density of $1 \times 10^{12} \text{ cm}^{-3}$, $\delta = -0.5 \text{ MHz}$, and $\theta = 2.8 \text{ mrad}$. Clearly there is the range of Δ near 900 MHz when modest gains are at maximum and probe transmission is high. We recommend this set of parameters for the new measurements of squeezing in K. Results of gains and transmissions are presented with [Fig. 9(a)] and without Doppler averaging [Fig. 9(b)]. Apparently, corrections due

to Doppler broadening are small for gains, as found to be the case also for Rb [15], but are considerable for the probe transmission. Results obtained for squeezing in potassium [38] for Δ of 500 MHz and probe transmission below 50% are below values for Rb [16,29] and Cs [19]. Parameters of FWM in Ref. [38] are outside ranges we believe, based on present results, are optimal for squeezing.

V. CONCLUSION

A nonperturbative numerical model was applied to the double- Λ atomic system in potassium vapor, and gains of probe and conjugate were calculated under the conditions of FWM. Results are in agreement with experimental results and show high gains when Δ is slightly larger than the Doppler width and δ is in the range -10 – 0 MHz . This system is a strong parametric amplifier with gains of several hundred, larger than observed with other alkali-metal atoms for similar pump laser power. On the other hand, potassium is the only alkali metal whose hfs of the ground state is smaller than the Doppler width, i.e., both pump and probe couple simultaneously both ground hfs levels to the excited level.

The model was also used to find parameters of FWM in K vapor that would be optimal for relative amplitude squeezing. In search for these parameters we included results that take into account Doppler averaging of density matrix elements. We have found that the density of $1 \times 10^{12} \text{ cm}^{-3}$, the angle between the pump and the probe $\theta = 2.8 \text{ mrad}$, while δ and Δ are -0.5 MHz , and $\sim 900 \text{ MHz}$, respectively, and for the pump and the probe Rabi frequencies 1.938 GHz and 23.72 MHz , respectively, are the set of parameters required for strong squeezing in hot potassium vapor.

ACKNOWLEDGMENTS

The authors acknowledge financial help from grants III45016 and OI131038 of the Ministry of Education, Science and Technological Development of Serbia. M.Ć. and I.R. acknowledge support from MP COST (BE) 4103 NQO and IZ73Z0_152511, Joint research projects (SCOPES).

APPENDIX

Far-detuned FWM is treated here as an atomic system with two ground and two excited levels. The pump couples two transitions, $|1\rangle \rightarrow |3\rangle$ and $|2\rangle \rightarrow |4\rangle$, while the probe and conjugate couple $|2\rangle \rightarrow |4\rangle$ and $|4\rangle \rightarrow |1\rangle$, respectively. Transitions to $|3\rangle$ are highly detuned, which justifies introducing another far detuned level $|4\rangle$, with a similarly weak coupling strength from the levels $|1\rangle$ and $|2\rangle$.

The explicit form for the spontaneous emission in Eq. (3) is given by

$$\widehat{SE} = \begin{pmatrix} \Gamma_{1,3}\rho_{33} + \Gamma_{1,4}\rho_{44} & 0 & -\frac{\Gamma_{1,3}+\Gamma_{2,3}}{2}\rho_{13} & -\frac{\Gamma_{1,4}+\Gamma_{2,4}}{2}\rho_{14} \\ 0 & \Gamma_{2,3}\rho_{33} + \Gamma_{2,4}\rho_{44} & -\frac{\Gamma_{1,3}+\Gamma_{2,3}}{2}\rho_{23} & -\frac{\Gamma_{1,4}+\Gamma_{2,4}}{2}\rho_{24} \\ -\frac{\Gamma_{1,3}+\Gamma_{2,3}}{2}\rho_{31} & -\frac{\Gamma_{1,3}+\Gamma_{2,3}}{2}\rho_{32} & -\Gamma_{1,3}\rho_{33} + \Gamma_{2,3}\rho_{33} & -\frac{\Gamma_{1,3}+\Gamma_{2,3}+\Gamma_{1,4}+\Gamma_{2,4}}{2}\rho_{34} \\ -\frac{\Gamma_{1,4}+\Gamma_{2,4}}{2}\rho_{41} & -\frac{\Gamma_{1,4}+\Gamma_{2,4}}{2}\rho_{42} & -\frac{\Gamma_{1,3}+\Gamma_{2,3}+\Gamma_{1,4}+\Gamma_{2,4}}{2}\rho_{43} & -\Gamma_{1,4}\rho_{44} - \Gamma_{2,4}\rho_{44} \end{pmatrix}, \quad (\text{A1})$$

and the relaxation term is

$$\hat{R} = -\gamma \left[\hat{\rho} - \text{diag}\left(\frac{1}{2}, \frac{1}{2}, 0, 0\right) \right] - \gamma_{\text{deph}} [\hat{\rho} - \text{diag}(\rho_{11}, \rho_{22}, \rho_{33}, \rho_{44})]. \quad (\text{A2})$$

Optical Bloch equations are

$$\dot{\rho}_{11} = \gamma \left(\frac{1}{2} - \rho_{11} \right) + \Gamma_{1,3}\rho_{33} + \Gamma_{1,4}\rho_{44} + \frac{i}{\hbar} (E_d^{(+)*} d\rho_{31} - E_d^{(+)} d\rho_{13} + E_c^{(+)*} d\rho_{41} - E_c^{(+)} d\rho_{14}), \quad (\text{A3a})$$

$$\dot{\rho}_{22} = \gamma \left(\frac{1}{2} - \rho_{22} \right) + \Gamma_{2,3}\rho_{33} + \Gamma_{2,4}\rho_{44} + \frac{i}{\hbar} (E_p^{(+)*} d\rho_{32} - E_p^{(+)} d\rho_{23} + E_d^{(+)*} d\rho_{42} - E_d^{(+)} d\rho_{24}), \quad (\text{A3b})$$

$$\dot{\rho}_{33} = -\rho_{33}\gamma - \Gamma_{3}\rho_{33} + \frac{i}{\hbar} (E_d^{(+)} d\rho_{13} - E_d^{(+)*} d\rho_{31} + E_p^{(+)} d\rho_{23} - E_p^{(+)*} d\rho_{32}), \quad (\text{A3c})$$

$$\dot{\rho}_{44} = -\rho_{44}\gamma - \Gamma_{4}\rho_{44} + \frac{i}{\hbar} (E_c^{(+)} d\rho_{14} - E_c^{(+)*} d\rho_{41} + E_d^{(+)} d\rho_{24} - E_d^{(+)*} d\rho_{42}), \quad (\text{A3d})$$

$$\dot{\rho}_{12} = -(\gamma + \gamma_{\text{deph}} + i\Delta_{132})\rho_{12} + \frac{i}{\hbar} (E_d^{(+)*} d\rho_{32} - e^{iz\Delta k} E_d^{(+)} d\rho_{14} + e^{iz\Delta k} E_c^{(+)*} d\rho_{42} - E_p^{(+)} d\rho_{13}), \quad (\text{A3e})$$

$$\dot{\rho}_{13} = -\left(\gamma + \gamma_{\text{deph}} + \frac{\Gamma_3}{2} + i\Delta_{13} \right) \rho_{13} + \frac{i}{\hbar} (E_d^{(+)*} d\rho_{33} - E_d^{(+)*} d\rho_{11} + E_c^{(+)*} d\rho_{43} - E_p^{(+)*} d\rho_{12}), \quad (\text{A3f})$$

$$\dot{\rho}_{14} = -\left(\gamma + \gamma_{\text{deph}} + \frac{\Gamma_4}{2} + i\Delta_{1324} \right) \rho_{14} + \frac{i}{\hbar} (E_d^{(+)*} d\rho_{34} - e^{-iz\Delta k} E_d^{(+)*} d\rho_{12} + E_c^{(+)*} d\rho_{44} - E_c^{(+)*} d\rho_{11}), \quad (\text{A3g})$$

$$\dot{\rho}_{23} = -\left(\gamma + \gamma_{\text{deph}} + \frac{\Gamma_3}{2} + i\Delta_{13} \right) \rho_{23} + \frac{i}{\hbar} (E_p^{(+)*} d\rho_{33} - E_d^{(+)*} d\rho_{21} + e^{-iz\Delta k} E_d^{(+)*} d\rho_{43} - E_c^{(+)*} d\rho_{22}), \quad (\text{A3h})$$

$$\dot{\rho}_{24} = -\left(\gamma + \gamma_{\text{deph}} + \frac{\Gamma_4}{2} + i\Delta_{1324} \right) \rho_{24} + \frac{i}{\hbar} (E_d^{(+)*} d\rho_{44} - E_d^{(+)*} d\rho_{22} + e^{iz\Delta k} E_p^{(+)*} d\rho_{34} - e^{iz\Delta k} E_c^{(+)*} d\rho_{21}), \quad (\text{A3i})$$

$$\dot{\rho}_{34} = -\left(\gamma + \gamma_{\text{deph}} + \frac{\Gamma_3}{2} + \frac{\Gamma_4}{2} + i\Delta_{1324} - i\Delta_{13} \right) \rho_{34} + \frac{i}{\hbar} (E_d^{(+)} d\rho_{14} - e^{-iz\Delta k} E_d^{(+)*} d\rho_{32} + e^{iz\Delta k} E_p^{(+)} d\rho_{24} - E_c^{(+)*} d\rho_{31}). \quad (\text{A3j})$$

Here Δk is the phase mismatch defined as $\Delta k = 2k_d - k_p - k_c$, where k_d is the pump wave vector. $\Gamma_{i,j}$ is the decay rate from level j to level i , while $\Gamma_i = \Gamma_{i,1} + \Gamma_{i,2}$. $\gamma = 10^5$ Hz is spontaneous decay from the excited state, and $\gamma_{\text{deph}} = 0$ is the dephasing rate.

-
- [1] L. M. Duan, M. D. Lukin, J. I. Cirac, and P. Zoller, *Nature (London)* **414**, 413 (2001).
[2] C. Shu, P. Chen, T. K. A. Chow, L. Zhu, Y. Xiao, M. Loy, and S. Du, *Nat. Commun.* **7**, 12783 (2016).
[3] R. C. Pooser, A. M. Marino, V. Boyer, K. M. Jones, and P. D. Lett, *Phys. Rev. Lett.* **103**, 010501 (2009).
[4] V. Boyer, C. F. McCormick, E. Arimondo, and P. D. Lett, *Phys. Rev. Lett.* **99**, 143601 (2007).
[5] J. Okuma, N. Hayashi, A. Fujisawa, and M. Mitsunaga, *Opt. Lett.* **34**, 1654 (2009).
[6] Y. Wu and X. Yang, *Phys. Rev. A* **70**, 053818 (2004).
[7] J. Wu, Y. Liu, D. S. Ding, Z. Y. Zhou, B.-S. Shi, and G.-C. Guo, *Phys. Rev. A* **87**, 013845 (2013).
[8] R. M. Camacho, P. K. Vudyasetu, and J. C. Howell, *Nat. Photon.* **3**, 103 (2009).
[9] A. Eilam, A. D. Wilson-Gordon, and H. Friedmann, *Opt. Lett.* **33**, 1605 (2008).

- [10] D. S. Ding, Z. Y. Zhou, B. S. Shi, X. B. Zou, and G. C. Guo, *Opt. Express* **20**, 11433 (2012).
- [11] A. Leszczyński, M. Parniak, and W. Wasilewski, *Opt. Express* **25**, 284 (2017).
- [12] K. I. Harada, K. Mori, J. Okuma, N. Hayashi, and M. Mitsunaga, *Phys. Rev. A* **78**, 013809 (2008).
- [13] K. I. Harada, T. Kanbashi, M. Mitsunaga, and K. Motomura, *Phys. Rev. A* **73**, 013807 (2006).
- [14] C. F. McCormick, V. Boyer, E. Arimondo, and P. D. Lett, *Opt. Lett.* **32**, 178 (2007).
- [15] M. T. Turnbull, P. G. Petrov, C. S. Embrey, A. M. Marino, and V. Boyer, *Phys. Rev. A* **88**, 033845 (2013).
- [16] C. F. McCormick, A. M. Marino, V. Boyer, and P. D. Lett, *Phys. Rev. A* **78**, 043816 (2008).
- [17] Q. Glorieux, L. Guidoni, S. Guibal, J. P. Likforman, and T. Coudreau, *Phys. Rev. A* **84**, 053826 (2011).
- [18] M. Jasperse, L. D. Turner, and R. E. Scholten, *Opt. Express* **19**, 3765 (2011).
- [19] M. Guo, H. Zhou, D. Wang, J. Gao, J. Zhang, and S. Zhu, *Phys. Rev. A* **89**, 033813 (2014).
- [20] V. Boyer, A. M. Marino, R. C. Pooser, and P. D. Lett, *Science* **321**, 544 (2008).
- [21] A. M. Marino, R. C. Pooser, V. Boyer, and P. D. Lett, *Nature (London)* **457**, 859 (2009).
- [22] S. L. Braunstein and P. van Loock, *Rev. Mod. Phys.* **77**, 513 (2005).
- [23] A. Gaeta, M. Gruneisen, and R. Boyd, *IEEE J. Quantum Electron.* **22**, 1095 (1986).
- [24] M. D. Lukin, P. R. Hemmer, M. Löffler, and M. O. Scully, *Phys. Rev. Lett.* **81**, 2675 (1998).
- [25] Q. Glorieux, R. Dubessy, S. Guibal, L. Guidoni, J. P. Likforman, T. Coudreau, and E. Arimondo, *Phys. Rev. A* **82**, 033819 (2010).
- [26] G. S. Agarwal, *Phys. Rev. A* **34**, 4055 (1986).
- [27] P. Kolchin, *Phys. Rev. A* **75**, 033814 (2007).
- [28] B. Ai, D. S. Glassner, R. J. Knize, and J. P. Partanen, *Appl. Phys. Lett.* **64**, 951 (1994).
- [29] R. C. Pooser, A. M. Marino, V. Boyer, K. M. Jones, and P. D. Lett, *Opt. Express* **17**, 16722 (2009).
- [30] Z. Qin, J. Jing, J. Zhou, C. Liu, R. C. Pooser, Z. Zhou, and W. Zhang, *Opt. Lett.* **37**, 3141 (2012).
- [31] G. Adenier, D. Calonico, S. Micalizio, N. Samantaray, I. Degiovanni, and I. R. Berchera, *Int. J. Quantum Inform.* **14**, 1640014 (2016).
- [32] W. V. Davis, M. Kauranen, E. M. Nagasako, R. J. Gehr, A. L. Gaeta, R. W. Boyd, and G. S. Agarwal, *Phys. Rev. A* **51**, 4152 (1995).
- [33] B. Zlatković, A. J. Krmpot, N. Šibalić, M. Radonjić, and B. M. Jelenković, *Laser Phys. Lett.* **13**, 015205 (2016).
- [34] J. A. Kleinfeld and A. D. Streater, *Phys. Rev. A* **53**, 1839 (1996).
- [35] D. S. Glassner and R. J. Knize, *Appl. Phys. Lett.* **66**, 1593 (1995).
- [36] M. Katharakis, N. Merlemis, A. Serafetinides, and T. Efthimiopoulos, *J. Phys. B* **35**, 4969 (2002).
- [37] M. Y. Lanzerotti, R. W. Schirmer, and A. L. Gaeta, *Appl. Phys. Lett.* **69**, 1199 (1996).
- [38] J. D. Swaim and R. T. Glasser, *Phys. Rev. A* **96**, 033818 (2017).
- [39] D. A. Steck, Quantum and Atom Optics, <http://steck.us/teaching> (revision 0.12.0, 16 May 2017).
- [40] D. McKay, Potassium $5p$ line data, http://fermionlattice.wdfiles.com/local-files/papers/5P_structure, 2009.



NIR photo-driven upconversion in NaYF₄:Yb,Er/PLGA particles for *in vitro* bioimaging of cancer cells

Lidija Mancic^{a,*}, Aleksandra Djukic-Vukovic^b, Ivana Dinic^c, Marko G. Nikolic^d, Mihailo D. Rabasovic^d, Aleksandar J. Krmpot^d, Antonio M.L.M. Costa^e, Dijana Trisic^f, Milos Lazarevic^g, Ljiljana Mojovic^b, Olivera Milosevic^a

^a Institute of Technical Sciences of the Serbian Academy of Sciences and Arts, Belgrade, Serbia

^b Department of Biochemical Engineering and Biotechnology, Faculty of Technology and Metallurgy, University of Belgrade, Serbia

^c Innovation Center of the Faculty of Chemistry, University of Belgrade, Serbia

^d Photonic Center, Institute of Physics Belgrade, University of Belgrade, Zemun, Belgrade, Serbia

^e Department of Chemical and Materials Engineering, Pontifical Catholic University of Rio de Janeiro, Rio de Janeiro, Brazil

^f Clinic for Pediatric and Preventive Dentistry, School of Dental Medicine, University of Belgrade, Serbia

^g Institute of Human Genetics, School of Dental Medicine, University of Belgrade, Serbia

ARTICLE INFO

Keywords:

Upconversion nanoparticles

PLGA

NaYF₄:Yb,Er

Bioimaging

Cancer cell

Human gingival cell

ABSTRACT

Lanthanide-doped fluoride up-converting nanoparticles (UCNPs) represent the new class of imaging contrast agents which hold great potential for overcoming existing problems associated with traditionally used dyes, proteins and quantum dots. In this study, a new kind of hybrid NaYF₄:Yb,Er/PLGA nanoparticles for efficient biolabeling were prepared through one-pot solvothermal synthesis route. Morphological and structural characteristics of the as-designed particles were obtained using X-ray powder diffraction (XRPD), scanning and transmission electron microscopy (SEM/TEM), energy dispersive spectroscopy (EDS), Fourier transform infrared (FTIR) and photoluminescence (PL) spectroscopy, while their cytotoxicity as well as up-conversion (UC) labeling capability were tested *in vitro* toward human gingival cells (HGC) and oral squamous cell carcinoma (OSCC). The results revealed coexistence of the cubic (*Fm-3m*) and hexagonal (*P6₃/m*) phase in spherical and irregularly shaped nanoparticles, respectively. PLGA [Poly(lactic-co-glycolic acid)] ligands attached at the surface of UCNPs particles provide their enhanced cellular uptake and enable high-quality cells imaging through a near-infrared (NIR) laser scanning microscopy ($\lambda_{\text{ex}} = 980 \text{ nm}$). Moreover, the fact that NaYF₄:Yb,Er/PLGA UCNPs show low cytotoxicity against HGC over the whole concentration range (10–50 $\mu\text{g/mL}$) while a dose dependent viability of OSCC is obtained indicates that these might be a promising candidates for targeted cancer cell therapy.

1. Introduction

Head and neck cancers represent the sixth most common cancer worldwide, with the highest incidence rates in Melanesia, South-Central Asia and Central and Eastern Europe [1]. Among them, oral squamous cell carcinoma (OSCC) is the most common malignant epithelial neoplasm affecting the oral cavity. The incidence of oral cavity cancer appearance is higher in males and as the major risk factors are considered smoking, alcohol use, smokeless tobacco use and human papillomavirus (HPV). Early stages of disease are asymptomatic and very similar to other mucosal diseases and if diagnosed at advanced stages result with a 5-year survival rate of around 50%. Fatal outcomes are mostly caused by local recurrence and neck lymph node metastasis [2]. Therefore, advancements in both, early diagnosis and therapy, are

necessary and most likely will come from innovative non-invasive selective optical techniques [3]. Among the various optical diagnostic methods, fluorescence imaging is of immense importance since that provides accurate visualization of the molecular and functional processes in the human body [4].

Moreover, with the current progress in designing of the new hybrid multifunctional lanthanide-doped up-conversion nanoparticles (UCNPs) whose excitation/emission falls into the biological tissue transparency window, superior optical diagnostic and targeted drug delivery is expectable in the near future [5, 6]. Due to efficient two-phonon excitation and the large anti-Stokes shift UCNPs are able to emit visible or UV photons under excitation by near-infrared (NIR) light, to achieve deeper tissue penetration, and to exhibit higher photochemical stability in comparison with a traditionally used fluorophores [7]. The

* Corresponding author.

E-mail address: lidija.mancic@itn.sanu.ac.rs (L. Mancic).

effectiveness of these materials is principally dependent on the crystal structure and phonon energy of a host matrix, as well as, on the choice and concentration of lanthanide dopants. Efficient lanthanide pairs which can easily upconvert low energy photons into higher ones comprise ytterbium (Yb^{3+}) as a sensitizer and erbium (Er^{3+}), thulium (Tm^{3+}) or holmium (Ho^{3+}) as activator. The rich energy levels and long-lived intermediate excited states of activators provide various energy transfer pathways for UC emissions in visible spectra. Following initial Yb^{3+} excitation by 980 nm laser, energy transfer upconversion (ETU), excited state absorption (ESA), photon avalanche (PA), cooperative energy transfer (CET) and cross-relaxation (CR) processes take place determining resulting fluorescence efficiency of UCNP [8]. Among many compounds, fluoride based cubic or hexagonal crystal lattices of NaYF_4 phase have been extensively studied as the most efficient hosts because of their low phonon energy (i.e., 350 cm^{-1}), which minimize harmful non-radiative relaxations, and high optical transparency necessary for migration of NIR photons. In particular, hexagonal phase exhibits approximately one order of magnitude higher UC emission in comparison to cubic counterpart since it possess a higher degree of asymmetry, multisite occupation with lanthanide dopant ions and shorter distance among them. Since that particle size also affects the luminescence efficiency (higher energy transfer loss is attributed to the higher density of the surface defects) different synthesis strategies were developed to highlight tailored performances of specially designed core-shell, hybrid and composite UCNP for cell imaging and tracking, drug delivery, photodynamic therapy and target recognition of bio-species [9, 10]. Although showing remarkable characteristics during both *in vitro* and *in vivo* investigations studied structures were usually obtain through complex multi-steps procedure which involves decomposition of organometallic compounds in oleic acid and subsequent ligand exchange (or oxidation, coating, intercalation, etc.). Usage of toxic and hazardous substances during synthesis raised deep concerns regarding potential toxicity of synthesized UCNP [11–13]. Recently, it was shown that such obtained UCNP could regain their cytotoxicity upon interaction with cells if weakly coordinated surface groups are used to render them biocompatible after synthesis [14]. Thus, the safe biological application of UCNP implies establishing of facile and reliable procedure which would minimize the usage of toxic solvents and provide hydrophilic reactive surface *in situ* toward enhanced conjugation of proteins and drugs. One-pot polymer assisted hydrothermal approach, originally reported by Wang et al. [15] is a simple procedure which enables direct synthesis of water-dispersible UCNP. To date, it was used for *in situ* functionalization of UCNP surface with a wide range of biocompatible capping ligands, including carboxylic and amine/imine groups of polymers, such as: polyethylenimine (PEI), polyacrylic acid (PAA), polyvinylpyrrolidone (PVP) and polyethylene glycol (PEG) [16–18]. Among others, we have also shown that PVP-, PEG- and EDTA-assisted hydro/solvothermal route, performed in a controlled manner, led to the generation of hydrophilic/biocompatible upconverting particles with a different shape (spherical, rod, prisms, octahedron and desert-rose) [19, 20]. Here, we reported for the first time usages of poly(lactic-co-glycolic acid) (PLGA) during solvothermal synthesis of $\text{NaYF}_4:\text{Yb}/\text{Er}$ nanoparticles. PLGA, approved by the United States Food and Drug Administration and European Medicine Agency for pharmaceutical application and human use, is one of the most widely utilized biodegradable polymer with a minimal toxicity associated with its use as scaffolds for tissue engineering or for delivery of macromolecular therapeutics [21–23]. For example, PLGA nanoparticles have been proposed as a delivery medium of an amphiphilic Gd^{3+} complex developed for the need of high sensitive magnetic resonance imaging (MRI) and imaging guided drug delivery applications [24]. Similarly, it was shown that pH-responsive PLGA(UCNP/doxorubicin hydrochloride) nanocapsules obtained through self-assembly strategy could act as T1-weighted contrast agents MRI, cell imaging label and effective chemotherapy drug delivery system [25]. Due to fact that PLGA comprises both, hydrophilic and hydrophobic moiety, it was

usually used in combination with PEG in the form of amphiphilic block-copolymer for posterior UCNP coating via flash nanoprecipitation. PEG-PLGA layer formed in such way provides excellent UCNP colloidal stability in deionized water, buffers and serum media, but in the case of a thicker layer formation decrease of the upconversion luminescence was observed [26]. Recently, fabrication of a multifunctional nanovector for simultaneous gene delivery and real-time intracellular tracking based on UCNP modified by positively charged amphiphilic polymer and PEG-PLGA copolymer was reported [27]. In accordance to the literature, PLGA solely was used, up to date, only for coating of the bare UCNP through intercalation process, but obtained biocompatible particles sized around 250 nm exhibited negligible cellular uptake and mild cytotoxicity (cellular viability of about 80%) when applied at concentration of $62.5 \mu\text{g}/\text{mL}$ to the human keratinocyte and fibroblast cells [28].

In this study, a new kind of hybrid $\text{NaYF}_4:\text{Yb},\text{Er}/\text{PLGA}$ nanoparticles for efficient cell labeling was prepared through one-pot solvothermal synthesis using non-toxic reagents. Hence, PLGA functional groups attached *in situ* to the UCNP surface ensure excellent biocompatibility without compromising upconverting process. Furthermore, $\text{NaYF}_4:\text{Yb},\text{Er}/\text{PLGA}$ UCNP demonstrated dose-dependent cytotoxicity against oral squamous cell carcinoma (OSCC) without damaging healthy non-cancerous human gingival cells (HGC), so could be considered as promising and reasonably safe candidate for theranostic.

2. Materials and methods

2.1. Synthesis and characterization of $\text{NaYF}_4:\text{Yb},\text{Er}/\text{PLGA}$ UCNP

All of the chemicals used for PLGA mediated solvothermal synthesis of $\text{NaY}_{0.8}\text{Yb}_{0.17}\text{Er}_{0.03}\text{F}_4$ were purchased from Sigma-Aldrich. Deionized water was used throughout. Defined stoichiometric amounts of rare earth nitrates (5 mmol in total) were dissolved in 15 ml of deionized water and then mixed with 5 ml of NaF solution (1.75-fold excess) and 0.1 g of PLGA (lactide:glycolide, 75:25; Mr. 66,000–107,000) dissolved in 40 ml of acetone. Obtained mixture was stirred for 15 min, transferred to 100 ml Teflon lined autoclave and sealed. Since that PLGA is thermally stable until $250 \text{ }^\circ\text{C}$ under atmospheric pressure [29] synthesis was carried out at twice lower temperature of $120 \text{ }^\circ\text{C}$ with a continual stirring (100 rpm) for 24 h. After cooling, the as-prepared $\text{NaYF}_4:\text{Yb},\text{Er}/\text{PLGA}$ UCNP were washed with acetone by centrifuging (8000 rpm, 10 min) and dried at $80 \text{ }^\circ\text{C}$ for 3 h.

The $\text{NaYF}_4:\text{Yb},\text{Er}/\text{PLGA}$ UCNP were characterized by the X-ray powder diffraction (XRPD) using Bruker D8 Discovery equipped with a Cu-K α source ($\lambda = 1.5406 \text{ \AA}$). The pattern was recorded with a step scan of 0.02° and accounting time of 5 s per step. Powders microstructural data were acquired through combined La Bail and Rietveld refinement in Topas 4.2 software. For cubic α - and hexagonal β - NaYF_4 phase refinements were carried out in *Fm-3m* (No. 225) and *P63/m* (No. 176) space groups, respectively. The morphological features of the as-prepared particles were investigated by means of both, scanning and transmission electron microscopy (JEOL JSM-6701F SEM and JEOL JEM 2010 TEM operating at 200 kV at phase contrast and selected area electron diffraction (SAED) modes) coupled with energy dispersive spectroscopy (EDS). For the aforementioned analyses the particles were suspended in isopropyl alcohol and dropped directly on the stub (for SEM) or on lacey carbon film supported on a Cu grid after 20 min sonication (for TEM). The SemAfore 5.21 JEOL software was used to construct particle size distribution diagrams, while Fourier processing of high resolution TEM images was performed with Digital Micrograph 3.7.4 Gatan Inc. software. Detection of the PLGA ligands on the particles surface was done by Fourier transform infrared spectroscopy (FTIR) using Thermo Scientific Nicolet 6700 spectrophotometer (Thermo Fisher Scientific) with a Smart iTR Diamond Attenuated Total Reflectance accessory. Spectra were recorded using typically 128 scans at the resolution of 4 cm^{-1} . Dynamic light scattering measurements of

the UCNPs hydrodynamic radius (R_H) were performed on a Malvern Zetasizer Nano ZS in the de-ionized water and medium used for testing of the cell viability and imaging. For that purpose, $\text{NaYF}_4\text{:Yb,Er/PLGA}$ UCNPs were dispersed at the concentration of 1 mg/ml and passed through a 0.45 μm cellulose syringe filter before DLS measurements. Photoluminescence emission measurement was performed at room temperature using Spex Fluorolog with C31034 cooled photomultiplier under diode laser excitation at 980 nm. From obtained spectrum the chromaticity coordinate calculation was done.

2.2. OSCC and HGC cultures

Human tumor and healthy gingival tissues were obtained from the patients at the Clinic of Maxillofacial Surgery of School of Dental Medicine, University of Belgrade immediately after the surgery, with signed informed consent approval from each patient prior to study participation. The planning experiments were approved by the Ethical Committee of the School of Dental Medicine (36/31), University of Belgrade.

Tumor tissues were oral squamous cell carcinoma (OSCC) of a tongue. Preparation of the cell cultures was performed using slightly modified procedure of Pozzi et al. [30]. Dulbecco's Modified Eagle Medium (DMEM) supplemented with 20% fetal bovine serum (FBS) and 100 U/ml penicillin-streptomycin seeded onto T25 cell culture flasks. The cells were maintained at 37 °C in humidified atmosphere containing 5% CO_2 . The medium was changed every 2–3 days and the cells were passaged prior to reaching 80% confluence. To avoid fibroblast contamination in cultures, brief exposure to TrypLE Express (Thermo Fisher Scientific, Waltham, USA) was used. OSCC used for the present study were obtained after the third passage.

Human gingival tissues were obtained from three different, healthy patients, aged 19–25 years, during extraction of the impacted third molar. The gingival tissue was transported in Gibco Dulbecco's modified Eagle's F12 medium (D-MEM/F12; Thermo Fisher Scientific), supplemented with 20% FBS and 1% antibiotic/antimycotic (ABAM; Thermo Fisher Scientific) solution. The gingival tissue was rinsed in phosphate-buffered saline (PBS) from Sigma-Aldrich (St. Louis, USA) and subjected to outgrowth isolation method. Tissue was minced into approximately 1 mm^2 fragments, and placed in 25- cm^2 culture flasks with DMEM/F12 supplemented with 10% FBS and 1% ABAM, and incubated at 37 °C in 5% CO_2 . The cells were allowed to reach 80% confluence prior to passage. The culture medium was changed every 2–3 days. HGC after the second passage were used in this study.

2.3. MTT assay

For assessment of cytotoxicity, $\text{NaYF}_4\text{:Yb,Er/PLGA}$ UCNPs suspensions with three different concentrations (10, 25 and 50 $\mu\text{g/ml}$) were prepared. For each concentration, adequate mass of $\text{NaYF}_4\text{:Yb,Er/PLGA}$ UCNPs was aseptically weighed and suspended in sterile water, shaken vigorously and sonicated for 3 min. OSCC and HGC were seeded in a 96-well plate (10,000 cells per well) and incubated at 37 °C in humidified 5% CO_2 atmosphere. After 24 h hours 100 μl of the $\text{NaYF}_4\text{:Yb,Er/PLGA}$ UCNPs were added (10, 25 or 50 $\mu\text{g/ml}$) in each plate. Incubation with the cell cultures was stopped after 24 h by discarding of spent media, and medium containing 3-(4,5-dimethylthiazol-2-yl)-2,5 diphenyltetrazolium bromide (MTT, 0.5 mg/ml) (Sigma-Aldrich, St. Louis, USA) was added to each well and then incubated for additional 4 h, as previous described by Castiglioni et al. [31]. The supernatant was discarded and formazan crystals were dissolved in 100 μl dimethyl sulfoxide (DMSO) (Sigma-Aldrich, St. Louis, USA) by shaking in duration of 20 min at 37 °C. Optical density was measured at 540 nm using ELISA

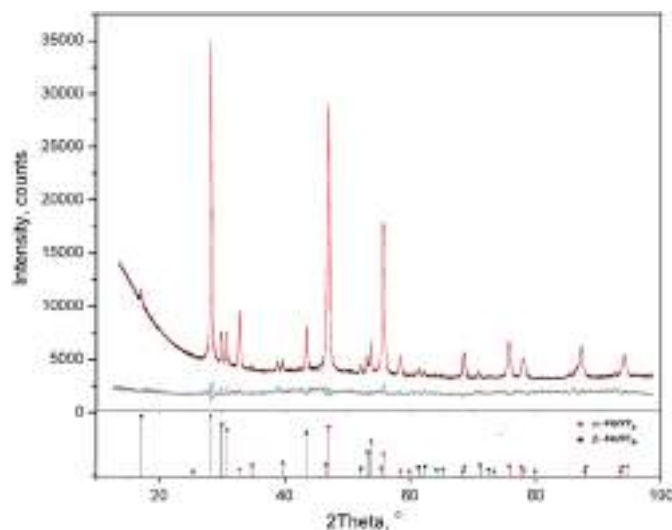


Fig. 1. XRPD pattern of $\text{NaYF}_4\text{:Yb,Er/PLGA}$ UCNPs (black), refined structure (red) and difference curve (gray); Standard patterns of cubic (PDF 01-077-2042) and hexagonal (PDF 01-016-0334) NaYF_4 phase are given as bottom bar line diagram. (For interpretation of the references to color in this figure legend, the reader is referred to the web version of this article.)

microplate reader (Enzyme-linked immunosorbent assay) RT-2100c, Rayto, China). Three wells without $\text{NaYF}_4\text{:Yb,Er/PLGA}$ UCNPs were used as a control group.

2.4. Statistical analysis

According to the cytotoxicity test procedure, the experiments were performed in triplicate and repeated three times in the independent experiments. Cells viability, expressed by the ratio of absorbance of the cells incubated with UCNPs to that of the cells incubated with culture medium only, were given in diagram as the mean \pm standard deviation (SD).

2.5. Cells imaging by laser scanning microscopy

For the visualization of $\text{NaYF}_4\text{:Yb,Er/PLGA}$ UCNPs uptake, the lowest concentration of $\text{NaYF}_4\text{:Yb,Er/PLGA}$ UCNPs suspension (10 $\mu\text{g/ml}$) was filtered through 0.45 μm syringe filter to separate large agglomerates and to avoid saturation during visualization. Filtered solution was used further for incubation with cells and preparation of samples for laser scanning microscopy. Sterilized 22 mm \times 22 mm glass coverslips were placed in 6-well plates, and 10,000 of OSCC and HGC were seeded per coverslip and incubated at 37 °C in humidified atmosphere containing 5% CO_2 . The next day cells were exposed to $\text{NaYF}_4\text{:Yb,Er/PLGA}$ UCNPs solution and incubated for another 24 h. Coverslips with adherent cells were gently rinsed with PBS twice and fixated with 4% paraformaldehyde (PFA) (Sigma-Aldrich, St. Louis, USA) for 20 min. Residuals of PFA were washed by PBS (3 \times 3 min), coverslips were dried, 10 μl of Mowiol (Sigma-Aldrich, St. Louis, USA) was placed on fixated cells, and coverslips were placed on microscopic slides with cells positioned in between. Samples were stored in a dark until they were observed under confocal microscopy.

The homemade nonlinear laser scanning microscope used in this study was described in detail elsewhere [32]. Ti:Sapphire laser (Coherent, Mira 900-F) was used as a laser light source. It operates in two regimes. The first regime generates femto-second (FS) pulses at 730 nm convenient for unlabeled cell imaging since that enables two photon excitation of auto-fluorescence in cells. Note that two photon excitation here is considered as excitation of the molecule with no intermediate levels between ground and excited state and it is not related to

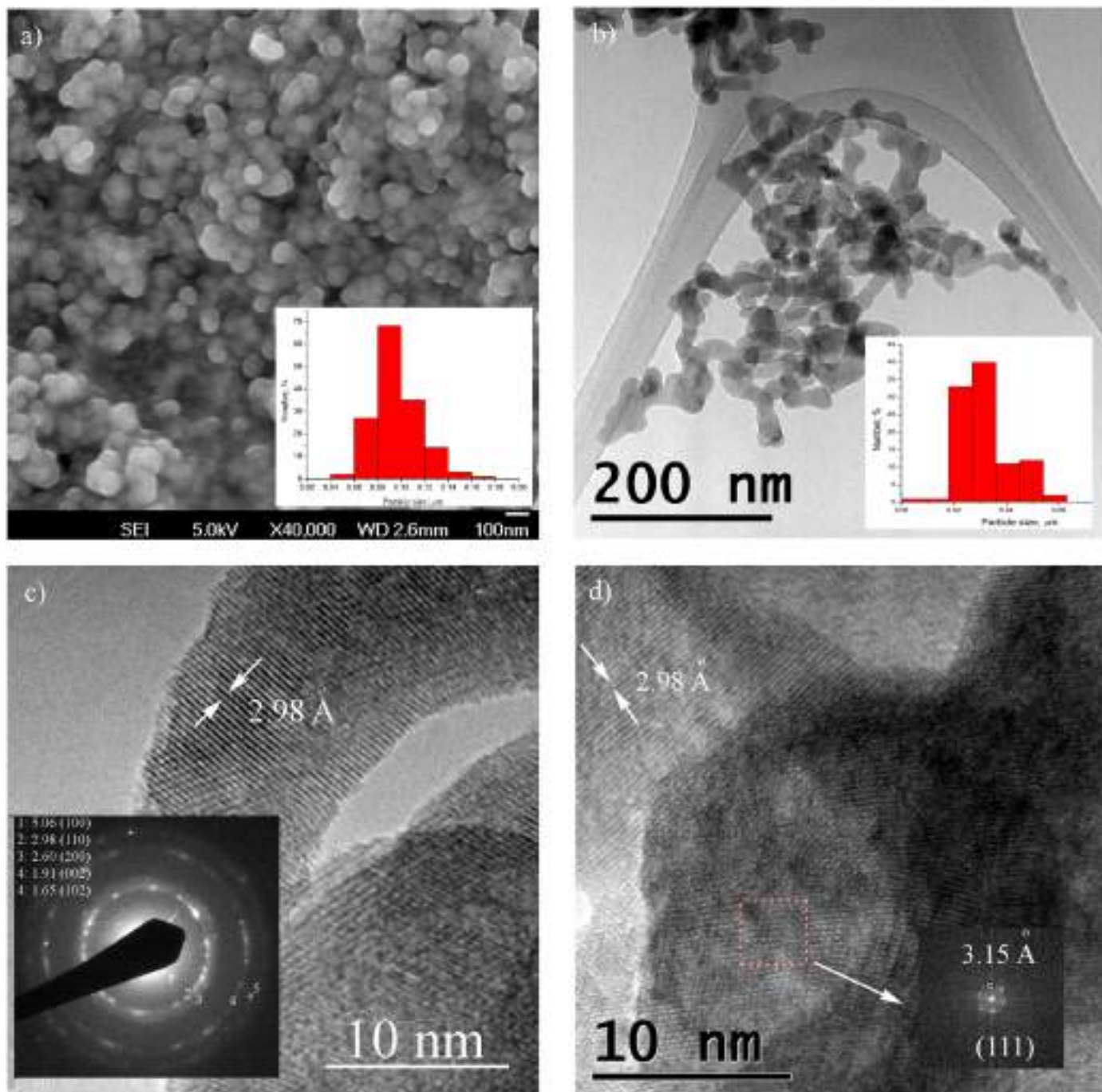


Fig. 2. SEM (a) and TEM (b–d) images of $\text{NaYF}_4:\text{Yb,Er}/\text{PLGA}$ UCNPs. Corresponding particle size distribution histograms are given as insets in a and b; SAED inset in c represents d values of the interplanar spacing of hexagonally crystallized elongated nanoparticles, while FFT (inset in d) confirms cubic crystal cell arrangements in a spherical ones.

upconversion process. The second regime comprises generation of continuous wave (CW) radiation at 980 nm and was used for the excitation of $\text{NaYF}_4:\text{Yb,Er}/\text{PLGA}$ UCNPs in cells. Due to the long UCNPs lifetime, the scanning rate was reduced during imaging in order to extend pixel dwell time. Hence the pixel dwell time was several times longer than fluorescence lifetime. Each fixed cell culture was imaged using Carl Zeiss, EC Plan-NEOFLUAR, 40×1.3 oil immersion objective for laser focusing and collection of the fluorescence. A visible interference filter (415 nm–685 nm) positioned in front of detector is used to remove scattered laser light. Thus, the whole visible range has been detected either for auto-fluorescence from cells or up-conversion from $\text{NaYF}_4:\text{Yb,Er}/\text{PLGA}$ UCNPs in cells.

3. Results and discussion

3.1. Structural and morphological properties of $\text{NaYF}_4:\text{Yb,Er}/\text{PLGA}$ UCNPs

To confirm the composition and the crystallinity of the synthesized $\text{NaYF}_4:\text{Yb,Er}/\text{PLGA}$ UCNPs XRPD analysis was performed. Pattern presented in Fig. 1. reflects that obtained sample is a mixture of well crystallized cubic ($Fm-3m$) and hexagonal ($P63/m$) phase since all of the reflections, i.e. their positions and intensities, are in a good agreement with the reported 01-077-2042 and 01-016-0334 ICDD data, presented as bottom bar line diagram in the same figure. In general, NaYF_4 material has three different polymorphs: low temperature cubic, hexagonal

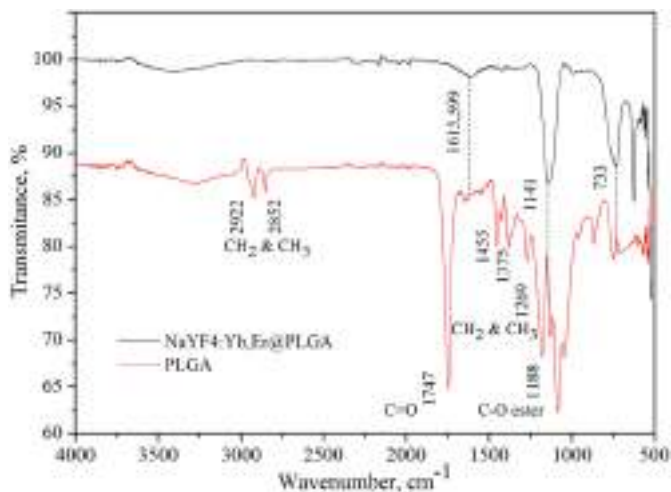


Fig. 3. FTIR of pure PLGA and NaYF₄:Yb,Er/PLGA UCNPs.

and high-temperature cubic – whose structure lacks detailed characterization [33]. In a low- temperature cubic phase (*Fm-3m*) there is only one site coordinated by eight fluoride anions over which Na⁺ and RE³⁺ ions are randomly distributed in the cationic sub-lattice, whereas in the hexagonal (*P63/m*) there are two types of low-symmetry sites at which dopants could be arranged. As it is indicated recently, high-temperature cubic phase could be described with the same space group as a low-temperature one, but with the well-ordered distribution of sodium and RE cations [34]. The unit cell parameters of low-temperature cubic phase and hexagonal one crystallized in the NaYF₄:Yb,Er/PLGA sample were determined from XRPD data to be (Å): a = 5.4764(1); and a = 5.9785(3), c = 3.5088(4); respectively. Since cubic phase prevails in the sample (~85 wt%), refinement of this phase was performed starting from the ICSD 6025 card data. Decreased occupation of the cation site by Na⁺ and Y³⁺ of 0.98(1) and 0.76(1) corresponds well with a nominal compound stoichiometry, while R_{Bragg} value of 1.79 reflects good compliance with the structural model used during refinement. The average crystallite size of 33(1) nm was calculated using volume weighted mean column height broadening

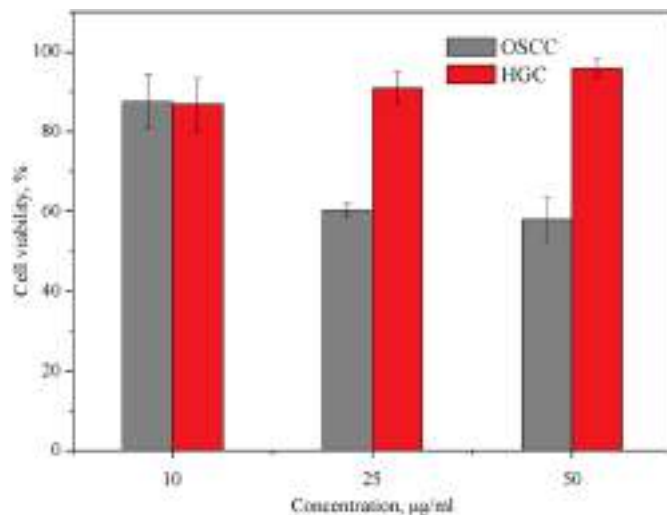


Fig. 5. MTT assay comparing viability of OSCC and HGC incubated with NaYF₄:Yb,Er/PLGA UCNPs for 24 h.

modeled by a Voigt function while Gaussian microstrain distribution was determined to be 0.113(4).

The morphological characteristic of the NaYF₄:Yb,Er/PLGA UCNPs were evaluated based on SEM and TEM analysis, Fig. 2. As presented in Fig. 2a, sample is composed of uniform and well defined spherical particles with average size around 100 nm. Backscattered electron images and EDS chemical analysis (not presented) implied compositional homogeneity and high particles purity. As it is notable from SEM, particles are stick together due to the PLGA presence. TEM analysis revealed existence of smaller nanoparticles with elongated shape and length up to 60 nm, Fig. 2b. The high resolution TEM image presented at Fig. 2c, exposes their good crystallinity, clear lattice fringes and the interplanar spacing of 2.98 Å which might be associated with a (110) plane of hexagonal phase. Furthermore, diffraction pattern via SAED mode presented as inset at the same figure pointed out that all of determined *d* values are consistent with the interplanar spacings of the hexagonal NaYF₄ phase (PDF 01-016-0334) confirming results derived

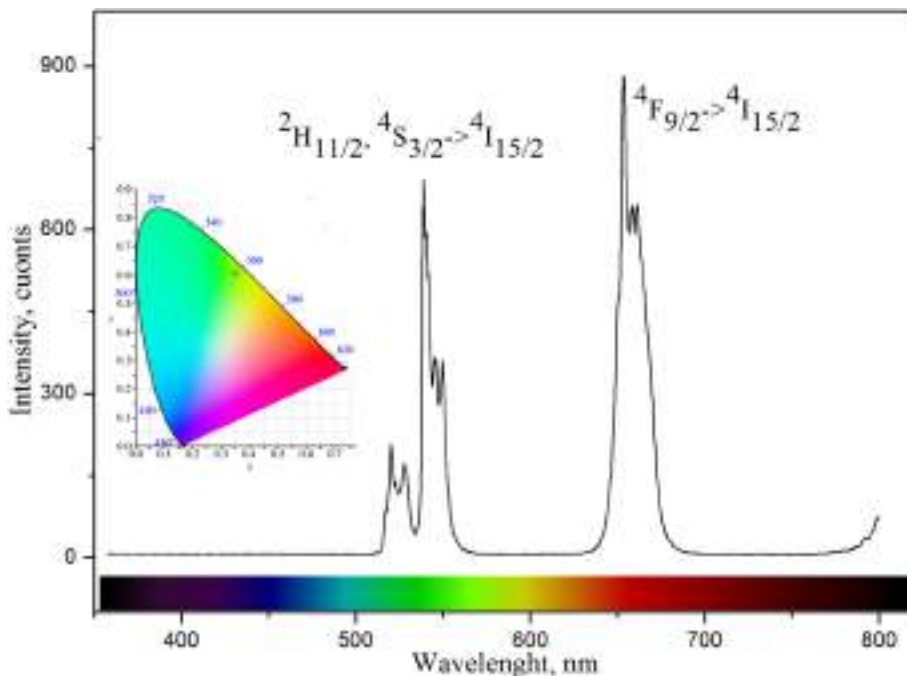


Fig. 4. Up-converted spectrum of NaYF₄:Yb,Er/PLGA UCNPs excited at 980 nm and corresponding CIE diagram (given as inset).

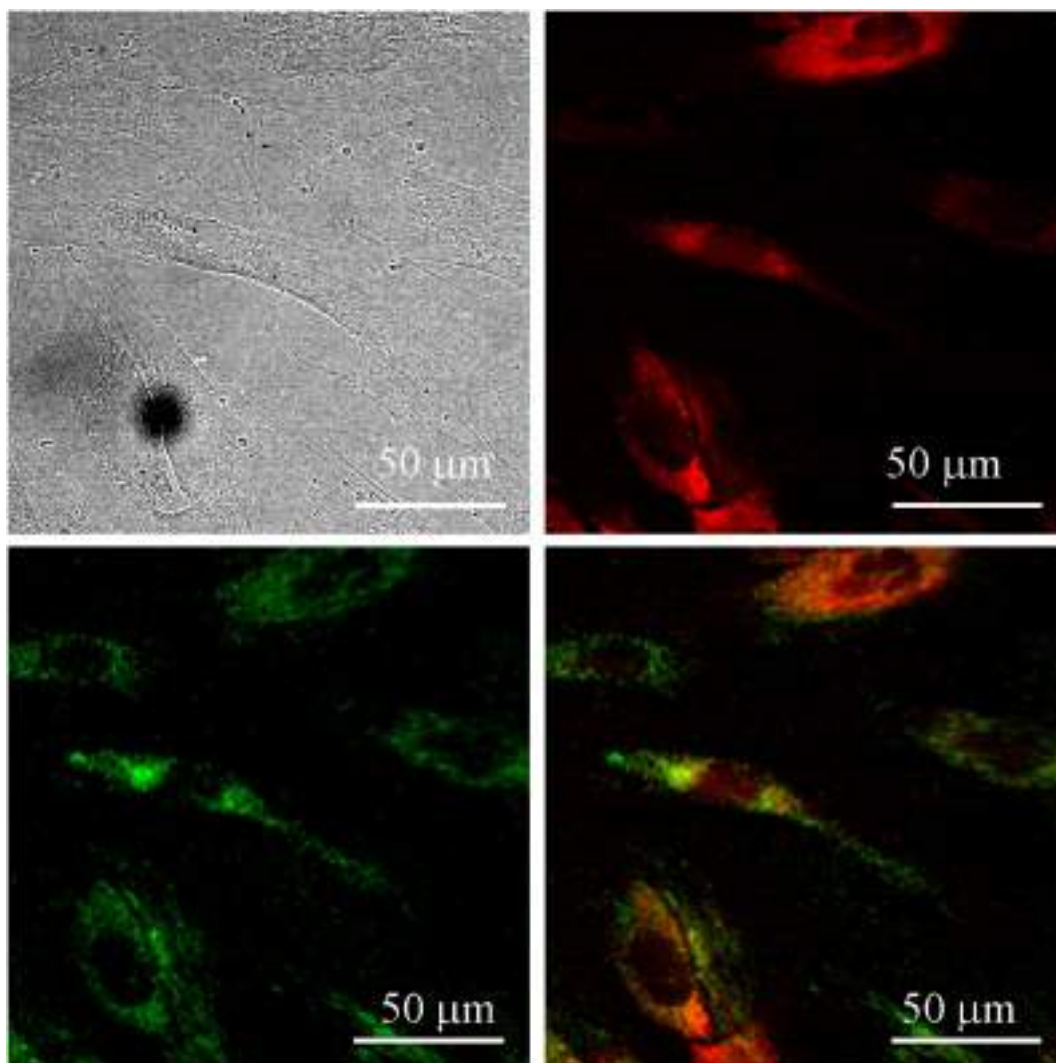


Fig. 6. Images of OSCC following 24 h incubation with 10 $\mu\text{g}/\text{ml}$ of $\text{NaYF}_4:\text{Yb,Er}/\text{PLGA}$: bright field (top-left) and cells auto-fluorescence upon femto-second excitation at 730 nm (top-right), pseudo color image of the $\text{NaYF}_4:\text{Yb,Er}/\text{PLGA}$ UCNPs upon CW excitation at 980 nm (bottom-left) and their positioning in cells, revealed through co-localization of the cell auto-fluorescence and the UCNPs emission (bottom-right). (For interpretation of the references to color in this figure legend, the reader is referred to the web version of this article.)

from XRPD. Cubic NaYF_4 phase was detected in somewhat smaller nanoparticles with a spherical shape, as it is shown in Fig. 2d. Confined growth of NaYF_4 nanocrystals was presumably caused by the interaction between the lanthanide ions and the carboxyl end groups of PLGA, which presence is verified further by FTIR analysis.

Colloidal size, polydispersity index (PDI) and stability of the $\text{NaYF}_4:\text{Yb,Er}/\text{PLGA}$ UCNPs solutions were estimated from dynamic light scattering measurements, Fig. S1. While a monomodal size distribution was obtained in water (due instant agglomeration of the nanoparticles sized below 20 nm), the bimodal one was preserved in a medium over time (24 h). As a result, slightly higher average hydrodynamic diameter (R_{Hav}) of the $\text{NaYF}_4:\text{Yb,Er}/\text{PLGA}$ UCNPs was detected in water (177 nm, PDI 0.32) than in medium (127 nm, PDI 0.31). Minimal changes distinguished after 1 h, confirms good stability of both colloids (195 nm, PDI 0.32; and 127 nm, PDI 0.31; in water and medium, respectively). With prolongation of time, after 24 h, magnitude of the $\text{NaYF}_4:\text{Yb,Er}/\text{PLGA}$ UCNPs R_{Hav} in water increased to 488 nm (PDI 0.3), while stayed unchanged in medium which is further used for cells bioimaging (122 nm, PDI 0.34).

Infrared absorption spectra of pure PLGA and $\text{NaYF}_4:\text{Yb,Er}/\text{PLGA}$ UCNPs were recorded and presented at Fig. 3. Pure PLGA exhibited characteristic absorption bands which are classified in accordance to

the literature [35] as follows: CH_3 and CH_2 asymmetric stretching at 2850 and 2920 cm^{-1} respectively; $\text{C}=\text{O}$ stretching around 1750 cm^{-1} , CH_3 and CH_2 symmetric angular deformation in the 1500–1250 cm^{-1} region and $\text{C}-\text{O}$ ester stretching in the 1300–1150 cm^{-1} region. FTIR analysis of $\text{NaYF}_4:\text{Yb,Er}/\text{PLGA}$ UCNPs revealed a decreased PLGA absorption due to side-chain vibrations as well as low-frequency shifting of its most intense band associated to the $\text{C}=\text{O}$ stretching, which might be due to the carboxylic acid salts formation, $\text{O}=\text{C}-\text{ONa}$, as it was suggested in the literature [36]. This evident that applied synthesis method preserves the highly reactive carboxylic acid groups on UCNPs surface which is very important for their conjugation with biomolecules containing $-\text{NH}_2$ group, like antibodies, streptavidin and DNA, creating in that way carriers with high binding potential for targeted imaging and therapy [13].

3.2. Optical properties of $\text{NaYF}_4:\text{Yb,Er}/\text{PLGA}$ UCNPs

The upconversion spectrum of $\text{NaYF}_4:\text{Yb,Er}/\text{PLGA}$ UCNPs is presented in Fig. 4. Following excitation with 980 nm into the $^2\text{F}_{5/2}$ state of Yb^{3+} and subsequent energy transfer from Yb^{3+} to Er^{3+} ions (and *vice versa*), three distinct Er^{3+} emission bands centered at 520, 539 and 653 nm are clearly observed in the visible part of spectrum. The double

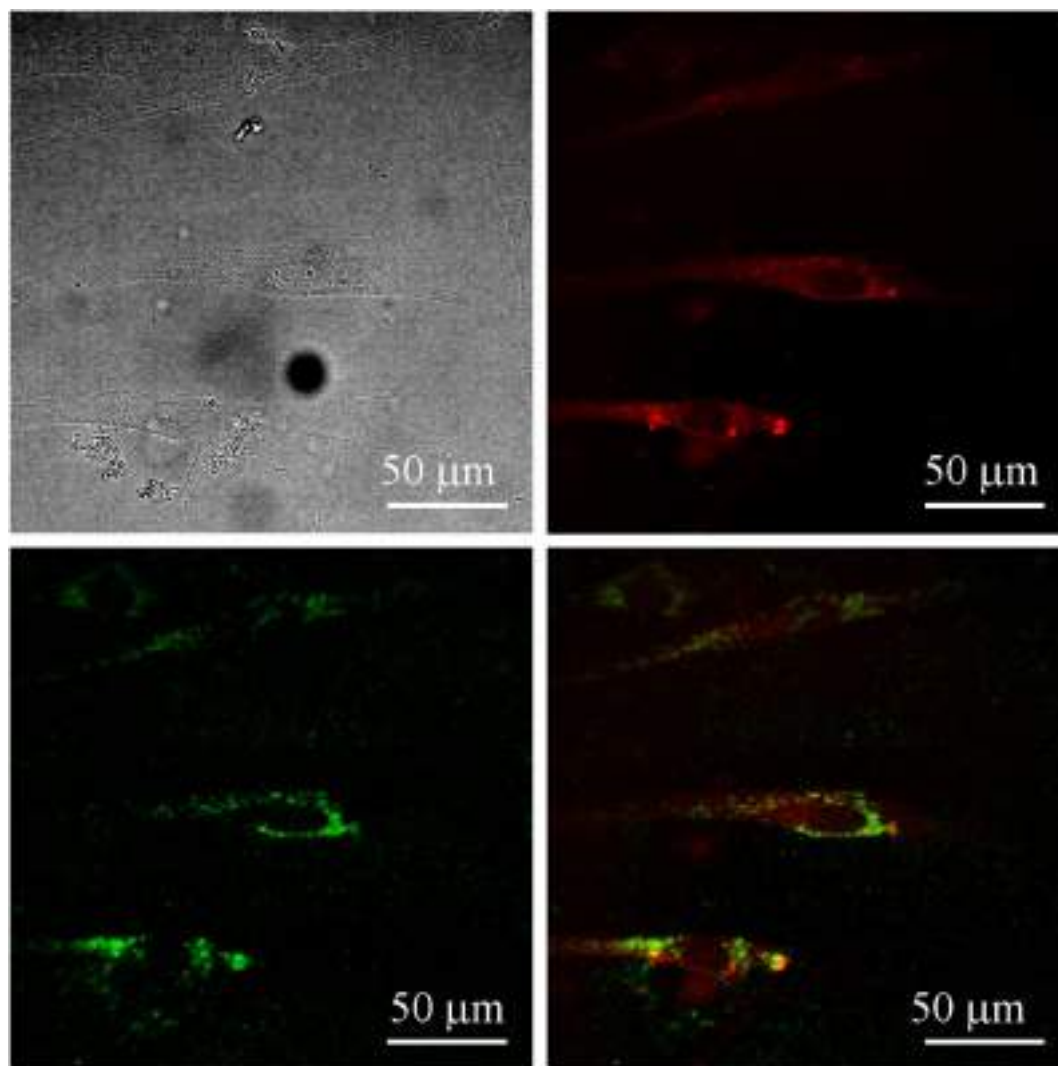


Fig. 7. Images of HGC following 24 h incubation with 10 $\mu\text{g/ml}$ of NaYF₄:Yb,Er/PLGA: bright field (top-left) and cells auto-fluorescence upon femto-second excitation at 730 nm (top-right), pseudo color image of the NaYF₄:Yb,Er/PLGA UCNPs upon CW excitation at 980 nm (bottom-left) and their positioning in cells, revealed through co-localization of the cell auto-fluorescence and the UCNPs emission (bottom-right). (For interpretation of the references to color in this figure legend, the reader is referred to the web version of this article.)

green emissions between 512 and 533 nm and between 533 and 560 nm are attributed to the $^2\text{H}_{11/2} \rightarrow ^4\text{I}_{15/2}$ and $^4\text{S}_{3/2} \rightarrow ^4\text{I}_{15/2}$ transitions respectively, while a red emission observed between 630 and 690 nm is due to the $^4\text{F}_{9/2} \rightarrow ^4\text{I}_{15/2}$ transition. Green band emission at 539 nm, characterized by several narrow lines associated with a splitting of the $^4\text{S}_{3/2}$ energy level by the matrix electric field, reflects the homogeneous distribution of Er^{3+} in the NaYF₄ phase [20]. On the other hand, the red emission appears due to a direct population of $^4\text{F}_{9/2}$ level from $^4\text{I}_{13/2}$ level (following the non-radiative decay from $^4\text{I}_{11/2}$ level which is intensified in nanocrystals) and a non-radiative relaxation from $^4\text{F}_{7/2}$ through the $^2\text{H}_{11/2}$ and $^4\text{S}_{3/2}$ levels. As a result, the integrated green to red emission ratios of 0.62 and CIE of (0.37, 0.61) determines the final color output of NaYF₄:Yb,Er/PLGA UCNPs, Fig. 4. Photostability of the NaYF₄:Yb,Er/PLGA UCNPs emission was also traced during 1 h, Fig. S2. As one could see, exceptionally stable UC luminescence signal was recorded.

3.3. Cytotoxicity of NaYF₄:Yb,Er/PLGA UCNPs

The viability of HSCC and HGC after 24 h exposure to NaYF₄:Yb,Er/PLGA UCNPs at concentrations of 10, 25 and 50 $\mu\text{g/ml}$, expressed in terms of percentages compared to the surviving cells in the control

group is presented at Fig. 5. As it is notable from Fig. 5, the viability of HGC was highly preserved after 24 h exposure, being above 88% for all examined concentrations of NaYF₄:Yb,Er/PLGA UCNPs. At the same time, the tolerance of OSCC was found variable with the increase of NaYF₄:Yb,Er/PLGA UCNPs concentration. Only in the case of the lowest concentration viability of OSCC implied non-significant cytotoxicity of 89%, while higher NaYF₄:Yb,Er/PLGA concentrations exerted in them certain level of cytotoxicity, i.e. cell viability of only 60% was detected. This is quite surprising since cancer cells are usually highly resistant to therapeutics. Obtained data regarding preserved viability of HGC corroborated well by recent conclusions about cytotoxicity of bare and PLGA coated NaYF₄:Yb,Er UCNPs tested on human skin cells [28]. Guller et al. [28] used the solvent evaporation technique for posterior formation of PLGA shell over the NaYF₄:Yb,Er nanoparticles that have been synthesized through decomposition of rare earth trifluoroacetates in oleic acid/octadecene mixture. Although the authors reported much lower internalization capacity, higher sensitivity of keratinocytes than of fibroblasts has been achieved, emphasizing the importance of studying normal cells. As it will be shown latter, maintaining of the high HGC viability in this study is not a consequence of the lower internalization of NaYF₄:Yb,Er/PLGA UCNPs in them, so evaluated differences in OSCC viability indicates that synthesized UCNPs could be

useful in therapeutic treatments of cancer cells.

3.4. *In vitro* laser scanning microscopy imaging of OSCC and HGC

For the evaluation of the NaYF₄:Yb,Er/PLGA UCNP's capability to be internalized in OSCC and HGC, the lowest NaYF₄:Yb,Er/PLGA UCNP's concentration of 10 µg/mL has been used. For this concentration, no significant cytotoxicity has been observed in both OSCC and HGC (Section 3.3) and therefore, it could be considered as the most promising concentration for diagnostic purpose.

Visualization of the OSCC and HGC labeled with the NaYF₄:Yb,Er/PLGA UCNP's was done using of a safe 980 nm laser intensity of 6 and 7.5 mW, respectively. The size of the imaged region was approximately 200 × 200 µm². Images of the OSCC are shown in Fig. 6. The top row, left panel shows bright field image of the sample. A pseudo color image of the cells auto-fluorescence upon femto-second excitation at 730 nm is shown in top-right panel. Bottom row - left panel shows the pseudo color image of the NaYF₄:Yb,Er/PLGA UCNP's upon CW excitation at 980 nm. Overlapping of the latter two images clearly implicates that observed fluorescence spots are related to the non-specific uptake of UCNP's through cell membrane and their positioning in a cytoplasmic area around cells nuclei. Size of the fluorescence spots indicates UCNP's aggregation in cells.

The consistent finding of the UCNP's internalization in the HGC has been drawn from Fig. 7, which presents HGCs labeled in the same way as OSCC. The fact that UCNP's are mainly localized in the vicinity of the cells nuclei, without visible entering in, designates that UCNP's didn't provoke gene disruption. In order to show comparable level of the NaYF₄:Yb,Er/PLGA UCNP's internalization in OSCC and HGC, quantification of the UCNP's signal from the Figs. 6 and 7, as well as additional one which show labeling of a single OSCC were done, and results obtained are presented in Supplement File (Figs. S3 and S4). Significant cellular internalization of NaYF₄:Yb,Er/PLGA UCNP's coupled with the preserved cells viability indicates that these could be useful theranostics for oral cavity cancers.

As it is pointed out before, the amount of literature showing cells viability and labeling with UCNP's is respectable and summarized in many reviews, but great majority is focused on cancer cells testing. At the same time, data about mucosal cytotoxicity and drug deliver capacity of UCNP's tested on primary cultures and normal cells are limited and inconsistent in achieved results due to the considerable disparity of the UCNP's characteristics and type of protective organic shell used [37–39]. Thus, it is not easy to compare these with data presented in this study but it is worth to note that realistic UCNP-assisted imaging depth nowadays is estimated to be up to 1 cm [28], which corresponds well with the depth of skin and mucosa, so successful OSCC and HGC labeling with NaYF₄:Yb,Er/PLGA UCNP's holds promise for these to be used as theranostic agents in the future.

4. Conclusion

In conclusion, we have demonstrated the successful fabrication of the new NaYF₄:Yb,Er/PLGA UCNP's that could be used as probes for NIR-excited fluorescence (*in vitro*) imaging of human mucosal cells. Comprehensive morphological and structural analyses implied crystallization of a low-temperature cubic phase in spherical nanoparticles (~100 nm), as well as, hexagonal one in elongated nanocrystals (~60 nm). As a consequence of the upconversion, green emission (between 512 and 533 nm and between 533 and 560 nm) and red emission (between 630 and 690 nm) are both prominent in spectra, yielding a final light green output (CIE 0.37, 0.61). PLGA functional groups present at NaYF₄:Yb,Er UCNP's surface make them accessible for further conjugation with biologically important molecules, while in the present form enable non-specific cellular uptake without compromising cells viability. Moreover, evidences about lower cytotoxicity under significant internalization of NaYF₄:Yb,Er/PLGA UCNP's in the vicinity of

the cell nucleus without gene disrupting, represent an important step toward application of UCNP-based particles for diagnosis or the treatment of cancer cells.

Acknowledgements

This work was financially supported by the Ministry of Education, Science and Technological Development of Serbia projects OI 172035 and III 45016.

Appendix A. Supplementary data

Supplementary data to this article can be found online at <https://doi.org/10.1016/j.msec.2018.05.081>.

References

- [1] N. Vigneswaran, M.D. Williams, Epidemiological trends in head and neck cancer and aids in diagnosis, *Oral Maxillofac. Surg. Clin. North Am.* 26 (2) (2014) 123–141.
- [2] A.K. Markopoulos, Current aspects on oral squamous cell carcinoma, *Open Dent. J.* 6 (2012) 126–130.
- [3] J.H. Wang, B. Wang, Q. Liu, Q. Li, H. Huang, L. Song, T.Y. Sun, H. Wang, X.F. Yu, C. Li, P.K. Chu, Bimodal optical diagnostics of oral cancer based on Rose Bengal conjugated gold nanorod platform, *Biomaterials* 34 (2013) 4274–4283.
- [4] P. Padmanabhan, A. Kumar, S. Kumar, R.K. Chaudhary, B. Gulyás, Nanoparticles in practice for molecular-imaging applications: an overview, *Acta Biomater.* 41 (2016) 1–16.
- [5] X. Huang, J. Lin, Active-core/active-shell nanostructured design: an effective strategy to enhance Nd³⁺/Yb³⁺ cascade sensitized upconversion luminescence in lanthanide-doped nanoparticles, *J. Mater. Chem. C* 3 (2015) 7652–7657.
- [6] K. Presley, J. Hwang, S. Cheong, R. Tilley, J. Collins, M. Viapiano, J. Lannutti, Nanoscale upconversion for oxygen sensing, *Mater. Sci. Eng. C* 70 (2017) 76–84.
- [7] X. Zhu, Q. Su, W. Feng, F. Li, Anti-stokes shift luminescent materials for bio-applications, *Chem. Soc. Rev.* 46 (2017) 1025–1039.
- [8] H. Dong, L.D. Sun, C.H. Yan, Energy transfer in lanthanide upconversion studies for extended optical applications, *Chem. Soc. Rev.* 44 (2015) 1608–1634.
- [9] P. Zhao, W. Ji, S. Zhou, L. Qiu, L. Li, Z. Qian, X. Liu, H. Zhang, X. Cao, Upconverting and persistent luminescent nanocarriers for accurately imaging-guided photothermal therapy, *Mater. Sci. Eng. C* 79 (2017) 191–198.
- [10] B. Hou, W. Yang, C. Dong, B. Zheng, Y. Zhang, J. Wu, H. Wang, J. Chang, Controlled co-release of doxorubicin and reactive oxygen species for synergistic therapy by NIR remote-triggered nanoimpellers, *Mater. Sci. Eng. C* 74 (2017) 94–102.
- [11] S. Chen, C. Zhang, G. Jia, J. Duan, S. Wang, J. Zhang, Size-dependent cytotoxicity of europium doped NaYF₄ nanoparticles in endothelial cells, *Mater. Sci. Eng. C* 43 (2014) 330–342.
- [12] X. Wu, G. Chen, J. Shen, Z. Li, Y. Zhang, G. Han, Upconversion nanoparticles: a versatile solution to multiscale biological imaging, *Bioconjug. Chem.* 26 (2015) 166–175.
- [13] J. Zhou, Z. Liu, F. Li, Upconversion nanophosphors for small-animal imaging, *Chem. Soc. Rev.* 41 (2012) 1323–1349.
- [14] G.K. Das, D.T. Stark, I.M. Kennedy, Potential toxicity of up-converting nanoparticles encapsulated with a bilayer formed by ligand attraction, *Langmuir* 30 (2014) 8167–8176.
- [15] F. Wang, D.K. Chatterjee, Z. Li, Y. Zhang, X. Fan, M. Wang, Synthesis of poly-ethyleneimine/NaYF₄ nanoparticles with upconversion fluorescence, *Nanotechnology* 17 (2006) 5786–5791.
- [16] M. Wang, C.-C. Mi, J.-L. Liu, X.-L. Wu, Y.-X. Zhang, W. Hou, F. Li, S.-K. Xu, One-step synthesis and characterization of water-soluble NaYF₄:Yb,Er/Polymer nanoparticles with efficient up-conversion fluorescence, *J. Alloys Compd.* 485 (2009) L24–L27.
- [17] T. Cao, Y. Yang, Y. Gao, J. Zhou, Z. Li, F. Li, High-quality water-soluble and surface-functionalized upconversion nanocrystals as luminescent probes for bioimaging, *Biomaterials* 32 (2011) 2959–2968.
- [18] A. Sedlmeier, H.H. Gorris, Surface modification and characterization of photon-upconverting nanoparticles for bioanalytical applications, *Chem. Soc. Rev.* 44 (2015) 1526–1560.
- [19] I. Dinic, M.E. Rabanal, K. Yamamoto, Z. Tan, S. Ohara, L.T. Mancic, O.B. Milosevic, PEG and PVP assisted solvothermal synthesis of NaYF₄:Yb³⁺/Er³⁺ up-conversion nanoparticles, *Adv. Powder Technol.* 27 (2016) 845–853.
- [20] I. Dinic, S. Ohara, T. Koji, M.E. Rabanal, A.M. Costa, B.A. Marinkovic, L. Mancic, O. Milosevic, Compositional and structural dependence of upconverting RE-fluorides obtained through EDTA assisted hydrothermal synthesis, *Adv. Powder Technol.* 28 (1) (2017) 73–82.
- [21] H.M. Mansour, M. Sohn, A. Al-Ghananeem, P.P. Deluca, Materials for pharmaceutical dosage forms: molecular pharmaceuticals and controlled release drug delivery aspects, *Int. J. Mol. Sci.* 11 (2010) 3298–3322.
- [22] H.K. Makadia, S.J. Siegel, Poly lactic-co-glycolic acid (PLGA) as biodegradable controlled drug delivery carrier, *Polymer* 3 (3) (2011) 1377–1397.
- [23] F. Danhier, E. Ansorena, J.M. Silva, R. Coco, A. Le Breton, V. Préat, PLGA-based

- nano particles: an overview of biomedical applications, *J. Control. Release* 161 (2) (2012) 505–522.
- [24] R.N. Mariano, D. Alberti, J.C. Cutrin, S.G. Crich, S. Aime, Design of PLGA based nanoparticles for imaging guided applications, *Mol. Pharm.* 11 (2014) 4100–4106.
- [25] J. Zhao, H. Yang, J. Li, Y. Wang, X. Wang, Fabrication of pH-responsive PLGA(UCNPs/DOX) nanocapsules with upconversion luminescence for drug delivery, *Sci. Rep.* 7 (2017) (Article No. 18014).
- [26] S.J. Budijono, J. Shan, N. Yao, Y. Miura, T. Hoye, R.H. Austin, Y. Ju, R.K. Prud'Homme, Synthesis of stable block-copolymer-protected NaYF₄:Yb³⁺, Er³⁺ up-converting phosphor nanoparticles, *Chem. Mater.* 22 (2010) 311–318.
- [27] X. Bai, S. Xu, J. Liu, L. Wang, Upconversion luminescence tracking of gene delivery via multifunctional nanocapsules, *Talanta* 150 (2016) 118–124.
- [28] A.E. Guller, A.N. Generalova, E.V. Petersen, A.V. Nechaev, I.A. Trusova, N.N. Landyshev, A. Nadort, E.A. Grebenik, S.M. Deyev, A.B. Shekhter, A.V. Zvyagin, Cytotoxicity and non-specific cellular uptake of bare and surface-modified upconversion nanoparticles in human skin cells, *Nano Res.* 8 (5) (2015) 1546–1562.
- [29] R.M. Mainardes, M.P.D. Gremião, R.C. Evangelista, Thermoanalytical study of praziquantel-loaded PLGA nanoparticles, *Braz. J. Pharm. Sci.* 42 (4) (2006) 523–530.
- [30] V. Pozzi, D. Sartini, R. Rocchetti, A. Santarelli, C. Rubini, S. Morganti, R. Giulante, S. Calabrese, G. Di Ruscio, F. Orlando, M. Provinciali, F. Saccucci, L. Lo Muzio, M. Emanuelli, Identification and characterization of cancer stem cells from head and neck squamous cell carcinoma cell lines, *Cell. Physiol. Biochem.* 36 (2015) 784–798.
- [31] S. Castiglioni, C. Caspani, A. Cazzaniga, J.A. Maier, Short- and long-term effects of silver nanoparticles on human microvascular endothelial cells, *World J. Biol. Chem.* 5 (2014) 457–464.
- [32] K. Bukara, S. Jovanic, I.T. Drvenica, A. Stancic, V. Ilic, M.D. Rabasovic, D. Pantelic, B. Jelenkovic, B. Bugarski, A.J. Krmpot, Mapping of hemoglobin in erythrocytes and erythrocyte ghosts using two photon excitation fluorescence microscopy, *J. Biomed. Opt.* 22 (2) (2017) 026003(8 pages).
- [33] T. Laihininen, M. Lastusaari, L. Pihlgren, L.C.V. Rodrigues, J. Holsa, Thermal behaviour of the NaYF₄:Yb³⁺, R³⁺ materials, *J. Therm. Anal. Calorim.* 121 (2015) 37–43.
- [34] L. Wang, X. Li, Z. Li, W. Chu, R. Li, K. Lin, H. Qian, Y. Wang, C. Wu, J. Li, D. Tu, Q. Zhang, L. Song, J. Jiang, X. Chen, Y. Luo, Y. Xie, Y. Xiong, A new cubic phase for α NaYF₄ host matrix offering high upconversion luminescence efficiency, *Adv. Mater.* 27 (2015) 5528–5533.
- [35] A.T.C.R. Silva, B.C.O. Cardoso, M.E.S.R. Silva, R.F.S. Freitas, R.G. Sousa, Synthesis, characterization, and study of PLGA copolymer in vitro degradation, *J. Biomater. Nanobiotechnol.* 6 (2015) 8–19.
- [36] J.B. Lee, Y.G. Ko, D. Cho, W.H. Park, B.N. Kim, B.C. Lee, I.K. Kang, O.H. Kwon, Modification of PLGA nanofibrous mats by electron beam irradiation for soft tissue regeneration, *J. Nanomater.* (2015) 10, <http://dx.doi.org/10.1155/2015/295807> (Article ID 295807).
- [37] U. Bazylińska, D. Wawrzyńczyk, J. Kulbacka, R. Frąckowiak, B. Cichy, A. Bednarkiewicz, M. Samoć, K.A. Wilk, Polymeric nanocapsules with upconverting nanocrystals cargo make ideal fluorescent bioprobes, *Sci. Rep.* 6 (2016) 29746.
- [38] H.C. Guo, R.Z. Hao, H.S. Qian, S.Q. Sun, D.H. Sun, H. Yin, Z.X. Liu, X.T. Liu, Upconversion nanoparticles modified with aminosilanes as carriers of DNA vaccine for foot-and-mouth disease, *Appl. Microbiol. Biotechnol.* 95 (2012) 1253–1263.
- [39] L. Zhao, A. Kutikov, J. Shen, C. Duan, J. Song, G. Han, Stem cell labeling using polyethylenimine conjugated (α-NaYbF₄:Tm³⁺)/CaF₂ upconversion nanoparticles, *Theranostics* 3 (4) (2013) 249–257.



PAPER

Optically-detected spin-echo method for relaxation times measurements in a Rb atomic vapor

OPEN ACCESS

RECEIVED

21 December 2016

REVISED

18 April 2017

ACCEPTED FOR PUBLICATION

17 May 2017

PUBLISHED

26 June 2017

Original content from this work may be used under the terms of the [Creative Commons Attribution 3.0 licence](#).

Any further distribution of this work must maintain attribution to the author(s) and the title of the work, journal citation and DOI.

M Gharavipour^{1,3}, C Affolderbach¹, F Gruet¹, I S Radojičić², A J Krmpot², B M Jelenković² and G Mileti^{1,3}¹ Laboratoire Temps-Fréquence (LTF), Institut de Physique, Université de Neuchâtel, Neuchâtel CH-2000, Switzerland² Institute of Physics Belgrade, University of Belgrade, Pregrevice 118, 11080 Belgrade, Serbia³ Authors to whom any correspondence should be addressedE-mail: mohammadreza.gharavipour@unine.ch and gaetano.mileti@unine.ch

Keywords: relaxation times, vapor cell atomic clock, spin-echo, optical detection, Ramsey scheme

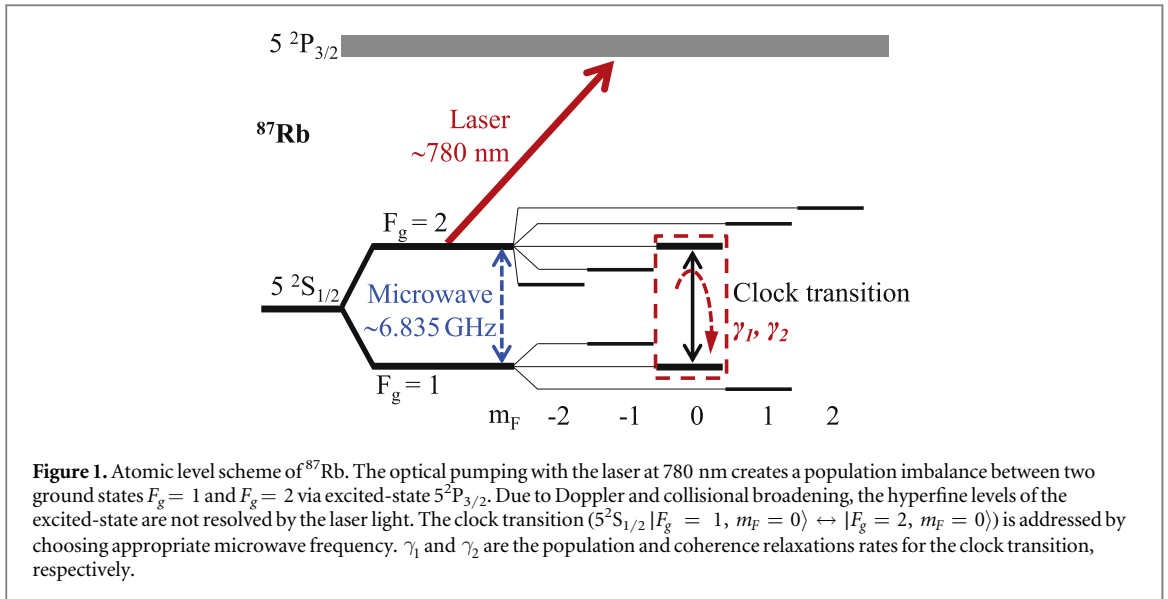
Abstract

We introduce and demonstrate an experimental method, optically-detected spin-echo (ODSE), to measure ground-state relaxation times of a rubidium (Rb) atomic vapor held in a glass cell with buffer-gas. The work is motivated by our studies on high-performance Rb atomic clocks, where both population and coherence relaxation times (T_1 and T_2 , respectively) of the ‘clock transition’ ($5^2S_{1/2}$ $|F_g = 1, m_F = 0\rangle \leftrightarrow |F_g = 2, m_F = 0\rangle$) are relevant. Our ODSE method is inspired by classical nuclear magnetic resonance spin-echo method, combined with optical detection. In contrast to other existing methods, like continuous-wave double-resonance (CW-DR) and Ramsey-DR, principles of the ODSE method allow suppression of decoherence arising from the inhomogeneity of the static magnetic field across the vapor cell, thus enabling measurements of intrinsic relaxation rates, as properties of the cell alone. Our experimental result for the coherence relaxation time, specific for the clock transition, measured with the ODSE method is in good agreement with the theoretical prediction, and the ODSE results are validated by comparison to those obtained with Franzen, CW-DR and Ramsey-DR methods. The method is of interest for a wide variety of quantum optics experiments with optical signal readout.

1. Introduction

Alkali atomic vapors are widely used in many types of high-resolution atomic physics experiments like nuclear magnetic resonance (NMR) [1] and precision measurements in applications such as optical magnetometry [2], vapor cell atomic frequency standards [3, 4], quantum entanglement and information storage [5], miniature atomic clocks [6], navigation systems [7–9], spin squeezing [10]. All these applications rely on long-lived ground-state spin-polarization of the alkali vapor in the cell [11]. Particularly in the vapor-cell atomic clocks, the clock stability critically depends on width and contrast of the atomic resonance line. The resonance linewidth is determined by various parameters, and ultimately, by the relaxation processes occurring in the cell. Like in NMR, alkali atoms in the vapor cell may lose their polarization due to various types of collisions, interactions with electro-magnetic fields, and also due to inhomogeneity of the static magnetic field.

Studies of relaxation processes in various spin-polarized systems have a long-standing history of more than 70 years. In the case of atomic relaxations in alkali vapors, Franzen presented the ‘relaxation in the dark’ method [12] in 1959 and measured the population relaxation time of optically-pumped Rb atoms in the vapor cell. Franzen’s method has been modified and used by other groups to determine both population and coherence relaxation times in Rb or Cs wall-coated vapor cells [13–16]. Moreover, methods of nonlinear magneto-optical rotation [11, 17], ground-state Hanle effect [18, 19] and optically detected magnetic resonance [19, 20] were employed to measure the hyperfine and the Zeeman relaxation times in wall-coated or in buffer-gas alkali vapor cells. Various modified NMR spin-echo techniques [21] have been studied both theoretically and experimentally for solid-state systems to extend the coherence time [22, 23]. Similar techniques like dynamical decoupling approach [24, 25] and gradient echo memory [26] applied in quantum memory studies aim for example to



minimize the detrimental effect of inhomogeneous broadening on the coherence storage time of the quantum bit (qubit) or to use the artificially created broadening for storage of broad-band optical pulses without deterioration of the storage time [27–29].

In this paper, we present our ‘optically-detected spin-echo’ (ODSE) method to measure the relaxation times in a Rb vapor cell with buffer-gas. This method is a combination of Franzen [12], Ramsey-DR [16] and NMR spin-echo [21] techniques. We apply the ODSE method to our high-performance ^{87}Rb atomic frequency-standard setup presented in [30, 31] and show how to determine the intrinsic coherence relaxation time (T_2) specifically for the ‘clock transition’ ($5^2S_{1/2} |F_g = 1, m_F = 0\rangle \leftrightarrow |F_g = 2, m_F = 0\rangle$), see figure 1). Here we use the term ‘intrinsic’ to describe the relaxations that do not include any influence of any electro-magnetic field but are influenced only by the various types of collisions that depend on the cell design and the temperature [19] (see section 2). Gradients in the static magnetic field across the vapor cell are some of the main sources of the relaxation processes. Such induced relaxation processes may mask the real intrinsic relaxation times during measurements, thus hindering their precise determination. The ODSE method enables measurements that are free of the influence of the static magnetic field gradients.

In section 2 we briefly recall the theory of relaxation processes in a buffer-gas vapor cell [3], and use it to estimate the ‘intrinsic’ population and coherence relaxation times (T_1 and T_2 respectively) of the clock transition in our ^{87}Rb vapor cell. In section 3, we introduce the experimental setup which is basically a Rb atomic clock [30, 31]. Finally in section 4, we present the results of relaxation times measured in the same ^{87}Rb vapor cell by using ODSE, Franzen, continuous-wave double-resonance (CW-DR), and Ramsey-DR methods. The advantages and limitations of these methods are discussed.

2. Theory of relaxation processes in a buffer-gas vapor cell

Ultra-narrow signal linewidths employed in atomic precision experiments and instrumentations, such as atomic clocks, are ultimately limited by the relaxation processes in the atomic sample. For example in a Rb atomic clock, the frequency of a quartz oscillator is stabilized to the frequency of the ^{87}Rb hyperfine clock transition [32] observed in a Rb vapor cell. Rb atoms are optically pumped with a laser to create a population imbalance and microwave interrogation creates a coherence between the two ground states $F_g = 1$ and $F_g = 2$ of ^{87}Rb atoms. Due to the relaxation processes, this population imbalance and coherence may be destroyed and the prepared Rb atoms lose their polarization. The dynamics of this process is characterized by the relaxation times on the atomic levels. The two parameters of longitudinal relaxation rate γ_1 and transverse relaxation rate γ_2 —which are inverse of the relaxation times T_1 and T_2 , respectively—describe the population and coherence relaxations for the clock transition, respectively (see figure 1).

We use the well-known relaxation theory [3] and the experimentally-determined parameters presented in [3] to estimate approximately γ_1 and γ_2 for our ^{87}Rb vapor cell. Collisions of polarized ^{87}Rb atoms with the cell walls, with buffer-gas particles and with other Rb atoms—the latter is known as spin-exchange—are the sources of relaxation processes occurring in a vapor cell. The total intrinsic population and coherence relaxation rates, γ_i (here and in the following index i stands for 1 and 2 for the population and coherence, respectively), are equal to

Table 1. Calculated intrinsic relaxation rates/times in Rb vapor cell, at $T = 336$ K.

	γ_1 (s ⁻¹)	γ_2 (s ⁻¹)
Buffer gas collisions (γ_{iBG})	12	79
Diffusion to cell walls (γ_{iW})	26	25
Spin-exchange (γ_{iSE})	185	116
Total rates	223	220
Calculated relaxation times (ms)	$T_1 = 4.5$ (3)	$T_2 = 4.5$ (3)

the sum of the three relaxation processes induced by the cell walls γ_{iW} , the buffer-gas γ_{iBG} and spin-exchange γ_{iSE} .

The presence of a buffer gas in the cell reduces the rate of depolarizing collisions between Rb atoms and the cell walls. Therefore, relaxation rates γ_{iW} , due to collisions of Rb atoms with the cell-walls, depend on the cell dimensions, cell temperature T and the total buffer-gas pressure, P , in the cell. In lowest order diffusion approximation, it is described by [3]:

$$\gamma_{iW} = ((2.405/a)^2 + (\pi/L)^2)D_i(P_0/P), \quad (1)$$

where $a = 1.25$ cm and $L = 2.5$ cm are the radius and length of our cylindrical ⁸⁷Rb vapor cell, respectively. D_i is the diffusion constant of Rb atoms in the buffer-gas particles of interest which is proportional to $T^{3/2}$, P_0 is the standard atmospheric pressure (1013.25 mbar) and P is about 33 mbar in our vapor cell.

Rb atoms also collide with the buffer-gas molecules in the vapor cell, which changes the electron density at the Rb nucleus and results in a change of hyperfine coupling in the Rb atoms [33]. The resulting buffer-gas relaxation rate γ_{iBG} is described as:

$$\gamma_{iBG} = L_0 \bar{v}_r \sigma_i (P/P_0), \quad (2)$$

where $L_0 = 2.686\,7774(47) \times 10^{25} \text{ m}^{-3}$ at 0 °C is Loschmidt's constant, \bar{v}_r is the mean relative velocity between a ⁸⁷Rb atom and a buffer-gas particle, and σ_i are the collisional cross-sections between colliding particles responsible for population and coherence relaxations. The temperature dependence of the above equation appears in the average relative velocity $\bar{v}_r = (8k_B T/\pi\mu)^{1/2}$ where k_B is the Boltzmann constant and μ is the reduced mass of the colliding particles (here Rb and buffer-gas atoms).

Note that in the case of anti-relaxation wall-coated cells the relaxation processes as described by equations (1) and (2) do not apply and the relaxation rates are instead governed by the properties and the quality (such as purity and coverage) of the coating [34–36]. Such wall-coated cells are however not considered in this study.

Collisions between Rb atoms in the vapor cell result in de-coherence due to spin exchange. The resulting population γ_{1SE} and coherence γ_{2SE} broadening are described by:

$$\gamma_{1SE} = n \bar{v}_s \sigma_{SE}, \quad (3)$$

$$\gamma_{2SE} = \gamma_{1SE}(6I + 1)/(8I + 4), \quad (4)$$

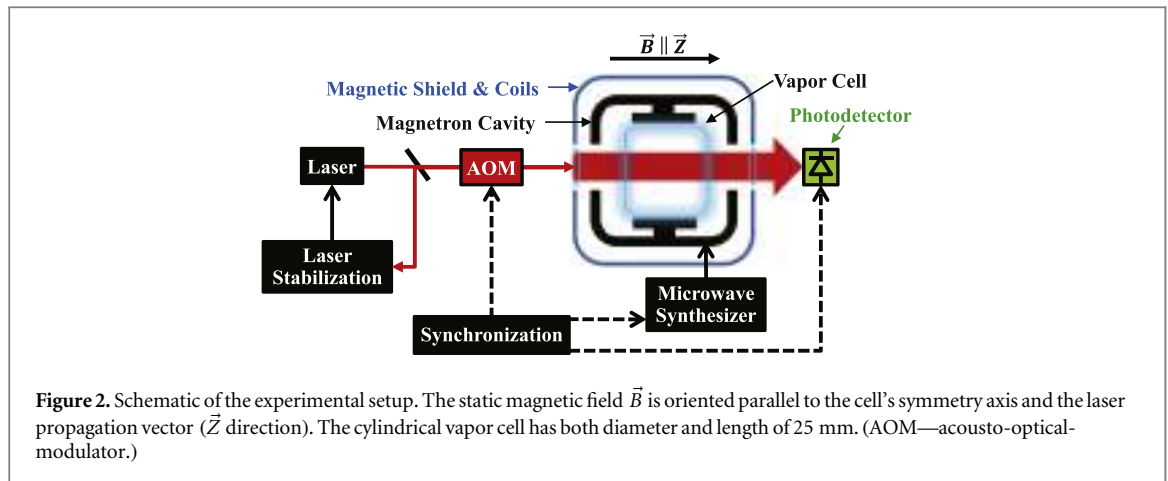
respectively, where n is the number density of the Rb vapor, \bar{v}_s is the average relative velocity between two ⁸⁷Rb atoms and $\sigma_{SE} = 1.6 \times 10^{-18} \text{ m}^2$ is the spin-exchange cross section. I is the nuclear spin and for ⁸⁷Rb is equal to 3/2.

The total expected relaxation rates in our cell are given by:

$$\gamma_i = \gamma_{iBG} + \gamma_{iW} + \gamma_{iSE}. \quad (5)$$

All these contributions to the intrinsic population and coherence relaxation rates are listed in table 1. They were calculated from equations (1)–(4) for the clock transition in our ⁸⁷Rb vapor cell using experimentally measured parameters for D_i and σ_i taken from [3]. Finally, both intrinsic relaxation times for the clock transition are calculated to be $T_1 \approx T_2 = 4.5$ ms. We note that the reported literature values for D_i and σ_i show considerable scatter, which results in a total uncertainty of 7% for both intrinsic T_1 and T_2 [12, 37–39].

In addition to the various presented types of collisions of the polarized Rb atoms in the vapor cell, their interactions with other electromagnetic fields may also be interpreted as sources of relaxations. The electromagnetic fields present in our atomic clock are the optical and the microwave fields that are used to prepare, drive and detect the resonance [30, 32] and the static magnetic field applied to lift the Zeeman degeneracy. The latter may have some residual inhomogeneity across the vapor cell. In a microscopic view, Rb atoms can move in the vapor cell and—due to the field inhomogeneity—they may experience various static magnetic fields. This effect introduces additional dephasing [40] which results in a decrease of the measured



coherence relaxation time depending on the method (see section 4). In NMR, the overall coherence relaxation time T_2^* due to the field inhomogeneity is given by [41]:

$$T_2^{*-1} = T_2^{-1} + \eta G^2, \quad (6)$$

where, T_2 is the intrinsic coherence relaxation time, G is the local gradient of the static magnetic field and η is a proportionality factor depending on atomic and experimental parameters.

In this study, we determine the coherence time T_2^* by using CW-DR and Ramsey-DR schemes (sections 4.2 and 4.3, respectively), while with ODSE method the intrinsic coherence relaxation time T_2 is obtained (section 4.4).

The system studied here is an alkali vapor cell with relatively high buffer-gas pressure, where the Rb atoms are effectively localized to a few micrometers over the measurement timescales. Due to this localization, the sample shows inhomogeneous shifts and broadenings because of the inhomogeneity of external fields [42]. This is fundamentally different from the case of anti-relaxation wall-coated cells without buffer gas where the atoms move freely through the entire cell volume and experience only homogeneous shifts and broadenings as well as narrowing [43].

3. Experimental setup

Figure 2 shows the schematics of our experimental setup, basically a Rb atomic clock, whose details were previously presented in [30, 31]. It consists of three main parts: (1) the physics package containing the microwave cavity and the vapor cell, (2) the compact frequency-stabilized laser head (LH), and (3) the microwave synthesizer. The physics package contains the in-house-made cylindrical glass cell with both diameter and length of 25 mm. The cell contains isotopically enriched ^{87}Rb and a mixture of Argon and Nitrogen as buffer gases. The vapor cell is placed in a compact magnetron-type microwave cavity which resonates at the ^{87}Rb clock transition frequency of ≈ 6.835 GHz, with a TE_{011} -like field-mode geometry [44]. A magnetic coil placed around the cavity generates a static magnetic field oriented parallel to the cell's symmetry axis and the laser propagation vector (\vec{Z} direction) to lift the degeneracy of ^{87}Rb hyperfine ground states into their respective Zeeman levels. The laser is a distributed-feedback laser diode emitting at 780 nm frequency stabilized on Rb D2 sub-Doppler absorption lines using a compact (1.4 cm^3) magnetically-shielded and thermally-controlled ^{87}Rb evacuated cell. An acousto-optical-modulator (AOM) is implemented in the LH and serves as a switch to control the duration and intensity of the laser pulses [45]. The AOM has the fall and rise times $< 5 \mu\text{s}$. The microwave synthesizer is used to generate the ≈ 6.835 GHz radiation for ^{87}Rb clock transition with a resolution below $1 \mu\text{Hz}$, and also controls the optical and microwave pulse sequences with a timing resolution at the level of $2 \mu\text{s}$, as used in the pulsed schemes [46]. All pulse durations and synchronization in the pulsed schemes are referenced to the high-stability quartz oscillator of the atomic clock setup, thus assuring a timing accuracy far below the nanosecond level over the duration of the pulse sequences employed (for typical pulse sequences, see sections 4.1, 4.3, and 4.4).

4. Characterization methods and results

We apply four methods, Franzen, CW-DR, Ramsey-DR and ODSE to measure the relaxation times in the buffer-gas ^{87}Rb vapor cell. The CW-DR and Ramsey-DR schemes were previously also used for analyses from a

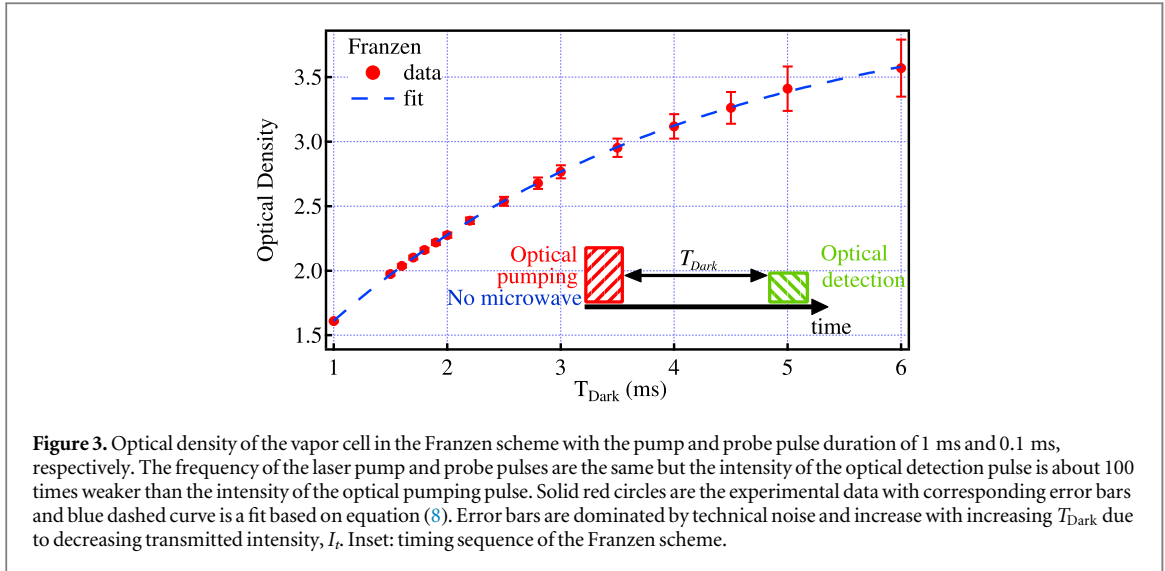


Figure 3. Optical density of the vapor cell in the Franzen scheme with the pump and probe pulse duration of 1 ms and 0.1 ms, respectively. The frequency of the laser pump and probe pulses are the same but the intensity of the optical detection pulse is about 100 times weaker than the intensity of the optical pumping pulse. Solid red circles are the experimental data with corresponding error bars and blue dashed curve is a fit based on equation (8). Error bars are dominated by technical noise and increase with increasing T_{Dark} due to decreasing transmitted intensity, I_t . Inset: timing sequence of the Franzen scheme.

metrological point of view including the short- and long-term frequency stability of our Rb atomic clock [47]. Franzen, Ramsey-DR and ODSE methods operate in pulse mode. In these three pulsed methods, first an optical pumping laser pulse creates a population imbalance by depopulating the ^{87}Rb $F_g = 2$ and filling the $F_g = 1$ ground state in the vapor cell (see figure 1). In the cases of Ramsey-DR and ODSE methods, optical pumping is followed by series of $\pi/2$ and/or π microwave pulses that create/modify coherence between the ground states. Finally—in all three pulse schemes—a laser probe pulse with the same frequency as during the optical pumping pulse is used to measure the optical density (OD) on the transition starting from $F_g = 2$ state by using a photodetector. To avoid re-pumping, this probe pulse has an approximately 100 times weaker intensity than the pump pulse. The variation of the OD as a function of time gives information about the population and/or coherence relaxation times. OD is defined to be the ratio of the incident I_0 and transmitted I_t laser probe pulse intensities:

$$\text{OD} = -\ln(I_t/I_0). \quad (7)$$

In the pulsed schemes, the laser probe pulse used for the detection does not resolve the atomic excited state because all the optical transitions to this $5^2\text{P}_{3/2}$ state are overlapped within Doppler linewidth. Furthermore, the clock transition cannot be addressed selectively by the laser alone either, because both the intrinsic transition linewidth and the Doppler linewidth are much larger than the Zeeman splitting in the $5\text{S}_{1/2}$ ground state. Hence, in these pulsed schemes, we can only address the population relaxation time between *all* m_F levels of the ground states $F_g = 1$ and $F_g = 2$ *simultaneously* (and not the clock transition only) which we write T_1' throughout this article. In Ramsey-DR and ODSE methods the frequency of the microwave field selects a particular hyperfine transition, which allows measuring its coherence relaxation time referring to the two involved m_F states only.

In the case of the CW-DR scheme, the linewidth of the resonance signal can be used to extract the coherence relaxation time for the clock transition. Also in the CW-DR scheme, the microwave frequency selects the specific Zeeman sublevels of interest. In all the above methods, no Doppler broadening occurs on the microwave transition, due to Dicke narrowing [43].

4.1. Franzen scheme

Franzen's well-known scheme of relaxation in the dark [12] for measuring population relaxation time is an all optical method, with absence of any microwave pulse. The timing sequence of the Franzen scheme is shown in inset in figure 3. First, a population imbalance is created between the ground states of ^{87}Rb atoms with the optical pumping. Then during the dark time T_{Dark} , the laser beam is switched off and the hyperfine population imbalance relaxes towards the thermal equilibrium. Finally, with a second laser pulse the sample's OD is probed which is a measure of the atomic population in $F_g = 2$. Figure 3 shows the experimentally obtained OD when T_{Dark} is varied, with the pump and probe pulse duration of 1 ms and 0.1 ms, respectively. By increasing the dark time, more atoms decay from $F_g = 1$ to $F_g = 2$ which results in increasing the OD. The data for the measurement is fitted with the equation:

$$\text{OD} = A - B \exp(-T_{\text{Dark}}/T_1'^{\text{Franzen}}), \quad (8)$$

where A , B and $T_1'^{\text{Franzen}}$ are the fitting parameters. As mentioned above, with this scheme only the population relaxation time of all m_F levels simultaneously is measured, which is determined as $T_1'^{\text{Franzen}} = 3.23$ (6) ms from

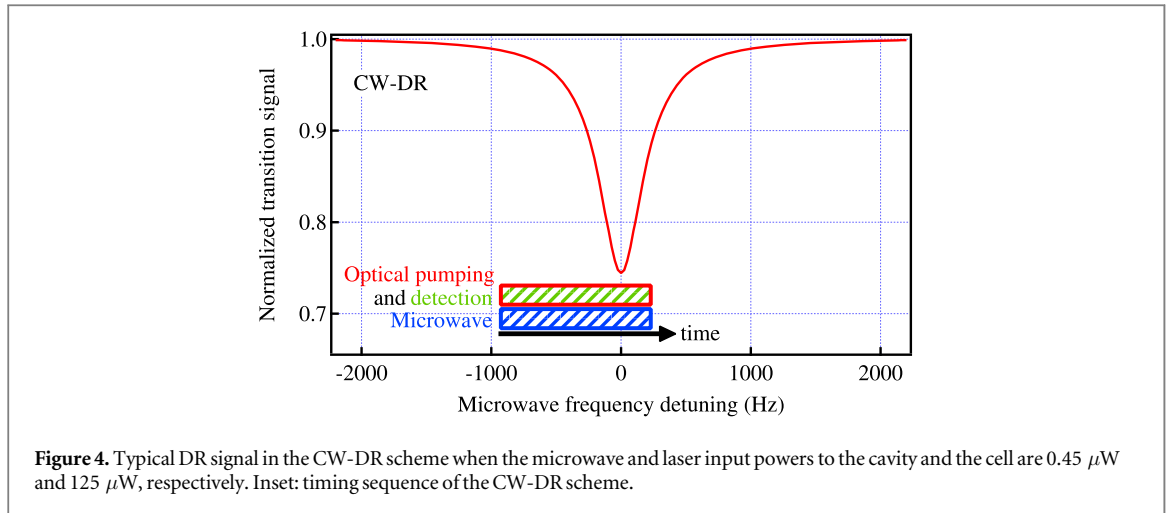


Figure 4. Typical DR signal in the CW-DR scheme when the microwave and laser input powers to the cavity and the cell are $0.45 \mu\text{W}$ and $125 \mu\text{W}$, respectively. Inset: timing sequence of the CW-DR scheme.

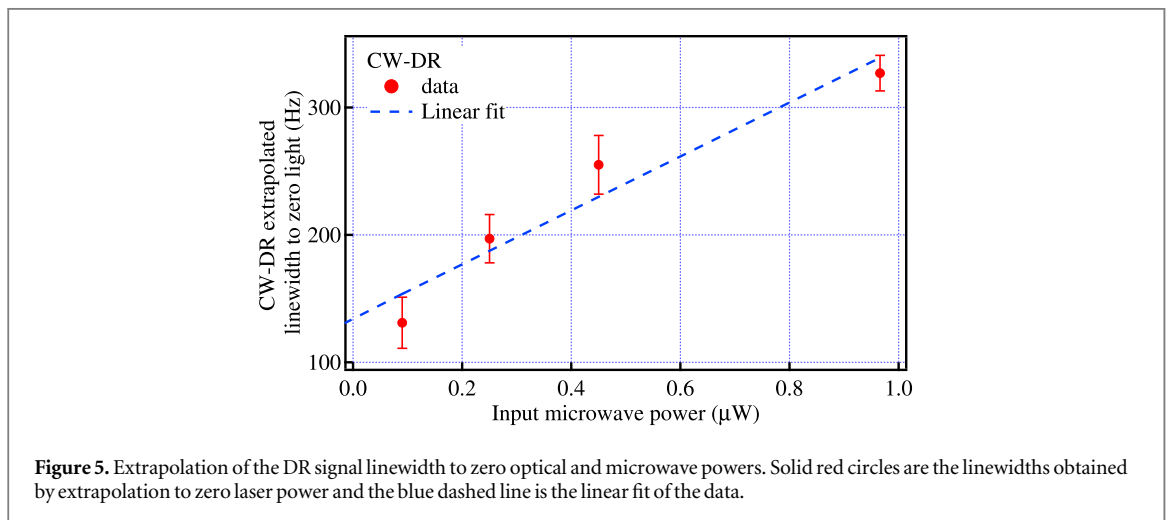


Figure 5. Extrapolation of the DR signal linewidth to zero optical and microwave powers. Solid red circles are the linewidths obtained by extrapolation to zero laser power and the blue dashed line is the linear fit of the data.

equation (8). This result did not change significantly when the measurement was repeated with the pump and probe pulse durations varied by $\pm 50\%$.

4.2. CW-DR scheme

In the case of CW-DR scheme [30], the laser optically pumps the Rb atoms in the vapor, while simultaneously a microwave field near-resonant with the ^{87}Rb hyperfine clock transition is applied. The transmitted light signal as a function of microwave frequency is a measure of the atomic ground state polarization known as DR signal. Figure 4 shows a typical DR signal which is obtained when the microwave frequency is scanned near resonance with $0.45 \mu\text{W}$ input power to the cavity and with $125 \mu\text{W}$ optical power to the cell. The linewidth of the DR signal is a measure of the coherence relaxation rate [32], but is additionally increased by optical and microwave power broadenings. To correct for this power broadening, the intrinsic DR signal linewidth, $\Delta\nu_{1/2}$, is determined by extrapolating the measured linewidth to zero with respect to both the optical and microwave powers, figure 5. By using this method, a coherence relaxation time for the clock transition, which is selectively driven by the applied microwave, is found to be $T_2^{\text{CW-DR}} = (\pi\Delta\nu_{1/2})^{-1} = 2.4(4) \text{ ms}$ [3]. However, this $T_2^{\text{CW-DR}}$ is significantly smaller than the predicted intrinsic T_2 from table 1. This can be attributed to uncertainties in the extrapolations and to additional relaxation due to gradients of the static magnetic field in the vapor cell which are well-known from NMR [40, 41].

4.3. Ramsey-DR scheme

In the Ramsey-DR scheme [48, 49], the three steps of optical pumping, microwave interrogation and optical detection are separated in time, see inset in figure 6. First, during the optical pumping a strong laser pulse creates a population imbalance between the two ground-state sublevels of ^{87}Rb . The optical pumping pulse has an input power to the vapor cell on the level of 14 mW and a duration of 0.4 ms . After this pumping pulse, in absence of light, two coherent $\pi/2$ microwave pulses are applied that are separated by the Ramsey time T_R . Both microwave

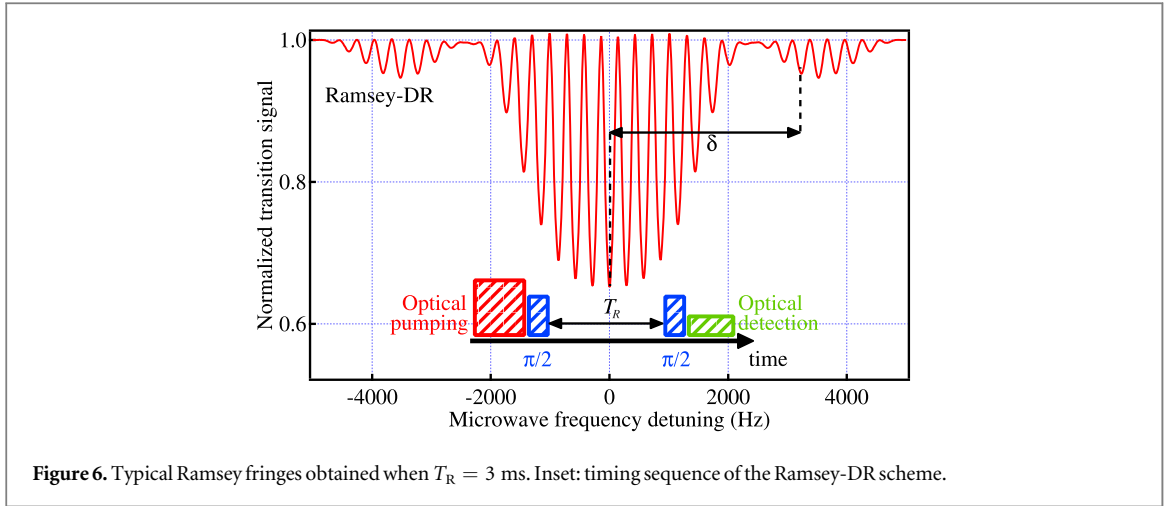


Figure 6. Typical Ramsey fringes obtained when $T_R = 3$ ms. Inset: timing sequence of the Ramsey-DR scheme.

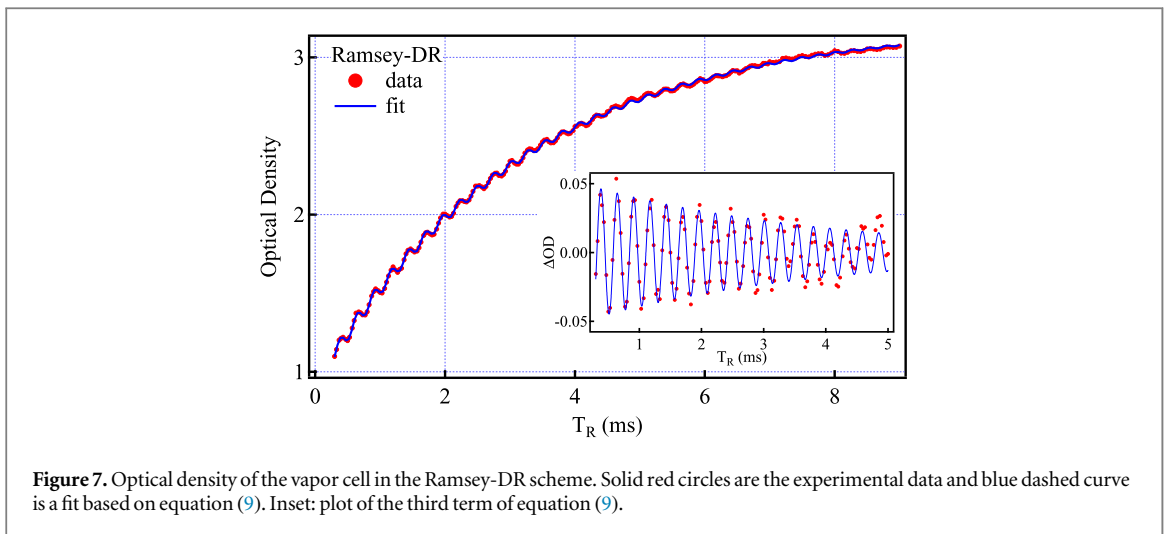


Figure 7. Optical density of the vapor cell in the Ramsey-DR scheme. Solid red circles are the experimental data and blue dashed curve is a fit based on equation (9). Inset: plot of the third term of equation (9).

pulses have the same duration of 0.4 ms, the same amplitude corresponding to a power of -18.2 dBm injected to the cavity and the same microwave frequency. The amplitude and duration of the $\pi/2$ microwave pulses in our Rb atomic clock were optimized according to the Rabi oscillation method presented in [50].

On the atomic level, the first $\pi/2$ microwave pulse creates a coherent superposition of the two hyperfine $m_F = 0$ states involved in the clock transition. During the Ramsey time, atoms evolve freely at the Larmor frequency. The second resonant microwave pulse converts the accumulated atomic phase into a population difference between the hyperfine states. Finally, in the last sequence the optical detection takes place with the laser. The laser frequency is the same for both optical pumping and detection steps, but the laser intensity is about 100 times weaker during the detection. In the Ramsey-DR scheme, the optical detection pulse duration is 0.7 ms [51] which results in an overall duration of one complete interrogation cycle of the scheme equal to $T_R + 1.9$ ms.

Figure 6 shows typical detected Ramsey fringes obtained by varying the microwave pulse frequency around the clock transition frequency, here for a Ramsey time of $T_R = 3$ ms. The OD of the Rb vapor is recorded for various values of T_R , with the microwave detuned from the clock transition by a fixed detuning δ (see figure 6) [16]. Figure 7 shows the recorded OD as a function of Ramsey time when the cavity is placed in a static magnetic field of 40 mG and the frequency of the microwave field is detuned from the resonance by $\delta = 3.8$ kHz. The data is fitted with the function [16]:

$$OD = A - B \exp(-T_R/T_1^{\text{Ramsey}}) + C \exp(-T_R/T_2^{\text{Ramsey}}) \sin(2\pi\delta T_R + \varphi), \quad (9)$$

where $A, B, C, T_1^{\text{Ramsey}}, T_2^{\text{Ramsey}}, \delta$ and φ are the fitting parameters. The fit gives the relaxation times with uncertainties $T_1^{\text{Ramsey}} = 3.20(1)$ ms and $T_2^{\text{Ramsey}} = 3.95(25)$ ms. Inset of figure 7 is the plot of the third term of equation (9) which shows the Ramsey oscillations in better contrast than the OD plot in figure 7.

In this method, like in the Franzen method, the T_1^{Ramsey} is a measurement of the population relaxation time for all m_F levels confounded and it is consistent with T_1^{Franzen} . However in contrast to the T_1^{Ramsey} population

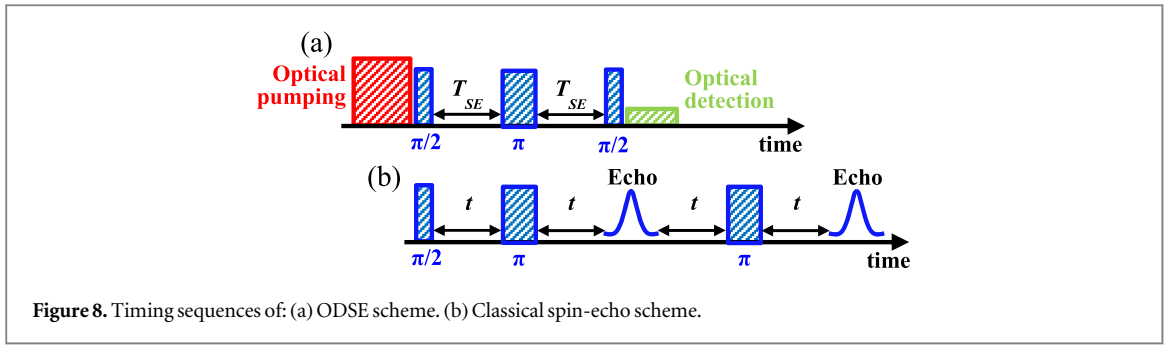


Figure 8. Timing sequences of: (a) ODSE scheme. (b) Classical spin-echo scheme.

relaxation time, $T_2^{*\text{Ramsey}}$ refers to the coherence relaxation time specific for the clock transition alone [16]. It is longer than T_2 from CW-DR method, but this $T_2^{*\text{Ramsey}}$ is still significantly shorter than the predicted coherence relaxation time ($T_2 = 4.5$ ms) from section 2. A likely reason for this can be the presence of the inhomogeneity of the static magnetic field inside our vapor cell that motivated us to propose our ODSE method to suppress this effect and measure the intrinsic T_2 (see section 4.4). Although, we note that such static magnetic field gradients are generally small across the vapor cell in our atomic clock, for example on the order of 4% in a similar physics package (see [52]).

In addition to the relaxation times, the microwave detuning from the resonance—which is given by the Ramsey oscillations—is obtained from the fit to equation (9) to be $\delta = 3.8 \pm 0.003$ kHz which is in excellent agreement with the measurement conditions.

4.4. ODSE scheme

In order to suppress coherence relaxation due to static magnetic field gradients (see section 2), we propose the new scheme of ODSE. The ODSE method is inspired by the NMR spin-echo method presented by Hahn [21] which is used to narrow the resonance line broadening in inhomogeneous static magnetic fields.

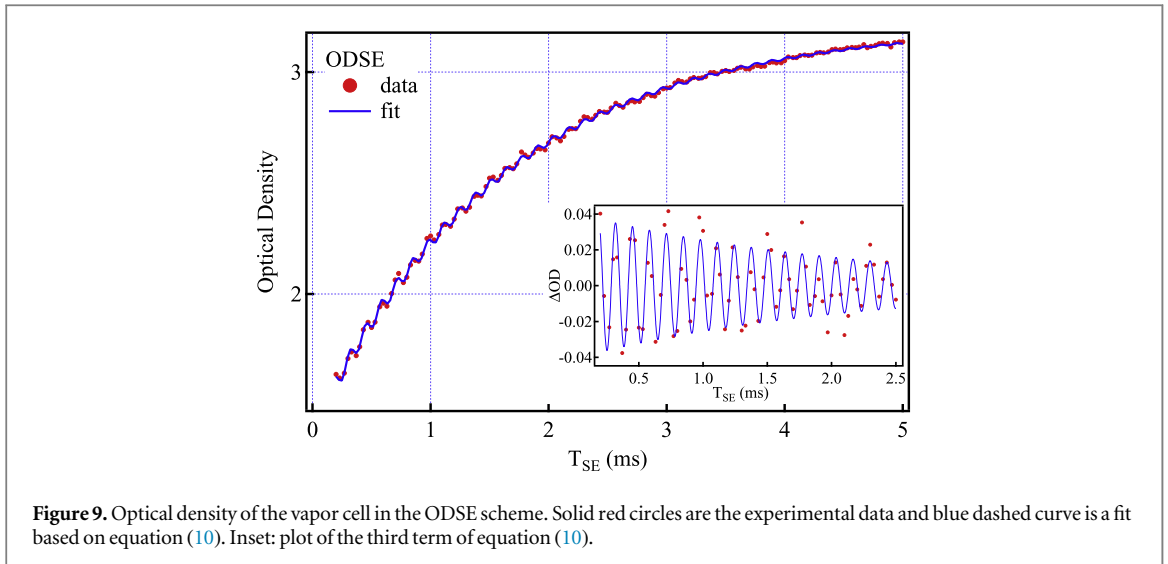
In classical NMR spin-echo, a pickup coil is required to detect the magnetic moments' precession of the sample [40], which on one hand cannot easily be integrated into an atomic clock using a microwave cavity and on the other hand can collect noise from the cell and reemit the collected microwaves through the wires outside of the cell, thus producing additional noise. In the proposed ODSE method a photodetector is used to measure the OD in the vapor cell which is much more robust, reliable and does not feedback noise to the atoms, thus circumventing the problems existing in the standard method of detection using pickup coil.

In the Ramsey-DR scheme, after the first $\pi/2$ microwave pulse, because of the inhomogeneity of the static magnetic field, the atomic spins dephase at different rates and their coherence starts to decay which finally results in a shorter coherence relaxation time compared to the intrinsic T_2 . To suppress this effect—like in NMR spin-echo—we apply a π microwave pulse added between the $\pi/2$ microwave pulses of the Ramsey-DR method and propose this resulting ODSE method for relaxation time measurements in an atomic vapor cell (see figure 8(a)). In the ODSE method, all the experimental conditions of optical pumping, optical detection and $\pi/2$ microwave pulses are the same as for the Ramsey-DR scheme (see section 4.3). The additional π pulse is separated from each of the two $\pi/2$ pulses by a dephasing time T_{SE} and has the same frequency and amplitude as the $\pi/2$ pulses, but its duration is two times longer so the duration of one complete cycle of ODSE scheme becomes $2T_{SE} + 2.7$ ms. The π pulse flips the direction of dephasing spins and reverses the spin phases (spin-flips). After some time equal to the dephasing time, T_{SE} , the dephased states are rephased at the instant of the second $\pi/2$ microwave pulse. Finally, the detection by the second $\pi/2$ pulse and the laser pulse destroys the atomic coherences so no more consecutive echoes (as observed in NMR, see figure 8(b)) can be detected. The OD of the vapor sample is recorded by varying the rephasing (and dephasing) time T_{SE} , with the same experimental conditions as in the case of Ramsey-DR scheme, i.e. a static magnetic field of 40 mG and microwave frequency detuning of $\delta = 3.8$ kHz from the clock transition. Like in the Ramsey-DR method, a trade-off exists for selecting δ in the ODSE method: for very small δ , big initial variations in I_t and thus in OD can be observed, but only few oscillations occur before they are damped away after about T_R or $T_{SE} \approx 2 \cdot T_2$. For very big δ on the other hand, many oscillations can be observed over this timescale but the maximum variation of I_t is small, which reduces the signal-to-noise ratio of the OD data.

The experimental data shown in figure 9 is fitted to the function:

$$\text{OD} = A - B \exp(-2T_{SE}/T_1^{\text{ODSE}}) + C \exp(-2T_{SE}/T_2^{\text{ODSE}}) \sin(4\pi\delta T_{SE} + \varphi), \quad (10)$$

where $A, B, C, T_1^{\text{ODSE}}, T_2^{\text{ODSE}}, \delta$ and φ are the fitting parameters. The fit gives both the relaxation times of $T_1^{\text{ODSE}} = 3.21$ (5) ms and $T_2^{\text{ODSE}} = 4.30$ (85) ms and $\delta = 3.8 \pm 0.005$ kHz. T_1^{ODSE} refers to the population relaxation time for the transitions between all m_F levels (like in the Franzen and Ramsey-DR methods). It shows



a very good consistency with the obtained T_1' from Franzen and Ramsey-DR methods. The measured T_2^{ODSE} is in a good agreement with the predicted intrinsic coherence relaxation time T_2 (≈ 4.5 ms).

In our proof-of-principle experiment, the measured relaxation times in ODSE method have larger uncertainties (3–5 times) compared to the ones from the Ramsey-DR method. We attribute this phenomena to: (1) the ODSE signal has a lower amplitude than the Ramsey-DR signal which is due to the longer duration of one complete interrogation cycle (2.7 ms + $2T_{\text{SE}}$ versus 1.9 ms + T_{R}), and (2) the residual instabilities of the microwave-synthesizer frequency over the entire measurement duration of about two hours may introduce additional noise on the signal (in Ramsey-DR and ODSE methods about 250 (figure 7) and 150 (figure 9) data points are presented, respectively).

To demonstrate the enhanced immunity of the ODSE method to inhomogeneity in the static magnetic field, the measurements were repeated with both Ramsey-DR and ODSE methods when the static magnetic field was doubled to 80 mG—resulting also in doubling of the static magnetic field gradient dominated by the geometry of the field coil—while all other parameters were kept unchanged. Under these conditions, with ODSE scheme the coherence relaxation time was measured to be $T_2^{\text{ODSE}} = 4.26$ (80) ms which is consistent to better than 1% with the measured coherence relaxation time when the magnetic field was 40 mG. But in the case of the Ramsey-DR scheme at higher magnetic field, the coherence relaxation time was measured to be $T_2^{\text{Ramsey}} = 3.80$ (25) ms which is about 4% shorter compare to $T_2^{\text{Ramsey}} = 3.95$ (25) ms obtained with lower magnetic field and its gradient. This comparison shows that the ODSE scheme is a promising method to suppress the effect of inhomogeneity of the static magnetic field across the vapor cell, even in the case of our well-controlled clock physics package with its highly homogeneous magnetic field.

5. Conclusion

We have introduced and demonstrated the method of ODSE to determine the population relaxation time (for all m_F -levels of the $F_g = 1$ and $F_g = 2$ ground states simultaneously) and the intrinsic coherence relaxation time, T_2 , specifically for the clock transition in a thermal atomic vapor with buffer-gas in view of its application to atomic clocks. This method was compared to other well established Franzen, CW-DR and Ramsey-DR methods using the same ^{87}Rb vapor cell. The population relaxation time measured with the ODSE method was very consistent with the ones from Franzen and Ramsey-DR methods. In all those pulsed methods, the obtained population relaxation time measured for all m_F -levels simultaneously (and not only for the clock transition). We have shown that the ODSE method suppresses coherence relaxation arising from gradients in the static magnetic field across the vapor cell and thus yields the intrinsic coherence relaxation time closer to the theoretically predicted T_2 . In contrast, the measured coherence relaxation times by both CW-DR and Ramsey-DR methods were shorter than the predicted T_2 , due to the inhomogeneity of the magnetic field.

Our proof-of-principle demonstrations shows that ODSE is a highly useful tool for measuring intrinsic relaxation rates in atomic vapors, independently of present magnetic field gradients. By measuring T_2 times with both the ODSE and Ramsey-DR schemes, it should also be possible to obtain experimental information on the magnetic field gradients across the atomic sample or vapor cell under study. Contrary to NMR spin-echo, our ODSE method does not need any pickup-coil but uses a photodetector to record the light absorbed in the vapor cell (OD), which is more robust and less noisy than detection in the radio-frequency or microwave regime.

Moreover, the photodetector can be conveniently placed outside the atomic vapor system under study—in our case outside the entire vapor-cell clock physics package—which makes the ODSE method an ideal candidate for characterizing relaxation times in atomic clocks with a cavity. While not covered by this present study, it would be of interest to study a potential extension of the ODSE technique to less localized atomic systems such as vapor cells without buffer-gas but equipped with an anti-relaxation wall coating. Similarly, the ODSE method is of high interest for characterizing relaxation rates in other quantum optics systems with optical readout, such as quantum information storage or processing [5, 53], cold-atom experiments [54], and other applications of quantum systems that rely on long-live atomic coherences.

Acknowledgments

This work was supported by the Swiss National Science Foundation (SNSF grants no. 140712 and 162346), the European Metrology Research Programme (EMRP project IND55-Mclocks), SNSF-Scopes project (152511) and Ministry of Education, Science and Technological Development of Republic Serbia (III 45016 and OI 171038) and COST Action 1403 Nanoscale Quantum Optics. The EMRP is jointly funded by the EMRP participating countries within EURAMET and the European Union. We thank A K Skrivervik and A Ivanov (both EPFL-LEMA) for their support on the microwave cavity, C Calosso (INRIM, Italy) for providing the microwave LO, W Moreno and M Pellaton (both LTF) for helpful discussions. We thank our former colleague S Kang for his contributions to the early phases of the work.

References

- [1] Keeler J 2010 *Understanding NMR Spectroscopy* 2nd edn (Chichester: Wiley)
- [2] Budker D and Romalis M 2007 *Nat. Phys.* **3** 227
- [3] Vanier J and Audoin C 1989 *The Quantum Physics of Atomic Frequency Standards* (Bristol: Adam Hilger)
- [4] Camparo J 2007 *Phys. Today* **60** 33
- [5] Julsgaard B, Kozhekin A and Polzik E S 2001 *Nature* **413** 400
- [6] Knappe S 2007 Emerging topics: MEMS atomic clocks *Comprehensive Microsystems* ed Y Gianchandani et al vol 3 (Amsterdam: Elsevier) p 571–612
- [7] Dupuis RT, Lynch T J and Vaccaro J R 2008 *Proc. IEEE Int. Frequency Control Symp.* ed B Jadsliwer (*Honolulu, Hawaii, USA, 19–21 May 2008*) pp 655–60
- [8] Waller P, Gonzalez S, Binda S, Sesia I, Hidalgo I, Tobias G and Tavella P 2010 *IEEE Trans. Ultrason. Ferroelect. Freq. Control* **57** 738
- [9] Chunhao H, Zhiwu C, Yuting L, Li L, Shenghong X, Lingfeng Z and Xianglei W 2013 *Int. J. Navig. Obs.* **2013** 371450
- [10] Kuzmich A, Mandel L and Bigelow N P 2000 *Phys. Rev. Lett.* **85** 1594
- [11] Budker D, Gawlik W, Kimball D F, Rochester S M, Yashchuk V V and Weis A 2002 *Rev. Mod. Phys.* **74** 1153
- [12] Franzen W 1959 *Phys. Rev.* **115** 850
- [13] Liberman V and Knize R J 1986 *Phys. Rev.* **34** 5115
- [14] Graf M T, Kimball D F, Rochester S M, Kerner K, Wong C and Budker D 2005 *Phys. Rev. A* **72** 23401
- [15] Corsini E P, Karaulanov T, Balabas M and Budker D 2013 *Phys. Rev. A* **87** 22901
- [16] Horsley A, Du G X, Pellaton M, Affolderbach C, Mileti G and Treutlein P 2013 *Phys. Rev. A* **88** 063407
- [17] Budker D, Hollberg L, Kimball D F, Kitching J, Pustelny S and Yashchuk V V 2005 *Phys. Rev. A* **71** 012903
- [18] Castagna N and Weis A 2011 *Phys. Rev. A* **84** 053421
Castagna N and Weis A 2012 *Phys. Rev. A* **85** 059907 (erratum)
- [19] Scholtes T, Woetzel S, IJsselstein R, Schultze V and Meyer H G 2014 *Appl. Phys. B* **117** 211
- [20] Castagna N, Bison G, Di Domenico G, Hofer A, Knowles P, Macchione C, Saudan H and Weis A 2009 *Appl. Phys. B* **96** 763
- [21] Hahn E L 1950 *Phys. Rev.* **80** 580
- [22] Bar-Gill N, Pham L M, Jarmola A, Budker D and Walsworth R L 2013 *Nat. Commun.* **4** 1743
- [23] Hodges J S, Yao N Y, Maclaurin D, Rastogi C, Lukin M D and Englund D 2013 *Phys. Rev. A* **87** 032118
- [24] Viola L and Lloyd S 1998 *Phys. Rev. A* **58** 4
- [25] Shim J H, Niemeyer I, Zhang J and Suter D 2012 *Europhys. Lett.* **99** 4
- [26] Hosseini M, Sparkes B M, Campbell G, Lam P K and Buchler B C 2011 *Nat. Commun.* **2** 174
- [27] Tittel W, Afzelius M, Chanelière T, Cone R L, Kröll S, Moiseev S A and Sellars M 2010 *Laser Photon. Rev.* **4** 244–67
- [28] Laplane C, Jobez P, Etesse J, Timoney N, Gisin N and Afzelius M 2016 *New J. Phys.* **18** 013006
- [29] Wolfowicz G, Maier-Flaig H, Marino R, Ferrier A, Vezin H, Morton J J L and Goldner P 2015 *Phys. Rev. Lett.* **114** 170503
- [30] Bandi T, Affolderbach C, Stefanucci C, Merli F, Skrivervik A K and Mileti G 2014 *IEEE Trans. Ultrason. Ferroelect. Freq. Control* **61** 1769–78
- [31] Kang S, Gharavipour M, Gruet F, Affolderbach C and Mileti G 2015 *Proc. Joint Conf. IEEE Int. Frequency Control Symp. & European Frequency and Time Forum (EFTF) (Denver, Colorado, USA, 12–16 April 2015)* pp 800–3
- [32] Vanier J and Mandache C 2007 *Appl. Phys. B* **87** 565–93
- [33] Oreto P J, Jau Y Y, Post A B, Kuzma N N and Happer W 2004 *Phys. Rev. A* **69** 042716
- [34] Robinson H G, Ensberg E S and Dehmelt H G 1958 *Bull. Am. Phys. Soc.* **3** 9
- [35] Bouchiat M A and Brossel J 1966 *Phys. Rev.* **147** 41
- [36] Bandi T, Affolderbach C and Mileti G 2012 *J. Appl. Phys.* **111** 124906
- [37] Vanier J, Simard J F and Boulanger J S 1974 *Phys. Rev. A* **9** 1031
- [38] Franz F A and Lüsher E 1964 *Phys. Rev.* **135** A582
- [39] Franz F A 1965 *Phys. Rev.* **139** A603
- [40] Carr H Y and Purcell E M 1954 *Phys. Rev.* **94** 630–8

- [41] Torrey H C 1956 *Phys. Rev.* **104** 563–5
- [42] Risley A, Jarvis S Jr and Vanier J 1980 *J. Appl. Phys.* **51** 4571
- [43] Dicke R H 1953 *Phys. Rev.* **89** 472
- [44] Stefanucci C, Bandi T, Merli F, Pellaton M, Affolderbach C, Mileti G and Skrivervik A K 2012 *Rev. Sci. Instrum.* **83** 104706
- [45] Gruet F, Pellaton M, Affolderbach C, Bandi T, Matthey R and Mileti G 2012 *Proc. Int. Conf. on Space Optics (ICSO) (Ajaccio, Corsica, 9–12 October 2012)* no 48
- [46] Calosso C E, Micalizio S, Godone A, Bertacco E K and Levi F 2007 *IEEE Trans. Ultrason. Ferroelectr. Freq. Control* **54** 1731
- [47] Gharavipour M, Affolderbach C, Kang S, Bandi T, Gruet F, Pellaton M and Mileti G 2016 *J. Phys.: Conf. Ser.* **723** 012006
- [48] Ramsey N 1956 *Molecular Beams* (Oxford: Oxford University Press)
- [49] Micalizio S, Godone A, Levi F and Calosso C 2009 *Phys. Rev. A* **79** 013403
- [50] Kang S, Gharavipour M, Affolderbach C, Gruet F and Mileti G 2015 *J. Appl. Phys.* **117** 104510
- [51] Kang S, Gharavipour M, Affolderbach C and Mileti G 2015 *Electron. Lett.* **51** 1767–9
- [52] Affolderbach C, Du G, Bandi T, Horsley A, Treutlein P and Mileti G 2015 *IEEE Trans. Instrum. Meas.* **64** 3629–37
- [53] Ardavan A, Rival O, Morton J J L, Blundell S J, Tyryshkin A M, Timco G A and Winpenny R E P 2007 *Phys. Rev. Lett.* **98** 057201
- [54] Maineult W, Deutsch C, Gibble K, Reichel J and Rosenbusch P 2001 *Phys. Rev. Lett.* **109** 020407

Scattering-enhanced absorption and interference produce a golden wing color of the burnished brass moth, *Diachrysia chrysitis*

Dejan Pantelić,^{1,*} Svetlana Savić-Šević,¹ Dejan V. Stojanović,² Srećko Ćurčić,³ Aleksandar J. Krmpot,¹ Mihailo Rabasović,¹ Danica Pavlović,¹ Vladimir Lazović,¹ and Vojislav Milošević¹

¹*Institute of Physics, University of Belgrade, Pregrevica 118, 11080 Zemun, Belgrade, Serbia*

²*Institute of Lowland Forestry and Environment, University of Novi Sad, Antona Čehova 13, 21000 Novi Sad, Serbia*

³*Institute of Zoology, University of Belgrade—Faculty of Biology, Studentski Trg 16, 11000 Belgrade, Serbia*

(Received 3 November 2016; published 8 March 2017)

Here we report how interference and scattering-enhanced absorption act together to produce the golden wing patches of the burnished brass moth. The key mechanism is scattering on rough internal surfaces of the wing scales, accompanied by a large increase of absorption in the UV-blue spectral range. Unscattered light interferes and efficiently reflects from the multilayer composed of the scales and the wing membranes. The resulting spectrum is remarkably similar to the spectrum of metallic gold. Subwavelength morphology and spectral and absorptive properties of the wings are described. Theories of subwavelength surface scattering and local intensity enhancement are used to quantitatively explain the observed reflectance spectrum.

DOI: [10.1103/PhysRevE.95.032405](https://doi.org/10.1103/PhysRevE.95.032405)

I. INTRODUCTION

Fascinating “inventions” of evolution have been discovered in a large number of recent studies dealing with the biophysics of living creatures. In that respect, insects are an excellent research subject due to their diversity and abundance.

Biophotonics of insects is a particularly active subject which aims to explain function and imitate intricate micro- and nanostructures on their bodies. Several studies present a comprehensive overview of the current research [1–3]. Surprising results are still being published, such as the photonic system of a Saharan silver ant, enabling radiative dissipation of heat, directly through the IR atmospheric window [4]. This and a number of other studies suggest that nature has developed many technologies which can be used to solve everyday problems, if successfully imitated [5,6].

Optical photonic structures in the living world are diverse and have been classified by Land [7], based on their biological function, including tapeta (light-path doubling or image forming), camouflage, display, optical filters (e.g., corneal nipples of insect compound eyes), and anatomical accidents (features whose optical properties have no obvious biological function, e.g., mother-of-pearl in some mollusks).

More specifically, the biophotonics of Lepidoptera draws much attention, mostly due to the attractiveness of butterflies. Much less is known about moths (suborder Heterocera), which represent a group of Lepidoptera, characterized by the wings mostly having drab colors (gray or brown), and feathery or saw-edged antennae (vs club-shaped in butterflies). While moths are more numerous than butterflies, the number of structural coloration studies is significantly smaller. Only attractive and conspicuous moth species were explored, such as the Madagascan sunset moth [8]. The lack of interest is, possibly, due to the simpler wing-scale structure of moths, compared to really complex features present on the scales of day flying butterflies (e.g., Bragg gratings or photonic crystals).

Golden wing patches are prominent features of some noctuid moths. The patches might be just small marks as in *Autographa jota* (Linnaeus, 1758) and *A. bractea* (Denis & Schiffermüller, 1775), or large areas, as in *Diachrysia balluca* Geyer, 1832. The physics behind the golden moth color was previously analyzed using the diffraction theory of Stratton-Silver-Chu [9] in the case of *Thysanoplusia orichalcea* (Fabricius, 1775) (previously included in the genus *Trichoplusia* McDunnough, 1944) (Noctuidae family). However, a correspondence between theory and experimentally recorded spectra was qualitative, probably due to approximations of the mathematical formalism.

Other insects with a golden cuticle do exist, such as *Chrysin aurigans* (Rothschild & Jordan, 1894) (Coleoptera: Scarabaeidae) [10], whose broadband metallic reflection is due to a chirped Bragg mirror within the cuticle. Some species have a tunable color, which depends on atmospheric humidity [11] or stressful events [12], enabling the insects to change the color from red to golden.

Rothschild *et al.* [13] found that carotenoid pigments may also contribute to golden metallic areas of Danainae butterfly pupae. Similar results were obtained by Taylor [14] and Neville [15]. In contrast, Steinbrecht *et al.* [16] proved that golden reflections of *Euploea core* (Cramer, 1780) (Lepidoptera: Nymphalidae) pupae have an entirely physical nature. They showed that reflectance spectra of the cuticle (possessing multiple endocuticular thin alternating layers) and metallic gold are very similar, with a characteristic edge at 450–550 nm. The authors also emphasize that the carotenoids in the epidermis cannot contribute to the color effects because the cuticle practically does not transmit yellow light at all.

Scattering from an irregular surface is a secondary mechanism of structural coloration—interference and diffraction being dominant ones. For example, lycaenid butterflies (in particular, subfamily Polyommatae) scatter light from the internal, pepper-pot-like, Bragg layers (having holes of 100 nm average diameter). The wing-scale laminae are almost hollow and permit the blue radiation to escape [17]. Pieridae can also be mentioned due to the nanobeads (pigment granules), which fill the space between the laminae [18], where the scattering

*pantelic@ipb.ac.rs

and fluorescence extend the reflection spectrum [19,20]. Scattering in the living world is sometimes accompanied by light trapping, as in diatoms [21]. This seems to be a significant mechanism for efficient light harvesting in photosynthetic organisms.

Here we describe how several optical mechanisms interact to produce the golden wing color of the burnished brass moth, *Diachrysia chrysitis* (Linnaeus, 1758). We have studied spectral properties of the golden wing patches, as well as the internal and external ultrastructure of the wing scales and wing membranes. It was found that the scattering from irregular internal surfaces of each scale suppresses the UV-blue reflection, while interference efficiently reflects the red-infrared spectral range. A theoretical model is proposed, which combines interference and scattering from the scale laminae. The finite element method (FEM) is used to confirm the trapping and local intensity enhancement of light inside the laminae, while the modified transfer matrix method is used to calculate the reflection spectrum.

II. OPTICAL PROPERTIES AND STRUCTURE OF *D. CHRYSITIS* WING

The burnished brass moth (*D. chrysitis*; shown in Fig. 1) is a common species of the Noctuidae family (Insecta: Lepidoptera). It inhabits temperate climates in the Palearctic region [22]. *D. chrysitis* is a remarkable moth with big, golden (sometimes brassy-green) areas on each forewing. The wingspan is 28–35 mm, while the length of each forewing is 16–18 mm [23]. The burnished brass moth is usually found in marshy areas or in slightly moist forb communities. The larvae feed on plants such as *Urtica* spp., *Lamium* spp., or *Cirsium* spp. [24]. The moth flies from May to October depending on the location. It flies regularly in dusk, and was seen visiting flowers of various plants. Sometimes it can be noticed during the day, even sucking nectar. The species is widespread in Serbia [25].

It is supposed that irregular golden patches in the forewings of *D. chrysitis* are an example of disruptive coloring, as an excellent way of hiding oneself by breaking up the body contours [26]. Additionally, it was also postulated that specular



FIG. 1. Burnished brass moth (*D. chrysitis*) with golden areas on its forewings.

reflection of the sun's rays may imitate the glittering of dew droplets. Even more, it seems that the wing color is optimized to efficiently reflect the yellowish light of the sun. As a dusk species, the moth may emit a signal in the IR spectral range from the golden patches, which might be used as a signal for intraspecific recognition. Anatomical accidents seem unlikely because metallic areas on *D. chrysitis* forewings form species-specific patterns [27].

From the optical point of view, the most prominent features of the studied moth are golden-color wing patches, as seen in Fig. 1. The corresponding wing spectra were recorded in reflection using a fiber optic spectrometer (manufactured by Ocean Optics, HR2000CG-UV-NIR), with a 400- μm core diameter fiber. A halogen lamp was used as a light source, and spectra were referenced to a standard white surface. The light collection angle was limited by the numerical aperture of the fiber ($\text{NA} = 0.22$, which is equivalent to an angular range of $\pm 12.7^\circ$), positioned such that an approximately 40- mm^2 area is observed. This means that the spectra of individual scales are integrated both angularly and across the wing surface. This fact was accounted for in the numerical simulations.

The spectrum of *D. chrysitis* is broad, with a cutoff wavelength at approximately 500 nm. Its exact shape slightly depends on the angle between light source, wing, and detector. There is a close similarity with the spectrum of metallic gold, as shown in Fig. 2. The specular reflectance spectrum of gold is taken tabulated from Ref. [28], where it is treated as a reference standard.

Optical reflection microscopy of the *D. chrysitis* forewing reveals an almost uniform, intense golden sheen as shown in Fig. 3(a). In contrast, reflection from individual scales is yellowish, with occasional red and green bands, presented in Fig. 3(b). Overlapped scales show increased reflection and color bands, as can be observed in the same image. If observed in transmission, an individual scale in air [see Fig. 3(c)] is quite transparent, with a slight residual absorption. By immersing

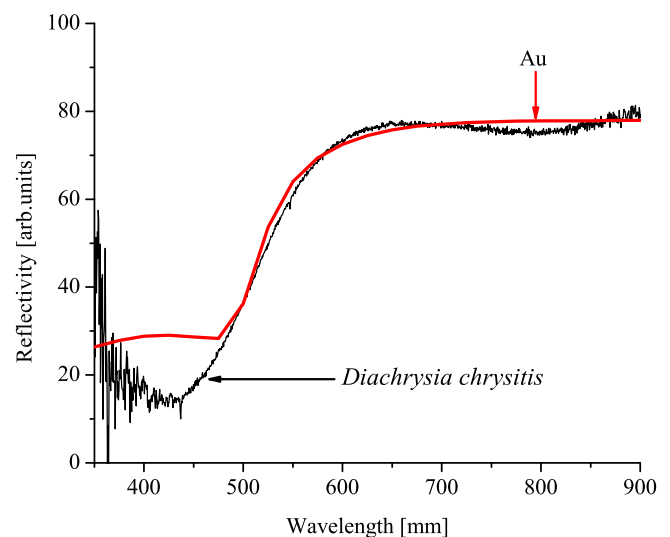


FIG. 2. Spectral reflectance of metallic gold (red curve) and golden wing patch of *D. chrysitis* forewings (black curve). Reflectance of *D. chrysitis* is scaled to emphasize the similarity with the gold.

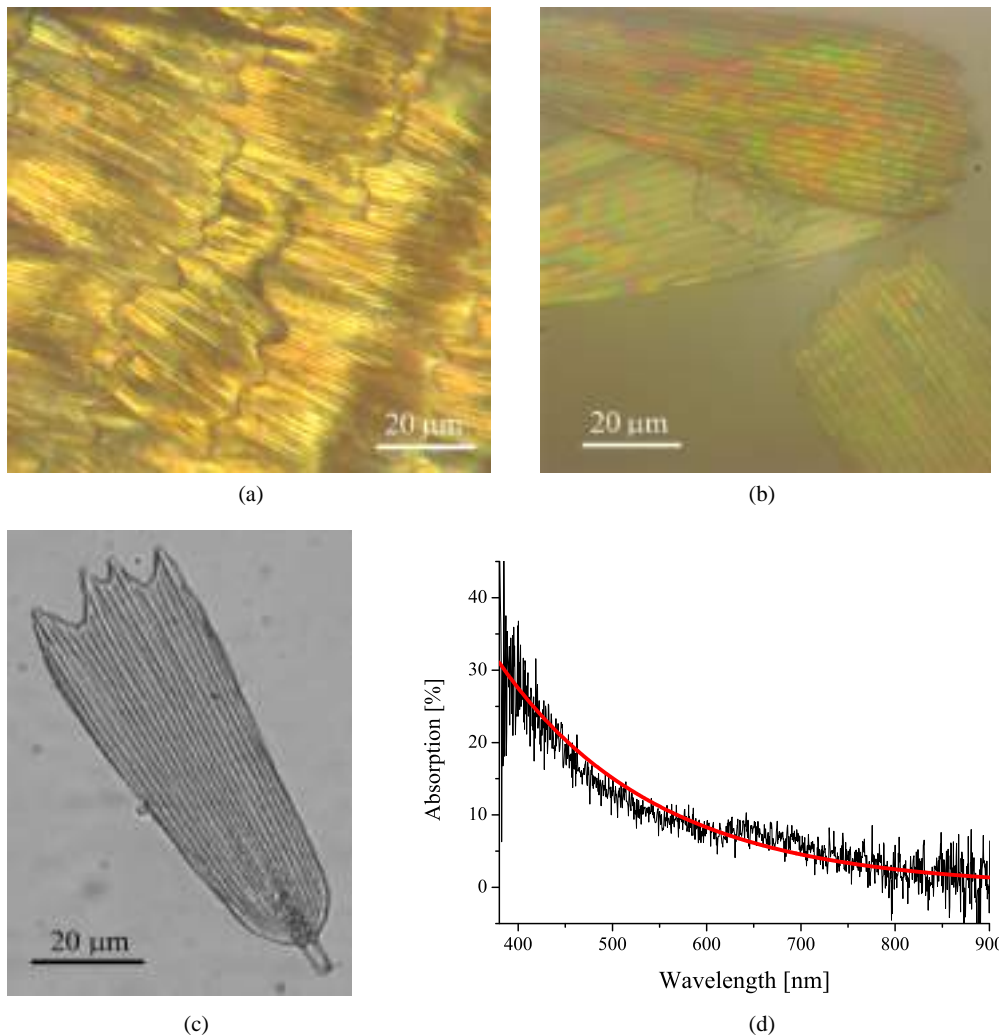


FIG. 3. Optical microscope images of *D. chrysitis*: (a) Scales on the forewing showing the uniformly golden reflection. (b) A microscope reflection image of two individual, overlapped scales. (c) A transmission image of an individual scale in air. (d) Absorption spectrum of a single scale placed in an immersion oil (black line) and the corresponding exponential fit (red line).

the scale in an index matching liquid (manufactured by Cargile, series A, with the certified refractive index 1.5700 ± 0.0002) Fresnel reflection was suppressed. We measured the absorption spectrum [Fig. 3(d)], which is very similar to that of melanin [29], showing exponential decrease from the UV to the IR part of the spectrum. We were able to estimate the value of the absorption coefficient α (or the imaginary part of the complex index of refraction $k = \alpha\lambda/4\pi$), and use it in further calculations. We have found that k ranges between 0.081 (at 380 nm) and 0.0013 (at 800 nm).

A field-emission gun scanning electron microscope (FEGSEM) was used to study the fine anatomy of the moth scales. The *D. chrysitis* forewing possesses a number of overlapping scales [as in Fig. 4(a)], but we were not able to see a difference between cover and ground scales. At higher magnification, as in Fig. 4(b), we can see that the upper lamina is ornamented with very thin lamellar ridges (separated by approximately $1.8 \mu\text{m}$). They are connected with herringbone shaped cross ribs, which constitute a subwavelength diffraction grating with the period of roughly 150 nm. A dual wing membrane seems to be an important optical component, too.

Its thickness is of the order of 500 nm and contains a number of 300-nm diameter, randomly dispersed, hemispherical protuberances [see inset in Fig. 4(a)].

Individual scales were prepared for scanning electron microscopy by the double transfer method, which was begun by detaching a scale with a low-surface-energy adhesive (adhesive layer of “Post-it” sticky note), followed by the transfer to a high-surface-energy tape (conductive carbon). By that means, the original scale orientation was preserved. Figure 5 shows one of the partially destroyed scales and its internal and external laminae structures. We see that the external side of the upper lamina (the one facing outwards) is strongly patterned, as explained above, while its internal surface is very irregular, with linear grooves directly beneath the ridges. The external side of the lower lamina (the one facing the wing membrane) is smooth, while its internal surface is completely irregular, similar to nanometer-sized “pebbles,” with a diameter less than 60 nm.

We have observed a strong autofluorescence of scales, which is enough for nonlinear (NL) fluorescence microscopy. We used a nonlinear microscope for laser processing and

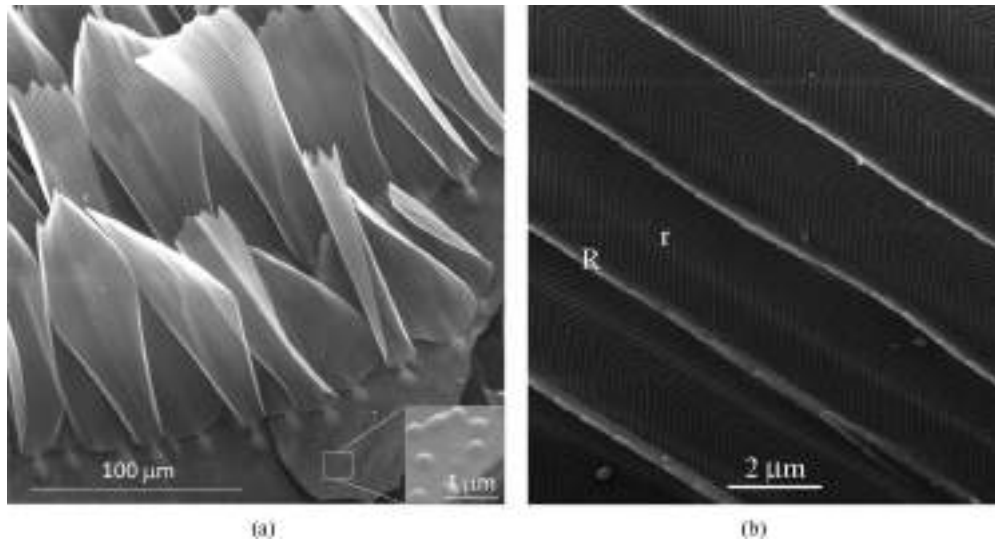


FIG. 4. (a) Scales of *D. chrysitis* in their natural position on the wing. The inset shows the enlarged part of the wing membrane with 300-nm-diameter protuberances. (b) Enlarged image of a single scale, showing lamellar ridges (R) and herringbone shaped cross ribs (r).

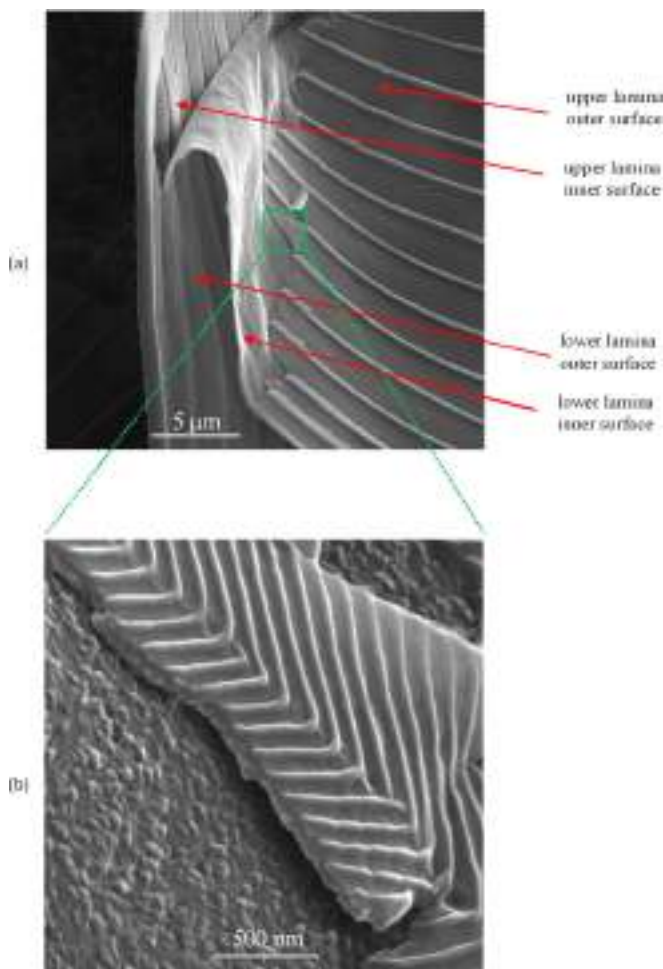


FIG. 5. FEGSEM images of a single *D. chrysitis* scale at two different magnifications. (a) This image reveals the internal and external structure of a single scale. (b) Enlarged zone of a scale showing rough internal surfaces.

cutting, too, which turned out to be a good tool for exposing otherwise hidden features. The beam power was increased above the threshold level and software was modified to enable drawing arbitrary shapes using vector images. At 840 nm and ~ 100 fs pulse length we were cutting moth chitinous structures with as low as a few milliwatts of laser power. However, continuous wave (cw) radiation at the same wavelength required an order of magnitude higher power. It was interesting that the laser-cut lines were rather irregular in the case of *D. chrysitis*, in contrast to scales of other lepidopteran species, which produced clear, well defined, lines.

To further reveal the cross-sectional geometry of *D. chrysitis* moth scales, we cut them as explained above. A SEM image of a laser-cut scale is shown in Fig. 6. The internal space of the scale is not visible due to the welding of the upper and lower laminae, but we were able to estimate the thickness of the scale at 300 nm, and the height of the ridge at 400 nm. Based on the scanning electron microscope images we are able to draw a general scheme of an individual scale as presented in Fig. 7.

We emphasize that the external features of the wing scale (such as the distance between the ridges) can be measured accurately from FEGSEM images, because they are recorded at normal incidence. Other characteristics, such as laminae thickness, are more complicated to quantify due to difficulty in determining the exact relative position of the scale and the scanning electron microscope optics (see Fig. 6, where the scale is partially lifted from the substrate). In such cases, measurements were performed using external features as a reference—e.g., lamina thickness was determined at approximately 75 nm by observing that it is approximately one half of the distance between the cross ribs (150 nm). Anyway, such measurements served just as a starting point for a wing-scale model.

Variability of the moth scales is another source of uncertainty. We recorded a number of SEM images, measured relevant features at several positions, and were able to find that they vary between 15% and 20% (depending on the measured characteristics).

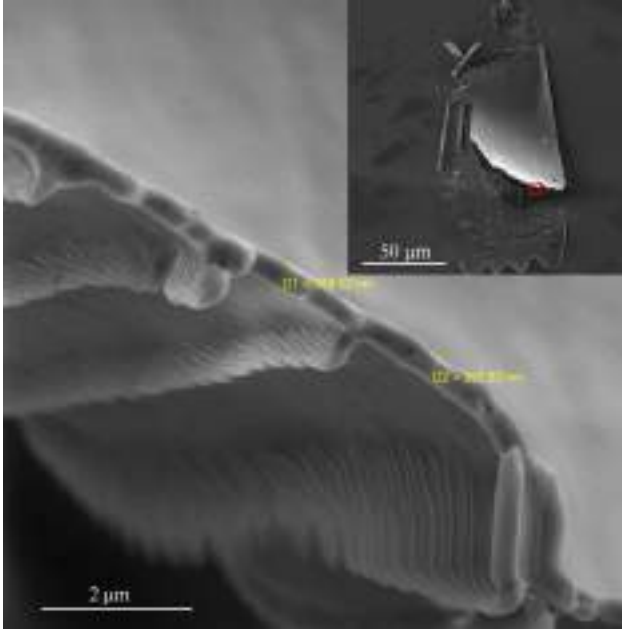


FIG. 6. A cross-sectional image of a femtosecond-laser-cut *D. chrysitis* wing scale. The image of the whole, laser-cut scale is shown in the inset.

III. OPTICAL MODELING OF THE *D. CHRYSITIS* WING SCALES

The transparency of *D. chrysitis* scales and the apparent simplicity of their internal and external structure pose a problem in explaining the golden wing color. We show that all the wing components (a double layer of scales and a wing membrane, possibly also the pigmented scales on the wing underside) work together to produce the final effect. Several features operate synergistically: slight absorbance of each scale, scattering on internal scale surfaces, interference of light within the scale, reflection of light from the wing membrane, and diffraction on the upper lamina grating.

We first demonstrate that the scattering on the internal scale surfaces leads to significant dispersal of incident light. As shown in Fig. 5, the internal scale surfaces are highly irregular, with the root mean squared (RMS) roughness estimated between 10 and 30 nm. The wavelength of the incident visible light (inside material) is much larger than the roughness and

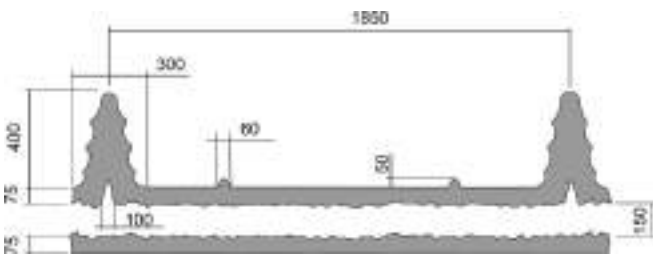


FIG. 7. A dimensional scheme of a *D. chrysitis* scale cross section. All dimensions (expressed in nanometers) are estimated from SEM images and vary across the scales. Due to the variability of features in the living world, uncertainty of all the dimensions is between 15% and 20%.

the widely used scalar surface-scattering theory [30,31] is applicable. Under these circumstances, the light is split into two parts: one, regular, propagating as if the surface is perfectly flat, and the other diffusely scattered (haze).

Quantitatively, both components are described relative to transmittance T_0 and reflectance $R_0 = 1 - T_0$ of an ideally flat surface, when Fresnel equations hold. Accordingly, the haze transmittance $T_H(\lambda)$ and reflectance $R_H(\lambda)$ of a rough surface are described by [31]

$$T_H(\lambda) = T_0 \left(1 - \exp \left\{ - \left[\frac{2\pi\sigma}{\lambda} (n_i \cos \phi_i - n_t \cos \phi_t) \right]^2 \right\} \right), \quad (1)$$

$$R_H(\lambda) = R_0 \left\{ 1 - \exp \left[- \left(\frac{4\pi\sigma}{\lambda} n_i \cos \phi_i \right)^2 \right] \right\}, \quad (2)$$

where T_0 and R_0 are the transmittance and the reflectance of a perfectly flat surface, respectively; λ is the wavelength in vacuum; ϕ_i and ϕ_t are the angles of incidence and refraction; n_i and n_t are corresponding refractive indices; σ is the surface RMS roughness.

A simple calculation, based on Eqs. (1) and (2), shows that between 1% and 3% of incident radiation is scattered at each interface, depending on the wavelength and assuming normal angle of incidence ($\phi_i = 0$), RMS roughness $\sigma = 20$ nm, and the refractive index of chitin $n_i = 1.57$. As expected, short wavelengths are scattered more than long ones. The scattered light has a tendency to be trapped inside chitin layers, in a manner similar to textured solar cells [32]. It was shown in [33] that the local light intensity is increased by $2n^2$, and absorption by $4n^2$, where n is the refractive index. This was verified for the *D. chrysitis* moth by using the finite element method (FEM) with periodic boundary conditions, applied to the model simulating a double layer of scales, as shown in Fig. 8(a). The corresponding electromagnetic field distributions can be seen in Fig. 8(b) showing the strong electromagnetic field enhancement.

Local field enhancement due to scattering is accompanied by increased absorption as predicted by the model described in [33]. We made slight modifications to correctly describe the scales of *D. chrysitis*.

The change of the beam cross section is ignored due to the thinness of the scales. This is justified by the following arguments: Assume that the angle of divergence is $\theta = 40^\circ$ and scale laminae thickness is $D = 75$ nm; then the beam spread is defined by $2Dt \tan(\theta/2) = 55$ nm. This is insignificant for a beam width of approximately 7 mm, as used in our spectral measurement. The surface absorption was disregarded, too, because the residual melanin is expected to be distributed inside the laminae.

Under these assumptions, the absorption A_{int} inside the planar layer can be described by

$$A_{int} = \frac{4n^2 T_{inc}}{T_{esc} + 4n^2 \alpha l}, \quad (3)$$

where α is absorption coefficient, n is the refractive index, I_{inc} is incident light intensity, l is the layer thickness, and T_{inc} is a fraction of light transmitted through the interface. T_{esc} is an

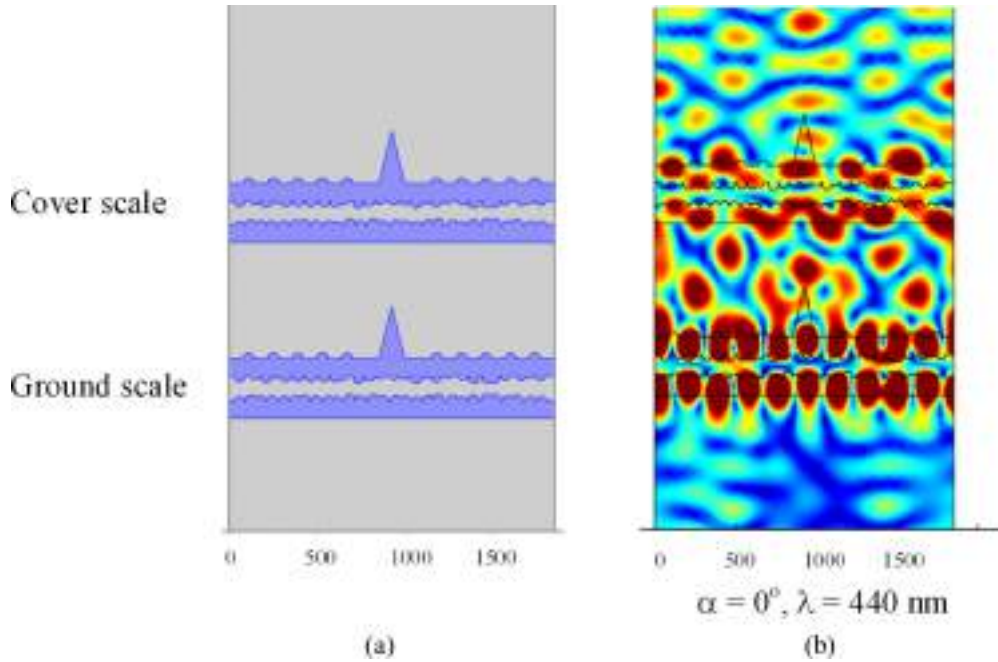


FIG. 8. (a) Geometry of the FEM model. (b) Intensity enhancement at 440 nm wavelength. The electromagnetic field is enhanced both in the ground and cover scales. Calculations were performed assuming that the angle of incidence is $\alpha = 0$ and there is no absorption.

average transmission factor of the escaping radiation, due to partial (Fresnel) transmission at the interface. According to the same model, fraction of the incident radiation escaping the layer is described by

$$F_{\text{esc}} = \frac{T_{\text{inc}} T_{\text{esc}}}{T_{\text{esc}} + 4n^2 \alpha l}. \quad (4)$$

Now we have tools to treat the problem of the golden coloration of the burnished brass moth. Its geometry includes two layers of scales and two wing membranes as shown in Fig. 9(a). It is assumed that the outside surfaces of the scales are flat, which is strictly true only for the lower lamina. The upper lamina is structured with two gratings. The coarse one

will produce diffraction orders which will be treated similarly during the propagation through the scales, the only difference being the angle of incidence. The dense grating is incapable of generating any propagating modes and will not enter the calculations. The inside scale surfaces are rough with RMS roughness of 10–30 nm, and the wing membranes are treated as flat. Fresnel reflection and transmission will be taken into account at flat surfaces, while rough surfaces will also include haze in reflection and transmission as schematically shown in Fig. 9(b). In the latter case, haze $R_H(\lambda)$ and $T_H(\lambda)$ diminish Fresnel coefficients R_0 and T_0 by the amounts $R_0 R_H(\lambda)$ and $T_0 T_H(\lambda)$. The resulting transmission and reflection coefficients are described by $R_0 - R_0 R_H(\lambda)$ and $T_0 - T_0 T_H(\lambda)$.

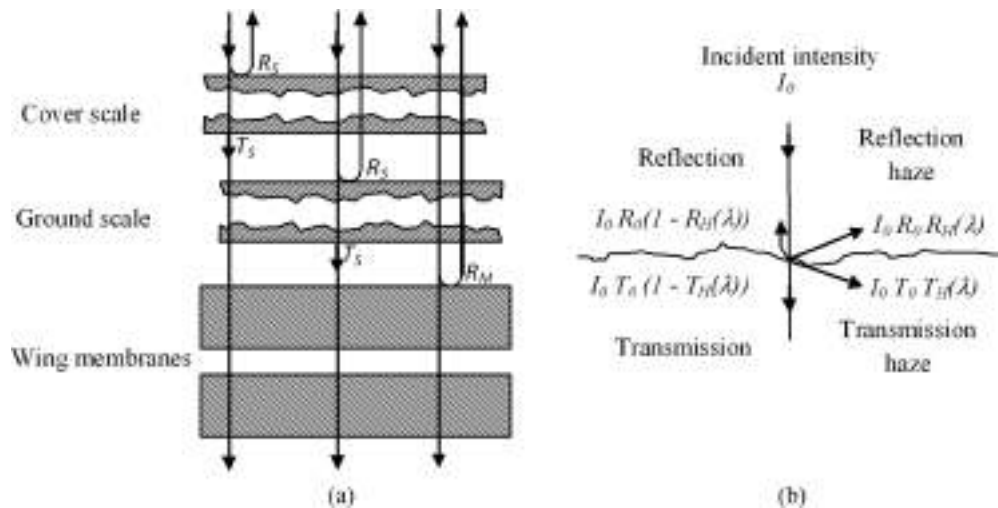


FIG. 9. (a) Geometry of the model used to simulate the wing of *D. chrysitis*. R_S and R_M are reflectance of a scale and a wing membrane, respectively. T_S is a transmittance of a single scale. (b) Reflection and transmission through the interface, as treated in a model. Incident intensity I_0 is split into four components: Fresnel reflectance (R_0), Fresnel transmittance (T_0), reflection haze (R_H), and transmission haze (T_H).

TABLE I. Numerical values of the parameters used for modeling optical reflection from *D. chrysitis* moth scales.

Parameter	Meaning	Value
N	Refractive index of chitin	1.57
α_0	Melanin absorption parameter, Eq. (5)	0.23 (1/nm)
A	Melanin absorption parameter, Eq. (5)	90 (nm)
λ_0	Melanin absorption parameter, Eq. (5)	380 (nm)
σ	RMS surface roughness	30 (nm)

The interference problem will be solved for an individual wing scale, as well as for the wing membranes, but not for the wing as a whole. This is a reasonable assumption, because the relative distances between the scales and the wing membrane are highly variable and the resulting effect is averaged across the wing surface. As a consequence, the resulting reflection spectral intensities of scales and membranes will be incoherently added.

Optical parameters of the model were estimated from the measurements performed on the scale embedded in an immersion liquid ($n = 1.57$), as described in the previous section. Therefore, the refractive index was taken to be 1.57 (consistent with the results published in [34]). According to the same study [34], the refractive index dispersion is less than 4% within the wavelength range of interest (380–900 nm) and the resulting effects were found to be insignificant. The coefficient of absorption α was modeled with an exponential function (assuming that the residual pigment is most probably melanin):

$$\alpha = \alpha_0 \exp\left(-\frac{\lambda - \lambda_0}{A}\right). \quad (5)$$

All parameters of the model are summarized in Table I.

Finding the exact solution to the multilayer interference is a problem requiring numerical tools. Here we adopt the transfer matrix method, described and used in [35] to analyze light scattering and trapping in silicon thin film solar cells. We divide incident light into two components: a scattered one, which is mostly absorbed and diffused, and an unscattered one, which interferes in wing scales and wing membranes. For the unscattered component we apply a transfer matrix method, where scattering from subwavelength rough surfaces is treated as a wavelength-dependent correction for Fresnel coefficients.

Reflection and transmission from a single scale are treated coherently using the transfer matrix method. As a result, the spectral reflectance R_S and transmittance T_S were found. Similarly, the reflection from the double wing membrane was treated coherently (with the resulting reflectance R_M). Scattering from the wing membrane was not included in calculations due to the sparsity and large dimensions of scattering inclusions (as illustrated in Fig. 4). The resulting spectrum of the wing as a whole is composed of three components: one which is reflected from the cover scales, the other reflected from the ground scales, and the final one due to the wing membranes. We combine them incoherently, because the mutual position between scales and membranes is stochastic and highly variable. The final reflected spectral

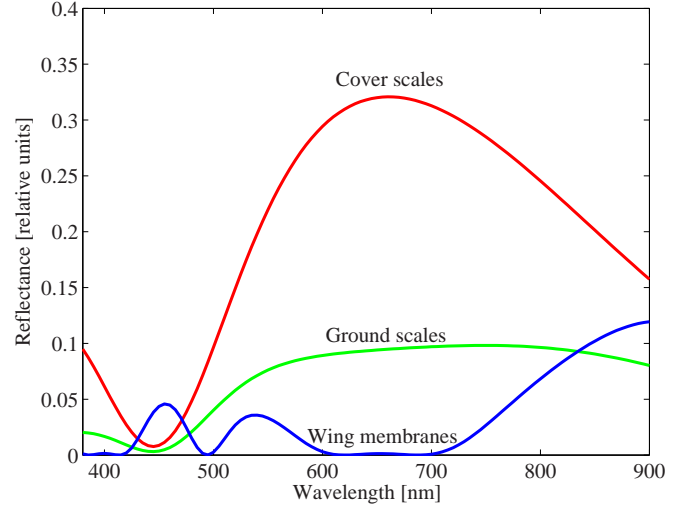


FIG. 10. Contributions of wing membranes, cover scales, and ground scales to the resulting wing spectrum. They are calculated using the transfer matrix method and normalized to the intensity of the incident light before being transmitted through the layers.

distribution of the whole wing is thus

$$R = R_S + T_S R_S T_S + T_S^2 R_M T_S^2. \quad (6)$$

The first term corresponds to the reflection from the cover scale, the second to the transmission through the cover scale, followed by the reflection from the ground scale and return path through the cover scale. The third term describes transmission through the cover and ground scales, followed by the reflection from the wing membrane, and return path through both layers of the scales. The calculated contribution of each term to the final spectrum is shown in Fig. 10 (normalized to the intensity of light before being transmitted through the layers).

Spectral contributions of wing components significantly depend on their geometry, i.e., scale laminae and wing membrane thicknesses. For some combination of dimensional parameters, even a single scale can quite faithfully reproduce an experimentally recorded spectrum (as in Fig. 11). However, there are slight modulations within the whole spectral range, due to thin film interference effects. They disappear when spatial and angular averaging is included, as further explained. As explained above, losses are much higher inside the blue-UV spectral range, as can be seen in Fig. 11. According to Eqs. (3) and (4), most of the light energy is absorbed, and the rest of the radiation is scattered. It is interesting to note that a significant amount of radiation is transmitted through the wing membranes (green curve in Fig. 11). However, the UV component of transmitted radiation is efficiently absorbed by the dark, pigmented scales, on the wing underside.

There is an important word of caution. In order to get a consistently golden wing color, the dimensional and optical parameters of each individual scale should be kept within quite tight tolerances—a task completely impossible in the living world. It is more realistic to expect significant variability of all the parameters. Thus they were varied in our simulations (according to the normal distribution) within $\pm 15\%$ of the values producing fit in Fig. 11. The angle of incidence was also

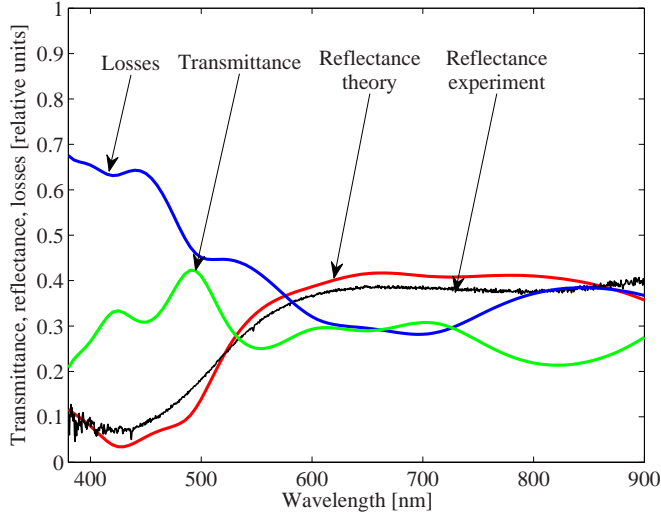


FIG. 11. A spectral reflectivity (red curve) of a *D. chrysitis* moth wing, calculated by the transfer matrix method is shown. The corresponding experimental curve (black curve) is added for reference. Losses (due to scattering and absorption, blue curve) and the wing transmittance (green curve) are displayed, too.

allowed to fluctuate within $\pm 20^\circ$, which imitates variability of scale orientations.

As a result, 100 different spectra were calculated (for clarity, only 25 of them are displayed in Fig. 12 as light blue curves). They were consequently averaged, in agreement with our experimental procedure where the light is collected from the wing area and within an angular range (the resulting curve is shown in blue). By comparing the calculated spectrum with the experimentally recorded one (red curve in the same figure), agreement appears remarkably good, except for the radiation above 800 nm.

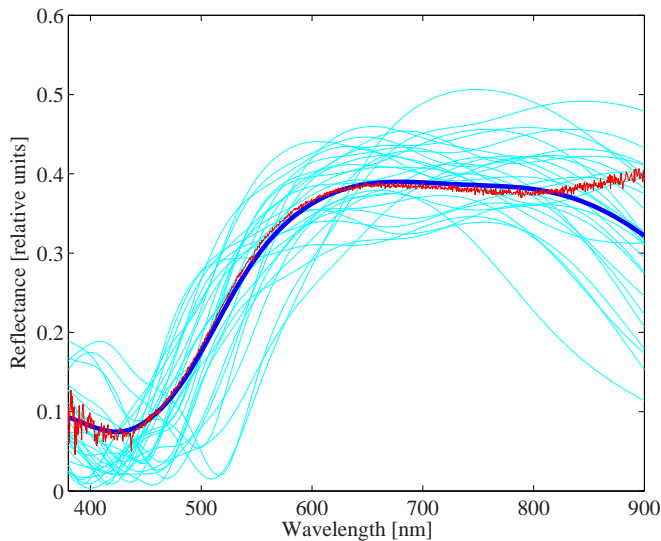


FIG. 12. Spectral averaging of light reflected from *D. chrysitis* wing, calculated by the transfer matrix method which includes scattering and local field enhancement. Light blue curves are individual spectra, blue curve is the averaged spectrum, and the red curve is the experimentally recorded spectrum.

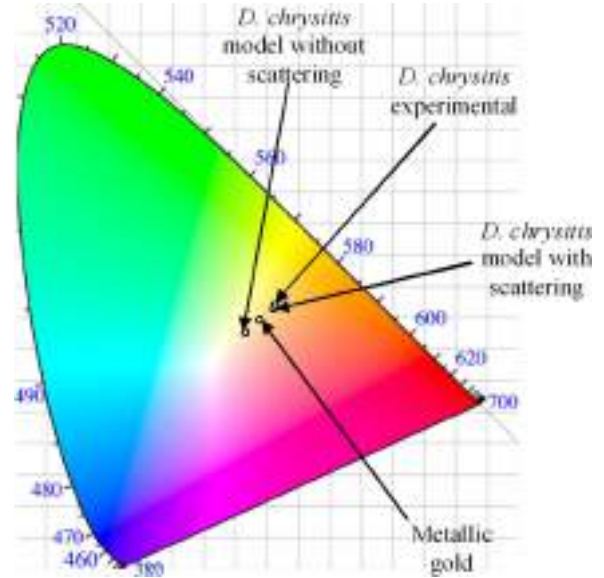


FIG. 13. CIE color coordinates of metallic gold and *D. chrysitis* forewing golden patches, with and without scattering.

The final shape of the spectrum is influenced by the layer thicknesses and the RMS surface roughness. They collectively influence the final calculated spectrum, but in general terms we have observed that increased thickness shifts the spectrum towards the red, while increased roughness depletes the blue part of the spectrum and decreases overall reflectivity.

All the computations are based on a transfer-matrix code, developed in [36] (declared free to use and made public at the URL provided therein). The program was modified by including scattering and local field enhancement effects [as defined by Eqs. (1)–(4)].

IV. DISCUSSION AND CONCLUSIONS

In contrast to most other lepidopteran species, each and every wing structure of *D. chrysitis* plays a certain role in iridescent color production. The same goes for the optical mechanisms—interference, diffraction, absorption, and surface scattering. They seem to be intricately intertwined in a synergistic manner—by omitting any of them, a significant change of the spectral profile would result. To demonstrate the fact, we calculated the resulting spectrum without taking into account scattering-enhanced absorption. As expected, reflection in the UV-blue spectral range is not attenuated. The corresponding CIE color coordinate testifies that the resulting color is whitish, as presented on a CIE 1931 diagram (Fig. 13). For reference, we have also displayed points corresponding to metallic gold, experimentally recorded spectrum, and full simulation of *D. chrysitis* wing. It is obvious that without scattering, the color coordinate would approach the achromatic center of the diagram—i.e., the wing will have only a slight coloration. It is interesting to note that the moth wing looks “yellower” than the gold.

As noted before, scattering stimulates confinement of light and increases the intensity by the $2n^2$ factor. It seems that the ground scale layer further amplifies the confinement [see Fig. 8(b)]. One possible explanation is that the cover scales

diffuse the incoming light, while the ground scales additionally disperse it and make it amenable for wave guiding within the layer.

Angular variability of *D. chrysitis* wing coloration is noticeable, and the golden color is observable within the $\pm 20^\circ$ from the specular direction. Beyond that, the color abruptly changes from golden to brown-gray. However, within the specular range, dependence of the reflected spectrum is slight for several reasons. On one hand, it results from irregular internal surfaces of the scale laminae and irregular mutual position of scales in ground and cover layers. The other reason is that the reflectivity at air-chitin interfaces is almost constant between 0° and 30° , as predicted by Fresnel equations. Therefore, the overall shape of the spectrum is not altered, but slightly shifted with the angle of incidence. Coarse diffraction grating on the upper lamina additionally diminishes angular dependence. From whichever direction light enters the scale, at least one of the diffraction orders is being reflected. This is what gives the notable stability of the optical effect with respect to the illumination direction (within the stated angular range).

We have not observed polarization sensitivity of the described reflection spectra, even though it certainly exists at the single wing-scale level. If observed macroscopically, across the whole wing, polarization effects cancel out due to strong variability of individual scale orientations with respect to incident radiation.

It is also interesting to note that the scales from brown-gray and golden areas of the wing have very similar morphology if observed under the scanning electron microscope. The most important difference is optical: while the golden area scales are almost transparent, the others contain a significant amount of absorbing pigment which leads to suppression of the specular component in the brown wing regions. Also, the brown scales are flatter, while the golden ones are slightly curled.

Calculations, according to Eqs. (3) and (4), have shown that approximately 70% of incoming radiation at 380 nm is scattered. Forty percent of the scattered component is absorbed, while the rest is uniformly dispersed all over the full solid angle. At the other end of the spectrum (above 800 nm), only 20% of light is scattered, without being absorbed to any significant extent. As a whole, the spectrum of unabsorbed light is quite flat from UV to IR. Its contribution to the wing

reflection is really small, because it is dispersed over the 4π solid angle, while the reflected light is concentrated around the specular direction.

A dual wing membrane is densely covered with nanosized spherical inclusions, conveniently situated, just beneath the scales. It seems that this could be an additional mechanism to scatter light back through the layer of scales. Transmission of the membranes is high and light further propagates to underside scales. They are gray, most probably due to melanin, which will further absorb the UV-blue part of the spectrum. In the red-infrared range, melanin absorbance is insignificant, and scales are again capable of reflecting light back through all the previous layers. This might account for the increased reflectivity in the infrared, which is not predicted by the theory described in the previous section.

Insects with golden body parts are rare and interesting from the biological point of view. The roles of the golden color may be diverse and are related mostly to possible defense mechanisms. We suppose that in *D. chrysitis* the golden forewing patches may appear to predators as warning and/or they can facilitate the conspecific recognition [15].

To summarize: All the structures—cover and ground scales, wing membranes, and underside wing scales—contribute to the golden wing color of the burnished brass moth. Interference, scattering, and absorption enhancement are optical mechanisms responsible for the effect. In short, interference on the scales produces a broad reflection spectrum with a peak in the green part of the spectrum. The blue part of the spectrum is absorbed due to scattering-enhanced absorption on a residual pigment. The red part of the spectrum is transmitted to the wing membrane, where it reflects, goes back through the scales, and combines with the reflection from the scales. The resulting spectrum is strongly attenuated below 520 nm, being almost flat up to 800 nm. The forewings of the *D. chrysitis* moth seem to be a remarkable, finely tuned, optical filter.

ACKNOWLEDGMENTS

This research was supported by Projects No. ON171038, No. III45016, and No. ON173038 funded by the Ministry of Education, Science and Technological Development of the Republic of Serbia.

-
- [1] J. Sun, B. Bhushan, and J. Tong, Structural coloration in nature, *RSC Adv.* **3**, 14862 (2013).
 - [2] J. Zi, B. Dong, T. Zhan, and X. Liu, in *Bioinspiration: From Nano to Micro Scales*, edited by X. Y. Liu (Springer, Berlin, 2012), pp. 275–329.
 - [3] T. Starkey and P. Vukusic, Light manipulation principles in biological photonic systems, *Nanophotonics* **2**, 289 (2013).
 - [4] N. N. Shi, C.-C. Tsai, F. Camino, G. D. Bernard, N. Yu, and R. Wehner, Keeping cool: Enhanced optical reflection and radiative heat dissipation in Saharan silver ants, *Science* **349**, 298 (2015).
 - [5] O. Karthaus, *Biomimetics in Photonics* (CRC Press, Boca Raton, FL, 2013).
 - [6] Z. Gan, M. D. Turner, and M. Gu, Biomimetic gyroid nanostructures exceeding their natural origins, *Sci. Adv.* **2**, e1600084 (2016).
 - [7] M. F. Land, The physics and biology of animal reflectors, *Prog. Biophys. Mol. Biol.* **24**, 75 (1972).
 - [8] S. Yoshioka, T. Nakano, Y. Nozue, and S. Kinoshita, Coloration using higher order optical interference in the wing pattern of the Madagascan sunset moth, *J. R. Soc., Interface* **5**, 457 (2008).
 - [9] D. J. Brink, J. E. Smith, M. E. Lee, and A. Möller, Optical diffraction by the microstructure of the wing of a moth, *Appl. Opt.* **34**, 6049 (1995).
 - [10] M. Hernández-Jiménez, D. E. Azofeifa, E. Libby, C. Barboza-Aguilar, Á. Solís, L. Arce-Marenco, I. García-Aguilar, A. Hernández, and W. E. Vargas, Qualitative correlation between structural chirality through the cuticle of *Chrysina aurigans* scarabs and left-handed circular polarization of the reflected light, *Opt. Mater. Express* **4**, 2632 (2014).

- [11] F. Liu, B. Q. Dong, X. H. Liu, Y. M. Zheng, and J. Zi, Structural color change in longhorn beetles *Tmesisternus isabellae*, *Opt. Express* **17**, 16183 (2009).
- [12] J. P. Vigneron, J. M. Pasteels, D. M. Windsor, Z. Vértesy, M. Rassart, T. Seldrum, J. Dumont, O. Deparis, V. Lousse, L. P. Biró, D. Ertz, and V. Welch, Switchable reflector in the Panamanian tortoise beetle *Charidotella egregia* (Chrysomelidae: Cassidinae), *Phys. Rev. E* **76**, 031907 (2007).
- [13] M. Rothschild, B. Gardiner, and R. Mummery, The role of carotenoids in the “golden glance” of danaid pupae (Insecta: Lepidoptera), *J. Zool.* **186**, 351 (1978).
- [14] R. L. Taylor, The metallic gold spots on the pupa of the monarch butterfly, *Entomol. News* **75**, 253 (1964).
- [15] A. C. Neville, Metallic gold and silver colours in some insect cuticles, *J. Insect Physiol.* **23**, 1267 (1977).
- [16] R. A. Steinbrecht, W. Mohren, H. K. Pulker, and D. Schneider, Cuticular interference reflectors in the golden pupae of danaine butterflies, *Proc. R. Soc. London, Ser. B* **226**, 367 (1985).
- [17] B. D. Wilts, H. L. Leertouwer, and D. G. Stavenga, Imaging scatterometry and microspectrophotometry of lycaenid butterfly wing scales with perforated multilayers, *J. R. Soc., Interface* **6**, S185 (2009).
- [18] N. I. Morehouse, P. Vukusic, and R. Rutowski, Pterin pigment granules are responsible for both broadband light scattering and wavelength selective absorption in the wing scales of pierid butterflies, *Proc. R. Soc. London, Ser. B* **274**, 359 (2007).
- [19] D. G. Stavenga, S. Stowe, K. Siebke, J. Zeil, and K. Arikawa, Butterfly wing colours: Scale beads make white pierid wings brighter, *Proc. R. Soc. London, Ser. B* **271**, 1577 (2004).
- [20] S. M. Luke, P. Vukusic, and B. Hallam, Measuring and modelling optical scattering and the colour quality of white pierid butterfly scales, *Opt. Express* **17**, 14729 (2009).
- [21] X. Chen, C. Wang, E. Baker, and C. Cun, Numerical and experimental investigation of light trapping effect of nanostructured diatom frustules, *Sci. Rep.* **5**, 11977 (2015).
- [22] A. Hille, M. A. Miller, and S. Erlacher, DNA sequence variation at the mitochondrial cytochrome oxidase I subunit among pheromotypes of the sibling taxa *Diachrysia chrysitis* and *D. tutti* (Lepidoptera: Noctuidae), *Zool. Scr.* **34**, 49 (2005).
- [23] A. Seitz, *The Macrolepidoptera of the World. A Systematic Description of the Known Macrolepidoptera. I Section. 3. Volume: The Palearctic Noctuidae. Plates* (Verlag des Seitz'schen Werkes, Stuttgart, 1914).
- [24] G. S. Robinson, P. R. Ackery, I. J. Kitching, G. W. Beccalon, and L. M. Hernández, *HOSTS—a Database of the World's Lepidopteran Hostplant* (Natural History Museum, London, 2010).
- [25] D. V. Stojanović and S. B. Čurčić, The diversity of noctuid moths (Lepidoptera: Noctuidae) in Serbia, *Acta Zool. Bulg.* **63**, 47 (2011).
- [26] M. Boardman, R. R. Askew, and L. M. Cook, Experiments on resting site selection by nocturnal moths, *J. Zool.* **172**, 343 (1974).
- [27] I. Svensson, P. Douwes, and B. O. Stille, Are *Diachrysia chrysitis* (L.) and *D. tutti* (Kostrowicki) different species? (Lepidoptera: Noctuidae), *Insect Syst. Evol.* **20**, 15 (1989).
- [28] A. D. Rakic, A. B. Djuricic, J. M. Elazar, and M. L. Majewski, Optical properties of metallic films for vertical-cavity optoelectronic devices, *Appl. Opt.* **37**, 5271 (1998).
- [29] D. G. Stavenga, H. L. Leertouwer, T. Hariyama, H. A. De Raedt, and B. D. Wilts, Sexual dichromatism of the damselfly *Calopteryx japonica* caused by a melanin-chitin multilayer in the male wing veins, *PLoS One* **7**, e49743 (2012).
- [30] H. Davies, The reflection of electromagnetic waves from rough surface, *Proc. IEE-Part IV: Inst. Monogr.* **101**, 209 (1954).
- [31] D. Domine, F.-J. Haug, C. Battaglia, and C. Ballif, Modeling of light scattering from micro- and nanotextured surfaces, *J. Appl. Phys.* **107**, 044504 (2010).
- [32] Y. A. Akimov, W. S. Koh, S. Y. Sian, and S. Ren, Nanoparticle-enhanced thin film solar cells: Metallic or dielectric nanoparticles? *Appl. Phys. Lett.* **96**, 073111 (2010).
- [33] E. Yablonovich and G. D. Cody, Intensity enhancement in textured optical sheets for solar cells, *IEEE Trans. Electron Devices* **29**, 300 (1982).
- [34] H. L. Leertouwer, B. D. Wilts, and D. G. Stavenga, Refractive index and dispersion of butterfly chitin and bird keratin measured by polarizing interference microscopy, *Opt. Express* **19**, 24061 (2011).
- [35] J. Springer, A. Porube, and M. Vanacek, Improved three-dimensional optical model for thin film silicon solar cells, *J. Appl. Phys.* **96**, 5329 (2004).
- [36] J. Junesch, T. Sannomiya, and A. B. Dahlin, Optical properties of nanohole arrays in metal-dielectric double films prepared by mask-on-metal colloidal lithography, *ACS Nano* **6**, 10405 (2012). Transfer matrix code can be found in <http://adahlin.com/onewebmedia/TransferMatrix3.m>.

Mapping of hemoglobin in erythrocytes and erythrocyte ghosts using two photon excitation fluorescence microscopy

Katarina Bukara,^a Svetlana Jovanić,^b Ivana T. Drvenica,^{a,c} Ana Stančić,^c Vesna Ilić,^c Mihailo D. Rabasović,^b Dejan Pantelić,^b Branislav Jelenković,^b Branko Bugarski,^a and Aleksandar J. Krmpot^{b,d,*}

^aUniversity of Belgrade, Department of Chemical Engineering, Faculty of Technology and Metallurgy, Belgrade, Serbia

^bUniversity of Belgrade, Institute of Physics Belgrade, Belgrade, Serbia

^cUniversity of Belgrade, Institute for Medical Research, Belgrade, Serbia

^dTexas A&M University at Qatar, Science Program, Doha, Qatar

Abstract. The present study describes utilization of two photon excitation fluorescence (2PE) microscopy for visualization of the hemoglobin in human and porcine erythrocytes and their empty membranes (i.e., ghosts). High-quality, label- and fixation-free visualization of hemoglobin was achieved at excitation wavelength 730 nm by detecting visible autofluorescence. Localization in the suspension and spatial distribution (i.e., mapping) of residual hemoglobin in erythrocyte ghosts has been resolved by 2PE. Prior to the 2PE mapping, the presence of residual hemoglobin in the bulk suspension of erythrocyte ghosts was confirmed by cyanmethemoglobin assay. 2PE analysis revealed that the distribution of hemoglobin in intact erythrocytes follows the cells' shape. Two types of erythrocytes, human and porcine, characterized with discocyte and echinocyte morphology, respectively, showed significant differences in hemoglobin distribution. The 2PE images have revealed that despite an extensive washing out procedure after gradual hypotonic hemolysis, a certain amount of hemoglobin localized on the intracellular side always remains bound to the membrane and cannot be eliminated. The obtained results open the possibility to use 2PE microscopy to examine hemoglobin distribution in erythrocytes and estimate the purity level of erythrocyte ghosts in biotechnological processes. © 2017 Society of Photo-Optical Instrumentation Engineers (SPIE) [DOI: [10.1117/1.JBO.22.2.026003](https://doi.org/10.1117/1.JBO.22.2.026003)]

Keywords: multiphoton fluorescence microscopy; ultrafast lasers; hemoglobin; label-free imaging; erythrocytes; erythrocyte ghosts.

Paper 160493RR received Jul. 14, 2016; accepted for publication Jan. 24, 2017; published online Feb. 9, 2017.

1 Introduction

Two photon excitation fluorescence (2PE) microscopy as an advanced technique offers the possibility for noninvasive, label-free high resolution imaging of living cells and deep tissues by using the fluorescence emission from the endogenous fluorescent molecules.¹⁻³ The near-infrared radiation generates 2PE signals of endogenous fluorophores, such as tryptophan, riboflavines, nicotinamides, collagen, elastin, and so on, and thus provides rich morphological and biochemical information of biological systems.⁴⁻⁶ Less investigated and reported is the intrinsic fluorescence of hemoglobin, the main intracellular component of erythrocytes, which emits a strong Soret fluorescence with the peak at 438 nm upon two-photon excitation by femtosecond pulses in red and near-infrared region (600 to 750 nm).^{7,8} Such optical properties of hemoglobin opened the possibility to use 2PE microscopy as a tool for label-free imaging of erythrocytes, even *in vivo*.⁹

In addition to the well-known physiological functions of erythrocytes, they serve as a natural blood compartment participating at the same time in biodistribution, metabolism, and action of certain drugs.¹⁰ Furthermore, intentional usage of human and animal erythrocytes, erythrocyte membranes (i.e., ghosts), and their nanoderivatives presents modern approach in terms of prolonged and controlled drug delivery systems.¹¹⁻¹⁴

Recently, we have reported the production of drug encapsulated porcine and bovine erythrocyte ghosts by gradual hypotonic hemolysis in much higher quantities than those described in literature so far.¹³ However, it was noted that after the hemolysis process a certain amount of hemoglobin remains in the final suspension of the resulting erythrocyte ghosts.¹³ The fraction of this so called residual hemoglobin, which cannot be easily eliminated from the system, significantly affects subsequent encapsulation processes and encapsulated drug releasing profile.¹⁵ Although this residual hemoglobin can be determined by the spectrophotometric method (e.g., cyanmethemoglobin method), data on spatial distribution of hemoglobin at the single cell level in erythrocytes and remaining erythrocytes ghosts are scarce. Demonstrated spatial redistribution of hemoglobin throughout intact erythrocytes in patients with vascular disorders¹⁶ promotes the importance of this parameter monitoring in disease diagnosis as well.

Based on the aforementioned wide applicability of erythrocytes in biomedical research and diagnostic tests, it is important to have a reliable microscopy method for single cell analysis, including spatial distribution of hemoglobin. Although phase contrast microscopy traditionally represents a fast method for tracking changes of erythrocytes during the gradual hypotonic hemolysis and appearance of erythrocyte ghosts,^{17,13,18} it does not provide enough information for detailed morphological analysis. Unlike the phase contrast microscopy that visualizes

*Address all correspondence to: Aleksandar J. Krmpot, E-mail: krmpot@ipb.ac.rs

all the changes of the index of refraction regardless of their origin, 2PE microscopy has high chemical selectivity, thus enabling the visualization of the distribution of certain chemical compounds. Confocal microscopy, scanning electron microscopy, transmission electron microscopy, and atomic force microscopy are considered as the most powerful tools for structural analysis of various cells, including erythrocytes. However, these methods mandatorily include cell fixation and/or labeling which might influence the fragile cell structure.¹⁹ So far, large numbers of optical microscopic techniques have been utilized for erythrocyte imaging. Comparative study of stained cells by confocal and unstained cells by holographic microscopy has been elaborated as shown in the work of Rappaz et al.²⁰ Scanning microphotolysis (Scamp), also referred to as fluorescence recovery after photobleaching, has been employed for erythrocyte examination either in a linear²¹ or in a two photon, i.e., nonlinear, regime.²² Volumetric imaging of erythrocytes using photoacoustic microscopy has been described by Shelton et al.,²³ while the same method in combination with confocal microscopy is used for hemoglobin oxygen saturation measurements, as shown by Wang et al.²⁴ 2PE was combined with stimulated Raman scattering for hemoglobin imaging in mouse retina.²⁵ Even second harmonic generation (SHG) microscopy, usually accompanied with 2PE as another modality of nonlinear microscopy, has been utilized for label free imaging of human erythrocytes membrane exposed to various glucose concentrations in phosphate buffered saline (PBS).²⁶ In addition to demonstration of the imaging possibilities of hemoglobin by the aforementioned techniques, 2PE has recently been applied in examination of particular biomedical problems related to erythrocytes: tracking blood vessels within the tissues²⁷ and photo-physical characterization of sickle cell disease hemoglobin.²⁸

In this work, we report label-free imaging of two kinds of erythrocytes, porcine and outdated human ones, at single cell level by 2PE microscopy, with the specific aim of investigating the spatial distribution (i.e., for mapping) of hemoglobin within intact erythrocytes and residual hemoglobin in erythrocyte membranes obtained after a gradual hypotonic hemolysis process. Furthermore, the quantity of residual hemoglobin was determined by analysis of 2PE images relative to the hemoglobin concentration in intact erythrocytes. This investigation opens the possibility to use 2PE microscopy as a tool for quality assessment of erythrocytes and erythrocyte membranes as a starting material in various biotechnological processes, such as the production of erythrocyte-based drug delivery systems^{13,15} or isolation of hemoglobin.^{18,29} Additionally, 2PE microscopy could help in revealing the ability of erythrocyte membranes, originating from different species, to bind different amounts of hemoglobin. Since various processes require various levels of purity, this information is important for the selection of raw material.

2 Materials and Methods

2.1 Blood Samples

Porcine slaughterhouse blood and human outdated blood were used as starting biological materials. Porcine blood was taken from the jugular veins of Swedish Landrace swine and collected in a sterile glass bottle with 3.8% sodium-citrate as an anticoagulant, at slaughterhouse “PKB Imes” in Belgrade, Serbia. Blood samples were transported at ambient temperature and processing started 2 h after the collection. The outdated

human erythrocyte concentrates were from the Institute for Transfusiology and Hemobiology, Military Medical Academy, Belgrade, Serbia. The erythrocytes were enriched by the standard procedure and preserved in saline-adenine-glucose-mannitol solution (each 100 mL contains 0.900 g dextrose monohydrate, 0.877 g sodium chloride, 0.0169 g adenine, and 0.525 g mannitol) for 42 days at 4°C. The outdated cell packs were anonymized prior to distribution, and the link to the donor was broken. If not used for the research, the cell packs would have been discarded.

2.2 Preparation of Erythrocytes and Erythrocyte Membranes (i.e., Ghosts)

Both porcine and human erythrocytes were precipitated by blood centrifugation at $2450 \times g$ for 20 min at 4°C. The plasma and leucocytes were carefully discarded by vacuum aspiration. The precipitated erythrocytes were resuspended in isotonic saline solution (0.9% NaCl), washed twice by centrifugation, and finally resuspended in an isotonic PBS, pH 7.2 to 7.4 (0.8% saline buffered with 10 mM sodium phosphate). Porcine and human erythrocyte ghosts were prepared by gradual hypotonic hemolysis^{13,29} by using hypotonic 35-mM sodium phosphate/NaCl buffer for porcine and 5-mM sodium phosphate buffer for human erythrocytes (30 min, flow rate 150 mL/h.) After the hemolysis, the erythrocyte ghosts were precipitated by 40 min centrifugation at $3220 \times g$, at 4°C. Erythrocyte ghosts were washed out three times in the buffer solution used for hemolysis and finally in PBS solution. Concentration of hemoglobin in suspensions of erythrocytes and residual hemoglobin in erythrocyte ghosts were determined by the cyanmethemoglobin method.³⁰ To quantify residual hemoglobin, prior to the determination of the concentration, erythrocyte ghosts were dispersed in 1 mL of isotonic PBS containing 1% w/w of Triton X100 detergent.

2.3 Experimental Setup for 2PE

The homemade two-photon microscopy experimental setup is similar to that reported in our previous study.³¹ The schematic of the setup is given in Fig. 1. The train of the femtosecond

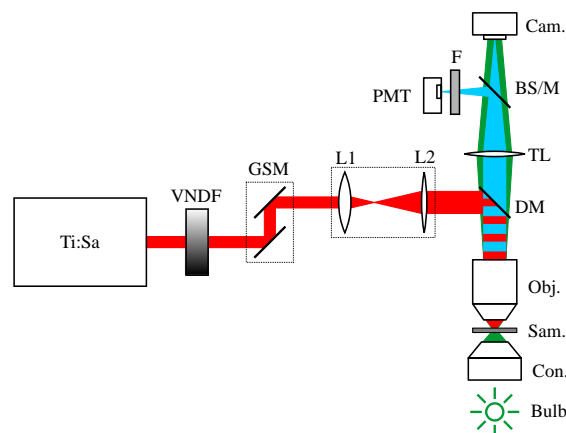


Fig. 1 Schematic of the imaging system: Ti:Sa, Ti:Sapphire laser, VNDF, variable neutral density filters, GSM, galvo scanning mirrors, L1 and L2, lenses, DM, dichroic mirror (short pass), Obj., microscope objective, Sam., sample, Con., condenser, Bulb, bulb for bright-field imaging illumination, TL, tube lens, BS/M, beam splitter or mirror, Cam., camera, F, filter, PMT, photomultiplier tube.

pulses is generated by the Ti:Sapphire laser (Coherent, Mira 900-F). The repetition rate is 76 MHz, and pulse duration is 160 fs. The galvoscaning mirrors (Cambridge Technologies, 6215H) are used to raster-scan the samples.

The laser beam is expanded in order to fill the entrance pupil of an objective (Carl Zeiss, EC Plan-NEOFLUAR, $40\times/1.3$ oil). A short-pass dichroic mirror (Thorlabs, M254H45) reflects the laser beam toward the objective, and transmits the signal toward the camera (Canon, EOS 50D) and the photomultiplier tube (PMT) (RCA, PF1006). The tube lens forms the sample image on the camera and/or PMT. The camera is used to take the bright-field image of the samples (green light in Fig. 1). The high intensity fluorescence can be seen by camera (blue light in Fig. 1). The commercial cameras usually have an infrared blocking filter. We removed this filter from our camera in order to see the backscattering/backreflection of the laser spot from the sample/cover slip which facilitated the alignment of the system. This is possible due to the fact that a small portion of the laser light leaks through the dichroic mirror (leakage of the laser is not shown in Fig. 1). A drawback of the infrared filter removing is the false coloring of the bright-field images. Thus, our bright-field images are greenish.

A beam-splitter or the mirror is used to reflect part of the signal or the complete signal to the PMT. An interference filter in front of the PMT removes scattered laser light. This filter is transparent for visible (415 to 685 nm) light, while blocking the IR and UV. Since the excitation wavelength is chosen in such a way that fluorescent signal comes predominantly from hemoglobin (Soret fluorescence), using the broadband filter ensures that all the fluorescent light will be collected, even from the wings of the fluorescent spectrum which is important in the case of relatively low excitation efficiency (see Sec. 2.4). This provides good signal-to-noise ratio and high contrast of images. Erythrocytes (hematocrit 5%, i.e., 5% suspension) and ghosts in the amount of $20\ \mu\text{L}$ were allowed to settle onto a microscopic slide. Afterward, coverslips were put above settled cells and fixed to microscope slides. Imaging of erythrocytes and erythrocyte ghosts was performed at 730-nm excitation wavelength.

2.4 Excitation Wavelength

The excitation wavelength is of the great importance in this study and it has to be carefully selected according to its availability and the properties of the samples. Selection of the wavelength can significantly affect the chemical selectivity of the imaging, providing excitation of the specific and desired objects, and quality of the images by means of excitation efficiency and fluorescence strength. The excitation wavelength in this study is selected to be 730 nm by the following criteria:

- We have tested different excitation wavelengths within a Ti:Sapphire laser tuning range (700 to 1000 nm). Our excitation spectrum is consistent with the spectrum shown in study of Zheng et al.,⁷ i.e., the excitation is the most efficient for the shortest wavelengths.
- The 2PE signal from hemoglobin at 650-nm excitation wavelength is reported to be more efficient⁷ but we were not able to utilize shorter wavelengths than 700 nm due to the laser tuning range (700 to 1000 nm). Also, there is a significant leakage of the laser light to the PMT for wavelengths shorter than 730 nm. The cut-off wavelength

of the dichroic mirror (hot mirror M254H45, Thorlabs, Inc.) is (700 ± 10) nm with transmission $>97\%$ for wavelengths longer than 710 nm, whereas full width at half maximum of the laser line is ~ 12 nm.

- The 2PE signal from glass (coverslips and microscope slides) is pronounced for wavelengths shorter than 730 nm. Thus, 730 nm is the shortest possible choice for the excitation wavelength to produce still high quality images.

3 Results and Discussion

In this study, erythrocyte membranes (ghosts) were prepared by gradual hypotonic hemolysis starting from slaughterhouse porcine and outdated human erythrocytes. During the process of gradual decrease of ionic strength of the solution surrounding erythrocytes, they swell and hemoglobin molecules leak out, leaving intact erythrocyte membranes.^{13,17,18,29} Preparation of ghosts was followed by an extensive washing out procedure (to remove extracellular hemoglobin released from lysed erythrocytes). However, a small amount of hemoglobin, so called residual hemoglobin, always remains bound to membranes in resulting erythrocyte ghosts.¹³

Here, 2PE microscopy was used to quantify the relative decrease in hemoglobin's content at the end of the applied process of hemolysis and reveal its localization in the examined samples. All 2PE images are of the high quality by means of good signal-to-noise ratio, high visibility (contrast), high pixel resolution, and without or with minimal postmeasurement processing.

Bright-field microscopy images and corresponding auto-fluorescence 2PE images of starting porcine and human erythrocytes are presented in Figs. 2 and 3, respectively. 2PE images are acquired in 1024×1024 pixels resolution upon 30 times averaging of raw fluorescence signal. Intensity of pseudo-red color corresponds to the 2PE signal intensity.

According to image dimensions ($30 \times 30\ \mu\text{m}^2$) and physical resolution of our experiment, which is limited by diffraction and measured to be ~ 300 nm,³¹ the minimal pixel resolution for faithful imaging of the object is set by Nyquist criterion to 200×200 pixels. In our case, 1024×1024 pixel resolution ensures that we overfill the Nyquist criterion and contribute to the high quality of the images.

As evident from Figs. 2(b) and 3(b), it is possible to notice localization of hemoglobin's content even from suspensions of

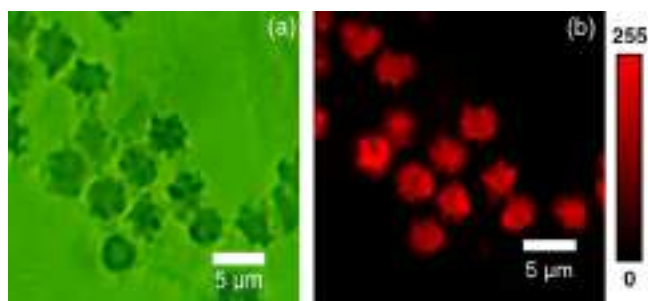


Fig. 2 Suspension of porcine erythrocytes: (a) bright-field microscopy image, (b) corresponding 2PE image revealing localization of hemoglobin; black, the lowest 2PE signal, red, the highest 2PE signal. 3-D model of examined human erythrocytes. (Video 1. MPEG, 6.16 MB [URL: <http://dx.doi.org/10.1117/1.JBO.22.2.026003.1>]).

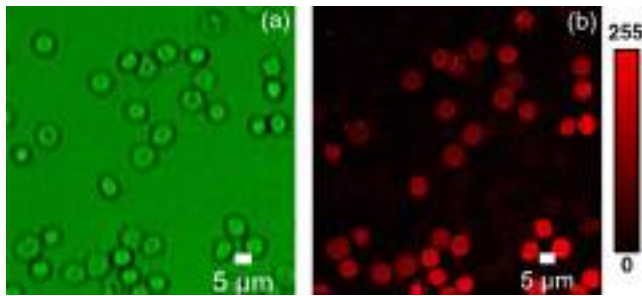


Fig. 3 Suspension of human erythrocytes: (a) bright-field microscopy image, (b) corresponding 2PE image revealing localization of hemoglobin; black, the lowest 2PE signal, red, the highest 2PE signal. Note that field of view (scale bar) is different than in a Fig. 2. It was changed because the region of interest was wider.

erythrocytes. Also, a 3-D model of examined human erythrocytes is displayed in Video 1.

Due to the presence of erythrocytes' methemoglobinreductase, hemoglobin in blood is predominately in its native ferrous form³² which is desirable for the 2PE signal measurement. 2PE images and examination of hemoglobin distribution in a single erythrocyte for both examined types are given in Fig. 4. This result demonstrates that the resolution of the 2PE microscopy is good enough for the analysis of erythrocytes at the single cell level. As with the images in Fig. 3, these 2PE images are the results of averaging 30 individual images. Pseudocoloring corresponds to the 2PE signal intensity. No further processing of the image was performed, the data points in graphs represent the raw 2PE signal levels.

Based on the results in Fig. 4, we have confirmed that human erythrocytes have the normal morphology of biconcave discs, whereas porcine erythrocytes have an echinocyte morphology. Such morphology of porcine erythrocytes is not a sign

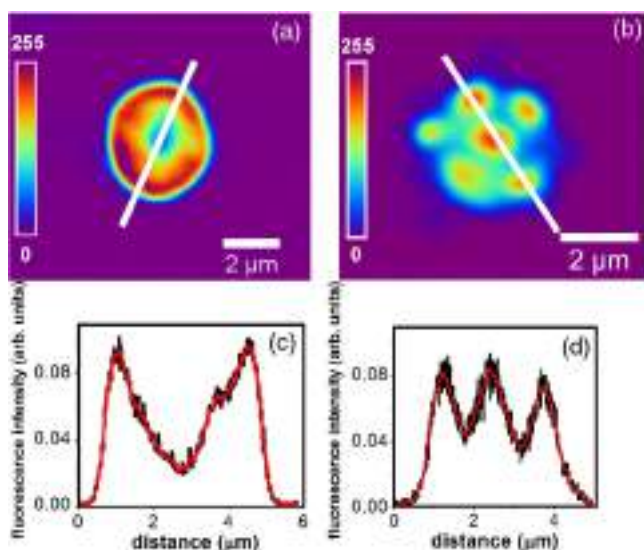


Fig. 4 Representative raw 2PE image of (a) human and (b) porcine erythrocyte. 2PE signal is presented in pseudocolor. Distribution of 2PE signals, i.e., hemoglobin concentration through the diameter of (c) human and (d) porcine erythrocyte. Black curves are raw data plot, red curves are obtained upon adjacent points averaging. Note that the two images are not recorded under the same experimental conditions; the intensities are not mutually normalized, thus they cannot be compared.

of some pathological condition but represents a common artifact in handling of porcine blood.³⁴

Hemoglobin, which is the dominant component of erythrocytes, follows the cells' shape which can be easily observed by comparing the bright field and 2PE images. For human erythrocytes, its lowest density is observed to be in the central area [Fig. 4(a)], and in peripheral parts, its distribution was homogeneous. This finding is in agreement with the reported spatial distribution of hemoglobin in healthy human erythrocytes examined by confocal Raman spectroscopy³⁵ and atomic force microscopy.³⁶ On the other hand, for porcine erythrocytes, 2PE revealed a significant accumulation of hemoglobin in cells' protrusions. As shown in the study by Parshina et al.,³⁶ amphibian (frog) nucleated and mammalian (rat) nonnucleated healthy erythrocytes have a homogeneous distribution of cytosolic hemoglobin. Our results indicate that the deviations from the biconcave morphology of porcine erythrocytes probably affect the distribution of hemoglobin and lead to its accumulation in the cell protrusions. Taking into account that various pathological conditions are accompanied by uneven distribution of hemoglobin,^{16,37} the developed method might be useful in their diagnosis. Until now it was described that isolated sickle cell disease hemoglobin (HbS) and malaria-infected red blood cells could be analyzed and photophysically characterized by multiphoton microscopy.^{28,38}

The overall presence of residual hemoglobin in the final suspensions of erythrocyte ghosts was primarily determined by cyanmethemoglobin assay (Fig. 5). The concentration of residual hemoglobin was 7.21 and 1.76 g/L for the porcine and human samples, respectively. This reflects the decrease in concentrations of hemoglobin by 95% and 99% in the suspension of erythrocyte ghosts compared to the starting suspensions of porcine and outdated human erythrocytes, respectively. These amounts of residual hemoglobin in erythrocyte ghosts are consistent with the range reported in other studies.^{39,40} However, the localization of residual hemoglobin in the suspension still remains unknown.

In addition to the spatial distribution of hemoglobin in intact human and porcine erythrocytes, images of residual hemoglobin in erythrocyte ghosts also can be obtained by 2PE (Figs. 6 and 7, respectively). The intensity of the 2PE signal depends on the concentration of the hemoglobin, but also on the pulse peak power, pulse duration, repetition rate, focal volume, excitation wavelength, etc. It is a nontrivial and time consuming task to quantify the dependence of the 2PE signal on hemoglobin concentration. In other words, it is almost impossible to determine

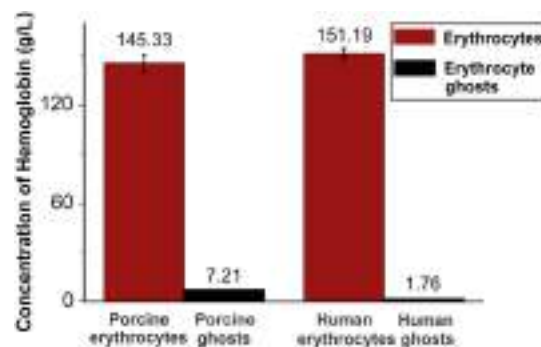


Fig. 5 Concentration of hemoglobin in erythrocytes and their ghosts obtained by gradual hemolysis. The concentration was determined by spectrophotometric cyanmethemoglobin method.

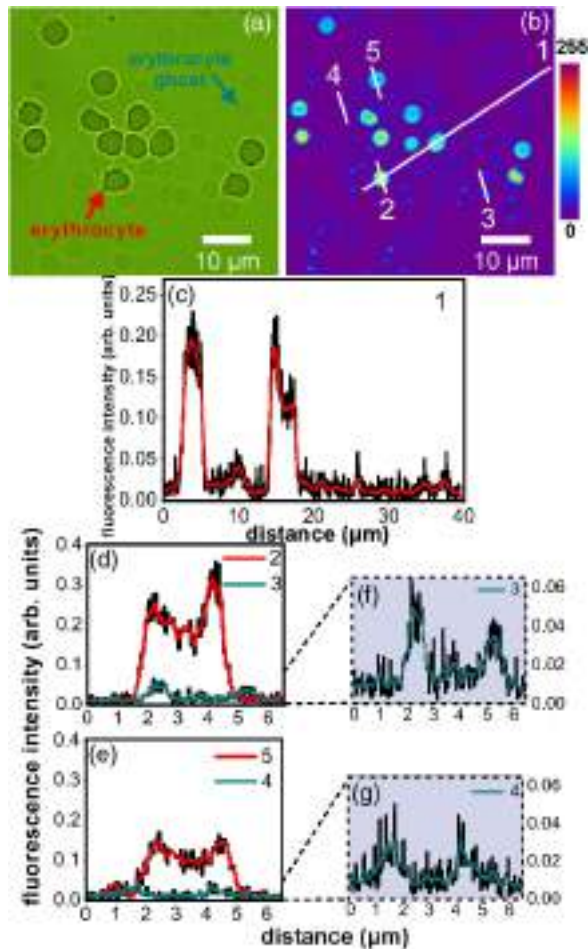


Fig. 6 Mixed suspension of human erythrocytes and resulting erythrocyte ghosts: (a) bright-field microscopy image; (b) 2PE image; (c–g) 2PE signal profiles along the corresponding lines at (b) image. Profiles 3 and 4 are given in magnified vertical scale in (f) and (g) graphs. Black curves are raw data plot, red and green curves are obtained upon adjacent points averaging.

absolute concentration from the 2PE signal since one has to keep all other parameters constant in separate measurements. In order to evaluate the local change (i.e., decrease) in hemoglobin content after the hemolysis, we mixed the ghosts with intact erythrocytes. In this way, we can evaluate the local content of hemoglobin, i.e., distribution of hemoglobin across erythrocytes and ghosts, and not just an average value for a whole cell or suspension. From the image data we obtained, the variation of intensity along appropriately chosen representative lines is shown in Figs. 6(b) and 7(b). The line is chosen in a way to intercept at least two erythrocytes and two ghosts which provide up to eight representative points positioned in the proximity of the membrane within the cells for comparison of 2PE signals. Note that the signals from the chosen points provide highly localized data for the comparison, opposite to the cyanmethemoglobin assay, which is intrinsically an averaging method. This ensures the same excitation parameters for both erythrocytes and erythrocyte ghosts. The above procedure ensures that the peak ratio from the 2PE intensity profile is equal to the concentration ratio in the untreated erythrocyte(s) and the ghost(s). We emphasize that this simple step enables us to determine changes in the content of residual hemoglobin in ghosts relative to the starting

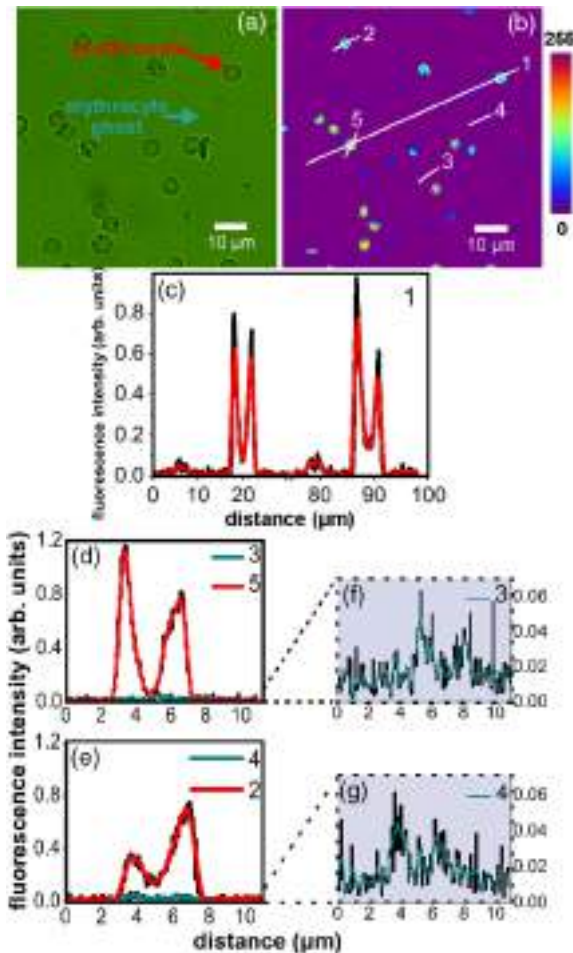


Fig. 7 Mixed suspension of porcine erythrocytes and resulting erythrocyte ghosts: (a) bright-field microscopy image; (b) 2PE image; (c–g) 2PE signal profiles along the corresponding lines at (b) image. Profiles 3 and 4 are given in magnified vertical scale in (f) and (g) graphs. Black curves are raw data plot, red and green curves are obtained upon adjacent points averaging.

content of hemoglobin in intact erythrocytes, but not the absolute concentration.

There is no significant autofluorescence signal upon two photon excitation at 730 nm from any other common molecular species that can be found in erythrocytes and which could significantly affect the obtained results, except hemoglobin. Namely, lipids and saccharides are essentially nonfluorescent,⁴¹ while aromatic amino acids as constituents of proteins, such tryptophan, phenylalanine, and tyrosine, have an absorption maximum of 280 nm⁴¹ and cannot contribute significantly to autofluorescence generated by two-photon excitation at 730 nm. Pyridine nucleotides NADH and NADPH have an absorption maximum of 340 nm⁴² and FAD has two excitation maxima at 360 and 450 nm. According to their excitation maximum, they could contribute the autofluorescence generated by two-photon excitation at 730 nm. However, their molar ratios to hemoglobin within erythrocytes (calculated based on data given in several studies)^{43–45} are completely negligible.

As can be seen from Figs. 6 and 7, after the conversion of erythrocytes to empty erythrocyte membranes, fluorescence emission from hemoglobin significantly decreased, but was still detectable. Therefore, the applied process that we used allows the production of ghosts; however, a certain amount

of the hemoglobin always remains bound to the membrane. Comparing the peak values from Figs. 6(d) and 6(e) (red curves) to those in Figs. 6(f) and 6(g), one can estimate lower fluorescence emissions for both porcine and human erythrocyte ghosts in comparison to respective erythrocytes. Our results suggest that residual hemoglobin in the suspension was localized on the intracellular side of the ghost membranes. The 2PE signal in the internal volume of both, human and porcine erythrocyte ghosts, is at the noise level, thus hemoglobin content is negligible.

These results support already reported data on hemoglobin's ability to bind to erythrocyte membranes via a transmembrane protein, e.g., band 3⁴⁶ or some other cytoskeleton proteins via α globin chains.⁴⁷ This phenomenon that we have confirmed by 2PE microscopy could be used as a valuable marker of inevitable oxidative damages⁴⁸ emerged during *in vitro* storage and erythrocytes handling. The higher concentration of residual hemoglobin obtained in porcine ghosts relative to initial concentration can be explained by specific membrane lipid composition and their high susceptibility to oxidative stress induced by reactive oxygen species⁴⁹ related to a lower level of enzymes protectants against oxidative damages.⁵⁰

Erythrocyte ghosts are extensively studied systems and have numerous potential applications. In addition to their usage as controlled drug delivery systems, they represent one of the most promising *in vitro* systems for drug partitioning studies and determination of the drug partition coefficient Kps.⁵¹ In food science they are used for an estimation of antioxidant activity of different nutritional compounds.^{52,53} Erythrocyte ghosts are suitable models for investigating membrane transport phenomena,⁵⁴ glucose translocation through biological membranes,⁵⁵ uptake and metabolism of different compounds,⁵⁶ etc. It is interesting to note that despite their widespread application, there are no studies estimating residual hemoglobin although it may significantly affect the quality of the final product. Apart from the mentioned study that suggests a positive correlation between the total content of membrane-bound hemoglobin and the level of oxidant stress,⁴⁸ it has been shown that iron from membrane-bound hemoglobin catalyzes the formation of reactive oxygen species which attack the cell membrane. This leads to peroxidation of membrane unsaturated lipids and disturbed structure and function of the membrane⁵⁷ and may directly affect the quality of the final product and/or obtained results.

In addition to using 2PE microscopy for analysis of erythrocyte ghosts as in the mentioned model or drug delivery systems, the results of this study also open a possibility of using 2PE microscopy in analysis of the spatial distribution of hemoglobin in erythrocytes in different physiological and pathological conditions. The spatial distribution of hemoglobin within erythrocytes can give information of the oxygen-transport capability and help by providing accurate diagnosis and appropriate treatment in erythrocytes disorders both in humans and animals.

4 Conclusion

In this study, we have demonstrated that 2PE microscopy can be used in analysis of the spatial distribution of hemoglobin in erythrocytes and erythrocyte ghosts, at an individual cell level. Although the maximal excitation efficiency for hemoglobin is at shorter wavelengths, high quality images can still be obtained using femtosecond pulses at 730 nm directly from a Ti:Sa oscillator. As opposed to the common spectroscopic

methods such as cyanmethemoglobin assay that is intrinsically averaging, providing results for hemoglobin concentration drop after the hemolysis process in the bulk sample, 2PE microscopy gives results on hemoglobin localization and its fluorescence intensity change in randomly chosen points within the ghost-erythrocytes sample. Obtained results suggest that residual hemoglobin in erythrocyte ghosts, either human or porcine ones, is located mainly near the cell membrane rather than uniformly distributed. In addition, 2PE microscopy enables imaging of the distribution of hemoglobin in the protrusions of erythrocytes with morphology of echinocytes, thus it can be used for mapping of hemoglobin in erythrocytes morphologically different from the normal discocytes.

High-quality, label- and fixation-free visualization of hemoglobin can be achieved at 730-nm excitation wavelength. The 2PE fluorescence signal from residual hemoglobin at representative points near the cell membrane in the ghosts was reported to have lower intensity than at the corresponding points in intact erythrocytes. Obtained results suggest that residual hemoglobin in erythrocyte ghosts is located mainly near the cell membrane rather than uniformly distributed.

In such a way, through an application of 2PE microscopy hemoglobin distribution in erythrocytes together with residual hemoglobin content and distribution in the resulting erythrocyte ghosts can be directly and relatively easily estimated. The proposed method could be of significant importance for identifying different pathological or nonpathological conditions and application in material selection in biotechnological processes.

Disclosures

The authors declare no conflicts of interest.

Acknowledgments

This work has been supported by Ministry of Education, Science and Technological Development of the Republic of Serbia (Project Nos. III 46010, OI 171005, OI 171038, and III45016) and by the project NPRP 6-021-1-005 from the Qatar National Research Fund (member of the Qatar Foundation).

References

1. K. König et al., "Multiplex FISH and three-dimensional DNA imaging with near infrared femtosecond laser pulses," *Histochem. Cell Biol.* **114**(4), 337–345 (2000).
2. R. Weigert et al., "Intravital microscopy: a novel tool to study cell biology in living animals," *Histochem. Cell Biol.* **133**(5), 481–491 (2010).
3. B. R. Masters and P. So, *Handbook of Biomedical Nonlinear Optical Microscopy*, Oxford University Press, New York (2008).
4. H. Kolesová et al., "Comparison of different tissue clearing methods and 3D imaging techniques for visualization of GFP-expressing mouse embryos and embryonic hearts," *Histochem. Cell Biol.* **146**, 141–152 (2016).
5. L. Peralta et al., "In vivo evaluation of cervical stiffness evolution during induced ripening using shear wave elastography, histology and 2 photon excitation microscopy: insight from an animal model," *PLoS One* **10**, e0133377 (2015).
6. B. G. Wang et al., "Intraocular multiphoton microscopy with subcellular spatial resolution by infrared femtosecond lasers," *Histochem. Cell Biol.* **126**(4), 507–515 (2006).
7. W. Zheng et al., "Two-photon excited hemoglobin fluorescence," *Biomed. Opt. Express* **2**, 71–79 (2010).
8. G. O. Clay, C. B. Chaffer, and D. Kleinfeld, "Large two-photon absorptivity of hemoglobin in the infrared range of 780–880 nm," *J. Chem. Phys.* **126**, 025102 (2007).

9. D. Li et al., "Time-resolved detection enables standard two-photon fluorescence microscopy for *in vivo* label-free imaging of microvasculature in tissue," *Opt. Lett.* **36**(14), 2638–2640 (2011).
10. P. H. Hinderling, "Red blood cells: a neglected compartment in pharmacokinetics and pharmacodynamics," *Pharmacol. Rev.* **49**(3), 279–295 (1997).
11. V. Leuzzi et al., "Erythrocyte-mediated delivery of recombinant enzymes," *Inherit. Metab. Dis.* **39** (4), 519–530 (2016).
12. V. Bourgeaux et al., "Drug-loaded erythrocytes: on the road toward marketing approval," *Drug Des. Dev. Ther.* **10**, 665–676 (2016).
13. I. Kostić et al., "Erythrocyte membranes from slaughterhouse blood as potential drug vehicles: isolation by gradual hypotonic hemolysis and biochemical and morphological characterization," *Colloids Surf. B* **122**, 250–259 (2014).
14. R. Deak et al., "Physicochemical characterization of artificial nanoerythrocytes derived from erythrocyte ghost membranes," *Colloids Surf. B* **135**, 225–234 (2015).
15. I. T. Drvenica et al., "Biomembranes from slaughterhouse blood erythrocytes as prolonged release systems for dexamethasone sodium phosphate," *Biotechnol. Prog.* **32**, 1046–1055 (2016).
16. V. V. Revin et al., "Study of the structure, oxygen-transporting functions, and ionic composition of erythrocytes at vascular diseases," *Biomed. Res. Int.* **2015**, 973973 (2015).
17. D. Danon, "Osmotic hemolysis by a gradual decrease in the ionic strength of the surrounding medium," *J. Cell. Comp. Physiol.* **57**, 111–117 (1961).
18. R. Stojanović et al., "Isolation of hemoglobin from bovine erythrocytes by controlled hemolysis in the membrane bioreactor," *Appl. Biochem. Biotechnol.* **166**, 1491–1506 (2012).
19. E. Wisse et al., "Fixation methods for electron microscopy of human and other liver," *World J. Gastroenterol.* **16**, 2851–2866 (2010).
20. B. Rappaz et al., "Comparative study of human erythrocytes by digital holographic microscopy, confocal microscopy, and impedance volume analyzer," *Cytometry* **73A**, 895–903 (2008).
21. M. Tschödrich-Rotter et al., "Optical single-channel analysis of the aerolysin pore in erythrocyte membranes," *Biophys. J.* **70**, 723–732 (1996).
22. U. Kubitschek et al., "Two-photon scanning microphotolysis for three-dimensional data storage and biological transport measurements," *J. Microsc.* **182**, 225–233 (1996).
23. R. L. Shelton, S. P. Mattison, and B. E. Applegate, "Volumetric imaging of erythrocytes using label-free multiphoton photoacoustic microscopy," *J. Biophotonics* **7**, 834–840 (2014).
24. Y. Wang et al., "In vivo integrated photoacoustic and confocal microscopy of hemoglobin oxygen saturation and oxygen partial pressure," *Opt. Lett.* **36**, 1029–1031 (2011).
25. S. He et al., "Label-free nonlinear optical imaging of mouse retina," *Biomed. Opt. Express* **6**, 1055–1066 (2015).
26. D. Lev et al., "d-Glucose-induced second harmonic generation response in human erythrocytes," *J. Phys. Chem.* **113**, 2513–2518 (2009).
27. N. L. Garrett et al., "Exploring uptake mechanisms of oral nanomedicines using multimodal nonlinear optical microscopy," *J. Biophotonics* **5**, 458–468 (2012).
28. G. D. Vigil and S. S. Howard, "Photophysical characterization of sickle cell disease hemoglobin by multi-photon microscopy," *Biomed. Opt. Express* **6**, 4098–4104 (2015).
29. B. Bugarski and N. Dovezenski, "Hemofarm Konzern. Verfahren zur Herstellung von Hemoglobin," Deutsches Patentamt DE 19707508 (2000).
30. O. W. Van Assendelft, A. H. Holtz, and S. M. Lewis, *Recommended Method for the Determination of the Haemoglobin Content of Blood*, I. C. S. H. Publications, World Health Organization (1984).
31. M. D. Rabasović et al., "Nonlinear microscopy of chitin and chitinous structures: a case study of two cave-dwelling insects," *J. Biomed. Opt.* **20**(1), 016010 (2015).
32. A. Mansouri and A. A. Lurie, "Concise review: methemoglobinemia," *Am. J. Hematol.* **42**, 7–12 (1993).
33. M. Diez-Silva et al., "Suresh shape and biomechanical characteristics of human red blood cells in health and disease," *MRS Bull.* **35**(5), 382–388S (2010).
34. J. D. Weiss and K. J. Wardrop, Eds., *Schalm's Veterinary Haematology*, 6th ed., pp. 144–151, Blackwell Publishing Ltd., Ames (2010).
35. L. Kang et al., "Confocal Raman microscopy on single living young and old erythrocytes," *Biopolymers* **89**, 951–959 (2008).
36. E. Y. Parshina et al., "Combined Raman and atomic force microscopy study of hemoglobin distribution inside erythrocytes and nanoparticle localization on the erythrocyte surface," *Laser Phys. Lett.* **10**, 075607 (2013).
37. J. P. Greer et al., *Wintrobe's Clinical Hematology*, 13th ed., Lippincott Williams & Wilkins, Philadelphia (2014).
38. J. Mauritz et al., "Biophotonic techniques for the study of malaria-infected red blood cells," *Med. Biol. Eng. Comput.* **48**, 1055–1063 (2010).
39. S. S. Bernstein et al., "Method for the preparation of posthemolytic residue or stroma of erythrocytes," *J. Biol. Chem.* **122**, 507–514 (1938).
40. D. Danon, A. Nevo, and Y. Marikovsky, "Preparation of erythrocyte ghosts by gradual haemolysis in hypotonic aqueous solution," *Bull. Res. Counc. Israel* **6E**, 36 (1956).
41. J. R. Lakowicz, "Protein fluorescence," Chapter 16 in *Principles of Fluorescence Spectroscopy*, 3rd ed., J. R. Lakowicz, Ed., pp. 530–578, Springer US, New York (2006).
42. H. Andersson et al., "Autofluorescence of living cells," *J. Microsc.* **191**(Pt 1), 1–7 (1998).
43. Y. Ogasawara, M. Funakoshi, and K. Ishii, "Determination of reduced nicotinamide adenine dinucleotide phosphate concentration using high-performance liquid chromatography with fluorescence detection: ratio of the reduced form as a biomarker of oxidative stress," *Biol. Pharm. Bull.* **32**(11), 1819–1823 (2009).
44. S. Hustad et al., "Riboflavin, flavin mononucleotide, and flavinadenine dinucleotide in human plasma and erythrocytes at baseline and after low-dose riboflavin supplementation," *Clin. Chem.* **48**(9), 1571–1577 (2002).
45. K. J. Smock and S. L. Perkins, "Examination of the blood and bone marrow," Chapter 1 in *Wintrobe's Clinical Hematology*, J. P. Greer et al., Eds., pp. 1–64, Lippincott Williams & Wilkins, Philadelphia (2014).
46. J. Eisinger, J. Flores, and J. M. Salhany, "Association of cytosol hemoglobin with the membrane in intact erythrocytes," *Proc. Natl. Acad. Sci. U. S. A.* **79**, 408–412 (1982).
47. K. Murakami and S. Mawatari, "Oxidation of hemoglobin to methemoglobin in intact erythrocyte by a hydroperoxide induces formation of glutathionylhemoglobin and binding of alpha-hemoglobin to membrane," *Arch. Biochem. Biophys.* **417**(2), 244–250 (2003).
48. R. Sharma and B. R. Premachandra, "Membrane-bound hemoglobin as a marker of oxidative injury in adult and neonatal red blood cells," *Biochem. Med. Metab. Biol.* **46**(1), 33–44 (1991).
49. E. Brzezińska-Slebodzińska, "Species differences in the susceptibility of erythrocytes exposed to free radicals *in vitro*," *Vet. Res. Commun.* **27**(3), 211–217 (2003).
50. J. K. Vodela and R. R. Dalvi, "Erythrocyte glutathione-S-transferase activity in animal species," *Vet. Hum. Toxicol.* **39**, 9–11 (1997).
51. A. A. Omran, "An *in vitro* spectrometric method for determining the partition coefficients of non-steroidal anti-inflammatory drugs into human erythrocyte ghost membranes," *Spectrochim. Acta. A* **104**, 461–467 (2013).
52. S. Kumazawa et al., "Antioxidant activity of polyphenols in carob pods," *J. Agric. Food Chem.* **50**, 373–377 (2002).
53. S. Chaudhuri et al., "Interaction of flavonoids with red blood cell membrane lipids and proteins: antioxidant and antihemolytic effects," *Int. J. Biol. Macromol.* **41**, 42–48 (2007).
54. U. Kubitschek et al., "Two-photon scanning microphotolysis for three-dimensional data storage and biological transport measurements," *J. Microsc.* **182**, 225–233 (1996).
55. R. D. Taverna and R. G. Langdon, "Reversible association of cytochalasin B with the human erythrocyte membrane. Inhibition of glucose transport and the stoichiometry of cytochalasin binding," *Biochim. Biophys. Acta* **323**, 207–219 (1973).
56. J. Schrader, R. M. Berne, and R. Rubio, "Uptake and metabolism of adenosine by human erythrocyte ghosts," *Am. J. Physiol.* **223**, 159–166 (1972).
57. A. W. Girotti and J. P. Thomas, "Damaging effects of oxygen radicals on resealed erythrocyte ghosts," *J. Biol. Chem.* **3**, 1744–1752 (1984).

Katarina Bukara graduated from Faculty of Pharmacy, University of Belgrade. Currently, she is doing a joint PhD at University of Belgrade,

Serbia (biotechnology and biochemical engineering) and University of Antwerp, Belgium (pharmaceutical sciences). Her research concerns the development of controlled drug delivery systems for steroids and nonsteroidal anti-inflammatory drugs based on empty erythrocyte membranes and biodegradable polymers.

Svetlana Jovanić obtained her master's degree in biophysics at the University of Belgrade, Serbia. Currently, she is a junior research associate at the Institute of Physics in Belgrade and a member of the Laboratory for Biophotonics. Her PhD research is based on investigation of neurodegeneration disorders by usage of nonlinear laser scanning microscopy (two photon excitation fluorescence and second harmonic generation) on cells and tissues.

Ivana T. Drvenica is a research associate at Innovation Centre of Faculty of Technology and Metallurgy, University of Belgrade (TMF). She obtained her MSc degree in pharmaceutical sciences from the Faculty of Pharmacy, University of Belgrade, in 2009. In collaboration with Institute for Medical Research, University of Belgrade, she obtained her PhD in biotechnology at TMF in 2015 on development and characterization of erythrocyte membranes from wasted slaughterhouse blood as prolonged drug delivery vehicles.

Ana Stančić is a third-year PhD student at the Faculty of Biology, carrying out experiments for her thesis at the Institute for Medical Research, University of Belgrade. She is the stipendist of the Ministry of Education, Science and Technological Development of the Republic of Serbia. Her work is focused on *in vitro* testing of biological effects of empty erythrocyte membranes (i.e., ghosts), hemoglobin-based products and development of modern glucocorticoid derivatives.

Vesna Ilić is a molecular biologist and physiologist. She received her PhD in immunobiology. She is a head of the Group of Immunology, Institute for Medical Research, University of Belgrade. Her areas of interests include immunoglobulins and immune complexes, signaling in cells of immune and hematopoietic systems, biological effects of mesenchymal stem cells, systems for prolonged drug delivery based on erythrocytes, and heme iron formulations for prevention or treatment of anemia.

Mihailo D. Rabasović obtained his BS, MS, and PhD degrees from the physics department of the University of Belgrade in field of applied physics. His current research interests include photoacoustics, microscopy, and correlation spectroscopy. In the field of microscopy, he is interested in nonlinear and label-free techniques.

Dejan Pantelić is a research professor at the Institute of Physics in Belgrade, Serbia. His interests include holography, biophotonics, biomimetics, and microscopy. He has published more than 100 papers in refereed journals and conferences. He is a member of the Optical Society of America.

Branislav Jelenković is a research professor and head of the Photonic Center, Institute of Physics, University of Belgrade. He earned his bachelor's degree at Faculty of Electrical Engineering, University of Belgrade (1977) and PhD in physics at Faculty of physics, University of Belgrade (1985). He is a member of Serbian Academy of Science and Art, Optical Society of Serbia (copresident), American Optical Society. He won Institute of Physics Award in 2010. He has over 100 publications in peer-reviewed journals, with over 2500 citations.

Branko Bugarski obtained a PhD in 1992 at the University of Queens, Canada. Currently, he is a professor of chemical engineering at Faculty of Technology and Metallurgy, University of Belgrade, Serbia. During 1998, he was a guest professor at Oregon State University and Massachusetts Institute of Technology. The majority of his research interests are focused on immobilization, encapsulation, nanoparticles, and their application in medicine and pharmacy.

Aleksandar J. Krmpot, assistant research professor at the Institute of Physics Belgrade received his PhD in quantum optics from the University of Belgrade, Serbia. His research activities are in quantum optics (coherent optical effects) and biophotonics (microscopy and imaging). His current research activities are the development and application of nonlinear microscopy for bioimaging at Institute of Physics, Belgrade, Serbia and multifocal correlation microscopy for studies of molecular diffusion dynamics at Karolinska Institute, Stockholm, Sweden.

Photon diagnostics at the FLASH THz beamline¹

Rui Pan,^a Ekaterina Zapolnova,^a Torsten Golz,^a Aleksandar J. Krmpot,^b Mihailo D. Rabasovic,^b Jovana Petrovic,^{c,d} Vivek Asgekar,^e Bart Faatz,^a Franz Tavella,^f Andrea Perucchi,^g Sergey Kovalev,^h Bertram Green,^h Gianluca Geloni,ⁱ Takanori Tanikawa,ⁱ Mikhail Yurkov,^a Evgeny Schneidmiller,^a Michael Gensch,^{j,k} and Nikola Stojanovic^{a*}

Received 17 October 2018

Accepted 11 March 2019

Edited by M. Yabashi, RIKEN SPring-8 Center, Japan

¹This article will form part of a virtual special issue on X-ray free-electron lasers.

Keywords: FLASH; intense THz; THz diagnostic; electro-optic; FTIR.

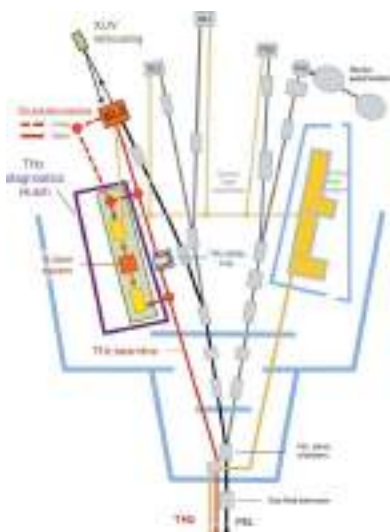
^aDeutsches Elektronen-Synchrotron (DESY), Notkestrasse 85, D-22607 Hamburg, Germany, ^bInstitute of Physics Belgrade, Pregrevica 118, 11080 Belgrade, Serbia, ^cVinca Institute of Nuclear Sciences, Belgrade, Serbia, ^dCenter for Free-Electron Laser Science, Deutsches Elektronen-Synchrotron (DESY), Notkestrasse 85, D-22607 Hamburg, Germany, ^eDepartment of Physics, S. P. Pune University, Pune, India, ^fSLAC National Accelerator Laboratory, Menlo Park, California, USA, ^gElettra – Sincrotrone Trieste S.C.p.A., 34149 Basovizza, Trieste, Italy, ^hHelmholtz-Zentrum Dresden-Rossendorf (HZDR), Bautzner Landstraße 400, 01328 Dresden, Germany, ⁱEuropean XFEL, Holzkoppel 4, 22869 Schenefeld, Germany, ^jGerman Aerospace Center (DLR), Institute of Optical Sensor Systems, Rutherfordstraße 2, 12489 Berlin, Germany, and ^kInstitute of Optics and Atomic Physics, Technical University of Berlin, Strasse des 17 Juni 135, 10623 Berlin, Germany. *Correspondence e-mail: nikola.stojanovic@desy.de

The THz beamline at FLASH, DESY, provides both tunable (1–300 THz) narrow-bandwidth ($\sim 10\%$) and broad-bandwidth intense (up to 150 μJ) THz pulses delivered in 1 MHz bursts and naturally synchronized with free-electron laser X-ray pulses. Combination of these pulses, along with the auxiliary NIR and VIS ultrashort lasers, supports a plethora of dynamic investigations in physics, material science and biology. The unique features of the FLASH THz pulses and the accelerator source, however, bring along a set of challenges in the diagnostics of their key parameters: pulse energy, spectral, temporal and spatial profiles. Here, these challenges are discussed and the pulse diagnostic tools developed at FLASH are presented. In particular, a radiometric power measurement is presented that enables the derivation of the average pulse energy within a pulse burst across the spectral range, jitter-corrected electro-optical sampling for the full spectro-temporal pulse characterization, spatial beam profiling along the beam transport line and at the sample, and a lamellar grating based Fourier transform infrared spectrometer for the on-line assessment of the average THz pulse spectra. Corresponding measurement results provide a comprehensive insight into the THz beamline capabilities.

1. Introduction

FLASH, the free-electron laser (FEL) in Hamburg at DESY, provides ultrafast XUV and soft X-ray radiation for users to perform pump–probe experiments. FLASH has two independent FEL undulator beamlines (Faatz *et al.*, 2016): FLASH1 and FLASH2. Each FEL branch ends with a dedicated experimental hall that has a number of beamlines.

FLASH1 has a unique feature, a dedicated THz undulator installed downstream of the XUV undulators. This feature allows the generation of intense THz pulses by the same electron bunch that generates XUV pulses (Stojanovic & Drescher, 2013), as shown in Fig. 1. As THz and XUV undulators are separated by empty drift space, XUV and THz pulses generated by the same electron bunch are naturally synchronized with no more than 5 fs timing jitter (Frühling *et al.*, 2009). Furthermore, THz pulses are carrier envelope phase (CEP) stable. Downstream of the THz undulator, the electron beam is deflected to ground by the so-called electron beam dump magnet (hereon referred to as the dump magnet). This



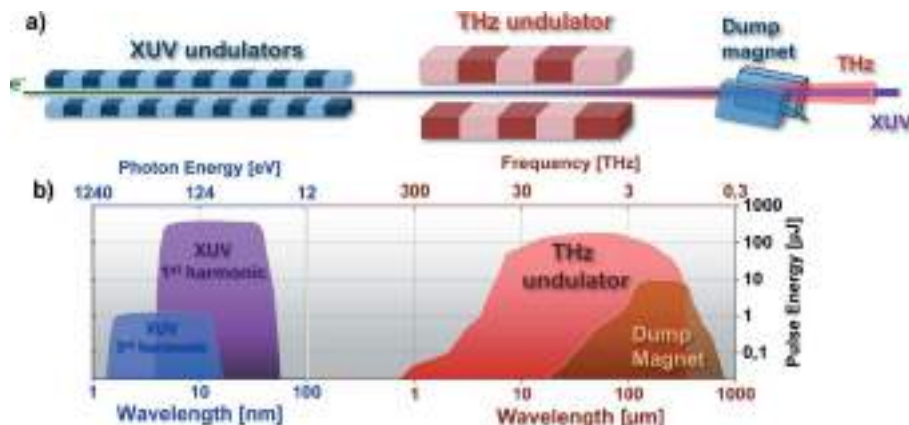


Figure 1
 Scheme of the FLASH1 THz photon sources. (a) The THz undulator is located downstream of the XUV undulators, separated by free space. The electron beam dump magnet follows the THz undulator. (b) Representation of the pulse energies that can be obtained at FLASH1 from the XUV and THz sources over a wide spectral range.

stage separates the electron beam from the photon (THz and XUV) beams. The dump magnet on its own generates an intense THz transient, mainly by the edge and bending radiation process (Tavella *et al.*, 2011; Geloni *et al.*, 2009a,b). Only a fraction of the total bending radiation is collected in the THz beamline downstream (estimated to be 11.4%), as beamline design is optimized for the radiation in the forward direction, while bending radiation is created tangentially along the bend. THz and XUV beams are separated by a large flat mirror (210 mm × 140 mm) with a 10 mm aperture for the XUV beam (Gensch *et al.*, 2008). Transport of the THz beam into the experimental hall over ~70 m requires multiple collimations and this is provided by all-reflective optics. By this unique photon generation scheme, the photon spectrum of FLASH1 is extended to the long-wavelength range. As shown in Fig. 1, FLASH1 covers the XUV range from 1.4 nm to 52 nm including harmonics (Tiedtke *et al.*, 2009), and the THz range from 1 μm to above 300 μm (300 THz to 1 THz). With an independent and synchronized near-infrared (NIR) laser (Redlin *et al.*, 2011) having a center wavelength of 800 nm, FLASH1 can provide XUV, THz and NIR laser beams for users at the same time to study photon–matter interactions.

Based on the scheme shown in Fig. 1, there are two types of intense THz sources. The first is a THz undulator (Grimm *et al.*, 2010) that generates tunable, linearly polarized (horizontally), narrow-bandwidth ($\Delta\lambda/\lambda = 10\%$) radiation. The wavelength is tunable from 1 μm to above 300 μm. The longest wavelength that can be reached depends on the electron beam energy for a given THz undulator period and peak field (see Fig. 2). Pulse energies delivered to the experiment can reach up to 150 μJ, depending on the FLASH accelerator parameters (mainly the electron bunch charge and its compression).

The second source of THz radiation is the dump magnet that generates edge and bending radiation. The edge radiation is generated by the longitudinal acceleration of the electron beam at the interface between the free space and the dump

magnet magnetic field (Tavella *et al.*, 2011; Geloni *et al.*, 2009a,b). This kind of radiation has a broad spectral bandwidth (quasi single-cycle temporal profile), is radially polarized and generated in the forward direction to the electron beam propagation. Electrons also generate the bending radiation along the bending arc of the dump magnet. The dump magnet vacuum chamber acceptance angle for the bending radiation is relatively small (2.4°) compared with 21° of the complete bend that the electrons experience. Thus only a fraction of the bending radiation radiated in the forward direction is collected into the THz beamline. Also, the bending radiation has a broad bandwidth (quasi single-cycle temporal profile) and is linearly polarized. The bending radiation is collected by the THz beamline mostly from the bending plane and is thus polarized mainly in the vertical direction, orthogonal to the THz undulator pulse polarization. Combined edge and bending dump magnet radiation can reach a pulse energy of over 10 μJ. This radiation is generated parasitically and can be used independently from the undulator radiation.

The THz beamline delivers the beam to the end-station at the end of the BL3 XUV beamline in the FLASH1 experimental hall (see Fig. 3). The THz beam can be delivered to the experiment via two branches, a short one with ultra-high-vacuum transport (10^{-9} mbar) and a long one via THz diagnostics hutch with high-vacuum transport (10^{-7} mbar). Due to the difference in optical path, the THz pulse arrives later than the XUV pulse to the end-station, 12 ns for the short branch and 21 ns for the long branch. We use two approaches to achieve temporal overlap of the XUV and THz pulses in the experiment: the first is delaying the XUV pulse by refocusing via multilayer mirrors; the second is to generate two electron bunches at the FLASH electron gun timed to achieve temporal overlap of the respective THz and XUV pulses in the experiment (Zapolnova *et al.*, 2018).

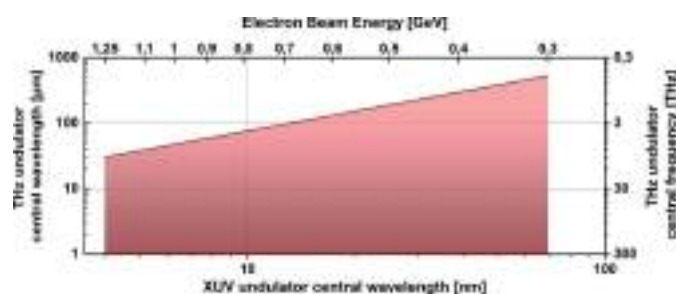


Figure 2
 THz undulator spectral range. The shaded area represents the range where the fundamental frequency of the THz undulator radiation can be reached for FLASH1 as a function of the FEL XUV wavelength (lower horizontal axis) and the electron beam energy in the linac (upper horizontal axis).

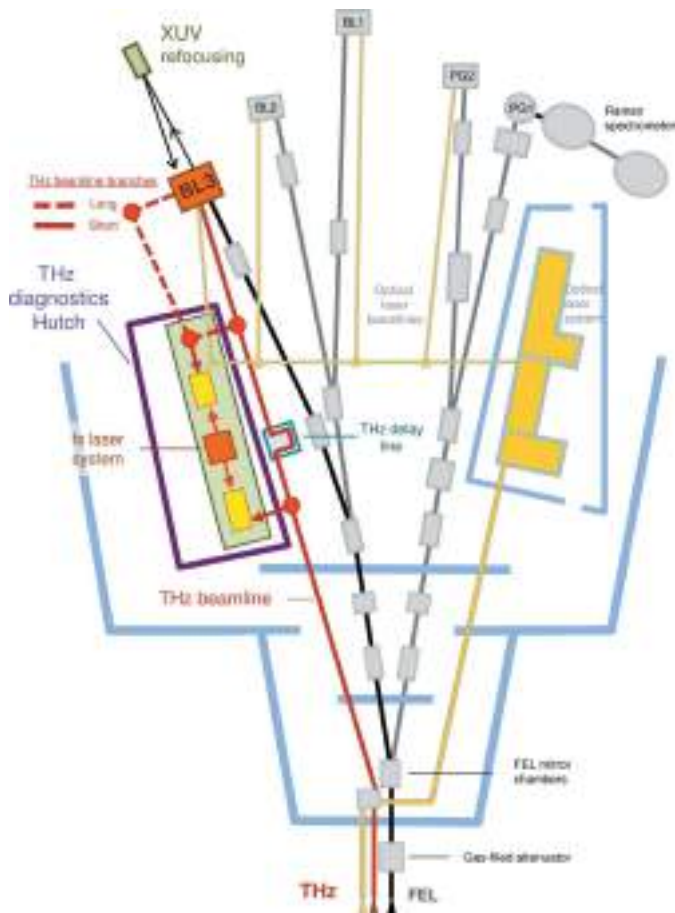


Figure 3
Scheme of the THz beamline in the FLASH1 experimental hall. THz beam is delivered to the end-station at the BL3 XUV beamline, via one of the two branches.

There are many unique applications for the CEP stable intrinsically synchronized THz pulses from the FLASH THz beamline. One important scientific area is in atomic and molecular physics. Here the THz field can act as a streak camera, allowing molecular reactions to be clocked and processes induced by the femtosecond-long XUV pulses from FLASH on a timescale of a few femtoseconds (Frühling *et al.*, 2009; Schütte *et al.*, 2012; Oelze *et al.*, 2017; Schmid *et al.*, 2019). An emerging new class of experiments at FLASH is the application of the strong THz fields for these tunable narrow-band pulses in selective excitation or selective THz control of matter [for a description of this field see, for example, Green *et al.* (2016), Buzzi *et al.* (2018), Kampfrath *et al.* (2013) and Kovalev *et al.* (2017)]. The first experiments performed at FLASH have focused on driving the magnetization dynamics in magnetic thin films by selective phonon excitation (Radu, 2019) and on the THz control of dynamic surface processes (Waltar *et al.*, 2018).

2. THz diagnostics

In a typical THz-pump/XUV-probe experiment at FLASH, determination of the properties of the driving THz pulse is of key importance. Based on the needs of the user experiments in

past years, we have developed diagnostics tools to fully characterize the THz beam at the experiment. Presently, all the tools are developed in the THz diagnostics hutch at FLASH1 experimental hall and will be transferred to the end-station at BL3 beamline (see Fig. 3). In this paper we present tools for the full spectral, temporal and spatial characterization of the THz pulses and the pulse-energy measurement. Thereby we discuss some of the major challenges for diagnostics, *i.e.* the extremely broad THz spectral range of FLASH sources, 1 MHz repetition rate in 10 Hz bursts and jitter to externally synchronized lasers (Azima *et al.*, 2009; Tavella *et al.*, 2011), that can be used for THz waveform characterization.

2.1. THz power measurement

We measure the THz pulse energies using a radiometer (RM3700, head RjP-735/RF, by Laser Probe). We have cross-referenced this detector to a PTB (The National Metrology Institute of Germany) traceable 3A-P-THz, by Ophir Optronics Solutions (Green *et al.*, 2016). The radiometer detector has a cavity pyroelectric probe and it has a time constant of 1 ms. Its temporal response prevents us from resolving individual pulses of the FLASH micro-pulses within a 1 MHz burst. However, the detector time constant is well matched to the maximal duration of the 1 MHz burst (with duration of 0.8 ms, containing up to 800 pulses) defined by the FLASH accelerator. Therefore, the integration is performed over all micro-bunches in a burst, which allows for determination of the average THz pulse energy with good accuracy.

Fig. 4 depicts the THz pulse energy as a function of the central wavelength of the THz undulator. The total THz beamline transmission (from the source until the end of beamline) as a function of wavelength is depicted as well. We calculate the beamline transmission by modeling the THz source and the optical transport with the *Synchrotron Radia-*

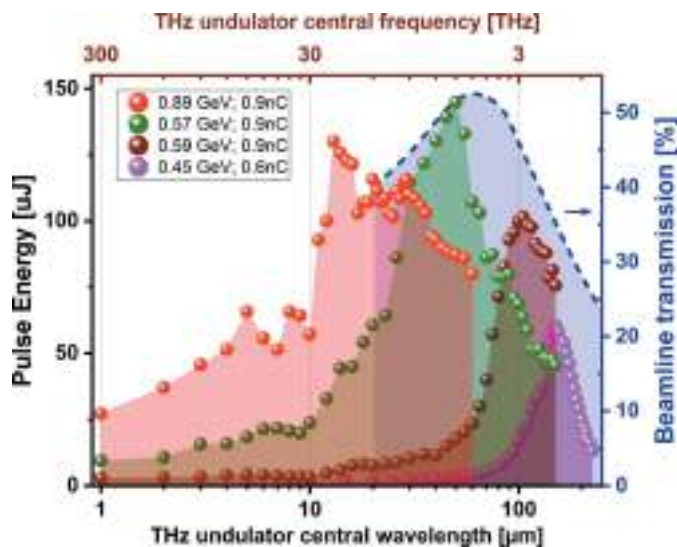


Figure 4
THz pulse energies measured at the beamline end-station for different conditions of the FLASH accelerator. The blue dashed line shows the beamline transmission, calculated using the *SRW* software package (Chubar & Elleaume, 1998).

tion Workshop (SRW) software package (Chubar & Elleaume, 1998). We also account for the Fresnel losses in the diamond window that separates the beamline from the accelerator vacuum (Gensch *et al.*, 2008). We present examples of four measurements taken for different electron beam settings of the FLASH accelerator. Note that the abrupt end of the THz undulator tuning range at long wavelengths relates to the maximal wavelength that can be reached at a particular electron beam energy and is determined by the maximum field (1.2 T) inside the undulator (see also Fig. 2).

2.2. THz temporal profile measurements

The THz time domain spectroscopy (TDS) via electro-optic sampling (EOS) method is a well established technique for the full characterization of the THz pulse temporal structure (Wu & Zhang, 1995; Schmuttenmaer, 2004), in a broad spectral range. The electric field of the THz pulse changes the birefringence of the EOS crystal. This transient change is sampled by an ultrashort laser pulse. By scanning the laser pulse in time, the complete THz pulse shape can be reconstructed.

At an accelerator-based light source, such as FLASH, the laser system is synchronized to the master clock of the FLASH accelerator (Schulz *et al.*, 2015). One of the main limiting factors for the use of an externally synchronized laser for EOS detection is the temporal jitter between the FEL and the laser pulses. Jitter limits the temporal resolution and subsequently the spectral bandwidth of EOS detection. We have measured the jitter of the probe laser (pulse duration 20 fs FWHM) in the THz hutch to the FLASH THz pulses to be around 100 fs RMS (~ 200 fs peak-to-peak). To solve this, we chose to detect the THz pulses' arrival time on a single-shot basis using spectral decoding electro-optic detection (EOSD) (Jiang & Zhang, 1998). This technique enables single-shot THz detection by imprinting the THz pulse electric field onto a stretched probe laser pulse, thus defining the arrival time of one with respect to the other. Spectral decoding is photon efficient (for a single-shot method) and enables the arrival time detection even with femtosecond oscillator pulses, which allows for a high-repetition-rate arrival time detection scheme that can be matched to the FLASH pulse pattern. Full EO detection of the THz pulses at FLASH then comprises two main components: arrival time monitoring by spectral decoding in combination with scanning electro-optic sampling (EOS). EOS data are sorted for their arrival time and the THz pulse shape is retrieved. The complete detection setup is installed in a high-vacuum chamber (10^{-7} mbar) to avoid measurement distortions by absorption in ambient air. We achieved a temporal resolution of the arrival time sorting of 9.7 fs RMS. Most importantly, the EOS sampling has a bandwidth of 37–3000 μm (0.1–8 THz) limited by the gallium phosphide (GaP) EOS crystal (100 μm thick). The setup has been developed in collaboration with the TELBE team at HZDR and details can be found in the literature (Kovalev *et al.*, 2017; Golz, 2018).

Two typical examples of measured THz waveform profiles are shown in Figs. 5(a) and 5(b). The THz and the probing laser beam are overlapped and focused on the GaP EOS

crystal, with beam sizes of 350 μm FWHM and 70 μm FWHM, respectively. The THz undulator was set to nominal wavelengths of 155 μm and 42 μm (corresponding to frequencies of 1.93 THz and 7.1 THz, respectively). For the long-wavelength example, unfiltered and spectrally filtered pulses are presented. The wire-grid THz bandpass filter used has been centered at 155 μm wavelength (1.93 THz) with 15% spectral bandwidth. For the unfiltered pulse, it is interesting to observe that the electric field and high-harmonic content increase along the pulse. This indicates the change of the electron bunch form factor (Nodvick & Saxon, 1954) inside the undulator. In the respective unfiltered THz pulse spectrum [see Fig. 5(c)] we clearly observe the first harmonic peaking at 169 μm (1.77 THz) and the third harmonic at 52 μm (5.68 THz), and the baseline includes the broadband spectrum from the dump magnet radiation. As expected, the measurement with the THz bandpass filter shows a strong peak around 160 μm (1.87 THz), with a small (few percent) leakage between 75 and 100 μm (3 and 4 THz). Similarly, in the spectrum of the short-wavelength pulse (tuned to 42 μm) we observe the first harmonic peaking at 43 μm (7 THz).

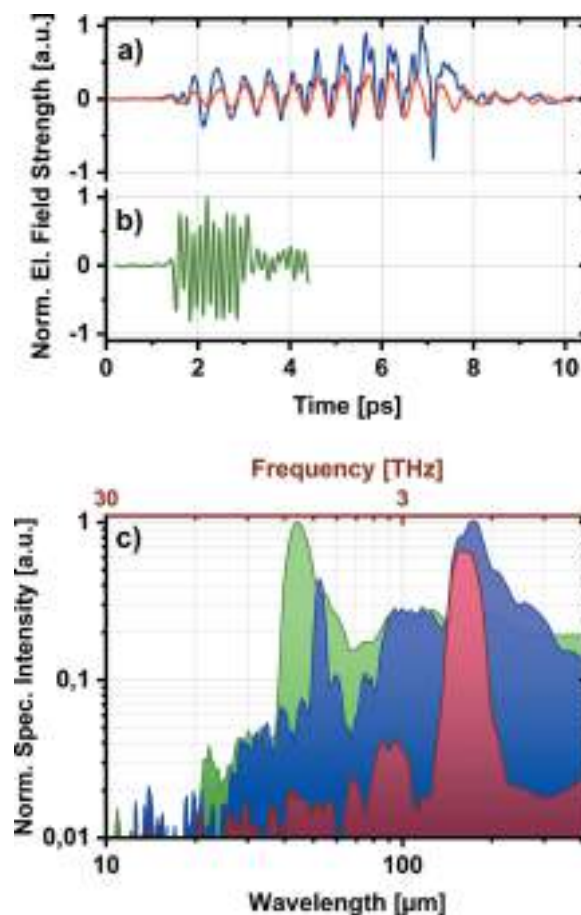


Figure 5 THz pulse waveforms measured by arrival-time-sorted time domain spectroscopy (TDS). (a) The THz pulse produced by the undulator set at the nominal wavelength of 155 μm (1.93 THz). The unfiltered temporal profile is shown by the blue line and the filtered by the red line, with 155 μm (1.93 THz) bandpass filter (15% bandwidth). (b) The unfiltered THz pulse at 43 μm (7 THz) (green line). (c) The corresponding THz pulse spectra.

It is worth noting that the EOSD scheme can be used as a THz arrival-time detection tool in other experiments. A recent application evaluated the timing jitter between two electron bunches with 21 ns delay timed for temporal overlap of THz and XUV pulses at the experimental end-station at BL3 (Zapolnova *et al.*, 2018).

2.3. THz beam profile

Knowledge of the transverse THz beam profile is important as it allows precise determination of the fluence (and the peak field) on the sample, as well as optimal optical design to maximize the beam transmission in the experiment. We model the THz source and the radiation transport using the *SRW* software package (Chubar & Elleaume, 1998) and observe the strong interference effects between undulator and dump magnet radiation (edge and bending radiation) at FLASH (Asgekar *et al.*, 2014).

An example of the measured THz beam profile from the dump magnet, with the THz undulator switched off, is shown in Fig. 6(a). An example of the THz undulator beam tuned to 88 μm (3.4 THz) is shown in Fig. 6(b). The beams have been imaged in the THz diagnostics hutch so that they image the plane approximately 10 m downstream of the radiation source. We perform 2D raster scanning of the beams. As a detector we employ an amplified pyroelectric detector (LME-501 from InfraTec). Both measurements have been performed with 30 μm long-pass THz spectral filter. The profiles have been reproduced by *SRW* calculation, whereby the integration of the output power was performed over the 30–300 μm

(1–10 THz) spectral range to account for the filtering, and the form factor of a 50 fs RMS long electron bunch was used.

For the dump magnet, both the measurement and calculation render a half-moon-like structure that can be explained by interference of the edge radiation with the bending radiation from the dump magnet. For the THz undulator beam we observe slight asymmetry in the horizontal plane which can be explained by interference of the undulator and the dump magnet radiation (Asgekar *et al.*, 2014).

We focus both beams with an off-axis parabolic mirror of focal length 150 mm and measure the beam profile with a Pyrocam III camera from Ophir Photonics for the dump magnet and with a microbolometer camera for the undulator beam. The results are shown in Figs. 6(c) and 6(d), respectively. We observe a beam size of 600 μm FWHM for the dump magnet and 350 μm FWHM for the undulator beam.

Moreover, we follow the THz undulator beam profile evolution, by wavefront propagation in *SRW*. The undulator radiation wavelength is set to 160 μm (1.87 THz). For an experimental confirmation, we measure the beam profile in the THz diagnostics hutch at five different positions along the beam path [see Fig. 7(a)], using the knife-edge technique. Zero

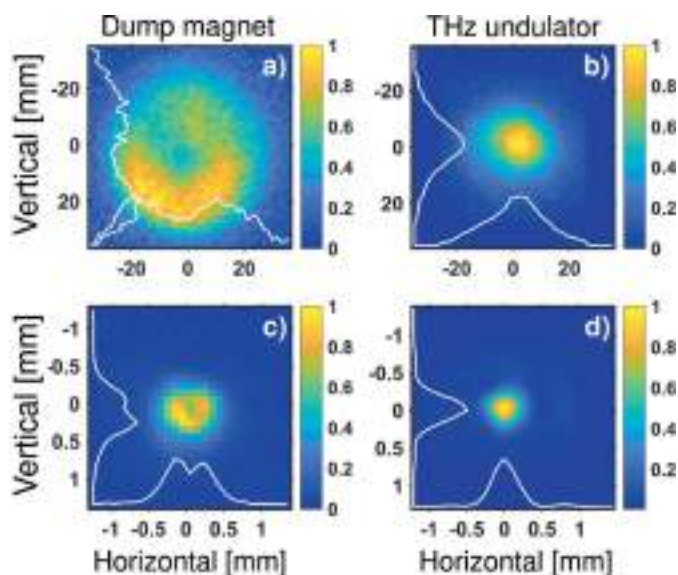


Figure 6
(Top) THz transverse beam profiles at FLASH. (a) Dump magnet (the THz undulator is off), and (b) THz undulator tuned to 88 μm (3.4 THz), unfocused beam profiles measured in the THz hutch; beam position imaged 10 m from the virtual source. Note that the undulator profile is padded with zeros to fill in the same image size. (Bottom) The same beams focused. (c) Dump magnet beam (600 μm FWHM), and (d) THz undulator beam (350 μm FWHM).

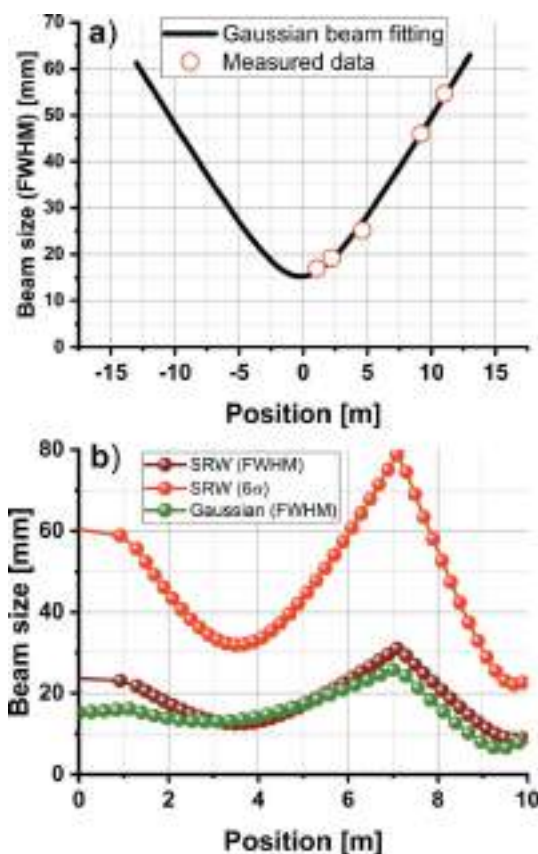


Figure 7
THz undulator beam size at 160 μm (1.87 THz) and its propagation. (a) Beam size measured at five different locations along the beam path (red circles) fitted by a Gaussian beam propagation. (b) THz beam propagation over the 10 m path, with the focusing mirrors inserted at the 1 m and 7 m position marks. The THz beam was approximated by fitted Gaussian beam (FWHM) (green curve) and calculated from the source by *SRW* (FWHM) (brown curve) and 6σ (red curve).

position denotes the THz beamline window at which the beam is extracted into the THz diagnostics station. We assume a Gaussian beam profile and obtain the beam parameters by fitting. The plot in Fig. 7(b) compares the beam size evolution (FWHM) calculated by SRW (brown curve) with the approximated Gaussian beam propagation (ABCD matrix formalism), fitted from the measured data (green curve), for the last 10 m of the THz beamline transport. Two toroidal mirrors with focal lengths of 3.8 m and 1.8 m are inserted at the 1 m and 7 m position marks, respectively. In this particular example, the goal was to couple the THz beam into an experimental chamber through a 25 mm aperture, located at the 10 m position mark, with highest possible transmission. The red curve depicts the THz beam size at the equivalent of 6σ (or 99.7% beam energy), and at the 10 m position mark we achieve the desired sub-25 mm beam size. We observe a reasonable agreement between these two numerical models, with the big advantage of the Gaussian beam propagation providing very fast and efficient evaluation of the beam sizes in the optical system.

2.4. THz spectrum measurement

For a quick THz spectral characterization, when temporal pulse structure is not necessary, we have developed the variation of the Fourier transform infrared (FTIR) spectrometer based on a reflective lamellar grating. Unlike the most commonly used Michelson interferometer (based on amplitude division), the reflective lamellar grating interferometer (Richards, 1964; Bell, 1972) divides the wavefront spatially. Because of this, the reflective lamellar grating design has a key advantage: a high (close to 100%) and smooth efficiency response (*e.g.* typical Fabry–Perot interferences that plague Michelson interferometers are absent). A comparison of the efficiency of the lamellar grating and the Michelson interferometer can be found in Fig. 3 of Richards (1964). As a side note, owing to a large spectral bandwidth, the lamellar gratings have found application in extreme ultraviolet (XUV) spectroscopy and metrology (Gebert *et al.*, 2014; Usenko *et al.*, 2017).

As shown in Fig. 8, the lamellar grating spectrometer consists of two interleaved gratings, manufactured from a 100 mm-diameter gold-coated copper mirror. One is fixed and the other is mounted on the motorized stage responsible for introducing the optical delay between the split beams. For detection a pyroelectric detector (LME-501 from InfraTec) with a 2 mm × 2 mm chip size was used.

The THz beam is collimated in a way that uniformly illuminates the gratings. The period of the grating ($h = 2$ mm) is chosen to match the spectral range of the THz sources at FLASH. The long-wavelength limit (Bell, 1972) for lamellar gratings is $\lambda_{\max} < h/2$, which is 1 mm (corresponding to

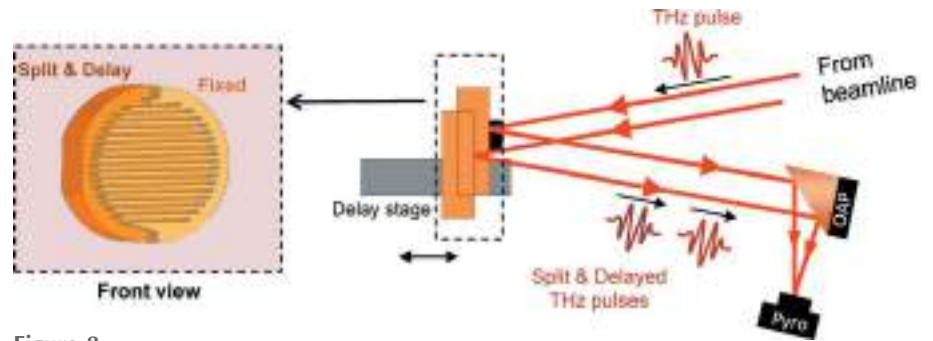


Figure 8 Scheme of the lamellar grating interferometer. OAP: off-axis parabolic mirror.

0.3 THz) in our case. For wavelengths longer than λ_{\max} , a cavity effect starts decreasing the modulation depth of the THz waves, which are polarized parallel to the fringes. The high-frequency limit for this geometry is 30 μm (corresponding to 10 THz), which is determined by diffraction theory and depends on the geometry of the device (Strong & Vanasse, 1960; Naftaly *et al.*, 2008; Ferhanoglu *et al.*, 2009): $\lambda_{\min} = hsf$, where $f = 130$ mm is the focal length of the parabolic mirror and $s = 2$ mm is the width of the exit slit of the detector (defined by the detector effective aperture).

An example of the measured interferogram and the calculated spectrum is shown in Fig. 9. The THz pulse was generated by the edge radiation and filtered by a 215 μm (1.4 THz) bandpass filter. The fluctuations of the shot-to-shot THz pulse energy at FLASH can be as high as 20% RMS, depending on the FLASH accelerator settings. We split a small portion of the beam for a reference measurement that is then used to

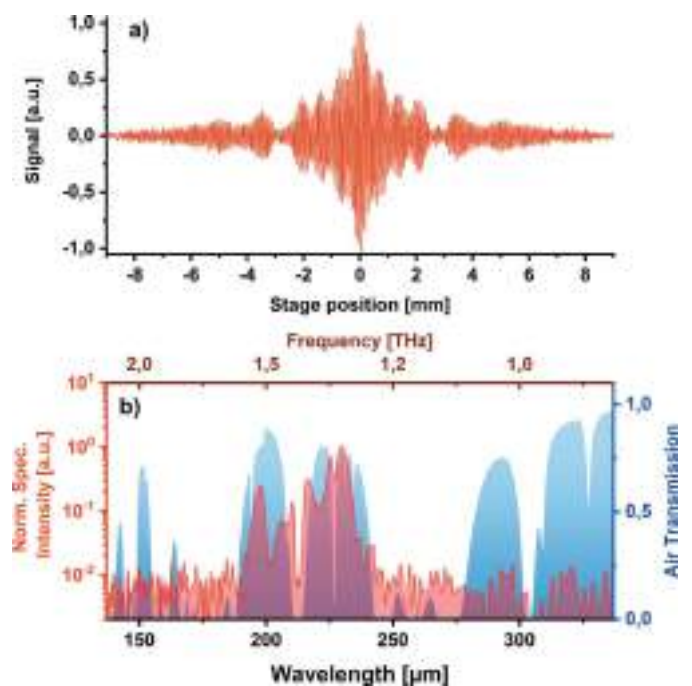


Figure 9 FTIR measurement for THz edge radiation with 215 μm (1.4 THz) THz bandpass filter. (a) Double-sided interferogram. (b) Respective spectrum (red curve) and air transmission with water vapor (in blue) show the strong absorption lines in this spectral range.

normalize the measured interferogram on a single-shot basis. The normalized interferogram in Fig. 9(a) was obtained during 20 min of scanning at 10 Hz repetition rate (12000 shots). Fig. 9(b) shows the normalized spectrum, obtained by taking a Fourier transform of the measured interferogram. We observe the spectral content as expected from the filter response with a signal-to-noise ratio exceeding 100.

Measurement has been performed in ambient air and we observe a strong modulation from the water vapor absorption lines. We are currently upgrading it to an all-in-vacuum spectrometer.

3. Conclusion

We have presented a range of THz diagnostic tools developed for THz/XUV pump–probe experiments at FLASH1, DESY. The THz pulse energy is an important parameter for optimization of the FLASH accelerator, and it reaches values from tens of μJ up to 150 μJ . The upgrade of a currently used radiometer to an online monitor is in progress. The THz temporal profile can be measured with 10 fs timing resolution and covers the spectral range from 37 to 3000 μm (0.1 to 8 THz). The ongoing development of this technique will explore the use of different EOS crystals to extend the measured bandwidth to shorter wavelengths, GaSe (Kübler *et al.*, 2005) and SiC (Naftaly *et al.*, 2016) being good candidates that should allow THz detection in the 10–40 THz and 0.1–15 THz spectral windows, respectively. To fully exploit the high THz pulse energies at FLASH, we are upgrading the single-shot EOSD THz detection technique to one via tilted laser pulse front (Teo *et al.*, 2015). This technique is free from the spectral distortions that plague EOSD (Jamison *et al.*, 2008) and allows for the full bandwidth of the pulse to be retrieved (limited only by the EOS crystal). The measurements of the transversal THz beam profile are used for the design of the beam transfer line and calibration of the peak field and intensity in the experiment. A broadband FTIR spectrometer, covering the spectral range 30–1000 μm (0.3–10 THz), based on a reflective lamellar grating is developed for spectral measurements. It will be permanently installed inside the THz beamline vacuum environment for distortion-free THz spectrum measurements, enabling quick and robust spectral studies [*e.g.* suitable for THz shaping by emerging THz meta-materials (Yen *et al.*, 2004; Monticone & Alù, 2017; Stojanović *et al.*, 2018; Polley *et al.*, 2018)].

Funding information

RP, EZ, AK, MR and NS acknowledge financial support from German Academic Exchange Service (DAAD Grant Numbers 57219839 and 57393513). NS acknowledge financial support from Bundesministerium für Bildung und Forschung (grant No. 05K12CH4). JP and AP were supported by the ‘Stephenson Distinguished Visitor Programme’ at DESY in Hamburg (Germany). JP, MR and AK acknowledge support from the Ministry of Education, Science and Technological Development of Serbia, under Grant No. III45010 and OI

171038 and bilateral projects 451-03-01732/2017-09/6 and 451-03-01038/2015-09/1. MG and BG acknowledge support from the European Cluster of Advanced Laser Light Sources (EUCALL) project which has received funding from the European Union’s Horizon 2020 research and innovation program under grant agreement No 654220. VA acknowledges support from the Alexander von Humboldt Foundation, Germany.

References

- Asgekar, V., Geloni, G., Kocharyan, V., Stojanovic, N., Michel, P. & Gensch, M. (2014). *Infrared Phys. Technol.* **64**, 26–32.
- Azima, A., Düsterer, S., Radcliffe, P., Redlin, H., Stojanovic, N., Li, W., Schlarb, H., Feldhaus, J., Cubaynes, D., Meyer, M., Dardis, J., Hayden, P., Hough, P., Richardson, V., Kennedy, E. T. & Costello, J. T. (2009). *Appl. Phys. Lett.* **94**, 144102.
- Bell, R. J. (1972). *Introductory Fourier Transform Infrared Spectroscopy*. New York: Academic Press.
- Buzzi, M., Först, M., Mankowsky, R. & Cavalleri, A. (2018). *Nat. Rev. Mater.* **3**, 299–311.
- Chubar, O. & Elleaume, P. (1998). *Proceedings of the Sixth European Particle Accelerator Conference (EPAC’98)*, 22–26 June 1998, Stockholm, Sweden, pp. 1177–1179.
- Faatz, B., Plönjes, E., Ackermann, S., Agababyan, A., Asgekar, V., Ayvazyan, V., Baark, S., Baboi, N., Balandin, V., Bargen, N., Bican, Y., Bilani, O., Bödewadt, J., Böhnert, M., Böspflug, R., Bonfigt, S., Bolz, H., Borges, F., Borkenhagen, O., Brachmanski, M., Braune, M., Brinkmann, A., Brovko, O., Bruns, T., Castro, P., Chen, J., Czwalińska, M. K., Damker, H., Decking, W., Degenhardt, M., Delfs, A., Delfs, T., Deng, H., Dressel, M., Duhme, H., Düsterer, S., Eckoldt, H., Eislage, A., Felber, M., Feldhaus, J., Gessler, P., Gibau, M., Golubeva, N., Golz, T., Gonschior, J., Grebentsov, A., Grecki, M., Grün, C., Grunewald, S., Hacker, K., Hänisch, L., Hage, A., Hans, T., Hass, E., Hauberg, A., Hensler, O., Hesse, M., Heuck, K., Hidvegi, A., Holz, M., Honkavaara, K., Höppner, H., Ignatenko, A., Jäger, J., Jastrow, U., Kammering, R., Karstensen, S., Kaukher, A., Kay, H., Keil, B., Klose, K., Kocharyan, V., Köpke, M., Körfer, M., Kook, W., Krause, B., Krebs, O., Kreis, S., Krivan, F., Kuhlmann, J., Kuhlmann, M., Kube, G., Laarmann, T., Lechner, C., Lederer, S., Leuschner, A., Liebertz, D., Liebing, J., Liedtke, A., Lilje, L., Limberg, T., Lipka, D., Liu, B., Lorbeer, B., Ludwig, K., Mahn, H., Marinkovic, G., Martens, C., Marutzky, F., Maslovc, M., Meissner, D., Mildner, N., Miltchev, V., Molnar, S., Mross, D., Müller, F., Neumann, R., Neumann, P., Nölle, D., Obier, F., Pelzer, M., Peters, H., Petersen, K., Petrosyan, A., Petrosyan, G., Petrosyan, L., Petrosyan, V., Petrov, A., Pfeiffer, S., Piotrowski, A., Pizarov, Z., Plath, T., Pototzki, P., Prandolini, M. J., Prenting, J., Priebe, G., Racky, B., Ramm, T., Rehlich, K., Riedel, R., Roggli, M., Röhling, M., Rönsch-Schulenburg, J., Rossbach, J., Rybnikov, V., Schäfer, J., Schaffran, J., Schlarb, H., Schlesselmann, G., Schlösser, M., Schmid, P., Schmidt, C., Schmidt-Föhre, F., Schmitz, M., Schneidmiller, E., Schöps, A., Scholz, M., Schreiber, S., Schütt, K., Schütz, U., Schulte-Schrepping, H., Schulz, M., Shabunov, A., Smirnov, P., Sombrowski, E., Sorokin, A., Sparr, B., Spengler, J., Staack, M., Stadler, M., Stechmann, C., Steffen, B., Stojanovic, N., Sychev, V., Syresin, E., Tanikawa, T., Tavella, F., Tesch, N., Tiedtke, K., Tischer, M., Treusch, R., Tripathi, S., Vagin, P., Vetrov, P., Vilcins, S., Vogt, M., Wagner, A. Z., Wamsat, T., Weddig, H., Weichert, G., Weigelt, H., Wentowski, N., Wiebers, C., Wilksen, T., Willner, A., Wittenburg, K., Wohlenberg, T., Wortmann, J., Wurth, W., Yurkov, M., Zagorodnov, I. & Zemella, J. (2016). *New J. Phys.* **18**, 062002.
- Ferhanoglu, O., Seren, H. R., Lüttjohann, S. & Urey, H. (2009). *Opt. Express*, **17**, 21289–21301.

- Frühling, U., Wieland, M., Gensch, M., Gebert, T., Schütte, B., Krikunova, M., Kalms, R., Budzyn, F., Grimm, O., Rossbach, L., Plönjes, E. & Drescher, M. (2009). *Nat. Photon.* **3**, 523.
- Gebert, T., Rompotis, D., Wieland, M., Karimi, F., Azima, A. & Drescher, M. (2014). *New J. Phys.* **16**, 073047.
- Geloni, G., Kocharyan, V., Saldin, E., Schneidmiller, E. & Yurkov, M. (2009a). *Nucl. Instrum. Methods Phys. Res. A*, **605**, 409–429.
- Geloni, G., Kocharyan, V., Saldin, E., Schneidmiller, E. & Yurkov, M. (2009b). *Nucl. Instrum. Methods Phys. Res. A*, **607**, 470–487.
- Gensch, M., Bittner, L., Chesnov, A., Delsim-Hashemi, H., Drescher, M., Faatz, B., Feldhaus, J., Fruehling, U., Geloni, G., Gerth, C., Grimm, O., Hahn, U., Hesse, M., Kapitzki, S., Kocharyan, V., Kozlov, O., Matyushevsky, E., Morozov, N., Petrov, D., Ploenjes, E., Roehling, M., Rossbach, J., Saldin, E. L., Schmidt, B., Schmueser, P., Schneidmiller, E. A., Syresin, E., Willner, A. & Yurkov, M. V. (2008). *Infrared Phys. Technol.* **51**, 423–425.
- Golz, T. (2018). PhD thesis, Hamburg University, Germany.
- Green, B., Kovalev, S., Asekar, V., Geloni, G., Lehnert, U., Golz, T., Kuntzsch, M., Bauer, C., Hauser, J., Voigtlaender, J., Wustmann, B., Koesterke, I., Schwarz, M., Freitag, M., Arnold, A., Teichert, J., Justus, M., Seidel, W., Ilgner, C., Awari, N., Nicoletti, D., Kaiser, S., Laplace, Y., Rajasekaran, S., Zhang, L., Winnerl, S., Schneider, H., Schay, G., Lorincz, I., Rauscher, A. A., Radu, I., Mährlein, S., Kim, T. H., Lee, J. S., Kampftrath, T., Wall, S., Heberle, J., Malnasi-Csizmadia, A., Steiger, A., Müller, A. S., Helm, M., Schramm, U., Cowan, T., Michel, P., Cavalleri, A., Fisher, A. S., Stojanovic, N. & Gensch, M. (2016). *Sci. Rep.* **6**, 22256.
- Grimm, O., Morozov, N., Chesnov, A., Holler, Y., Matushevsky, E., Petrov, D., Rossbach, J., Syresin, E. & Yurkov, M. (2010). *Nucl. Instrum. Methods Phys. Res. A*, **615**, 105–113.
- Jamison, S., Gillespie, W. & Phillips, P. (2008). *Signal*, **1**, 2.
- Jiang, Z. & Zhang, X.-C. (1998). *Appl. Phys. Lett.* **72**, 1945–1947.
- Kampftrath, T., Tanaka, K. & Nelson, K. A. (2013). *Nat. Photon.* **7**, 680.
- Kovalev, S., Green, B., Golz, T., Mährlein, S., Stojanovic, N., Fisher, A. S., Kampftrath, T. & Gensch, M. (2017). *Struct. Dyn.* **4**, 024301.
- Kübler, C., Huber, R. & Leitenstorfer, A. (2005). *Semicond. Sci. Technol.* **20**, S128–S133.
- Monticone, F. & Alù, A. (2017). *Rep. Prog. Phys.* **80**, 036401.
- Naftaly, M., Dean, P., Miles, R. E., Fletcher, J. R. & Malcoci, A. (2008). *Quantum Electron.* **14**, 443–448.
- Naftaly, M., Molloy, J., Magnusson, B., Andreev, Y. & Lanskii, G. (2016). *Opt. Express*, **24**, 2590–2595.
- Nodvick, J. S. & Saxon, D. S. (1954). *Phys. Rev.* **96**, 180–184.
- Oelze, T., Schütte, B., Müller, M., Müller, J. P., Wieland, M., Frühling, U., Drescher, M., Al-Shemmary, A., Golz, T., Stojanovic, N. & Krikunova, M. (2017). *Sci. Rep.* **7**, 40736.
- Polley, D., Hagström, N. Z., Schmising, C. K., Eisebitt, S. & Bonetti, S. (2018). *J. Phys. B At. Mol. Opt. Phys.* **51**, 224001.
- Radu, I. (2019). In preparation.
- Redlin, H., Al-Shemmary, A., Azima, A., Stojanovic, N., Tavella, F., Will, I. & Dusterer, S. (2011). *Nucl. Instrum. Methods Phys. Res. A*, **635**, S88–S93.
- Richards, P. L. (1964). *J. Opt. Soc. Am.* **54**, 1474–1484.
- Schmid, G., Schnorr, K., Augustin, S., Meister, S., Lindenblatt, H., Trost, F., Liu, Y., Stojanovic, N., Al-Shemmary, A., Golz, T., Treusch, R., Gensch, M., Kübel, M., Foucar, L., Rudenko, A., Ullrich, J., Schröter, C. D., Pfeifer, T. & Moshhammer, R. (2019). *Phys. Rev. Lett.* **122**, 073001.
- Schmittenmaer, C. A. (2004). *Chem. Rev.* **104**, 1759–1779.
- Schulz, S., Grguraš, I., Behrens, C., Bromberger, H., Costello, J., Czwilina, M., Felber, M., Hoffmann, M., Ilchen, M., Liu, H., Mazza, T., Meyer, M., Pfeiffer, S., Prędko, P., Schefer, S., Schmidt, C., Wegner, U., Schlarb, H. & Cavalieri, A. L. (2015). *Nat. Commun.* **6**, 5938.
- Schütte, B., Bauch, S., Frühling, U., Wieland, M., Gensch, M., Plönjes, E., Gaumnitz, T., Azima, A., Bonitz, M. & Drescher, M. (2012). *Phys. Rev. Lett.* **108**, 253003.
- Stojanović, D. B., Beličev, P. P., Gligorić, G. & Hadžievski, L. (2018). *J. Phys. D Appl. Phys.* **51**, 045106.
- Stojanovic, N. & Drescher, M. (2013). *J. Phys. B At. Mol. Opt. Phys.* **46**, 192001.
- Strong, J. & Vanasse, G. A. (1960). *J. Opt. Soc. Am.* **50**, 113–118.
- Tavella, F., Stojanovic, N., Geloni, G. & Gensch, M. (2011). *Nat. Photon.*, **5**, 162.
- Teo, S. M., Ofori-Okai, B. K., Werley, C. A. & Nelson, K. A. (2015). *Rev. Sci. Instrum.* **86**, 051301.
- Tiedtke, K., Azima, A., von Barga, N., Bittner, L., Bonfigt, S., Dusterer, S., Faatz, B., Frühling, U., Gensch, M., Gerth, C., Guerrasimova, N., Hahn, U., Hans, T., Hesse, M., Honkavaar, K., Jastrow, U., Juranic, P., Kapitzki, S., Keitel, B., Kracht, T., Kuhlmann, M., Li, W. B., Martins, M., Núñez, T., Plönjes, E., Redlin, H., Saldin, E. L., Schneidmiller, E. A., Schneider, J. R., Schreiber, S., Stojanovic, N., Tavella, F., Toleikis, S., Treusch, R., Weigelt, H., Wellhöfer, M., Wabnitz, H., Yurkov, M. V. & Feldhaus, J. (2009). *New J. Phys.* **11**, 023029.
- Usenko, S., Przystawik, A., Jakob, M. A., Lazzarino, L. L., Brenner, G., Toleikis, S., Haunhorst, C., Kip, D. & Laermann, T. (2017). *Nat. Commun.* **8**, 15626.
- Waltar, K., Haase, J., Lucchini, M., van Bokhoven, J. A., Hengsberger, M., Osterwalder, J. & Castiglioni, L. (2018). *Opt. Express*, **26**, 8364–8374.
- Wu, Q. & Zhang, X. (1995). *Appl. Phys. Lett.* **67**, 3523–3525.
- Yen, T.-J., Padilla, W., Fang, N., Vier, D., Smith, D., Pendry, J., Basov, D. & Zhang, X. (2004). *Science*, **303**, 1494–1496.
- Zapolnova, E., Golz, T., Pan, R., Klose, K., Schreiber, S. & Stojanovic, N. (2018). *J. Synchrotron Rad.* **25**, 39–43.



Cite this: *RSC Adv.*, 2018, 8, 27429

One-step synthesis of amino-functionalized up-converting NaYF₄:Yb,Er nanoparticles for *in vitro* cell imaging†

Lidija Mancic,^a Aleksandra Djukic-Vukovic,^b Ivana Dinic,^c Marko G. Nikolic,^d Mihailo D. Rabasovic,^d Aleksandar J. Krmpot,^d Antonio M. L. M. Costa,^e Bojan A. Marinkovic,^e Ljiljana Mojovic^b and Olivera Milosevic^a

The emerging up-conversion nanoparticles (UCNPs) offer a wide range of biotechnology applications, from biomarkers and deep tissue imaging, to single molecule tracking and drug delivery. Their successful conjugation to biocompatible agents is crucial for specific molecules recognition and usually requires multiple steps which may lead to low reproducibility. Here, we report a simple and rapid one-step procedure for *in situ* synthesis of biocompatible amino-functionalized NaYF₄:Yb,Er UCNPs that could be used for NIR-driven fluorescence cell labeling. X-ray diffraction showed that UCNPs synthesized through chitosan-assisted solvothermal processing are monophasic and crystallize in a cubic α phase. Scanning and transmission electron microscopy revealed that the obtained crystals are spherical in shape with a mean diameter of 120 nm. Photoluminescence spectra indicated weaker green (²H_{11/2}, ⁴S_{3/2} → ⁴I_{15/2}) and stronger red emission (⁴F_{9/2} → ⁴I_{15/2}), as a result of enhanced non-radiative ⁴I_{11/2} → ⁴I_{13/2} Er³⁺ relaxation. The presence of chitosan groups at the surface of UCNPs was confirmed by Fourier transform infrared spectroscopy, thermogravimetry and X-ray photoelectron spectroscopy. This provides their enhanced internalization in cells, at low concentration of 10 μg ml⁻¹, without suppression of cell viability after 24 h of exposure. Furthermore, upon 980 nm laser irradiation, the amino-functionalized NaYF₄:Yb,Er UCNPs were successfully used *in vitro* for labeling of two human cell types, normal gingival and oral squamous cell carcinoma.

Received 16th May 2018
 Accepted 25th July 2018

DOI: 10.1039/c8ra04178d

rsc.li/rsc-advances

Introduction

Nanotechnology research in the last few decades has been driven by both technological and fundamental interests, in an effort to develop advanced multifunctional biomaterials for a broad range of applications. It has been shown already that functionalized inorganic nanoparticles could be used as therapeutic nanoplatfroms when grafting of drugs/antigens is successfully completed at their surface.^{1,2} Particularly, tailored coupling of optically active lanthanide doped inorganic fluorides and oxides, that have the ability to convert long-

wavelength near infrared (NIR) excitation into shorter-wavelength emission of visible light (up-conversion, UC), with a variety of biomolecules, generates hybrid nanoparticles which possess superior bioimaging and therapeutic characteristics.^{3,4} Compared with traditional fluorescent dyes, up-converting nanoparticles (UCNPs) offer several advantages, including excellent chemical and thermal stability, narrow-band emission, a large anti-Stokes shift and a long lifetime. The absence of photobleaching and blinking are other advantages that meet the requirements of background free detection in deeper tissues, as well as time-resolved imaging of morphological details from cells. Intrinsic optical properties of UCNPs originate from abundant energy states of lanthanide ions doped in a host matrix. The electron transitions between partially filled 4f orbitals which are effectively shielded by 5s and 5p are Laporte forbidden, so gaining of their intensity occurs through the mixing in higher electronic states of opposite parity, either by “vibronic coupling” or through the effect of a ligand field.⁵ To enhance probability of radiative transitions, at least two lanthanide ions (sensitizer and activator) are usually doped in host material with a strong crystal field and low phonon energy (like oxides and fluorides). The UC goes on through following mechanisms: excited state absorption (ESA), energy transfer

^aInstitute of Technical Sciences of the Serbian Academy of Sciences and Arts, Belgrade, Serbia. E-mail: lidija.mancic@itn.sanu.ac.rs

^bDepartment of Biochemical Engineering and Biotechnology, Faculty of Technology and Metallurgy, University of Belgrade, Serbia

^cInnovation Center of the Faculty of Chemistry, University of Belgrade, Serbia

^dPhotonic Center, Institute of Physics Belgrade, University of Belgrade, Zemun, Belgrade, Serbia

^eDepartment of Chemical and Materials Engineering, Pontifical Catholic University of Rio de Janeiro, Rio de Janeiro, Brazil

† Electronic supplementary information (ESI) available: Photostability, HRTEM/FFT and XPS analyses of the amino-functionalized UCNP. See DOI: 10.1039/c8ra04178d



(ET), photon avalanche (PA), cooperative energy transfer (CET) and energy migration-mediated up-conversion (EMU). For ET to occur, the excited energy levels of both ions must be resonant, and ions should be in close spatial proximity.⁶ For instance, $^2F_{5/2}$ level of ytterbium resonates well with energy levels of erbium, thulium and holmium, so it is used as a very efficient sensitizer for achieving efficient UC in NaYF_4 host. In $\text{Yb}^{3+}/\text{Er}^{3+}$ co-doped NaYF_4 nanoparticles, green (520 nm and 540 nm) and red (660 nm) emissions are most commonly observed under 980 nm excitation, while violet emission at 415 nm is usually weakened. The emission is dependent on dopants concentration and crystal arrangement of the NaYF_4 phase. In the structure of cubic α phase lanthanide and sodium ions occupy eight-coordinated cation site randomly, whilst in hexagonal β phase cation sites are of three types: a one-fold site occupied solely by lanthanides; a one-fold site occupied randomly by 1/2 lanthanides and 1/2 sodium; and a two-fold site occupied by sodium and vacancies stochastically.⁷ As a result, green and red emissions are both prominent in the spectra of cubic phase, whereas green dominates in spectra of hexagonal one.

The rapid progress in development of different protocols which give rise to the synthesis of monodisperse lanthanide doped NaYF_4 UCNPs through decomposition of organometallic precursors, proposed initially by Mai *et al.*,⁸ is replaced nowadays with studies devoted to *in situ* obtaining of biocompatible UCNPs.^{9,10} This is due to the fact that synthesis from toxic organometallic, performed in an oxygen-free environment, must be followed by SiO_2 encapsulation, ligands exchange/oxidation or by coating with a biocompatible polymer towards achieving a demanded chemical functionality for conjugation of the targeting molecular moiety. Although well established, the reproducibility of multiple steps involved in such synthesis is not trivial, since toxicity of UCNPs produced throughout is not easily predictable.¹¹ In order to obtain physiologically stable $\text{NaYF}_4:\text{Yb}^{3+}/\text{Er}^{3+}$ nanoparticles *in situ*, some biopolymers are already being used as surfactants during hydro/solvothermal synthesis. Wang *et al.*¹² were the first who reported a simple one-step approach for the synthesis of hydrophilic UCNPs which comprises polyethylenimine (PEI), polyacrylic acid (PAA), polyvinylpyrrolidone (PVP) and polyethylene glycol (PEG) usage during hydrothermal treatment. Many years later it was shown that such functionalized particles could be easily conjugated to folic acid, a commonly used cancer targeting agent, and then loaded with doxorubicin hydrochloride to achieve pH-responsive release at target cells.¹³ Furthermore, PEGylated nanoparticles of $\alpha\text{-NaYF}_4:\text{Yb,Er}$, prepared under the cooperative influence of two ligands, demonstrated low cytotoxicity and excellent distribution in small animals.¹⁴ Under the guidance of the same concept we have shown that PEG, PVP and EDTA capped $\text{NaYF}_4:\text{Yb,Er}$ nano- and micro-particles could be easily obtained in a controlled manner through tuning of hydro/solvothermal processing conditions.^{15,16}

In this study, amino-functionalized $\text{NaYF}_4:\text{Yb,Er}$ nanoparticles with a high degree of size uniformity and efficient up-conversion were prepared through solvothermal treating of rare earth nitrates in the presence of chitosan (CS). Chitosan is a linear polysaccharide composed of randomly distributed β -

linked D -glucosamine and N -acetyl- D -glucosamine. Inter-dispersed acetamido groups, as well as an abundance of external $-\text{NH}_2$ and $-\text{OH}$ functional groups offer excellent biocompatibility and bio-reactivity, making it to be one of the most valuable polymer for medical and pharmaceutical applications. It is widely used today in encapsulation and controlled delivery of drugs, wound dressing, construction of contact lenses and artificial skin substitutes.^{17,18} An immense array of depicted benefits was recently complemented with its prominent antitumor activity.¹⁹ Lately, several reports related to chitosan coupling to inorganic UCNPs were also reported. Thus, an effective coating of DMSA-modified $\text{NaYF}_4:\text{Yb/Er}$ UC with folic acid-chitosan conjugates was achieved through a robust approach which comprised covalent bonding of amine groups with carboxyl groups located at particle surface.²⁰ Besides, amphiphilic N -succinyl- N' -octyl chitosan modified UCNPs coupled with Zn(II) -phthalocyanine photosensitizer, in form of novel drug delivery system, ZnPc -loaded SOC-UCNPs, demonstrated promising potential for NIR triggered photodynamic therapy of human breast adenocarcinoma.²¹ More recent studies shown that quaternized chitosan hydrogels incorporated with $\text{NaYF}_4:\text{Er/Yb/Mn}$ @photosensitizer-doped silica could be used for effective killing of both Gram-positive and Gram-negative bacteria,²² whilst spherical chitosan- $\text{NaYF}_4:\text{Yb}^{3+}/\text{Tm}^{3+}$ composite beads have excellent drug loading capacity and release performance upon near-infrared (NIR) laser irradiation.²³ Although presented results provide evidence of the significant therapeutic effects, all of aforementioned hybrid UCNPs were actually obtained through multiple steps. It is worth noting that there is only one report, as far as the authors are aware of, on the usages of O -carboxymethyl chitosan during solvothermal preparation of $\text{NaYF}_4:\text{Yb}^{3+}/\text{Tm}^{3+}/\text{Er}^{3+}$ nanoparticles (UCNPs@OCMC), but successful staining of the HeLa cancer cells was achieved only after additional bio-conjugation of synthesized UCNPs@OCMC with folic acid.²⁴

Hence, the main goal of the present study is *in situ* synthesis of chitosan functionalized $\text{NaYF}_4:\text{Yb,Er}$ nanoparticles capable of transforming continual NIR radiation into visible light and their successful utilization in visualization of the oral squamous cell carcinoma (OSCC). OSCC is the most common malignant tumor of the head and neck. Its incidence has increased in the recent years, thus development of a new contrast-enhanced agent useful for its detection at an early stage is essential. The potential cytotoxicity of the as-obtained UCNPs synthesized in this study was additionally tested against human gingival cells (HGC) isolated from healthy gingival tissue.

Materials and methods

Reagents and materials

Chitosan (low molecular weight, 50 000–190 000 Da), sodium fluoride (NaF, 99.99%), yttrium(III) nitrate hexahydrate ($\text{Y}(\text{NO}_3)_3 \cdot 6\text{H}_2\text{O}$, 99.9%), ytterbium(III) nitrate pentahydrate ($\text{Yb}(\text{NO}_3)_3 \cdot 5\text{H}_2\text{O}$, 99.9%), erbium(III) nitrate pentahydrate ($\text{Er}(\text{NO}_3)_3 \cdot 5\text{H}_2\text{O}$, 99.9%), anhydrous ethylene glycol ($\text{C}_2\text{H}_6\text{O}_2$, 99.8%), phosphate-buffered saline (PBS), fetal bovine serum (FBS), dimethyl sulfoxide (DMSO), Dulbecco's Modified Eagle



Medium (DMEM), penicillin–streptomycin (100 U ml⁻¹), 3-(4,5-dimethylthiazol-2-yl)-2,5 diphenyltetrazolium bromide (MTT, 0.5 mg ml⁻¹), paraformaldehyde (PFA) and Mowiol were all purchased from Sigma-Aldrich, St. Louis, USA. TrypLE Express enzyme, Gibco™ Dulbecco's modified Eagle's F12 medium (D-MEM/F12) and antibiotic/antimycotic solution (ABAM, 1%) were bought from Thermo Fisher Scientific. Deionized water was used throughout the experiments.

Synthesis of amino modified NaYF₄:Yb,Er

Monodispersed NaY_{0.8}Yb_{0.17}Er_{0.03}F₄ nanoparticles were synthesized using facile one-pot solvothermal synthesis. Stoichiometrically defined amounts of rare earth nitrates (5 mmol in total) were dissolved initially in 10 ml of water and then added to a chitosan solution (0.1 g CS in 15 ml of water). Obtained clear solution was then gradually dropped into NaF solution (1.75-fold excess, 10 ml) and mixed further with 35 ml of ethylene glycol (EG). Stirring of the mixture is performed until homogeneous transparent solution was obtained at pH = 4, then transferred into a 100 ml Teflon-lined stainless steel autoclave and sealed. Solvothermal treating was carried out at temperature of 200 °C (2 h) with a slow continual stirring (~100 rpm). Afterwards, the autoclave was cooled to room temperature, the precipitate was centrifuged at 8000 rpm and then washed with ethanol three times. The as-obtained white powder was dried at 60 °C for 2 h.

Characterization of amino-functionalized NaYF₄:Yb,Er

Structural and morphological characteristics of amino-functionalized NaYF₄:Yb,Er powder were obtained through the X-ray powder diffraction (XRPD), scanning and transmission electron microscopy (JEOL JSM-6701F SEM and JEOL JEM 2010 TEM), Fourier transform infrared spectroscopy (FTIR, Thermo Scientific Nicolet 6700 with a Smart iTR Diamond Attenuated Total Reflectance accessory) and thermogravimetric analysis (Perkin-Elmer Simultaneous Thermal Analyzer, STA 6000). The XRPD pattern was recorded using Bruker D8 Discovery equipped with a Cu-K α source ($\lambda = 1.5406 \text{ \AA}$) with a step scan of 0.02° and accounting time of 5 s per step. Structure refinement was done in Topas 4.2 software²⁵ using a fundamental parameter approach. The background was refined using a fifth-order Chebyshev polynomial. Refinement of the cubic phase was carried out in *Fm-3m* (no. 225) space group, starting from ICSD 60257 data. Isotropic size-strain analysis was performed using a predefined double-Voigt approach (volume weighted mean column height, FWHM based LVol). Due to the observed preferential orientation, the spherical harmonic formulation, also referred as “orientation distribution function”, is included in fitting of diffraction lines intensities. The size, shape and chemical purity of the nanoparticles were determined by SEM coupled with energy dispersive spectroscopy (EDS). The SemAfore 5.21 JEOL software was used to construct histogram of particle size from backscatter SEM images presenting more than 300 particles. Dynamic light scattering measurements of hydrodynamic radius (R_H) were performed on a Malvern Zetasizer Nano ZS in the de-ionized water and medium used for

testing of the cell viability and imaging. For that purpose UCNPs were dispersed at the concentration of 1 mg ml⁻¹ and passed through a 0.45 μm cellulose syringe filter before DLS measurements. For TEM analysis nanoparticles were sonicated 20 min in isopropyl alcohol and dropped directly on lacey carbon film supported on a Cu grid. Confirmation of the crystal structure was carried out using selected area electron diffraction (SAED) and Fourier processing in Digital Micrograph 3.7.4 (Gatan Inc.) software. Presence of the chitosan ligands on the nanoparticles surface was investigated by FTIR, TG and XPS analyses. FTIR spectrum was recorded using typically 128 scans at the resolution of 4 cm⁻¹. TGA was conducted in nitrogen flux (100 ml min⁻¹) in the temperature range between 30 and 730 °C, applying a heating rate of 5 °C min⁻¹. XPS was carried out using an Alpha 100 hemispherical analyser from VG thermo and the K α line from Mg (1486.6 eV) radiation. Photoluminescence spectrum was recorded at room temperature using Spex Fluorolog with C31034 cooled photomultiplier under diode laser excitation at 980 nm, and based on it CIE chromaticity coordinates were calculated.

OSCC and HGC cultures

Healthy gingival and tumor tissues were obtained from the patients at the Clinic of Maxillofacial Surgery of School of Dental Medicine, University of Belgrade immediately after surgical procedure. Signed informed consent approval from each patient was assured prior to participation in this study. Experiments were authorized by the Ethical Committee of the School of Dental Medicine, University of Belgrade (resolution 36/31).

Tumor cell lines were derived from tumor tissue taken from localized squamous cell carcinoma of the oral tongue. Preparation of the cell culture was performed using slightly modified procedure of Pozzi *et al.*²⁶ Briefly, DMEM supplemented with 20% fetal bovine serum (FBS) and 100 U ml⁻¹ penicillin–streptomycin was used for tissue transport. The cells isolated from minced tissue were seeded onto T25 cell culture flasks and grown in DMEM supplemented with 10% FBS and 100 U ml⁻¹ penicillin–streptomycin. Incubation was performed at 37 °C in a humidified atmosphere of 5% CO₂. The medium was changed thrice weekly and cells were passaged prior to reaching 80% confluence. To avoid fibroblast contamination, brief exposure to TrypLE Express (Thermo Fisher Scientific, Waltham, USA) was performed. OSCC used in this study were obtained after the third passage.

Human gingival tissues were obtained from three different, healthy patients, aged 19–25 years, during extraction of the impacted third molar. The gingival tissue was transported in Gibco™ D-MEM/F12 supplemented with 20% FBS and 1% ABAM solution. The gingival tissue was rinsed in PBS and subjected to outgrowth isolation method. Tissue was minced into approximately 1 mm² fragments, and placed in 25 cm² culture flasks with DMEM/F12 supplemented with 10% FBS and 1% ABAM. Incubation was performed at 37 °C in a humidified atmosphere of 5% CO₂. The cells were allowed to reach 80% confluence prior to passage. The medium was changed every 2–3 days. HGC used in this study were obtained after the second passage.



Cytotoxicity assay

MTT assays were carried out to evaluate the potential cytotoxicity of amino-functionalized NaYF₄:Yb,Er in both, HGC and OSCC. Cells were seeded into a 96-well cell culture plate at 10⁴ per well and incubated at 37 °C in humidified 5% CO₂ atmosphere. Then, aseptically weighted UCNPs in concentrations of 10, 25 and 50 μg ml⁻¹ were dispersed in sterile water by sonication (3 min). After 24 h hours of cells incubation 100 μl of UCNPs were added in each plate. Incubation of UCNPs with the cell cultures was stopped after 24 h by discarding of spent media, and medium containing MTT (0.5 mg ml⁻¹) was added to each well. After additional incubation for 4 h, supernatant was discarded and the precipitated formazan crystals were dissolved by DMSO (100 μl) under shaking at 37 °C for 20 min. Optical density was measured at 540 nm using ELISA microplate reader (enzyme-linked immunosorbent assay) RT-2100c, Rayto, China. Three wells without UCNPs were used as a control group. All experiments were performed in triplicate and repeated three times in the independent experiments. Cell viability, expressed by the ratio of absorbance of the cells incubated with UCNPs to that of the cells incubated with culture medium only, was given in diagram as the mean ± standard deviation (SD).

Cell imaging by laser scanning microscopy

For the visualization of UCNPs uptake by cells 10 μg ml⁻¹ of sterile UCNPs suspension was filtered through 0.45 μm syringe filter to separate agglomerates that could provoke saturation during imaging. Sterilized 22 × 22 mm glass coverslips were placed in 6-well plates and 10⁴ of cells were seeded per coverslip. Incubation was performed at 37 °C in humidified 5% CO₂ atmosphere. The next day cells were exposed to UCNPs and incubated for another 24 h. Coverslips with adherent cells were gently rinsed with fresh PBS twice and fixed with 4% PFA for 20 min. PFA residue was then washed by PBS (3 × 3 min), coverslips were dried, 10 μl of Mowiol was placed on fixed cells, and coverslips were placed on microscopic slides with cells positioned in between. Samples were stored in a dark until they were observed under laser scanning microscopy.

The homemade nonlinear laser scanning microscope used in this study was described in detail elsewhere.²⁷ The Ti:Sapphire laser (Coherent, Mira 900-F) was used as a laser light source operating either in femto-second (FS) pulse mode or continuous wave (CW) mode. FS mode at 730 nm was used for unlabeled cell imaging since it enables two photon excitation of cells auto-fluorescence. Please note that two-photon excitation is considered here as excitation of the molecule with no intermediate levels between ground and excited state and it is not related to UC process. From the other hand, 730 nm light do not interact with UCNPs. The CW radiation at 980 nm was used for the excitation of UCNPs in cells. Analogously to the previous case, CW 980 nm light cannot excite any other molecule except UCNPs. Due to the long UCNPs lifetime, the acquisition time at a single point has to be reduced during scanning in order to extend pixel dwell time. Hence, the pixel dwell time was several times longer than fluorescence lifetime. The laser focusing and

collection of the fluorescence during cell imaging were done using 40 × 1.3 oil immersion objective (Carl Zeiss, EC Plan-NEOFLUAR). A visible interference filter (415–685 nm) positioned in front of detector was used to remove scattered laser light. Thus, the whole visible range has been detected either for auto-fluorescence from cells or for up-conversion from amino-functionalized NaYF₄:Yb,Er UCNPs in cells.

Results and discussion

The morphology and size of amino-functionalized NaYF₄:Yb,Er UCNPs was evaluated by scanning electron microscopy (Fig. 1a). The SEM image showed that the as-obtained nanoparticles were spherical in shape, monodispersed and without obvious aggregation. Particle size varied between 50 and 200 nm and the bulk of the particles (>65%) are with diameter of 120 nm. The purity and expected chemical composition of the as-obtained NaYF₄:Yb,Er phase were confirmed by an energy dispersive spectrometer coupled to TEM, Fig. 1b. Based on the elemental analysis (inset at Fig. 1b), it is evident the presence of all constituting elements: sodium (K α at 1.041), yttrium (L α at 1.92 keV), ytterbium (L α at 7.414 and M α at 1.521 keV), erbium (L α at 6.947 and M α at 1.404 keV) and fluorine (K α at 0.677). TEM/SAED analyses, Fig. 1c, showed a mixture of distinct spots and rings in the SAED pattern which correspond to *d* values of 3.119, 2.705, 1.923 and 1.104 Å and match fine with (111), (200), (220) and (423) crystal planes of the cubic α NaYF₄ phase (JCPDS 77-2042). Coexistence of much smaller crystallites of α phase at the UCNPs surface is evident from Fig. 1c and HRTEM/FFT images, Fig. S1.†

The XRPD pattern of the as-obtained sample was indexed to cubic α structure of NaYF₄:Yb,Er phase (JCPDS no. 77-2042, *a* = 5.47 Å, *V* = 163.67 Å³), Fig. 1d. However, structural refinement confirmed the coexistence of two different particle populations (two NaYF₄:Yb,Er phases were used to adjust experimental pattern), both adopting the same *Fm-3m* space group with a similar unit cell parameters (Å): *a*₁ = 5.51830(9) and *a*₂ = 5.53074(1), and a quite different crystallite size (nm): 84(4) and 12(1), respectively. Calculated crystallites sizes were in agreement with the size observed during TEM analysis. Small change of the refined unit cell volume (168.04 Å³) might be due to the Yb³⁺ and Er³⁺ incorporation at Y³⁺ site. Occupation of 0.41(1) for Y³⁺ site, correlates well with the nominal NaY_{0.8}Yb_{0.17}Er_{0.3}F₄ composition (the value of 0.5 corresponds to the full occupation of the general site occupied by rare earths in the cubic NaYF₄ phase), whilst *R*_{Bragg} value of 5.7 confirmed good agreement between observed and computed patterns. The relevant information about Y³⁺ sites occupancy with rare earth ions in the phase with the smaller crystallite size were not acquired, due to the fact that better refinement was achieved when fixed values of occupation factor were used.

Hydrodynamic radius (*R*_H), polydispersity index (PDI) and stability of amino-functionalized NaYF₄:Yb,Er UCNPs colloids over time were estimated from dynamic light scattering measurements, Fig. 2. As one could see, the coexistence of different particle populations (one sized up to 30 nm and another bigger than 100 nm), indicated by TEM an XRPD



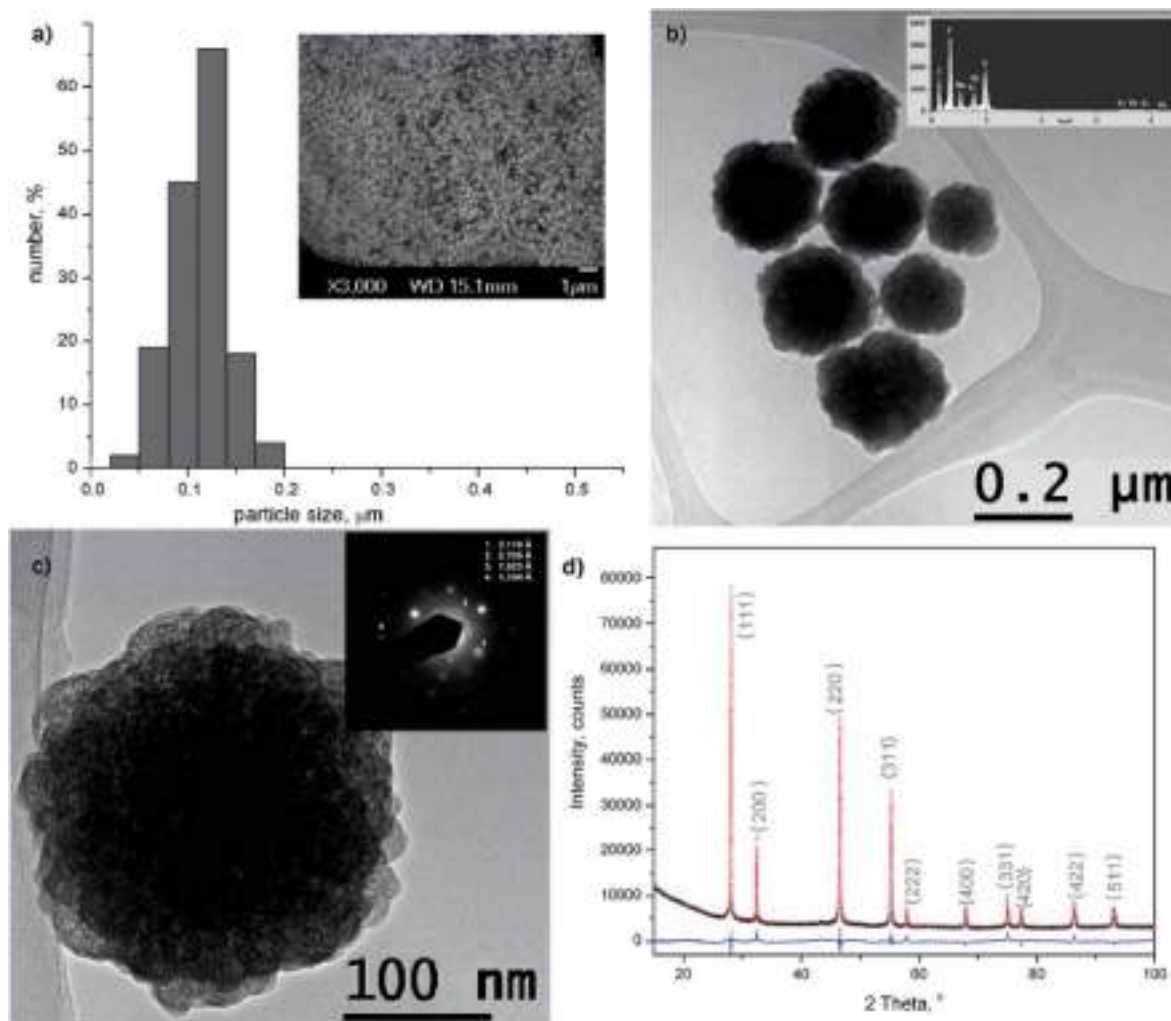


Fig. 1 Particle size distribution histogram (a) and TEM images (b and c) of amino-functionalized NaYF₄:Yb,Er UCNPs. Corresponding SEM, EDS, SAED and FFT were given as insets in (a), (b) and (c), respectively; XRPD pattern of amino-functionalized NaYF₄:Yb,Er (black), refined structure (red) and difference curve (blue) is presented in (d). Miller indices are indicated in {} by gray marks.

analysis is well preserved in medium solution over time confirming the long-term stability of this colloid (Fig. 2a). Since DLS measures actual particle size plus thickness of the strongly

bounded solvent shell around particles, obtained average values are different (60 nm with PDI 1 in medium, and 311 nm with PDI 0.34 de-ionized water, respectively) than determined ones

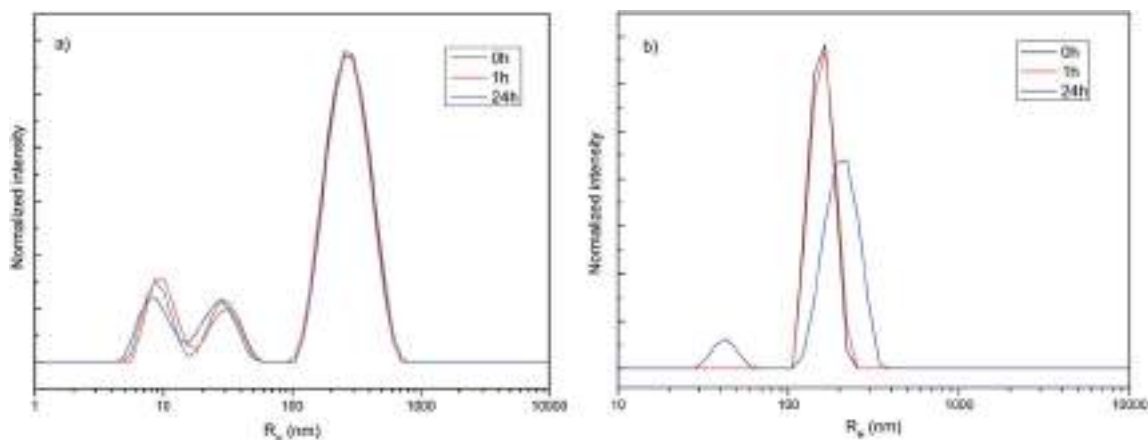


Fig. 2 Hydrodynamic radius distribution over time of amino-functionalized NaYF₄:Yb,Er UCNPs (1 mg ml⁻¹) in medium used for testing of cell viability and imaging (a) and deionized water (b).



from TEM images (120 nm). While average R_H and PDI of amino-functionalized $\text{NaYF}_4:\text{Yb,Er}$ UCNPs in medium stay unchanged with time, slight increase of both parameters were detected after one hour (380 nm and PDI 0.4) in water (Fig. 2b). Decrease of R_H to 211 nm (PDI 0.34) after 24 h is observed and is due to appearance of a significant fraction of clusters (~ 50 nm) composed from nanoparticles sized up to 20 nm.

The successful *in situ* modification of the UCNPs surface with chitosan ligands was confirmed by FTIR spectroscopy (Fig. 3a). In accordance to the literature^{28–30} observed bands in spectrum of pure chitosan were classified as follows: broad band in the range from 3500 to 3000 cm^{-1} is due to stretching vibration of OH groups, which partially overlaps stretching vibration of amine N–H; band at 2870.1 cm^{-1} is due stretching of C–H bond in $-\text{CH}_3$; band at 1651.7 cm^{-1} corresponds to vibrations of carbonyl bonds of the amide group CONHR (C=O stretching, secondary amide); band at 1587.1 cm^{-1} is due to protonated amine stretching; bands at 1417.9 cm^{-1} and 1374.1 cm^{-1} are due CH_3 and CH_2 bending vibrations; band at 1318.6 cm^{-1} is associated to the amide III (C–N stretching) and CH_2 wagging; band at 1149.8 cm^{-1} reflects asymmetric vibration of C–O group, whilst band at 1060.156 cm^{-1} is assigned to CO bending vibration of pyranose ring. The small band at 890 cm^{-1} corresponds to wagging of the saccharide structure of chitosan. The FTIR spectrum of the as-synthesized UCNPs showed a decrease in adsorption and slight shifting of chitosan related bands at: 3399.9 cm^{-1} (O–H and amine N^{3+} –H group stretching), 1651.7 cm^{-1} (C=O stretching), 1557 cm^{-1} (protonated amine stretching), 1373.5 cm^{-1} (CH_2 bending) and 1080.4 cm^{-1} (CO bending) implying their existence on the UCNPs surface. This confirmed that chitosan-assisted solvothermal synthesis of $\text{NaYF}_4:\text{Yb,Er}$ was an effective way for *in situ* obtaining of biocompatible UCNPs.

The TGA also show chitosan presence at the UCNPs surface, Fig. 3b. TGA curve shows total weight loss of 9.5% in the temperature region from 30–730 $^\circ\text{C}$. The initial weight loss of 2% (< 200 $^\circ\text{C}$) is ascribed to the dehydration of adsorbed moisture and possible ethanol impurity, whilst the more intense loss of 7.5% at higher temperatures is, predominantly, due to the

vaporization of the chitosan groups present on the UCNPs surface. In accordance to literature, the thermal degradation of chitosan in nitrogen is an one-step reaction which starts at 326.8 $^\circ\text{C}$.³¹ Meanwhile, a total mass loss of ca. 2–4% has been reported for bare $\text{NaYF}_4:\text{Yb,R}$ (R: Pr, Nd, Sm, Eu, Tb, Dy or Er) UCNPs owing to the removal of water, ethanol and slow evaporation of NaF in the same temperature range.^{32,33}

XPS analysis was also used to verify surface chemical composition of the amino-functionalized $\text{NaYF}_4:\text{Yb,Er}$ UCNPs. All of the lanthanide elements, as well as, Na, F, C, N and O are detected in XPS spectrum, Fig.S2.† The peak at 1073.5 eV is assigned to the binding energy of Na 1s; peaks at 160.96, 174.29 and 185.72 eV were assigned to the binding energies of Y 3d, Er 4d and Yb 4d respectively; and peak at 685.71 eV is related to F 1s.^{34,35} Peaks of C 1s, O 1s and N 1s were further decomposed in the fine-scan mode to confirm the bonding of chitosan at the $\text{NaYF}_4:\text{Yb,Er}$ UCNPs surface. The C 1s peak showed three components: at 284.8 eV, typical of carbon bonding to carbon and hydrogen [C–(C,N)]; at 282.92 eV due carbon bonding to oxygen or nitrogen [C–(O,N)]; and at 286.59 eV typical for acetal or amide group [O–C–O, N–C=O]. The O 1s contributions at 532.70 and 531.4 eV were due to oxygen of the polysaccharide backbone and amide respectively.³⁶ The first two N 1s contributions at 399.71 and 397.9 eV confirm coexistence of the non-protonated and protonated amine groups, implying that approximately half of chitosan terminal amine groups are covalently bounded at UCNPs surface.

The up-conversion luminescence spectra of the amino-functionalized $\text{NaYF}_4:\text{Yb,Er}$ UCNPs is given at Fig. 4a. It can be split into two emission segments, a green region of 520–550 nm and a red region of 630–690 nm, attributed to $^4\text{S}_{3/2} \rightarrow ^4\text{I}_{15/2}$ and $^4\text{F}_{9/2} \rightarrow ^4\text{I}_{15/2}$ transitions of Er^{3+} ions, respectively. According to energy transfer and relaxation pathways depicted at the energy level diagram of the Er^{3+} – Yb^{3+} couple (Fig. 4b), both were determined by the non-radiative decay from $^4\text{F}_{7/2}$ excited state.

Upon the 980 nm excitation, Yb^{3+} absorbs energy and promotes $^2\text{F}_{7/2} \rightarrow ^2\text{F}_{5/2}$ transitions. Afterward, it resonantly transfers the energy to the $^4\text{I}_{11/2}$ state of the neighbouring Er^{3+} ion. The $^4\text{I}_{11/2}$

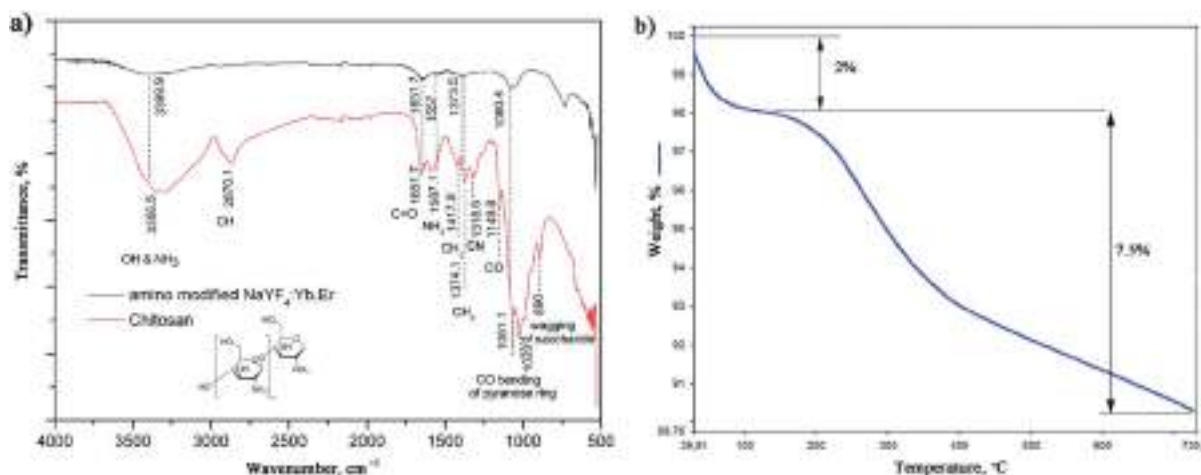


Fig. 3 FTIR of chitosan and amino-functionalized $\text{NaYF}_4:\text{Yb,Er}$ (a) TGA of amino-functionalized $\text{NaYF}_4:\text{Yb,Er}$ UCNPs (b).



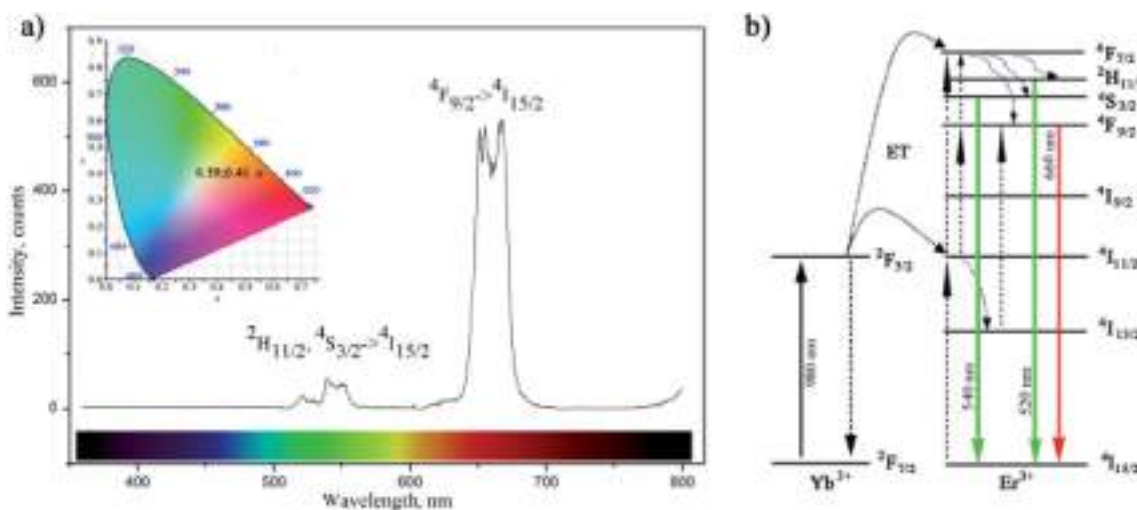


Fig. 4 Up-conversion luminescence of amino-functionalized NaYF₄:Yb,Er UCNPs upon excitation at 980 nm with corresponding CIE diagram given as inset (a) and energy level diagram of the Er³⁺–Yb³⁺ couple (b).

level of Er³⁺ ion can be also populated by direct excitation of Er³⁺ ion from its ⁴I_{15/2} ground state. Thus, the higher excited states of Er³⁺, ⁴F_{7/2} and ⁴F_{9/2}, will be further populated either through energy transfer from another excited Er³⁺ ion which is in close proximity, or through a two-step energy transfer from Yb³⁺ to the neighbouring Er³⁺ ions. The populated ⁴F_{7/2} level of Er³⁺ then relaxes non-radiatively to the ²H_{11/2} and ⁴S_{3/2} levels, and further radiatively to the ground ⁴I_{15/2} state generating green emissions at 520 nm (²H_{11/2} → ⁴I_{15/2}) and 540 nm (⁴S_{3/2} → ⁴I_{15/2}). Meanwhile, red emission appears due to the ⁴F_{9/2} → ⁴I_{15/2} de-excitation, which could be additionally intensified by the non-radiative ⁴F_{7/2} → ⁴F_{9/2} relaxation. Therefore, green and red emissions were obtained simultaneously through two-photon UC processes. Furthermore, due to the enhanced non-radiative relaxation of ⁴I_{11/2} → ⁴I_{13/2} in nanocrystals^{16,31} which proceeds to the direct population of ⁴F_{9/2} level emission of red/orange light (defined by CIE 0.59, 0.41) was observed by bare eyes at room temperature. Photostability of amino-functionalized up-converting NaYF₄:Yb,Er nanoparticles emission was also traced during 1 h, Fig. S3.† As one could see at Fig. S3,† exceptionally stable UC luminescence signal was recorded.

The viability of OSCC and HGC following 24 h incubation with the amino-functionalized NaYF₄:Yb,Er UCNPs, expressed in terms of percentages evaluated through comparison to the number of surviving cells in the control group, was determined by MTT assay (Fig. 5). One could see that viability of HGC was highly preserved after 24 h exposure, being above 90% for all examined concentrations of UCNPs. However, viability of OSCC was found variable with the increase of UCNPs concentrations. Only in the case of the lowest concentration non-significant cytotoxicity (*i.e.* viability of 98%) was detected, whilst at higher UCNPs concentrations noteworthy cytotoxicity was observed, as reflected in a concentration dependent decrease in the percentage of viable cells up to the value of 66% for 50 μg ml⁻¹. Previous study reported low cytotoxicity of the ZnPe-loaded SOC-UCNPs toward the adenocarcinoma cells for concentrations up to 200 μg ml⁻¹.²¹ Also, insignificant

difference in HeLa carcinoma cell viability (~85%) has been observed when the concentrations of UCNPs@OCMC went up to 200 μg ml⁻¹.²⁴ When compared with latter two, the results obtained in this study are unanticipated and indicate certain theranostic effect of amino-functionalized NaYF₄:Yb,Er UCNPs toward OSCC at much lower doses.

To monitor the intracellular uptake and non-specific cell labelling *in vitro*, 10 μg ml⁻¹ of amino-functionalized NaYF₄:Yb,Er UCNPs were incubated with OSCC and HGC and after 24 h laser scanning microscopy was performed. Images of the OSCC are shown at Fig. 6, top row. Fig. 6a shows bright field image of the cell, a pseudo color image of the cell auto-fluorescence upon femto-second excitation at 730 nm is shown at Fig. 6b, whilst the pseudo color image of the amino-functionalized NaYF₄:Yb,Er UCNPs upon CW excitation at 980 nm is given in Fig. 6c.

Overlapping the last two images (Fig. 6d), revealed that the UCNPs (green fluorescence spots) are positioned inside the cell, mainly in the cytoplasmic area adjacent to the plasma membrane. Images of the HGCs are shown in bottom row of

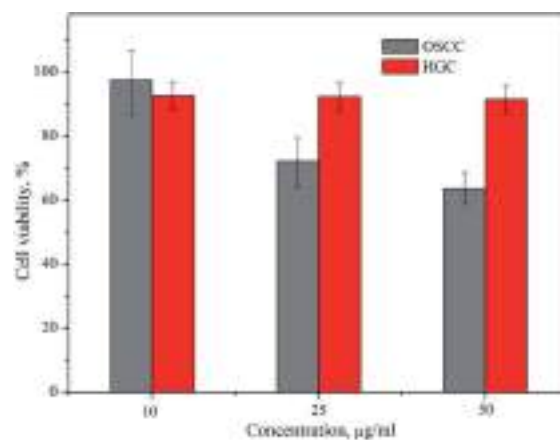


Fig. 5 Cytotoxicity assays of the amino-functionalized NaYF₄:Yb,Er UCNP in OSCC and HGC after 24 h exposure.



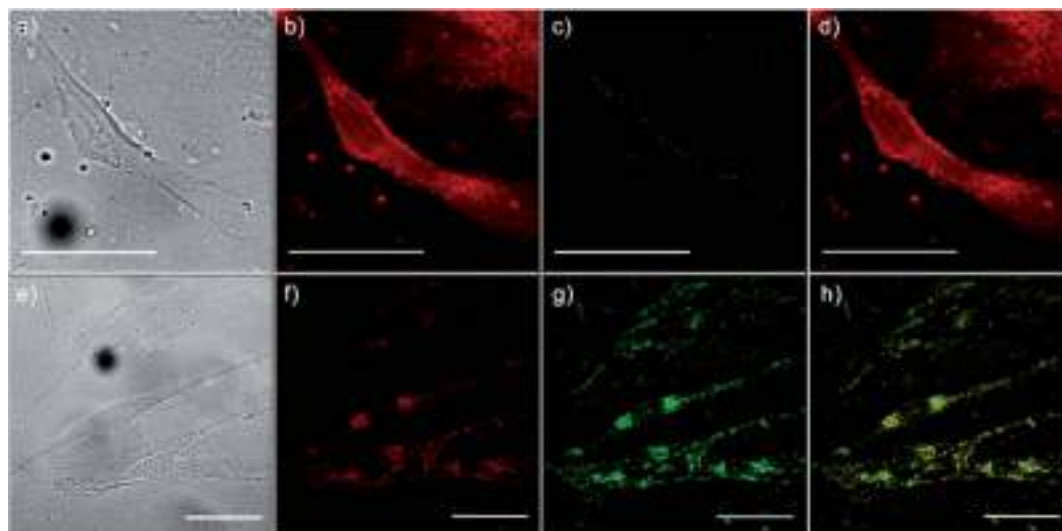


Fig. 6 Laser scanning microscopy images of OSCC (top row) and HGC (bottom row) following 24 h incubation with $10 \mu\text{g ml}^{-1}$ of amino-functionalized $\text{NaYF}_4:\text{Yb,Er}$ UCNP; bright field image of cells (a and e), cells auto-fluorescence upon femto-second excitation at 730 nm (b and f), image of the amino-functionalized $\text{NaYF}_4:\text{Yb,Er}$ UCNP upon CW excitation at 980 nm (c and g), and their positioning in cells, revealed through co-localization of the cell auto-fluorescence and the UCNP emission (d and h); the scale bars correspond to 50 μm .

Fig. 6 following the same scanning procedure. As in a previous case, successful internalization of UCNP in the cytoplasmic region of cells was achieved without disturbing cell nuclei. Since no auto-fluorescence was observed from cells upon NIR excitation (Figs. 6c and g), successful cells visualization with UCNP demonstrated the possibility of utilizing the amino-functionalized $\text{NaYF}_4:\text{Yb,Er}$ nanoparticles for nonspecific cell labelling. Furthermore, abundance of the chitosan ligands present at their surface (particularly amino groups), make them accessible for further conjugation with anti-cancer drugs, monoclonal antibodies or photosensitizers towards developing of specific theranostic agents.³⁷ As it is pointed out before, in prior studies which involved UCNP surface modification with chitosan, multistep procedures were used to achieve the benefits of both, biocompatibility and near-infrared triggered up-conversion in cells. We believe that facile approach presented in this study may be extended to the synthesis of UCNP with other biocompatible ligands too, raising at that way their potential use in biomedicine.

Conclusions

Monodisperse, hydrophilic and biocompatible $\text{NaYF}_4:\text{Yb,Er}$ UCNP were synthesized *in situ* using chitosan-assisted solvothermal synthesis. Spherical particles sized around 120 nm contain a single crystal structure of a cubic α phase ($Fm-3m$) and emit intense orange light (CIE 0.59, 0.41) upon 980 nm laser excitation. Due to the presence of amino functional groups at their surface, $\text{NaYF}_4:\text{Yb,Er}$ UCNP presented suitable properties for application in non-specific *in vitro* cell labelling. The superior biocompatibility detected toward normal human gingival cells with regard to oral squamous cell carcinoma, under similar cellular internalization, indicates their great potential in diagnostic and cancer therapy, particularly in a deeper tissue up to the penetration depth of NIR light.

Conflicts of interest

There are no conflicts of interest to declare.

Acknowledgements

This work was financially supported by the Ministry of Education, Science and Technological Development of Serbia project OI 172035 and III 45016. B. A. M. is grateful to CNPq (National Council for Scientific and Technological Development) for a Research Productivity Grant.

References

- Z. Yaari, D. da Silva, A. Zinger, E. Goldman, A. Kajal, R. Tshuva, E. Barak, N. Dahan, D. Hershkovitz, M. Goldfeder, J. Shainsky Roitman and A. Schroeder, *Nat. Commun.*, 2016, 7, 13325.
- Y. Chen, H. Zhang, X. Cai, J. Ji, S. He and G. Zhai, *RSC Adv.*, 2016, 6, 92073–92091.
- F. Zhang, *Photon Upconversion Nanomaterials*, Springer-Verlag Berlin Heidelberg, 2015.
- D. Li, W.-Y. Lai, Q. Shao and W. Huang, *RSC Adv.*, 2017, 7, 11491–11495.
- S. Cotton, *Lanthanide and Actinide Chemistry*, John Wiley & Sons, Inc., 2006.
- D. J. Naczynski, M. C. Tan, R. E. Riman and P. V. Moghe, *J. Mater. Chem. B*, 2014, 2, 2958–2973.
- H. Dong, L.-D. Sun and C.-H. Yan, *Chem. Soc. Rev.*, 2015, 44, 1608–1634.
- H.-X. Mai, Y.-W. Zhang, R. Si, Z.-G. Yan, L.-d. Sun, L.-P. You and C.-H. Yan, *J. Am. Chem. Soc.*, 2006, 128, 6426–6436.
- L. Grana-Suarez, W. Verboom, S. Sarkar, V. Mahalingam and J. Huskens, *ChemistrySelect*, 2016, 1, 4068–4074.



- 10 Z. Zhang, X. Ma, Z. Geng, K. Wang and Z. Wang, *RSC Adv.*, 2015, **5**, 33999–34007.
- 11 A. Gautam and F. C. J. M. van Veggel, *J. Mater. Chem. B*, 2013, **1**, 5186–5200.
- 12 M. Wang, C.-C. Mi, J.-L. Liu, X.-L. Wu, Y.-X. Zhang, W. Hou, F. Li and S.-K. Xu, *J. Alloys Compd.*, 2009, **485**, L24–L27.
- 13 X. Liang, J. Fan, Y. Wang, Y. Zhao, R. Jin, T. Sun, M. Cheng and X. Wang, *J. Rare Earths*, 2017, **35**, 419–429.
- 14 T. Cao, Y. Yang, Y. Sun, Y. Wu, Y. Gao, W. Feng and F. Li, *Biomaterials*, 2013, **34**, 7127–7134.
- 15 I. Dinic, M. E. Rabanal, K. Yamamoto, Z. Tan, S. Ohara, L. T. Mancic and O. B. Milosevic, *Adv. Powder Technol.*, 2016, **27**, 845–853.
- 16 I. Dinic, S. Ohara, T. Koji, M. E. Rabanal, A. M. Costa, B. A. Marinkovic, L. Mancic and O. Milosevic, *Adv. Powder Technol.*, 2017, **28**, 73–82.
- 17 M. N. V. R. Kumar, *React. Funct. Polym.*, 2000, **46**, 1–27.
- 18 F. Croisier and C. Jérôme, *Eur. Polym. J.*, 2013, **49**, 780–792.
- 19 L. Gibot, S. Chabaud, S. Bouhout, S. Bolduc, F. A. Auger and V. J. Moulin, *Int. J. Biol. Macromol.*, 2015, **72**, 370–379.
- 20 Q. Chen, X. Wang, F. Chen, Q. Zhang, B. Dong, H. Yang, G. Liu and Y. Zhu, *J. Mater. Chem.*, 2011, **21**, 7661–7667.
- 21 S. Cui, H. Chen, H. Zhu, J. Tian, X. Chi, Z. Qian, S. Achilefu and Y. Gu, *J. Mater. Chem.*, 2012, **22**, 4861–4873.
- 22 M. Yin, Z. Li, L. Zhou, K. Dong, J. Ren and X. Qu, *Nanotechnology*, 2016, **27**, 125601.
- 23 H. Yan, X. Chen, J. Shi, Z. Shi, W. Sun, Q. Lin, X. Wang and Z. Dai, *Mater. Sci. Eng., C*, 2017, **71**, 51–59.
- 24 L. Hao and L. Y. Wang, *Chin. Sci. Bull.*, 2013, **58**, 4051–4056.
- 25 TOPAS, *General Profile and Structure Analysis Software for Powder Diffraction Data, V4.2*, Bruker AXS GmbH, Karlsruhe, Germany.
- 26 V. Pozzi, D. Sartini, R. Rocchetti, A. Santarelli, C. Rubini, S. Morganti, R. Giuliante, S. Calabrese, G. Di Ruscio, F. Orlando, M. Provinciali, F. Saccucci, L. Lo Muzio and M. Emanuelli, *Cell. Physiol. Biochem.*, 2015, **36**, 784–798.
- 27 K. Bukara, S. Jovanic, I. T. Drvenica, A. Stancic, V. Ilic, M. D. Rabasovic, D. Pantelic, B. Jelenkovic, B. Bugarski and A. J. Krmpot, *J. Biomed. Opt.*, 2017, **22**, 026003.
- 28 I. A. Latif, H. M. Abdullah and M. Hameed Saleem, *Am. J. Polym. Sci.*, 2016, **6**, 50–57.
- 29 S. M. L. Silva, C. R. C. Braga, M. V. L. Fook, C. M. O. Raposo, L. H. Carvalho and E. L. Canedo, in *Infrared spectroscopy – Material Science, Engineering and Technology*, ed. T. Theophile, InTechOpen, 2012, pp. 44–61.
- 30 Y. Yang, J. Cui, M. Zheng, C. Hu, S. Tan, Y. Xiao, Q. Yang and Y. Liu, *Chem. Commun.*, 2012, **48**, 380–382.
- 31 P.-Z. Hong, S.-D. Li, C.-Y. Ou, C.-P. Li, L. Yang and C.-H. Zhang, *Appl. Polym. Sci.*, 2007, **105**, 547–551.
- 32 T. Laihininen, M. Lastusaari, L. Pihlgren, L. C. V. Rodrigues and J. Hölsä, *J. Therm. Anal. Calorim.*, 2015, **121**, 37–43.
- 33 J. Hölsä, T. Laamanen, T. Laihininen, M. Lastusaari, L. Pihlgren and C. V. Rodrigues, *Opt. Mater.*, 2014, **6**, 1627–1630.
- 34 H. Guo, Z. Li, H. Qian, Y. Hu and I. N. Muhammad, *Nanotechnology*, 2010, **21**, 125602.
- 35 M. Ding, D. Chen, S. Yin, Z. Ji, J. Zhong, Y. Ni, C. Lu and Z. Xu, *Sci. Rep.*, 2015, **5**, 12745.
- 36 H. Maachou, M. J. Genet, D. Aliouche, C. C. Dupont-Gillain and P. G. Rouxhet, *Surf. Interface Anal.*, 2013, **45**, 1088–1097.
- 37 A. Zhou, Y. Wei, B. Wu, Q. Chena and D. Xing, *Mol. Pharmaceutics*, 2012, **9**, 1580–1589.



Remodeling of extracellular matrix of the lamina propria in the uninvolved human rectal mucosa 10 and 20 cm away from the malignant tumor

Tumor Biology

July 2017: 1–10

© The Author(s) 2017

Reprints and permissions:

sagepub.co.uk/journalsPermissions.nav

DOI: 10.1177/1010428317711654

journals.sagepub.com/home/tub

Sanja Z Despotović¹, Novica M Miličević¹, Dragoslav P Milošević^{2,3}, Nebojša Despotović^{2,3}, Predrag Erceg^{2,3}, Petar Svorcan^{2,4}, Udo Schumacher⁵, Sebastian Ullrich⁵, Gordana Mihajlović³, Dragan Kalem⁴, Srđan Marković⁴, Ivana M Lalić¹, Aleksandar J Krmpot⁶, Mihailo D Rabasović⁶, Dejan V Pantelić⁶, Svetlana Z Jovanić⁶, Thomas Rösch⁷ and Živana Miličević¹

Abstract

In recent years, it has been demonstrated that malignancy arises and advances through the molecular interplay between tumor cells and non-malignant elements of the tumor stroma, that is, fibroblasts and extracellular matrix. However, in contrast to the mounting evidence about the role of tumor stroma in the genesis and progression of the malignant disease, there are very few data regarding the uninvolved stromal tissue in the remote surrounding of the tumor. Using the objective morphometric approach in patients with adenocarcinoma, we demonstrate the remodeling of extracellular matrix of the lamina propria in the uninvolved rectal mucosa 10 and 20 cm away from the neoplasm. We show that the representation of basic extracellular matrix constituents (reticular and collagen fibers and ground substance) is decreased. Also, the diameter of empty spaces that appear within the extracellular matrix of the lamina propria is increased. These spaces do not represent the blood or lymphatic vessel elements. Very likely, they reflect the development of tissue edema in the remote, uninvolved lamina propria of the mucosa in patients with the malignant tumor of the rectum. We hypothesize that the remodeling of extracellular matrix in lamina propria of the rectal mucosa may increase its stiffness, modulating the mechano-signal transduction, and thus promote the progression of the malignant disease.

Keywords

Rectum, cancer, human, extracellular matrix

Date received: 8 September 2016; accepted: 3 April 2017

¹Institute of Histology and Embryology, Faculty of Medicine, University of Belgrade, Belgrade, Serbia

²Faculty of Medicine, University of Belgrade, Belgrade, Serbia

³Department of Geriatrics, Zvezdara University Clinical Center, Belgrade, Serbia

⁴Center for Gastroenterology and Hepatology, Zvezdara University Clinical Center, Belgrade, Serbia

⁵Institute of Anatomy and Experimental Morphology, University Cancer Center, University Medical Center Hamburg-Eppendorf, Hamburg, Germany

⁶Institute of Physics, University of Belgrade, Belgrade, Serbia

⁷Department of Interdisciplinary Endoscopy, University Hospital Hamburg-Eppendorf, Hamburg, Germany

Corresponding author:

Živana Miličević, Institute of Histology and Embryology, Faculty of Medicine, University of Belgrade, Višegradska 26 | 1000 Belgrade, Serbia.

Email: emilicen@etf.bg.ac.rs



Table 1. Demographic characteristics of patients included in the study.

Patients	Number	Age (years)	Gender	
			Male	Female
Cancer	32	72.12	18	14
Healthy	30	70.90	16	14

Introduction

The surrounding tissue of colorectal cancers has attracted considerable interest in recent years for two main reasons. The first reason is that carcinogens act on an entire tissue exposed to this carcinogen, and consequently, genetic alterations are expected to occur at sites distant from the tumor itself. Therefore, several malignant or pre-malignant lesions may occur in the vicinity of an actual tumor. This concept of field carcinogenesis has originally been proposed for the oral mucosa but has been expanded to practically all tissues of the human body.^{1–3} While the field carcinogenesis primarily targets the epithelial cells of the colorectum, the connective stroma has attracted considerable interest too. The masters of colorectal carcinogenesis Vogelstein and Kinzler⁴ stated recently that “Despite intensive efforts, no genetic alterations have been shown to be required to convert a malignant primary tumor into a metastatic lesion.” With reference to distant metastasis formation, the decreased presence of lymphatic vessels and reduced immune cytotoxicity have recently been highlighted as hallmarks for the occurrence of metastasis,⁵ thus putting the tumor stroma into the focus of metastasis research. Malignancies arise and advance through the interactions with the elements of the neighboring tissues, that is, the tumor microenvironment.^{6,7} Special significance has been attributed to the molecular interplay between tumor cells and non-malignant elements of the tumor stroma, that is, fibroblasts and extracellular matrix (ECM).⁸ Tumor progression and aggressiveness are promoted by the surrounding tissue through cell-to-cell contacts or secreted molecules.^{9,10} In return, tumor cells uphold the recruitment of fibroblasts into a tumor mass and their transdifferentiation into myofibroblasts, which produce factors stimulating cancer progression.^{11–14} In this way, the interplay between the cancer cells and stromal cells is established, a positive feedback loop is closed and the advancement of malignant disease is promoted.

However, despite the mounting evidence about the role of tumor stroma in the genesis and progression of the malignant disease, there are very few data regarding the uninvolved stromal tissue in the remote surrounding of the tumor. Only very recently, we performed a morphometric study of the mucosa of rectum and revealed the alterations of Lieberkühn crypts, as well as reduced cellularity, 10 and 20 cm away from the malignant tumor. Our study also provided indications that ECM of the lamina propria could be affected.¹⁵

Therefore, the aim of this study was to investigate the organization of ECM components of the lamina propria of the rectal mucosa in the remote surrounding of the malignant tumor and quantitate them using an objective morphometric approach.

Our work is the first to reveal a profound remodeling of ECM of the lamina propria of the uninvolved human rectal mucosa in the remote surrounding of the malignant tumor. Thus, we document the interactions between the cancer and distant mucosal tissue of the affected organ.

Materials and methods

Tissue samples

This study has been approved by the Ethics Committee of Zvezdara Clinical Center, Belgrade, Serbia (27 November 2013) and performed in accordance with ethical standards laid down in the 1964 Declaration of Helsinki. All individuals involved received detailed verbal information and gave their informed consent prior to their inclusion into the study.

Only patients with newly discovered tumor were included in the study. Thus, they had not received any previous treatment for the malignant disease. Tissues were endoscopically sampled at the Center for Gastroenterology and Hepatology, Zvezdara Clinical Center, Belgrade, Serbia, from patients suspected on clinical grounds to suffer from a rectal cancer, which all were subsequently diagnosed as adenocarcinoma according to World Health Organization (WHO) histological classification of tumors. Patients with diverticular disease of the colon, previous infectious colitis, or inflammatory bowel disease were excluded from the study. Patients were divided into groups according to their gender. All patients were on standard mixed meals regimen and not on any particular form of diet.

Samples of rectal mucosa were obtained from 32 patients older than 60 years (18 males and 14 females; Table 1). Cancers were located in the sigmoid colon 25–30 cm from the external anal verge and the biopsies were taken 10 and 20 cm away from the malignant tumor in the caudal direction. The samples of rectal mucosa collected at the same institution from 30 healthy persons of the corresponding age (16 males and 14 females; Table 1) during the active endoscopy screening of individuals with a family history of intestinal malignancy, possibly suffering from an as yet unidentified, asymptomatic cancer in which no disease involving the rectal mucosa was found, were used as control. Samples were collected from the upper third of rectum.

Tissue preparation, staining, and morphometric measurements

The biopsies of the rectal mucosa were fixed in 10% neutral buffered formalin, processed to Paraplast. Tissue sections (3–5 μ m thick) were routinely stained with hematoxylin–eosin, while Gomori’s silver impregnation

and Masson trichrome staining were used for demonstration of reticular and collagen fibers, respectively.¹⁶

Microphotographs were acquired with a digital camera Olympus C3030-Z (Olympus Deutschland GmbH, Hamburg, Germany) connected to a light microscope Opton Photomicroscope III (Carl Zeiss AG, Oberkochen, Germany) or digital camera Leica DFC295 (Leica, Heerbrugg, Switzerland) connected to a light microscope Leica DM4000 B LED (Leica, Wetzlar, Germany).

Gomori's silver impregnation technique was used to identify the reticular fibers which stained black. A random selection of three fields per slide from the subepithelial region, between the crypts, and above the lamina muscularis mucosae was assessed for further analysis.

The diameters of spaces between reticular fibers were measured at the magnification 630 \times . In order to avoid the inclusion of crypts in the measurement of the spaces between reticular fibers, a rectangle was drawn that always occupied the same area of the lamina propria (3600 μm^2) excluding the crypts, and our measurements were performed within this rectangle. The plugin BoneJ within open-source software Fiji¹⁷ was used to estimate the diameter of spaces between reticular fibers in the lamina propria of the rectal mucosa of healthy individuals ($n=30$), as well as 10 cm ($n=27$) and 20 cm ($n=22$) away from the malignant tumor. BoneJ determines the diameter (μm) of the largest sphere that can be inserted into the spaces between the reticular fibers and assigns different colors to these spaces according to their diameter.

The presence of reticular fibers in colonic lamina propria was determined in the following manner. A random selection of 15 fields per slide (5 fields in subepithelial region, 5 fields between the crypts of lamina propria, and 5 fields above lamina muscularis mucosae) was assessed at the magnification of 400 \times (n =as above). Reticular fibers were extracted using Color Picker Threshold Plugin within open community platform for bioimage informatics Icy.¹⁸ For each slide, 10 positive and 10 negative colors were selected as recognition patterns of stained and unstained tissue elements. The resulting images were systematically compared with the corresponding originals, and in cases in which the detection of reticular fibers was not accurate, the threshold was fixed manually. The presence of reticular fibers in rectal lamina propria was expressed as the relative percentage of the area occupied by the reticular fibers divided by the area of the lamina propria selected with an imaging processor.

Masson's trichrome staining identified collagen fibers, which were green. The presence of collagen fibers of healthy individuals ($n=30$), as well as 10 cm ($n=32$) and 20 cm ($n=32$) away from the malignant tumor, was determined in the same manner as described above for reticular fibers.

Also, for the identification of collagen fibers, the unfixed and label-free colon tissue samples were imaged on an original labframe nonlinear laser scanning microscope (NLM). The microscope is described elsewhere.¹⁹

Experimental setup for NLM was used for second harmonic generation (SHG) imaging of 3D collagen distribution from the samples. The incoming infrared femtosecond pulses from the tunable mode-locked Ti:sapphire laser (Coherent, Mira 900) were directed onto the sample by a dichroic mirror through the Zeiss EC Plan-Neofluar 40 \times /1.3 NA Oil objective. The laser wavelength was 840 nm. The SHG was selected by narrow bandpass filter at 420 nm (Thorlabs FB420-10, FWHM 10 nm). The average laser power on the sample was 30 mW and the peak laser power was 2.5 kW.

Immunohistochemical analysis was performed on formalin-fixed, paraffin-embedded sections using following antibodies and dilution ratios: monoclonal mouse anti-human CD34 (M7165, dilution 1:100; Dako, Carpinteria, CA, USA), CD105 (clone SN6h, MA5-11854, dilution 1:100; Thermo Fisher Scientific, Rockford, IL, USA), podoplanin (clone D2-40, M3619, dilution 1:100; Dako), as well as hyaluronic acid binding protein (HABP, biotinylated, 385911-50 UG, dilution 1:75; Calbiochem, Spring Valley, CA, USA).

For anti-CD34, -CD105, and -podoplanin antibodies, the following procedure was used. Briefly, after dewaxing and rehydration, a heat-inducing antigen retrieval procedure using Tris-EDTA at pH 9.0 for 30 min was performed on all tissue sections, with subsequent washing in Tris-buffered saline (TBS) with Tween and incubation with primary antibodies for 60 min. The sections were treated by applying the commercial Ultra Vision/3,3'-diaminobenzidine (DAB) staining kit (Thermo Scientific Lab Vision TL-060-HD, Rockford, IL, USA). Immunoreactions were developed by DAB substrate.

For HABP antibody, Dako retrieval solution (S1699 at pH=6) was used. After washing in TBS, protein blocking was performed with 1% bovine serum albumin (BSA) in TBS. After incubation with primary biotinylated antibodies for 60 min and with VECTASTAIN ABC-AP kit (Vector Laboratories, Burlingame, CA, USA) for 30 min, staining with Permanent Red (Dako K0640, Carpinteria, CA, USA) was used for visualization. The sections were counter-stained with Mayer's hematoxylin. Negative controls were performed on colon sections using the same methodology, but with the omission of primary antibody. For CD105 antibody, sections of human colon cancers were used as a positive control and for HABP antibody, sections of human nasal mucosa.

The number of blood vessels demonstrated with CD34 or CD105 in rectal lamina propria (per 0.1 mm^2 of the tissue) was determined at 5 fields per slide at 200 \times magnification using the open-source software Fiji. A region of interest was drawn on each field, which excluded the crypts and included only the lamina propria. Counting of blood vessels was performed on healthy tissue ($n=25$), 10 and 20 cm away from tumor ($n=10$), using the Multi-point tool.

The diameter of spaces within ECM and the representation of hyaluronan, as demonstrated with HABP staining, in healthy tissues (n=4) 10 cm (n=10) and 20 cm (n=12) away from the malignant tumor, were determined as described for reticular fibers.

Statistical analysis

The statistical package SPSS for Windows 12.0 (SPSS Inc., Chicago, IL, USA) was used to calculate the means and standard deviations, as well as to indicate significant differences (Student's t-test and one-way analysis of variance (ANOVA) at $p < 0.05$).

Results

Morphological alterations of the uninvolved rectal mucosa in cancer patients

The mucosa of normal, healthy persons exhibited an orderly organization. The crypts were well developed, generally regular and round in shape, with luscious epithelium consisting mostly of goblet cells and fewer enterocytes (Figure 1(a)). The connective tissue of lamina propria also displayed a tidy appearance with very little free space within ECM (Figure 1(a)).

At the distance of 10 cm away from the tumor, the number of crypts appeared decreased, with diminished diameter, slightly irregular in shape, and with frail epithelium (Figure 1(b)). The connective tissue of lamina propria showed a disorderly organization, whereby the prominent spaces were notable within the ECM (Figure 1(b)). Similar alterations of lamina propria of the rectal mucosa, but less prominent in comparison with the normal tissue, were observed in cancer patients 20 cm away from the tumor (not shown).

Therefore, we wished to objectively investigate the extent of disorderly organization of the mucosal lamina propria 10 and 20 cm away from the adenocarcinoma of the rectum and quantify the basic components of ECM (namely, reticular and collagen fibers, as well as ground substance). To this end, we used the computer-aided image analysis of the affected tissue to estimate the diameter of spaces and the representation of the components of ECM in the lamina propria of the rectal mucosa 10 and 20 cm away from the malignant tumor.

Disorganization of reticular fibers in the lamina propria of the uninvolved rectal mucosa in cancer patients

In normal tissue, the reticular fibers were orderly organized and showed a tidy appearance. They were thick and intimately appositioned to the epithelium of the crypts. The basal lamina of the crypts was surrounded by three to

four layers of reticular fibers. A dense meshwork of reticular fibers leaving little space for non-fibrous ground substance connected the crypts with each other (Figure 1(c)).

At the distance of 10 and 20 cm away from the tumor, the reticular fibers around the crypts consisted only of one thin layer, and those fibers spanning the ECM were also thin, thus leaving the prominent empty spaces between the reticular fibers (Figure 1(d)). We revealed that the diameter of spaces between the reticular fibers was significantly increased at the distance of 10 cm away from the tumor lesion ($5.66 \pm 2.21 \mu\text{m}$), in comparison with both healthy controls ($3.32 \pm 0.81 \mu\text{m}$; $p < 0.01$; Figures 1(e)–(h)) and tissue samples taken 20 cm away from the tumor ($3.72 \pm 1.27 \mu\text{m}$; $p < 0.01$). There was no statistically significant difference between samples taken 20 cm away from the tumor and control (Table 2). These results clearly documented the disturbed organization of the lamina propria in the remote, uninvolved rectal mucosa 10 cm away from the malignant lesion.

Furthermore, we wished to explore whether the increased diameter of spaces was accompanied by a decreased representation of reticular fibers in the lamina propria of the remote rectal mucosa 10 and 20 cm away from the neoplasia. We revealed that the representation of reticular fibers was significantly decreased in the lamina propria of rectal mucosa 10 cm (27.99 ± 7.86 ; $p < 0.01$) but not 20 cm (38.76 ± 10.01) away from the tumor in comparison with the tissue of healthy individuals (42.72 ± 11.33 ; Table 2). The representation of reticular fibers was significantly lower ($p < 0.01$) in the lamina propria at the distance of 10 cm away from the tumor compared with the representation at the distance of 20 cm (Table 2).

Disorganization of collagen fibers in the lamina propria of the uninvolved rectal mucosa in cancer patients

In normal tissue, the collagen fibers showed a notably tidy appearance: the fibers were massive, intimately appositioned, and orderly organized (Figure 2(a)).

At the distance of 10 and 20 cm away from the tumor, the collagen fibers were frail and loosely arranged. Thus, the prominent spaces were notable between the collagen fibers (Figure 2(b)).

We further wished to exclude the possibility that the observed changes of the collagen fibers in the mucosal lamina propria were artificially produced (i.e. due to fixation or staining procedure). Therefore, NLM was used for SHG imaging of collagen distribution. In this method, the fresh, unfixed, and unstained tissue is used for demonstration of collagen fibers. SHG images wholly confirmed the above-described findings: in healthy individuals, the collagen fibers were massive, closely appositioned, and orderly organized around the crypts and throughout the lamina propria (Figure 2(c) and Online Resource 1). In the lamina

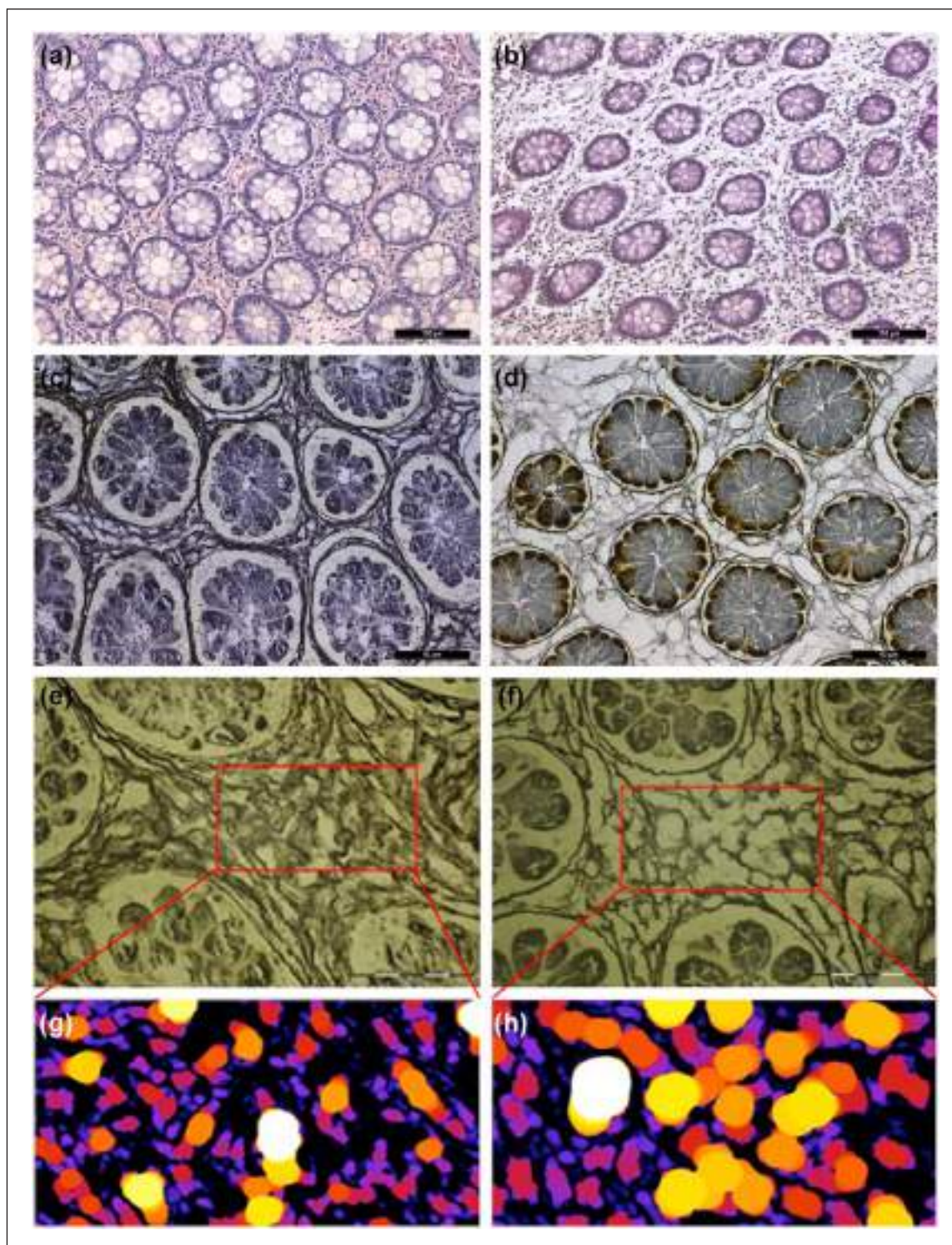


Figure 1. Representative photomicrographs of rectal mucosa in healthy persons (a, c, e, and g) and cancer patients 10 cm away from the tumor (b, d, f, and h). (a) On hematoxylin–eosin staining, the connective tissue of lamina propria of healthy person shows orderly organization with very little free space within extracellular matrix, (b) while at the distance of 10 cm away from the tumor, lamina propria is disorganized with prominent spaces notable within extracellular matrix. Gomori's silver impregnation technique identified reticular fibers which were (c) thick and closely appositioned in normal mucosa and (d) feeble and loosely arranged at the distance 10 cm away from the tumor. Measurement of the spaces between reticular fibers in (e) a healthy person and (f) 10 cm away from tumor was performed within the rectangle using plugin BoneJ (Fiji). BoneJ determines the diameter of the largest sphere that can be inserted into the spaces between reticular fibers and assigns different colors to these spaces according to their diameter. Brighter spheres have larger diameter. Graphical output from (g) BoneJ of healthy tissue and (h) 10 cm away from tumor.

Table 2. Morphometric measurements of the rectal mucosa in healthy subjects and cancer patients 10 and 20 cm away from tumor.

	Healthy controls	10 cm away from tumor	20 cm away from tumor
Diameter of spaces between reticular fibers (μm)	3.32 \pm 0.81	5.66 \pm 2.21*	3.72 \pm 1.27 ⁺
Representation of reticular fibers (%)	42.72 \pm 11.33	27.99 \pm 7.86*	38.76 \pm 10.01 ⁺
Representation of collagen fibers (%)	48.05 \pm 8.92	26.43 \pm 6.22*	35.15 \pm 8.34** ⁺
Diameter of spaces between HABP (μm)	2.00 \pm 0.40	4.27 \pm 1.58*	3.78 \pm 1.45 [§]
Representation of HABP (%)	60.41 \pm 9.31	42.71 \pm 11.81*	45.42 \pm 13.35**

HABP: hyaluronic acid binding protein.

*10 cm away from tumor versus healthy controls ($p < 0.01$).

⁺10 cm away from tumor versus 20 cm away from tumor ($p < 0.01$).

**20 cm away from tumor versus healthy controls ($p < 0.01$).

[§]20 cm away from tumor versus healthy controls ($p < 0.05$).

propria 10 cm away from tumor, the collagen fibers were thinner, disordered, and loosely arranged with noticeable spaces between them (Figure 2(d) and Online Resource 2).

We also wished to explore whether the presence of free spaces between the collagen fibers was accompanied by a decreased representation of collagen in the lamina propria of the uninvolved rectal mucosa 10 and 20 cm away from the neoplasia. We revealed that the representation of collagen fibers in the lamina propria in the remote rectal mucosa 10 and 20 cm away from the cancer was significantly lower (26.43 \pm 6.22 and 35.15 \pm 8.34, respectively; $p < 0.01$) in comparison with the control, healthy individuals (48.05 \pm 8.92; Table 2). Notably, the representation of collagen fibers was significantly lower ($p < 0.01$) in the lamina propria at the distance of 10 cm away from the tumor compared with that at the distance of 20 cm (Table 2).

Disorganization of ground substance in the lamina propria of the uninvolved rectal mucosa in cancer patients

The ECM ground substance was visualized by demonstration of HABP binding to hyaluronan in affinity histochemically stained tissue sections of healthy individuals and cancer patients and analyzed using computer-aided morphometric approach.

In normal tissue, the ECM ground substance was organized in confluent, uniform bands between the crypts with very few small spaces within it (Figure 2(e)).

At the distance of 10 and 20 cm away from the tumor, the ECM ground substance recapitulated the structural organization similar to that observed for reticular and collagen fibers: namely, the prominent spaces were notable within it (Figure 2(f)). The morphometric analysis revealed that the diameter of spaces within the ground substance was significantly increased at the distance of 10 and 20 cm away from the tumor lesion (4.27 \pm 1.58 μm , $p < 0.01$ and 3.78 \pm 1.45 μm , $p < 0.05$, respectively), in comparison with healthy controls (2.00 \pm 0.40 μm ; Table 2). Furthermore, we revealed that the representation of ECM ground substance in the lamina propria of the remote rectal mucosa 10 and 20 cm away from

the cancer was significantly lower (42.71 \pm 11.81 and 45.42 \pm 13.35, respectively; $p < 0.01$) in comparison with the control, healthy individuals (60.41 \pm 9.31; Table 2).

Edema of the lamina propria of the uninvolved rectal mucosa in cancer patients

Finally, we wanted to elucidate whether the enlarged spaces within the ECM in the lamina propria of the remote, unaffected rectal mucosa 10 and 20 cm away from the tumor could represent the blood or lymphatic vessel elements.

On the routinely stained sections of the healthy tissue, the small blood vessels and capillaries were readily discernible, but infrequently seen. On the contrary, in lamina propria of the rectal mucosa 10 and 20 cm away from the tumor, the small blood vessels and capillaries were abundant and much more frequent than in the healthy tissue. To more specifically uphold our observation, we stained the tissue samples immunohistochemically with CD34 and CD105 antibodies for total and newly formed blood vessels, respectively. We counted the number of blood vessel profiles per unit area of tissue (0.1 mm² of the lamina propria).

The CD34-positive blood vessels were abundant in healthy tissue (Figure 3(a)), as well as 10 and 20 cm away from the malignant tumor (Figure 3(b)). However, their number per 0.1 mm² of the lamina propria 10 cm away (65.15 \pm 18.94, $p < 0.01$) and 20 cm away from the tumor (45.77 \pm 16.48; $p < 0.01$) was significantly higher compared with the lamina propria of healthy tissue (36.57 \pm 7.59). The number of CD34-positive blood vessels 10 cm away from the tumor was significantly increased compared with lamina propria 20 cm away from the tumor ($p < 0.01$; Table 3).

The microvessels in rectal lamina propria from healthy controls were either minimally positive or totally CD105-negative. Rare CD105-positive blood vessels were preferentially located either superficially immediately below the basement membrane or at the cryptal base (Figure 3(c)). The number of CD105-positive blood vessels was significantly increased 10 and 20 cm away from the rectal adenocarcinoma (Figure 3(d), 14.93 \pm 5.65 and 9.53 \pm 4.97, respectively; $p < 0.01$) in comparison with the control,

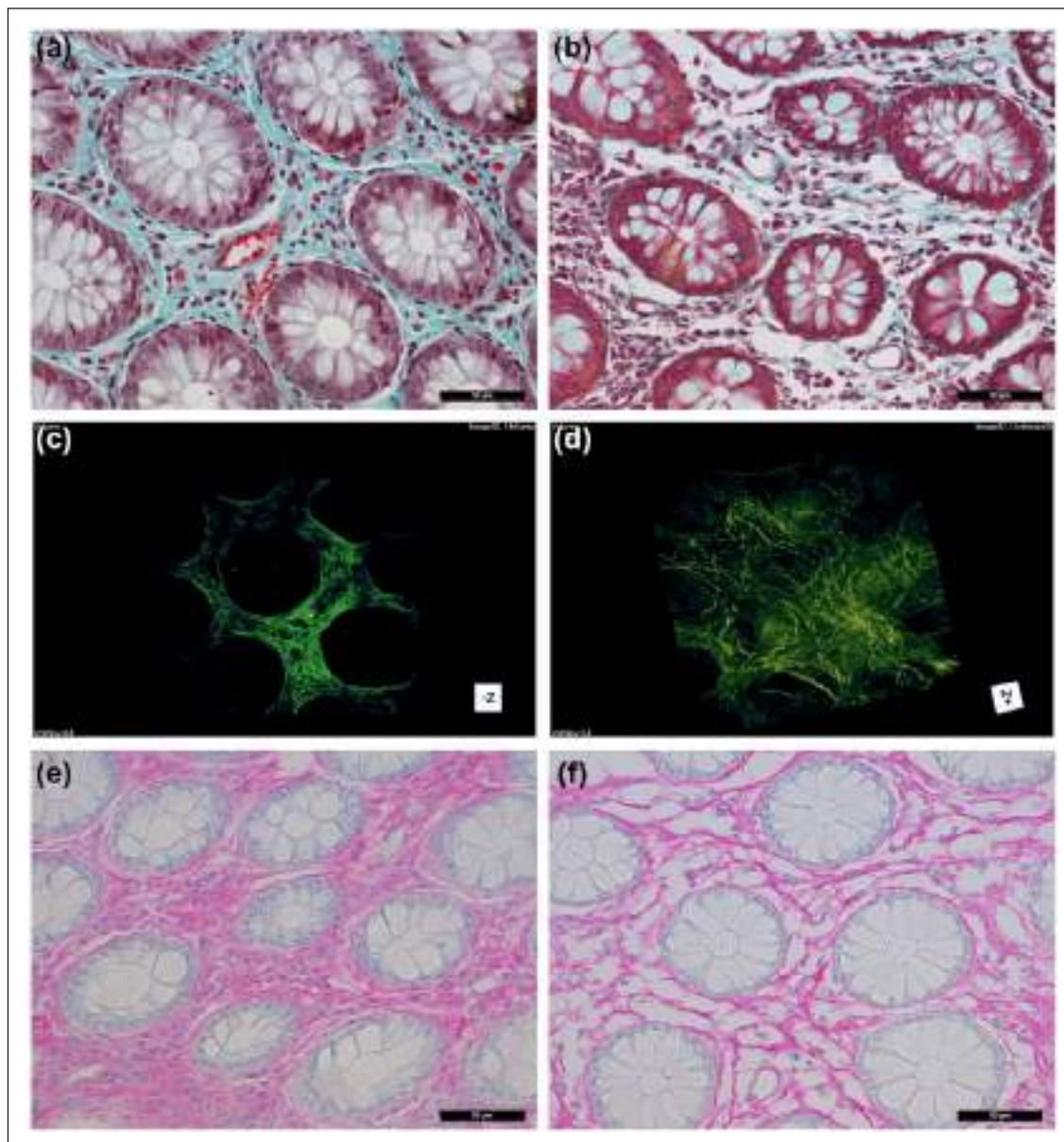


Figure 2. Representative photomicrographs of rectal mucosa in healthy persons (a, c, and e) and cancer patients 10 cm away from the tumor (b, d, and f). Masson's trichrome staining identified collagen fibers, which were massive, intimately appositioned, and orderly organized in (a) normal rectal tissue and (b) frail and loosely arranged 10 cm away from the tumor. NLM was used for SHG imaging of collagen fibers in (c) unfixed and unstained healthy tissue and (d) tissue 10 cm away from the tumor. SHG images confirmed the findings described above. (e) Immunohistochemical staining for hyaluronan using HABP in healthy person shows hyaluronan (red) organized in confluent bands between the crypts with small spaces within it. (f) At the distance 10 cm away from the tumor, hyaluronan formed thin bands with prominent spaces notable within it.

healthy tissue (5.8 ± 2.52). Also, the number of CD105-positive blood vessels 10 cm away from the tumor was significantly increased compared with lamina propria 20 cm away from the tumor ($p < 0.01$; Table 3).

So, we demonstrate that both the number of total and newly formed blood vessels in the lamina propria 10 and 20 cm away from the tumor was increased in comparison with the lamina propria of healthy tissue. However, as the large spaces within the ECM of diseased rectal lamina propria remained CD34- and CD105-negative, we concluded

that they do not represent the blood vessel elements. Thus, the question of their nature remained unanswered.

Therefore, we decided to investigate whether these spaces could represent newly developed lymphatic vessels. To clarify this issue, we immunostained the tissue samples with anti-podoplanin that labels lymphatic endothelium, whereas it is unreactive with vascular endothelium. We did not reveal any lymphatic vessels in the lamina propria of healthy colon and they were present only at the level of lamina muscularis mucosae where an abundant array could

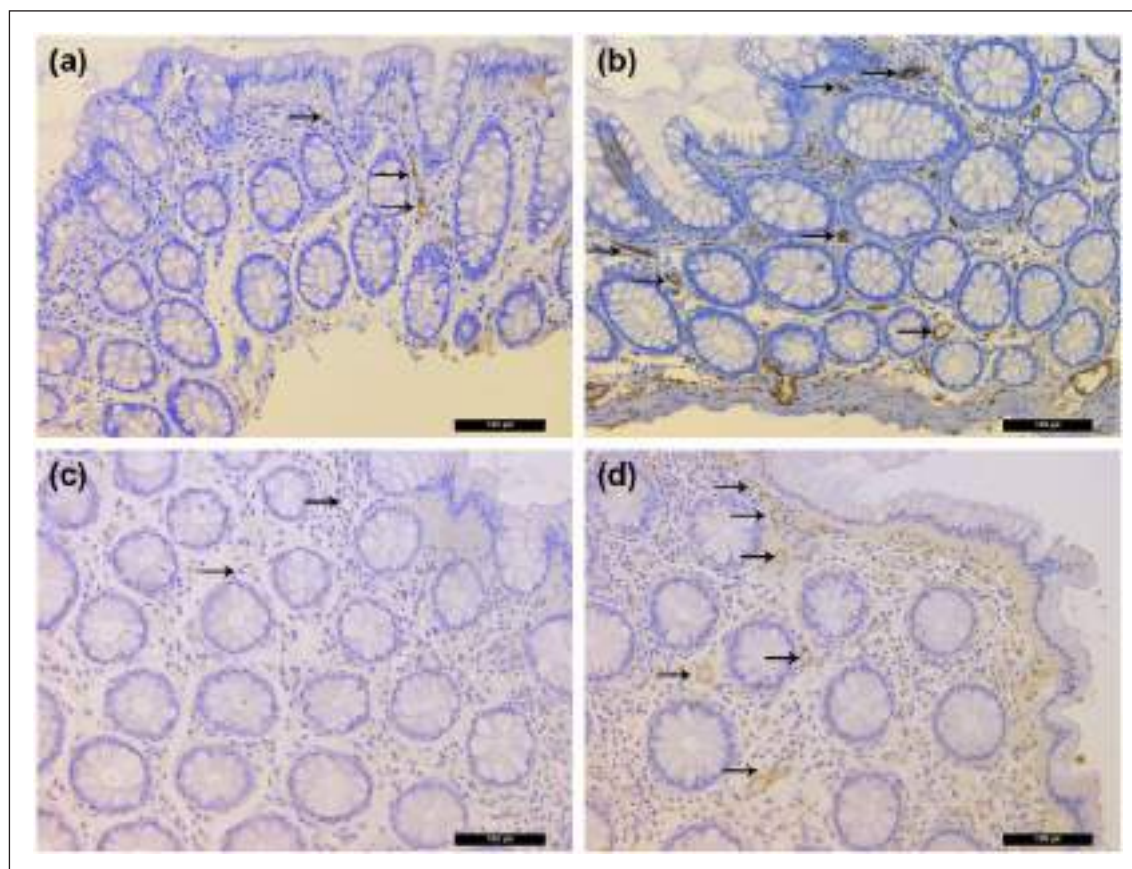


Figure 3. Immunohistochemical staining for CD34 and CD105 of rectal mucosa in healthy persons (a and c) and cancer patients 10 cm away from the tumor (b and d). (a) The CD34-positive blood vessels were abundant in healthy tissue. (b) Their number was significantly increased 10 cm away from the tumor. (c) The blood vessels in healthy lamina propria were either minimally positive or totally CD105-negative. (d) The number of CD105-positive blood vessels was significantly increased 10 cm away from the rectal adenocarcinoma (some blood vessels are indicated by arrows).

Table 3. Number of CD34- and CD105-positive blood vessels per 0.1 mm² of the rectal mucosa in healthy subjects and cancer patients 10 and 20 cm away from tumor.

	Healthy controls	10 cm away from tumor	20 cm away from tumor
Number of CD34-positive blood vessels (per 0.1 mm ² of lamina propria)	36.57 ± 7.59	65.15 ± 18.94*	45.77 ± 16.48**+
Number of CD105-positive blood vessels (per 0.1 mm ² of lamina propria)	5.8 ± 2.52	14.93 ± 5.65*	9.53 ± 4.97**+

*10 cm away from tumor versus healthy controls ($p < 0.01$).

**20 cm away from tumor versus healthy controls ($p < 0.01$).

+10 cm away from tumor versus 20 cm away from tumor ($p < 0.01$).

be seen (not shown). On the contrary, tiny profiles of lymphatic vessels were sometimes identifiable within the lamina propria 10 and 20 cm away from the tumor (not shown). These results neatly corresponded to those of Kenney and Jain.²⁰ However, the lymphatic vessels in such cases were very few and could not account for numerous spaces in the lamina propria, which were podoplanin-negative. Therefore, we concluded that these spaces do not represent the newly developed lymphatic vessels.

It should be notified that no differences in structure of the mucosal elements were observed between male and female healthy persons. Also, no gender difference for any

structural element of the rectal mucosa was observed neither at 10 cm nor at 20 cm distance away from the tumor.

Taking our results together, we concluded that they reflect the development of a veritable tissue edema in the remote, uninvolved lamina propria of the mucosa in patients with the neoplastic tumor of the rectum.

Discussion

Our present work, to the best of our knowledge, is the first to document the remodeling of lamina propria in the uninvolved rectal mucosa remote from the malignant lesion

using an exact morphometric analysis. We demonstrate the decreased representation of basic ECM constituents (reticular and collagen fibers, and ground substance), as well as the increased diameter of free spaces within the ECM in the lamina propria of the distant, uninvolved rectal mucosa.

These findings are in line with the finding that collagen is reduced in tumor-associated lamina propria.^{21,22} Recent studies show that modifications of collagen fibers (e.g. cross-linking), associated with changes of pore sizes, strongly affect the ECM stiffness.^{7,23–25} The cells grown in fibrillar collagen gels, which are nowadays extensively used to study tumor–microenvironment interactions in vitro, adopted a motile phenotype in gels with larger pores and a less motile phenotype in gels with small pores.²⁶ The increased rigidity of the ECM modulates the mechano-signal transduction and promotes the aggressiveness of neoplastic cells.^{27,28} One is tempted to speculate that the remodeling of the lamina propria in the remote rectal mucosa that we registered in vivo corresponds to these in vitro modifications of ECM, which sustain the aggressive behavior of tumor cells.

Two main questions arise from our study. First, what do the free spaces observed within the ECM represent? Second, does the remodeling of the remote rectal lamina propria reflect the influence of the malignant tissue, or conversely, denotes the intrinsic modifications of the stromal tissue which provide a suitable ground for tumor development?

Regarding the first question, and having in mind that enlarged spaces in the remote rectal lamina propria of cancer patients are CD34-, CD105-, and podoplanin-negative, we favor the possibility that these changes disclose a tissue edema at the greater distance from the tumor. This observation extends the finding that edema is observed in the immediate vicinity of tumors.²⁹

Regarding the second question, the former hypothesis is strengthened by the fact that neoplastic tissues can affect the structure and function of very distant organs.^{30,31} It is also supported by our finding that the changes of lamina propria are somewhat more prominent at the distance of 10 cm than at 20 cm away from the tumor. The latter notion is underpinned by our finding that the remodeling of the rectal lamina propria still remains evident at a greater distance (20 cm) away from the tumor. This is in line with the concept of “field carcinogenesis”: it postulates that genetic and environmental risk factors induce large areas of tissue injury suitable for cancer development.^{32,33} So, it remains possible that the remodeling of lamina propria that we observed in cancer patients reflects the overall alteration of larger fields of the colorectal mucosa and its connective tissue. At this moment, based on our data, it cannot be concluded with certainty which hypothesis holds true. However, studies currently in progress in our laboratories—in which the samples of mucosal lamina propria are taken from the part of the large bowel the most distant from the neoplastic lesion—are expected to greatly clarify the situation.

In very recent time, a view has emerged that the role of stroma is not secondary to that of epithelium in the

phenomenon of “field carcinogenesis.”^{34,35} Our results strongly support this opinion and suggest that the concept of “field carcinogenesis” should incorporate not only the changes in epithelial component, but the stroma of the malignantly affected organ as well.²

Our findings are in fine agreement with the results of genetic studies which showed that the significant gene expression alterations exist in the unaffected colon mucosa from patients with colon tumor.^{36–38} In addition to changes in ECM components, we also found an increased number of CD34- and CD105-positive capillaries and small blood vessels in the remote rectal mucosa. This was also detected in endoscopically normal rectal mucosa in patients with multiple adenomas anywhere in the colon and was completely absent in patients with benign colonic diseases.³³ Together, these data show that the use of remote uninvolved mucosa from patients with tumors of the gut as control tissue³⁹ should be regarded as unjustified. Despite its unremarkable endoscopic appearance, this tissue is not normal and only truly healthy tissue should be used as controls.

In conclusion, our study reveals profound remodeling of the ECM of lamina propria in the rectal mucosa 10 and 20 cm away from the malignant lesion. It documents the complex interplay between the tumor and stromal tissues not only of the neoplasm itself, but of the distant, uninvolved rectal lamina propria, as well. The search for these changes may be used as a diagnostic tool and a valuable indicator of occult tumors of the large bowel.

Acknowledgement

The authors are grateful to Luca Vannucci for critically reading the manuscript and Jovanka Ognjanović for excellent technical assistance.

Declaration of conflicting interests

The author(s) declared no potential conflicts of interest with respect to the research, authorship, and/or publication of this article.

Funding

The author(s) disclosed receipt of the following financial support for the research, authorship, and/or publication of this article: This work was supported by the Ministry of Education, Science and Technological Developments of the Republic of Serbia (grant nos 175005, and 45016).

References

1. Hawthorn L, Lan L and Mojica W. Evidence for field effect cancerization in colorectal cancer. *Genomics* 2014; 103(2–3): 211–221.
2. Lochhead P, Chan AT, Nishihara R, et al. Etiologic field effect: reappraisal of the field effect concept in cancer predisposition and progression. *Mod Pathol* 2015; 28(1): 14–29.
3. Patel A, Tripathi G, Gopalakrishnan K, et al. Field cancerization in colorectal cancer: a new frontier or pastures past? *World J Gastroenterol* 2015; 21(13): 3763–3772.

4. Vogelstein B and Kinzler KW. The path to cancer—three strikes and you're out. *N Engl J Med* 2015; 373(20): 1895–1898.
5. Mlecnik B, Bindea G, Kirilovsky A, et al. The tumor microenvironment and immunoscore are critical determinants of dissemination to distant metastasis. *Sci Transl Med* 2016; 8(327): 327ra26.
6. Goubran HA, Kotb RR, Stakiw J, et al. Regulation of tumor growth and metastasis: the role of tumor microenvironment. *Cancer Growth Metastasis* 2014; 7: 9–18.
7. Vannucci L. Stroma as an active player in the development of the tumor microenvironment. *Cancer Microenviron* 2015; 8(3): 159–166.
8. Hemmings C. Is carcinoma a mesenchymal disease? The role of the stromal microenvironment in carcinogenesis. *Pathology* 2013; 45(4): 371–381.
9. Hale MD, Hayden JD and Grabsch HI. Tumour-microenvironment interactions: role of tumour stroma and proteins produced by cancer-associated fibroblasts in chemotherapy response. *Cell Oncol* 2013; 36(2): 95–112.
10. Valcz G, Sipos F, Tulassay Z, et al. Importance of carcinoma-associated fibroblast-derived proteins in clinical oncology. *J Clin Pathol* 2014; 67(12): 1026–1031.
11. Fuyuhiro Y, Yashiro M, Noda S, et al. Upregulation of cancer-associated myofibroblasts by TGF- β from scirrhous gastric carcinoma cells. *Br J Cancer* 2011; 105: 996–1001.
12. Mazzocca A, Dituri F, Lupo L, et al. Tumor-secreted lysophosphatidic acid accelerates hepatocellular carcinoma progression by promoting differentiation of peritumoral fibroblasts in myofibroblasts. *Hepatology* 2011; 54: 920–930.
13. Polanska UM and Orimo A. Carcinoma-associated fibroblasts: non-neoplastic tumour-promoting mesenchymal cells. *J Cell Physiol* 2013; 228(8): 1651–1657.
14. Martinez-Outschoorn UE, Curry JM, Ko YH, et al. Oncogenes and inflammation rewire host energy metabolism in the tumor microenvironment: RAS and NF κ B target stromal MCT4. *Cell Cycle* 2013; 12(16): 2580–2597.
15. Despotović SZ, Milićević NM, Milosević DP, et al. Morphometric study of uninvolved rectal mucosa 10 cm and 20 cm away from the malignant tumor. *Histol Histopathol* 2014; 29(2): 229–234.
16. Bradbury P and Gordon KC. Connective tissues and stains. In: JD Bancroft and A Stevans (eds) *Theory and practice of histological techniques*. Edinburgh: Churchill Livingstone, 1982, pp. 121–144.
17. Doube M, Klosowski MM, Arganda-Carreras I, et al. BoneJ: free and extensible bone image analysis in ImageJ. *Bone* 2010; 47: 1076–1079.
18. de Chaumont F, Dallongueville S, Chenouard N, et al. Icy: an open bioimage informatics platform for extended reproducible research. *Nat Methods* 2012; 9(7): 690–696.
19. Rabasović MD, Pantelić DV, Jelenković BM, et al. Nonlinear microscopy of chitin and chitinous structures: a case study of two cave-dwelling insects. *J Biomed Opt* 2015; 20(1): 016010.
20. Kenney BC and Jain D. Identification of lymphatics within the colonic lamina propria in inflammation and neoplasia using the monoclonal antibody D2–40. *Yale J Biol Med* 2008; 81(3): 103–113.
21. Tarpey SG and White FH. Ultrastructural morphometry of collagen from lamina propria during experimental oral carcinogenesis and chronic inflammation. *J Cancer Res Clin Oncol* 1984; 107(3): 183–194.
22. Fu Z, Song P, Li D, et al. Cancer-associated fibroblasts from invasive breast cancer have an attenuated capacity to secrete collagens. *Int J Oncol* 2014; 45(4): 1479–1488.
23. Ng MR and Brugge JS. A stiff blow from the stroma: collagen crosslinking drives tumor progression. *Cancer Cell* 2009; 16(6): 455–457.
24. Yi J, Radosevich AJ, Stypula-Cyrus Y, et al. Spatially resolved optical and ultrastructural properties of colorectal and pancreatic field carcinogenesis observed by inverse spectroscopic optical coherence tomography. *J Biomed Opt* 2014; 19(3): 36013.
25. Sapudom J, Rubner S, Martin S, et al. The phenotype of cancer cell invasion controlled by fibril diameter and pore size of 3D collagen networks. *Biomaterials* 2015; 52: 367–375.
26. Carey SP, Kraning-Rush CM, Williams RM, et al. Biophysical control of invasive tumor cell behavior by extracellular matrix microarchitecture. *Biomaterials* 2012; 33(16): 4157–4165.
27. Parekh A and Weaver AM. Regulation of cancer invasiveness by the physical extracellular matrix environment. *Cell Adh Migr* 2009; 3(3): 288–292.
28. Seewaldt V. ECM stiffness paves the way for tumor cells. *Nat Med* 2014; 20(4): 332–333.
29. White LM, Wunder JS, Bell RS, et al. Histologic assessment of peritumoral edema in soft tissue sarcoma. *Int J Radiat Oncol Biol Phys* 2005; 61(5): 1439–1445.
30. Lopez DM, Charyulu V and Adkins B. Influence of breast cancer on thymic function in mice. *J Mammary Gland Biol Neoplasia* 2002; 7(2): 191–199.
31. Carrio R and Lopez DM. Insights into thymic involution in tumor-bearing mice. *Immunol Res* 2013; 57(1–3): 106–114.
32. Vannucci L, Fiserova A, Horvath O, et al. Cancer evolution and immunity in a rat colorectal carcinogenesis model. *Int J Oncol* 2004; 25(4): 973–981.
33. Backman V and Roy HK. Advances in biophotonic detection of field carcinogenesis for colon cancer risk stratification. *J Cancer* 2013; 4: 251–261.
34. Dotto GP. Multifocal epithelial tumors and field cancerization: stroma as a primary determinant. *J Clin Invest* 2014; 124(4): 1446–1453.
35. Ge L, Meng W, Zhou H, et al. Could stroma contribute to field cancerization? *Med Hypotheses* 2010; 75(1): 26–31.
36. Chen LC, Hao CY, Chiu YS, et al. Alteration of gene expression in normal-appearing colon mucosa of APC(min) mice and human cancer patients. *Cancer Res* 2004; 64(10): 3694–3700.
37. Belshaw NJ, Pal N, Tapp HS, et al. Patterns of DNA methylation in individual colonic crypts reveal aging and cancer-related field defects in the morphologically normal mucosa. *Carcinogenesis* 2010; 31(6): 1158–1163.
38. Lian J, Ma L, Yang J, et al. Aberrant gene expression profile of unaffected colon mucosa from patients with unifocal colon polyp. *Med Sci Monit* 2015; 21: 3935–3940.
39. Genovese L, Zawada L, Tosoni A, et al. Cellular localization, invasion, and turnover are differently influenced by healthy and tumor-derived extracellular matrix. *Tissue Eng Part A* 2014; 20(13–14): 2005–2018.



8th Regional Biophysics Conference



Dr. Aleksandar Jovan Krmopot

Photonics Center, Institute of Physics Belgrade,

University of Belgrade

Serbia

Dear Dr. Krmopot,

8th Regional Biophysics conference invitation to invited speaker

On behalf of the organizing committee of Regional Biophysics Conference 2018 I would like to invite you to present your work as an invited speaker at 8th Regional Biophysics conference. The conference will take place in Zreče, Slovenija between 16 and 20 May 2018. We would also like to invite your PhD students Tanja Fajc and Katarina Stevanovic to attend the event.

Sincerely,

prof. Janez Strancar

President of the RBC 2018 organizing committee

Mapping of hemoglobin residuals in erythrocyte ghosts using two photon excited fluorescence microscopy

Ivana Drvenica (1), Katarina Bukara (2), Svetlana Jovanić (3), Ana Stančić (1), Vesna Ilić (1), Mihailo D Rabasović (3), Dejan V Pantelić (3), Branislav M Jelenković (3), Branko Bugarski (2), Aleksandar Jovan Krmpot (3)

(1) Institute for Medical Research, University of Belgrade, Dr Subotića br 4, 11 129 Belgrade, Serbia

(2) Department of Chemical Engineering, Faculty of Technology and Metallurgy, University of Belgrade, Karnegijeva 4, 11 000 Belgrade, Serbia

(3) Photonics Center, Institute of Physics Belgrade, University of Belgrade, Pregrevica 118, 11080 Belgrade, Serbia

We have utilized the two photon excitation fluorescence (TPEF) microscopy to map the spatial distribution of residual hemoglobin. The home-made experimental set up for NLSM utilizes the train of the femtosecond pulses from Ti:Sapphire laser at 730nm, repetition rate 76MHz, and pulse duration 160fs. Porcine slaughterhouse blood and human outdated blood were used as a starting biological material. The erythrocyte ghosts were prepared by gradual hypotonic hemolysis [3]. First we used TPEF microscopy to image the intact erythrocytes at single cell level and to study their morphologies, discocyte of human and echynocyte of porcine erythrocytes. We have shown that the distribution of hemoglobin in intact erythrocytes follows the cells' shape with pronounced abundance in the proximity of cell membrane [4]. The TPEF images have also revealed that despite an extensive washing out procedure after gradual hypotonic hemolysis, residual hemoglobin localized on intracellular side of the ghost membranes [4]. The TPEF estimated hemoglobin distribution in intact erythrocytes and residual hemoglobin distribution in erythrocyte ghosts could be of importance in biotechnological processes but also in diagnosis of different pathological conditions.

[1] W. Zheng et al, Biomed Opt Express 2, 71-79 (2010)

[2] V. Leuzzi, et al, J. Inherit. Metab. Dis., 1-12 (2016)

[3] I. Kostić, et al, Colloids Surf B 122, 250-259 (2014)

[4] K. Bukara et al, J. Biomed. Opt. 22, 26003 (2017)

Keywords: multiphoton fluorescence microscopy, ultrafast lasers, hemoglobin, label-free imaging, erythrocytes, erythrocyte ghosts

[Back to programme](#)

北海道大学

〒 060-0812
札幌市北区北条西五丁目
Tel : 011-706-9005
Fax : 011-706-9006
E-mail : ku@hokkaido-u.ac.jp
URL : <http://www.hokkaido-u.ac.jp>



Hokkaido University

Kita21-1, Nishi11-1, Kita-ku
Sapporo 060-0812, JAPAN
Tel : +81-(0)11-706-9005
Fax : +81-(0)11-706-9006
E-mail : ku@hokkaido-u.ac.jp
URL : <http://www.hokkaido-u.ac.jp>

Monday, March 25, 2019

To: Dr. Aleksandar J. Krmpot,
Associate Professor
DePhotonics center
Institute of Physics,
Pregrevica 118, 11080
Belgrade- Zemun, SERBIA

Ref: Invitation letter

Dear Prof. Aleksandar J. Krmpot,

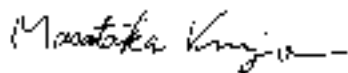
I am pleased to invite you to give a lecture at “Life Science Special Lecture III (Advanced Fluorescence Microscopy in Life Science Research)” in Hokkaido Summer Institute 2019, on Sep 9 – 15, 2019 at Hokkaido University, Sapporo, JAPAN. I would also like to use this opportunity to discuss with you our future collaboration, a joint research grant application and Hokkaido University Summer course in 2020.

We think that you will enjoy a lively exchange of ideas with a diverse audience of faculty and graduate students in our course. We will most certainly enjoy the opportunity to meet you and exchange ideas in this collegial atmosphere.

We will cover accommodation costs for your stay in Sapporo, Sep. 9 – 15, 2019.

I am looking forward to seeing you in Sapporo.

Sincerely yours



Masataka Kinjo
Professor
Faculty of Advanced Life Science
Hokkaido University,
Sapporo, 060-0812,
Japan,

Nonlinear Laser Scanning Microscopy (NLSM)

Aleksandar Krmpot

Institute of Physics, University of Belgrade, Belgrade, Serbia

E-mail: krmpot@ipb.ac.rs

Nonlinear laser scanning microscopy (NLSM) is advanced imaging technique particularly suitable for deep tissue and in vivo imaging. It utilizes ultra-short laser pulses (femto second pulses) in near infrared spectral region and due to nonlinearity the interaction with specimen material occurs only in the tiny focal volume which enables deep penetration. There are three modalities of NLSM: Two Photon Excitation Fluorescence (TPEF), Second Harmonic Generation (SHG) and Third Harmonic Generation (THG) imaging. Each of them provide complementary and valuable information and is used for various types of imaging. TPEF is the most similar to the single photon excitation fluorescence in confocal microscopy, but it has much higher penetration depth and axial resolution. TPEF relays very often on auto fluorescence, that originates from NADH and FAD mostly, when vertebrate specimens are imaged or chitin in arthropods. SHG imaging reveals ordered structures such as collagen (type I), myosin and starch with no need for labeling and with extremely high contrast. Also, it is the only optical technique that is used for quantification of degree of collagen molecules organization. THG is also used for unstained samples imaging providing information on steep changes of refractive index inside the specimen. With some limitations it is mostly used for in vivo imaging and real time tracking of some physiological processes, e.g. *C. Elegance* embryogenesis, physiological processes in zebra fish etc.

In the presentation, the physical background of TPEF, SHG and THG process will be explained. The properties of the technique such as axial and lateral resolution, information on samples that NLSM provides and basic applications will be discussed. 3D models and examples for imaging using each of modalities will be presented.

Suggested reading:

- 1. B. R. Masters, and P. So, Handbook of Biomedical Nonlinear Optical Microscopy. Oxford University Press (2008).**
- 2. Jerome Mertz, Introduction to Optical Microscopy, Roberts and Company Publishers (2009)**
- 3. 2014 - Francesco S Pavone_ Paul J Campagnola-Second harmonic generation imaging-CRC Press Taylor & Francis**

4. 2003 - Campagnola - Second-harmonic imaging microscopy for visualizing of biomolecular arrays in cell, tissues and organisms - Nat. Biotechn. 894
5. 2001 - Mertz, Moreaux - SHG by focused excitation of inhomogenously distributed scatterers - Opt Com 196
6. 2000 - Koenig-Multiphoton microscopy in life science-J Microscopy 200
7. <https://www.ncbi.nlm.nih.gov/pubmed/16369553>
8. <http://www.mitr.p.lodz.pl/evu/lectures/Filippidis.pdf>
9. G.J. Tserevelakis, G. Filippidis, A.J. Krmpot, M. Vlachos, C. Fotakis, N. Tavernarakis, "Imaging Caenorhabditis elegans embryogenesis by third-harmonic generation microscopy," Micron, 41 444 (2010), doi: 10.1016/j.micron.2010.02.006
10. Katarina Bukara, Svetlana Jovanić, Ivana T. Drvenica, Ana Stančić, Vesna Ilić, Mihailo D. Rabasović, Dejan Pantelić, Branislav Jelenković, Branko Bugarski, Aleksandar J. Krmpot, "Mapping of hemoglobin in erythrocytes and erythrocyte ghosts using two photon excitation fluorescence microscopy," J. Biomed. Opt. 22(2), 026003 (2017), doi: 10.1117/1.JBO.22.2.026003
11. Mihailo D. Rabasović, Dejan V. Pantelić, Branislav M. Jelenković, Srećko B. Ćurčić, Maja S. Rabasović, Maja D. Vrbica, Vladimir M. Lazović, Božidar P. M. Ćurčić, Aleksandar J. Krmpot, "Nonlinear microscopy of chitin and chitinous structures: a case study of two cave-dwelling insects," Journal of Biomedical Optics 20 016010 (2015). doi: 10.1117/1.JBO.20.1.016010



1st International Conference on Chemo and Bioinformatics
ICCBIKG 2021

BOOK OF PROCEEDINGS

October 26-27, 2021
Kragujevac, Serbia

Sponsored by



ART WINE



1st International Conference on Chemo and BioInformatics, Kragujevac, October 26-27, 2021
Serbia

Editors:

Professor Zoran Marković

Professor Nenad Filipović

Technical Editors:

Vladimir Simić

Izudin Redžepović

Nikola Srećković

Illustrations:

Igor Stanković, „Vector Alchemist“ d.o.o.

Publisher:

Institute for Information Technologies, University of Kragujevac, Serbia, Jovana Cvijića bb,
2021

Press:

„Grafo Ink“, Kragujevac

Impression:

120 copies

CIP - Каталогизacija u publikaciji - Narodna biblioteka Srbije, Beograd

54:004(048)(0.034.2)

57+61]:004(082)(0.034.2)

INTERNATIONAL Conference on Chemo and BioInformatics (1 ; 2021 ;
Kragujevac) Book of Proceedings [Elektronski izvor] / 1st International Conference
on Chemo and BioInformatics, ICCBIKG 2021, October 26-27, 2021 Kragujevac,
Serbia ; [editors Zoran Marković, Nenad Filipović]. - Kragujevac :
University, Institute for Information Technologies, 2021 (Kragujevac :
Grafo Ink). - 1 USB fleš memorija ; 3 x 2 x 1 cm

Sistemski zahtevi: Nisu navedeni. - Nasl. sa naslovne strane dokumenta. -
Tiraž 120. - Bibliografija uz svaki rad.

ISBN 978-86-82172-01-7

a) Хемија - Информациона технологија - Зборници b) Биомедицина -
Информациона технологија - Зборници

COBISS.SR-ID 48894473

THE EFFECTS OF SELENITE ON FILAMENTOUS FUNGI LIPID DROPLETS MONITORED *IN VIVO* LABEL FREE USING ADVANCED NONLINEAR MICROSCOPY TECHNIQUE

Tanja Pajic¹, Natasa Todorovic², Dunja Stefanovic¹, Mihailo D. Rabasovic³, Aleksandar Krmpot³, Miroslav Zivic¹

¹ Faculty of Biology, University of Belgrade, Studentski trg 16, 11158 Belgrade, Serbia

e-mail: tpajic@bio.bg.ac.rs

² Institute for Biological Research "Sinisa Stankovic", University of Belgrade, Institute of National Importance for the Republic of Serbia, Bulevar Despota Stefana 142, 11000 Belgrade, Serbia

³ Institute of Physics Belgrade, University of Belgrade, Pregrevica 118, 11000 Belgrade, Serbia

e-mail: nara@ibiss.bg.ac.rs, rabasovic@ipb.ac.rs, krmpot@ipb.ac.rs, mzivic@bio.bg.ac.rs

Abstract:

Third Harmonic Generation (THG) microscopy was employed as a method of choice for lipid droplet (LD) measurements and quantification of the effect of selenite on LDs.

Nonlinear laser scanning microscopy (NLSM) employs ultra-short laser pulses for imaging. THG microscopy is the modality of NLSM. Strong THG signals can only be observed from regions with non-uniformities with respect to their refractive index. Such regions in biological samples are lipid-water interfaces, and by far the brightest features in cells are LDs. For that reason, THG microscopy is the appropriate method for imaging of LDs from live unfixed cells, without the need for additional labeling.

The biological effects of spore- to- end- of- exponential- phase duration (27 - 30 h) of exposure to 1 mM selenite were monitored *in vivo* on the cells of filamentous fungi in liquid culture. We measured the lipid droplet density and size distribution in a model fungi *Phycomyces blakesleeanus*. The in-house built microscope frame complemented with Yb KGW laser (1040 nm, 200 fs pulses) was used, while detection was enabled in the transmission arm by PMT through the Hoya glass UV filter (peak at 340 nm).

From THG images of control and Se⁺⁴-treated hyphae, LD size and number were measured, showing that LD density was increased by more than 60% in Se⁺⁴-treated hyphae, compared to control. The average LD size distribution seemed slightly changed by Se⁺⁴-treatment. The obtained results suggest that 1 mM selenite treatment probably induces cellular stress response in filamentous fungi.

Keywords: Lipid droplets, Selenite, Third Harmonic Generation Microscopy, *Phycomyces blakesleeanus*

1. Introduction

Selenium is an essential trace element for humans and animals, while it is not necessary for plants and fungi. The availability and biological activity of selenium depend on its dose and chemical form [1]. In trace amounts, selenium enhances antioxidant capacity in a number of selenoproteins while at higher concentrations, selenium is toxic due to its prooxidative effects like oxidation of protein thiols and reactive oxygen species generation [2]. Since the oxidative stress is among the main intracellular signals sustaining autophagy [3], and lipid droplet (LD) biogenesis seems to be a general cellular response to high autophagic flux according to recent studies [4], we hypothesized that increased LD formation could be an immediate cellular response to a high selenium exposure.

In order to reliably monitor LDs *in vivo* by imaging, and measure the effects of selenite-induced oxidative stress- mediated cellular changes, it would be necessary to employ the imaging method that causes minimal additional phototoxicity. Otherwise, the oxidative stress induced by, for example, confocal imaging of labeled LDs, could potentially interfere with the processes underlying the measurements. For those reasons, Third Harmonic Generation (THG) microscopy was employed as a method of choice for LD measurements and quantification of the effect of selenite on LD number and sizes. THG microscopy is one of the modalities of nonlinear laser scanning microscopy (NLSM). In NLSM, the high laser intensity, and low average power due to employing ultra-short laser pulses, allow for the generation of nonlinear imaging signals. Although THG microscopy is not chemically specific, strong THG signals can only be observed from regions with non-uniformities with respect to their refractive index. Such regions in biological samples are lipid-water interfaces, and by far the brightest features in live cells are LDs [5]. For that reason, THG microscopy is especially appropriate method for LD imaging from live unfixed cells, without the need for additional labeling.

The biological effects (on the lipid droplet density and size distribution) of exposure to 1mM selenite were monitored *in vivo* on the cells of filamentous fungi in liquid culture. Filamentous fungi are one of the main pathways for selenium entrance into ecosystems and able to concentrate selenium in the mycelia [6]. Additionally, fungi are simple to manipulate, unicellular model system, that is naturally without selenoproteins encoded in genome [7]. Therefore, in fungi the prooxidative effects of selenium can be observed unhindered with simultaneous beneficial selenium-mediated effects.

2. Materials and Methods

Model organism was unicellular wild-type strain of the oleaginous filamentous fungus *Phycomyces blakesleeanus* (Burgeff 1925) (NRRL 1555(-)), grown in lighted stationary plates from the spore stock as previously described [8]. To observe the effect of treatment with 1mM sodium selenite, the prepared fungi activated spore culture volume was divided to control culture and treatment culture (same as control, with addition of sodium selenite in final concentration 1mM). The experiments were performed in triplicate.

As a method of choice for label free *in vivo* LD measurements, the application of THG microscopy was employed: 1040 nm, 200 fs pulses from Yb KGW laser were used; THG signal was detected by PMT in the transmission arm after passing through the Hoya glass UV filter with the peak at 340 nm. The obtained images were analyzed in ImageJ to quantify LDs number and size. The results are reported as mean \pm Standard error (SE) and statistically tested by student t-test with 95% confidence level.

3. Results and Discussion

In THG images obtained from control and selenite (Se^{+4})-treated hyphae, LDs can be readily observed (Figure 1a).

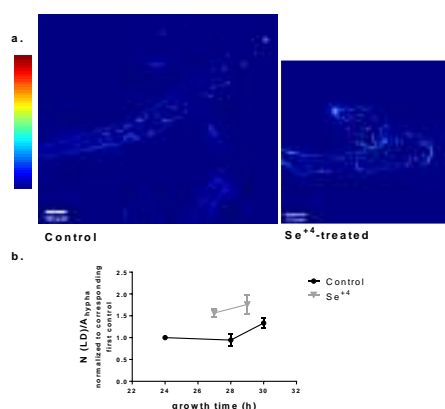


Figure 1. a.) THG images of: Control (28h), in the left panel; Se^{+4} -treated hypha (26h) in the right panel. Calibration bar is shown on the left (bottom: minimal; top: maximal intensity). Brightest spots represent LDs, and the faint cell wall THG signal can be seen as well. The increased LD density in treated group is visible. b.) LD density (LD number per unitary hypha area) was normalized for each independent experiment (n=3) to the LD

density value of the first control (24h) and plotted as a function of growth time. Control: black circles; Se⁺⁴-treated: gray triangles.

From THG images of control and Se⁺⁴-treated hyphae, LD number (Figure 1b) and size were measured (Figure 2). Fig. 1b. graph shows that average LD density increased by more than 60% in Se⁺⁴-treated hyphae, compared to control. LD density was calculated as: (LD number in the hypha) / (Area of that hypha (μm²)). Trend for slight increase of LD density in oldest controls is also evident, although it is less pronounced than in treated group (33 ± 16% increase in aged controls vs. 88 ± 26% in aged Se⁺⁴-treated). Average LD size was unchanged (Fig.2b.), not supporting the expectation that the stress induces generation of new LDs. Distribution of LD sizes on the other hand, shows that Se⁺⁴-treated LDs are more frequently small (around 1 μm) compared to LDs in controls. In addition, LD distribution in controls, but not in treated group, always had a “right side shoulder”-telltale sign that the separate population of LDs with diameters larger than group average is present. Same finding is more clearly seen in Fig 2c. graph, where the obtained parameters of Gauss function fits to the distribution of LD diameters are shown.

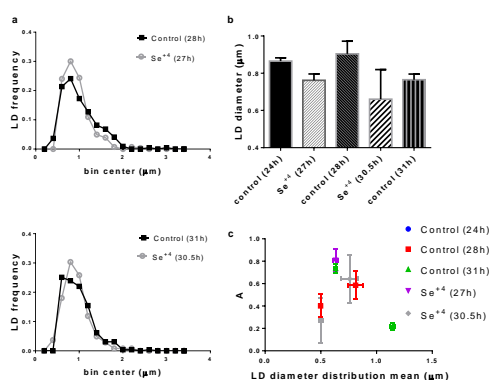


Figure 2. Size of LDs in the control and the Se⁺⁴-treated group. a.) Distributions of LD size for the Se⁺⁴-treated and for the age closest control. Top: 27 h treatment / 28 h control. Bottom: 30.5 h treatment / 31 h control. b.) Mean ± SD diameters of LDs in all groups (n = 200 - 400 LDs for each group). c.) Obtained parameters of the Gauss fit to LD size distribution. A - frequency of the component fitted. Some group distributions could be fitted with one normal distribution, but most often, two components were present.

LDs in the model fungus *Phycomyces blakesleeanus* are very small (mean diameters in all groups are less than 1 μm), while the resolution limit of the images presented is at around 0.4 μm. Smaller than average LDs were barely above the limit. Therefore, the close proximity to resolution limit is probably the cause for our inability to reliably detect the Se⁺⁴-induced generation of the smallest LDs and subsequent lowering of the mean diameter.

3. Conclusions

We were able to measure shift of the distribution of sizes, and the increase of the number of LDs induced by 1 mM selenite treatment. THG modality of NLSM enabled *in vivo* and label free physiological study that provided data in support of the hypothesis presented. Based on our data, it can be concluded that selenite induces cellular stress leading to autophagy and subsequent LD formation.

References

[1] C.M. Weekley, H.H. Harris, *Which form is that? The importance of selenium speciation and metabolism in the prevention and treatment of disease*. Chemical Society Reviews, 42 (2013) 8870 – 8894.
 [2] J.E. Spallholz, V.P. Palace, T.W. Reid, *Methioninase and selenomethionine but not Se-methylselenocysteine generate methylselenol and superoxide in an in vitro chemiluminescent assay*:

- implications for the nutritional carcinostatic activity of selenoamino acids*, Biochemical pharmacology, 67 (2004) 547-54.
- [3] G. Filomeni, D. De Zio, F. Cecconi, *Oxidative stress and autophagy: the clash between damage and metabolic needs*. Cell death and differentiation, 22 (2015) 377-88.
- [4] T.B. Nguyen, J.A. Olzmann, *Lipid droplets and lipotoxicity during autophagy*. Autophagy, 13 (2017) 2002-2003.
- [5] T. Watanabe, A. Thayil, A. Jesacher, K. Grieve, D. Debarre, T. Wilson, M. Booth, S. Srinivas, *Characterisation of the dynamic behaviour of lipid droplets in the early mouse embryo using adaptive harmonic generation microscopy*, BMC Cell Biology, 11 (2010) 38.
- [6] J. Falandysz, *Selenium in edible mushrooms*, Journal of Environmental Science and Health. Part C, Environmental Carcinogenesis & Ecotoxicology Reviews, 26 (2008) 256-99.
- [7] M. Mariotti, G. Salinas, T. Gabaldón, V.N. Gladyshev, *Utilization of selenocysteine in early-branching fungal phyla*, Nature Microbiology, 4 (2019) 759-765.
- [8] M. Stanić, J. Zakrzewska, M. Hadžibrahimović, M. Zičić, Z. Marković, Z. Vučinić, M. Zivić, *Oxygen regulation of alternative respiration in fungus *Phycomyces blakesleeanus*: connection with phosphate metabolism*. Research in Microbiology, 164 (2013) 770-8.

2017 Joint Conference of the European Frequency and Time Forum and IEEE International Frequency Control Symposium (EFTF/IFC 2017)

**Besancon, France
9 – 13 July 2017**



**IEEE Catalog Number: CFP17FRE-POD
ISBN: 978-1-5386-2917-8**

**Copyright © 2017 by the Institute of Electrical and Electronics Engineers, Inc.
All Rights Reserved**

Copyright and Reprint Permissions: Abstracting is permitted with credit to the source. Libraries are permitted to photocopy beyond the limit of U.S. copyright law for private use of patrons those articles in this volume that carry a code at the bottom of the first page, provided the per-copy fee indicated in the code is paid through Copyright Clearance Center, 222 Rosewood Drive, Danvers, MA 01923.

For other copying, reprint or republication permission, write to IEEE Copyrights Manager, IEEE Service Center, 445 Hoes Lane, Piscataway, NJ 08854. All rights reserved.

****** This is a print representation of what appears in the IEEE Digital Library. Some format issues inherent in the e-media version may also appear in this print version.***

IEEE Catalog Number:	CFP17FRE-POD
ISBN (Print-On-Demand):	978-1-5386-2917-8
ISBN (Online):	978-1-5386-2916-1
ISSN:	1075-6787

Additional Copies of This Publication Are Available From:

Curran Associates, Inc
57 Morehouse Lane
Red Hook, NY 12571 USA
Phone: (845) 758-0400
Fax: (845) 758-2633
E-mail: curran@proceedings.com
Web: www.proceedings.com

CURRAN ASSOCIATES INC.
proceedings
.com

EFTF-IFCS 2017 TABLE OF CONTENTS

Low-Power and Low-Profile Miniature Atomic Clock: Ceramic Based Flat Form Factor Miniature Atomic Clock Physics Package (C-MAC)55

Jacques Haesler¹, Laurent Balet¹, Sylvain Karlen¹, Thomas Overstolz¹, Benjamin Gallinet¹, Steve Lecomte¹, Fabien Droz¹, Kari Kautio³, Pentti Karioja³, Markku Lahti³, Antti Määttänen², Ossi Lahtinen², Ville Hevonkorpi²
¹CSEM SA, Switzerland; ²Primoceler Oy, Finland; ³VTT Technical Research Centre of Finland Ltd, Finland

Impact of Static-Magnetic-Field-Gradients on Relaxation Times in a Rb Vapor Cell57

Mohammadreza Gharavipour¹, Christoph Affolderbach¹, Florian Gruet¹, Gaetano Mileti¹, Ivan S. Radojčić², Aleksandar J. Krmpot², Brana M. Jelenković²
¹Université de Neuchâtel, Switzerland; ²University of Belgrade, Serbia

Microfabrication of Cs-Filled MEMS Cell Using Sequential Plasma Activated Bonding.....60

Kenta Terashima, Yoshikazu Hirai, Toshiyuki Tsuchiya, Osamu Tabata
Kyoto University, Japan

Cell-Based Stabilized Laser Sources and Light-Shifts in Pulsed Rb Atomic Clocks.....63

Nil Almat, William Moreno, Matthieu Pellaton, Mohammadreza Gharavipour, Florian Gruet, Christoph Affolderbach, Gaetano Mileti
Université de Neuchâtel, Switzerland

A2L-D Oscillators Design

Date: Monday, July 10, 2017
Time: 14:00 - 15:40
Room: Room 5, 6 & 7
Chair(s): Fabrice Sthal; FEMTO-ST
Jean-Pierre Aubry; FEMTO-ST

SPINTRONIC Based RF Components.....66

Ursula Ebels¹, Jérôme Hem³, Anike Purbawati³, Ana Ruiz Calafora³, Chandrasekhar Murapaka¹, Laurent Vila¹, Karla Jaimes Merazzo⁷, Erika Jimenez⁷, Marie-Claire Cyrille¹, Ricardo Ferreira², Martin Kreissig⁴, Rui Ma⁴, Frank Ellinger⁴, Romain Lebrun⁶, Steffen Wittrock⁶, Vincent Cros⁶, Paolo Bortolotti⁵
¹Commissariat à l'Énergie Atomique et aux Énergies Alternatives, France; ²International Iberian Nanotechnology Laboratory, Braga, Portugal; ³SPINTEC / Université Grenoble Alpes, France; ⁴Technische Universität Dresden, Germany; ⁵Thales Research & Technology, France; ⁶Unite Mixte de Physique CNRS-Thales / Université Paris-Sud / Université Paris Saclay, France; ⁷Université Grenoble Alpes / Commissariat à l'Énergie Atomique et aux Énergies Alternatives, France

A Fully Integrated Quartz MEMS VHF TCXO68

Randall Kubena¹, Frederic Stratton¹, Hung Nguyen¹, Deborah Kirby¹, David Chang¹, Richard Joyce¹, Yook-Kong Yong³, Jeffrey Garstecki², Matthew Cross², S. E. Seman²
¹HRL Laboratories, LLC, United States; ²Johns Hopkins University Applied Physics Laboratory, United States; ³Rutgers University, United States

DORIS-Class Oscillator Under Radiations: the Jason Family of Satellites.....72

Alexandre Belli², Pierre Exertier², Christian Jayles¹, François Vernotte³
¹Centre National d'Études Spatiales, France; ²Géoazur / Université de Nice Sophia-Antipolis / Observatoire de la Côte d'Azur, France; ³Université de Franche-Comté, France

High Precision Time Measurement Using a Self-Timed Ring Oscillator Based TDC77

Assia El-Hadbi², Abdelkarim Cherkaoui², Oussama Elissati¹, Laurent Fesquet²
¹Institut National des Postes et Télécommunications, Morocco; ²Université Grenoble Alpes, France

Impact of Static-Magnetic-Field-Gradients on Relaxation Times in a Rb Vapor Cell

Mohammadreza Gharavipour, Christoph Affolderbach, Florian Gruet and Gaetano Mileti
Laboratoire Temps-Fréquence (LTF), Institut de Physique
Université de Neuchâtel, Switzerland
Email: mohammadreza.gharavipour@unine.ch

Ivan S. Radojičić, Aleksandar J. Krmpot and
Branica M. Jelenković
Institute of Physics
University of Belgrade, Serbia

Abstract—We apply an innovative method called **Optically-Detected Spin-Echo** to measure the intrinsic coherence relaxation time in the buffer-gas vapor cell of a Rb atomic clock [1]. This method suppresses the influence of static-magnetic-field-gradients across the cell which is a source of relaxation processes. Such studies are of interest for high-performance Rb atomic clocks, where both intrinsic population and coherence relaxation times (T_1 and T_2 , respectively) of the “clock transition” ($5^2S_{1/2} |F_g = 1, m_F = 0\rangle \leftrightarrow |F_g = 2, m_F = 0\rangle$) are relevant.

Keywords—Relaxation times; Spin-Echo; Rb atomic clock;

I. INTRODUCTION

Alkali vapor cells are used in precision measurements applications such as vapor cell atomic frequency standards, navigation systems, optical magnetometry and quantum information storage [2-6]. They rely on long-lived ground-state spin-polarization of the alkali vapor in the cell [7]. In a vapor-cell atomic clock, the clock stability is limited by the linewidth and contrast of the atomic resonance line, which both are influenced by the relaxation processes in the cell. Alkali atoms in a buffer-gas vapor cell may lose their polarizations due to collisions with the cell-walls, with the buffer-gas atoms, and among themselves (spin-exchange). These processes are well described by the relaxation theory in [2]. Based on this theory and above mentioned processes, we determine both intrinsic population and coherence relaxation times T_1 and T_2 , respectively, approximately equal to 4.5 ms specifically for the “clock transition” ($5^2S_{1/2} |F_g = 1, m_F = 0\rangle \leftrightarrow |F_g = 2, m_F = 0\rangle$) of Rb atoms in our particular buffer-gas cell (see section II). The term “intrinsic” describes the relaxations that depend on the cell’s properties only, such as cell temperature, pressure and the cell geometry, but do not depend on any external electro-magnetic field. In a vapor-cell atomic clock, a static magnetic field is applied to lift the Zeeman degeneracy. The alkali atoms may experience various static magnetic fields due to some residual static-magnetic-field-gradients (SMFG) across the cell. The SMFG may also give rise to an additional relaxation source like in Nuclear Magnetic Resonance (NMR)

This work was supported by the Swiss National Science Foundation (SNSF grant no. 162346), the European Metrology Research Programme (EMRP project IND55-Mclocks), SNSF-Scopes project (152511) and Ministry of Education Science and Technological Development of Republic Serbia (III 45016 and OI 171038). The EMRP is jointly funded by EMRP participating countries within EURAMET and the European Union.

[8]. In NMR experiments the total coherence relaxation time, conventionally denoted T_2^* , is shorter than the intrinsic coherence relaxation time T_2 due to the static magnetic field inhomogeneity in the system that can be described by the local static magnetic field gradients, G . Then, the total coherence relaxation time is given by [9]:

$$T_2^{*-1} = T_2^{-1} + \eta G^2, \quad (1)$$

where η is a proportionality factor depending on atomic and experimental parameters.

In this article, we apply Optically-Detected Spin-Echo (ODSE) method demonstrated in [1] to suppress the impact of SMFG across a Rb vapor cell and measure T_2 time, while T_2^* is accessed using Ramsey method [10].

II. EXPERIMENTAL SETUP

Our experimental setup is a Rb atomic clock, whose details were presented in [11]. It contains three main components: 1) a frequency-stabilized laser system, 2) the clock physics package (PP), and 3) a microwave synthesizer. The laser system [12] consists of a distributed-feedback laser diode that emits at 780 nm, an evacuated ^{87}Rb reference cell and an acousto-optical-modulator (AOM). The AOM is used as a fast switch to control the duration and intensity of the laser pulses. The PP is based on a compact magnetron-type microwave cavity [13]. It resonates at the ^{87}Rb clock transition frequency ≈ 6.835 GHz, with a TE_{011} -like field-mode geometry. The microwave cavity surrounds a cylindrical glass cell with both diameter and height of 25 mm. The cell is filled with ^{87}Rb atomic vapor and a mixture of Argon and Nitrogen buffer-gases with a partial pressure ratio of $P_{\text{Ar}}/P_{\text{N}_2} = 1.6$. The microwave cavity is placed inside a C-field coil that generates a static magnetic field parallel to the cell’s symmetry axis and the laser propagation vector. The microwave synthesizer is used to generate a ≈ 6.835 GHz radiation resonant with the ^{87}Rb clock transition [14].

III. EXPERIMENTAL RESULTS AND DISCUSSIONS

The ODSE method is inspired by the Ramsey method [10] combined with the NMR spin-echo method presented in [15]. The timing sequence of the ODSE scheme is shown in the inset of Fig. 1. First, an optical pumping laser pulse creates a

population imbalance by depopulating the ^{87}Rb $F_g = 2$ and filling the $F_g = 1$ ground state. Then, in absence of light, a $\pi/2$ microwave pulse creates a coherent superposition of the two hyperfine $m_F = 0$ states involved in the clock transition. The spins dephase at different rates and their coherences start to decay due to the SMFG across the cell. After a free evolution time, T_{SE} (dephasing time), a phase-reversal π microwave pulse flips the spins and inverts the dephasing effect. After an additional free evolution time equal to the initial dephasing time, T_{SE} , the dephased states are rephased at the instant of the second $\pi/2$ microwave pulse. The second $\pi/2$ pulse converts the accumulated atomic phase into a population difference between the hyperfine states. Finally, optical density (OD) is measured in the cell with a laser pulse on the transition from $F_g = 2$ by using a photodetector. OD is defined by:

$$\text{OD} = -\ln(I_t/I_0), \quad (2)$$

where, I_0 and I_t are the incident and transmitted laser probe pulse intensities respectively.

In the ODSE method the detection of OD, i.e. of atomic population, is done with the laser. The Zeeman splitting in the $5S_{1/2}$ ground state is much smaller than the intrinsic optical and Doppler linewidths, thus laser detection delivers the population relaxation time, T_1 , involving *all* the Zeeman levels in the ground states $F_g = 1$ and $F_g = 2$ *simultaneously* (and not the clock levels only). However, because the microwave radiation does resolve the different Zeeman sublevels *individually*, we can selectively access T_2 of the clock transition *alone*. We vary T_{SE} and record OD consequently when the microwave frequency is detuned from the clock transition by a fixed amount of δ [10]. The experimental data shown in Fig. 1 is fitted by the equation:

$$\text{OD} = A + B \exp(-2T_{SE}/T_1^{\text{ODSE}}) + C \exp(-2T_{SE}/T_2^{\text{ODSE}}) \sin(4\pi\delta T_{SE} + \varphi), \quad (3)$$

where A , B , C , T_1^{ODSE} , T_2^{ODSE} , δ and φ are the fitting parameters. The fit gives both the relaxation times of $T_1^{\text{ODSE}} = 3.21 \pm 0.05$ ms and $T_2^{\text{ODSE}} = 4.30 \pm 0.85$ ms. T_1^{ODSE} refers to the population relaxation time for the transitions between all m_F levels and T_2^{ODSE} is specific to the clock transition. The measured T_2^{ODSE} is in a good agreement with the predicted intrinsic coherence relaxation time T_2 (≈ 4.5 ms).

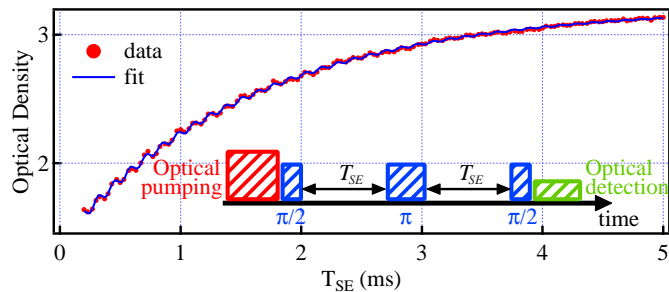


Fig. 1. Optical density of the vapor cell in the ODSE scheme. Solid red circles are the experimental data and blue curve is a fit based on equation (3). Inset: Timing sequences of ODSE scheme.

The relaxation times were also measured using the Ramsey method [10], in the same vapor cell and the same static magnetic field as used for the ODSE measurements. We found $T_1^{\text{Ramsey}} = 3.20 \pm 0.01$ ms and $T_2^{\text{Ramsey}} = 3.95 \pm 0.25$ ms. The obtained T_1 's were consistent in both methods, while T_2^{Ramsey} was shorter than T_2^{ODSE} (and also the predicted T_2) due to SMFG across the vapor cell. The measured relaxation times with ODSE method show higher uncertainties compared to the ones from Ramsey method. This can be attributed to the lower signal contrast due to the longer complete interrogation cycle in the case of ODSE.

IV. CONCLUSION

We have demonstrated that by using the ODSE method, the additional dephasing contributions arising from SMFG across a vapor cell can be suppressed. Such SMFG-induced dephasing can be considerable, even for our well-designed atomic clock PP with field gradients on the order of 2 – 4 % (obtained by measuring the broadening of the Zeeman linewidths and from [16]). Thus, the ODSE method allows measuring the intrinsic T_2 , in good agreement with the relaxation theory. The current uncertainties in T_2^{ODSE} could be reduced by enhancing the signal contrast and by reducing the signal noise. The ODSE method is also of high interest to characterize T_2 in other quantum-optics systems, e.g. cold atoms or solid-state systems such as nitrogen-vacancy centres in diamond, for applications in quantum information, quantum memories, quantum sensing or quantum metrology [17-20].

ACKNOWLEDGMENT

We thank A. K. Skrivervik and A. Ivanov (both EPFL-LEMA) for their support on the microwave cavity, C. Calosso (INRIM) for providing the microwave LO, and M. Pellaton (LTF) for helpful discussions. We thank our former colleague S. Kang for his contributions to the early phases of the work.

REFERENCES

- [1] M. Gharavipour, C. Affolderbach, F. Gruet, I. S. Radojčić, A. J. Krmpot, B. M. Jelenković, and G. Miletì, "Optically-Detected Spin-Echo method for relaxation times measurements in a Rb atomic vapor," *New J. Phys.*, 19 063027, 2017.
- [2] J. Vanier and C. Audoin, "The Quantum Physics of Atomic Frequency Standards". Bristol, U.K.: Adam Hilger, 1989.
- [3] J. Camparo, "The Rb atomic clock and basic research," *Phys. Today* 60 33, 2007.
- [4] F. X. Esnault *et al.* "HORACE: a compact cold atom clock for Galileo," *J. Adv. Space Res.* 47 (5), 854, 2011.
- [5] D. Budker and M. Romalis, "Optical magnetometry," *Nature Physics* 3 227, 2007.
- [6] B. Julsgaard, A. Kozhokin and E. S. Polzik, "Experimental long-lived entanglement of two macroscopic objects," *Nature* 413 400, 2001.
- [7] D. Budker *et al.* "Resonant nonlinear magneto-optical effects in atoms," *Rev. Mod. Phys.* 74 115, 2002.
- [8] H. Y. Carr and E. M. Purcell, "Effects of diffusion on free precession in NMR experiments," *Phys. Rev.*, 94, no. 3, pp. 630, 1954.
- [9] H. C. Torrey, "Bloch equations with diffusion terms," *Phys. Rev.*, 104, 3, 563, 1956.
- [10] A. Horsley, G.-X. Du, M. Pellaton, C. Affolderbach, G. Miletì, and P. Treutlein, "Imaging of relaxation times and microwave field strength in a microfabricated vapor cell," *Phys. Rev. A*, vol. 88, p. 063407, 2013.

- [11] M. Gharavipour, C. Affolderbach, S. Kang, T. Bandi, F. Gruet, M. Pellaton and G. Mileti "High performance vapour-cell frequency standards," *Jour. of Phys.: Conf. Series* 723 012006, 2016.
- [12] F. Gruet, M. Pellaton, C. Affolderbach, T. Bandi, R. Matthey and G. Mileti "Compact and frequency stabilized laser heads for Rubidium atomic clocks", *Proc. ICSO- Ajaccio, Corsica*, 9-12 Oct. 2012 no. 48.
- [13] C. Stefanucci, T. Bandi, F. Merli, M. Pellaton, C. Affolderbach, G. Mileti and A. K. Skrivervik "Compact microwave cavity for high performance Rb frequency standards," *Rev. Sci. Instrum.* 83 104706, 2012.
- [14] C. E. Calosso, S. Micalizio, A. Godone, E. K. Bertacco and F. Levi "Electronics for the pulsed Rb clock: design and characterization," *IEEE Trans. Ultrason. Ferroelectr. Freq. Cont.* 54 1731, 2007.
- [15] E. L. Hahn "Spin echos," *Phys. Rev.* 80 580, 1950.
- [16] C. Affolderbach, G. Du, T. Bandi, A. Horsley, P. Treutlein and G. Mileti "Imaging microwave and DC magnetic fields in vapour-cell Rb atomic clock," *IEEE Trans. on Instrum. and Meas.* 64, no 12, 3629, 2015.
- [17] G. Wolfowicz, H. Maier-Flaig, R. Marino, A. Ferrier, H. Vezin, J. J. L. Morton and P. Goldner "Coherent Storage of Microwave Excitations in Rare-Earth Nuclear Spins," *Phys. Rev. Lett.* 114 170503, 2015.
- [18] J. H. Shim, I. Niemeyer, J. Zhang and D. Suter "Robust dynamical decoupling for arbitrary quantum states of a single NV center in diamond," *Europhysics Letters* 99 4, 2012.
- [19] M. Hosseini, B. M. Sparkes, G. Campbell, P. K. Lam and B. C. Buchler, "High efficiency coherent optical memory with warm rubidium vapour," *Nature Comms.* 2 174, 2011.
- [20] W. Tittel, M. Afzelius, T. Chanelière, R. L. Cone, S. Kröll, S. A. Moiseev and M. Sellars "Photon-echo quantum memory in solid state systems," *Laser & Photon. Rev.* 4 244, 2010.

<p style="text-align:center">ICTON III Chair: Jarmila Müllerová (16:50-18:30 Monday, July 11)</p>	<p style="text-align:center">OWW II Chair: Goran Djordjevic (16:40-18:10 Monday, July 11)</p>	<p style="text-align:center">FiWiN5G I Chair: Nikos Pleros (16:10-17:45 Monday, July 11)</p>	<p style="text-align:center">SWP III Chair: Oksana Shramkova (16:50-18:30 Monday, July 11)</p>	<p style="text-align:center">NAON II Chair: Judy Rorison (16:50-18:25 Monday, July 11)</p>	<p style="text-align:center">CTS I Chair: Kira Kastell (17:00-18:40 Monday, July 11)</p>
<p>16:50 Mo.D1.1 On the group delay statistics of few-mode fibres with intermediate linear mode coupling (<i>Invited</i>) F.M. Ferreira, N. Mac Suibhne, C. Sánchez, M. Sorokina, S. Sygletos, A. Ellis</p> <p>17:10 Mo.D1.2 Accurate modal characterization of optical fibers using acousto-optics (<i>Invited</i>) E. Alcusa-Sáez, A. Díez, M.V. Andrés</p> <p>17:30 Mo.D1.3 Long period gratings in multicore fibers: Components for space division multiplexing systems (<i>Invited</i>) A.M. Rocha, T. Almeida, M. Facção, R.N. Nogueira</p> <p>17:50 Mo.D1.4 The role of distributed Raman amplification in the times of the "capacity crunch" (<i>Invited</i>) J.D. Ania-Castañón, P. Rosa, G. Rizzelli, F. Gallazzi, J. Nuño, P. Corredera</p> <p>18:10 Mo.D1.5 Higher order mode optical fiber Raman amplifiers (<i>Invited</i>) K. Rottwitz, S.M.M. Friis, M.A. Usuga Castaneda, E.N. Christensen, J.G. Kofoed</p>	<p>16:40 Mo.D2.1 Cognitive optical wireless network (<i>Invited</i>) V.W.S. Chan</p> <p>17:00 Mo.D2.2 Continuous tracking in free space optical balloon mesh networks (<i>Invited</i>) M.B. Awan, S. Mohan</p> <p>17:20 Mo.D2.3 Synchronization and channel estimation for optical block-transmission systems with IM/DD (<i>Invited</i>) M. Wolf, S.A. Cheema, M. Haardt</p> <p>17:40 Mo.D2.4 Performance investigation of OCT precoding for MIMO-OFDM based indoor visible light communications Yang Hong, Lian-Kuan Chen</p> <p>17:55 Mo.D2.5 Reduction of inter-cell interference in asynchronous multi-cellular VLC by using OFDMA-based cell partitioning Sun-Young Jung, Do-Hoon Kwon, Se-Hoon Yang, Sang-Kook Han</p>	<p>16:10 Mo.D3.1 Photonics-based transceivers for fiber-wireless networks (<i>Invited</i>) P. Ghelfi, F. Laghezza, F. Scotti, G. Serafino, C. Porzi, A. Bogoni</p> <p>16:30 Mo.D3.2 The new flexible mobile fronthaul: Digital or analog, or both? (<i>Invited</i>) N.J. Gomes, P. Assimakopoulos, M.K. Al-Hares, U. Habib, S. Noor</p> <p>16:50 Mo.D3.3 5G radio over fiber for small-cells (<i>Invited</i>) F. Ponzini, L. Giorgi</p> <p>17:10 Mo.D3.4 The effect of different queuing regimes on a switched Ethernet fronthaul M.K. Al-Hares, P. Assimakopoulos, S. Hill, N.J. Gomes</p> <p>17:25 We.C2.1 Requirements for 5G fronthaul (<i>Invited, moved from session We.C2</i>) L. Valcarenghi, K. Kondepu, F. Giannone, P. Castoldi</p>	<p>16:50 Mo.D4.1 Optical sensing from plasmonic metamaterials (<i>Invited</i>) I. Mbonson, S. Tabor, S.G. McMeekin, B. Lahiri, R.M. De la Rue, N.P. Johnson</p> <p>17:10 Mo.D4.2 New microphotonic resonant devices for label-free biosensing (<i>Invited</i>) C. Ciminelli, F. Dell'Olio, D. Conteduca, F. Innone, T. Tatoli, M.N. Armenise</p> <p>17:30 Mo.D4.3 Technology of hybrid plasmonic devices for optical bio-sensing (<i>Invited</i>) L. Wosinski, Xu Sun, L. Thylén</p> <p>17:50 Mo.D4.4 Nonlinear optical effects used for investigations on biological samples at micro and nanoscale (<i>Invited</i>) G.A. Stanciu, D.E. Tranca, S.G. Stanciu, C. Stoichita, A. Toma</p> <p>18:10 Mo.D4.5 Influence of laser beam quality on modal selection in tapered optical fibers for multipoint optogenetic control of neural activity (<i>Invited</i>) A. Della Patria, M. Pisanello, L. Sileo, M. De Vittorio, F. Pisanello</p>	<p>16:50 Mo.D5.1 Monolithic high contrast grating VCSELs: Concept and prospects (<i>Invited</i>) M. Gebbski, M. Marciniak, M. Dems, J.A. Lott, T. Czyszanowski</p> <p>17:10 Mo.D5.2 Performance characteristics of GaSb-based TJ-VCSELs with emission wavelength above 2.6 µm (<i>Invited</i>) Ł. Piskorski, J. Walczak, M. Marciniak, P. Belling, M. Dems, W. Nakwaski</p> <p>17:30 Mo.D5.3 Single-mode 1.5-µm VCSELs with small-signal bandwidth beyond 20 GHz (<i>Invited</i>) S. Spiga, A. Andrejew, G. Boehm, M-C. Amann</p> <p>17:50 Mo.D5.4 Electro-optical modulation processes in Si-MOS LEDs operating in the avalanche light emission mode (<i>Invited</i>) Kaikai Xu</p> <p>18:10 Mo.D5.5 Characterization and equalization of nonlinearities in directly modulated resonant cavity light-emitting diodes M. Schüppert, C-A. Bunge</p>	<p>17:00 Mo.D6.1 Replacement of the controller area network (CAN) protocol for future automotive bus system solutions by substitution via optical networks (<i>Invited</i>) D. Kraus, E. Leitgeb, T. Plank, M. Löschnigg</p> <p>17:20 Mo.D6.2 Optical backhaul network planning for DSRC-based public intelligent transportation system: A case study (<i>Invited</i>) E. Grigoreva, C. Mas Machuca, W. Kellerer</p> <p>17:40 Mo.D6.3 Tip timing measurements for structural health monitoring in the first stage of the compressor of an aircraft engine (<i>Invited</i>) I. García, R. Przynsowa, J. Zubia, J. Villatoro, J. Mateo, C. Vázquez</p> <p>18:00 Mo.D6.4 Research of opportunities of short-range radar to prevent flight accidents (<i>Invited</i>) A. Ananenkov, Y. Likharev, V. Rastorguev, P. Sokolov</p> <p>18:20 Mo.D6.5 Experimental characterization of transmission properties in multi-core plastic optical fibers (<i>Invited</i>) A. López, S. Ramón, M. Chueca, M.A. Losada, F.A. Domínguez-Chapman, J. Mateo</p>

19:00 **Social event at Gallerie Piedicastello**
Tuesday, July 12

FOCUS Chair: **Prince Anandarajah** (9:00-11:00 Tuesday, July 12) **Track 7 – ROOM 227**

9:00 Tu.A7.1 Numerical simulation and analysis of single section quantum dot lasers for optical comb generation (<i>Invited</i>), M. Gioannini, P. Bardella, L. Columbo, I. Montrosset	9:20 Tu.A7.2 Investigation of novel materials for future communication needs: Quantum dots and highly-mismatched alloys (<i>Invited</i>), J.M. Rorison, C. Broderick, W. Xiong, Q. Wang	9:40 Tu.A7.3 Pulse train stability of multi-gigahertz passively mode-locked semiconductor lasers (<i>Invited</i>), O. Nikiforov, L. Jaurigue, C. Weber, L. Drzewietzki, K. Lüdge, S. Breuer	10:00 Tu.A7.4 On-chip multi-wavelength laser sources fabricated using generic photonic integration technology (<i>Invited</i>), S. Latkowski, K. Williams, E. Bente	10:20 Tu.A7.5 Terahertz wireless communications using photonic and electronic devices (<i>Invited</i>), G. Ducournau, P. Szriftgiser, F. Pavanello, P. Latzel, M. Zaknoune, E. Peytavit, D. Bacquet, J-F. Lampin	10:40 Tu.A7.6 Nanoseconds wavelength and space optical cross-connect switches for high performance optical network (<i>Invited</i>), N. Calabretta, Wang Miao, K. Williams
--	---	---	---	--	--

Track 1 – ROOM 3	Track 2 – ROOM 7	Track 3 – ROOM 6	Track 4 – ROOM 221	Track 5 – ROOM 223	Track 6 – ROOM 224
<p style="text-align:center">ICTON IV Chair: Masatoshi Suzuki (8:30-10:20 Tuesday, July 12)</p>	<p style="text-align:center">OWW III Chair: Wen-De Zhong (8:30-10:00 Tuesday, July 12)</p>	<p style="text-align:center">WAOR I Chair: Xavier Hesselbach (8:30-10:10 Tuesday, July 12)</p>	<p style="text-align:center">SWP IV Chair: Brana Jelenković (8:30-10:25 Tuesday, July 12)</p>	<p style="text-align:center">NAON III Chair: Adonis Bogris (8:30-9:50 Tuesday, July 12)</p>	<p style="text-align:center">CTS II Chair: Vladimir Rastorguev (8:30-10:05 Tuesday, July 12)</p>
<p>8:30 Tu.A1.1 Multi-dimensional demappers for optical fiber systems with soft-decision forward error correction (<i>Invited</i>) T. Fehenberger N. Hanik</p>	<p>8:30 Tu.A2.1 Approaching terabit serial optical transmission over strong atmospheric turbulence channels (<i>Invited</i>) Zhen Qu, I.B. Djordjevic</p>	<p>8:30 Tu.A3.1 Optical layer-driven network restoration and redesign for improved fast reroute reliability (<i>Invited</i>) Zhen Lu, Y. Jayabal, M. Razo, M. Tacca, A. Fumagalli, G.M. Galimberti, G. Martinelli, G. Swallow</p>	<p>8:30 Tu.A4.1 Surface enhanced Raman scattering in surgery and forensics (<i>Invited</i>) C. Micsa, C. Rizea, M.I. Rusu, N.D. Becherescu-Barbu, R. Munteanu, M.V. Udrea, B. Chircuta, A. Parau, A. Tonetto, R. Notonier, I.A. Birtoiu, C.E.A. Grigorescu</p>	<p>8:30 Tu.A5.1 Improving SOA direct modulation capability with optical filtering (<i>Invited</i>) Z.V. Rizou, K.E. Zoiros, P. Morel</p>	<p>8:30 Tu.A6.1 Analysis of planning constraints for wireless access in vehicular environments with respect to different mobility and propagation models (<i>Invited</i>) K. Kastell</p>
<p>8:50 Tu.A1.2 Layered LDPC decoding for turbo-differential decoding in presence of cycle slips in optical communications (<i>Invited</i>) C. Cabiroi, W. Sauer-Greff, R. Urbansky</p>	<p>8:50 Tu.A2.2 Design of high speed free space optical channels (<i>Invited</i>) M. Cvijetic</p>	<p>8:50 Tu.A3.2 State-dependent connection admission control and routing and spectrum assignment in multirate flex-grid optical networks (<i>Invited</i>) R. Romero Reyes, T. Bauschert</p>	<p>8:50 Tu.A4.2 Pulse and multifrequency near-field subsurface diagnostics (<i>Invited</i>) K.P. Gaikovich</p>	<p>8:50 Tu.A5.2 40 GBd D(Q)PSK and OOK amplification using O-band quantum-dot semiconductor optical amplifiers (<i>Invited</i>) H. Schmeckeber, A. Zeghuzi, D. Arsenijević, M. Stubenrauch, C. Meuer, C. Schubert, C.A. Bunge, D. Bimberg</p>	<p>8:50 Tu.A6.2 Radio-over-fibre based high-speed millimetre-wave backhaul system for high-speed trains (<i>Invited</i>) T. Kawanishi, A. Kanno, P.T. Dat, N. Yamamoto</p>
<p>9:10 Tu.A1.3 Hammerstein-based equalizer for nonlinear compensation in coherent OFDM long-reach PONs (<i>Invited</i>) J. Torres-Zugaide, I. Aldaya, G. Campuzano, G. Castanon</p>	<p>9:10 Tu.A2.3 Moderate-to-strong turbulence generation in a laboratory indoor free space optics link and error mitigation via RaptorQ codes (<i>Invited</i>) R. Pernice, A. Andò, A. Parisi, A.C. Cino, A.C. Busacca</p>	<p>9:10 Tu.A3.3 Spectrally efficient operation of mixed fixed/flexible-grid optical networks with sub-band virtual concatenation (<i>Invited</i>) Ya Zhang, Longfei Li, Yongcheng Li, S.K. Bose, Gangxiang Shen</p>	<p>9:10 Tu.A4.3 Optical single pixel detection for compressive sensing with unitary circulant matrices (<i>Invited</i>) D. Pastor-Calle, A. Pastuszczak, M. Mikołajczyk, R. Kotyński</p>	<p>9:10 Tu.A5.3 All-optical memory based on quantum dot semiconductor optical amplifiers (QD-SOAs) for advanced modulation formats (<i>Invited</i>) Y. Ben Ezra, B.I. Lembrikov</p>	<p>9:10 Tu.A6.3 Coordination and agreement among traffic signal controllers in urban areas (<i>Invited</i>) M-D. Cano, R. Sanchez-Iborra, F. Garcia-Sanchez, A-J. Garcia-Sanchez, J. Garcia-Haro</p>
<p>9:30 Tu.A1.4 Multidimensional OFDM for programmable adaptive optical transceivers (<i>Invited</i>) J.M. Fabrega M. Svaluto Moreolo</p>	<p>9:30 Tu.A2.4 Performance analysis of a hybrid QAM-MPPM technique under gamma-gamma turbulent channels H.S. Khallaf, T. Ismail, H.M.H. Shalaby, S. Sampei</p>	<p>9:30 Tu.A3.4 Modulation format-aware restoration and re-optimization in flexgrid optical networks (<i>Invited</i>) L. Gifre, M. Ruiz, L. Velasco</p>	<p>9:30 Tu.A4.4 Design of silicon ring resonators for CO₂ detection (<i>Invited</i>) Yaping Zhang, Siyu Zhao, Beinuo Lu</p>	<p>9:30 Tu.A5.4 Stabilization of semiconductor amplifiers with large linewidth enhancement factors (<i>Invited</i>) S. Kumar, M. Botey, R. Herrero, K. Staliunas</p>	<p>9:30 Tu.A6.4 On-board computer network for information support of unmanned mobile vehicles control systems (<i>Invited</i>) S.M. Sokolov, A.A. Boguslavsky</p>
<p>10:05 Tu.A1.5 Phase noise impact on directly detected optical OFDM transmission in uncompensated links S. Mandelli, A. Gatto, M. Magarini, P. Boffi, P. Martelli, S. Pecorino, A. Spalvieri</p> <p>10:05 Tu.A1.6 Bit loading-based irregular LDPC coded-modulation for high-speed optical communications Ding Zou, I.B. Djordjevic</p>	<p>9:45 Tu.A2.5 Performance analysis of SIM-DPSK FSO system over lognormal fading with pointing errors T. Ismail, E. Leitgeb</p>	<p>9:50 Tu.A3.5 Indirect crosstalk-aware routing and wavelength assignment in transparent optical networks with the use of generic algorithms (<i>Invited</i>) D. Monoyios, K. Manousakis, C. Christodoulou, A. Hadjiantonis, K. Vlachos, G. Ellinas</p>	<p>9:50 Tu.A4.5 Ultrasensitive sensors based on specialty optical fibres (<i>Invited</i>) J. Villatoro, J. Zubia</p> <p>10:10 Tu.A4.6 Modified noiselet transform and its application to compressive sensing with optical single pixel detectors A. Pastuszczak, B. Szczygieł, M. Mikołajczyk, R. Kotyński</p>		<p>9:50 Tu.A6.5 Access and resource reservation in vehicular visible light communication networks M. Garai, M. Siliti, N. Boudriga</p>

Coffee break (10:20-10:50) / Coffee break (10:00-10:30) / Coffee break (10:10-10:40) / Coffee break (10:25-10:50) / Coffee break (9:50-10:20) / Coffee break (10:05-10:30)					
Track 1 – ROOM 3	Track 2 – ROOM 7	Track 3 – ROOM 6	Track 4 – ROOM 221	Track 5 – ROOM 223	Track 6 – ROOM 224
<p style="text-align:center">ICTON V Chair: Stefan Wabnitz (10:50-12:30 Tuesday, July 12)</p> <p>10:50 Tu.B1.1 Bright and dark vector rogue waves (<i>Tutorial</i>) S.V. Sergeyev, Chengbo Mou, S. Kolpakov, V. Kalashnikov</p>	<p style="text-align:center">OWW IV Chair: Mike Wolf (10:50-12:00 Tuesday, July 12)</p> <p>10:30 Tu.B2.1 BER analysis of WiMAX on FSO (<i>Invited</i>) G.T. Djordjevic, I.B. Djordjevic</p>	<p style="text-align:center">WAOR II Chair: Andrea Fumagalli (10:50-12:20 Tuesday, July 12)</p> <p>10:40 Tu.B3.1 Scalable elastic optical path networking models (<i>Invited</i>) B. Jaumard, M. Daryalal</p>	<p style="text-align:center">SWP V Chair: Satoshi Ishii (10:50-12:30 Tuesday, July 12)</p> <p>10:50 Tu.B4.1 Graphene and polarisable nanoparticles: Looking good together? (<i>Invited</i>) M.I. Vasilevskiy, J.E. Santos, R.M. Pereira, Yu.V. Bludov, F. Vaz, N.M.R. Peres</p>	<p style="text-align:center">NAON IV Chair: Stefan Breuer (10:20-12:00 Tuesday, July 12)</p> <p>10:20 Tu.B5.1 Silicon photonics based on Ge/SiGe quantum well structures (<i>Invited</i>) D. Marris-Morini, V. Vakarin, P. Chaisakul, J. Frigerio, M. Rahman, J.M. Ramirez, M-S. Rouifed, D. Chrastina, X. Le Roux, G. Isella, L. Vivien</p>	<p style="text-align:center">ESPC III Chair: Martina Gerken (10:30-12:20 Tuesday, July 12)</p> <p>10:30 Tu.B6.1 Hybrid photonic crystal lasers (<i>Invited</i>) A.A. Liles, A.P. Bakoz, A.A. Gonzalez, T. Habruseva, S. Persheyev, G. Huyet, S.P. Hegarty, L. O’Faolain</p>

Slow and Stored Light in Amplifying Four Way Mixing Process

Bojan Zlatković, Aleksandar Krmpot, Ivan Radojičić, Dušan Arsenović, Milan Minić,
and Brana Jelenković

Institute of physics, University of Belgrade, Pregrevica 118, 11080 Belgrade, Serbia

Tel: (38111) 3713 107, e-mail: branaj@ipb.ac.rs

ABSTRACT

We have investigated experimentally and theoretically four-wave mixing (FWM) in hot potassium vapor as a medium for producing slow and store light. Two pump and a single probe photon were mixed in double- Λ system, characterized by parametric amplification of coupled co-propagating probe and conjugate beams. We have observed very high gains of probe and conjugate, up to 60 and 80 respectively, at two photon Raman resonance, under large one photon detuning, and high K-cell temperature. Using an amplifying medium to alleviate the absorption and distortion of propagating pulses are important for slow-light propagation. We observed ultraslow propagation of probe and conjugate pulses under conditions when parametric amplification of twin beams is well below their maximum values. A fractional delays of close to 5 at a gain ~ 1.5 , for the probe pulse of 20 ns, have been achieved simultaneously for both probe and accompanying conjugate pulse. FWM mixing process under conditions of the experiment results in broadening of twin beams, close to observed delays.

Keywords: four way mixing, electromagnetically induced transparency, slow light, potassium.

1. INTRODUCTION

Four-wave mixing (FWM) in the double lambda configuration in alkalis has been intensively studied since electromagnetically induced transparency (EIT) in double-atomic systems allows control of the FWM process, and often brings large parametric gains of twin beams, probe and conjugate. There are only few works on FWM in potassium vapor [1,2], all done with counter propagating pump and probe beams. On the other hand, potassium ^{39}K ground state hyperfine splitting is only 461 MHz, lower than in any other alkali atom, In potassium, transitions originating from both ground state hyperfine sublevels are completely overlapped because of Doppler broadening. This affects the dynamics of pumping and repopulating ground state hyperfine sublevels in a different way than in other alkali atoms. Moreover, atomic susceptibilities that govern the FWM process should be higher in atoms with lower hyperfine splitting [3].

In this work we have studied slow light in hot K vapor under different parametric gains of twin beams. The transmission line shape of the twin beams under FWM conditions look like a Lorentzian transmission, and the dispersion within the gain profile give rise to slow light. We have investigated, experimentally and theoretically, gains of twin beams and their fractional delays and broadening under different two photon Raman detuning, one photon (pump) detuning, K atom density and pump beam intensity.

In the experiment and in the model, pump and probe beams are co-propagating and intersect under a small angle in the K - cell. Probe and conjugate are detected as they exit the cell. This scheme is suitable to investigate other properties of FWM, like relative intensity squeezing between twin beams, since FWM has been identified as a very efficient process to generate non classical beams [4].

We show experimentally and numerically that a double-Lambda system in K vapor, characterized by parametric amplification of coupled probe and four-wave mixing pulses, is promising medium for producing slow light and also stored light. Moreover, this system can compensate for the absorption and broadening processes that usually occur without destroying the coherent properties of the medium. We are currently experimenting with storage of light pulses in Potassium.

2. EXPERIMENT AND MODEL

We use co-propagating orthogonally polarized pump and probe to couple three hyperfine levels via double- Λ scheme in D1 line in ^{39}K (Fig. 1a).

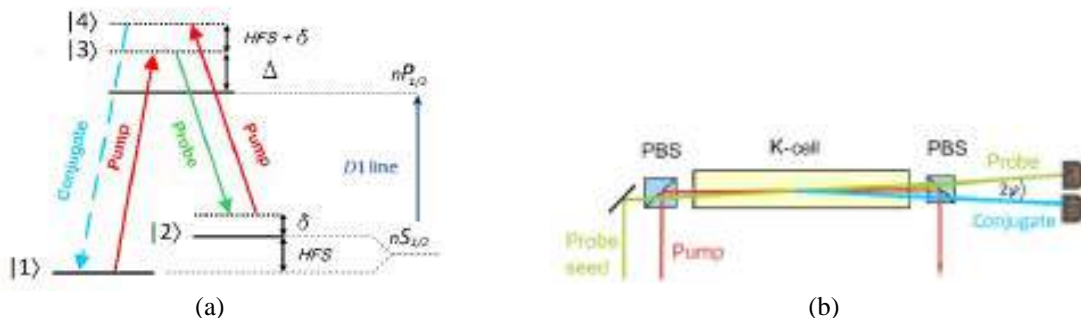


Figure 1. Schematic of a) atomic level diagram for FWM in K and b) experimental the setup.

Level $|3\rangle$ from Fig. 1 is $4P_{1/2}$ while two lower levels $|1\rangle$ and $|2\rangle$ are $4S_{1/2}$, $F=1$ and $4S_{1/2}$, $F=2$ respectively. Important feature of this set up (Fig. 1b) is the amplification in the FWM process and generation of the conjugate pulse, coupled to the probe and propagating alongside the probe.

In the experiment (Fig. 1b) pump (red) and probe (green) are combined on the polarization beam splitter (PBS). They intersect at a small angle φ inside the potassium vapor cell (K-cell). Exciting the cell are probe and conjugate (blue), detected by two photodiodes. The only light source is the single mode, frequently stabilized Ti:Sapphire at ~ 770 nm, used for both pump and probe seed beams. The probe seed (≈ 200 μ W), derived by extracting a small fraction of the pump is frequency shifted by the pair of AOM making the overall frequency offset between pump and probe close to the hyperfine splitting of the ^{39}K ground state. Two-photon detuning δ is scanned by changing the RF frequency fed to one of the AOM. The K cell temperature and thus the density of K atoms are controlled by the temperature of hot air flowing inside the ceramic cylinder with the K cell.

To obtain the physical insight in to the FWM processes, we first solve the Maxwell-Bloch equations for the probe and FWM fields and then the coupled equations for field propagation, equations (1) and 2),

$$\frac{d\hat{\rho}}{dt} = -\frac{i}{\hbar} [\hat{H}_A + \hat{H}_{AF}, \hat{\rho}] + S\hat{E} + \gamma(\hat{\rho}_0 - \hat{\rho}) \quad (1)$$

$$\left(\frac{\partial}{\partial z} + \frac{1}{c} \frac{\partial}{\partial t} \right) E^{(+)} = i \frac{k}{2\epsilon_0} P^{(+)} \quad (2)$$

where \hat{H}_A and \hat{H}_{AF} are free and atom-laser interaction Hamiltonians, $S\hat{E}$ denotes spontaneous emission, γ is relaxation rate to ground states $\hat{\rho}_0$, $E^{(+)}$ is positive frequency part of the electric fields and $P^{(+)}$ for macroscopic polarizations.

3. RESULTS AND DISCUSSION

We first made detailed analyses of parameters that affects gains of the probe and conjugate. Next, we compared waveforms of the reference (probe pulse before the K – cell) with the probe and conjugate pulses behind the cell for conditions corresponding to different gain levels. Optimal parameters for probe and conjugate gains, and for time delays between reference probe and probe and conjugate exciting the K-cell were selected after varying pump intensity, K-cell temperature (gas density), OPD and TPD.

3.1 Gain of Probe and Conjugate

We have investigated the dependence of the probe and the conjugate gain on two-photon detuning δ (TPD), one-photon detuning Δ (OPD), pump laser intensity and the density of K atoms. The gain of the probe and the conjugate is defined as $G_p = P_p/P_{p,in}$ and $G_c = P_c/P_{c,in}$, where P_p and P_c are measured powers of the probe and the conjugate, respectively, and P_{in} is initial power of the probe seed inside the amplifying medium.

Optimal parameters for high probe and conjugate gains are summarized in Fig. 2 where we have shown gains as a function of TPD for various OPD, for K cell temperature of 120°C ($\approx 3 \times 10^{12}$ atoms/cm 3), pump power of 400 mW and the probe seed power of 200 μ W. The angle between the pump and the probe was $\varphi = 3$ mrad.

The maximal gains of the probe and the conjugate were ~ 80 and ~ 60 respectively, for OPD = 700 MHz and TPD = -6 MHz. The maximum of gains at a particular OPD is due to competition between photon amplification and absorption^{13,20}. The trade-off is for OPD ~ 700 MHz which is close to Doppler broadening in K. Since the frequency of the conjugate is offset much further from the hyperfine splitting, for $\sim 2 \times 460$ MHz = 920 MHz, its absorption is weaker than the probe., leading to higher gains for the conjugate, as long as OPD is not very large, for instance over 1.3 GHz.

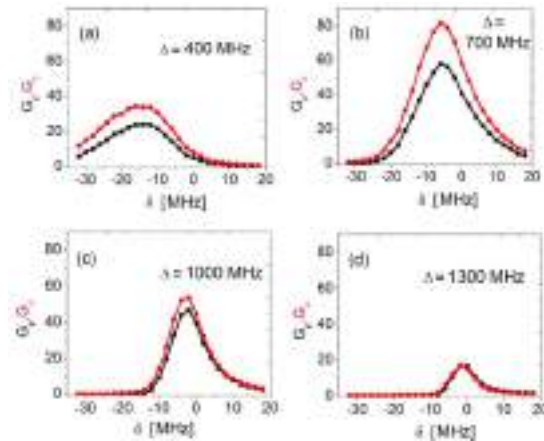


Figure 2. Schematic of a) atomic level diagram for FWM in K and b) experimental setup.

3.2 Slow Light

The probe pulses were either Gaussian or triangle. The necessary fast (10 – 100 ns) quasi-Gaussian excitation pulse was made by the fine shaping of the trapezoid pulse with a passive CLC pi-filter. Parameters of the trapezoid pulse (height, FWHM and rise time) were obtained by fitting the unit-height and unit-half-width Gaussian pulse with the symmetrical trapezoid waveform, in the range of ± 5 . After appropriate scaling for the half-widths of necessary Gaussian pulses, these optimal trapezoidal pulses were made by a pulse generator and sent to the CLC pi-filter with 50 ohms characteristic impedance and characteristic time constant $2\pi\sqrt{LC}/2$ equal to the pulse FWHM. In this way the breakpoints of the trapezoid pulse were well filtered with only a small asymmetry added. Each quasi-Gaussian pulse was generated with its own appropriate filter. The pulse was sent to EOM for shaping the fast probe pulse.

The main parameters affecting the propagation of twin beams, pulse fractional delays and broadening are pump power and pump OPD. Waveforms of the input (reference) probe and the probe and conjugate pulse at the output of the cell, for 20 ns reference pulse, OPD = 1.5 GHz, TPD = -1 MHz at the temperature of the cell 130 °C are given in Fig. 3.

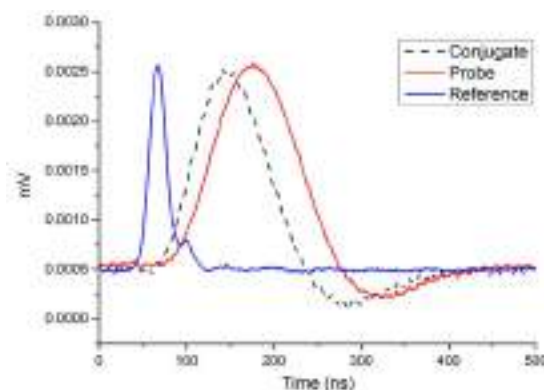


Figure 3. Waveforms of the reference (solid blue), probe (solid red) and conjugate (dashed black) at low gain and high OPD. The pump power was 400 mw, the probe power was OPD = 1.5 GHz.

The delay time of both probe and conjugate can be made longer when the gain is set lower. The conjugate pulse always precedes the probe pulse. Like in sodium [5] the model gives wider pulses at the output of the cell than what we observed. The theory and numerical simulation show similar behavior of twin beams. In the low pump power and low-gain regime the probe-pulse velocity is close to the EIT group velocity, at a low gain high pump power the conjugate velocity can be nearly twice as the probe. In the high-gain regime, the probe accelerates and twin beams propagate with the similar velocity $v_s = 2v_g$.

4. CONCLUSIONS

We explored experimentally and numerically generation process of non-degenerate FWM in Potassium, under double-Lambda atomic scheme. We have observed exceptionally high gain of twin beams, around 60 and 80 for probe and conjugate, under moderate pump power of 400 mW, near the Raman resonance of the pump and the probe, and at one-(pump) photon detuning close to Doppler broadening in K. Such high gain can be attributed to high atomic susceptibility in K, i.e., the lowest hyperfine splitting of the ground state of all alkalis.

We have shown slow light propagation of twin beams, with the conjugate pulse exciting the cell first. For very short input probe pulses of 10 – 20 ns, ultra-slow light effect and large fractional delay of 5 are observed. Pulse broadening at the cell output is large, nearly large as the delay between the reference pulse and the probe. Further optimization of parameters should help in narrowing the pulse widths, which is very important for applications of such systems in pulse repetition mode.

ACKNOWLEDGEMENTS

Authors acknowledge grant III45016 of the Serbian Ministry of education and science and technological development.

REFERENCES

- [1] D. S. Glassner and R. J. Knize: Reduced angular dependence for degenerate four-wave mixing in potassium vapor by including nitrogen buffer gas, *Appl. Phys. Lett.*, vol. 66, pp. 1593-1595 (1995).
- [2] M. Y. Lanzerotti *et al.*: High-reflectivity, wide-bandwidth optical phase conjugation via four-wave mixing in potassium vapor, *Appl. Phys. Lett.*, vol. 69, pp. 1199-1204 (1996).
- [3] M.T. Turnbull *et al.*: Role of the phase-matching conditions in nondegenerate four-way mixing in hot vapors for the generation of squeezed light, *Phys. Rev. A*, vol. 88, 033845-10 (2013).
- [4] C. F. McCormick *et al.*: Strong relative intensity squeezing by four-wave mixing in rubidium vapor, *Opt. Lett.*, vol. 32, 178-180 (2007).
- [5] J. Okuma *et al.*: Ultraslow matched-pulse propagation in sodium vapor, *Opt. Lett.*, vol. 64, pp. 1654-1656 (2009).



Serbian Ceramic Society Conference
ADVANCED CERAMICS AND APPLICATION IX
New Frontiers in Multifunctional Material Science and Processing

Serbian Ceramic Society
Institute of Technical Sciences of SASA
Institute for Testing of Materials
Institute of Chemistry Technology and Metallurgy
Institute for Technology of Nuclear and Other Raw Mineral Materials

PROGRAM AND THE BOOK OF ABSTRACTS

Serbian Academy of Sciences and Arts, Knez Mihailova 35
Serbia, Belgrade, 20-21. September 2021.

Serbian Ceramic Society Conference
ADVANCED CERAMICS AND APPLICATION IX
New Frontiers in Multifunctional Material Science and Processing

Serbian Ceramic Society
Institute of Technical Science of SASA
Institute for Testing of Materials
Institute of Chemistry Technology and Metallurgy
Institute for Technology of Nuclear and Other Raw Mineral Materials
PROGRAM AND THE BOOK OF ABSTRACTS

Serbian Academy of Sciences and Arts, Knez Mihailova 35
Serbia, Belgrade, 20-21. September 2021

Book title: Serbian Ceramic Society Conference - ADVANCED CERAMICS AND APPLICATION IX Program and the Book of Abstracts

Publisher:

Serbian Ceramic Society

Editors:

Prof.dr Vojislav Mitić

Dr Lidija Mančić

Dr Nina Obradović

Technical Editors:

Ivana Dinić

Marina Vuković

Printing:

Serbian Ceramic Society, Belgrade, 2021

Edition:

100 copies

CIP - Каталогизacija у публикацији
Народна библиотека Србије, Београд

666.3/.7(048)

66.017/.018(048)

SRPSKO KERAMIČKO DRUŠTVO. CONFERENCE ADVANCED CERAMICS AND APPLICATION : NEW FRONTIERS IN MULTIFUNCTIONAL MATERIAL SCIENCE AND PROCESSING (9 ;2021 ; BEOGRAD)

Program ; and the Book of abstracts / Serbian Ceramic Society Conference Advanced Ceramics and Application IX : New Frontiers in Multifunctional Material Science and Processing, Serbia, Belgrade, 20-21. September 2021 ; [organized by Serbian Ceramic Society ... [et al.] ; [editors Vojislav Mitić, Lidija Mančić, Nina Obradović]. - Belgrade : Serbian Ceramic Society, 2021 (Belgrade : Serbian Ceramic Society). - 93 str. : ilustr. ; 30 cm

Tiraž 100.

ISBN 978-86-915627-8-6

а) Керамика -- Апстракти б) Наука о материјалима -- Апстракти в) Наноматеријали -- Апстракти

COBISS.SR-ID 45804553



EUROPEAN ACADEMY
of Sciences and Arts

Dear colleagues and friends,

We have great pleasure to welcome you to the Advanced Ceramic and Application IX Conference organized by the Serbian Ceramic Society in cooperation with the Institute of Technical Sciences of SASA, Institute of Chemistry Technology and Metallurgy, Institute for Technology of Nuclear and Other Raw Mineral Materials and Institute for Testing of Materials.

It is nice to host you here in Belgrade in person. As you probably know, Serbia launched a vaccination campaign at the beginning of this year, so up to date more than 50 percent of the adult population has been vaccinated. Since there is no one statistic to compare the COVID19 outbreaks and fears for loved ones in different countries, we believe that we all suffer similarly during this pandemic. That is why we appreciate even more your positive attitude and readiness to travel in this uncertain time. We understand that some of you had to cancel your lectures in the last minute due to the travel limitation in your countries, but we hope that you will come next year. We deeply hope that the ACA IX Conference will be worth remembering, that you will respect all COVID-19 safety measures at SASA building, that you will have a nice time here and that ultimately you will return to your home safely. We are very proud that we succeeded in bringing the scientific community together again and fostering the networking and social interactions around an interesting program on emerging advanced ceramic topics. The chosen topics cover contributions from fundamental theoretical research in advanced ceramics, computer-aided design and modeling of new ceramics products, manufacturing of nanoceramic devices, developing of multifunctional ceramic processing routes, etc.

Traditionally, ACA Conferences gather leading researchers, engineers, specialists, professors and PhD students trying to emphasize the key achievements which will enable the widespread use of the advanced ceramics products in the High-Tech industry, renewable energy utilization, environmental efficiency, security, space technology, cultural heritage, etc.

Serbian Ceramic Society was initiated in 1995/1996 and fully registered in 1997 as Yugoslav Ceramic Society, being strongly supported by American Ceramic Society. Since 2009, it has continued as the Serbian Ceramic Society in accordance with Serbian law procedure. Serbian Ceramic Society is almost the only one Ceramic Society in South-East Europe, with members from more than 20 Institutes and Universities, active in 16 sessions. Part of our members are also members of the Serbian Chapter of ACerS since 2019. Their activities in the organization of this conference is highly recognized. To them and all of you thanks for being with us here at ACA IX.

Prof. Dr Vojislav Mitić
President of the Serbian Ceramic Society
World Academy Ceramics Member
European Academy of Sciences & Arts Member

Prof. Dr Olivera Milošević,
President of the General Assembly of the
Serbian Ceramic Society
Academy of Engineering Sciences of Serbia Member

Conference Topics

- Basic Ceramic Science & Sintering
- Nano-, Opto- & Bio-ceramics
- Modeling & Simulation
- Glass and Electro Ceramics
- Electrochemistry & Catalysis
- Refractory, Cements & Clays
- Renewable Energy & Composites
- Amorphous & Magnetic Ceramics
- Heritage, Art & Design

Conference Programme Chairs:

Dr. Lidija Mančić SRB
Dr. Nina Obradović SRB

Conference Co-chairs:

Prof. Dr. Vojislav Mitić SRB
Prof. Dr. Rainer Gadow GER

Scientific Committee

Academician Zoran Popović SRB
Academician Zoran Đurić SRB
Prof. Dr. Vojislav Mitić SRB
Prof. Dr. Rainer Gadow DEU
Prof. Dr. Marcel Van de Voorde EEZ
Prof. Dr. Wei Pan
Prof. Dr. Reuben Jin-Ru Hwu
Dr. Richard Todd GBR
Prof. Dr. Hans Fecht DEU
Prof. Dr. Olivera Milošević SRB
Prof. Dr. Vladimir Pavlović SRB
Dr. Nina Obradović SRB
Dr. Lidija Mančić SRB
Prof. Dr. Bojan Marinković BRA
Dr. Takashi Goto, Japan
Dr. Steven Tidrow, USA
Dr. Snežana Pašalić SRB
Prof. Dr. Zoran Nikolić SRB
Dr. Nebojša Romčević SRB
Dr. Zorica Lazarević SRB
Prof. Dr. Nebojša Mitrović SRB
Dr. Aleksandra Milutinović–Nikolić SRB
Dr. Predrag Banković SRB
Dr. Zorica Mojović SRB

Prof. Dr. Branislav Vlahović USA
Prof. Dr. Stevo Najman SRB
Prof. Dr. Vera Pavlović

Organizing Committee

Prof. Dr. Vojislav Mitić SRB
Dr. Lidija Mančić SRB
Dr. Nina Obradović SRB
Dr. Ivana Dinić SRB
Dr. Marina Vuković SRB
Dr. Suzana Filipović SRB
Dr. Maria Čebela
Dr. Nataša Jović Jovičević SRB
Dr. Vesna Paunović SRB
Dr. Vladimir Blagojević SRB
Dr. Darko Kosanović SRB
Dr. Vladimir Dodevski SRB
Dr. Ivana Radović SRB
Dr. Jelena Vujančević SRB
Dr. Jelena Živojinović SRB
Dr. Adriana Peleš Tadić SRB
Dr. Ana Radosavljević Mihajlović, SRB
Bojana Marković SRB

arrangement which could accommodate higher concentration of dopants at shorter distance. Stabilization of this phase in nanoparticles is usually achieved through thermal decomposition of organic precursors in the presence of solvents with a high boiling point. Here, for the same purpose, we used gadolinium co-doping during chitosan assisted solvothermal processing of inorganic precursor salts. Precursor concentration, solvent type, and synthesis time were varied in order to determine their influence on the β - $\text{NaY}_{0.65}\text{Gd}_{0.15}\text{F}_4:\text{Yb}_{0.18}\text{Er}_{0.02}$ phase crystallization. The XRPD analysis showed that lower surplus of fluoride ions during synthesis leads to formation of $\text{Y}_{0.65}\text{Gd}_{0.15}\text{F}_4:\text{Yb}_{0.18}\text{Er}_{0.02}$ orthorhombic phase, while the increase of fluoride content or prolongation of the processing time enhances formation α - $\text{NaY}_{0.65}\text{Gd}_{0.15}\text{F}_4:\text{Yb}_{0.18}\text{Er}_{0.18}$ phase. Along with it, the changes of UCNPs morphology from spindle to spherical shape is detected. All samples emit intense green emission due to the ($^2\text{H}_{11/2}$, $^4\text{S}_{3/2}$) \rightarrow $^4\text{I}_{15/2}$ electronic transitions, after been excited with infrared light ($\lambda=978$ nm).

INV

Nonlinear laser scanning microscopy for imaging of the cells labeled by up-converting $\text{NaYF}_4:\text{Yb,Er}$ nanoparticles

Mihailo D. Rabasovic¹, Ivana Dinic², Aleksandra Djukic-Vukovic³, Milos Lazarevic⁴, Marko G. Nikolic¹, Aleksandar J. Krmpot¹, Lidija Mancic²

¹Photonic Center, Institute of Physics Belgrade, University of Belgrade, Zemun, Belgrade, Serbia

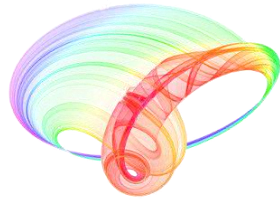
²Institute of Technical Sciences of the Serbian Academy of Sciences and Arts, Belgrade, Serbia

³Department of Biochemical Engineering and Biotechnology, Faculty of Technology and Metallurgy, University of Belgrade, Serbia

⁴Institute of Human Genetics, School of Dental Medicine, University of Belgrade, Serbia

The Nonlinear Laser Scanning Microscopy (NLSM) contributes to the cell labeling through addressing two main issues: photobleaching and phototoxicity. Moreover, an increase of the penetration depth and a reduction of background autofluorescence are achieved. We have used a multidisciplinary approach combining expertise in material science, nanoparticles synthesis and characterization, cancer cell and tissue labeling, and high resolution imaging, in order to accomplish *in vitro* imaging of the cancer cells. We have imaged the oral squamous carcinoma cells and human gingival cells. We have demonstrated that we are able to take high contrast images. We have shown position of the nanoparticles in cells, through co-localization of the cell auto-fluorescence and the nanoparticles up-conversion. We plan to improve our abilities through further optimization of the up-converting nanoparticles (smaller and brighter particles) and microscopy technique.

Book of abstracts



PHOTONICA2021

VIII International School and Conference on Photonics

& HEMMAGINERO workshop

23 - 27 August 2021,

Belgrade, Serbia

Editors

Mihailo Rabasović, Marina Lekić and Aleksandar Krmpot

Institute of Physics Belgrade, Serbia

Belgrade, 2021

ABSTRACTS OF TUTORIAL, KEYNOTE, INVITED LECTURES,
PROGRESS REPORTS AND CONTRIBUTED PAPERS

of

VIII International School and Conference on Photonics
PHOTONICA2021

23 - 27 August 2021

Belgrade Serbia

Editors

Mihailo Rabasović, Marina Lekić and Aleksandar Krmpot

Publisher

Institute of Physics Belgrade

Pregrevica 118

11080 Belgrade, Serbia

Printed by

Serbian Academy of Sciences and Arts

Number of copies

200

ISBN 978-86-82441-53-3

CIP - Каталогизacija у публикацији - Народна библиотека Србије, Београд

535(048)

621.37/.39:535(048)

621.37/.39:535]:61(048)

66.017/.018(048)

INTERNATIONAL School and Conference on Photonic (8; 2021; Beograd)

Book of abstracts / VIII International School and Conference on Photonics PHOTONICA2021 & HEMMAGINERO workshop, 23 - 27 August 2021, Belgrade, Serbia; editors Mihailo Rabasović, Marina Lekić and Aleksandar Krmpot. - Belgrade: Institute of Physics, 2021 (Belgrade: SASA). - V, 192 str.: ilustr.; 30 cm

Tiraž 200. - Bibliografija uz većinu apstrakata. - Registar.

ISBN 978-86-82441-53-3

1. Hemmaginero Workshop (2021; Beograd)

а) Оптика -- Апстракти б) Оптички материјали -- Апстракти в) Оптоелектроника -- Апстракти г) Оптоелектроника -- Биомедицина -- Апстракти д) Телекомуникације -- Апстракти

COBISS.SR-ID 44290057

PHOTONICA 2021 (VIII International School and Conference on Photonics - www.photonica.ac.rs) is organized by Institute of Physics Belgrade, University of Belgrade (www.ipb.ac.rs), Serbian Academy of Sciences and Arts (www.sanu.ac.rs), and Optical Society of Serbia (www.ods.org.rs).



PHOTONICA 2021 is organized under auspices and with support of the Ministry of Education, Science and Technological Development, Serbia (www.mpd.gov.rs).

The support of the sponsors of PHOTONICA 2021 is gratefully acknowledged:



Committees

Scientific Committee

- Aleksandar Krmpot, Serbia
- Aleksandra Maluckov, Serbia
- Bojan Resan, Switzerland
- Boris Malomed, Israel
- Branislav Jelenković, Serbia
- Carsten Ronning, Germany
- Concita Sibilica, Italy
- Darko Zibar, Denmark
- Dmitry Budker, Germany
- Dragan Inđin, United Kingdom
- Edik Rafailov, United Kingdom
- Francesco Cataliotti, Italy
- Giannis Zacharakis, Greece
- Goran Isić, Serbia
- Goran Mašanović, United Kingdom
- Ivana Vasić, Serbia
- Jasna Crnjanski, Serbia
- Jelena Radovanović, Serbia
- Jelena Stašić, Serbia
- Jerker Widengren, Sweden
- Jovan Bajić, Serbia
- Ljupčo Hadžievski, Serbia
- Luca Antonelli, UK
- Marco Canepari, France
- Marko Krstić, Serbia
- Marko Spasenović, Serbia
- Milan Kovačević, Serbia
- Milena Milošević, Serbia
- Milivoj Belić, Qatar
- Mirjana Novaković, Serbia
- Nikola Stojanović, Germany
- Nikola Vuković, Serbia
- Nikos Pleros, Greece
- Pavle Andjus, Serbia
- Petra Beličev, Serbia
- Sergei Turitsyn, UK
- Vladan Pavlović, Serbia
- Vladan Vuletić, USA
- Vladana Vukojević, Sweden
- Zoran Grujić, Serbia

Organizing Committee

- Marina Lekić, Institute of Physics Belgrade (Chair)
- Aleksandar Krmpot, Institute of Physics Belgrade (Co-Chair)
- Danica Pavlović, Institute of Physics Belgrade (Secretary)
- Stanko Nikolić, Institute of Physics Belgrade (Webmaster)
- Mihailo Rabasović, Institute of Physics Belgrade
- Tanja Pajić, Faculty of Biology, University of Belgrade
- Aleksandra Gočanin, Faculty of Physics, University of Belgrade
- Jadranka Vasiljević, Institute of Physics Belgrade
- Uroš Ralević, Institute of Physics Belgrade

Technical Organizer



Lufthansa City Center
Panacomp Wonderland
Travel

<http://www.panacomp.net/>

Tel: +381 21 466 075

Tel: +381 21 466 076

Tel: +381 21 466 077

Interaction of ultrashort laser pulses with hemoglobin as a tool for selective erythrocytes photo-labeling

M. Radmilovic¹, I. Drvenica², M. D. Rabasovic¹, V. Ilic², D. Pavlovic¹, S. Nikolic¹, M. Matic³ and A. Krmpot¹

¹*Institute of Physics Belgrade, Serbia*

²*Institute for Medical Research, University of Belgrade, Serbia*

³*Institute of Oncology and Radiology of Serbia*

e-mail: mihajlo.radmilovic@ipb.ac.rs

Interaction of hemoglobin (Hb) with ultrashort laser pulses is followed by fluorescence detection [1, 2]. The photophysical nature of fluorescence from Hb-containing specimens is not completely understood so far. There is some evidence of photoproduct formation in the process of Hb interaction with ultrashort laser pulses [3].

We measured Uv-Vis and Two-photon emission spectra of formed photoproduct in the way that Hb thin film was previously treated with a femtosecond Ti: Sapphire laser operating on 730nm. A relative relation and position of Uv-Vis Hb characteristic peaks such as Soret peak (410 nm), α and β peaks (577 nm and 541 nm respectively) served as a marker of structural changes in the laser treated Hb films [4].

Results suggest that the interaction of Hb with ultrashort laser pulses probably leads to the photodegradation of Hb, due to changes in α , β peaks relative relation and red shift of Soret peak in photoproduct Fig. 1 a).

Moreover, we emphasize that the photoproduct formed on thin Hb films has long durability, since we were able to detect its fluorescence after several months. This opens a possibility to apply the formed photoproduct as optical data storage and security tag.

We have also induced photoproduct formation in the human healthy erythrocytes Fig. 1 b) in order to selectively “label” and make them fluorescent in a whole blood. Two-photon selective labeling of erythrocytes can be used as a tool for studying red blood cells with different fluorescence detection methods, due to photoproduct fluorescence. This can be potentially applied in studying hemoglobin and erythrocytes in various physiological and pathophysiological states.

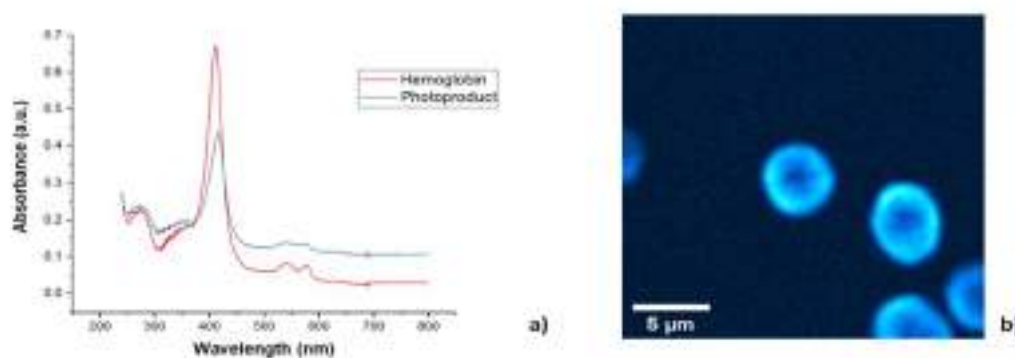


Figure 1. a) Uv-Vis absorption spectra of hemoglobin (red) and formed photoproduct (blue), b) Two-photon fluorescence image of selectively chosen erythrocytes with induced photoproduct formation.

Funding: Project HEMMAGINERO, No 6066079

REFERENCES

- [1] D. Li, W. Zheng, Y. Zeng, *Optics Lett.* 36, 834 (2011).
- [2] K. Bukara, S. Jovanic, I. Drvenica, *J. Biomed. Opt.* 22.2, 026003 (2017).
- [3] E.A. Shirshin, B.P. Yakimov, S.A. Rodionov, *Laser Phys. Lett.* 15, 075604 (2018).
- [4] E.H. Hanson, J. Ballantyne, *PLoS One* 5, e12830 (2010).

Label-free Third Harmonic Generation Imaging of Lipid Droplets in Live Filamentous Fungi

T. Pajić¹, N. Todorović², M. Zivić¹, M. D. Rabasović³, A.H.A. Clayton⁴, and A. Krmpot³

¹University of Belgrade – Faculty of Biology, Belgrade, Serbia

²Institute for Biological Research “Siniša Stanković”, University of Belgrade, Serbia

³Institute of Physics, Belgrade, Serbia

⁴Optical Sciences Centre, Swinburne University of Technology, Victoria, Australia

e-mail:tpajic@bio.bg.ac.rs

Oleaginous fungi can accumulate significant amounts of lipids in their mycelium (up to 80% of their biomass), primarily in the form of lipid droplets (LDs). LDs have optical properties that differ from the surrounding aquatic environment, which causes sudden changes in the refractive index. Here, we present *in vivo* and label-free imaging of individual hyphae of the oleaginous filamentous fungus *Phycomyces blakesleeanus* by Third Harmonic Generation (THG) microscopy method [1], where LDs are the main source of contrast [2] (Figure 1). The LDs quantification from THG images was performed by two image analysis techniques: Image Correlation Spectroscopy (ICS) and software particle counting – Particle Size Analysis (PSA). ICS measures the spatial variation of fluorescence intensity fluctuations in the images, which can then be related to particle density and aggregation state. In order to test and compare the two methods, we used hyphae that undergo nitrogen starvation, which is known to cause alterations in lipid metabolism and the increase in LDs number.

For *in vivo* THG imaging of label-free, > 24-hour old hyphae, we used 1040 nm, 200 fs pulses from Yb KGW laser. Detection was performed in the transmission arm by PMT through Hoya glass UV filter with peak transmission at 340nm. The laser beam was focused with the Zeiss Plan Neofluar 40x1.3 objective lens. For the imaging, the fungi were placed between two cover glasses of 0.17 μm thickness to match the objective lens requirements and for better transmission of the THG signal.

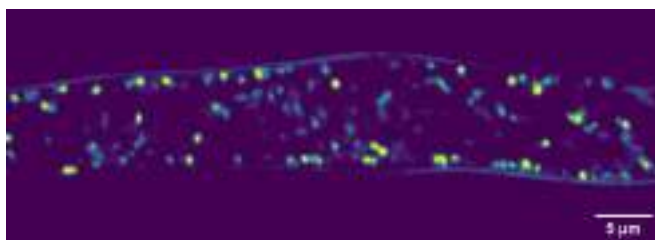


Figure 1. THG image of lipid droplets in hyphae of the fungus *Phycomyces blakesleeanus*. The bright objects are lipid droplets.

An increased number of LDs under nitrogen starvation was observed in THG images and their number and size were analyzed using two quantification methods. The comparison of LDs number and size obtained by ICS and PSA shows that the number of LDs is approximately the same on average, but that ICS consistently detects slightly larger LD number in older group. The mean ICS measured diameter was slightly lower. Using the THG method *in vivo* and label-free, we can accurately and reliably, over time, detect changes in the localization, total number, and size of LDs in hyphae of the oleaginous filamentous fungus *Phycomyces blakesleeanus*.

Acknowledgement: Project HEMMAGINERO, No. 6066079 from Program PROMIS, Science Fund of the Republic of Serbia, and Project „Minimally invasive, selective ablation of dental caries by femtosecond laser “Move for the science/2019

REFERENCES

[1] R. W. Boyd, Academic Press (2008).

[2] D. Débarre, W. Supatto, A. M. Pena, A. Fabre, T. Tordjmann, L. Combettes, E. Beaurepaire, *Nature Methods*, 3(1), 47–53. (2006).

Nonlinear Imaging of Dentin-Adhesive Interface Treated by Cold Atmospheric Plasma

T. Lainović¹, A. Krmpot², M. D. Rabasović, N. Selaković, I. Plešić¹, L. Blažić^{1,3}, N. Škoro², N. Puač²

¹*Faculty of Medicine, School of Dental Medicine, University of Novi Sad, Novi Sad, Serbia*

²*Institute of Physics, University of Belgrade, Belgrade, Serbia*

³*Dental Clinic of Vojvodina, Novi Sad, Serbia*

e-mail: tijana.lainovic@mf.uns.ac.rs

The Nonlinear Laser Scanning Microscopy (NLSM) could be considered as a useful tool for the analysis of hard dental tissues, and tissue-material interfaces in dental medicine. Two-photon excitation fluorescence microscopy (TPEF) is able to detect the two-photon excited autofluorescence of dental tissues, and the second harmonic generation (SHG) can detect second-order nonlinear susceptibility of collagen type I, the most abundant dentinal organic substance [1,2].

The objective of this study was to microscopically test the effect of Cold Atmospheric Plasma (CAP) [3,4] on the morphology of the dentin-adhesive interface, using NLSM.

Human molar teeth were cut in half for the CAP-treated and control samples. The influence of CAP on standard etch-and-rinse (ER) or self-etch (SE) procedures was investigated. The following CAP configurations were used: feeding gas He, gas flow 1 slm, deposited power in the plasma power input 1 W or 2 W, and tip-to-surface distance 2 mm or 4 mm. The CAP-treated ER group was firstly etched and treated by CAP, before adhesive application. The SE group was treated by CAP before the adhesive placement. The control groups underwent the same process omitting the CAP phase. NLSM was used to image the morphology of hybrid layers.

The results demonstrated that the CAP causes the removal of the smear layer and opens the tubules. The tubules are not only more open but changed by CAP regarding their surface properties so that the permeation of the adhesive is highly favored. Compared to the control groups of around 20-30 μm hybrid layers, the length of resin tags in the CAP treated ER group was measured to even up to 600 μm , and in the CAP-treated SE group they were extended up to 100 μm .

CAP treatment of dentin drastically changes the morphology of the hybrid layer and the extension of resin tags. There is a need for additional analysis in the field to examine the influence of these changes on the quality of the dentin-adhesive interface.

Acknowledgment: Supported by the Ministry of Education, Science and Technological Development of Republic of Serbia (under contract No. NIO 200114 and No. 451-03-68/2021-14/200024), Project HEMMAGINERO, No. 6066079 from Program PROMIS, Science Fund of the Republic of Serbia and by the program "Start up for science. Explore. Make a change.", Funded by Leadership Development Center, Phillip Morris for Serbia, 2019.

REFERENCES

- [1] T. Lainović, J. Margueritat, Q. Martinet, X. Dagany, L. Blažić, D. Pantelić, M.D. Rabasović, A.J. Krmpot and T. Dehoux, *Acta Biomater* 105, 214-222 (2020).
- [2] T. Cloitre, I.V. Panayotov, H. Tassery, C. Gergely, B. Levallois and F.J.G. Cuisinier, *J Biophotonics* 6, 330-337 (2013)
- [3] J.N. Stašić, N. Selaković, N. Puač, M. Miletić, G. Malović, Z.Lj. Petrović, D.N. Veljović and V. Miletić, *Clin Oral Invest* 23, 1383–1396 (2019).
- [4] A. Stancampiano, D. Forgione, E. Simoncelli, R. Laurita, R. Tonini, M. Gherardi and V. Colombo, *J Adhes Dent* 21, 229-237 (2019).

50,000 deaths each year. Despite major advances in treatment (i.e., surgery, radiation therapy, chemotherapy, biologic/immune therapy) and resultant improved outcomes over time, it has been demonstrated that failure of treatment in patients with metastatic breast cancer portends a poor prognosis. As the number of potential FDA-approved cancer drugs increases, the likelihood of identifying effective combination strategies tailored to an individual patient's tumor increases. Therefore, to provide significant advances in cancer treatment and enable the most effective chemotherapy, development of more quantitative and objective means for assessing drug sensitivity of an individual patient's tumor that is safer, faster, sensitive and capable for single- or multi-drug testing is urgently needed for advancing personalized therapies. To develop such an approach, fluorescence spectroscopic technologies may serve as a non-invasive means of revealing cell health. We applied phasor-fluorescence lifetime imaging microscopy (phasor-FLIM) to measure drug response using human colorectal cancer cell line HCT116 and patient samples. FLIM can be served as a promising new approach for reading the metabolic states of cancer cells treated with anti-cancer therapeutics and identified specific alterations of metabolic states that are early indicators of irreversible cell demise and that such metabolic changes can be detected using a label-free imaging assay for single-cell drug testing of rare and/or heterogeneous cancer cells. Based on these findings, we apply the label-free imaging platform to measure drug response using patient samples.

1502-Pos

Phasor-FLIM Quantification of Changes in Keratinocyte Metabolism and Tissue Architecture in a Longitudinal Study of UV-induced Skin Cancer

Michael G. Nichols¹, Molly Myers¹, Dominick Myers¹, Kelsey A. Jackson¹, Ben G. Huertner¹, Duyen Nguyen¹, Connor J. Kalthorn¹, George Varghese¹, Katie D. Sotelo¹, Marifel Frances Gabriel¹, Dan L. Che¹, Emiliano Altuzar¹, Anya Long¹, Jackson W. Morris¹, Laura A. Hansen².

¹Physics, Creighton University, Omaha, NE, USA, ²Biomedical Sciences, Creighton University, Omaha, NE, USA.

Two of the recognized hallmarks of cancer include fundamental shifts in energy metabolism toward a glycolytic phenotype and a reorganization of tissue architecture to enable tumor cell invasion and metastasis. Phasor-FLIM imaging of NAD(P)H and flavoproteins enables a rapid assessment of changes in metabolism, while fluorescence and scattering from structural proteins reveal changes in tissue architecture. Here, we demonstrate the practicality of conducting a long-term longitudinal study, monitoring the development and progression of UV-induced skin cancer in SKH1 mice. Linear Mixed Model Analysis of the entire dataset of more than 2000 repeated observations reveals statistically significant changes in bound NADH fraction as well as the degree of collagen fluorescence. Recent developments, including modifications to the instrument design to include a three-color, macro-fluorescence imaging mode to guide the selection of suspect regions will be discussed.

This publication was made possible by grants from the National Institute for General Medical Science (NIGMS) (5P20GM103427), a component of the National Institutes of Health (NIH), and its contents are the sole responsibility of the authors and do not necessarily represent the official views of NIGMS or NIH.

1503-Pos

Mapping the Spatiotemporal Heterogeneity of Biomolecules Concentration, Mobility and Local Environment in Live Cells using Quantitative Time-Resolved Confocal Fluorescence Microscopy Imaging Without Scanning and Fluorescence Lifetime Imaging Microscopy

Sho Oasa¹, Aleksandar Krmpot², Stanko Nikolic², Lars Terenius¹, Rudolf Rigler³, Vladana Vukojevic¹.

¹Clinal Neuroscience, Karolinska Inst, Stockholm, Sweden, ²Inst of Physics Belgrade, Univ of Belgrade, Belgrade, Serbia, ³Dept Med Biophysics, Karolinska Inst, Stockholm, Sweden.

In living cells, biomolecules are integrated *via* chemical reactions and transport processes into self-regulated dynamical networks. Through these networks of interactions life-sustaining biological functions, such as gene transcription and signal transduction, emerge at the higher level of organization and at longer spatiotemporal scales. To quantitatively characterize in live cells biomolecules concentration, mobility and properties of their immediate surroundings, we have developed functional Fluorescence Microscopy Imaging (fFMI), a scanning-free time-resolved quantitative confocal fluorescence microscopy imaging technique that integrates massively parallel Fluorescence Correlation Spectroscopy with fluorescence lifetime imaging (Krmpot AJ. *et al. Analytical Chemistry*, 2019 **91**(17): 11129-11137). In our approach, a single-photon avalanche photodiode (SPAD) matrix camera simultaneously records fluorescence signal from 256 or 1024 observation volume elements generated by passing the incident laser light through a Diffractive Optical

Element (DOE) designed to match the SPAD matrix detector geometry. fFMI is characterized with single-molecule sensitivity, high spatial (≈ 240 nm) and temporal (≈ 10 μ s/frame) resolution, and can map fluorescence lifetimes (1-7 ns). We demonstrate here fFMI to characterize in live cells the dynamic landscape of a transcriptional regulatory factor (the glucocorticoid receptor) and map the spatial heterogeneity of cell surface receptor (the opioid receptor) dynamics.

1504-Pos

AO-DIVER Advances the Depth Limits of Multiphoton Microscopy in Scattering Media

Simon W. Leemans¹, Alexander Dvornikov¹, Tara Gallagher², Enrico Gratton¹.

¹Biomedical Engineering Department, UC Irvine, Irvine, CA, USA, ²Molecular Biology & Biochemistry, UC Irvine, Irvine, CA, USA.

The long wavelengths used in multiphoton microscopy have facilitated volumetric imaging of scattering samples by reducing the effects of scattering and absorption. However, the imaging depth in multiphoton microscopy is still limited by sample-induced phase aberrations and out-of-focus (top surface) fluorescence. To counteract image degradation and enable high-resolution 3D imaging in tissue samples, we built the AO-DIVER, Adaptive Optics enhanced- Deep Imaging Via Emission Recovery, a multiphoton microscope specifically designed for imaging deep in scattering samples. We demonstrate here that the AO-DIVER can image nearly 3 orders of magnitude deeper into scattering samples than typical epi-detection methods due to the enhanced signal acquisition, with near diffraction-limited resolution due to our improved ability to focus the excitation light. Traditional direct wavefront sensing approaches are impossible at such depths, so we have developed a feedback-based approach to find the optimal wavefront correction. We use a modified version of the Downhill Simplex algorithm to leverage the high speed of the BMC Hex-DM (10's of kHz) and correct aberrations within 20 seconds per isoplanatic patch, with intensity improvements relative to a flat DM surface reaching up to a factor of 10 deep in heterogeneous samples. We have also developed software to guide users in producing large volumetric phase corrections quickly and effectively for 3D imaging. This work is supported by NIH P41-GM103540 and NIH P50-GM076516 grants and the NSF through the Integrative Graduate Education and Research Traineeship (IGERT) Program (DGE-1144901).


1505-Pos

Non-destructively Analyzing the Metabolic Dysregulation of Invasive Cancer Cells on an Intracellular Scale

Austin E.Y.T. Lefebvre¹, Freddie A. Adame², Mingjuan Liu², Michelle A. Digman¹.

¹Biomedical Engineering, UC Irvine, Irvine, CA, USA, ²Developmental and Cell Biology, UC Irvine, Irvine, CA, USA.

Cancer has overtaken cardiovascular disease's top spot in non-communicable deaths. However, it is not cancer itself that looms as the largest killer, but rather cancer's spread to distant organs – a process known as metastasis – that finishes the job. Capturing metabolic alterations of migrating cells intracellularly, and in a non-destructive manner to both the surrounding environment and the cell is technically challenging. In this study, we use fluorescence lifetime imaging (FLIM) of the reduced form of nicotinamide adenine dinucleotide (NADH) and phasor analysis to examine metabolic changes on a single cell level. Additionally, we use phosphorescence lifetime imaging (PLIM) and phasor analysis of an oxygen sensitive probe ruthenium-tris(2,2'-bipyridyl) (Ru(BPY)₃²⁺), whose lifetime is quenched in the presence of oxygen, in order to observe intracellular changes of oxygen concentration. Finally, we use spectral imaging and phasor analysis to quantify changes in intracellular lipid order using the fluorescent probe 6-dodecanoyl-N,N-dimethyl-2-naphthylamine (Laurdan). In these studies, we observe a time-dependent recovery of metabolic processes in triple negative breast cancer (TNBC) cells with pharmacological inhibition of mitochondrial respiration via metformin, but not oligomycin. Furthermore, we observe high intracellular lipid order in TNBC cells but not in other breast cancer or non-cancerous breast cells. Finally, we spatially map intracellular oxygen concentration using the phasor approach to PLIM with Ru(BPY)₃²⁺. Combining these non-destructive techniques to analyze alterations in metabolically important parameters in breast cells of varying invasive potentials may reveal potential therapeutically actionable targets of metastatic disease that may otherwise remain hidden due to limitations of existing analysis methods. This work is supported by the National Institutes of Health grant P41-GM103540, and the National Science Foundation's Career Award #1847005 and its Graduate Research Fellowship Award DGE-1839285.

 Presentation

Select Language ▼

[Translator Disclaimer](#)

13 March 2019

Mapping mechanical properties and structure of dentin by Brillouin spectroscopy and nonlinear optical microscopy (Conference Presentation)

Tijana Lainović (</profile/Tijana.Lainovic-4138090>), *J r mie Margueritat*, *Larisa Bla i c*, *Dejan Panteli c* (</profile/Dejan.Pantelic-7796>), *Mihailo Rabasovi c*, *Aleksandar Krmpot* (</profile/Aleksandar.Krmpot-133598>), *Thomas Dehoux*

[Author Affiliations + \(\)](#)

Proceedings Volume 10880, *Optical Elastography and Tissue Biomechanics VI*; </conference-proceedings-of-spie/10880.toc> 1088018 (2019) <https://doi.org/10.1117/12.2506858> (<https://doi.org/10.1117/12.2506858>)

Event: [SPIE BiOS](/conference-proceedings-of-spie/browse/SPIE-Photonics-West/SPIE-BIOS/2019) (</conference-proceedings-of-spie/browse/SPIE-Photonics-West/SPIE-BIOS/2019>), 2019, San Francisco, California, United States

ARTICLE

CITED BY

Abstract

Mechanical and optical properties are the main criteria for assessing the health of dental tissue in contemporary dentistry. Dentinal pathological changes can be detected by visuo-tactile and radiographic methods to guide clinicians in establishing a relevant diagnosis and an adapted therapy. However, such approaches cannot give information on the dentinal microstructure. Recently, laser ultrasonic techniques have been deployed to evaluate the mechanical properties of enamel [1,2] However, such techniques lack the resolution to reveal the transitions differences between tissue layers. In this work, we used Brillouin light scattering spectroscopy as a non-contact alternative to probe mechanical changes in dentin and dentin-resin interface at GHz hypersonic frequencies. We obtained maps of the Brillouin frequency shift and linewidth that can be interpreted as maps of sound velocity and viscosity. In addition, we observed the specimens by a homemade nonlinear microscopy setup [3]. A 730 nm wavelength Titanium-sapphire laser was used as an excitation source for two-photon excitation fluorescence microscopy (TPEF), while 1040 nm wavelength Yb:KGW laser was used for second harmonic generation (SHG). Our results show significant changes between healthy tissues and pathological lesions. Such results can help to precisely delineate destructed dentin during clinical procedures, paving the way to minimally invasive strategies. In addition, our simultaneous analysis of Brillouin maps and nonlinear images brings valuable information on structure-related mechanical properties of dentin and dentin-resin adhesive interface. 1. Wang et al, Experimental and numerical studies for nondestructive evaluation of human enamel using laser ultrasonic technique. *Appl Opt* 52, 6896-6905 (2013). 2. Wang et al., Laser ultrasonic evaluation of human dental enamel during remineralisation treatment. *Biomed Opt Express* 2, 345-355 (2011). 3. Rabasovi c M et al. Nonlinear microscopy of chitin and chitinous structures: a case study of two cave-dwelling insects. *J Biomed Opt* 20, 016010 (2015)

Conference Presentation

PROCEEDINGS
PRESENTATION


WATCH
PRESENTATION

SAVE TO MY LIBRARY

SHARE

GET CITATION

CITATIONS

[Explore citations on Lens.org](#)
(<https://www.lens.org/lens/scholar/article/05929-839-423-772/main>). 

Advertisement

Advertisement

KEYWORDS

[Microscopy](/search?keyword=Microscopy) (</search?keyword=Microscopy>)

▼ Show Transcript

© (2019) COPYRIGHT Society of Photo-Optical Instrumentation Engineers (SPIE). Downloading of the abstract is permitted for personal use only.

Citation [Download Citation](#) ▼

Tijana Lainović (</profile/Tijana.Lainovic-4138090>), Jérémie Margueritat, Larisa Blažić, Dejan Pantelić (</profile/Dejan.Pantelic-7796>), Mihailo Rabasović, Aleksandar Krmpot (</profile/Aleksandar.Krmpot-133598>), and Thomas Dehoux "Mapping mechanical properties and structure of dentin by Brillouin spectroscopy and nonlinear optical microscopy (Conference Presentation)", Proc. SPIE 10880, Optical Elastography and Tissue Biomechanics VI, 1088018 (13 March 2019); <https://doi.org/10.1117/12.2506858> (<https://doi.org/10.1117/12.2506858>)

[Spectroscopy \(/search?keyword=Spectroscopy\)](/search?keyword=Spectroscopy)

[Laser dentistry \(/search?keyword=Laser_dentistry\)](/search?keyword=Laser_dentistry)

[Ultrasonics \(/search?keyword=Ultrasonics\)](/search?keyword=Ultrasonics)

[Dentistry \(/search?keyword=Dentistry\)](/search?keyword=Dentistry)

[Interfaces \(/search?keyword=Interfaces\)](/search?keyword=Interfaces)

[Medicine \(/search?keyword=Medicine\)](/search?keyword=Medicine)

[Show All Keywords](#)

RELATED CONTENT


[Polarization control in optical fibers and applications in optical microscopy... \(/conference-proceedings-of-spie/8693/86930Q/Polarization-control-in-optical-fibers-and-applications-in-optical-microscopy/10.1117/12.2009585.full\)](#)
 Proceedings of SPIE (April 11 2013)


[Label-free imaging of acanthamoeba using multimodal nonlinear optical microscopy \(/conference-proceedings-of-spie/10498/104982J/Label-free-imaging-of-acanthamoeba-using-multimodal-nonlinear-optical-microscopy/10.1117/12.2288136.full\)](#)
 Proceedings of SPIE (February 23 2018)

[The influence of hypericin mediated photodynamic therapy on secretion of... \(/conference-proceedings-of-spie/11070/11070A2/The-influence-of-hypericin-mediated-photodynamic-therapy-on-secretion-of/10.1117/12.2525516.full\)](#)
 Proceedings of SPIE (August 07 2019)

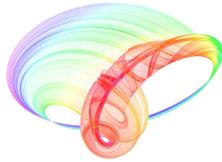
[Charaterization of cyanobiphenyl-cyanoterphenyl mixtures in Langmuir films \(/conference-proceedings-of-spie/4147/0000/Charaterization-of-cyanobiphenyl-cyanoterphenyl-mixtures-in-Langmuir-films/10.1117/12.385686.full\)](#)
 Proceedings of SPIE (May 12 2000)

[Root canal microleakage investigation after Nd:YAG laser-assisted treatment \(/conference-proceedings-of-spie/7373/73731U/Root-canal-microleakage-investigation-after-NdYAG-laser-assisted-treatment/10.1117/12.831914.full\)](#)
 Proceedings of SPIE (July 17 2009)

 [Subscribe to Digital Library \(/subscribe-page\)](#)

 [Receive Erratum Email Alert \(\)](#)

Book of abstracts



PHOTONICA2019

The Seventh International School and Conference on
Photonics, 26 August – 30 August 2019, Belgrade, Serbia

& Machine Learning with Photonics Symposium
(ML-Photonica 2019)



& ESUO Regional Workshop



& COST action CA16221



Editors: Milica Matijević, Marko Krstić and Petra Beličev

Belgrade, 2019

ABSTRACTS OF TUTORIAL, KEYNOTE, INVITED LECTURES,
PROGRESS REPORTS AND CONTRIBUTED PAPERS

of

The Seventh International School and Conference on Photonics
PHOTONICA2019, 26 August – 30 August 2019, Belgrade, Serbia

and

Machine Learning with Photonics Symposium

and

ESUO Regional Workshop

Editors

Milica Matijević, Marko Krstić and Petra Beličev

Technical Assistance

Danka Stojanović and Goran Gligorić

Publisher

Vinča Institute of Nuclear Sciences

Mike Petrovića Alasa 12-14, P.O. Box 522

11000 Belgrade, Serbia

Printed by

Serbian Academy of Sciences and Arts

Number of copies

300

ISBN 978-86-7306-153-5

PHOTONICA2019 (The Seventh International School and Conference on Photonics-www.photonica.ac.rs) is organized by Vinča Institute of Nuclear Sciences, University of Belgrade (www.vinca.ac.rs), Serbian Academy of Sciences and Arts (www.sanu.ac.rs), and Optical Society of Serbia (www.ods.org.rs).



Other institutions that helped the organization of this event are: Institute of Physics Belgrade, University of Belgrade (www.ipb.ac.rs), School of Electrical Engineering, University of Belgrade (www.etf.bg.ac.rs), Institute of Chemistry, Technology and Metallurgy, University of Belgrade (www.ihtm.bg.ac.rs), Faculty of Technical Sciences, University of Novi Sad (www.ftn.uns.ac.rs), Faculty of Physics, University of Belgrade (www.ff.bg.ac.rs), and Faculty of Biology, University of Belgrade (www.bio.bg.ac.rs). Joint event “Machine learning with Photonics Symposium” has been co-organized with programme partners H2020-RISE-CARDIALLY, H2020 – MULTIPLY and H2020-EID-FONTE.

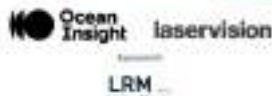
PHOTONICA2019 is organized under auspices and with support of the Ministry of Education, Science and Technological Development, Republic of Serbia (www.mpn.gov.rs). PHOTONICA2019 is supported and recognized by OSA - The Optical Society (www.osa.org), Integrated Initiative of European Laser Research Infrastructures Laser Lab-Europe (www.laserlab-europe.eu) and European Physical Society (www.eps.org).



The support of the sponsors of PHOTONICA2019 is gratefully acknowledged:



Development Center Serbia



Committees:

Scientific committee:

Aleksandar Krmpot, Serbia
Antun Balaž, Serbia
Arlene D. Wilson-Gordon, Israel
Bojan Resan, Switzerland
Boris Malomed, Israel
Branislav Jelenković, Serbia
Dejan Gvozdić, Serbia
Detlef Kip, Germany
Dragan Indjin, United Kingdom
Edik Rafailov, United Kingdom
Feng Chen, China
Francesco Cataliotti, Italy
Giannis Zacharakis, Greece
Goran Isić, Serbia
Goran Mašanović, United Kingdom
Isabelle Philippa Staude, Germany
Jelena Radovanović, Serbia
Jerker Widengren, Sweden
Jovana Petrović, Germany
Laurent Sanchez, France
Ljupčo Hadžievski, Serbia
Marco Santagiustina, Italy
Milan Mashanović, United States of America
Milan Trtica, Serbia
Miloš Živanov, Serbia
Milutin Stepić, Serbia
Milivoj Belić, Qatar
Nikola Stojanović, Germany
Pavle Anđus, Serbia
Peđa Mihailović, Serbia
Peter Schaaf, Germany
Radoš Gajić, Serbia
Sergei Turitsyn, United Kingdom
Suzana Petrović, Serbia
Ticijana Ban, Croatia
Vladana Vukojević, Sweden
Zoran Jakšić, Serbia
Željko Šljivančanin, Serbia

Organizing Committee:

Petra Beličev (Chair)
Marko Krstić (Co-chair)
Milica Matijević (Secretary)
Goran Gligorić (Webmaster)
Ljupčo Hadžievski
Aleksandra Maluckov
Milutin Stepić
Maja Nešić
Marija Ivanović
Danka Stojanović
Marjan Miletić
Jelena Kršić
Mirjana Stojanović

ML-Photonica 2019 Symposium Steering Committee:

Sergei Turitsyn, United Kingdom
Darko Zibar, Denmark
Sugavam Srikanth, UK

Technical Organizer:



Strain of MoS₂ mapped with second harmonic generation microscopy

M. Spasenović¹, A. J. Krmpot², M. D. Rabasović², N. Vujičić³,
V. Jadriško³, D. Čapeta³ and M. Kralj³

¹*Center for Microelectronic Technologies, Institute of Chemistry, Technology and Metallurgy, Belgrade, Serbia*

²*Institute of Physics, Belgrade, Serbia*

³*Center of Excellence for Advanced Materials and Sensing Devices, Institute of Physics, Zagreb, Croatia*

e-mail: spasenovic@nanosys.ihm.bg.ac.rs

2D materials are an extremely intense and current field of research. After the experimental realization of graphene and the immense body of results that highlighted its spectacular properties, attention has started to shift to other 2D materials, namely those that might be of interest for various applications in flexible electronics, optoelectronics, sensing, and in other industrial branches. 2D semiconductors in particular are now drawing the interest of researchers, due to the existence of a bandgap.

Although the potential for applications is enormous, production processes for these materials are still being studied and refined. Chemical vapor deposition (CVD) is widely regarded as a good candidate growth process for wide-scale applications. Nevertheless, it is well known that CVD yields materials that consist of grains with varying orientation and size. Due to the ultrathin nature of these materials, studying the crystallographic orientation and grain size is not trivial.

Optical methods provide a useful tool to study the properties of 2D materials with high resolution. In particular, second harmonic generation (SHG) has been used to map crystal orientation of CVD-grown 2D semiconductors on standard growth and use substrates [1]. Further studies have shown high-resolution strain mapping using the same principles of nonlinear optics [2].

Here we show SHG microscopy studies of crystal orientation and the presence of strain of MoS₂ grown on quartz. We show that the growth substrate as well as the speed of cooling during growth can have an influence on strain, and we propose to engineer strain by selecting or patterning the substrate, or tuning the growth process. Strain control on the nanoscale is an enabling tool for the emerging technology of straintronics.

REFERENCES

[1] S. Psilodimitrakopoulos et al., *Light Sci. Appl.* 7, 18005 (2018).

[2] L. Mennel et al., *Nat. Commun.* 9, 516 (2018).

Nonlinear microscopy and time resolved fluorescence spectroscopy of *Chelidonium majus* L.

M. S. Rabasovic, D. Sevic, B. P. Marinkovic, A. J. Krmpot and M. D. Rabasovic

¹*Institute of Physics, Belgrade, Serbia*

e-mail: majap@ipb.ac.rs

Greater celandine (*Chelidonium majus* L.) is a well-known healing plant. It has segmented laticifers filled with yellowish - brown content that is rich in biologically active substances (alkaloids, flavonoids and phenolic acids) [1, 2]. The concentration of these components can change significantly, depending on the time of year, from flowering period in spring to the fruit - bearing time in autumn [3]. Flavonoids (plant pigments) are responsible for the yellow color of the greater celandine flower [4]. The antioxidant activity was also correlated with the concentration of total phenolics (including flavonoids), which is the highest in the spring months [4].

This study presents the analysis of the physical phenomena diagnosed in *Chelidonium majus* components. Time resolved optical characteristics were analyzed by using TRLS (Time Resolved Laser Spectroscopy) experimental setup. Nonlinear optical properties of the plant have been studied using two-photon excited autofluorescence (TPEF), second - harmonic generation (SHG) and upconversion luminescence (UCL) simultaneously. The benefits of using UCL for biological applications are in reducing the photobleaching and providing photostability. Upconversion emission is also more efficient than the TPEF and SHG. Moreover, UCL could be achieved with a low power continuous wave (CW) laser.

REFERENCES

- [1] K. Seidler-Łożykowska et al., *Acta Sci. Pol. Hortorum Cultus* 15, 161 (2016).
- [2] V. N. Deulenko et al., *Biochem Anal Biochem* 7, 1000370 (2018).
- [3] Z. D. Jakovljevic, M. S. Stankovic, M. D. Topuzovic, *EXCLI J.* 12, 260 (2013).
- [4] P. C. H. Hollman, *Pharm. Biol.* 42, 74 (2004).

In vivo Third Harmonic Generation Imaging of *Phycomyces blakesleeanus*

T. Pajic¹, K. Stevanovic¹, N. Todorovic², A. Krmpot³,
M. Rabasovic³, B. Jelenkovic³ and M. Zivic¹

¹Faculty of Biology, University of Belgrade, Serbia

²Institute for Biological Research, University of Belgrade, Serbia

³Institute of Physics, University of Belgrade, Serbia

e-mail: tpajic@bio.bg.ac.rs

Third Harmonic Generation is a nonlinear optical effect in which the incident laser beam interacts with a medium producing the light of exactly three times shorter wavelength than the incidental one. THG is generated in medium that have third order nonlinearity, but it is particularly pronounced at the interfaces where the steep change of refractive index takes a place [1]. THG phenomenon is employed in laser scanning microscopy that utilizes ultrashort laser pulses for imaging. The THG microscopy is a label free techniques that provides important information on the sample such as membrane imaging and lipid droplets distribution [2]. It is mostly used for *in vivo* imaging of small model organisms like zebrafish [3] and *C. Elegance* [4].

We present THG imaging of filamentous fungus organism *Phycomyces blakesleeanus*, combined with Two Photon Excitation fluorescence (TPEF). The hyphae were grown in various conditions on glass coverslips coated with collagen and concanavalin A. For THG imaging of label-free, 16-24 hour old hyphae, we used 1040 nm, 200 fs pulses from Yb KGW laser, while for TPEF, Ti:Sa pulses at 730 nm, 160 fs duration, were used. Both laser beams were focused with the same objective lens, Zeiss Plan Neofluar 40x1.3. Detection of THG was performed by PMT through Hoya glass UV filter with peak transmission at 340nm, while for TPEF 400-700 nm band pass filter was used. THG images revealed the chitinous cell wall and the membrane that are clearly separated. The appearance of the cell wall was confirmed by colocalization with TPEF images. Most prominent observation on the THG images is presence of numerous, seemingly randomly dispersed, round shiny features throughout the cytoplasm, for which we suspect that could be lipid droplets as indicated in Débarre et al., 2006.

REFERENCES

- [1] R. W. Boyd, *Nonlinear Optics*, Academic Press, (2008).
- [2] D. Débarre et al., *Nat. Methods* 3, 47 (2006).
- [3] N. Olivier et al., *Science* 329, 967 (2010).
- [4] G. J. Tservelakis et al., *Micron* 41, 444 (2010).

Successful Ti:Sapphire laser cell surgery of *Phycomyces blakesleeanus* cell wall

Tanja Pajić (1), Katarina Stevanović (1), Nataša Todorović (2), Aleksandar Krmpot (3),
Mihailo Rabasović (3), Vladimir Lazović (3), Dejan Pantelić (3), Brana Jelenković (3),
Miroslav Živić (1)

(1) University of Belgrade - Faculty of Biology, Serbia

(2) Institute for Biological Research, University of Belgrade, Serbia

(3) Institute of Physics, University of Belgrade, Serbia

Application of patch-clamp method for investigation of membrane ion channels of filamentous fungi is nontrivial task due to presence of chitinous cell wall. Complete removal of the wall patch is needed to make the membrane accessible to glass pipette. We use the model filamentous fungus organism, *Phycomyces blakesleeanus* which is undertaken to the cell surgery procedure by means of tightly focused femtosecond laser beam. The hyphae were grown on glass coverslips coated with collagen plasmolysed and imaged by homemade non-linear laser scanning microscope by detecting two photon excitation fluorescence signal. Although intrinsic autofluorescence of chitin enables imaging of the cell wall the hyphae were stained by Calcofluor White dye prior to the imaging in order to improve signal to noise ratio. Ti:Sa laser, used for both imaging and surgery, was operating at 730nm, with 76MHz repetition rate and 160fs pulse duration. Carl Zeiss, EC Plan-NEOFLUAR, 401.3 oil immersion objective was used for tight focusing of the laser beam and for the collection of the fluorescence signal. A visible interference filter (415nm - 685nm) was placed in front of detector in order to remove scattered laser light. The successful cutting of cell wall could be achieved within the range of laser intensities and cutting speeds (dwell times). The hyphae were kept in azide throughout the experiment in order to block the regeneration of the cell wall. After the surgery, hyphae were slowly deplasmolysed to induce exit of a portion of the protoplast through the laser made incision in the cell wall.

Financing: This work was supported by Ministry of Education, Science and Technological Development, Republic of Serbia (grant no. III 45016).

Keywords: Cell surgery; Ti:Sapphire

[Back to programme](#)

Programme & The Book of Abstracts

Twentieth Annual Conference

YUCOMAT 2018

Herceg Novi, Montenegro, September 3–7, 2018

Organised by



endorsed by



ENDORSED MEETING



TWENTIETH ANNUAL CONFERENCE

YUCOMAT 2018

Hunguest Hotel Sun Resort Herceg Novi, Montenegro,
September 3-7, 2018
<http://www.mrs-serbia.org.rs>

Programme and The Book of Abstracts

Organised by:
Materials Research Society of Serbia

Endorsed by:
**Materials Research Society,
European Materials Research Society
and
Federation of European Material Societies**

Title: THE TWENTIETH ANNUAL CONFERENCE
YUCOMAT 2018
Programme and The Book of Abstracts

Publisher: Materials Research Society of Serbia
Knez Mihailova 35/IV, P.O.Box 433, 11000 Belgrade, Serbia
Phone: +381 11 2185-437
<http://www.mrs-serbia.org.rs>

Editors: Prof. Dr. Dragan P. Uskokovi and Prof. Dr. Velimir R. Radmilovi

Technical editor: Sava Stoisavljevi

Front cover: Modified Photo by Hons084; Wikimedia Commons
(https://commons.wikimedia.org/wiki/File:Widoki_z_twierdzy_Forte_Mare_na_Herceg_Novi_03.jpg); CC BY-SA 4.0

Back cover: Modified Photo by Dani Lavi 0007; Wikimedia Commons
(https://commons.wikimedia.org/wiki/File:Belgrade_at_night.jpg); CC BY-SA 4.0

Copyright © 2018 Materials Research Society of Serbia

Acknowledgments: This conference is celebrating 20 years of YUCOMAT



Printed in: Biro Konto
Sutorina bb, Igalo – Herceg Novi, Montenegro
Phones: +382-31-670123, 670025, E-mail: bkonto@t-com.me
Circulation: 220 copies. The end of printing: August 2018

P.S.C.3.

One-pot synthesis of biocompatible NaYF₄:Yb,Er nanoparticles for cell labeling

Ivana Dini¹, Marina Vukovi¹, Lidija Manić², Aleksandar Krmpot³, Olivera Milošević²

¹Innovation Center of the Faculty of Chemistry, University of Belgrade, Serbia;

²Institute of Technical Sciences of SASA, Belgrade, Serbia;

³Photonic Center, Institute of Physics Belgrade, University of Belgrade, Belgrade, Serbia

In modern medical research, great attention has been focused to the development of the new biomarkers which include up-converting nanoparticles (UCNPs). Their optical response is triggered by NIR radiation that achieves deeper tissue penetration when compared with traditionally used fluorophores. In this work, biocompatible NaYF₄: Yb, Er nanoparticles were synthesized by polymer assisted one-pot solvothermal processing using chitosan or poly(lactic-co-glycolic acid). X-ray powder diffraction and electron microscopy results revealed differences in crystal arrangement and morphology of the as-synthesized particles. Fourier transform infrared spectroscopy confirmed the presence of corresponding polymers moiety on UCNPs surface providing their biocompatibility and low cytotoxicity towards human gingival fibroblasts (HFG). As a consequence of efficient up-conversion, prominent green emission (between 512-533nm and between 533-560nm) as well as red emission (630-690nm) were recorded in the particles photoluminescence spectra, and these are applied further in the visualization of the HFG using the laser scanning microscopy with a NIR laser source.

This work was financially supported by the Ministry of Education, Science and Technological Development of Serbia projects OI 172035.

CIP-

66.017/.018(048)

MATERIALS Research Society of Serbia (Beograd). Conference (20 ; 2018 ; Herceg Novi)

Programme ; and The Book of Abstracts / Twentieth Annual Conference YUCOMAT 2018, Herceg Novi, September 3-7, 2018 ; organised by Materials Research Society of Serbia ; [editors Dragan P. Uskokovi and Velimir R. Radmilovi]. - Belgrade : Materials Research Society of Serbia, 2018 (Herceg Novi : Biro Konto). - XLIV, 159 str. : ilustr. ; 23 cm

Tiraž 220. - Bibliografija uz pojedine apstrakte. - Registar.

ISBN 978-86-919111-3-3

1. Materials Research Society of Serbia (Beograd)

a) -

b) -

COBISS.SR-ID 266944524



Serbian Ceramic Society Conference
ADVANCED CERAMICS AND APPLICATION VI
New Frontiers in Multifunctional Material Science and Processing

Serbian Ceramic Society
Institute of Technical Sciences of SAsA
Institute for Testing of Materials
Institute of Chemistry Technology and Metallurgy
Institute for Technology of Nuclear and Other Raw Mineral Materials

PROGRAM AND THE BOOK OF ABSTRACTS

Serbian Academy of Sciences and Arts, Knez Mihailova 35
Serbia, Belgrade, 18-20. September 2017.

Serbian Ceramic Society Conference
ADVANCED CERAMICS AND APPLICATION VI
New Frontiers in Multifunctional Material Science and Processing

Serbian Ceramic Society
Institute of Technical Science of SASA
Institute for Testing of Materials
Institute of Chemistry Technology and Metallurgy
Institute for Technology of Nuclear and Other Raw Mineral Materials

PROGRAM AND THE BOOK OF ABSTRACTS

Serbian Academy of Sciences and Arts, Knez Mihailova 35
Serbia, Belgrade, 18-20. September 2017

Book title: Serbian Ceramic Society Conference - ADVANCED CERAMICS AND APPLICATION VI Program and the Book of Abstracts

Publisher:

Serbian Ceramic Society

Editors:

Prof.dr Vojislav Mitić

Dr Lidija Mančić

Dr Nina Obradović

Technical Editors:

Dr Lidija Mančić

Dr Nina Obradović

Ivana Dinić

Printing:

Serbian Ceramic Society

Edition:

200 copies

CIP - Каталогизacija y yyybykacuji
Hapodna byblyyoteka Cpbyje, Beograd

666.3/.7(048)

66.017/.018(048)

SRPSKO keramicko drustvo. Conference Advanced Ceramics and Application
: New Frontiers in Multifunctional Material Science and Processing (6 ; 2017 ;
Beograd)

Program ; and the Book of Abstracts / Serbian Ceramic Society Conference
Advanced Ceramics and Application VI : New Frontiers in Multifunctional
Material Science and Processing, Serbia, Belgrade, 18-20. September 2017. ;
[organized by] Serbian Ceramic Society ... [et al.] ; [editors Vojislav Mitić, Lidi-
ja Mančić, Nina Obradović]. - Belgrade : Serbian Ceramic Society, 2017 (Bel-
grade : Serbian Ceramic Society). - 86 str. : ilustr. ; 30 cm

Tiraž 200.

ISBN 978-86-915627-5-5

a) Kepamuka - AnctpaKTI b) Hayka o MaTepиjajиMa - AnctpaKTI c)
HanoMaTepиjajи - AnctpaKTI
COBISS.SR-ID 244577036

Dear Colleagues,

We have great pleasure to welcome you to the Advanced Ceramic and Application Conference VI organized by the Serbian Ceramic Society in cooperation with the Institute for Testing of Materials, Institute of Technical Sciences of SASA, Institute of Chemistry Technology and Metallurgy and Institute for Technology of Nuclear and Other Raw Mineral Materials.

Advanced Ceramics today include many old-known ceramic materials produced through newly available processing techniques as well as broad range of the innovative compounds and composites, particularly with plastics and metals. Such developed new materials with improved performances already bring a new quality in the everyday life. The chosen Conference topics cover contributions from a fundamental theoretical research in advanced ceramics, computer-aided design and modeling of a new ceramics products, manufacturing of nanoceramic devices, developing of multifunctional ceramic processing routes, etc. Traditionally, ACA Conferences gather leading researchers, engineers, specialist, professors and PhD students trying to emphasize the key achievements which will enable the wide spread use of the advanced ceramics products in High-Tech industry, renewable energy utilization, environmental efficiency, security, space technology, cultural heritage, prosthesis, etc.

Serbian Ceramic Society has been initiated in 1995/1996 and fully registered in 1997 as Yugoslav Ceramic Society, being strongly supported by American Ceramic Society. Since 2009, it has continued as Serbian Ceramic Society in accordance to the Serbian law procedure. Serbian Ceramic Society is almost the only one Ceramic Society in the South-East Europe, with members from more than 20 Institutes and Universities, active in 16 sessions, by program and the frames which are defined by the American Ceramic Society activities.

For the first time Advanced Ceramic and Application Conference hosting delegations from Republics of Ghana, Nigeria, Niger and Cameroon with the idea to connect, share and provide positive influence to the scientific and industrial communities all around world.



Prof. Dr Vojislav Mitić
President of the Serbian Ceramic Society
World Academy Ceramics Member
European Academy of Sciences&Arts Member



Prof. Dr Olivera Milošević,
President of the General Assembly of the
Serbian Ceramic Society
Academy of Engineering Sciences of Serbia Member

Conference Topics

- Basic Science & Sintering of Ceramics
- Nano, Bio- & Opto Ceramic
- Electro & Multifunctional Ceramics
- Magnetic, Catalytic & Composite Materials
- Renewable Energy, Heritage & Archeology
- Industrial Talks

Conference Co-chairmen:

Prof. Dr. Vojislav Mitić SRB
Prof. Dr. Olivera Milošević SRB
Prof. Dr. Marcel Van de Voorde EU
Prof. Dr. Rainer Gadow GER

Conference Programme Chairs:

Dr. Lidija Mančić SRB
Dr. Nina Obradović SRB

Scientific Committee

Academician Zoran Đurić SRB
Academician Ninoslav Stojadinović SRB
Academician Zoran Popović SRB
Academician Pantelija Nikolić SRB
Academician Miroslav Gašić SRB
Academician Laszlo Forro CHE
Academician Dragoljub Mirjanić BiH(RS)
Prof. Dr. Vojislav Mitić SRB
Prof. Dr. Marcel Van de Voorde EEZ
Prof. Dr. David Johnson GBR
Prof. Dr. Slavcho Rakovsky BGR
Prof. Dr. Jurgen G. Heinrich DEU
Prof. Dr. Masohiro Yoshimura JPN
Dr. Mrityunjay "Jay" Singh USA
Prof. Dr. Rainer Gadow DEU
Dr. Richard Todd GBR
Dr. Moritz von Witzleben DEU
Dr. Jon Binner, UK
Dr. Fiqiri Hodaj FRA
Prof. Dr. Hans Fecht DEU
Dr. Dušan Jovanović SRB
Prof. Dr. Olivera Milošević SRB
Prof. Dr. Vladimir Pavlović SRB
Dr. Nina Obradović SRB
Dr. Lidija Mančić SRB
Prof. Dr. Steven Tidrow USA
Dr. Wilhelm Siemen DEU
Dr. Jonjaua Ranogajec SRB
Dr. Snežana Pašalić SRB
Prof. Dr. Zoran Nikolić SRB
Dr. Zagorka Radojević SRB
Dr. Nebojša Romčević SRB
Dr. Zorica Lazarević SRB

Prof. Dr. Ljubica Pavlović SRB
Prof. Dr. Nebojša Mitrović SRB
Prof. Dr. Ljubiša Kocić SRB
Dr. Aleksandra Milutinović–Nikolić SRB
Dr. Predrag Banković SRB
Dr. Zorica Mojović SRB
Dr. Dušan Milivojević SRB
Dr. Miomir Korać SRB
Prof. Dr. Branislav Vlahović SRB
Dr. Radomir Žikić SRB
Prof. Dr. Stevo Najman SRB
Dr. Biljana Djordjević SRB
Dr. Anja Terzić SRB

Organizing Committee

Prof. Dr. Vojislav Mitić SRB
Dr. Nina Obradović SRB
Dr. Lidija Mančić SRB
Prof. Dr. Vladimir Pavlović SRB
Dr. Dušan Jovanović SRB
Dr. Zorica Lazarević SRB
Prof. Dr. Ljubica Pavlović SRB
Dr. Vesna Paunović SRB
Dr. Darko Kosanović SRB
Dr. Anja Terzić SRB
Dr. Suzana Filipović SRB
Dr. Vladimir Blagojević SRB
Prof. Zvonko Petković SRB
Ivana Dinić SRB
Zoran Gajić SRB
Jelena Živojinović SRB

Sponsors & Endorsements:

Analysis - Lab equipment, Belgrade (Serbia), Direktna Banka a.d. Kragujevac, Exchange office „Hulk“, LMB Soft, Niš (Serbia), SCAN doo. Preddvor (Slovenia), Voda Vrnjci (Serbia), Regular Authority of Electronic Media (Serbia), Turisticka organizacija Beograd, Štamparija "Format" and GRAND doo (Serbia).

Acknowledgements:

The Conference Organizers are grateful to the Ministry of Education and Science of the Republic of Serbia for financial support, as well as to the Serbian Academy of Sciences and Arts, European Academy of Sciences and Arts, American Ceramics Society, Institute of Technical Sciences of SASA, Archeological Institute of SASA, Institute of Physics UB, Vinča Institute of Nuclear Sciences - Laboratory of Physics (010), Electrical Engineering Institute Nikola Tesla and High School-Academy for Arts and Conservation, Serbian Orthodox Church.

OR-NOP2

In-vitro visualization of primary tumor cells using up-conversion nanophosphors

Lidija Mancic¹, Aleksandra Djukic-Vukovic², Ljiljana Mojovic², Mihailo Rabasovic³,
Aleksandar J. Krmpot³, Ivana Dinic⁴, Antonio MLM. Costa⁵, Olivera Milosevic¹

¹*Institute of Technical Sciences of SASA, Belgrade, Serbia*

²*Department of Biochemical Engineering and Biotechnology, Faculty of Technology and Metallurgy, University of Belgrade, Serbia*

³*Photonic Center, Institute of Physics Belgrade, University of Belgrade, Zemun, Belgrade, Serbia*

⁴*Innovation Center of the Faculty of Chemistry, University of Belgrade, Serbia*

⁵*Department of Chemical and Materials Engineering, Pontifical Catholic University of Rio de Janeiro, Rio de Janeiro, Brazil*

Due to their unique luminescent features, lanthanide doped up-converting nanoparticles (Ln-UCNPs) have an important role in biomedical use, particularly in the area of NIR-excited fluorescent cell imaging. For such purpose, Ln-UCNPs should have specific morphological characteristics and efficient luminescence response. In this work, a biocompatible and water dispersible NaYF₄:Yb,Er@PLGA nanoparticles synthesized using a one-step hydrothermal synthesis were tested as fluorescent bio-labels of primary cell cultures obtained after passage of head and neck squamous carcinoma cells (HNSCC). Structural, morphological and optical properties of particles were obtained using X-ray powder diffraction (XRPD), field emission scanning and transmission electron microscopy (FESEM/TEM), energy dispersive X-ray (EDX), Fourier transform infrared (FTIR) and photoluminescence (PL) spectroscopy. The results revealed coexistence of the cubic (*Fm-3m*) and hexagonal (*P6₃/m*) phase in spherical and irregularly shaped nanoparticles, respectively. Moreover, preservation of the PLGA ligands at the particles surface facilitates their interactions with the cell membrane and provides permeation into cells. To assess a biological safety of their use, viability of human gingival fibroblasts (HFG) was additionally evaluated by a colorimetric MTT assay.

OR-EM1

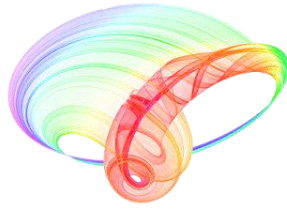
Effect of annealing temperature on structural and surface morphology of ceramic electrolyte for IT-SOFC applications

Shabana P. S. Shaikh, Kiran P. Adhi

*Center for Advanced Studies in Materials Science & Condensed Matter Physics
Department of Physics, Savitribai Phule Pune University, Pune 411007, India*

In the present work the powder of Gd_{0.1}Ce_{0.9}O_{1.95} Gadolinium-doped ceria (10GDC) is procured from Sigma Aldrich with 99.9% purity. Using powder 10GDC the electrolyte material in pellets form were sintered at different temperature of 800, 900, 1100 and 1200 °C for 4 hr in microwave high temperature furnace to investigate the effect of sintering temperature on density, structural and morphological properties of 10GDC. Density was measured using the Archimedes's method.

Book of abstracts



PHOTONICA2017

The Sixth International School and Conference on Photonics

& COST actions: MP1406 and MP1402



&H2020-MSCA-RISE-2015 CARDIALLY workshop



28 August – 1 September 2017

Belgrade, Serbia

Editors

Marina Lekić and Aleksandar Krmpot

Institute of Physics Belgrade, Serbia

Belgrade, 2017

ABSTRACTS OF TUTORIAL, KEYNOTE, INVITED LECTURES,
PROGRESS REPORTS AND CONTRIBUTED PAPERS

of

The Sixth International School and Conference on Photonics
PHOTONICA2017

28 August – 1 September 2017
Belgrade Serbia

Editors

Marina Lekić and Aleksandar Krmpot

Technical assistance

Marko Nikolić and Danica Pavlović

Publisher

Institute of Physics Belgrade
Pregrevica 118
11080 Belgrade, Serbia

Printed by

Serbian Academy of Sciences and Arts

Number of copies

300

ISBN 978-86-82441-46-5

PHOTONICA 2017 (The Sixth International School and Conference on Photonica - www.photonica.ac.rs) is organized by Institute of Physics Belgrade, University of Belgrade (www.ipb.ac.rs), Serbian Academy of Sciences and Arts (www.sanu.ac.rs), and Optical Society of Serbia (www.ods.org.rs).

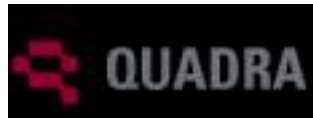


Other institution that helped the organization of this event are: Vinča Institute of Nuclear Sciences, University of Belgrade (www.vinca.rs), Faculty of Electrical Engineering, University of Belgrade (www.etf.bg.ac.rs), Institute of Chemistry, Technology and Metallurgy, University of Belgrade (www.ihtm.bg.ac.rs), Faculty of Technical Sciences, University of Novi Sad (www.ftn.uns.ac.rs), Faculty of Physics, University of Belgrade (www.ff.bg.ac.rs), and Faculty of Biology, University of Belgrade (www.bio.bg.ac.rs).

PHOTONICA 2017 is organized under auspices and with support of the Ministry of Education, Science and Technological Development, Serbia (www.mpn.gov.rs). PHOTONICA 2017 is supported and recognized by The Integrated Initiative of European Laser Research Infrastructures LaserLab-Europe (www.laserlab-europe.eu) and European Physical Society (www.eps.org).



The support of the sponsors of PHOTONICA 2017 is gratefully acknowledged:



Committees

Scientific Committee

Aleksandar Krmpot, Serbia
Antun Balaž, Serbia
Arlene D. Wilson-Gordon, Israel
Bojan Resan, Switzerland
Boris Malomed, Israel
Branislav Jelenković, Serbia
Dejan Gvozdić, Serbia
Detlef Kip, Germany
Dragan Indjin, United Kingdom
Edik Rafailov, United Kingdom
Feng Chen, China
Francesco Cataliotti, Italy
Giannis Zacharakis, Greece
Goran Isić, Serbia
Goran Mašanović, United Kingdom
Isabelle Philippa Staude, Germany
Jelena Radovanović, Serbia
Jerker Widengren, Sweden
Jovana Petrović, Serbia
Laurent Sanchez, France
Ljupčo Hadžievski, Serbia
Marco Santagiustina, Italy
Milan Mashanović, United States of America
Milan Trtica, Serbia
Miloš Živanov, Serbia
Milutin Stepić, Serbia
Milivoj Belić, Qatar
Nikola Stojanović, Germany
Pavle Andus, Serbia
Peđa Mihailović, Serbia
Radoš Gajić, Serbia
Schaaf Peter, Germany
Sergei Turitsyn, United Kingdom
Suzana Petrović, Serbia
Ticijana Ban, Croatia
Vladana Vukojević, Sweden
Zoran Jakšić, Serbia
Željko Šljivančanin, Serbia

Organizing Committee

Aleksandar Krmpot, (Chair)
Marina Lekić (Secretary)
Stanko Nikolić (webmaster)
Marko Nikolić,
Vladimir Veljić
Danica Pavlović

Technical Organizer



Two-photon excited hemoglobin fluorescence for *ex vivo* microscopy analysis of erythrocytes at single cell level

I. T. Drvenica¹, A. Stančić¹, S. Jovanić², V. Lj. Ilić¹, M. D. Rabasović², D. V. Pantelić², B. M. Jelenković², B.M. Bugarski³, A. J. Krmpot²

¹Institute for Medical Research, University of Belgrade, Dr Subotića 4, 11 129 Belgrade, Serbia

²Institute of Physics Belgrade, University of Belgrade, Pregrevica 118, 11 080 Belgrade, Serbia

³Department of Chemical Engineering, Faculty of Technology and Metallurgy, University of Belgrade, Karnegijeva 4, 11 000 Belgrade, Serbia

e-mail:ivana.drvenica@imi.bg.ac.rs

Fluorescence of hemoglobin, the main intracellular component of erythrocytes, upon excitation by ultra-short pulses in red and near infrared region [1-3], allows two-photon excited fluorescence (TPEF) microscopy to be used as a tool for label-free imaging of these cells, even *in vivo* [4]. Despite wide applicability of erythrocytes in diagnostic tests, and distribution of hemoglobin as a marker of their functional status under physiological or pathological conditions [5], data on spatial distribution of hemoglobin at the single cell level are scarce.

Based on findings reported by Zheng and co-workers [1], we have utilized TPEF microscopy to map the spatial distribution of hemoglobin in porcine erythrocytes *ex vivo*. Porcine erythrocytes were used as extremely susceptible cells to stress and thus represent a good model system to study influence of different factors (heat, humidity, malnutrition, infections...) on erythrocyte morphology and hemoglobin distribution. The custom made experimental set up for NLSM utilized the train of the femtosecond pulses from Ti:Sapphire laser (Coherent, Mira 900-F) at 730 nm. The repetition rate was 76MHz, and pulse duration was 160fs.

The results demonstrate that the resolution of the TPEF microscopy is good enough for the analysis of erythrocytes at single cell level. Two different morphological types of porcine erythrocytes, normocytes and echinocytes, collected during mild autumn and extremely hot summer, respectively, were clearly differed by TPEF microscopy. Besides, erythrocytes having intermediate morphology i.e. having some characteristics of both abovementioned morphological extremes were also found. The distribution of hemoglobin in erythrocytes noticeably followed the cells' shape, where erythrocytes with altered morphology demonstrated significant accumulation of hemoglobin in cells' protrusions. During TPEF microscopy experiments fluorescence emission from the exposed cells increased, but longer exposure led to irreversible change of erythrocytes, as already shown in literature [3]. Since functional status of erythrocytes *in vivo* (both in physiological or pathological states) and *ex vivo* (e.g. transfusion bag) [3] is accompanied with change of morphology and consequently altered distribution and functionality of hemoglobin, result of this study even though obtained on animal cell model, confirmed strong potential of TPEF microscopy for such application in biomedical research. However, *in vivo* tests by TPEF microscopy merit further experimental optimization.

This work is supported by bilateral project 451-03-01038/2015-09/1 between Ministry of Education, Science and Technological Development -MESTD of Republic of Serbia and German Academic Exchange Service-DAAD and by projects III45016, III 46010 and OI 171038 of MESTD of Republic of Serbia.

REFERENCES

- [1] W. Zheng, D. Li, Y. Zeng, Y. Luo, J. Y. Qu, Biomed. Opt. Express. 2, 71 (2010).
- [2] G. O. Clay, C. B. Chaffer, D. Kleinfeld, J. ChemPhys. 126, 025102 (2007).
- [3] I. Saytashev, R. Glenn, G.M. Murashova, S.Osseiran, D. Spence, C. L. Evans, M. Dantus, Biomed. Opt. Express. 7, 3449 (2016).
- [4] D. Li, W. Zheng, W. Zhang, S. K. Teh, Y. Zeng, Y. Luo, J. Y. Qu, Opt. Lett. 36, 2638 (2011).
- [5] V. V. Revin, et al. BioMed. Res. Int. 973973 (2015).

Second harmonic generation imaging of collagen fibers in the uninvolved human rectal mucosa 10 cm and 20 cm away from the malignant tumor

Sanja Despotović¹, Ivana Lalić¹, Novica Milićević¹, Živana Milićević¹, Mihailo Rabasović², Dejan Pantelić², Svetlana Jovanić² and Aleksandar Krmpot²

¹*Institute of Histology and embryology, Medical faculty, University of Belgrade, Serbia*

²*Institute of Physics Belgrade, University of Belgrade, Serbia*

e-mail: sanjadesp@med.bg.ac.rs

The aim of our study was to investigate the organization of collagen fibers utilizing second harmonic generation (SHG) microscopy in the lamina propria of the rectal mucosa in the remote surrounding of the malignant tumor. We demonstrated the structural alterations (reduced cellularity, alterations of Lieberkühn crypts and tissue edema) of the lamina propria of the mucosa 10 cm and 20 cm away from the rectal adenocarcinoma. Our study also provided indications that the collagen fibers in the rectal lamina propria could be affected [1].

Tissue samples were endoscopically collected from 30 patients with adenocarcinoma located in the sigmoid colon. The biopsies were taken 10 cm and 20 cm away from the malignant tumor in the caudal direction. The samples of rectal mucosa collected at the same institution from 30 healthy persons with a family history of intestinal malignancy, were used as control.

Masson trichrome staining on formalin-fixed, paraffin-embedded tissue was used to visualize collagen fibers. Also, to exclude the possibility that the observed changes could be due to methodology used (fixation or staining), an original labframe nonlinear laser scanning microscope (NLM) [2] was used for SHG imaging of collagen distribution on fixation- and label-free colon tissue samples. The incoming infrared femtosecond pulses from the tunable mode-locked Ti:Sapphire laser (Coherent, Mira 900) were directed onto the sample by a dichroic mirror through the Zeiss EC Plan-Neofluar 40x/1.3 NA oil immersion objective. The laser wavelength was 840 nm, and the SHG was selected by narrow bandpass filter at 420 nm (Thorlabs FB420-10, FWHM 10 nm). The average laser power on the sample was 30 mW with pulse duration of 160 fs and repetition rate of 76 MHz which produced 2.5 kW of peak power.

On Masson trichrome stained tissue, the collagen fibers in the lamina propria of healthy persons were massive, intimately appositioned and orderly organized. At the distance 10 cm away from the tumor the collagen fibers were feeble and loosely arranged. The enlarged spaces were notable between the collagen fibers, indicating the presence of tissue edema. Similar alterations of collagen fibers, but less prominent, were observed 20 cm away from the tumor.

SHG images on fresh, label-free tissue completely confirmed the aforementioned findings. The profound remodeling of collagen fibers is even more clearly noticeable on 3D reconstruction model obtained from SHG images. In the lamina propria 10 cm away from the tumor collagen fibers became fragile, increasingly disordered and the crypts architecture appeared disturbed.

We documented the profound alterations of collagen fibers in the rectal lamina propria 10 cm and 20 cm away from the malignant tumor.

Acknowledgment: This work is supported by bilateral project 451-03-01038/2015-09/1 between Ministry of Education, Science and Technological Development -MESTD of Republic of Serbia and German Academic Exchange Service-DAAD and by projects 175005, III45016 and OI 171038 of MESTD of Republic of Serbia.

REFERENCES

- [1] Despotović SZ, Milićević NM et al. *Histol Histopathol* **29**, 229-234(2014).
 [2] Rabasović MD, Pantelić DV et al. *J Biomed Opt* **20**, 016010(2015).

Second order optical autocorrelator for measuring ultra short laser pulses duration

Andreja Vladković¹, Mihailo Rabasović¹, Torsten Golz², Nikola Stojanović², Dejan Pantelić¹, Branislav Jelenković¹, Aleksandar Krmpot¹

¹*Institute of physics Belgrade, University of Belgrade,
Pregrevica 118,
11080 Belgrade, Serbia*

²*Deutsches Elektronensynchrotron (DESY),
Notkestrasse 85,
22607 Hamburg, Germany
e-mail: andrejav@ipb.ac.rs*

Second order, i.e. intensity, optical autocorrelation is well established and commonly used technique for ultrashort laser pulse duration measurements [1]. More advanced technique that combines autocorrelation and spectral measurements provides even exact temporal shape of the pulse [2]. We report on development of an intensity autocorrelator for measuring femtosecond pulses duration using a nonlinear crystal. Autocorrelator setup is based on Michelson interferometer with BBO (β Barium Borate) crystal in the detection arm for second harmonic generation. Corner cube prism on a motorised stage provides variable delay line. Photodiode with spectral filter was used for signal detection. Data acquisition, the stage driving and the autocorrelation traces display is performed by computer, acquisition card and specially developed software. The software performs simple data processing: filtering and calculation of the pulse duration as Full Width at Half Maximum (FWHM) of autocorrelation curve. Autocorrelator was used to measure duration of ultrashort pulses from a modelocked lasers. We have tested the set-up and the software for various pulse duration and wave lengths from two ultrafast lasers: Coherent Mira 900 (160fs, 700-1000nm) and Timebandwidth products, Yb GLX (200fs, 1040nm). For the longer pulse duration (150fs-5ps) regenerative amplifier Coherent RegA with external pulse compressor/stretcher was used.

Acknowledgments: This work is supported by bilateral project 451-03-01038/2015-09/1 between Ministry of Education, Science and Technological Development -MESTD of Republic of Serbia and German Academic Exchange Service-DAAD and by projects III45016 and OI 171038 of MESTD of Republic of Serbia.

REFERENCES

- [1] W. Demtroeder, Laser Spectroscopy, Springer (1996).
- [2] Rick Trebino, Frequency-Resolved Optical Gating: The Measurement of Ultrashort Laser Pulses, Springer (2002).

УНИВЕРЗИТЕТ У БЕОГРАДУ
Институт за физику



Конференција
**Десета радионица фотонике
(2017)**

Зборник апстраката



10th Photonics Workshop
Book of Abstracts
Копоник, 26.2–2.3, 2016

Копоник, 26.2–2.3.2016.

Конференција Десета радионица фотонице (2017)

Зборник апстраката

Копаоник 26.2.-2.3.2017.

Издаје

Институт за физику Универзитета у Београду

За издавача

др Александар Богојевић, директор

Уредник

др Драган Лукић

Тираж

100 примерака

ИСБН 978-86-82441-45-8

Штампа

Развојно-истраживачки центар,
Технолошко-металуршког факултета у Београду
Карнегијева 4, Београд

Програмски одбор:

др Бранислав Јеленковић, научни саветник Института за физику (председник)

др Дејан Пантелић, научни саветник Института за физику

др Љупчо Хаџиевски, научни саветник Института за нуклеарне науке „Винча“

др Павле Анђус, редовни професор Биолошког факултета

др Радош Гајић, научни саветник Института за физику

др Александер Ковачевић, виши научни сарадник Института за физику

др Александар Крмпот, виши научни сарадник Института за физику

Организациони одбор:

др Александер Ковачевић, виши научни сарадник Института за физику (председник)

др Драган Лукић, виши научни сарадник Института за физику

др Александар Крмпот, виши научни сарадник Института за физику

др Дарко Васиљевић, виши научни сарадник Института за физику

др Бранислав Јеленковић, научни саветник Института за физику

Спонзори Конференције:

Министарство просвете, науке и технолошког развоја Републике Србије

Оптичко друштво Србије

„Сензор инфиз“ д.о.о.

Hemoglobin imaging using two photon excitation fluorescence microscopy

Katarina Bukara¹, Svetlana Jovanić², Ivana T. Drvenica¹, Ana Stančić³, Vesna Ilić³, Mihailo D. Rabasović², Dejan Pantelić², Branislav Jelenković², Branko Bugarski¹, Aleksandar J. Krmpot²

(1) *Department of Chemical Engineering, Faculty of Technology and Metallurgy, University of Belgrade, Karnegijeva 4, 11 000 Belgrade, Serbia*

(2) *Institute of Physics Belgrade, University of Belgrade, Pregrevica 118, 11 080 Belgrade, Serbia*

(3) *Institute for Medical Research, University of Belgrade, Dr Subotića br. 4, 11 129 Belgrade, Serbia*

Contact: A. Krmpot (krmpot@ipb.ac.rs)

Abstract. Two photon excitation fluorescence (TPEF) microscopy as an advanced technique offers the possibility for noninvasive, label-free imaging by using the fluorescence emission from the endogenous fluorescent molecules in living cells and tissues. It has been shown recently that, hemoglobin, emits strong Soret fluorescence peaked at 438 nm upon two-photon excitation by femtosecond pulses in red and near infrared region (600-750 nm) [1]. This finding opened the possibility to use two-photon fluorescence microscopy as a powerful tool for label-free imaging of erythrocytes, even in vivo [2]. In this work we show the possibility to use TPEF microscopy for label-free 3D imaging of porcine and outdated human erythrocytes based on findings from [1]. Moreover, TPEF microscopy was employed to investigate the spatial distribution (i.e. for mapping) of hemoglobin within intact erythrocytes and residual hemoglobin in the resulting erythrocyte membranes obtained after the process of gradual hypotonic hemolysis. Quantity of residual hemoglobin is determined by analysis of TPEF images relative to the hemoglobin concentration in intact erythrocytes.

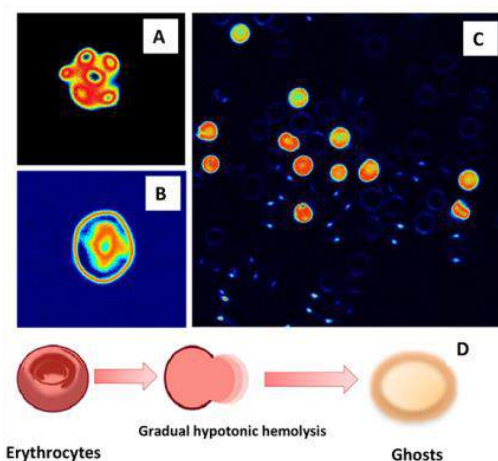


Figure 1. a) TPEF image of a porcine erythrocyte; b) TPEF image of a human erythrocyte; c) TPEF image of mixture of human erythrocytes and their membranes; d) schematic of gradual hypotonic hemolysis process.

This work has been supported by Ministry of Education, Science and Technological Development of the Republic of Serbia (Project No. III 46010, OI 171005, OI 171038 and III45016).

REFERENCES

- [1] W. Zheng, D. Li, Y. Zeng, Y. Luo, and J. Y. Qu, *Biomed Opt Express* **2** (2010).
- [2] D. Li, W. Zheng, W. Zhang, S. KhoonTeh, Y. Zeng, Y. Luo, and J. Y. Qu, *Opt. Lett.* **36**(2011)



СРПСКА АКАДЕМИЈА НАУКА И УМЕТНОСТИ

ЕКОЛОШКИ И ЕКОНОМСКИ ЗНАЧАЈ ФАУНЕ СРБИЈЕ



ЕКОЛОШКИ И ЕКОНОМСКИ
ЗНАЧАЈ ФАУНЕ СРБИЈЕ

SERBIAN ACADEMY OF SCIENCES AND ARTS

SCIENTIFIC MEETINGS
Book CLXXI

DEPARTMENT OF CHEMICAL AND BIOLOGICAL SCIENCES
Book 12

ECOLOGICAL AND ECONOMIC SIGNIFICANCE OF FAUNA OF SERBIA

PROCEEDINGS OF THE SCIENTIFIC MEETING
held on November 17, 2016

E d i t o r
Corresponding Member
RADMILA PETANOVIĆ

BELGRADE 2018

СРПСКА АКАДЕМИЈА НАУКА И УМЕТНОСТИ

НАУЧНИ СКУПОВИ
Књига CLXXI

ОДЕЉЕЊЕ ХЕМИЈСКИХ И БИОЛОШКИХ НАУКА
Књига 12

ЕКОЛОШКИ И ЕКОНОМСКИ ЗНАЧАЈ ФАУНЕ СРБИЈЕ

ЗБОРНИК РАДОВА СА НАУЧНОГ СКУПА
одржаног 17. новембра 2016.

Уредник
дописни члан
РАДМИЛА ПЕТАНОВИЋ

БЕОГРАД 2018

Издаје
Српска академија наука и уметности
Београд, Кнез Михаилова 35

Лектура и коректура
Тања Рончевић

Прелом и дизајн корица
Никола Стевановић

Технички уредник
Мира Зебић

Тираж 400 примерака

Штампа
Colorgrafx, Београд

Српска академија наука и уметности © 2018

САДРЖАЈ
CONTENTS

Предговор	9
Preface	13
Александар Ћетковић, Владимир Стевановић ОЧУВАЊЕ И ВРЕДНОВАЊЕ БИОДИВЕРЗИТЕТА: КОНЦЕПТ ЕКОСИСТЕМСКИХ УСЛУГА И БИОЛОШКИ РЕСУРСИ ФАУНЕ	17
Aleksandar Ćetković, Vladimir Stevanović PRESERVATION AND EVALUATION OF BIODIVERSITY: THE CONCEPT OF ECOSYSTEM SERVICES AND BIOLOGICAL RESOURCES OF FAUNA	36
Душко Ћировић, Срђан Стаменковић ФАУНА СИСАРА СРБИЈЕ – ВРЕДНОВАЊЕ ФУНКЦИОНАЛНЕ УЛОГЕ И ЗНАЧАЈА ВРСТА У ЕКОСИСТЕМИМА	39
Duško Ćirović, Srđan Stamenković MAMMALS FAUNA OF SERBIA – VALORISATION OF FUNCTIONAL ROLE AND SPECIES IMPORTANCE IN ECOSYSTEMS	62
Воислав Васић О ВАЖНОСТИ ПТИЦА: ПРИМЕРИ ЕГЗИСТЕНЦИЈАЛНЕ ВРЕДНОСТИ И ПРАКТИЧНОГ ЗНАЧАЈА У СРБИЈИ	67
Voislav Vasić ON THE IMPORTANCE OF BIRDS: EXAMPLES OF THE EXISTENTIAL VALUE AND PRACTICAL SIGNIFICANCE OF THE BIRDS IN SERBIA	100

Имре Кризманић, Тања Вуков ВОДОЗЕМЦИ У СРБИЈИ ДАНАС И СУТРА – ЕКОЛОШКИ И ЕКОНОМСКИ ЗНАЧАЈ	103
Imre Krizmanić, Tanja Vukov AMPHIBIANS IN SERBIA TODAY AND TOMORROW – ECOLOGICAL AND ECONOMIC VALUE	138
Мирјана Ленхардт, Весна Ђикановић, Александар Хегедиш, Желјка Вишњић-Јефтић, Стефан Скорић, Марија Смедеревац-Лалић КВАЛИТАТИВНО-КВАНТИТАТИВНЕ ПРОМЕНЕ ИХТИОФАУНЕ У ПРОТОЧНИМ ДУНАВСКИМ АКУМУЛАЦИЈАМА ПОСЛЕ ИЗГРАДЊЕ БРАНА ЂЕРДАПСКИХ ХИДРОЕЛЕКТРАНА	143
Mirjana Lenhardt, Vesna Đikanović, Aleksandar Hegediš, Željka Višnjić-Jeftić, Stefan Skorić, Marija Smederevac-Lalić QUALITATIVE AND QUANTITATIVE CHANGES IN THE ICTHYOFAUNA OF THE DANUBIAN RESERVOIRS AFTER THE CONSTRUCTION OF THE IRON GATES HYDROPOWER PLANT DAMS	168
Зоран Марковић, Марко Станковић, Божидар Рашковић, Ненад Секулић, Весна Полексић АКВАКУЛТУРА У СЛУЖБИ ЗАШТИТЕ УГРОЖЕНИХ ВРСТА РИБА У СРБИЈИ	173
Zoran Marković, Marko Stanković, Božidar Rašković, Nenad Sekulić, Vesna Poleksić AQUACULTURE IN SERVICE OF EDANGERED FISH SPECIES PROTECTION IN SERBIA	195
Ивана Живић, Александар Остојић, Бранко Миљановић, Зоран Марковић МАКРОИНВЕРТЕБРАТЕ ТЕКУЋИХ ВОДА СРБИЈЕ И ЊИХОВ БИОИНДИКАТОРСКИ ЗНАЧАЈ У ПРОЦЕНИ КВАЛИТЕТА ВОДЕ	199
Ivana Živić, Aleksandar Ostojić, Branko Miljanović, Zoran Marković MACROINVERTEBRATES OF SERBIAN STREAMS AND THEIR SIGNIFICANCE AS BIOINDICATORS IN ESTIMATION OF WATER QUALITY	226

Дејан Пантелић, Срећко Ђурчић, Александар Крмпот, Дејан В. Стојановић, Михаило Рабасовић, Светлана Савић-Шевић МОРФОЛОШКЕ СТРУКТУРЕ НЕКИХ ПРЕДСТАВНИКА ЕНТОМОФАУНЕ СРБИЈЕ КАО МОДЕЛИ У БИОМИМЕТИЦИ	231
Dejan Pantelić, Srećko Ćurčić, Aleksandar Krmpot, Dejan V. Stojanović, Mihailo Rabasović, Svetlana Savić-Šević THE MORPHOLOGICAL STRUCTURES OF SOME REPRESENTATIVES OF THE ENTOMOFAUNA OF SERBIA AS MODELS IN BIOMIMETICS	250
Михаела Кавран, Александра Игњатовић Ђупина, Марија Згомба, Душан Петрић ЈЕСТИВИ ИНСЕКТИ – БЕЗБЕДНА ХРАНА ЗА ЉУДЕ И ДОМАЋЕ ЖИВОТИЊЕ	251
Mihaela Kavran, Aleksandra Ignjatović Ćupina, Marija Zgomba, Dušan Petrić EDIBLE INSECTS – SAFE FOOD FOR HUMANS AND LIVESTOCK	295
Жељко Томановић, Владимир Жикић КОМПЛЕКСИ БРАКОНИДНИХ ОСА (HYMENOPTERA, ICHNEUMONOIDEA, BRACONIDAE) У СРБИЈИ И ЊИХОВ ЗНАЧАЈ У БИОЛОШКОЈ КОНТРОЛИ	301
Željko Tomanović, Vladimir Žikić BRACONID COMPLEXES (HYMENOPTERA, ICHNEUMONOIDEA, BRACONIDAE) IN SERBIA; THE IMPORTANCE IN BIOLOGICAL CONTROL	308
Љубодраг Михајловић ЕКОЛОШКИ И ЕКОНОМСКИ ЗНАЧАЈ ФАУНЕ НАДФАМИЛИЈЕ CHALCIDOIDEA СРБИЈЕ (INSECTA:HYMENOPTERA)	313
Ljubodrag Mihajlović ENVIRONMENTAL AND ECONOMIC SIGNIFICANCE OF ZOOLOGY OF THE SUPERFAMILIA CHALCIDOIDEA IN SERBIA (INSECTA: HYMENOPTERA)	337

- Иво Тошевски, Оливер Крстић, Јелена Јовић,
Биљана Видовић, Радмила Петановић
ИНСЕКТИ И ГРИЊЕ У ФАУНИ СРБИЈЕ ОД ЗНАЧАЈА
ЗА КЛАСИЧНУ БИОЛОШКУ КОНТРОЛУ КОРОВА 341
- Ivo Toševski, Oliver Krstić, Jelena Jović,
Biljana Vidović, Radmila Petanović
INSECTS AND MITES IN THE FAUNA OF SERBIA –
IMPORTANCE FOR THE CLASSICAL BIOLOGICAL
CONTROL OF WEEDS 363
- Љубиша Станисављевић, Анте Вујић, Предраг Јакшић, Злата Марков,
Александар Ћетковић
ФУНКЦИОНАЛНО-ЕКОЛОШКИ СТАТУС, УГРОЖЕНОСТ И
ЕКОНОМСКО ВРЕДНОВАЊЕ ИНСЕКТА ОПРАШИВАЧА У
СРБИЈИ 367
- Ljubiša Stanisavljević, Ante Vujić, Predrag Jakšić, Zlata Markov,
Aleksandar Ćetković
FUNCTIONAL AND ECOLOGICAL STATUS, VULNERABILITY
AND ECONOMIC EVALUATION OF INSECT POLLINATORS IN
SERBIA 411

ПРЕДГОВОР

Тематски скуп о еколошком и економском значају фауне Србије, који је иницирао Академијски одбор за проучавање фауне Србије САНУ, одржан је у јубиларној години обележавања 175. годишњице САНУ, 17. новембра 2016. године.

Откада је појам **биодиверзитета** званично ушао у употребу 1992. године доношењем Конвенције о биолошкој разноврсности а потом и њеном ратификацијом којом су све државе потписнице преузеле **обавезу** да донесу законска акта и успоставе потребне активности на **заштити и вредновању** биодиверзитета, истраживања флоре, фауне и фунгије добила су на значају, а класичне биолошке дисциплине – таксономија, биогеографија и екологија – нашле су се у жижи интересовања не само научне већ и шире јавности. Таксономија, систематика и фаунистика, односно флористика, традиционалне биолошке дисциплине са најдужом традицијом у биологији, доживеле су свој препород или тријумфални повратак.

Важно је истаћи да је Српска академија наука и уметности, од свог оснивања, препознала значај изучавања живог света Србије и околних земаља и да је увидела да је повратак ових биолошких дисциплина важан задатак биолога у Србији на почетку новог миленијума. Два Академијска одбора, Одбор за изучавање флоре и вегетације и Одбор за проучавање фауне Србије, покренула су и остварила капитална дела флористике, фитоценологије и фаунистике у Србији. Едиција Флоре Србије доживљава друго, ново и значајно измењено издање, објављују се нови прилози у едицији Вегетација Србије, а едиција Фауна Србије већ има неколико вредних монографија: *Фауна мрава Србије*, *Крпељи Србије*, *Репати водоземци Србије*. Овим публикацијама САНУ се представила као најрелевантнија институција у Србији, фокусирана, преко одбора, на истраживања флоре и фауне, што имплицира свеобухватно сагледавање биодиверзитета у Србији.

Одржани научни скупови посвећени, директно или индиректно овој проблематици додатно потврђују спремност и разумевање САНУ да

истраживања флоре и фауне, као и биодиверзитета Србије, одлучно подржи. У том контексту би требало и разумети овај научни скуп.

Примена Конвенције о биолошкој разноврсности и њених полазних идеја и концепција временом је довела до разраде, унапређивања и усредсређивања на неке друге аспекте очувања и коришћења биодиверзитета, а не само његове вредности као више или мање обновљивог ресурса, већ и читавих екосистема, односно до функционалности њихових кључних компоненти или процеса који омогућавају корист и добробит за било коју људску заједницу. То је остварено дефинисањем **екосистемских услуга** као **кључног теоријског приступа и практичног механизма** за свеобухватно **вредновање** реалног значаја очувања биодиверзитета.

Подсетићемо се овим приликом да је 2005. године у организацији Одбора „Човек и животна средина“ Српске академије наука и уметности, одржан научни скуп **„Биодиверзитет на почетку новог миленијума“** који је **сумирао фундаменталне теме** које се тичу биодиверзитета, развоја идеје о потреби заштите и парадигми одрживости са циљем да пружи одговоре на значајна питања: колико је у нашем друштву порасла свест о потреби заштите биодиверзитета; шта је у међувремену урађено на плану инвентаризације биодиверзитета и колики су трошкови заштите биодиверзитета, односно који су економски модалитети потребни за остваривање склада између заштите биодиверзитета и коришћења биолошких ресурса.

Научни скуп „Еколошки и економски значај фауне Србије“ комплементаран је, у извесној мери, наведеном, и надовезује се темама које обрађује на неке аспекте очувања и заштите биодиверзитета, примарно на **вредновање** фауне Србије као елемената биодиверзитета у функцији **биолошких ресурса**, али и у складу са савременим приступом о **екосистемским услугама биодиверзитета** пре свега у доменима „снабдевања/обезбеђивања“ и регулације, али и „културних“ вредности/добара.

Сви научни радови, у Зборнику, подвлаче циљеве научног скупа, одржаног 17. новембра 2016. године:

- сагледавање напретка који је постигнут разрадом концепата из Конвенције и доношењем допунских стратешких докумената чији је циљ да олакшају комплексне задатке очувања биодиверзитета и коришћења биолошких ресурса, генерално, а посебно у Србији, као и да се укаже на неодрживу праксу експлоатације и недовољне бриге о ресурсима фауне;
- сагледавање функционалне улоге и значаја припадника фауне Србије и указивање на њихове вредности у контексту новоуспостављеног концепта **екосистемских услуга** пре свега као биоиндикатора загађења средине, те илустративних и инспиративних примера у биомиметици и биофизици, као чинилаца биолошке контроле штет-

них организама, опрашивања биљака или као елемената естетске и других нематеријалних вредности, у различитим доменима људске егзистенције и делатности у Србији;

- сагледавање значаја које поједине врсте или фаунистичке групе имају као ресурси хранљивих и лековитих супстанци и других, за човека корисних и употребљивих својстава.

Очекујемо да ће резултати анализа у Зборнику са научног скупа „Еколошки и економски значај фауне Србије“, допринети планирању пројеката вредновања и очувања биодиверзитета, процени угрожености и заштити фауне Србије, као и одрживом коришћењу биолошких ресурса фауне и омогућити сагледавање садашњег стања у националној легислативи и активностима надлежних сектора и однос заједнице према живом свету као природној баштини у Србији данас. Очекујемо да ће се истаћи и економски значај, односно вредновање појединих таксона животиња, не само у контексту биолошких ресурса, већ вредности њихове улоге у склопу екосистемских услуга које пружају, а уколико не постоје одговарајући подаци у Србији, да се процене могу извести на основу аналогних података из других земаља, са циљем очувања биодиверзитета Србије.

У Београду, 17. јануара 2018. године

Радмила Петановић, дописни члан

PREFACE

The thematic conference on ecological and economic importance of Serbian fauna, initiated by the SASA Academic committee for the study of the fauna of Serbia, was held in the jubilee year of marking the 175 years of SASA, on 17th November 2016.

Since the term biodiversity was officially put into use in 1992, with the Convention on Biological Diversity entering into force and its later ratification which led to all signatory states taking the obligation to impose legal acts and establish necessary activities regarding the protection and evaluation of biodiversity, the exploration of flora, fauna and fungi gained importance while classical biological disciplines such as taxonomy, biogeography and ecology were placed in the focus of not only scientific, but also wider public. Taxonomy, systematics and faunistics, i.e. floristics, traditional biological disciplines with the longest tradition in biology, have witnessed their rebirth and triumphal return.

It is important to highlight that the Serbian Academy of Sciences and Arts since its inception has recognized the importance of studying the living world of Serbia and surrounding countries, and that the return of these biological disciplines is an important task for Serbian biologists at the beginning of the new millennium.

Two Academic committees, the Academic committee for the study of flora and vegetation and the Academic committee for the study of the fauna of Serbia, have initiated and accomplished capital works in the field of floristics, phytocoenology and faunistics in Serbia.

The publication *Flora of Serbia* has had a new, second and significantly revised edition, new contributions within the edition *Vegetation of Serbia* have been published, and the edition *Fauna of Serbia* has already got several valuable monographs – the *Ant Fauna of Serbia*, *Ticks of Serbia*, *Tailed Amphibians of Serbia*. These publications show that SASA, through its committees, is like few institutions in Serbia, centered on the exploration of flora and fauna, which can ultimately be classified as an inevitable and comprehensive view on biodiversity in Serbia. The previous scientific conferences directly or indirectly

dedicated to this subject, additionally confirm the readiness and understanding of SASA to offer its strong support to the exploration of flora and fauna, as well as the biodiversity of Serbia. This scientific conference should also be understood through such context.

The application of the Convention on Biological Diversity and its initial ideas and conceptions, eventually led to the elaboration, improvement and focusing on some other aspects of conservation and use of biodiversity, not only its value as a more or less renewable resource, but also the whole ecosystems, i.e. the functionality of their key components or processes which provide benefit and well-being to any human community. This was accomplished by defining ecosystem services as a key theoretical approach and practical mechanism for comprehensive evaluation of the real importance of biodiversity conservation.

On this occasion, we would like to bring to mind the scientific conference “Biodiversity at the onset of a new millennium” held in 2005, organized by the “Man and Environment” Committee of SASA, summing up fundamental issues regarding biodiversity, development of the idea on the need of protection and paradigm of sustainability with the aim to offer answers to questions such as:

- how much has the awareness on the need of biodiversity preservation been developed in our society;
- what has been done about the plan of inventory of biodiversity in the meantime;
- and how big the expenses of protecting biodiversity are, i.e. which economic modalities are necessary for achieving harmony between the protection of biodiversity and the use of biological resources.

The scientific conference “Ecological and economic importance of Serbian fauna” is somewhat complementary to the above mentioned conference, with the areas of interest it explores, building on certain aspects of conservation and protection of biodiversity, above all the evaluation of fauna of Serbia as an element of biodiversity in the function of biological resources, and in accordance with the contemporary approach to ecosystem services of biodiversity, primarily in the domain of “supplying/providing” and regulation, but also “cultural” values/goods.

The aim of this scientific conference and the scientific papers to be published in the Proceedings is to enable:

- perceiving the progress made by elaborating concepts from the Convention and imposing additional strategic documents aimed at facilitating complex tasks of preserving biodiversity and using biological resources in general, especially in Serbia, as well as indicating the unsustainable exploitation practice and insufficient care for the resources of fauna;

- perceiving the functional role and importance of the members of Serbian fauna and indicating their values in the context of the newly established concept of ecosystem services, primarily as bioindicators of environmental pollution, as illustrative and inspirational examples in biomimetics and biophysics, as factors of biological control over harmful organisms, plant pollination or elements of esthetic and other immaterial values, in various domains of human existence and activity in Serbia;
- perceiving the importance that certain species or faunistic groups have as resources of nutritive and healing substances and other useful and usable properties to people.

We expect that the results of analysis, published in the Proceedings from the scientific conference “Ecological and economic significance of Fauna of Serbia”, will be useful for planning the projects of evaluating and preserving biodiversity, assessing the endangerment and protection of Serbian fauna, as well as sustainable use of biological resources of fauna, and that we will be able to perceive the current situation in national legislation and activities, along with the attitude of the community towards the living world as a natural heritage in Serbia today. We also expect to draw attention to the economic significance, i.e. the evaluation of certain animal taxa, not only in the context of biological resources but also the value of their role within the ecosystem services they offer, and if there are no sufficient data in Serbia, that assessments based upon corresponding data from other countries will be made, all in order to preserve the biodiversity of Serbia.

Belgrade, 17th January 2018

Radmila Petanović, corresponding member

МОРФОЛОШКЕ СТРУКТУРЕ НЕКИХ ПРЕДСТАВНИКА ЕНТОМОФАУНЕ СРБИЈЕ КАО МОДЕЛИ У БИОМИМЕТИЦИ

Дејан ПАНТЕЛИЋ*, Срећко ЋУРЧИЋ**, Александар КРМПОТ*, Дејан В.
СТОЈАНОВИЋ***, Михаило РАБАСОВИЋ*, Светлана САВИЋ-ШЕВИЋ*

С а ж е т а к. – Током веома дугог еволутивног развоја живи организми су развили добро адаптиране материјале и структуре који представљају напредна решења у области оптике, механике, термике или акустике, чак и са аспекта модерне науке, што је довело до интензивног развоја биомиметике као области која се бави стварањем нових технологија инспирисаних биолошким макроструктурама и микроструктурама. Код већег броја таксона лептира и тврдокрилаца, елемената фауне Србије, примећује се структурна обојеност њихових крила и покрилаца. Она настаје због присуства низа наизменичних ваздушних и хитинских слојева кутикуле (нпр. ребра, ламеле и гребени на љуспицама крила лептира), на којима се испољава таласна природа светлости кроз појаве интерференције, дифракције и расејања. При томе долази до селективне рефлексije светлосних таласа и појаве структурних боја. Овде су представљене методе генерисања биоморфних структура применом холографије, микролитиграфије и сродних оптичких техника. Указано је на могућности практичне примене морфолошких структура појединих врста инсеката из Србије у области сензора, заштите докумената и нових оптичких материјала.

Кључне речи: биофотоника, биомиметика, инсекти, структурне боје

* Институт за физику, Универзитет у Београду, pantelic@ipb.ac.rs, krmopot@ipb.ac.rs, rabasovic@ipb.ac.rs, svetlana.savic@ipb.ac.rs

** Институт за зоологију, Универзитет у Београду – Биолошки факултет, srecko@bio.bg.ac.rs

*** Институт за низијско шумарство и животну средину, Универзитет у Новом Саду, dvstojanovic@uns.ac.rs

УВОД

Природа је одувек била инспирација обичном човеку, уметнику или научнику. Сетимо се Ван Гогових пејзажа, слике са цветовима ириса или вазе са сунцокретима. Поменимо и писца научне фантастике Станислава Лема и његов роман „Непобедиви“, у коме ројеви минијатурних, летећих, инсектоликих робота, на далекој планети, нападају моћну интергалактичку крстарицу, исказујући своју колективну интелигенцију. Роман је превазишао уметност и имао је утицај на развој концепта „паметне прашине“ (енгл. smart dust) [1] као система бежично повезаних сензора.

И многе друге идеје, открића и проналасци су произашли из посматрања природе. Ото Лилијентал је објавио књигу „Лет птица као основа вештине летећа“ [2] и конструисао низ летећих машина инспирисаних птицама. Протезе спринтера Оскара Писторијуса, конструисане од композита са угљеничним влакнима, акумулирају механичку енергију и имају велику сличност са ногама кенгура. Поменимо и проналазача Жоржа де Местрала и његову чичак траку, чије само име указује на извор инспирације. Многе рачунарске и алгоритамске технике, попут целуларних аутомата [3], неуронских мрежа, еволуционих и генетских алгоритама, интелигенције роја [4] „позајмљене“ су из природе.

Тешко је одредити тачан историјски тренутак када је посматрање и имитирање природе претворено у посебну научну област. Пре ће бити да је целокупни развој цивилизације у доброј мери био везан за учење од природе, да би данас овај правац истраживања добио назив биомиметика. Њен циљ је да се посматрањем организама и биолошких система открију потенцијално корисне особине или „инжењерско-технолошка“ решења, која ће се затим копирати. Као пример ћемо навести сложене очи зглавкара, које имају веома широк видни угао, за разлику од стандардних оптичких система. Иако постоје панорамски објективи и технике панорамског снимања и међусобног повезивања слика, опрема је скупа, процедура компликована, а процес снимања је дуготрајан. Насупрот томе, еволуција је код већине зглавкара проблем решила на једноставан и ефикасан начин: уместо једног компликованог система, употребила је мноштво малих и једноставних (оматидије као делови сложеног ока) [5].

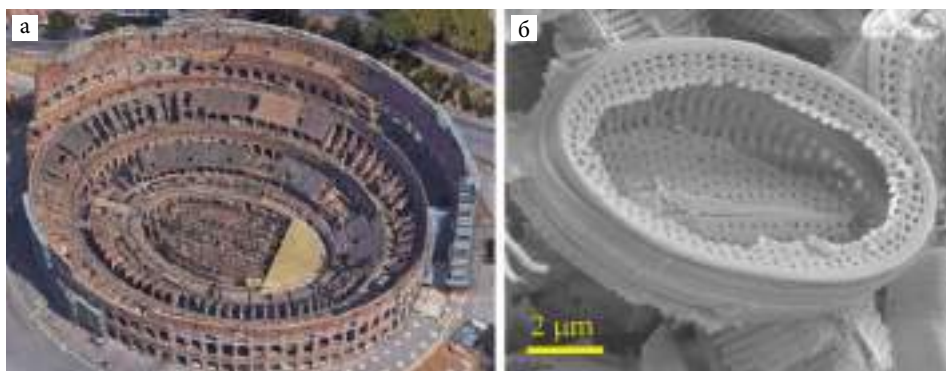
Сродна биомиметици је бионика, која означава инжењерски приступ имитацији природе, где није битно само разоткрити принципе функционисања живих организама, већ на ефикасан начин конструисати и направити производ. Као пример, наведимо фабрикацију материјала са суперхидрофобним својствима (способних да их не кваси вода). Одавно се зна да кутикула инсеката и површина листа лотоса одбијају воду [6], те да кожа ајкуле значајно смањује хидродинамички отпор [7]. У оба случаја, површина тела организама је покривена микронским и субмикронским избочинама, чиме се значајно мењају хидростатичке и хидродинамичке особине. Користећи ове принципе,

развијена је једноставна техника која користи савремени композитни материјал (полимер и угљеничне нанотубе) да рационално произведе суперхидрофобну површину [8].

Биомиметика понекад произлази из физичких услова који се постављају пред сложене системе, независно од тога да ли их је „конструисала“ природа или их је конструисао човек. Погледајмо само велику сличност између архитектуре римског Колосеума и „архитектуре“ дијатоме (сл. 1(а) и 1(б)). Као што је констатовано у раду [9], механичка отпорност фрустуле дијатома је веома добра, те се предлаже директно копирање биолошке механичке конструкције у архитектонску.

Често се среће и термин биоинспирација [10, 11], са прилично магловитом разликом у односу на биомиметику. Можда би се могло рећи да је то област којој биолошки системи служе само као полазна тачка за конципирање нових материјала, машина или уређаја. Не тежи се детаљном копирању биолошких функција, већ се неке од њих задржавају, а друге изостављају, са циљем задржавања жељене функције, уз могућност техничке реализације савременим технологијама. Истраживања сложеног ока рака *Odontodactylus scyllarus* (Linnaeus, 1758) показала су супериорна поларизациона својства у односу на савремене оптичке елементе овог типа [12]. У том смислу, ово је биоинспиративни путоказ за конструкцију нових оптичких компонената, као и других вештачких материјала, наравно, модерним технологијама.

На крају, један од интересантних праваца представља и функционализација биолошких структура или структура биолошког порекла. Овде се директно користе организми или њихови делови, који се затим модификује тако да раде ствари за које нису предвиђени својом биолошком природом. Занимљив је пример раније употребе (у XIX веку) нити паукове мреже као кончанице у окуларима оптичких инструмената и нишанских справа [13]. Све до појаве микролитиграфије, то је био једини начин да се у оптичке инструменте уграде веома fine нишанске линије, у распону дебљина од 2 до 10 μm (што је особина нити мреже паука крсташа – *Araneus diadematus* (Clerck, 1757)).



Слика 1. Сличност архитектуре (а) римског Колосеума и (б) дијатоме

Биомиметика, бионика, биоинспирација или функционализација нису термини којима се описује једна, добро дефинисана, област истраживања. У зависности који се аспект посматра, можемо бити инспирисани механиком, оптиком, термиком, трибологијом, адхезијом, акустиком, радиометријом, али и хемијом, организацијом или структуром. Истраживања су стога увек мултидисциплинарна, одређена знањем, искуством и интересовањем истраживача који их спроводе. Ми ћемо у овом раду приказати оне аспекте биомиметике који се тичу оптичких ефеката у живом свету [14] и могућности њихове практичне примене.

ИНСЕКТИ КАО ИНСПИРАЦИЈА У БИОФОТНИЦИ И БИОМИМЕТИЦИ

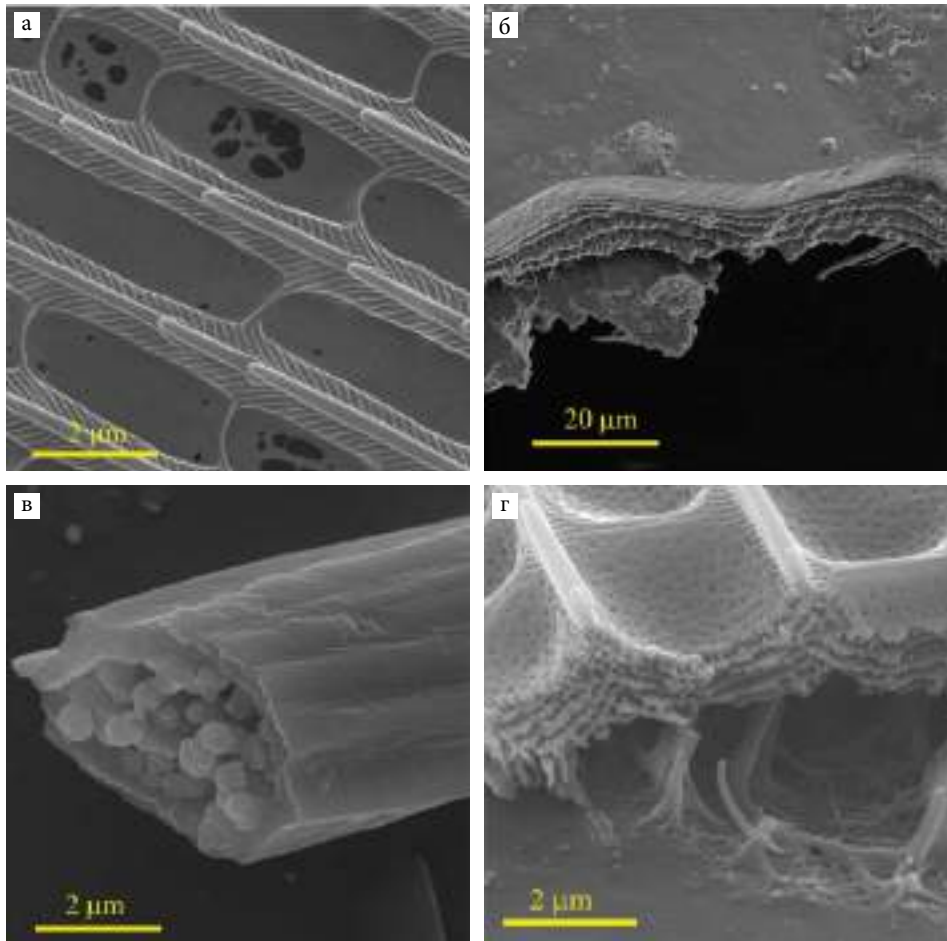
Инсекти су једна од најбројнијих група живих организама. Настајују скоро све екосистеме, а током еволуције су се развили различити механизми опстанка код бројних врста. Између осталог, на телу одређених инсеката се могу наћи зупчаник (*Issus coleopratus* (Fabricius, 1781) [15]), супер хидрофобне (*Morpho aega* (Hübner, 1822) [16]) и адхезивне структуре [17], као и сложене очи [18, 19].

Зато је поље биомиметике инсеката широко отворено за откривање нових принципа и њихово практично коришћење. Посебно је интересантна оптика, где постоји велики број студија заснованих на структурама инсеката – нпр. површински појачано Раманово расејање (енгл. surface-enhanced Raman scattering (SERS)), као метод детекције ниске концентрације анализата [20], љуспице крила лептира као сензори (*Euploea mulciber* (Cramer, 1777) [21], *Morpho sulkowskyi* (Kollar, 1850) [22]), инсектима инспирисани оптички филтери у заштити докумената (*Pierella luna* (Fabricius, 1793) [23]), радијативно хлађење (*Cataglyphis bombycina* Roger, 1850 [24]), ефикасни детектори инфрацрвеног зрачења (*Merimna atrata* (Gory & Laporte, 1837) [25], *M. sulkowskyi* [26]), итд.

Оптика кутикуле инсеката

Да би се добро разумела оптика инсеката, посветићемо ово кратко потглавље ефектима који постоје на њиховој кутикули. Основна намена им је да инсекту дају карактеристично обојење које му омогућава мимикрију, апосемију, дисруптивне ефекте (привидну промену контуре тела), што као последицу има ефикасније преживљавање у природном окружењу.

Са оптичке тачке гледишта, највише је заступљена апсорпција на различитим пигментима, попут меланина, птерина или каротеноида (пигментна обојеност) [27]. Дијапазон боја, који се на овај начин добија, је релативно ограничен, па је природа морала да посегне за напреднијим оптичким ме-



Слика 2. Примери (а) површинске (*Argynnis adippe* (Denis & Schiffermüller, 1775)) и (б) слојевите структуре кутикуле инсеката (*Calosoma sycophanta* (Linnaeus, 1758)), (в) запреминске структуре длачица (*Agapanthia violacea* (Fabricius, 1775)) и (г) мешовите површинско-запреминске структуре (*Jordanita globulariae* (Hübner, 1793))

ханизмима, као што су интерференција, расејање, поларизација, дифракција, преламање и таласоводна пропација. Већина поменутих ефеката се ослања на таласне особине светлости, што се у крајњем исходу своди на селективну рефлексију појединих спектралних интервала, чиме се постиже неопходна обојеност. Код инсеката се на овакав начин добијају боје из плавог и зеленог дела спектра, као и златне и сребрне боје. Занимљиво је да се код многих инсеката боје мењају са углом посматрања – ова појава се назива иридесценција.

Сви ови ефекти се виде само онда када је кутикула структурирана на микронском и субмикронском нивоу. Уочавају се паралелне линије (које

функционишу као дифракционе решетке – сл. 2(а)), слојевите структуре (сл. 2(б)), правилни (сл. 2(в)), комплексни (сл. 2(г)), запремински облици (фотонски кристали), низови брадавичастих испупчења, храпаве, неправилне површине, и све то у невероватном броју међусобних комбинација. Ове структуре се могу налазити у дубини кутикуле, као што је то најчешће случај код Coleoptera, или на љуспицама и длачицама које облажу кутикулу код Lepidoptera или неких Coleoptera. Боје настале на овакав начин (нпр. код лептира са сл. 3) називамо структурним.

Понекад морфолошке структуре немају улогу у стварању обојења, већ служе као помоћна компонента у смањивању губитака у оптичком систему ока. Велики број инсеката користи правилне структуре на површини корнее оматидија, које тада функционишу као антирефлексионни слој, који обезбеђује да највећи део светлосне енергије стигне до фоторецептора (кућна мува [28]).



Слика 3. Структурна обојеност крила лептира *Apatura metis* (Freyer, 1829).
На левом предњем крилу се види иридесцентна љубичаста боја,
која мења своју нијансу са променом угла посматрања

Кратак преглед техника анализе оптичких структура инсеката

Биомиметика суштински има два дела. Први се бави анализом природних структура, мерењем њихових оптичких особина (спектар, усмереност, поларизација) и разоткривањем физичких принципа који стоје иза примећених ефеката. Други покушава да искористи постојеће технологије ради имитације поменутих структура и ефеката.

С обзиром на минијатурност структура које се посматрају, најважније су микроскопске методе анализе: скенирајућа (SEM) и трансми-

сиона електронска микроскопија (ТЕМ), микроскопија атомских сила (AFM), конфокална и нелинеарна микроскопија (NLM) [29], микротомографија и нанотомографија, дигитална холографија [30, 31] и холографска микроскопија [32].

Дифрактометрија проучава распршивање светлости због дифракције на структурама чије су димензије поредиве са таласном дужином видљиве светлости. Тиме се зрачење расипа у широком просторном углу, а његово мерење омогућава да се стекне увид у природу самих структура. Ако се користе могућности холографије, могуће је добити и слику самих структура (дигитална холографска микроскопија).

Спектрална анализа је једна од важних техника, јер облик спектра одређује обојеност кутикуле [33] и служи као путоказ ка објашњењу оптичких ефеката. Анализа угаоне расподеле расејане светлости једнако је важна, јер суштински зависи од структура на кутикули [34, 35].

Полариметријом се утврђује да ли кутикуларне структуре утичу на поларизацију рефлектоване или пропуштене светлости. Ово има биолошку важност зато што су поједине врсте инсеката способне да виде и стање поларизације те да га користе као сигнал.

Разоткривање доминантних оптичких ефеката се највећим делом своди на симулирање простирања електромагнетног таласа кроз компликоване структуре кутикуле, те поређење са експерименталним мерењима. Примењују се следеће нумеричке технике: метод коначних елемената, метод преносне матрице, ригорозна анализа спрегнутих таласа и др.

Преглед техника за генерисање биомиметских оптичких структура

Анализа фотонских структура указује на доминантне оптичке ефекте, које је потребно имитирати на вештачки начин. С обзиром на микронске и субмикронске структуре и њихову тродимензионалност, оптику инсеката је могуће имитирати неком од мноштва литографских техника: двофотонском стереолитографијом [36], холографском и интерференционом литографијом [37], директним ласерским исписивањем, утискивањем (енгл. *embossing, nano-imprint*) [38], директним копирањем (енгл. *templating, molding, soft-lithography*) [39], јонском литографијом [40] или комбинацијом различитих метода [41]. Немогуће је дати детаљно објашњење поменутих техника у овом релативно кратком тексту па ћемо се концентрисати само на оне методе које су важне за даљи ток излагања.

Двофотонска стереолитографија се заснива на скенирању фотоосетљивог материјала ласерским снопом са ултракратким импулсима дужине трајања од неколико десетина фемтосекунди (један десетомилionити део милионитог дела секунде). У веома малој запремини око фокалне тачке снопа, интензитет светлости је довољно велики да изазове експозицију материјала – испред и иза фокуса материјал је неекспониран. Након

хемијске обраде, појављују се тродимензионалне структуре микронских и субмикронских димензија [42].

Холографска литографија је заснована на контролисаној интерференцији два и више снопова унутар фотоосетљивог материјала [43]. Као што је познато, интерференција формира области повећаног или смањеног интензитета, које различито експонирају материјал. Након хемијске обраде, а у зависности од броја снопова, њихове међусобне оријентације и стања поларизације, могуће је добити велики број правилних кристалних структура [44], сличних онима које се срећу код лептира (нпр. *Callophrys rubi* (Linnaeus, 1758) [45]).

Богатство фотонских морфолошких структура инсеката Србије

Ентомофауна Србије свакако није онако богата као у бразилској прашуми, али и даље пружа изворе инспирације за истраживања на граници биологије, физике, хемије, али и технике и технологије. Са гледишта оптике, визуелни показатељи присуства структура јесу иридесценција, присуство боја из плаво-зеленог дела спектра, као и сребрнкасте или златне боје. Веома често су бела или црна боја (које, стриктно физички говорећи, и нису боје) појачане и потпомогнуте присуством структура.

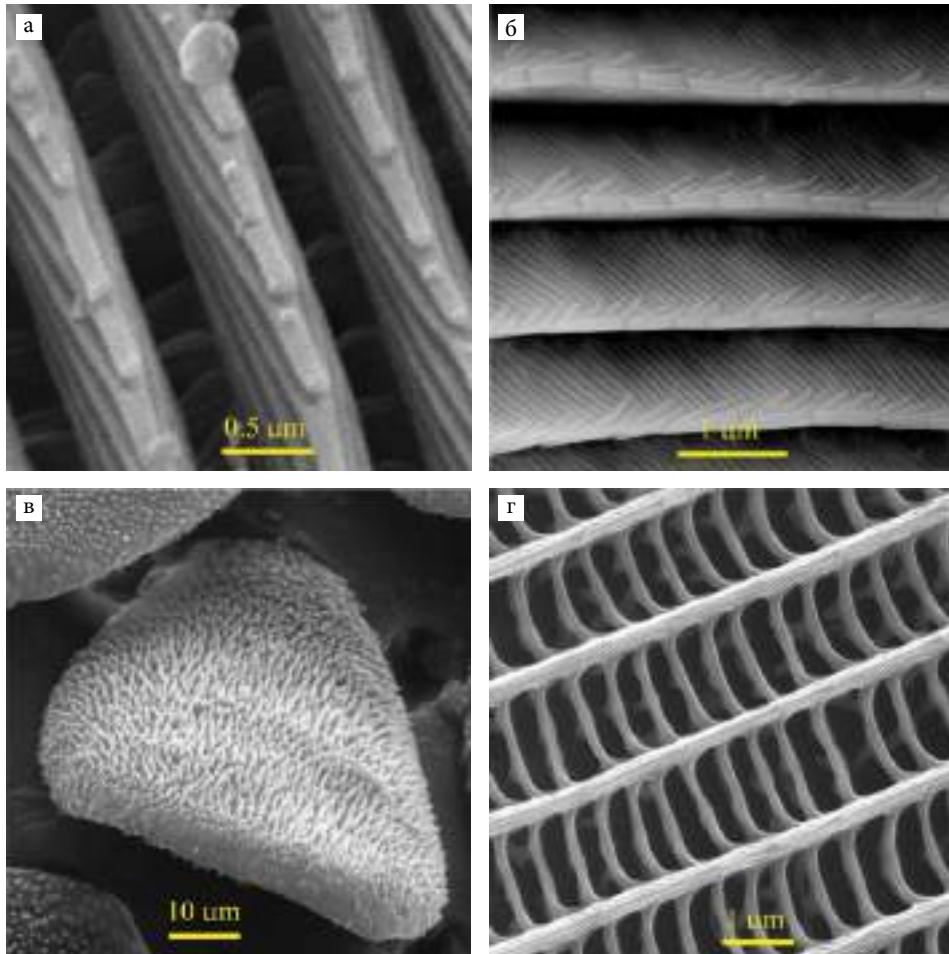
Посебно су интересантни лептири и мољци (Lepidoptera) и неки тврдокрилци (Coleoptera) (фамилије Vuprestidae, Cerambycidae, Rutelidae, Curculionidae и Carabidae), вилини коњици (Odonata), мрежокрилци (Neuroptera) и опнокрилци (Hymenoptera). Крилне љуспице лептира и мољаца могу бити структурно обојене (са типичном структуром као на сл. 4(а) и 4(б)), а код тврдокрилаца и љуспице (сл. 4(в)) и дубински делови кутикуле (сл. 2(б)) учествују у формирању структурних боја. Чак и пигментне љуспице крила лептира имају субмикронску структуру (сл. 4(г)), али се интерференциони ефекти не виде, због тога што је апсорпција светлости доминантна. У табели 1 су приказане неке од биомиметски занимљивих врста инсеката Србије.

У наредна два потпоглавља приказаћемо примере анализе фотонских морфолошких структура инсеката из Србије, њихове миметике и практичне употребе.

Табела 1. Неки од таксона инсеката Србије занимљиви са аспекта биомиметике

Таксон	Ред	Фамилија	Тип структуре
<i>Apatura ilia</i> (Denis & Schiffermüller, 1775)	Lepidoptera	Nymphalidae	Брегова структура љуспица, сл. 4(а)
<i>Apatura iris</i> (Linnaeus, 1758)	Lepidoptera	Nymphalidae	Брегова структура љуспица, сл. 4(а)

Таксон	Ред	Фамилија	Тип структуре
<i>Apatura metis</i> (Freyer, 1829)	Lepidoptera	Nymphalidae	Брегова структура љуспица, сл. 4(а)
<i>Argynnis adippe</i> (Denis & Schiffermüller, 1775)	Lepidoptera	Nymphalidae	Слојевита структура љуспица, сл. 2(а)
<i>Argynnis aglaja</i> (Linnaeus, 1758)	Lepidoptera	Nymphalidae	Слојевита структура љуспица, сл. 2(а)
<i>Argynnis paphia</i> (Linnaeus, 1758)	Lepidoptera	Nymphalidae	Слојевита структура љуспица, сл. 2(а)
<i>Autographa bractea</i> (Denis & Schiffermüller, 1775)	Lepidoptera	Noctuidae	Сложена дифракциона решетка, сл. 4(б)
<i>Autographa gamma</i> (Linnaeus, 1758)	Lepidoptera	Noctuidae	Површинска структура љуспица
<i>Autographa jota</i> (Linnaeus, 1758)	Lepidoptera	Noctuidae	Површинска структура љуспица
<i>Callophrys rubi</i> (Linnaeus, 1758)	Lepidoptera	Lycaenidae	Фотонски кристал
<i>Diachrysia chrysitis</i> (Linnaeus, 1758)	Lepidoptera	Noctuidae	Расејавајући планарни слој, сл. 5(в)
<i>Issoria lathonia</i> (Linnaeus, 1758)	Lepidoptera	Nymphalidae	Површинска структура љуспица, сл. 2(а)
<i>Jordanita globulariae</i> (Hübner, 1793)	Lepidoptera	Zygaenidae	Конкавна запреминска решетка, сл. 2(г)
<i>Pieris brassicae</i> (Linnaeus, 1758)	Lepidoptera	Pieridae	Флуоресцентне наночестице
<i>Pieris rapae</i> (Linnaeus, 1758)	Lepidoptera	Pieridae	Флуоресцентне наночестице
<i>Polyommatus bellargus</i> (Rottemburg, 1775)	Lepidoptera	Lycaenidae	Расејавајућа запреминска решетка
<i>Calosoma sycophanta</i> (Linnaeus, 1758)	Coleoptera	Carabidae	Кутикуларна запреминска структура, сл. 2(б)
<i>Hoplia argentea</i> (Poda, 1761)	Coleoptera	Rutelidae	Рандомизована површинска решетка, сл. 4(в)
<i>Laemostenus punctatus</i> (Dejean, 1828)	Coleoptera	Carabidae	Кутикуларна запреминска структура
<i>Morimus asper funereus</i> Mulsant, 1862	Coleoptera	Cerambycidae	Апсорпционе длачице
<i>Rosalia alpina</i> (Linnaeus, 1758)	Coleoptera	Cerambycidae	Апсорпционе длачице



Слика 4. Изглед (а) структурно обојених љуспица лептира *Apatura iris* (Linnaeus, 1758), (б) мољца *Autographa bractea* (Denis & Schiffermüller, 1775) и (в) тврдокрилца *Hoplia argentea* (Poda, 1761) и (г) пигментне љуспице лептира *A. adippe* (Denis & Schiffermüller, 1775)

Холографска биомиметика Diachrysia chrysitis (Linnaeus, 1758)

Совица *D. chrysitis* (сл. 5(а)) поседује изражену структурну обојеност на широким зонама дорзалне стране предњих крила. Златна обојеност ових области највероватније има дисруптивну функцију, која обезбеђује разбијање контуре тела и теже препознавање од стране предатора. Занимљиво је да посматрање под оптичким трансмисионим микроскопом показује да су појединачне љуспице веома провидне (сл. 5(б)), али њихов просторни распоред у виду двоструког слоја (који чине покровне и базне љуспице) даје интензивну златну рефлексију. Скенирајућа електронска

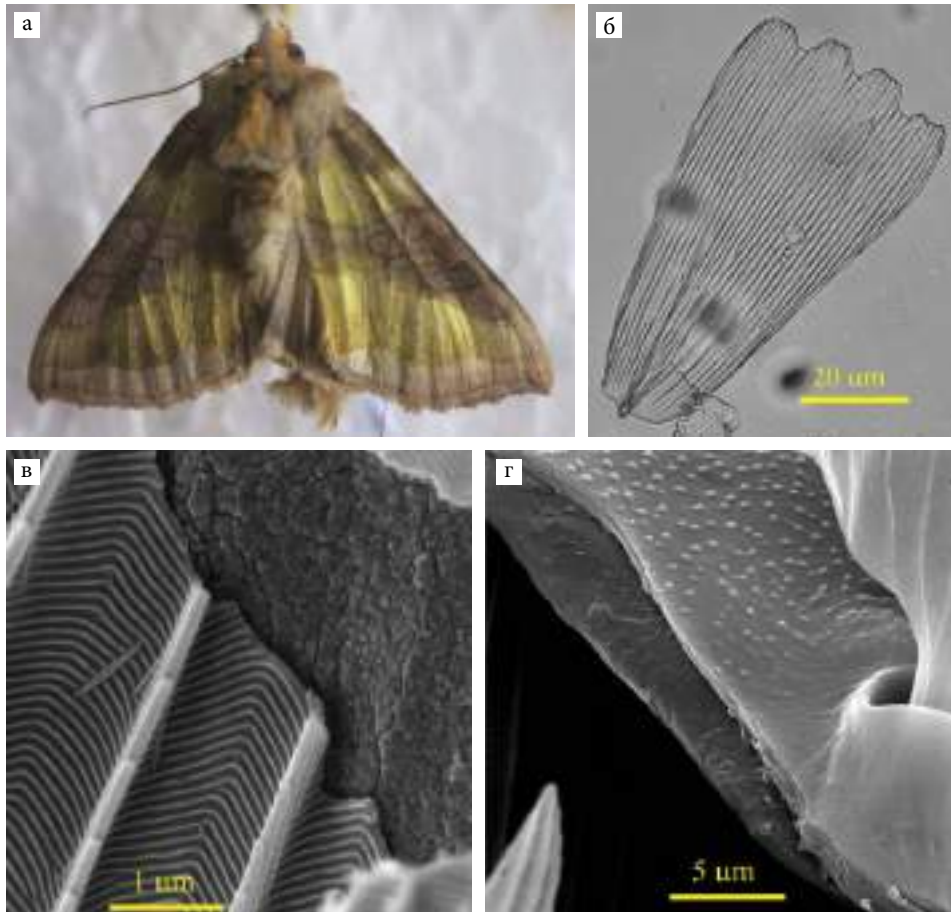
микроскопија (сл. 5(в)) показује једноставну површинску структуру, која се састоји од широко размакнутих гребена (на међусобном растојању од око 2 μm), који су повезани густо распоређеним попречним ребрима (на растојању од око 0.15 μm), облика рибље кости. Прорачун показује да је за златну боју одговорна неравна површина унутрашњости љуспице (сл. 5(в)). Расејање на овој површини уклања плави део спектра из светлости, док веће таласне дужине рефлектује, што одговара златној боји (сл. 5(г)).

Оптичке структуре овог мољца могуће је имитирати холографски. Ми смо користили интерференцију два контра-пропагирајућа ласерска снопа (таласне дужине 532 nm). Као фотоосетљиви материјал, коришћен је танак слој пулулана (природни полисахарид), са додатком јона хрома (дихромирани пулулан). Након хемијске обраде, формиран је низ слојева између којих се налази велики број наночестица (сл. 6(а)). У рефлексији овако добијен слој има златни одсејак попут оног код *D. chrysitis* (сл. 6(а) и 6(б)).

*Варијабилност, јединственост и функционализација љуспица крила
лептира *Issoria lathonia* (Linnaeus, 1758),
Argynnis aglaja (Linnaeus, 1758) и *A. adippe**

Посматрање љуспица крила лептира под оптичким микроскопом открива велику разноврсност њихових облика и боја (сл. 7(а)). На већим увеличањима, посматрајући скенирајућим електронским микроскопом, видимо да постоји одговарајућа варијабилност микронских и субмикронских морфолошких структура (сл. 7(б) и 7(в)). Математичка анализа распореда боја на слици снимљеној под оптичким трансмисионим микроскопом (сл. 7(а)) или међусобног положаја попречних ребара на слици добијеној помоћу скенирајућег електронског микроскопа (сл. 7(в)), показује да је вероватноћа проналажења две идентичне љуспице екстремно мала – чак 10^{-92} . У практичном смислу, можемо да тврдимо да је немогуће наћи две идентичне љуспице, тј. да је свака потпуно јединствена – онако како су јединствени отисци прста, боје дужице ока или распоред крвних судова очног дна код човека.

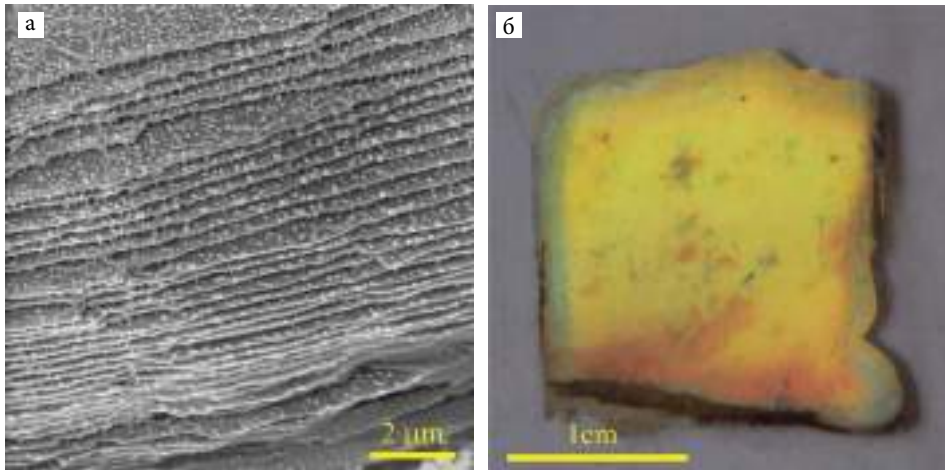
Јединственост указује на висок потенцијал коришћења љуспица крила *Lepidoptera* као елемената за заштиту докумената [46, 47]. Ако се љуспица перманентно интегрише у документ (новчаницу, личну карту, пасош), он постаје непоновљив и веома компликован за фалсификовање због тродимензионалне, субмикронске структуре љуспица. Ово је значајан напредак у односу на тренутно коришћене технике заштите [48], које се заснивају на сложености заштитних елемената (нпр. холограм), али без јединствености (сви холограми на новчаницама од 1000 динара су потпуно идентични). Тиме се приближавамо савременим настојањима да се документи персонализују [49]. Још једна од предности овог вида



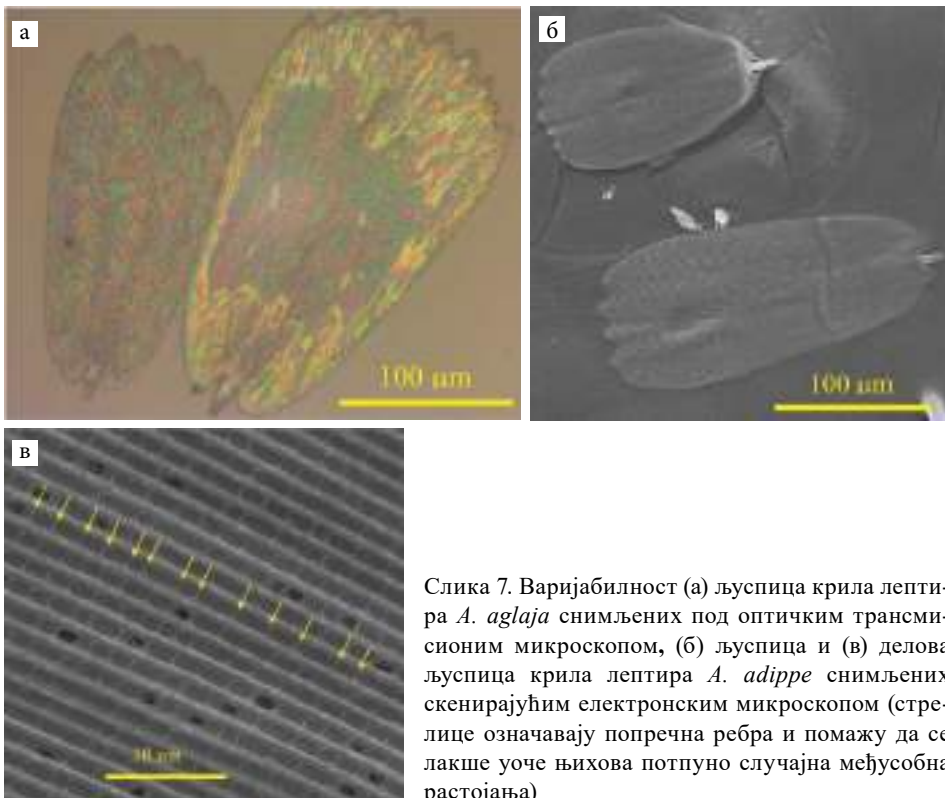
Слика 5. (а) Структурна обојеност предњих крила, (б) појединачна крилна љуспица снимљена под оптичким трансмисионим микроскопом, (в) неравна површина унутрашњости љуспице и (г) расејавајућа површина крилне мембране мољца *D. chrysitis*

заштите је и велика трајност хитинских структура, које у ентомолошким збиркама преживљавају десетине, па и стотине година без икакве промене оптичких својстава. Штавише, пронађени су фосилизовани остаци мољца старог 47 милиона година [50], чија је структурна обојеност била очувана!

Код свих елемената за оптичку заштиту важна је и могућност уписа додатних информација (попут личних података, слика или биометријских карактеристика). Показали смо да је применом ултракратких ласерских импулса могуће на контролисан начин уписивати податке на појединачне љуспице крила *Lepidoptera*. Модификован је раније развијен систем за ласерску микроскопију [29], тако да ласерски снап може да исписује про-

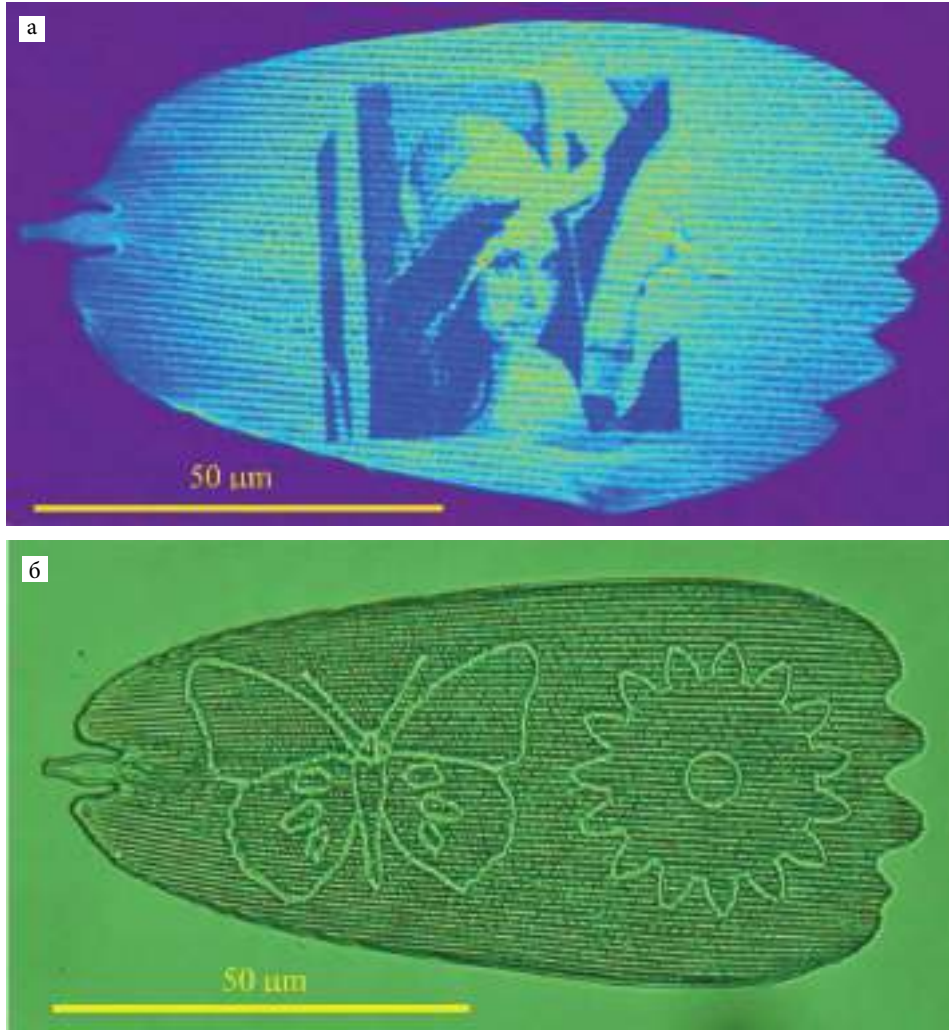


Слика 6. (а) Холографски добијени слојеви на дихромираном пулулану, као имитација унутрашње структуре љуспице *D. chrysitis*. Снимак је добијен скенирајућим електронским микроскопом. (б) Фотографија рефлексије са холографски модификованог слоја дихромираног пулулана



Слика 7. Варијабилност (а) љуспица крила лептира *A. aglaja* снимљених под оптичким трансмисионим микроскопом, (б) љуспица и (в) делова љуспица крила лептира *A. adippe* снимљених скенирајућим електронским микроскопом (стрелице означавају попречна ребра и помажу да се лакше уоче њихова потпуно случајна међусобна растојања)

извољно задату слику [51]. У зависности од интензитета ласерског снопа, исписивање је могуће реализовати променом флуоресцентних особина хитина, избелјивањем (сл. 8(а)) или сечењем (сл. 8(б)).



Слика 8. Слике добијене (а) ласерским избелјивањем и (б) ласерским сечењем луспице крила лептира *I. lathonia*

ЗАКЉУЧНА РАЗМАТРАЊА

Биомиметика, биоинспирација и функционализација биолошких структура су области које се веома интензивно развијају [52]. Широко су конципиране и тешко их је јасно дефинисати – можда је најисправније рећи да се више ради о погледу на свет него о јасно дефинисаном правцу истраживања [53]. Ипак, истраживања из ових области су обимна по броју објављених радова и веома значајна (мерено бројем цитата). Стога су се појавили и специјализовани часописи, попут “Bioinspiration and Biomimetics” или “Robotics and Biomimetics”, а у реномираним научним часописима, као што су “Nature” и “Science”, чести су радови из ових области. Сем тога, резултати су већ нашли и практичне, индустријске примене у области адхезива, дисплеја, козметике и др.

Свака техничка област истраживања лако може наћи свој пандан у живом свету: машинство – у необичној структури биолошких композита или механици покрета животиња, рачунарство – у комплексним неуронским мрежама животиња и еволуционим принципима, оптика – у интегументу или сложеним очима инсеката, хемија – у богатству биолошких супстанци, аеронаутика – у птицама и летећим инсектима а, нажалост, и војна наука има изванредног учитеља у живом свету, угледајући се на вечиту борбу за опстанак. Овом списку заиста нема краја и у томе је и велика привлачност биомиметике. У овој области, биолози и стручњаци из других области се налазе на заједничком задатку уочавања занимљивих особина живих организама и проналажењу начина да се ове особине искористе.

Инсекти су најбогатији извор инспирације због чињенице да је еволутивним развојем настало више милиона врста, а присутна је и велика разноврсност форми. И у Србији постоји велики број врста инсеката, али мало је доступних података о њиховим кутикуларним структурама од потенцијалног интереса за биомиметику. Мислимо да би било од великог практичног значаја да се направи нека врста илустрованог каталога микроструктура и нано-структура инсеката Србије, посебно за редове *Lepidoptera* и *Coleoptera*. Каталог би укључивао морфолошке карактеристике микроструктура и наноструктура кутикуле (очију, крила, антена, ногу и др.), али и њихове оптичке и механичке карактеристике. Тиме би се значајно олакшао посао будућим истраживачима у области биомиметике.

РЕФЕРЕНЦЕ

- [1] Wood, R., Nagpal, R., Wei, G.-Y. (2013): Flight of the robobees. *Sci. Am.*, 308: 60–65.
- [2] Lilienthal (1889): *Der Vogelflug als Grundlage der Fliegekunst. Ein Beitrag zur Systematik der Flugtechnik*, Berlin, R. Gaertners Verlagsbuchhandlung, p. 187.
- [3] Gardner, M. (1970): Mathematical games: the fantastic combinations of John Conway’s new solitaire game “life”. *Sci. Am.*, 223: 120–123.
- [4] Bonebeau, E., Dorigo, M., Theraulaz, G. (2000): Inspiration for optimization from social insect behaviour. *Nature*, 406: 39–42.
- [5] Song, Y.M., Xie, Y., Malyarchuk, V., Xiao, Y., Jung, I., Choi, K.-J., Liu, Z., Park, H., Lu, C., Kim, R.-H., Li, R., Crozier, K.B., Huang, Y., Rogers, J.A. (2013): Digital cameras with designs inspired by the arthropod eye. *Nature*, 497: 95–99.
- [6] Feng, L., Li, S., Li, Y., Li, H., Zhang, L., Zhai, J., Song, Y., Liu, B., Jiang, L., Zhu, D. (2002): Super-hydrophobic surfaces: from natural to artificial. *Adv. Mater.*, 14: 1857–1860.
- [7] Dean, B., Bhushan, B. (2010): Shark-skin surfaces for fluid-drag reduction in turbulent flow: a review. *Phil. Trans. R. Soc. A*, 368: 4755–4806.
- [8] Park, S.-H., Lee, S., Moreira, D., Bandaru, P.R., Han, I., Yun, D.-J. (2015): Bioinspired superhydrophobic surfaces, fabricated through simple and scalable roll-to-roll processing. *Sci. Rep.*, 5: 15430.
- [9] Hamm, C.E., Merkel, R., Springer, O., Jurkojc, P., Maier, C., Prechtel, K., Smetacek, V. (2003): Architecture and material properties of diatom shells provide effective mechanical protection. *Nature*, 421: 841–843.
- [10] Wegst, U.G.K., Bai, H., Saiz, E., Tomsia, A.P., Ritchie, R.O. (2015): Bio-inspired structural materials. *Nat. Mater.*, 14: 23–36.
- [11] Whitesides, G.M. (2015): Bioinspiration: something for everyone. *Interface Focus* 5: 20150031.
- [12] Roberts, N.W., Chiou, T.-H., Marshall, N.J., Cronin, T.W. (2009): A biological quarter-wave retarder with excellent achromaticity in the visible wavelength region. *Nat. Photonics*, 3: 641–644.
- [13] Darius, J., Thomas, P.K. (1981): Crosswires in a guiding eyepieces. *J. Phys. E: Sci. Instrum.*, 14: 761–765.
- [14] Parker, A.R., Townley, H.E. (2007): Biomimetics of photonic nanostructures. *Nat. Nanotechnol.* 2: 347–353.
- [15] Burrows, M., Sutton, G. (2013): Interacting gears synchronize propulsive movements in a jumping insect. *Science*, 341: 1254–1256.
- [16] Zheng, Y., Gao, X., Jiang, L. (2007): Directional adhesion of superhydrophobic butterfly wings. *Soft Matter*, 3: 178–182.
- [17] Dirks, J.-H. (2016): Adhesion in insects. In: Bhushan, B. ed. *Encyclopedia of Nanotechnology*, 2nd ed., Dordrecht, Springer, pp. 1–10.

- [18] Stavenga, D.G., Foletti, S., Palasantzas, G., Arikawa, K. (2006): Light on the moth-eye corneal nipple array of butterflies. *Proc. Roy. Soc. B*, 273: 661–667.
- [19] Jeong, K.-H., Kim, J., Lee, L.P. (2006): Biologically inspired artificial compound eyes. *Science*, 312: 557–561.
- [20] Garrett, N.L., Sekine, R., Dixon, M.W.A., Tilley, L., Bambery, K.R., Wood, B.R. (2015): Bio-sensing with butterfly wings: naturally occurring nano-structures for SERS-based malaria parasite detection. *Phys. Chem. Chem. Phys.*, 17: 21164–21168.
- [21] Tan, Y., Gu, J., Xu, W., Chen, Z., Liu, D., Liu, Q., Zhang, D. (2013): Reduction of CuO butterfly wing scales generates Cu SERS substrates for DNA base detection. *ACS Appl. Mater. Interfaces*, 5: 9878–9882.
- [22] Potyrailo, R.A., Ghiradella, H., Vertiatchikh, A., Dovidenko, K., Cournoyer, J.R., Olson, E. (2007): *Morpho* butterfly wing scales demonstrate highly selective vapour response. *Nat. Photonics*, 1: 123–128.
- [23] England, G., Kolle, M., Kim, P., Khan, M., Muñoz, P., Mazur, E., Aizenberg, J. (2014): Bioinspired micrograting arrays mimicking the reverse color diffraction elements evolved by the butterfly *Pierella luna*. *Proc. Natl. Acad. Sci. USA*, 111: 15630–15634.
- [24] Shi, N.N., Tsai, C.-C., Camino, F., Bernard, G.D., Yu, N., Wehner, R. (2015): Keeping cool: enhanced optical reflection and heat dissipation in silver ants. *Science*, 349: 298–301.
- [25] Kahl, T., Bousack, H., Schneider, E.S., Schmitz, H. (2014): Infrared receptors of pyrophilous jewel beetles as model for new infrared sensors. *Sensor Rev.*, 34: 123–134.
- [26] Pris, A.D., Utturkar, Y., Surman, C., Morris, W.G., Vert, A., Zalyubovskiy, S., Deng, T., Ghiradella, H.T., Potyrailo, R.A. (2012): Towards high-speed imaging of infrared photons with bio-inspired nanoarchitectures. *Nat. Photonics*, 6: 195–200.
- [27] Fox, D.L. (1976): *Animal Biochromes and Structural Colours: Physical, Chemical, Distributional & Physiological Features of Colored Bodies in the Animal World*, 2nd ed., Berkeley, University of California Press, p. 433.
- [28] Huang, J., Wang, X., Wang, L.W. (2008): Bio-inspired fabrication of antireflection nanostructures by replicating fly eyes. *Nanotechnology*, 19: 025602.
- [29] Rabasović, D.M., Pantelić, D.V., Jelenković, B.M., Ćurčić, S.B., Rabasović, M.S., Vrbica, M.D., Lazović, V.M., Ćurčić, B.P.M., Krmpot, A.J. (2015): Nonlinear microscopy of chitin and chitinous structures: a case study of two cave-dwelling insects. *J. Biomed. Opt.*, 20: 016010.
- [30] Aguayo, D.D., Mendoza Santoyo, F., De la Torre-I, M.H., Salas-Araiza, M.D., Caloca-Mendez, C., Gutierrez Hernandez, D. A. (2010): Insect wing deformation measurements using high speed digital holographic interferometry. *Opt. Express*, 18: 5661–5667.

- [31] Pantelić, D.V., Grujić, D.Ž., Vasiljević, D.M. (2014): Single-beam, dual-view digital holographic interferometry for biomechanical strain measurements of biological objects. *J. Biomed. Opt.*, 19: 127005.
- [32] Martinez-Leon, L., Pedrini, G., Osten, W. (2005): Applications of short-coherence digital holography in microscopy. *Appl. Opt.*, 19: 3977–3984.
- [33] Pantelić, D., Ćurčić, S., Savić-Šević, S., Korać, A., Kovačević, A., Ćurčić, B., Bokić, B. (2011): High angular and spectral selectivity of purple emperor (*Lepidoptera: Apatura iris* and *A. ilia*) butterfly wings. *Opt. Express*, 19: 5817–5826.
- [34] Savić-Šević, S., Pantelić, D., Grujić, D., Jelenković, B., Ćurčić, S., Ćurčić, B., Stojanović, D. (2012): *Localization of light in photonic crystals of biological origin*, Conference Proceedings, 14th International Conference on Transparent Optical Networks (ICTON), Coventry, 02–05 July 2012. pp. 1–3.
- [35] Pantelić, D., Savić-Šević, S., Grujić, D. (2013). Zoom system for measurement of coherent backscattering of light in micro- and nanomaterials. *Phys. Scr.*, T157: 014020.
- [36] Liu, Y., Nolte, D., Pyrak-Nolte, L.J. (2010): Large-format fabrication by two-photon polymerization in SU-8. *Appl. Phys. A*, 100: 181–191.
- [37] Siddique, R.H., Hünig, R., Faisal, A., Lemmer, U., Hölscher, H. (2015): Fabrication of hierarchical photonic nanostructures inspired by *Morpho* butterflies utilizing laser interference lithography. *Opt. Mater. Express*, 5: 996–1005.
- [38] Savić-Šević, S., Pantelić, D. (2005): Relief hologram replication using a dental composite as an embossing tool. *Opt. Express*, 13: 2747–2754.
- [39] Kang, S.-H., Tai, T.-Y., Fang, T.-H. (2010): Replication of butterfly wing microstructures using molding lithography. *Curr. Appl. Phys.*, 10: 625–630.
- [40] Juodkazis, S., Rosa, L., Bauerdick, S., Peto, L., El-Ganainy, R., John, S. (2011): Sculpturing of photonic crystals by ion beam lithography: towards complete photonic bandgap at visible wavelengths. *Opt. Express*, 19: 5802–5810.
- [41] Burgess, I.B., Aizenberg, J., Loncar, M. (2013): Creating bio-inspired hierarchical 3D-2D photonic stacks via planar lithography on self-assembled inverse opals. *Bioinspir. Biomim.*, 8: 045004.
- [42] Gan, Z., Turner, M.D., Gu, M. (2016): Biomimetic gyroid nanostructures exceeding their natural origins. *Sci. Adv.*, 2: e1600084.
- [43] Campbell, M., Sharp, D.N., Harrison, M.T., Denning, R.G., Turberfield, A.J. (2000): Fabrication of photonic crystals for the visible spectrum by holographic lithography. *Nature*, 404: 53–56.
- [44] Wang, X., Gao, W., Hung, J., Tam, W.Y. (2014): Optical activities of large-area SU8 microspirals fabricated by multibeam holographic lithography. *Appl. Opt.*, 53: 2425–2430.

- [45] Saranathan, V., Osuji, C.O., Mochrie, S.G., Noh, H., Narayanan, S., Sandy, A., Dufresne, E.R., Prum, R.O. (2010): Structure, function, and self-assembly of single network gyroid (I4132) photonic crystals in butterfly wing scales. *Proc. Natl. Acad. Sci. USA*, 107: 11676–11681.
- [46] Pantelic, D., Rabasovic, M., Krmpot, A., Lazovic, V., Pavlovic, D. (2015): Security device individualized with biological particles. *PCT/EP2015/081398*.
- [47] Pantelic, D., Rabasovic, M., Krmpot, A., Lazovic, V., Pavlovic, D. (2015): Security tag containing a pattern of biological particles. *PCT/EP2015/081400*.
- [48] Van Renesse, R.L. (2005): *Optical Document Security*, 3rd ed., Boston-London, Artech House, p. 386.
- [49] Nam, H., Song, K., Ha, D., Kim, T. (2016): Inkjet printing based mono-layered photonic crystal patterning for anti-counterfeiting structural colors. *Sci. Rep.*, 6: 30885.
- [50] McNamara, M.E., Briggs, D.E.G., Orr, P.J., Wedmann, S., Noh, H., Cao, H. (2011): Fossilized biophotonic nanostructures reveal the original colors of 47-million-years-old moths. *PLoS Biol.*, 9: e1001200.
- [51] Pantelic, D., Rabasovic, M., Krmpot, A., Lazovic, V., Pavlovic, D. (2015): Security tag with laser-cut particles of biological origin. *PCT/EP2015/081407*.
- [52] Lepora, N.F., Verschure, P., Prescott, T.J. (2013): The state of the art in biomimetics. *Bioinspir. Biomim.*, 8: 013001.
- [53] Vincent, J.F.V., Bogatyreva, O.A., Bogatyrev, N.R., Bowyer, A., Pahl, A.-K. (2006): Biomimetics: its practice and theory. *J. R. Soc. Interface*, 3: 471–482.

ЗАХВАЛНИЦА

Захваљујемо се Министарству просвете, науке и технолошког развоја Републике Србије за подршку кроз следеће пројекте: ОН171038, ОН173038, ИИИ45016 и ИИИ43002.

THE MORPHOLOGICAL STRUCTURES OF SOME REPRESENTATIVES OF THE ENTOMOFAUNA OF SERBIA AS MODELS IN BIOMIMETICS

Dejan PANTELIĆ, Srećko ĆURČIĆ, Aleksandar KRMPOT,
Dejan V. STOJANOVIĆ, Mihailo RABASOVIĆ, Svetlana SAVIĆ-ŠEVIĆ

S u m m a r y

Biomimetics, bioinspiration and functionalization of biological structures are disciplines of intense research. They are wide in scope but not easy to define – this is more a worldview, rather than a well defined research direction. Anyway, the research is voluminous measured by the number of scientific papers and very important by numerous citations. This is why specialized journals have appeared such as “Bioinspiration and Biomimetics” and “Robotics and Biomimetics”, while renowned journals “Nature” and “Science” frequently publish papers in this area. Apart from this, the practical results have found the application in adhesives, displays, cosmetics, etc.

Each and every technical research area can find its counterpart in the living world: machine engineering in the unusual properties of biological composites or mechanics of animals, computing in the complex neural networks or evolutionary principles, optics in the integument and compound eyes of insects, chemistry in the richness of biological substances, aeronautics in birds and flying insects, and, regrettably, military science has an excellent teacher in the living world too, inspired by the eternal battlefield of survival. There is no end of this list, which is one of the main appeals of biomimetics. In this area, biologists and specialists in other disciplines have a common task of finding interesting properties of living organisms and discovering ways to use their properties.

Insects are the richest source of inspiration due to the number of several million species created during the evolutionary history, with the enormous diversity in both form and function. There is a great diversity of insect species in Serbia as well, but with a small amount of available information on the cuticular structures of interest for biomimetics. We think that it would be of practical interest to make an illustrated catalogue of the micro- and nano-structures of insects of Serbia, in particular for the orders of Lepidoptera and Coleoptera. Catalogue would include morphological characteristic of the micro- and nano-structures of (cuticle, eyes, wings, antennas, legs, etc.), but also their optical and mechanical properties. This will significantly facilitate the future research in biomimetics.



(43) International Publication Date
6 July 2017 (06.07.2017)

- (51) International Patent Classification:
H42D 25/36 (2014.01) G09F 3/02 (2006.01)
G06K 1/08 (2006.01)
- (21) International Application Number:
PCT/EP2015/081400
- (22) International Filing Date:
30 December 2015 (30.12.2015)
- (25) Filing Language: English
- (26) Publication Language: English
- (71) Applicant: INSTITUTE OF PHYSICS, BELGRADE, UNIVERSITY OF BELGRADE (RS ES); Progresna 118, 11080 Belgrade (RS)
- (72) Inventors: PANTELIĆ, Dejan; Nemanjina 7, 11080 Belgrade (RS); RAHANOVIĆ, Mihalj; Srećkova Papica 171, 11080 Belgrade (RS); KRMPOT, Aleksandar; Jaserova 8/15, 11030 Belgrade (RS); LAZOVIĆ, Vladimir; Jurijsa Gagarina 127, 11070 Belgrade (RS); PAVLOVIĆ, Đorđica; Boška Živkovićeva 18c, 11260 Belgrade (RS)
- (74) Agent: WINKLER, Andrew; P.O. Box 347013, 28329 Bremen (DE)

(81) Designated States (unless otherwise indicated, for every kind of national protection available): AE, AG, AL, AM, AU, AT, AZ, BA, BB, BG, BR, BS, BY, BZ, CA, CH, CL, CN, CO, CR, CU, CZ, DE, DK, DM, DO, DZ, EC, EE, EG, ES, FI, GB, GD, GE, GR, GU, HK, HN, HR, HU, IL, IN, IR, IS, JP, KE, KG, KN, KP, KR, KZ, LA, LC, LK, LR, LS, LU, LY, MA, MD, ME, MG, MK, MN, MW, MX, MY, MZ, NA, NG, NI, NO, NZ, OM, PA, PE, PG, PH, PL, PT, QA, RO, RS, RU, RW, SA, SC, SD, SE, SG, SK, SL, SM, ST, SV, SY, TH, TJ, TN, TR, TT, TZ, UA, UG, US, UZ, VC, VN, ZA, ZM, ZW.

(84) Designated States (unless otherwise indicated, for every kind of regional protection available): ARIPO (BW, GH, GM, KE, LR, LS, MW, MZ, NA, RW, SD, SL, ST, SZ, TZ, UG, ZM, ZW), Eurasian (AM, AZ, BY, KG, KZ, RU, TJ, TM), European (AL, AT, BE, BG, CH, CY, CZ, DE, DK, EE, ES, FI, FR, GB, GR, HU, IE, IT, LT, LU, LV, MC, MK, ML, NL, NO, PL, PT, RO, RS, SE, SI, SK, SM, TR), OAPI (BF, BJ, CF, CG, CI, CM, GA, GN, GQ, GW, KM, MF, MR, NE, SN, TD, TG)

Published
with international search report (Art. 21bis)

(54) Title: SECURITY TAG CONTAINING A PATTERN OF BIOLOGICAL PARTICLES

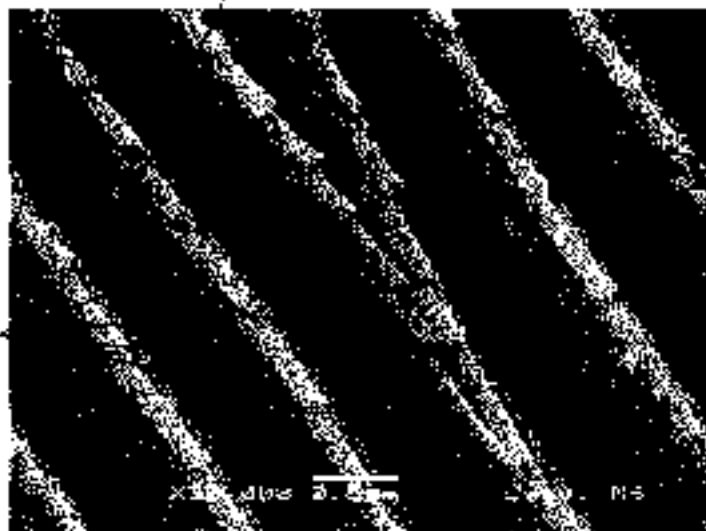


Fig. 1

(57) Abstract: The invention is directed to a security device individualized by permanently attaching particles of biological origin, possessing large variability of optical effects and complexity of internal structure. Biological species and corresponding particles are chosen to maximize variability and complexity, while having durability, tamper sensitivity and micron size thickness. A method to manufacture a tag, suitable for visual, machine and 3D/laser inspection, is disclosed.

WO 2017/114570 A1

Security tag containing a pattern of biological particles

FIELD OF INVENTION

The present invention relates to security tags for identification and authentication of goods, articles and documents.

5 BACKGROUND OF INVENTION

Optically variable devices (OVD) are a common protective element on various types of documents (e.g. identity cards, passports, visas, bank cards) – see the book “Optical Document Security”, ed. by R. L. Van Renesse, Artech House, (1998). Holograms and other diffractive elements are mainly used, because their protective value is based on complexity of micron and submicron structures. Manufacturing is a complicated and expensive process whose final result is a master hologram – a single, unique prototype. To make protection commercially acceptable, the master hologram is copied and multiplied, resulting in a replica shim used for embossing into a plastic foil, which is then integrated into a document using a hot tool. The final result is a series of documents possessing exactly the same protective OVD. This is a significant drawback, because, if the OVD is counterfeited, a large number of fake documents can be manufactured.

As a result, there is ongoing research for a simple and affordable document individualization method. This makes counterfeit much harder, because each and every document has to be copied individually, i.e. large scale production of false documents becomes impossible. However, the trivial individualization by simply printing numbers will not work, because it is too simple and affordable, if using modern printing technologies (e.g. laser printing). Therefore the individualization-bearing features must possess a significant amount of complexity together with strong, unrepeatable, individual properties. They have to be comparable in its uniqueness with biometric characteristics, such as: fingerprints, iris and retina pattern, but significantly more complex and miniscule. Currently used OVD security methods are not well suited for individualization (fingerprinting), as this will significantly increase the production prices.

Attempts to obtain “fingerprint” documents are based on the idea of physical one-way functions (C. Boehm, M. Hofer, “Physically unclonable functions in theory and practice”,

Springer, 2013) – which are physical devices simple to manufacture, yet extremely difficult to reverse engineer and copy. Random structures can be highly significant for document security, because they offer simple and cheap production, almost impossible re-origination and unique features. It was proposed to tag documents with randomly dispersed objects such as metal, fluorescent or optical fibers (van Rensse book, and references therein).

Natural fibrous structure of paper-based substrates was used (J. D. R. Buchanan, R. P. Cowburn, A-V. Clauszew, D. Petit, P. Seem, G. Xiang, D. Atkinson, K. Lenton, D. A. Allwood, M. E. Brynn, “‘Fingerprinting’ documents and packaging”, Nature 436, (2005) 475). Laser beam was scattered from the paper surface and its statistics was observed and recorded. This however requires a large scale scanning of the document surface which is a slow process, and paper structure may be strongly affected by printing and everyday usage.

Yet another technique was described in R. Pappu, B. Recht, J. Taylor, N. Gershenfeld, “Physical One-Way Functions,” Science 297, (2002) 2026 -2030), where mesoscopic scattering from disordered array of plastic spheres embedded in a transparent substrate was used to construct physical one-way function. The response of the system strongly depends on the illumination direction, again producing unique individual characteristics. The proposed method is limited by the physical requirements for the mesoscopic scattering, resulting in a 10 mm x 10 mm sized tag, with 2.5 mm thickness, which is unsuitable for the modern plastic card technology. Furthermore, the dimension of scattering particles is rather large – 500 - 800 µm in diameter, with 100 µm average spacing – resulting in a bulky system which can be reverse engineered by techniques like micro-tomography.

It is a common knowledge that certain natural characteristic of living creatures are essentially complex and hard to reproduce. This was first realized by Benjamin Franklin who used this for document protection (Barley Girbb, “Benjamin Franklin and the birth of the paper money economy”, Essay based on March 30, 2006 lecture, published by Federal Reserve Bank of Philadelphia). He made casts of plant leaves (correctly recognizing the uniqueness of their venation) and used them to print the first dollar bills. Due to further technological advancements, Franklin's method became obsolete, and was replaced with different printing techniques, such as: intaglio, guilloche, watermark, holograms, etc.

Complexity of natural structures was observed in art, too. Japanese painters used fish printing (gyotaku) to directly transfer fish features, instead of painting them. Later, Leonardo Da Vinci directly printed leaf venation on the paper, while Dutch painter Otto Marseus Van Schrieck transferred butterfly wing scales to his canvases (S. Berthier, J. Boulenguez, M. Menu, B. Mottin, "Butterfly inclusions in Van Schrieck masterpieces: Techniques and optical properties", *Appl. Phys. A*, 51 – 57, (2006)). Today, all the techniques have the common name: nature printing (R. Newcomb, "Method for producing nature prints", US 4279200 A, (1981), C.J.Cowan, "Butterfly wing prints", *J. Soc. Biblioph. Nat. Hist.*, 4 (1968): 368-369, D. G. Edwards, "A receipt for taking figures of butterflies on thin gummed paper", in *Essays upon natural history and other miscellaneous subjects*, pg. 117).

Patents WO 2007031077 (A1) 3/2007, C. Hamm-Dubischar, "Inorganic marking particles for characterizing products for proof of authenticity method for production and use thereof" and DE10238506 A1, 3/2004, H. Raube, "Producing information-bearing micro-particulate mixtures involves defining oxide that can be implemented using natural or subsequently applied particle characteristics selected from e.g. morphology", disclosed an idea for document protection which uses natural complexity of aquatic organism inorganic shells (like diatoms and radiolarians) according to characteristics of their surfaces. The practicing method is, however, not disclosed. Another problem is that the optical effects are not very pronounced, and the complexity can be observed only at the sub-wavelength levels, using electron microscopy. Technique for estimating the degree of complexity was not described, either. Variation among the specimens of the same species is rather small. In that respect, the method can be used only for the forensic level of document authentication.

Recently, there was a significant amount of research aimed at using the principles of optics in nature for document protection – biomimetics (J. Sun, B. Bhushan and J. Tong, "Structural coloration in nature", *RSC Adv.*, 2013, 3, 14862–14889, B. Yoon, J. Lee, I. S. Park, S. Jeon, J. Lee, J.-M. Kim, "Recent functional material based approaches to prevent and detect counterfeiting", *J. Mater. Chem. C* 1, (2013) 2388 - 2403). Variability of biological structures was also observed (L. P. Biro and J.-P. Vigneron, "Photonic nanoarchitectures in butterflies and beetles: valuable sources for bioinspiration", *Laser Photonics Rev.* 5, No. 1, 27–51 (2011)). Biotemplating was used to manufacture butterfly scale-like structures using metals

(S. Sotiropoulos, Y. Sierra-Sastre, S. S. Mark, and C. A. Ball, "Biostempled Nanostructured Materials", Chem. Mater. 2008, 20, 821-834).

The randomized systems described above must be machine inspected, based on radiation scattering with consequent optical or microwave detection (in the case of metal inclusions).
5 Recorded pattern is encrypted and stored in a central repository or on the document, itself. Public key encryption method is used, as described in the report: "Counterfeit deterrent features for the next generation currency design", Committee on Next-Generation Currency Design, National Materials Advisory Board, Commission on Engineering and Technical Systems, National Research Council, Publication NMAB 472, 419934, Section: Random Pattern/Encryption
10 Counterfeit-Deterrence Concept, pg. 74 - 75, and Appendix E: "Methods for authentication of unique random", pg. 117 - 119. A technique is based on two keys: a secret one, used for encryption, and a public one, used for the decryption.

All the methods used a complexity of natural structures but their variability remained completely unused in the context of the document protection. Document variability was rather
15 attained by randomly dispersing particle- or thread-like entities across the document, as described in the patent literature (US 8408470B2, 2013, N. Komatsu, S-I. Nanjo, "Object for authentication verification, authentication verifying chip reading device and authentication judging method").

20

SUMMARY OF THE INVENTION

This invention solves the problem of identicalness of, presently used, document security features (e.g. holograms and other OVDs), making them vulnerable to counterfeiting. Presently, security elements are identical on the same type of document (passport, visa, credit card),
25 without variability between the individual documents. This eases the counterfeiting process because, once the counterfeit is made, it can be applied to any number of documents. The invention uses naturally occurring biological particles, whose variability is guaranteed by the

large number of degrees of freedom of biological processes. They are used to manufacture a tag, which can be further applied to a document or a product, thus making it unique.

A security tag and a manufacturing method are disclosed.

5 The security tag of the present invention is characterized by a pattern of inimitable biological particles, directly transferred from an organism to a transparent adhesive layer on a substrate, covered with a transparent superstrate, such that said biological particles are encapsulated between said substrate and said superstrate.

In one embodiment of the present invention, the pattern of biological particles is in the shape of a bar-code or QR-code.

10 In another embodiment of the present invention, the pattern of biological particles is in the shape of a silhouette of a human head or, alternatively, in the shape of a fingerprint.

Preferably, the biological particles are overtly inscribed with information by mechanical or laser cutting.

15 Alternatively, the biological particles are covertly inscribed with information by permanently bleaching their fluorescence.

Preferably, the biological particles are selected from Lepidoptera scales, hairs or bristles, Coleoptera scales, Trichoptera hairs or bristles, and Arachnides scales.

More preferably, the biological particles are taken from several different species, and assembled on the substrate in a predetermined pattern.

20 In one embodiment of the present invention, selected parts of the superstrate are covered with a transparent layer of adhesive, which permanently adheres to the biological particles.

Furthermore, the invention is directed to the use of a security tag according to the present invention for identification and authentication of goods, articles and documents.

25 Finally, the invention is directed to a method of manufacturing a security tag according to the present invention, comprising the following steps:

- (1) providing for at least one biological particle on a surface;
- (2) cutting an optically transparent tape, with a low surface energy adhesive layer, in a predetermined shape to form a first pre-cut tape;
- (4) pressing the first pre-cut tape onto the surface with the biological particles;
- 5 (5) removing the first pre-cut tape from the surface with the biological particles, with a majority of the biological particles being attached to the first pre-cut tape;
- (6) bringing in contact the first pre-cut-tape with attached biological particles (1b) with a second, high surface energy, optically transparent, adhesive tape, such that the adhesive layers face each other;
- 10 (7) lifting-off the first pre-cut tape from the second tape;
- (8) covering the second tape with a third optically transparent tape, which is smaller than the second tape to form the security tag ready to be attached to goods, articles or documents.

A tag according to the present invention comprises a multiplicity of selected, micron-sized, parts of an insect body (biological particles), attached on a substrate surface within the
15 predetermined area having well defined, easily recognizable, shape. Biological particles are directly transferred to the substrate, retaining their original physical characteristics and spatial arrangement. Said biological particles are selected according to a high level of complexity and variability of their optical properties, observable under different image magnifications. Overall
20 tag size is such that it enables visual inspection and easy recognition by the user, as well as machine inspection at the microscopic level.

Complexity is measured by the statistically averaged volume to surface ratio of the biological particle (Fig. 1 and Fig. 2 show the typical complexity of insect body-scales found on the cuticle of some insects). Preferably, the volume/surface ratio is less than 50 nm. Variability is
25 defined through the number of degrees of freedom (G. T. di Francia, "Degrees of freedom of an image", *JOSA* 59, (1969) 799 - 804) of the observed biological particle image at the defined

magnification (Fig. 6 presents optical patterns of insect body-scales 7 recorded at different magnifications). Preferably, the number of degrees of freedom should be larger than 1000.

It is required that the observed optical effects are strongly localized, variable and individual and the result of interference, diffraction and scattering (including their polarization and angular dependence) from a complex three-dimensional structure. Additionally, tissues and cells are chosen to be durable, with permanent optical properties and capable of being transferred to the substrate and processing prior, during and after attachment to the substrate. A substrate which receives the biological structure thus becomes unique and unrepeatable. The resulting tag can be further attached on various types of objects demanding individualization and secure identification.

A tag substrate may contain three printed markers, which are used as a reference to generate a local coordinate system. Selected features of insect body parts attached to the tag are used as the machine-readable security code (second line of protection).

Tag manufacturing process consists of several stages, which use adhesive tapes with varying surface energy. The first tape is used to lift off the biological particles from the organism. They are transferred to a higher surface energy tape, where they remain permanently affixed and protected by an additional protective layer.

BRIEF DESCRIPTION OF THE DRAWINGS

- 20 Fig. 1: Butterfly scale observed under the scanning electron microscope (SEM).
- Fig. 2: Cross-section of the butterfly scale observed under the transmission electron microscope (TEM).
- Fig. 3: Magnified cross-section of the butterfly scale ridge, observed under the TEM microscope.
- 25 Fig. 4: Gamma corrected image of the butterfly scale from Fig. 3, where edges are emphasized.

- Fig. 5: Thresholded version of the image in Fig. 3, enabling calculation of the enclosed surface area.
- Fig. 6: Part of the butterfly wing is star shaped cut, such that an iridescent patch is included, whose magnified image reveals individual scales with number of dots of different intensity and spectral content.
- 5 Fig. 7: A Fourier transform of the scale in Fig. 6 is used to calculate signal bandwidth $\Delta\nu$.
- Fig. 8: A tag with transferred biological particles.
- Fig. 9: A tag with transferred biological particles and superstrate having an adhesive layer which changes the iridescence color.
- 10 Fig. 10: Square-shaped cuts in a butterfly wing (designated with white arrows), as observed under the scanning electron microscope.
- Fig. 11: A silhouette made of biological particles.
- Fig. 12: A fingerprint made of biological particles.
- 15 Fig. 13: A bar-code made of butterfly scales.
- Fig. 14: A manufacturing process of a tag with biological particles.
- Fig. 15: A flow chart of the manufacturing process of a tag with biological particles.
- Fig. 16: A manufacturing process of a tag with biological particles belonging to different biological species.

20

DETAILED DESCRIPTION OF THE INVENTION

In cooperation with the attached drawings, the technical contents and detailed embodiments of the present invention are described hereinafter, however, not limiting its scope of protection, which is exclusively defined by the claims. Any equivalent variation and

modification made according to the appended claims is to be included into their scope of protection.

An optical tag is disclosed which contains a number of biological particles selected according to their complexity and variability. Before describing the construction of a tag and its various embodiments, we assign concrete meaning to notions of complexity and variability. This is necessary in order to select the best species and biological particles, which guarantee the anti-counterfeit properties of a tag.

In reference to Fig. 1, the typical complexity of biological particles can be observed, e.g. Lepidoptera scales. Structure consists of two types of gratings: a volume grating which is characterized by ridges 1 having a number of lamellas 2, and a surface grating consisting of cross-ribs 3 connecting the ridges. By observing the cross-section of the scale (Fig. 2), it can be seen that the scale has two membranes: a lower one 4, which is unstructured, and an upper one 5, which contains ridges, lamellas and cross-ribs. By using magnified cross-section of a complex part of the butterfly scale in Fig. 3, the complexity can be quantified by determining the contour length to contour enclosed-surface ratio. Contour length is determined by first digitally emphasizing object edges (see Fig. 4) and calculating the total number of black pixels - L_{in} . Surface area is determined by digitally thresholding image in Fig. 3 (the result of the operation is shown in Fig. 5), and integrating the total number of black pixels S_k . Complexity C is thus $C = S_k/L_{in}$.

Natural variation in the internal structure of the biological particles, e.g. Lepidoptera scale (as shown in Figs. 1, 2 and 3), leads to variability of resulting optical effects. Fig. 6 shows a star-shaped part of the butterfly wing transferred on another substrate. Concrete Lepidoptera species and cut position are chosen such that the resulting piece contains at least one iridescent spot 6. Its magnified image reveal scales 7 having a number of dots of varying intensity and spectral content. Their position, optical spectrum and intensity are unpredictable and define degrees of freedom. Their number N is used a measure of variability. This can be estimated by calculating the ratio of the individual scale surface area S (easily calculated from an image) to the average dimension of a dot A_c (Fig. 6). The last feature is connected to spectral width of the signal via relation:

$$\Delta x \Delta v = 1/4\pi f$$

(see Fig. 7, where Fourier transform of the Lepidoptera scale image is shown). By measuring the spectral width Δv , average dot dimension Δx can be calculated. Finally, the number of the degrees of freedom is calculated as $N = S/\Delta x$.

5 In reference to Fig. 8, a preferred embodiment of an optical security tag according to the invention is shown by presenting it in two orthogonal projections. A substrate 8 is covered with a thin, transparent, adhesive layer 9. Biological particles 10 firmly adhere to the said adhesive layer, producing an easily recognizable pattern (e.g. a symbol, a letter, a barcode, a silhouette, etc.). Adhesion of the biological particles 10 is such that the attempt of removal destroys their
 10 submicron-sized structure. Three visible marks 11, 12 and 13 (e.g. crosses) are printed on the substrate 8, and are used for positioning the tag in a well defined position, with respect to the optical reading system. They also define a local coordinate system which can be curvilinear and non-orthogonal (designated with dashed lines). The exact mathematical nature of the coordinate system is known only to the issuer of the tag. The biological particles 10 are protected by a
 15 transparent cover 14. One or several particles 10' are randomly selected as bearers of individualization pattern. Their position with respect to markers 11, 12 and 13 is determined and memorized. In addition, their optical pattern (7 in Fig. 6) is recorded and memorized, too.

In another embodiment (Fig. 9) the superstrate 14 comprises a patterned adhesive layer 16 which permanently affixes to the biological particles. This serves a dual purpose. First, the
 20 refractive index of the layer changes the refractive index above the biological particles and alters the iridescent color of one part of the pattern 17. As in the previous embodiment, one or several scales 10', are randomly selected as bearers of individualization pattern. In addition, any attempt to disassemble the tag results in separation of biological particles – some of them remain on the substrate and others are lifted with the superstrate, thus producing a tamper sensitive tag.

25 In another embodiment, the substrate 8 is transparent, thus enabling two-sided observation of the biological particle 10. For some Lepidoptera species, the iridescence pattern is different on each side of the scale. In this embodiment, the optical pattern can be observed both in transmitted and reflected light. The pattern can be a result of diffraction, interference,

iridescence, scattering and fluorescence of coherent or incoherent light. Angular, focal and polarization changeability of the pattern is recorded and used as an authentication signal.

In yet another embodiment, transferred biological particles 10 are further patterned by mechanical means. A mechanical tool is engraved with the desired pattern, producing a system of raised and recessed portions. It is pressed onto the pattern, thus crushing the biological particles and changing their optical properties (e.g. iridescence, scattering), producing visually observable pattern.

In yet another embodiment, transferred biological particles are macroscopically patterned by laser cutting or engraving (e.g. square shaped areas designated with white arrows in Fig. 10). A beam from an ultrafast laser is introduced in a system with a computer controlled galvanometer-mirror scanner, which is used to angularly deflect a beam according to programmed trajectory. The beam is then expanded and focused to the tag with biological particles, using an f-theta lens, which enables flat scanning field and linear relation between the deflection angle and the focal beam position. The laser wavelength, scanning speed and power are chosen such that cutting or engraving is enabled. It is used to draw a personalized, biometric, pattern (e.g. silhouette as in Fig. 11, fingerprint as in Fig. 12, retinal blood vessel pattern, signature, or iris image) onto the surface of a tag with biological particles. In this manner an open pattern is produced, which can be used for visual and machine authentication.

A further embodiment is characterized by a bar-code or QR-code pattern made from biological particles (Fig. 13).

In another embodiment, fluorescence of transferred biological particles is selectively bleached using high intensity UV radiation. This can be done using an UV projection system consisting of a UV lamp and an objective. A mask, containing transparent and opaque areas which comprise an image, is inserted into the system such that an image is produced directly on a tag with biological particles. Bleaching action is controlled by the intensity of the illuminating beam and the illumination time. Alternatively, a beam from a continuous wave (CW) or ultrafast laser is introduced in a system with a computer-controlled galvanometer-mirror scanner, which is used to angularly deflect a beam according to programmed trajectory. The beam is then expanded and focused to the tag with biological particles, using an f-theta lens, which enables

flat scanning field and linear relation between the deflection angle and the focal beam position. Wavelength of a laser is chosen such that the bleaching action is enabled via single-photon process (in the case of a CW laser), or two-photon process (in the case of an ultrafast laser). The laser power and its scanning speed determine the intensity of the bleaching. The pattern is observable using low intensity UV radiation as a covert security feature.

The tag manufacturing process consists of several stages depicted in Fig. 14. First, a tape having an adhesive layer (pressure sensitive) with low peel strength (preferably, the surface energy of the order of 0.5 N/cm) is laser- or die-cut in the required shape. A tape is pressed on the surface covered with biological particles (e.g. a butterfly wing), with their iridescent surface facing up, and they adhere to the tape (phase (I) in Fig. 14). The tape is peeled, lifting-off cells or tissues (phase (II) in Fig. 14). Next, a tape is transferred to a second optically transparent tape having high peel strength and, preferably, surface energy of the order of 2.5 N/cm (phase (III) in Fig. 14). Tapes are pressed together with the adhesive layers facing each other, biological particles being trapped between the layers. After a certain dwell time, the tapes are separated (phase (IV) in Fig. 14). Due to the higher surface energy of the second tape, biological particles from the first plate remain on the second tape. The third, optically transparent, non-adhesive tape is used to cover the biological particles, protecting them from external influences (phase (V) in Fig. 14). The third tape is smaller than the second tape, thus exposing the remaining adhesive layer, which will be used for attachment to an object requiring individualization. A flow chart of the whole process is shown in Fig. 15.

In another embodiment, a tag and associated manufacturing process use biological particles of several species. The final pattern is assembled from two or more sub-patterns transferred from several insect species belonging to e.g. Lepidoptera order, as described in Fig. 16. First, a tape 18 having an adhesive layer (pressure sensitive) with low peel strength (preferably, with a surface energy of the order of 0.5 N/cm) is laser- or die-cut in the required shape. A tape is pressed on the surface 19 covered with biological particles (e.g. a Lepidoptera wing) belonging to one biological species, with their iridescent surface facing up. Biological particles adhere to the tape (phase (I) in Fig. 16). The tape is peeled, lifting off cells or tissues (phase (II) in Fig. 16). Next, a tape is transferred to a second optically transparent tape 20 having high peel strength and, preferably, a surface energy of the order of 2.5 N/cm (phase (III) in Fig.

140 Tapes are pressed together with the adhesive layers facing each other, biological particles being trapped between the layers. After a certain dwell time, the tapes are separated (phase (IV) in Fig. 16). Due to the higher surface energy of the second tape, biological particles from the first plate remain on the second tape. Another tape 21, having an adhesive layer (pressure sensitive) with a low peel strength (preferably, with a surface energy of the order of 0.5 N/cm) is laser- or die-cut in the required shape, complementary to the one described in Phase I of the process. A tape is pressed on the surface 22 covered with biological particles (e.g. a Lepidoptera wing) belonging to another biological species, with their iridescent surface facing up. Biological particles adhere to the tape (phase (V) in Fig. 16). The tape is peeled, lifting off cells or tissues (phase (VI) in Fig. 16). Next, a tape is transferred to, previously manufactured, transparent tape 20 having high peel strength and, preferably, a surface energy of the order of 2.5 N/cm (phase (VII) in Fig. 16). Tapes are pressed together with the adhesive layers facing each other such that patterns defined by tapes 18 and 21 complement each other. Consequently biological particles are trapped between the layers. After a certain dwell time, the tapes are separated (phase (VIII) in Fig. 16). Due to the higher surface energy of the second tape, biological particles from the first tape remain on the second tape.

In the next phase (IX in Fig. 16) the third, optically transparent, non-adhesive tape is used to cover the biological particles, protecting them from external influences. The third tape is smaller than the second tape, thus exposing the remaining adhesive layer, which will be used for attachment to an object requiring individualization.

The method described in the previous embodiment can be further extended to any number of different biological species.

Claims

1. A security tag, characterized by a pattern of inimitable biological particles (10), directly transferred from an organism to a transparent adhesive layer (9) on a substrate (8), covered with a transparent superstrate (14), such that said biological particles (10) are encapsulated between said substrate (8) and said superstrate (14).
2. The security tag according to claim 1, wherein the pattern of biological particles (10) is in the shape of a bar-code or QR-code.
3. The security tag according to claim 1, wherein the pattern of biological particles (10) is in the shape of a silhouette of a human head.
4. The security tag according to claim 1, wherein the pattern of biological particles (10) is in the shape of a fingerprint.
5. The security tag according to any of the preceding claims, wherein the biological particles (10) are overtly inscribed with information by mechanical or laser cutting.
6. The security tag according to any of claims 1 to 4, wherein the biological particles (10) are covertly inscribed with information by permanently bleaching their fluorescence.
7. The security tag according to any of the preceding claims, wherein the biological particles (10) are selected from Lepidoptera scales, hairs or bristles, Coleoptera scales, Trichoptera hairs or bristles, and Araneae scales.
8. The security tag according to claim 7, wherein the biological particles (10) are taken from several different species, and assembled on the substrate (8) in a predetermined pattern.
9. The security tag according to claim 7 or 8, wherein selected parts of the superstrate (14) are covered with a transparent layer of adhesive, which permanently adheres to the biological particles (10).
10. Use of a security tag according to any of the preceding claims for identification and authentication of goods, articles and documents.

- 11 A method of manufacturing a security tag according to any of claims 1 to 9, comprising the following steps:
- (1) providing for at least one biological particle (10) on a surface;
- (2) cutting an optically transparent tape, with a low surface energy adhesive layer, in a
5 predetermined shape to form a first pre-cut tape;
- (4) pressing the first pre-cut tape onto the surface with the biological particles (10);
- (5) removing the first pre-cut tape from the surface with the biological particles (10), with a majority of the biological particles (10) being attached to the first pre-cut tape;
- (6) bringing in contact the first pre-cut-tape with attached biological particles (10) with a
10 second, high surface energy, optically transparent, adhesive tape, such that the adhesive layers face each other;
- (7) lifting-off the first pre-cut tape from the second tape;
- (8) covering the second tape with a third optically transparent tape, which is smaller than the second tape to form the security tag ready to be attached to goods, articles or
15 documents.

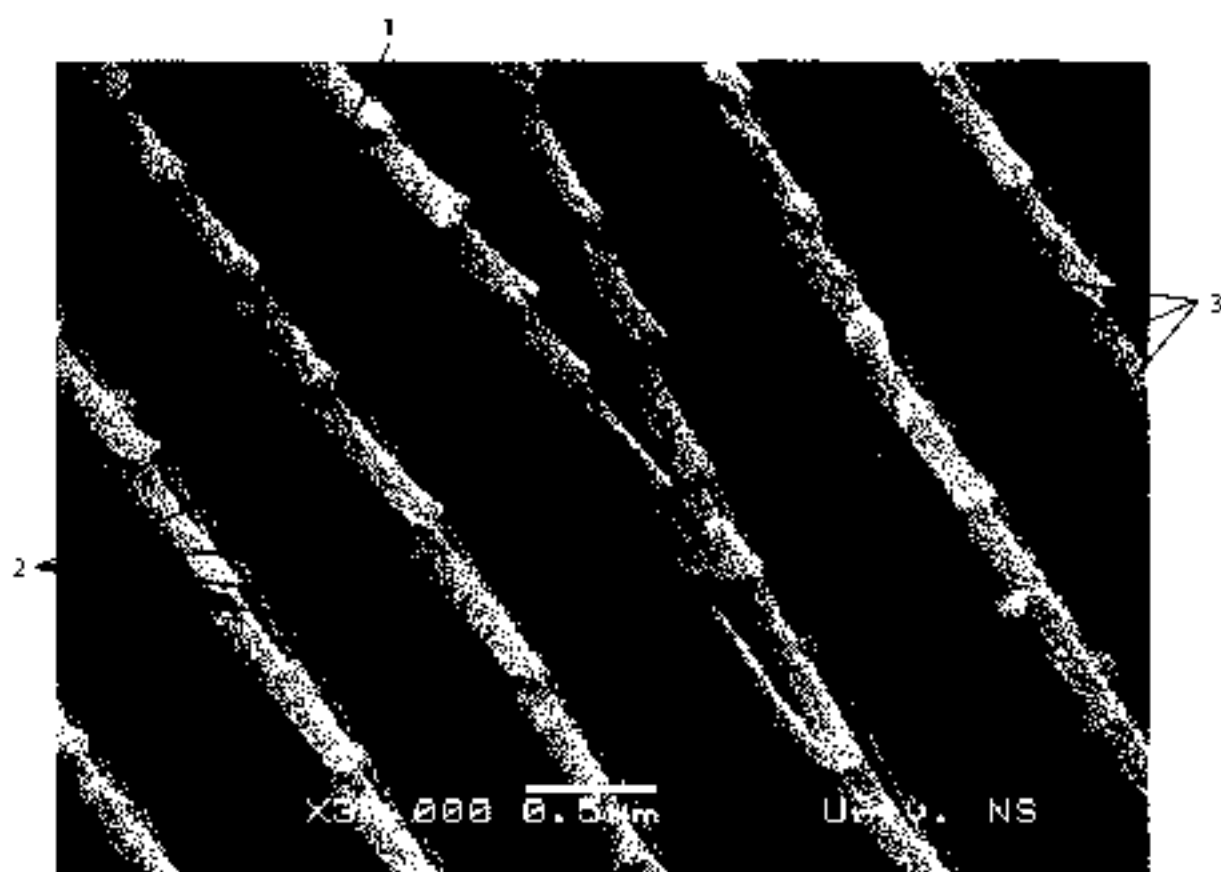


Fig. 1

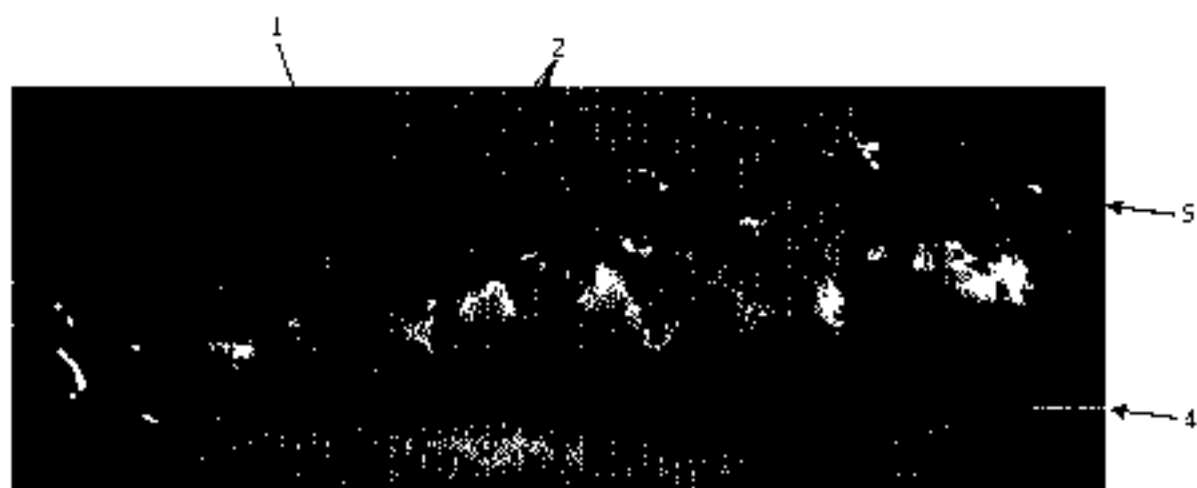


Fig. 2



Fig. 3

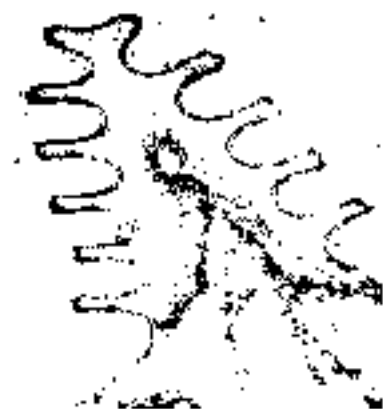


Fig. 4



Fig. 5

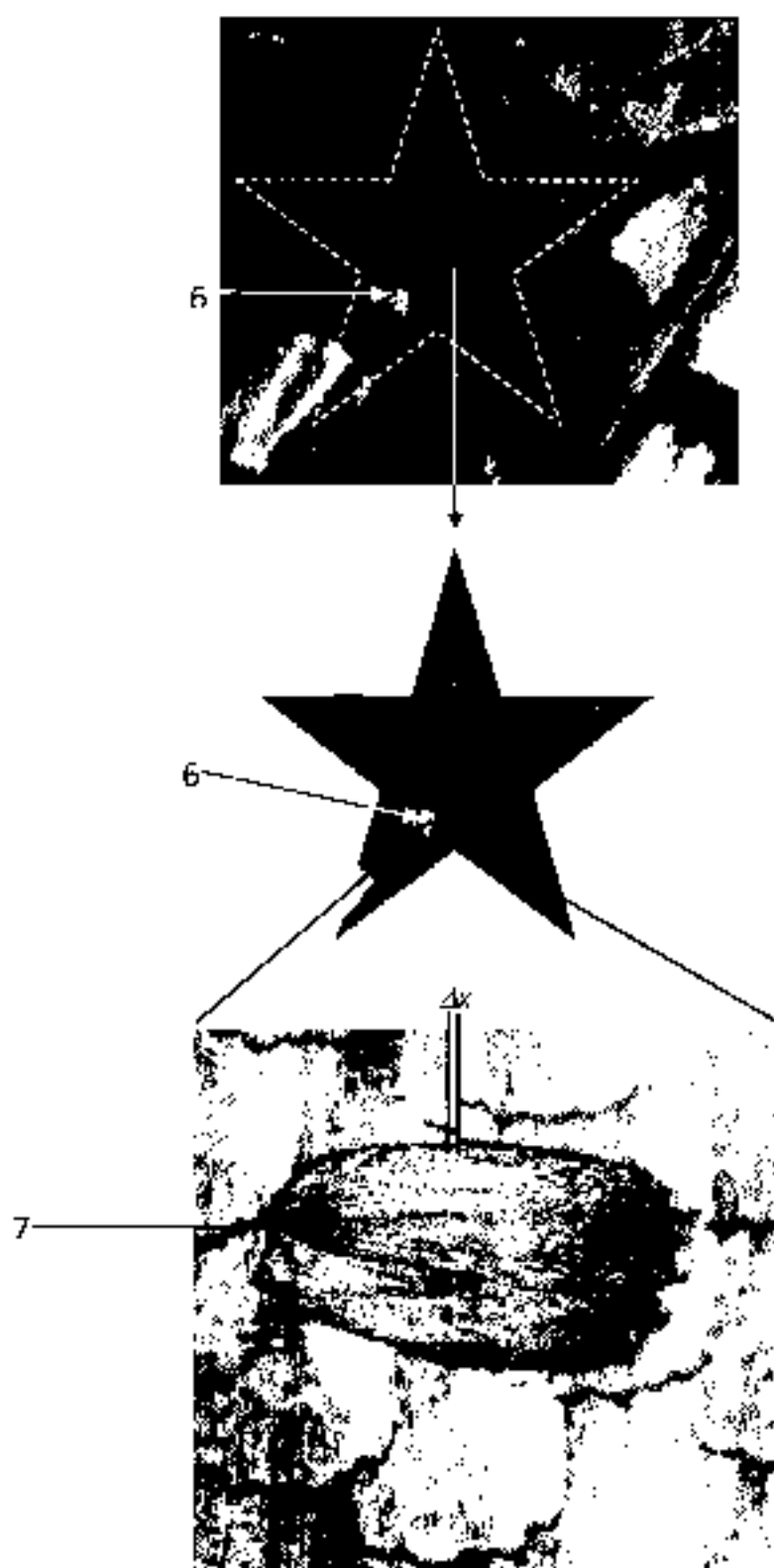


Fig. 6

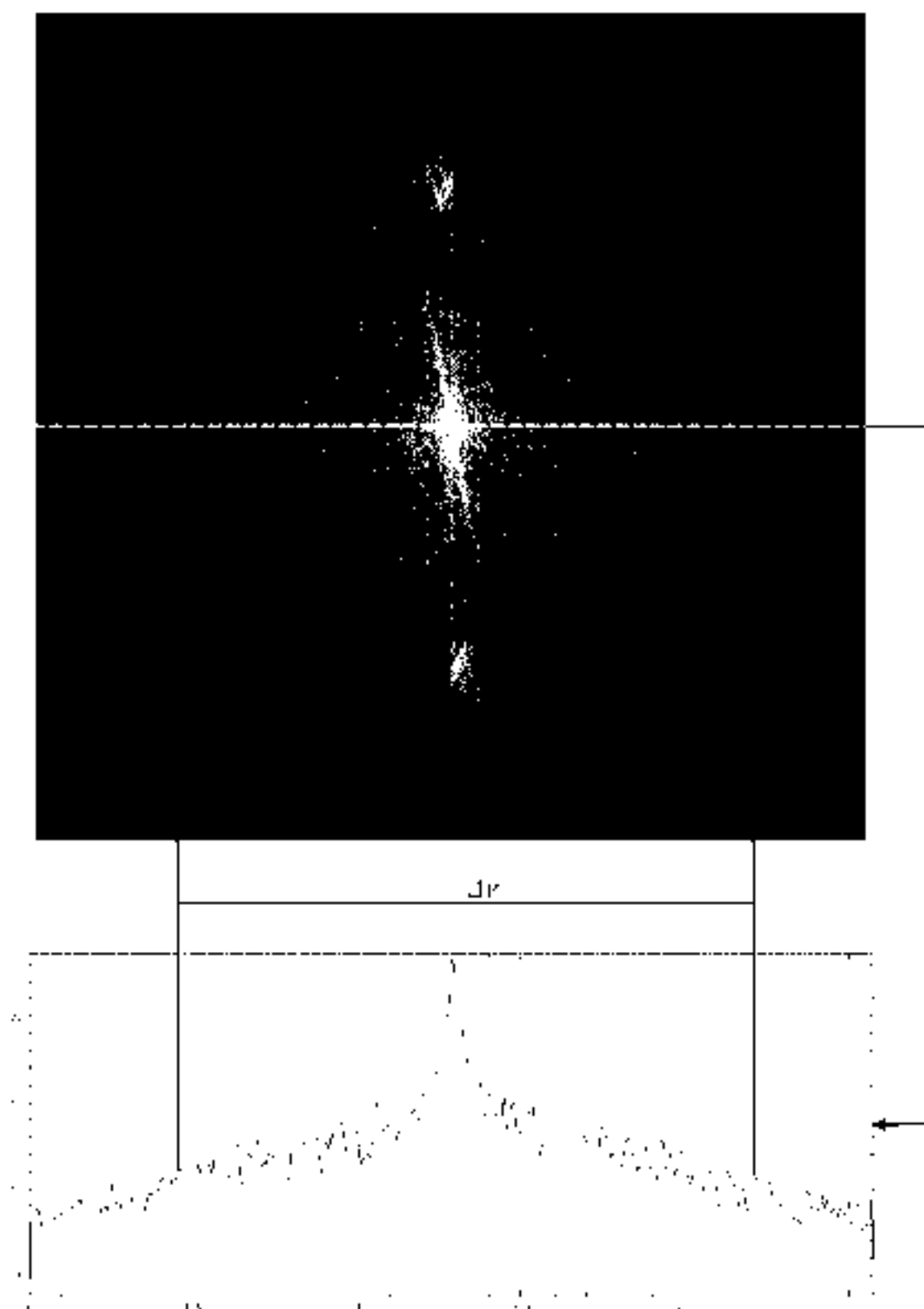


Fig. 7

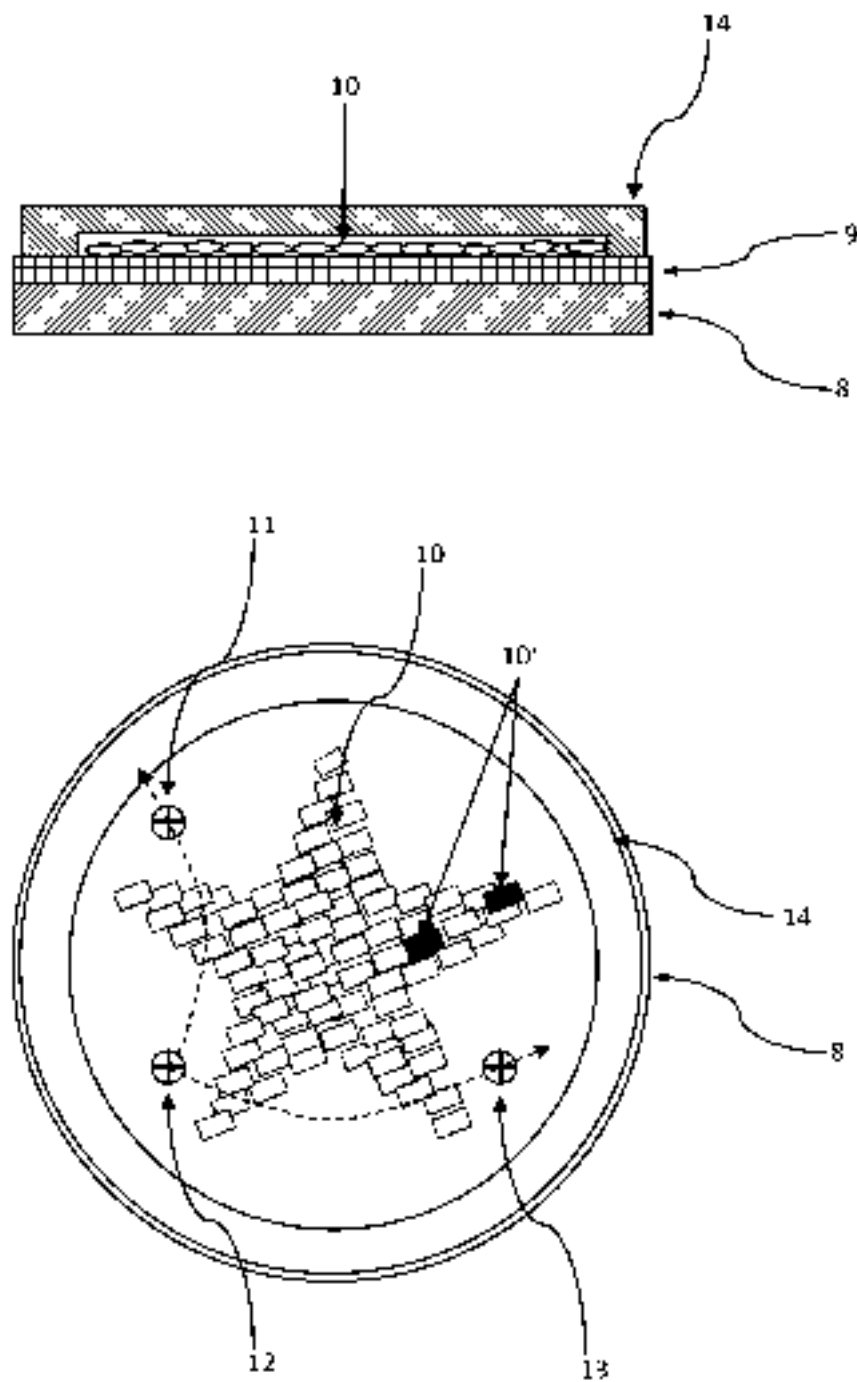


Fig. 8

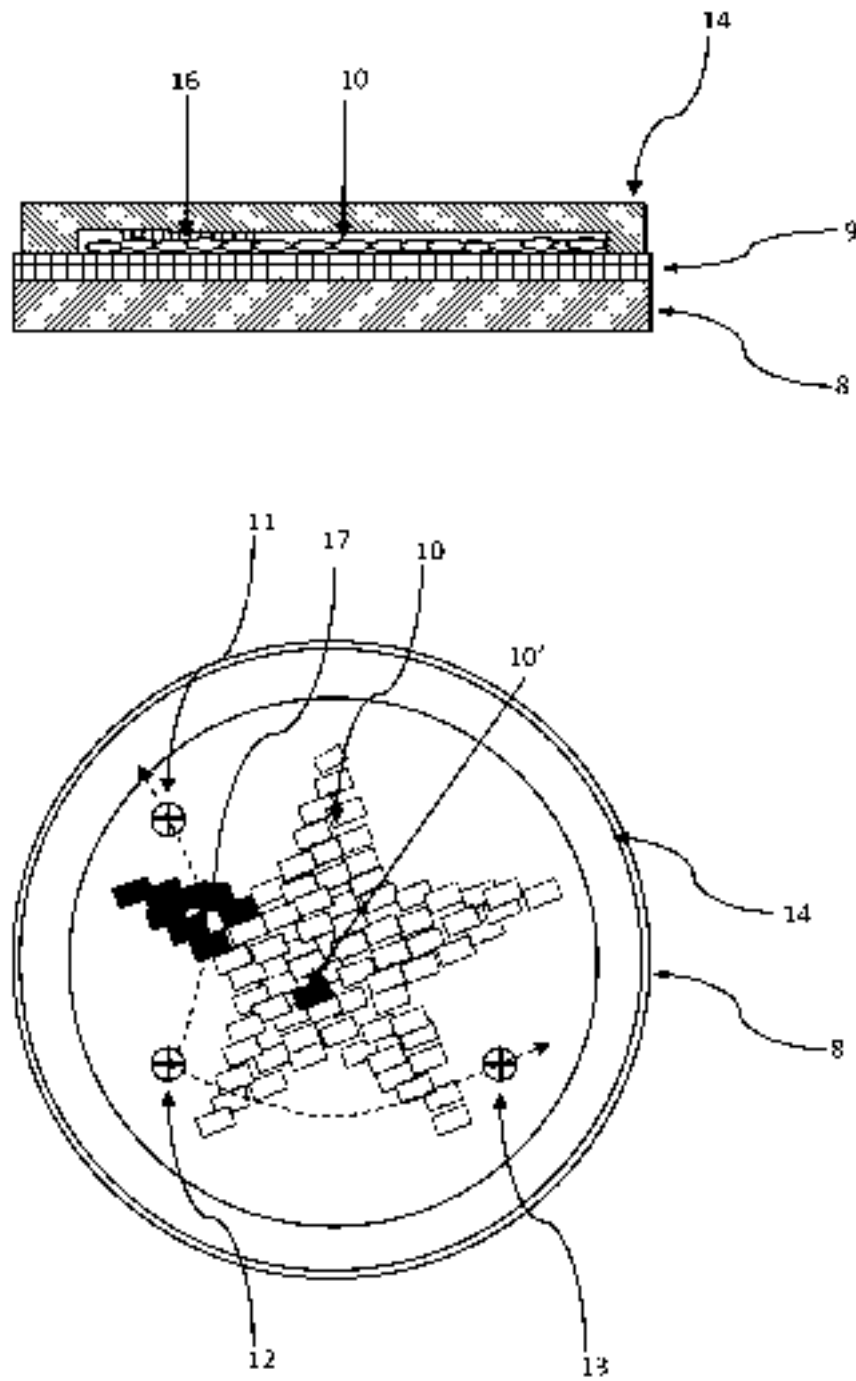


Fig. 9

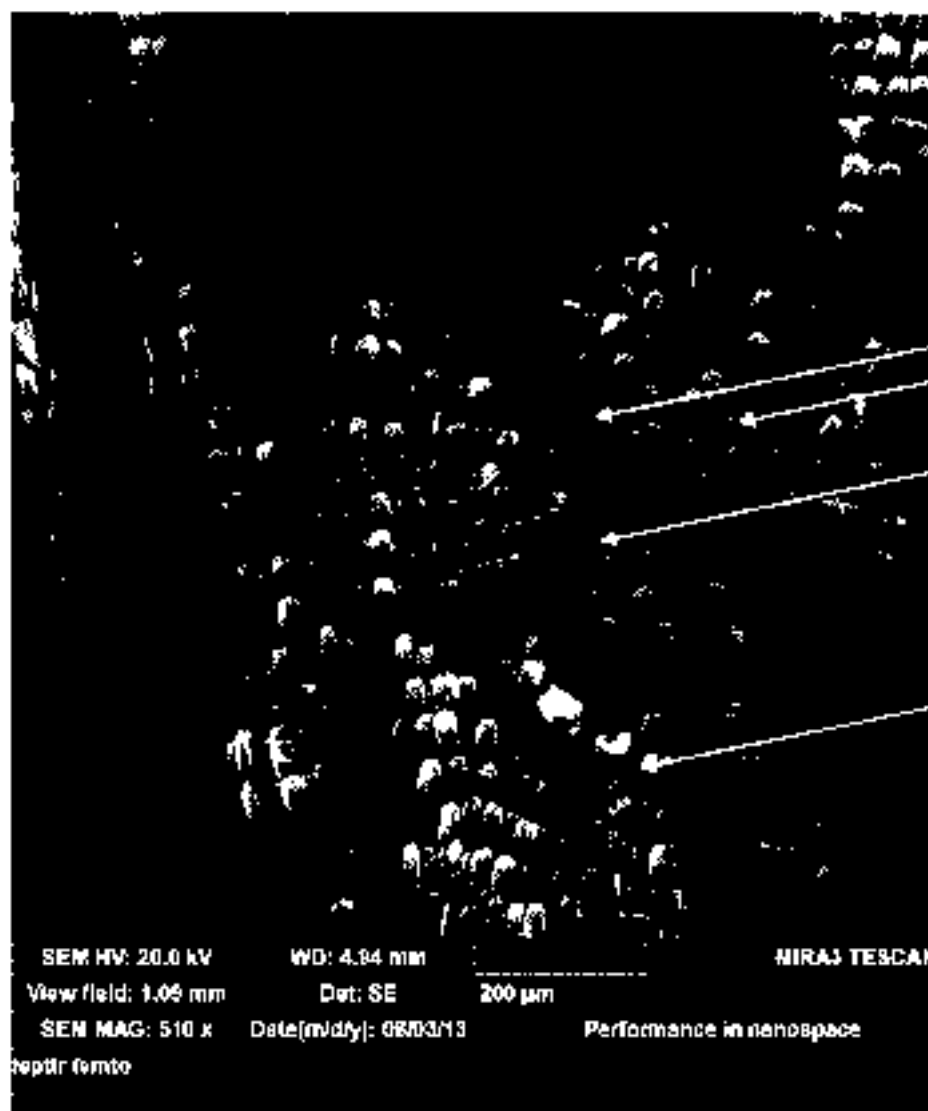


Fig. 10

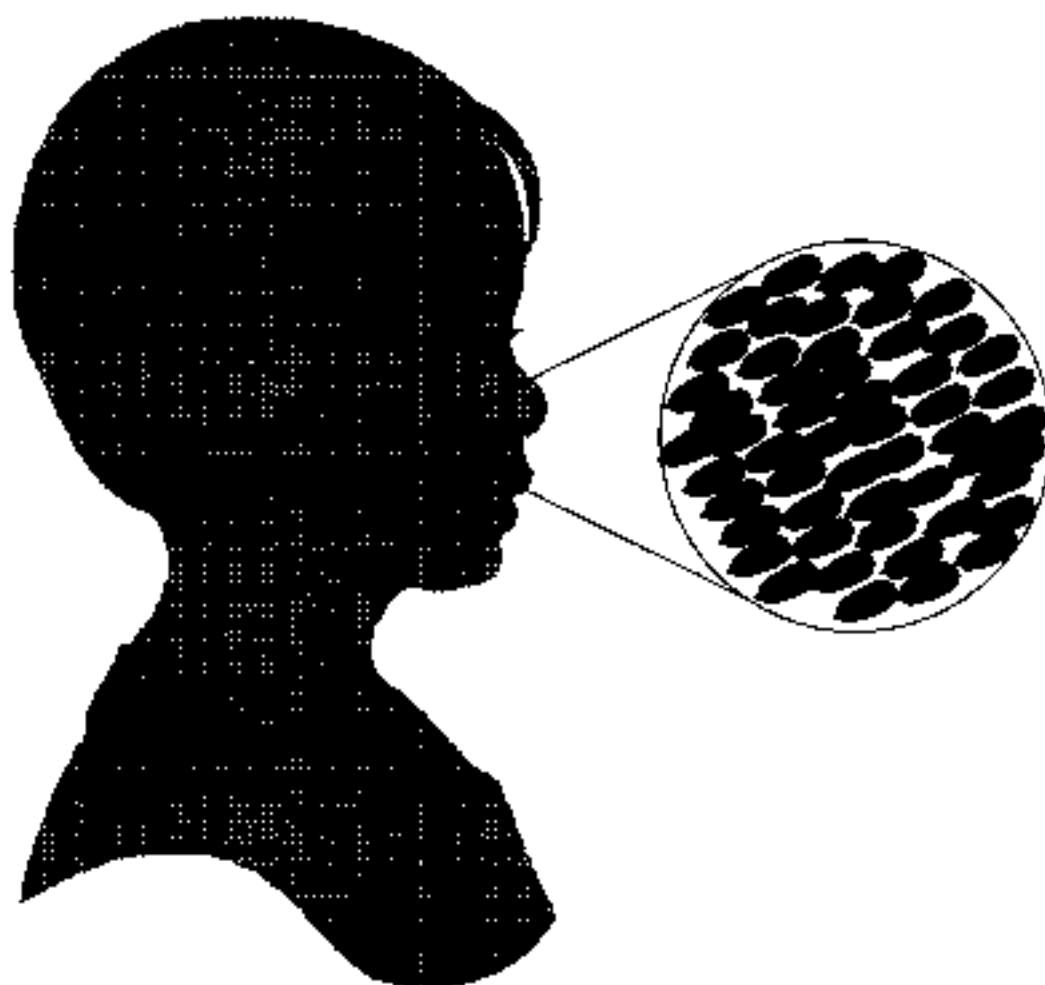


Fig. 11

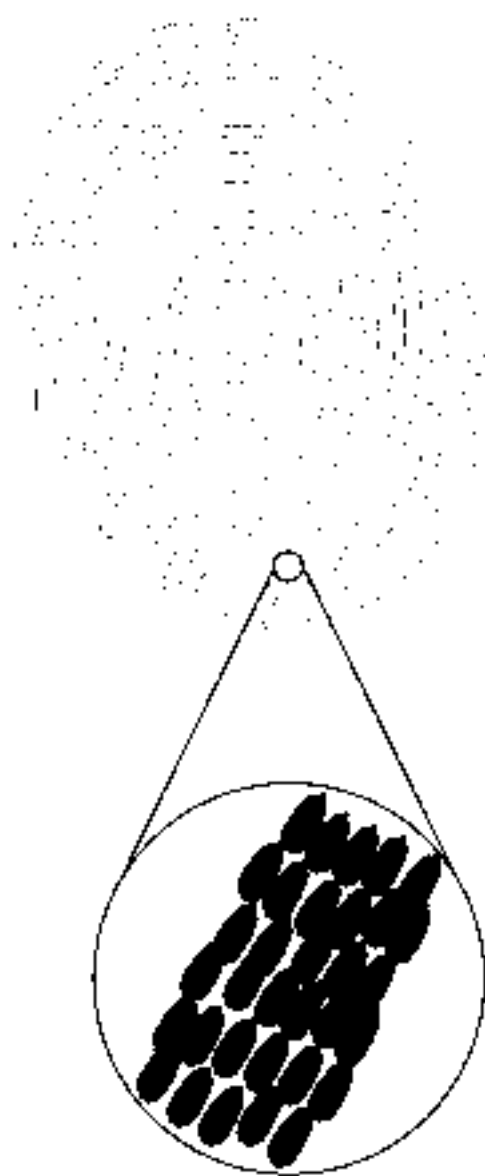


Fig. 12

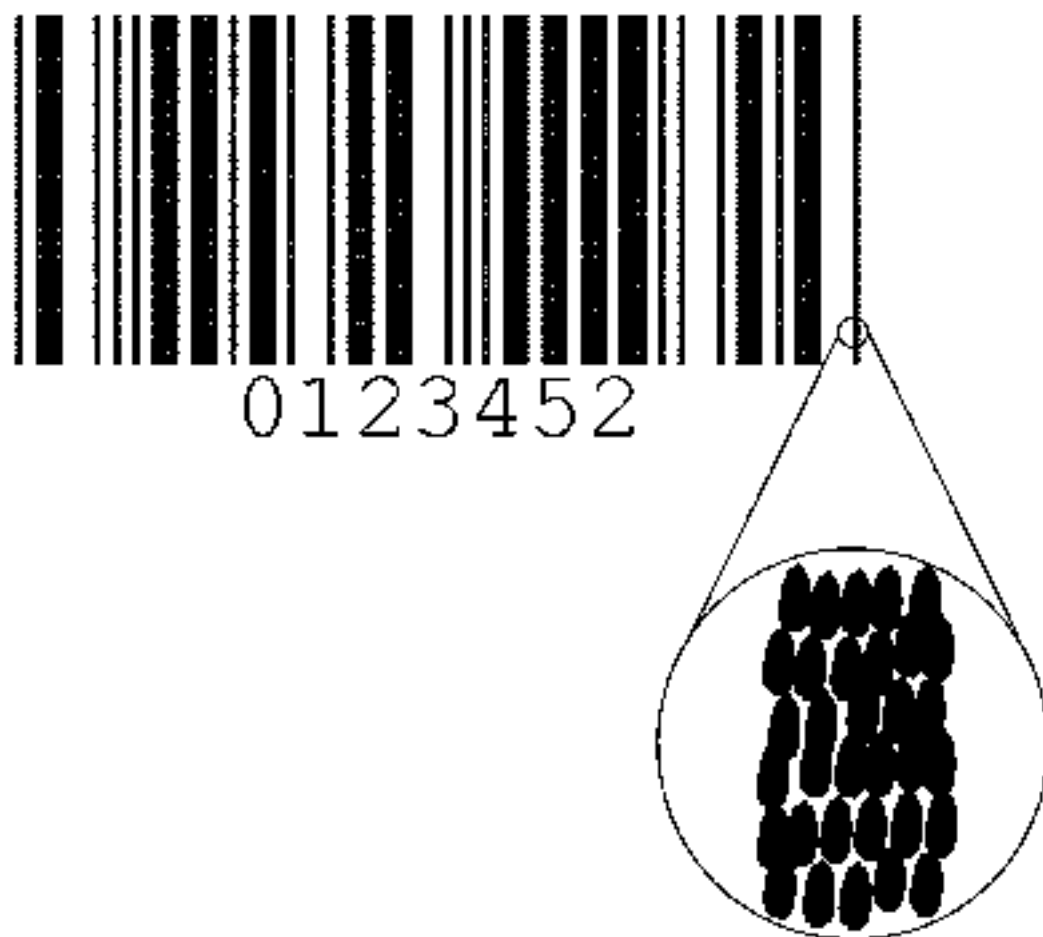


Fig. 13

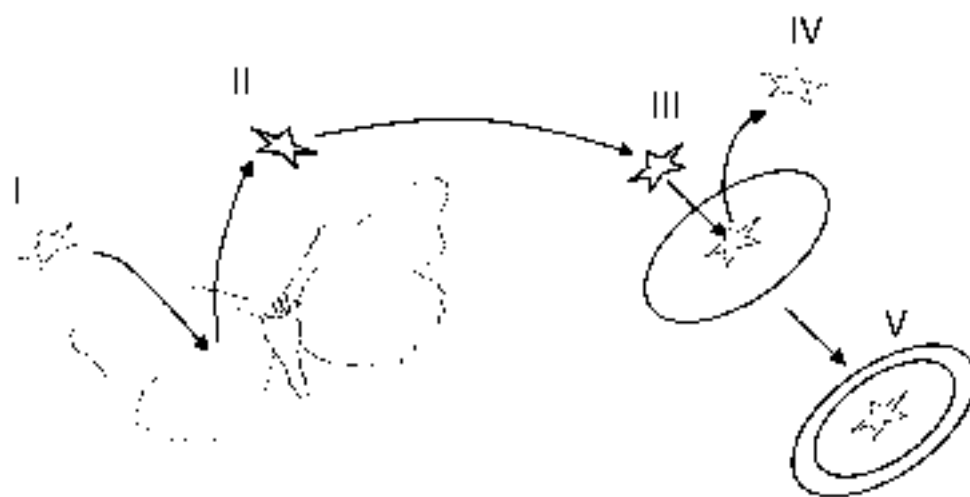


Fig. 14

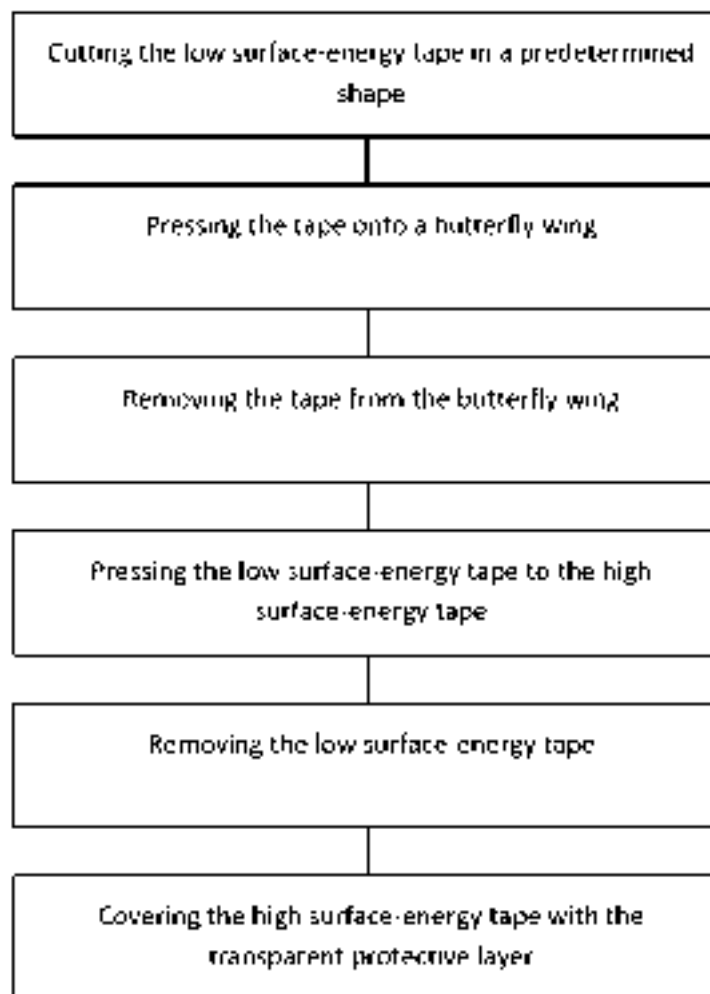


Fig. 15

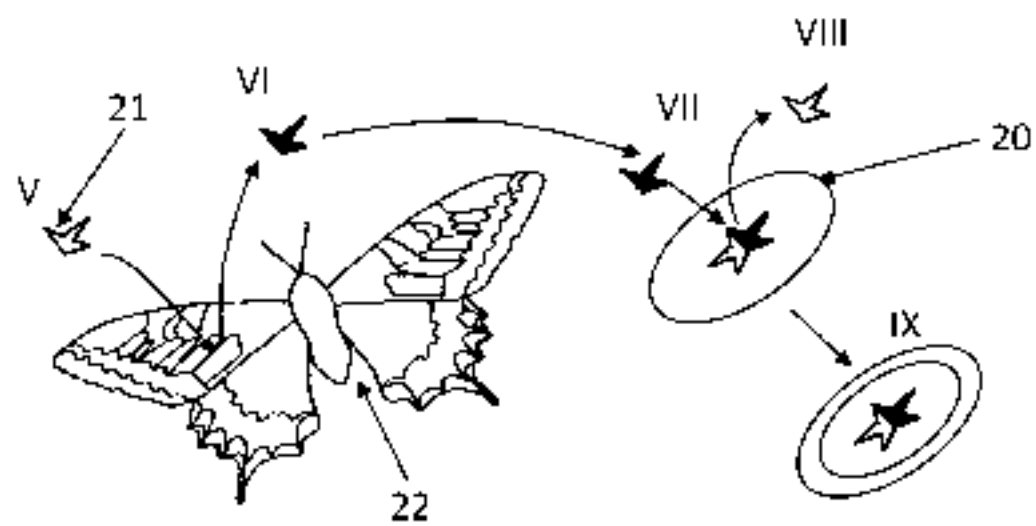
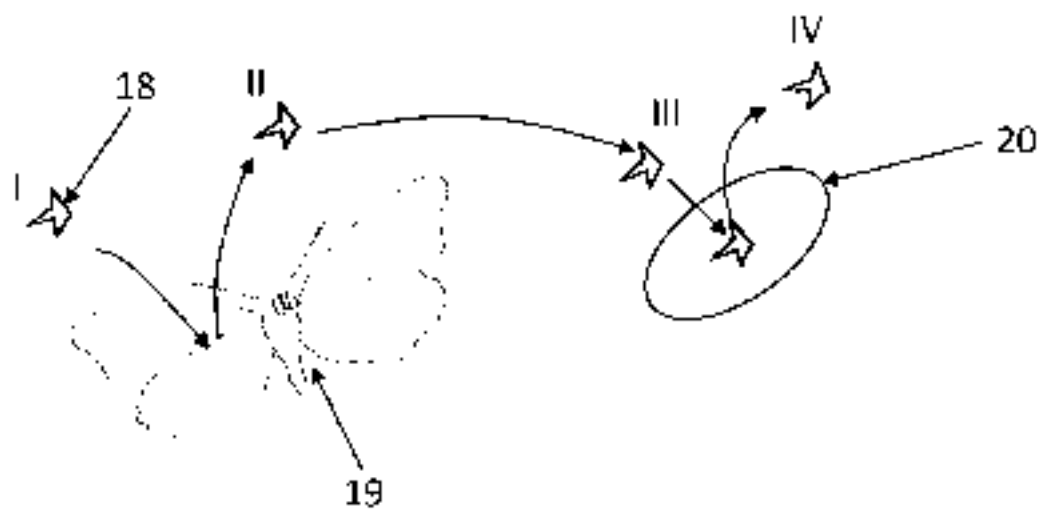


Fig. 16

INTERNATIONAL SEARCH REPORT

International application No
PCT/EP2015/081400

A. CLASSIFICATION OF SUBJECT MATTER

INV. B42D25/36 G06K19/08 G09F3/02
ADD.

According to International Patent Classification (IPC) or to both national classification and IPC

B. FIELDS SEARCHED

Minimum documentation searched (classification system followed by classification symbols)

B42D G06K B41M G09F

[Documentation searched other than minimum documentation to the extent that such documents are included in the fields searched]

Electronic data base consulted during the international search (name of data base and, where practicable, search terms used)

EPQ-Internal, WPI Data

C. DOCUMENTS CONSIDERED TO BE RELEVANT

Category	Citation of document, with indication, where appropriate, of the relevant passages	Relevant to claim No.
A	WO 2007/031077 A1 (STIFTUNG A WEGENER INST POLAR [DE]; HAMM-DUBISCHAR CHRISTIAN [DE]) 22 March 2007 (2007-03-22) cited in the application page 14, line 13 - page 15, line 23 page 19, line 5 - page 20, line 18; figures 1,3 -----	1-11
A	DE 10 2007 052009 B3 (HOCHSCHULE BREMERHAVEN [DE]; STIFTUNG A WEGENER INST POLAR [DE]) 4 December 2008 (2008-12-04) paragraphs [0032] - [0035]; figures 1A,1B,2 -----	1-11

 Further documents are listed in the continuation of Box C See patent family annex.

Special categories of cited documents:

"X" document defining the general state of the art which is not considered to be of particular relevance

"E" earlier application or patent but published on or after the international filing date

"L" document which may throw doubts on priority claim(s) or which is cited to establish the publication date of another citation or other special reason (as specified)

"O" document referring to an oral disclosure, use, exhibition or other means

"P" document published prior to the international filing date but later than the priority date claimed

"T" later document published after the international filing date or priority date and not in conflict with the application but cited to understand the principle or theory underlying the invention

"C" document of particular relevance: the claimed invention cannot be considered novel or cannot be considered to involve an inventive step when the document is taken alone

"Y" document of particular relevance: the claimed invention cannot be considered to involve an inventive step when the document is combined with one or more other such documents, such combination being obvious to a person skilled in the art

"B" document member of the same patent family

[Date of the actual completion of the international search]

18 August 2016

[Date of mailing of the international search report]

02/09/2016

Name and mailing address of the ISA/

European Patent Office, P. B. 5518 Patentlaan 2
NL - 2280 HX Rijswijk
Tel (+31-70) 340 2040,
Fax (+31-70) 340 3016

Authorized official:

O'Incecco, Raimondo

INTERNATIONAL SEARCH REPORT

Information on patent family members.

International application No.

PCT/EP2015/081400

Patent document cited in search report	Publication date	Patent family member(s)	Publication date
WO 2007031077 A1	22-03-2007	DE 102005045642 A1	29-03-2007
		WO 2007031077 A1	22-03-2007

DE 102007052009 B3	04-12-2008	AT 510275 T	15-06-2011
		DE 102007052009 B3	04-12-2008
		EP 2227788 A2	15-09-2010
		WO 2009052811 A2	30-04-2009

Tell us what you think of PATENTSCOPE in our [short survey](#).

1. CA3009382 - SECURITY TAG CONTAINING A PATTERN OF BIOLOGICAL PARTICLES

[National Biblio. Data](#) [Patent Family](#) [Documents](#)

[PermaLink](#) [Machine translation](#)

Office

Canada

Application Number

3009382

Application Date

Publication Number

3009382

Publication Date

06.07.2017

Publication Kind

A1

IPC

[B42D 25/36](#) [G06K 19/08](#) [G09F 3/02](#)

CPC

[B42D 25/36](#) [B42D 25/305](#) [B42D 25/313](#)

[B42D 25/43](#) [B42D 25/47](#) [B42D 25/45](#)

[View more classifications](#)

Applicants

INSTITUTE OF PHYSICS BELGRADE, UNIVERSITY OF BELGRADE

Title

[EN] SECURITY TAG CONTAINING A PATTERN OF BIOLOGICAL PARTICLES

[FR] ETIQUETTE DE SECURITE CONTENANT UN MOTIF DE PARTICULES BIOLOGIQUES

Abstract

[EN] The invention is directed to a security device individualized by permanently attaching particles of biological origin, possessing large variability of optical effects and complexity of internal structure. Biological species and corresponding particles are chosen to maximize variability and complexity, while having durability, tamper sensitivity and micron size thickness. A method to manufacture a tag, suitable for visual, machine and forensic inspection, is disclosed.

Related patent documents

[CN108472982](#) [KR1020180098620](#) [EP3397503](#) [US20190023055](#) [JP2019503916](#) [WO/2017/114570](#)



Tell us what you think of PATENTSCOPE in our [short survey](#).

1. CN108472982 - SECURITY TAG CONTAINING A PATTERN OF BIOLOGICAL PARTICLES

[National Biblio. Data](#) [Description](#) [Claims](#) [Drawings](#) [Patent Family](#) [Documents](#)

[PermaLink](#) [Machine translation](#)

Office

China

Application Number

201580085649.0

Application Date

30.12.2015

Publication Number

108472982

Publication Date

31.08.2018

Grant Number

108472982

Grant Date

07.02.2020

Publication Kind

B

IPC

G09F 3/02 G06K 19/08 B42D 25/36

CPC

B42D 25/36 B42D 25/305 B42D 25/313

B42D 25/43 B42D 25/47 B42D 25/45

[View more classifications](#)

Applicants

INSTITUTE OF PHYSICS BELGRADE UNIVERSITY OF BELGRADE
贝尔格莱德大学贝尔格莱德物理学院

Inventors

PANTELIC DEJAN
德扬·潘泰利奇
RABASOVIC MIHAILO
米哈伊洛·拉巴索维奇
KRMPOT ALEKSANDAR
亚历山大·克尔姆波蒂
LAZOVIC VLADIMIR
弗拉迪米尔·拉佐维奇
PAVLOVIC DANICA
达妮察·帕夫洛维奇

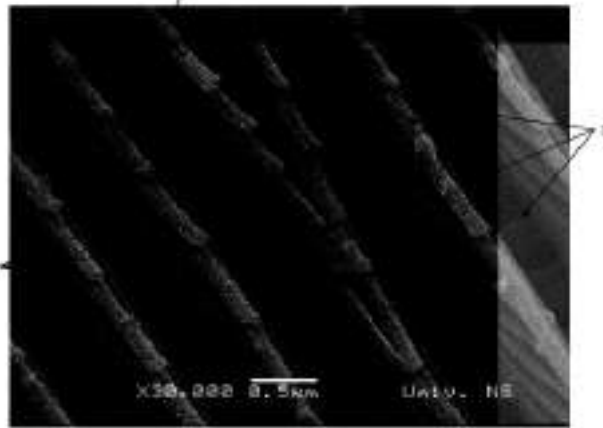
Agents

中科专利商标代理有限公司 11021

Title

[EN] SECURITY TAG CONTAINING A PATTERN OF BIOLOGICAL PARTICLES

[ZH] 含有生物粒子图案的安全标签



Abstract

[EN] The invention is directed to a security device individualized by permanently attaching particles of biological origin, possessing large variability of optical effects and complexity of internal structure. Biological species and corresponding particles are chosen to maximize variability and complexity, while having durability, tamper sensitivity and micron size thickness. A method to manufacture a tag, suitable for visual, machine and forensic inspection, is disclosed.

[ZH] 本发明涉及通过永久附着生物来源的粒子而个性化的安全装置，其具有大的光学效果可变性和内部结构复杂性。选择生物物种和相应粒子以将可变性和复杂性最大化，同时具有耐久性、篡改敏感性和微米尺寸厚度。本发明公开了制造适用于视觉、机器和法医检查的标签的方法。

Related patent documents

[KR1020180098620](#) [EP3397503](#) [US20190023055](#) [JP2019503916](#) [WO/2017/114570](#) [CA3009382](#)



Tell us what you think of PATENTSCOPE in our [short survey](#).

1. EP3397503 - SECURITY TAG CONTAINING A PATTERN OF BIOLOGICAL PARTICLES

[National Biblio. Data](#) [Description](#) [Claims](#) [Drawings](#) [Patent Family](#) [Documents](#)

[PermaLink](#) [Machine translation](#)

Office

European Patent Office

Application Number

15823174

Application Date

30.12.2015

Publication Number

3397503

Publication Date

07.11.2018

Publication Kind

B1

IPC

B42D 25/36

G06K 19/08

G09F 3/02

CPC

B42D 25/36

B42D 25/305

B42D 25/313

B42D 25/43

B42D 25/47

B42D 25/45

[View more classifications](#)

Applicants

INSTITUTE OF PHYSICS BELGRADE UNIV OF BELGRADE

Inventors

PANTELIC DEJAN
RABASOVIC MIHAILO
KRMPOT ALEKSANDAR
LAZOVIC VLADIMIR
PAVLOVIC DANICA

Designated States

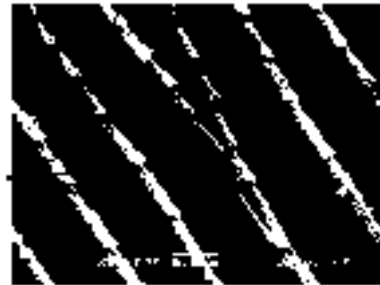
[View all](#)

Title

[DE] SICHERHEITSETIKETT ENTHALTEND EIN MUSTER AUS BIOLOGISCHEN PARTIKELN

[EN] SECURITY TAG CONTAINING A PATTERN OF BIOLOGICAL PARTICLES

[FR] ÉTIQUETTE DE SÉCURITÉ CONTENANT UN MOTIF DE PARTICULES BIOLOGIQUES



Abstract

[EN] The invention is directed to a security device individualized by permanently attaching particles of biological origin, possessing large variability of optical effects and complexity of internal structure. Biological species and corresponding particles are chosen to maximize variability and complexity, while having durability, tamper sensitivity and micron size thickness. A method to manufacture a tag, suitable for visual, machine and forensic inspection, is disclosed.

[FR] La présente invention concerne un dispositif de sécurité individualisé par la fixation permanente de particules d'origine biologique, possédant une grande variabilité d'effets optiques et une structure interne complexe. Les espèces biologiques et les particules correspondantes sont choisies pour maximiser la variabilité et la complexité, tout en ayant une durabilité, une sensibilité à la violation et une épaisseur de taille micrométrique. La présente invention concerne un procédé de fabrication d'une étiquette conçue pour l'inspection visuelle, mécanique et médico-légale.

Related patent documents

[CN108472982](#) [KR1020180098620](#) [US20190023055](#) [JP2019503916](#) [WO/2017/114570](#) [CA3009382](#)



Tell us what you think of PATENTSCOPE in our [short survey](#).

1. JP2019503916 - 生物粒子のパターンを含むセキュリティタグ

[National Biblio. Data](#)
[Full Text](#)
[Patent Family](#)
[Documents](#)
[PermaLink](#)
[Machine translation](#)
Office

Japan

Title

[JA] 生物粒子のパターンを含むセキュリティタグ

Application Number

2018553295

Abstract

[JA]

本発明は、光学的効果の大きな変異性と内部構造の複雑さを持つ生物起源の粒子を永続的に付着させることにより個別化されたセキュリティデバイスを対象としている。生物種および対応する生物粒子は、変異性および複雑さを最大にし、同時に、耐久性があり、改竄が感知しやすく、ミクロンサイズの厚さを有するものが選択される。目視、機械および裁判検査に適したタグを製造する方法が開示されている。

Application Date

30.12.2015

Publication Number

2019503916

Related patent documents
[CN108472982](#) [KR1020180098620](#) [EP3397503](#) [US20190023055](#) [WO/2017/114570](#) [CA3009382](#)
Publication Date

14.02.2019

Grant Number

6636174

Grant Date

27.12.2019

Publication Kind

B2

IPC
[B42D 25/36](#) [B42D 25/305](#) [B42D 25/313](#)
[B42D 25/40](#) [B42D 25/435](#) [B42D 25/44](#)
CPC
[B42D 25/36](#) [B42D 25/305](#) [B42D 25/313](#)
[B42D 25/43](#) [B42D 25/47](#) [B42D 25/45](#)
[View more classifications](#)
Applicants

インスティテュート オブ フィジックス ベ
オグラード、ユニバーシティ オブ ベオグラ
ード

Inventors

バンテリック, デジャン
ラボンビック, ミハイロ
クラムポット, アレクサンダー
ラゾヴィック, ウラジーミル
バプロヴィック, ダニカ

Agents

小林 浩
大森 規雄
日野 真美
大賀 沙央里
鈴木 康仁



Tell us what you think of PATENTSCOPE in our [short survey](#).

1. KR1020180098620 - 생물학적 입자의 패턴을 포함하는 보안 태그

National Biblio. Data Description Claims Drawings Patent Family Documents

PermaLink Machine translation

Office

Republic of Korea

Application Number

1020187021531

Application Date

30.12.2015

Publication Number

1020180098620

Publication Date

04.09.2018

Publication Kind

A

IPC

B42D 25/36

B42D 25/43

B42D 25/47

Applicants

인스티튜트 오브 피직스 베오그라드, 유니버시티 오브 베오그라드

Inventors

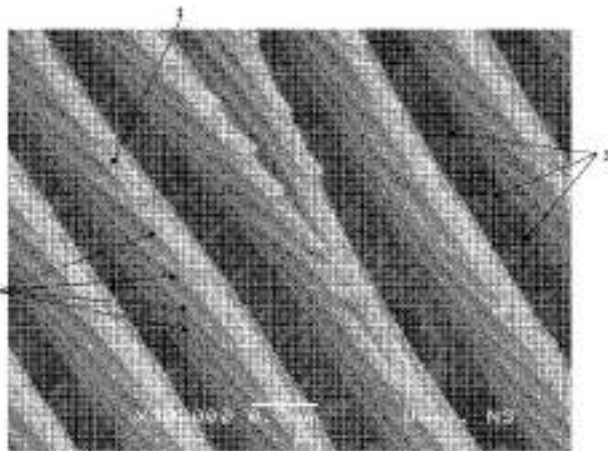
판테릭 데잔
라바소비크 미하일로
크름포트 알렉산다르
라조비크 블라디미르
파블로비크 다니카

Agents

유미특허법인

Title

[KO] 생물학적 입자의 패턴을 포함하는 보안 태그



Abstract

[KO] 본 발명은 광학 효과의 큰 가변성 및 내부 구조의 복잡성을 보유하는 생물학적 근원의 입자를 영구적으로 부착함으로써 개별화된 보안 장치에 관한 것이다. 생물학적 종 및 대응하는 입자는 내구성, 조작 민감성, 및 미크론 크기의 두께를 가지면서, 가변성 및 복잡성을 최대화하도록 선택된다. 시각적, 기계적, 및 법의학적 검사에 적합한 태그를 제조하는 방법이 개시된다.

Related patent documents

[CN108472982](#) [EP3397503](#) [US20190023055](#) [JP2019503916](#) [WO/2017/114570](#) [CA3009382](#)



Tell us what you think of PATENTSCOPE in our [short survey](#).

1. US20190023055 - SECURITY TAG CONTAINING A PATTERN OF BIOLOGICAL PARTICLES

[National Biblio. Data](#) [Description](#) [Claims](#) [Drawings](#) [Patent Family](#) [Documents](#)

[PermaLink](#) [Machine translation](#)

Office

United States of America

Application Number

16067283

Application Date

30.12.2015

Publication Number

20190023055

Publication Date

24.01.2019

Grant Number

10406847

Grant Date

10.09.2019

Publication Kind

B2

IPC

G09F 3/02

B42D 25/36

B42D 25/45

G06K 7/10

G09F 3/00

G09F 3/10

CPC

B42D 25/45

B42D 25/36

G06K 7/10366

G09F 3/0297

G09F 3/10

G09F 3/0292

[View more classifications](#)

Applicants

Institute of Physics Belgrade, University of Belgrade

Inventors

Dejan Pantelic
Mihailo Rabasovic
Aleksandar Krmpot
Vladimir Lazovic
Danica Pavlovic

Agents

Grüneberg and Myers PLLC

Title

[EN] Security tag containing a pattern of biological particles



Abstract

[EN]

A security tag can be used to identify or authenticate a substrate that has the security tag. The security tag includes a pattern of inimitable biological particles, a transparent adhesive layer, a substrate, and a transparent superstrate, where the pattern of inimitable biological particles is directly transferred from an organism to the transparent adhesive layer on the substrate, and where said biological particles are covered with the transparent superstrate, such that said inimitable biological particles are encapsulated between said substrate and said superstrate.

Related patent documents

[CN108472982](#) [KR1020180098620](#) [EP3397503](#) [JP2019503916](#) [WO/2017/114570](#) [CA3009382](#)





(51) International Patent Classification:

B42D 25/36 (2014.01) *B42D 25/45* (2014.01)
B42D 25/29 (2014.01) *B42D 25/28* (2014.01)
B42D 25/33 (2014.01) *B42D 25/35* (2014.01)

(21) International Application Number

PCT/EP2015/08195

(22) International Filing Date:

30 December 2015 (30.12.2015)

(25) Filing Language:

English

(26) Publication Language:

English

(71) Applicant: INSTITUTE OF PHYSICS BELGRADE, UNIVERSITY OF BELGRADE [RS/Sr]; Prigrevica 118, Be grade, 11080 (RS)

(72) Inventors: PANTIĆ, Dejan; Ne manjin 7, Be grade, 11080 (RS); KAJIĆ, Viliđin; Svetozna Papića 151, Be grade, 11080 (RS); KRMPOT, Aleksandar; Jesterova 8/15, Be grade, 11030 (RS); LAZOVIC, Vlado; m; Jurića Gagarina 177, Be grade, 11070 (RS); PAVLOVIC, Danica; Boška Žrnjina 18c, Be grade, 11260 (RS)

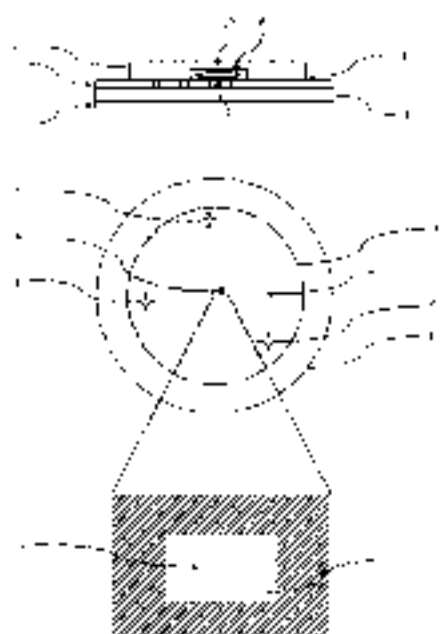
(74) Agent: WINKLER, Andreas; WINKLER IP, P.O. Box 547011, 28309 Bremen (DE)

(80) Designated States (unless otherwise indicated, for each kind of regional protection available): AE, AG, AL, AM, AO, AT, AU, AZ, BA, BB, BG, BH, BR, BW, BY, BZ, CA, CH, CL, CN, CO, CR, CU, CZ, DE, DK, DM, DO, DZ, EC, EE, EG, ES, FI, GB, GD, GE, GF, GG, GT, HN, HR, HU, ID, IL, IN, IR, IS, JP, KE, KG, KN, KP, KR, KZ, LV, LU, LY, MA, MD, ME, MG, MK, MN, MW, MX, MY, MZ, NA, NG, NI, NO, NZ, OM, PA, PE, PG, PH, PL, PT, QA, RO, RS, RU, RW, SA, SC, SD, SE, SG, SK, SL, SM, ST, SV, SY, TH, TJ, TL, TN, TR, TT, TZ, UA, UG, US, UZ, VC, VN, ZA, ZM, ZW.

(81) Designated States (unless otherwise indicated, for each kind of regional protection available): ARIPO (BW, GH, GM, KE, LR, LS, MW, MZ, NA, RW, SD, SI, ST, SZ, TZ, UG, ZM, ZW), Eurasia (AM, AZ, BY, KG, KZ, RU, TJ, TM), European (AT, BE, BG, CH, CY, CZ, DE, DK, EE, ES, FI, FR, GB, GR, HR, HU, IE, IS, IT, LT, LU, LV, MC, MK, MT, NL, NO, PL, PT, RO, RS, SE, SI, SK, SM, TR), OAPI (BF, BJ, CF, CG, CI, CM, GA, GN, GQ, GW, KM, ML, MR, NE, SN, TD, TG)

[Cont. on next page]

(54) TITLE: SECURITY DEVICE INDIVIDUALIZED WITH BIOLOGICAL PARTICLES



(57) Abstract: The invention is directed to a security device with hologram, individualized by permanently attaching particles of biological origin, possessing large variability of optical effects and complexity of internal structure. Biological species and corresponding particles are chosen to maximize variability and complexity, while having durability, narrow sensitivity and micron-size thickness. The security device comprises a transparent substrate (1) with at least one embedded hologram (2) on its top surface, at least one immutable biologic particle (3) affixed and attached on or above the upper surface of the substrate (1), a transparent superstrate (5), having a recess (10), and adhering to the substrate (1) and enclosing the biological particles (3).

Published

with international search report (Art. 21(2))

Security device individualized with biological particles

Field of Invention

The present invention relates to security devices for identification and authentication of goods, articles and documents.

5 Background of the Invention

Optically variable devices (OVD) are a common protective element on various types of documents (e.g. identity cards, passports, visas, bank cards) – see the book “Optical document security” ed. by R. L. Van Renesse, Artech House, (1998). Holograms and other diffractive elements are mainly used, because their protective value is based on complexity of micron and submicron structures. Manufacturing is a complicated and expensive process whose final result is a master hologram – a single, unique prototype. To make protection commercially acceptable, the master hologram is copied and multiplied, resulting in a replica shim used for embossing into a plastic foil, which is then integrated into a document using a hot tool. The final result is a series of documents possessing exactly the same protective OVD. This is a significant drawback, because, if the OVD is counterfeited, a large number of fake documents can be manufactured.

As a result, there is ongoing research for a simple and affordable document individualization method. This makes counterfeit much harder, because each and every document has to be copied individually, i.e. large scale production of false documents becomes impossible. However, the trivial individualization by simply printing numbers will not work, because it is too simple and affordable, if using modern printing technologies (e.g. laser printing). Therefore, the individualization-bearing features must possess a significant amount of complexity, together with unrepeatable, individual properties. They have to be comparable in its uniqueness with biometric characteristics, such as: fingerprints, iris and retina pattern, but significantly more complex and miniscule. Currently used OVD security methods are not well suited for individualization (fingerprinting), as this will significantly increase the production prices.

Attempts to obtain "fingerprint" documents are based on the idea of the physical one-way functions, which are alternatively called the physically unclonable functions (C. Boehm, M. Hofer, "Physically unclonable functions in theory and practice", Springer, 2013). These are physical devices simple to manufacture, yet extremely difficult to reverse engineer and copy. Random structures can be highly significant for document security, because they offer simple and cheap production, almost impossible re-origination and unique features. It was proposed to tag documents with randomly dispersed objects such as metal, fluorescent or optical fibers ("Optical document security" ed. by R. L. Van Renesse, Artech House, (1998), pg. 210 - 211, and references therein). More details can be found in: "Counterfeit deterrent features for the next generation currency design", Committee on Next-Generation Currency Design, National Materials Advisory Board, Commission on Engineering and Technical Systems, National Research Council, Publication NMAB-472, (1993), Section: Random Pattern/Encryption Counterfeit-Deterrence Concept, pg. 74 - 75, and in Appendix E of the same document: "Methods for authentication of unique random patterns", pg. 117 - 119. Yet another technique uses holographic platelets as fingerprinting device (US2010110514 (A1), 2010 - R. Hradency, T. Lethal, L. Kotacka, I. Jermolajev, J. Drinkwater, C. Hradency, "Security articles and devices containing coded holographic platelets and methods of manufacturing the same").

Natural fibrous structure of paper-based substrates was used (J. D. R. Buchanan, R. P. Cowburn, A-V. Jausevec, D. Petit, P. Seem, G. Xiong, D. Atkinson, K. Fenton, D. A. Allwood, M. T. Bryan, " 'Fingerprinting' documents and packaging", Nature 436, (2005) 475). Laser beam was scattered from the paper surface and its statistics was observed and recorded. This, however, requires a large scale scanning of the document surface which is a slow process, and paper structure may be strongly affected by printing and everyday usage.

Yet another technique was described in R. Pappu, B. Recht, J. Taylor, N. Gershenfeld, "Physical One-Way Functions," Science 297, (2002) 2026 - 2030, where mesoscopic scattering from disordered array of plastic spheres embedded in a transparent substrate was used to construct physical one-way function. The response of the system strongly depends on the illumination direction, again producing unique individual characteristics. The proposed method is limited by the physical requirements for the mesoscopic scattering, resulting in a 10 mm x 10 mm sized tag, with 2.5 mm thickness, which is unsuitable for the modern plastic card

technology. Furthermore, the dimension of scattering particles is rather large – 500 - 800 µm in diameter, with 100 µm average spacing – resulting in a bulky system which can be reverse engineered by techniques like micro tomography.

It is a common knowledge that certain natural characteristic of living creatures are inherently complex and hard to reproduce. This was first realized by Benjamin Franklin who used this for document protection (Farley Grubb, "Benjamin Franklin and the birth of the paper money economy", Essay based on March 30, 2006 lecture, published by Federal Reserve Bank of Philadelphia). He made casts of plant leaves (correctly recognizing the uniqueness of their venation) and used them to print the first dollar bills. Due to further technological advancements, Franklin's method became obsolete, and was replaced with different printing techniques, such as: intaglio, gulloche, watermark, holograms, etc

Two patents (WO 20070331077 (A1) 3/2007, C. Hamm-Dubischar, "Inorganic marking particles for characterizing products for proof of authenticity method for production and use thereof", and DE10238506 A1, 3/2004, H. Raabe, "Producing information bearing micro-particulate mixtures involves defining oxide that can be implemented using natural or subsequently applied particle characteristics selected from e.g. morphology") disclosed an idea for document protection which uses natural complexity of aquatic organism inorganic shells (like diatoms and radiolarians) according to characteristics of their surfaces. The practicing method is, however, not disclosed. Another problem is that the optical effects are not very pronounced, as well as their variability, and the complexity can be observed only at the sub-wavelength levels, using electron microscopy. Technique for estimating the degree of complexity was not described, either. Variation among the specimens of the same species is rather small. In that respect, the method can be used only for the forensic level of document authentication.

Recently, there was a significant amount of research aimed at using the principles of optics in nature for document protection (J. Sun, B. Bhushan and J. Tong, "Structural coloration in nature", RSC Adv., 2013, 3, 14862-14889). Variability of biological structures was also observed (L. P. Birn and J-P. Vigneron, "Photonic nanoarchitectures in butterflies and beetles: valuable sources for bioinspiration", Laser Photonics Rev. 5, No. 1, 27-51 (2011)). Biotemplating was used to manufacture butterfly scale-like structures using metals

(S. Sotiropoulos, Y. Sierra-Sastre, S. S. Mark, and C. A. Ball, "Biodepleted Nanostructured Materials", Chem. Mater. 2008, 20, 821-834).

Embossed holograms have been individualized by using a two-stage process (US7420720 (B2) — 2008-09-02, G. Dausmann, J. Ments, "Optical element and method for the production thereof"). The first one generates a master hologram with a background image. In the second, additional embossing stamper are used containing letters or numbers, capable of uniquely marking a hologram.

Another way of individualization is described (DE102007003504 (A1) 2009-05-07, J. Ehrcke, A. Leopold, "Individualized hologram manufacturing method for e.g. passport"), where a master hologram is used for the permanent part of holographic image, whereas a spatial light modulator is used for the variable information. Both images are combined on the third holographic medium.

The randomized systems described above must be machine-inspected, based on radiation scattering with consequent optical or microwave detection (in the case of metal inclusions). Recorded pattern is encrypted and stored in a central repository or on the document itself. Public key encryption method is used, as described in the report: Counterfeit deterrent features for the next generation currency design. A technique is based on two keys: a secret one, used for encryption, and a public one, used for the decryption.

All the methods use a complexity of natural structures, but their variability remained completely unused in the context of document protection. Document variability was rather attained by randomly dispersing particle- or thread-like entities across the document, as described in the patent literature (US 8408470B2, 2013, N. Komatsu, S-I. Nanjo, "Object for authentication verification, authentication verifying chip reading device and authentication judging method").

Summary of the Invention

The problem solved by the invention is individualization of mass-produced security devices with holograms. This is done by attaching biological particles with pronounced individuality

The invention is directed to a security device, comprising

- 5 a transparent substrate with at least one embedded hologram on its upper surface;

 at least one inimitable biological particle arranged and attached on or above the upper surface of the substrate;

 a transparent superstrate, having a recess, and adhering to the substrate and enclosing the biological particle(s)

10

The security device of the invention preferably comprises at least one predefined position without diffracting structures being formed on the substrate, and the inimitable biological particle(s) being placed at said position.

- 15 More preferably, the predefined position(s) without diffracting structures is (are) transparent, thus forming at least one window, wherein the inimitable biological particle(s) is (are) placed in at least one of said windows.

- 20 In one embodiment of the invention, more than one predefined positions are provided and arranged according to a predetermined pattern.

Preferably, the inimitable biological particle(s) is (are) selected from scales, hairs or bristles from the Lepidoptera wing or body.

Alternatively or additionally, the inimitable biological particle(s) is (are) selected from scales from the Coleoptera species cuticle and/or Araneae species body.

Furthermore, the inimitable biological particle(s) may be selected from hairs or bristles of the Trichoptera species.

In a preferred embodiment of the invention, the inimitable biological particle(s) is (are) firmly attached to the substrate by a transparent adhesive.

- 5 Alternatively, the inimitable biological particle(s) can be held in place on the substrate only by the natural attractive forces between the particle(s) and the substrate, without using adhesive substances.

In one embodiment of the invention, it is also proposed that the inimitable biological particle(s) is (are) cut in a predetermined shape, before arrangement on or above the substrate.

- 10 In another embodiment, more than one inimitable biological particles are used.

In one embodiment, the inimitable biological particles are stacked on one another, before arrangement on or above the substrate.

Preferably, the inimitable biological particle(s) is (are) inscribed with information, before or after arrangement on or above the substrate and/or enclosing of the biological particle.

- 15 More preferably, the inimitable biological particle(s) is (are) overtly inscribed with information by cutting through its (their) surface.

Alternatively, the inimitable biological particle(s) is (are) covertly inscribed with information by permanently bleaching its (their) fluorescence.

- 20 In a preferred embodiment of the invention, the inimitable biological particles of several species are chosen according to their variability of optical properties.

Preferably, the substrate comprises a transparent adhesive layer on its lower surface.

The invention is also directed to the use of the security device of the invention for identification and authentication of goods, articles and documents.

Finally, the invention is directed to a method of manufacturing a security device of the invention, comprising the following steps:

- (1) providing a transparent substrate with at least one embedded hologram on its upper surface;
- 5 (2) demetalizing the hologram at at least one predefined position to form at least one transparent window;
- (3) attaching at least one imitable biological particle in said window; and
- (4) placing a recess of a transparent superstrate over the window and adhering the superstrate to the substrate to enclose the biological particle(s).

10 There are several criteria which must be simultaneously fulfilled in order to provide the device with a unique fingerprint, usable for document protection purposes.

The first criterion for biological particle selection is according to variability of optical properties across their surface (near-field) or in the far-field of the scattered radiation. Detected optical properties include optical field amplitude and phase, field vorticity, reflection and
15 transmission spectral distribution, overall biological particle shape, moiré pattern, polarization pattern, iridescence, diffraction, and fluorescence. The second selection criterion is the underlying complexity of biological particle structure, which has to span the range from nano-meter to micron-size features, intricately distributed in three-dimensions. The third criterion is their fragility, necessary for tamper sensitivity. The fourth criterion is the non-degradability of
20 the structure, at least within the validity period of the document. The fifth criterion is the thinness of the structures such that they can be easily integrated within holographic OVDs, whose thickness is of the order of several tens of microns. The selection process requires fulfillment of all five criteria.

Preferred biological particles are those which can be found in the cuticle of various
25 species of Lepidoptera (scales, hairs or bristles), Coleoptera (scales), Trichoptera (hairs or bristles), Araneae (scales). There is a general ground-plan of these structures, with the details

significantly depending on the species. They are self-contained (Fig. 1), plate-like or cylindrical, having a wall of submicron thickness, which encloses the internal volume. Inside the particle, a number of features may exist, such as nano-pillars, photonic crystals, fluorescent nano-particles. One or both external surfaces are patterned with grating-like ridges and cross-ridges (Fig. 2).
5 Ridges have a lamellar structure, similar to the Bragg grating. The main constituent is chitin, a biological polysaccharide insoluble in water and many other solvents. They are permanent remnants of individual cells, and may endure without changing their optical properties for long periods. It is known that dried insects like butterflies may survive for decades in entomological collections. Iridescence, diffraction pattern or fluorescence of individual particles may strongly
10 vary across the surface (of the order of $50 \times 150 \mu\text{m}^2$), as can be seen in Fig. 1. Thickness is of the order of few microns, resulting in fragility of the whole structure, which is stable enough to be transferred and adhered to the hologram substrate.

A hologram may be prepared for individualization by making special marks on the hologram surface which define a local coordinate system. Particles are attached to the hologram
15 in the positions defined with respect to the said coordinate system. Large surface-energy adhesive may be used to permanently fix the particles to the hologram surface. A particle is protected from tampering by the transparent superstrate, which is permanently affixed to the hologram using high surface-energy adhesive or hot-stamping. A recess is made in a superstrate, such that the particle is protected from high pressures exerted during the stamping process.

20 A single particle or a plurality of them can be attached to the hologram in a predefined pattern. Only a subset of attached particles might be used for authentication purposes, while the rest is there as a distraction, which makes counterfeit harder, as a counterfeiter would not know which particles are used for authentication. Biological particles which possess different optical properties on their front and rear side may be used to produce security features which can be read
25 from both sides in perfect alignment (see-through register).

Brief Description of the Drawings

Fig. 1: Optical image of an individual butterfly scale, where the strong, local variability of iridescence can be observed

- Fig. 2: Scanning electron microscope image of the butterfly scale, where the complexity of its internal structure can be seen.
- Fig. 3: Exploded view of the security hologram presented in two orthogonal projections
- Fig. 4: A security hologram with a window, where a number of individually cut and shaped Lepidoptera or Coleopteran scales are positioned inside the window.
- Fig. 5: A security hologram with an array of windows where individual Lepidoptera or Coleopteran scales are attached.
- Fig. 6: A security hologram with an array of windows where the individually cut and shaped Lepidoptera or Coleopteran scales are attached
- Fig. 7: A security hologram with an array of windows where the individually overtly inscribed Lepidoptera or Coleopteran scales are attached.
- Fig. 8: A security hologram with an array of windows positioned in a rectangular grid. Windows are partially filled with Lepidoptera or Coleopteran scales as to produce a binary or bar-code
- Fig. 9: A security hologram without windows, where Lepidoptera or Coleopteran scales are randomly distributed across the hologram surface.
- Fig. 10: A security hologram with an array of windows positioned in a quasiperiodic or aperiodic tiling (e.g. Penrose tiling).

20 Detailed Description of the Invention

In cooperation with the attached drawings, the technical contents and detailed embodiments of the present invention are described hereinafter, however, not limiting its scope of protection which is exclusively defined by the claims. Any equivalent variation and

modification made according to the appended claims is to be included into their scope of protection.

Reference is made to Fig. 3 which presents two orthogonal views of one embodiment of the security device of the present invention. It is composed of a substrate 1, having a hologram 2 embedded on its upper surface. Additional marks 3, 4 and 5, whose dimensions are smaller than 200 μm , are incorporated into the hologram 2. The lower surface of the substrate 1 carries an adhesive layer 6, which can be activated either by heat or by pressure in order to integrate the security device with an article, good or document. The upper surface of the substrate 1 comprises a small patch of adhesive 7, whose surface is just large enough to receive a biological particle 8. The biological particle 8 is permanently attached onto the adhesive 7.

The biological particle 8 is then covered with a superstrate 9, having a recess 10 large enough to enclose the biological particle 8, without touching its upper surface. The lower surface of the superstrate 9 is covered with a transparent layer of heat or pressure activated adhesive 11, such that the recess 10 is left without adhesive layer. Superstrate 9 and substrate 1 are attached to each other, such that they enclose the biological particle 8.

In another embodiment, depicted in Fig. 4, the hologram 2 is demetalized at the places where the biological particles 8 are to be put, thus producing a window 12 which enables observation of the optical properties of the biological particle from underneath.

In a further embodiment as shown in Fig. 5 a number of cut shaped butterfly scales 8 are positioned inside the hologram window 12, following the previously described procedure.

Reference is made to Fig. 6, representing another embodiment of the security device of the present invention designed and manufactured to have an unspecified number of opaque or transparent windows without a diffraction grating 13, 14, 15, 16 and 17. The windows are positioned in an orderly manner, corresponding to certain symmetry, as in Fig. 6. The windows are of identical dimensions, width and height of each window being within the range of 150 μm - 300 μm . A transparent adhesive patch is placed inside each window and individual iridescent Lepidoptera or Coleopteran scales 8 are attached to each patch.

- Preferred, but not limited to, Lepidoptera species are those possessing silver spots or patches on their wings, such as: *Ixoria lathonia*, *Argyrophorus argenteus*, *Dione moneta*, *Dione juno*, *Agrotis vuilliae*, *Aryzitis addipe*, *Argyris aelaja*, *Argynis papua*. Other Lepidoptera species, possessing structurally colored scales, may be used, too, such as: *Diachrysa chrysis*,
 5 *Macdunnoughia confusa*, *Autographa gamma*, *Jordanita globularia*, *Callophrys rubi*. Preferred Coleoptera species are those possessing scales on their cuticle: *Hoplia caerulea*, *Pseudomyrmex waterhousei*, *Laoprosynopus angustus*, *Hypero diversipunctatus*, *Protoparce lactator*, *Cyphus harriseki*, *Ecdinus imperialis*, *Sphingonema mirabilis*, *Hoplia argentea*, some Curculionidae, some Collembola. Preferred Trichoptera species are:
 10 *Pseudoleptocerus chirindensis*, *Phyllocis abdominalis*, *Nectopsyche punctata*, *Banyalarga vicaria*, *Hesperophylax designatus*, *Polycentropus flavomaculatus*, *Mystacides azurea*, *Mystacides longicornis*, *Anthripsodes albifrons*, *Limnephilus bimaculatus*. Preferred Araneae species are those possessing scales on their cuticle, such as: *Moratus volans*, *Moratus splendidus*, *Philippus andax*, *Pauphabetes unimaculatus*, *Cyrtopogonites lividus*.
- 15 Windows can be either filled with scales from a single species, or with scales from several different species. The hologram 2 with scales 8 is covered with a transparent foil having recesses exactly matching the positions of windows on the hologram. A thin layer of a transparent adhesive is placed on the bottom side of a cover, without covering the recesses.

In yet another embodiment individual Lepidoptera or Coleopteran scales 8 are cut
 20 shaped, using laser machining, and then placed inside the hologram windows 12, as shown in Fig. 7, following the previously described embedding procedure.

In a further embodiment, depicted in Fig. 8, Lepidoptera or Coleopteran scales 8 are overtly inscribed with information 20 (e.g. text, numbers, image, barcode) by cutting through the scale 8, preferably by laser. Information 20 can be inscribed before or after the encapsulation of
 25 the scale 8 in the security device 1. The scales are cut by using short pulse laser - preferably pico-second or femto-second, whose energy is slightly above the damage threshold of scales. The laser beam is introduced in a microscope, where it is focused by the objective, directly onto the scale. The laser beam position is controlled using a pair of computer-controlled, galvanometer-scanning mirrors.

In an alternative embodiment Lepidoptera or Coleopteran scales 8 are covertly inscribed with information 20 (e.g. text, numbers, image, barcode), by bleaching the scale fluorescence. Information 20 can be inscribed before or after the encapsulation of the scale 8 in the security device 1. The scales are bleached by using short pulse laser - preferably pico-second or femto-second, whose energy is slightly below the damage threshold of scales. The laser beam is introduced in a microscope, where it is focused by the objective, directly onto the scale. The laser beam position is controlled using a pair of computer-controlled, galvanometer-scanning mirrors.

In yet another embodiment, windows 12 are arranged in a regular rectangular grid (Fig. 9), and their occupancy depends on the binary encoding of information, wherein a window occupied with a scale designates binary 1, and an unoccupied window designates binary 0.

In yet another embodiment, there are no windows on the hologram 2, and scales 8 are randomly distributed on the hologram surface (Fig. 10).

A further embodiment is depicted in Fig. 11, where windows 12 are placed according to quasiperiodic or aperiodic tiling (e.g. Penrose tiling).

Claims**1.** A security device comprising:

a transparent substrate (1) with at least one embedded hologram (2) on its upper
5 surface;

at least one inimitable biologic particle (8) arranged and attached on or above the
upper surface of the substrate (1);

a transparent superstrate (9), having a recess (10), and adhering to the substrate
(1) and enclosing the biological particle(s) (8).

10

2. The security device according to claim 1, wherein at least one predefined position without
diffracting structures is formed on the substrate (1), and the inimitable biological particle(s)
(8) is (are) placed at said position.

15

3. The security device according to claim 2, wherein the predefined position(s) without
diffracting structures is (are) transparent, thus forming at least one window (12), wherein
the inimitable biological particle(s) (8) is (are) placed in at least one of said windows.

20

4. The security device according to any of claims 2 or 3, wherein more than one predefined
positions are provided and arranged according to a predetermined pattern.

5. The security device according to any of the preceding claims, wherein the inimitable
biological particle(s) (8) is (are) selected from scales, hairs or bristles from the Lepidoptera
25 wing or body.

6. The security device according to any of the preceding claims, wherein the inimitable biological particle(s) (8) is (are) selected from scales from the Coleoptera species cuticle and/or Araneae species body.
- 5 7. The security device according to any of the preceding claims, wherein the inimitable biological particle(s) (8) is (are) selected from hairs or bristles of the Trichoptera species.
8. The security device according to any of the preceding claims, wherein the inimitable biological particle(s) (8) is (are) firmly attached to the substrate (1) by a transparent adhesive.
10
9. The security device according to any of claims 1 to 7, wherein the inimitable biological particle(s) (8) is (are) held in place on the substrate (1) only by the natural attractive forces between the particle(s) and the substrate..
15
10. The security device according to any of the preceding claims, wherein the inimitable biological particle(s) (8) is (are) cut in a predetermined shape, before arrangement on or above the substrate (1).
- 20 11. The security device according to any of the preceding claims, wherein more than one inimitable biological particles (8) are used.
12. The security device according to claim 11, wherein the inimitable biological particles (8) are stacked on one another, before arrangement on or above the substrate (1).
- 25 13. The security device according to any of the preceding claims, wherein the inimitable biological particle(s) (8) is (are) inscribed with information, before or after arrangement on or above the substrate (1) and/or enclosing of the biological particle.
- 30 14. The security device according to claim 13, wherein the inimitable biological particle(s) (8) is (are) overtly inscribed with information by cutting through its (their) surface.

15. The security device according to claim 13, wherein the inimitable biological particle(s) is (are) covertly inscribed with information by permanently bleaching its (their) fluorescence.
- 5 16. The security device according to any of the preceding claims, wherein the inimitable biological particles of several species are chosen according to variability of their optical properties.
17. The security device according to any of the preceding claims, wherein the substrate (1) comprises a transparent adhesive layer (6) on its lower surface.
- 10 18. Use of the security device according to any of the preceding claims for identification and authentication of goods, articles and documents.
- 15 19. A method of manufacturing a security device according to any of claims 1 to 17, comprising the following steps:
- (1) providing a transparent substrate (1) with at least one embedded hologram (6) on its upper surface;
- (2) demetalizing the hologram (6) at at least one predefined position to form at least one transparent window (7);
- 20 (3) attaching at least one inimitable biological particle (8) in said window (7); and
- (4) placing a recess (14) of a transparent superstrate (9) over the window (7) and adhering the superstrate (9) to the substrate (1) to enclose the biological particle(s) (8).
- 25

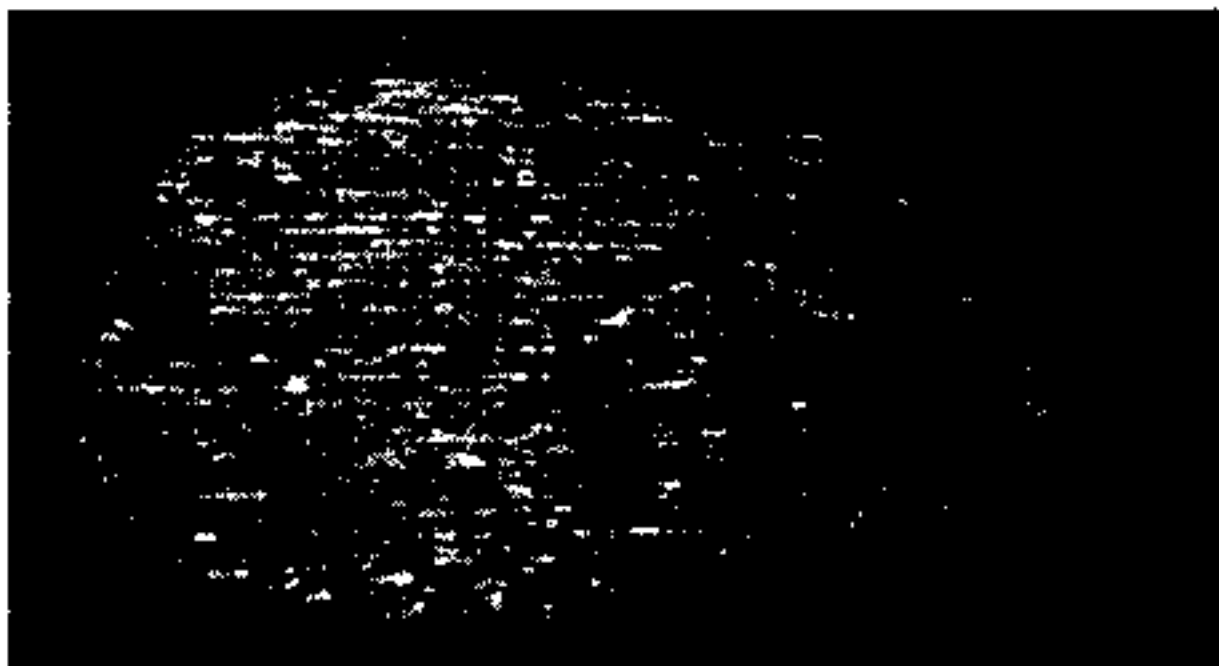


Fig. 1

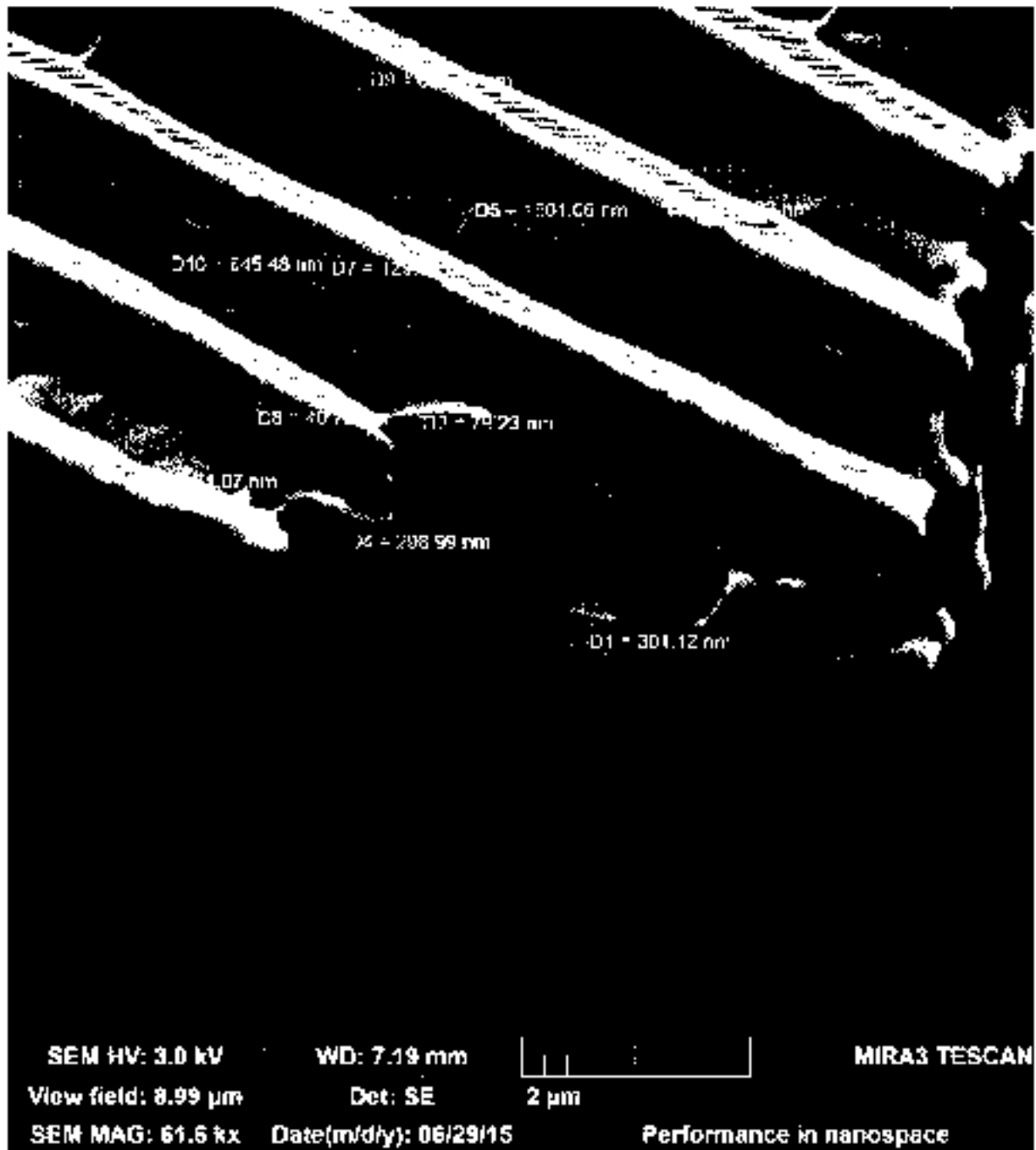


Fig. 2

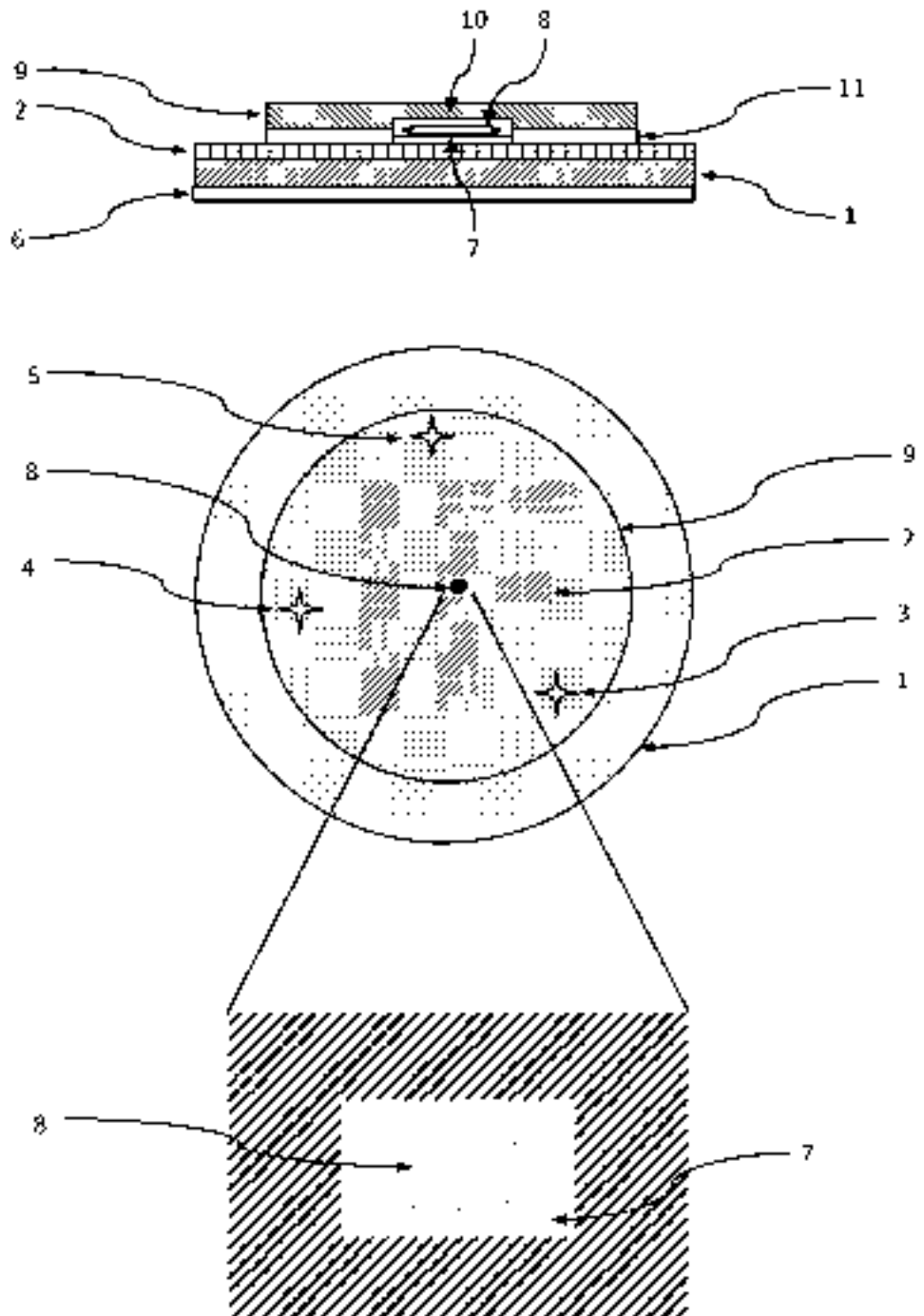


Fig. 3

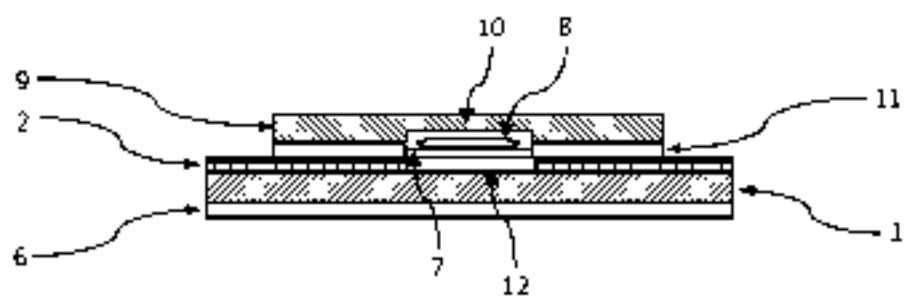


Fig. 4

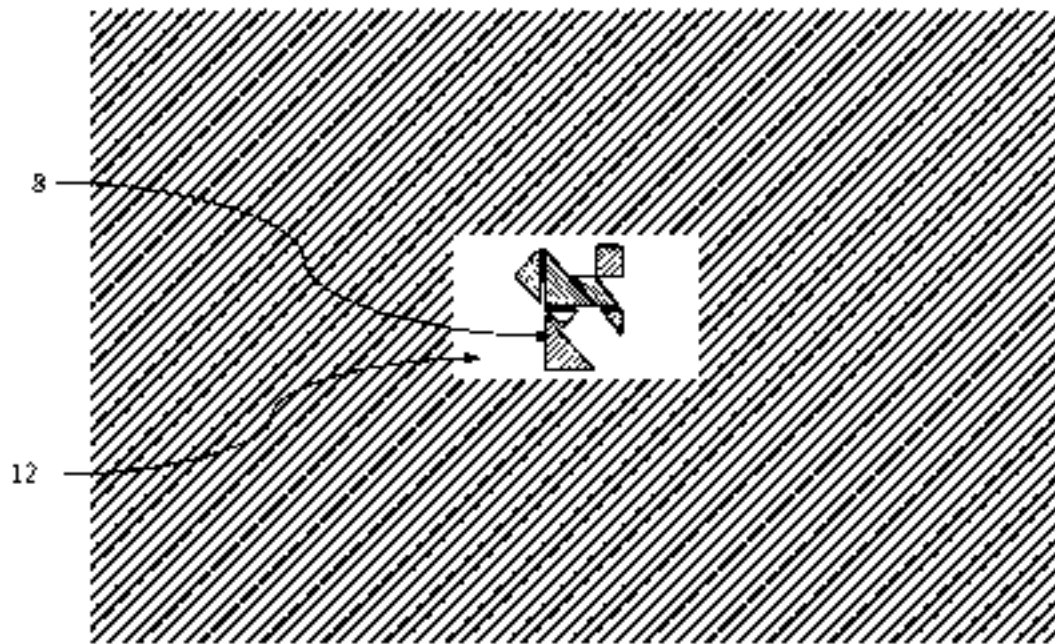


Fig. 5

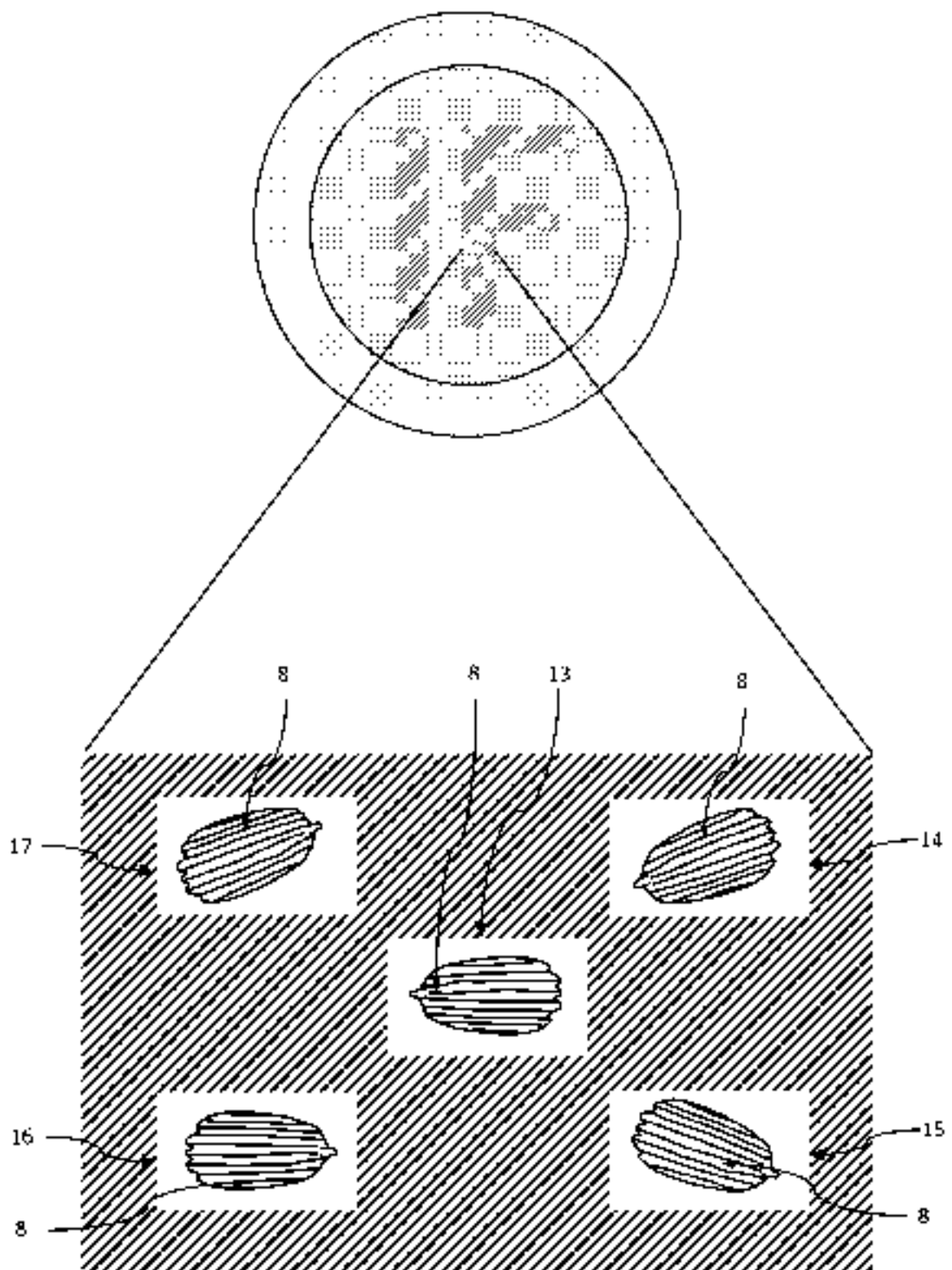


Fig. 6

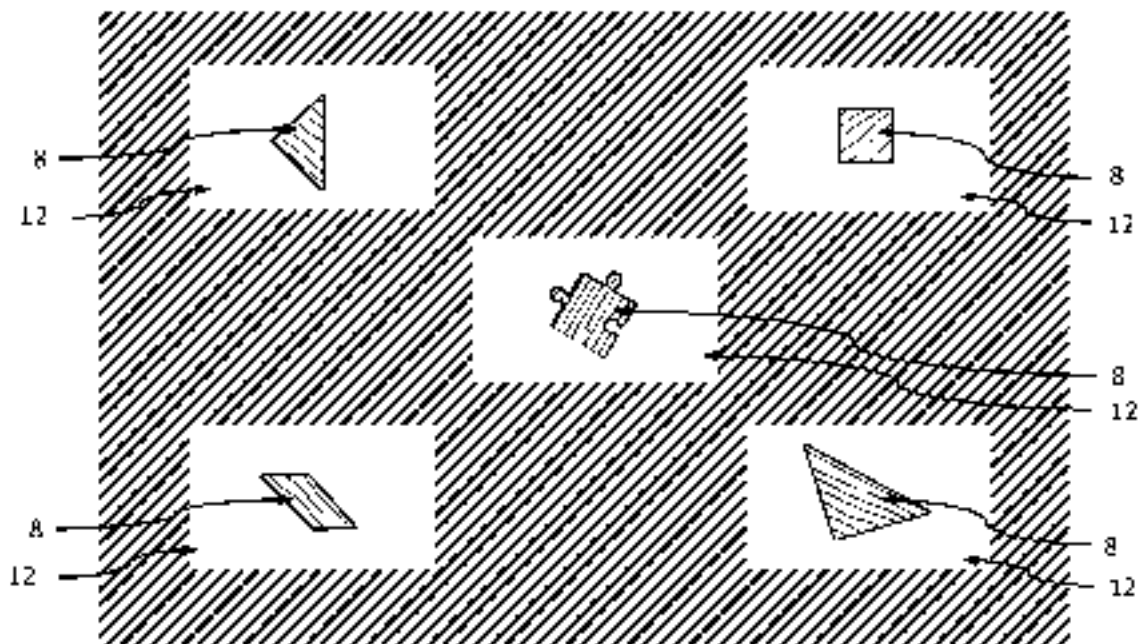


Fig. 7

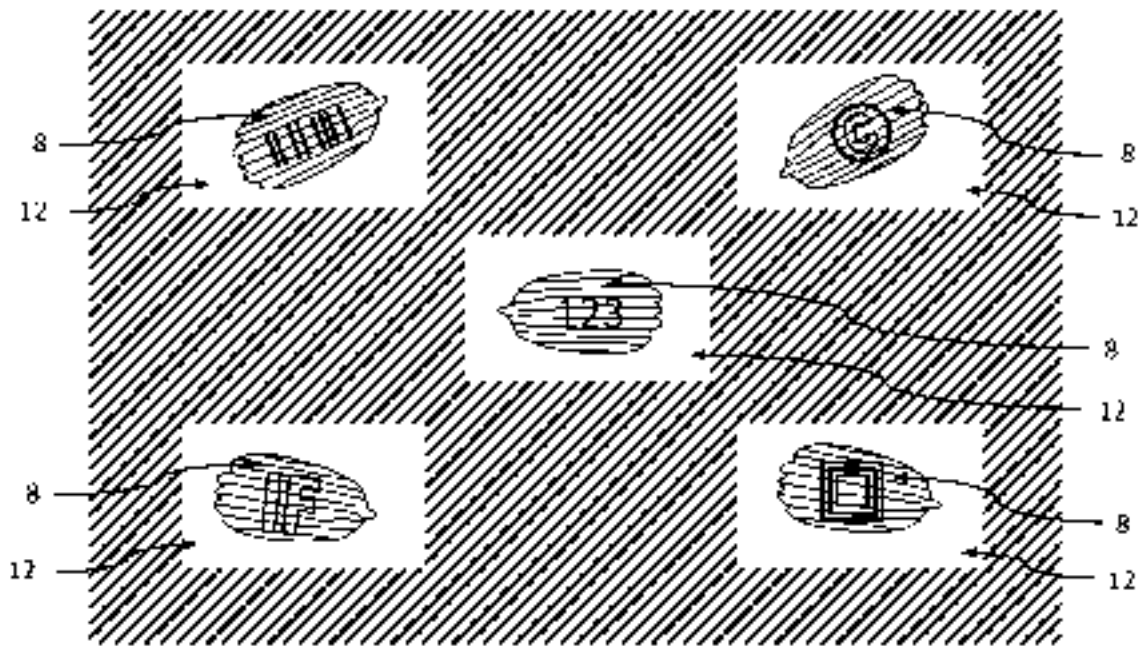


Fig. 8

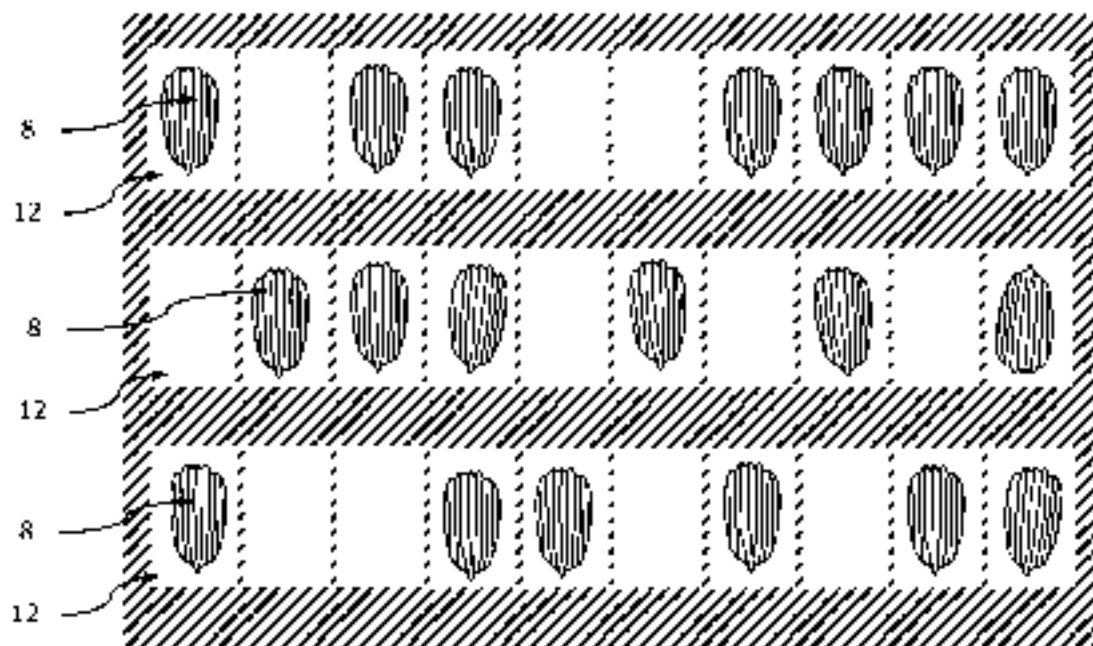


Fig. 9

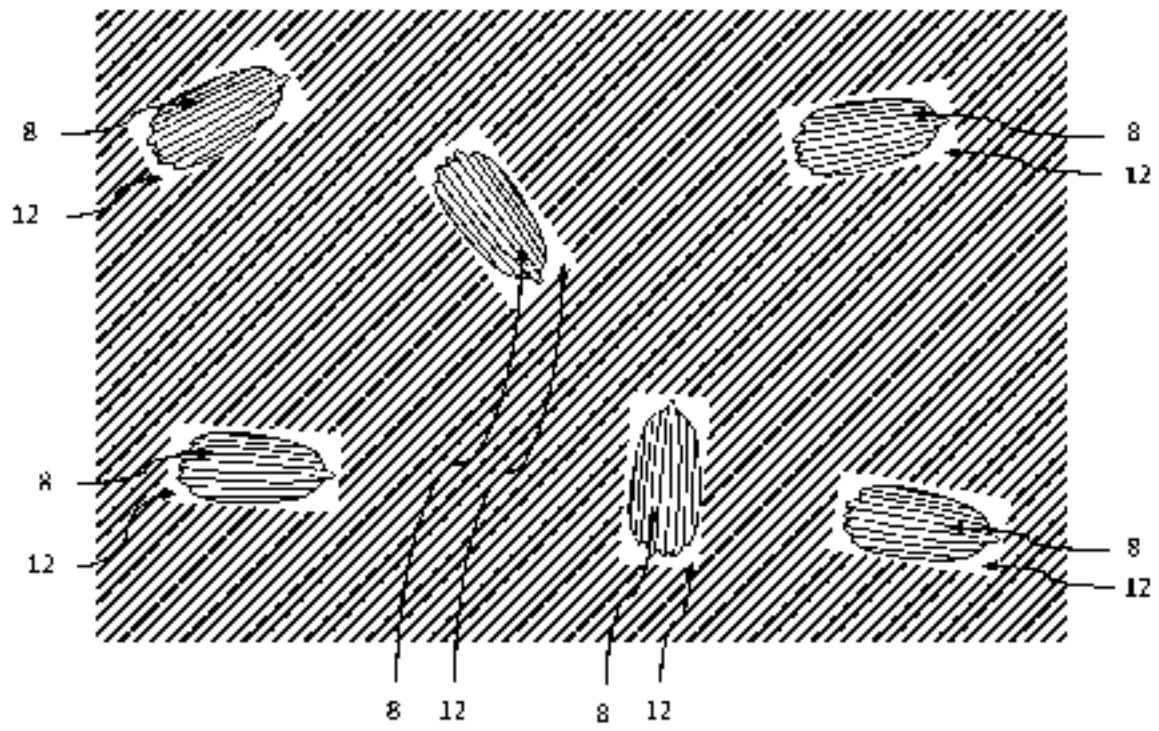


Fig. 10

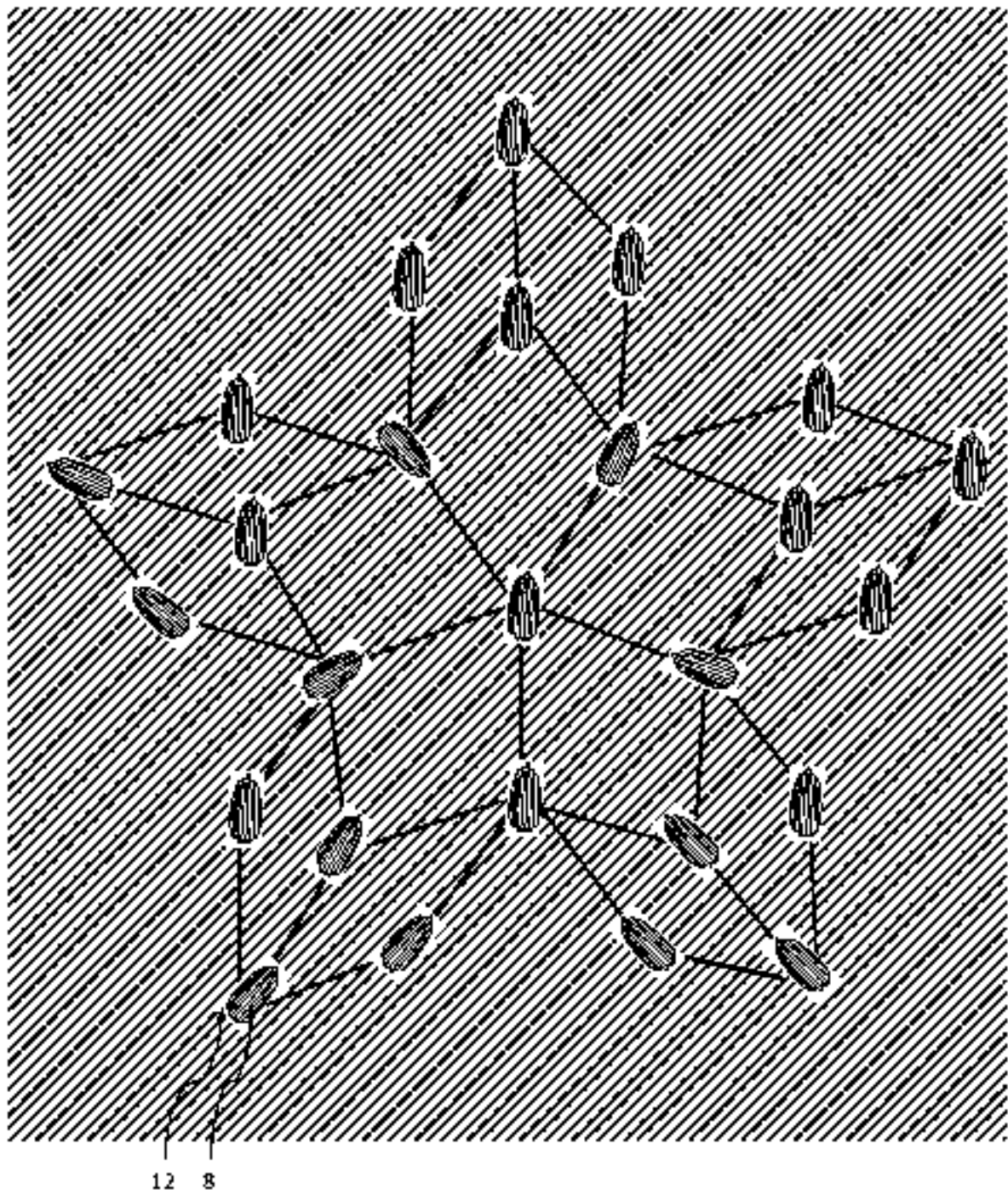


Fig. 11

INTERNATIONAL SEARCH REPORT

International application No
PCT/EP2015/081398

A. CLASSIFICATION OF SUBJECT MATTER		
INV.	B42D25/36 B42D25/351	B42D25/29 B42D25/43 B42D25/45 B42D25/328
ADD.		
According to International Patent Classification (IPC) or to both national classification and IPC		
B. FIELDS SEARCHED		
Minimum documentation searched (classification system followed by classification symbols)		
B42D		
Documentation searched other than minimum documentation to the extent that such documents are included in the fields searched		
Electronic data base consulted during the international search (name of data base and, where practicable, search terms used)		
EP0-Internal, WPI Data		
C. DOCUMENTS CONSIDERED TO BE RELEVANT		
Category	Citation of document, with indication, where appropriate, of the relevant passages	Relevant to claim No.
X	WO 2009/052811 A2 (STIFTUNG A WEGENER INST POLAR [DE]; HOCHSCHULE BREMERHAVEN [DE]; DUBIS) 30 April 2009 (2009-04-30)	1-3,18
A	page 5, line 23 - page 7, line 2 page 12, line 15 - page 13, line 3 page 14, lines 7-9 page 14, line 29 - page 15, line 26 page 16, line 27 - page 17, line 10; figures 1,2 ----- -/--	4-17,19
<input checked="" type="checkbox"/> Further documents are listed in the continuation of Box C <input checked="" type="checkbox"/> See patent family annex.		
* Special categories of cited documents: "X" document defining the general state of the art which is not considered to be of particular relevance "E" earlier application or patent but published on or after the international filing date "L" document which may throw doubts on priority claim(s) or which is cited to establish the publication date of another citation or other special reason (as specified) "O" document referring to an oral disclosure, use, exhibition or other means "P" document published prior to the international filing date but later than the priority date claimed "T" later document published after the international filing date or priority date and not in conflict with the application but cited to understand the principle or theory underlying the invention "X" document of particular relevance: the claimed invention cannot be considered novel or cannot be considered to involve an inventive step when the document is taken alone "Y" document of particular relevance: the claimed invention cannot be considered to involve an inventive step when the document is combined with one or more other such documents, such combination being obvious to a person skilled in the art "E" document member of the same patent family		
Date of the actual completion of the international search		Date of mailing of the international search report
25 August 2016		12/09/2016
Name and mailing address of the ISA/ European Patent Office, P. B. 5518 Patentlaan 2 NL - 2280 HX Rijswijk Tel (+31-70) 340 2040, Fax (+31-70) 340 3016		Authorized officer O'Incecco, Raimondo

INTERNATIONAL SEARCH REPORT

International application No
PCT/EP2015/081398

C(Continuation) DOCUMENTS CONSIDERED TO BE RELEVANT		
Category	Citation of document, with indication, where appropriate, of the relevant passages	Relevant to claim No.
A	<p>Mastercard ET AL: "Card Identification Features Card Front Security Features Overview Security Feature Current Requirement/Placement New Requirement/Placement MasterCard Brand Mark Card front No change MasterCard Card Front Features and Designs Card Front Requirements",</p> <p>31 December 2005 (2005-12-31), XP055297501, Retrieved from the Internet: URL:https://www.mastercard.com/uk/merchant/en/downloads/10862_MasterCard_Card_Identification_Features.pdf [retrieved on 2016-08-24] see the credit card on the upper left corner and the copyright icon dated 2005</p> <p>-----</p>	1-19
A	<p>WO 2007/031077 A1 (STIFTUNG A WEGENER INST POLAR [DE]; HAMM-DUBISCHAR CHRISTIAN [DE]) 22 March 2007 (2007-03-22) cited in the application page 14, line 13 - page 15, line 23 page 19, line 5 - page 20, line 18; figures 1,3</p> <p>-----</p>	1-19

INTERNATIONAL SEARCH REPORT

Information on patent family members.

International application No.

PCT/EP2015/081398

Patent document cited in search report	Publication date	Patent family member(s)	Publication date	
WO 2009052811	A2	30-04-2009	AT 510275 T	15-06-2011
			DE 102007052009 B3	04-12-2008
			EP 2227788 A2	15-09-2010
			WO 2009052811 A2	30-04-2009

WO 2007031077	A1	22-03-2007	DE 102005045642 A1	29-03-2007
			WO 2007031077 A1	22-03-2007



(51) International Patent Classification:

B42D 25/47 (2014.01) B42D 25/36 (2014.01)
G09F 3/02 (2006.01) B42D 25/45 (2014.01)

(21) International Application Number:

PCT/EP2015/081407

(22) International Filing Date:

30 December 2015 (30.12.2015)

(25) Filing Language:

English

(26) Publication Language:

English

(71) Applicant: INSTITUTE OF PHYSICS, BELGRADE, UNIVERSITY OF BELGRADE (RS); Progress 118, Belgrade, 11080 (RS)

(72) Inventors: PAVLOVIC, Danica; Boska Zivkovic, 18, Belgrade, 11260 (RS); LAZOVIC, Vladimir; Jutija Cvjetin, 127, Belgrade, 11070 (RS); KRMPOT, Aleksandar; Jovanica 8/5, Belgrade, 11030 (RS); RAJASOVIĆ, Mihalj; Svatoslava Papica 151, Belgrade,

11080 (RS); PAVELIĆ, Dejan; Nemanjina 7, Belgrade, 11080 (RS)

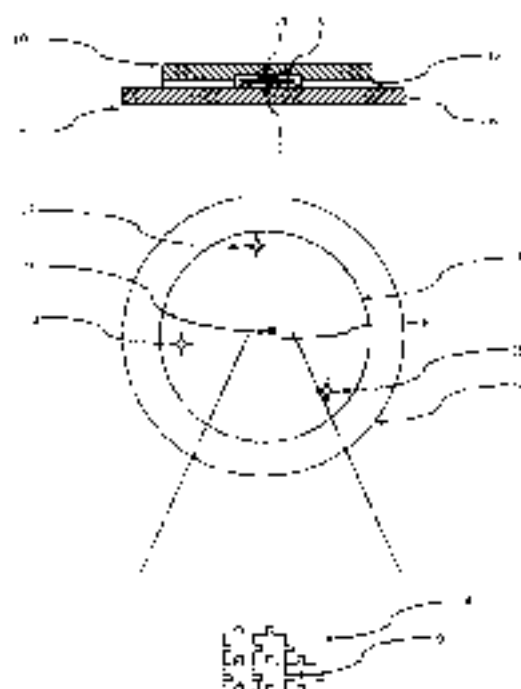
(74) Agent: WINKLER, Andreas; P.O. Box 3470-3, 28339 Bremen (DE)

(81) Designated States (unless otherwise indicated, for every kind of national protection available): AE, AG, AL, AM, AU, AT, AU, AZ, BA, BB, BG, BR, CA, CH, CN, CO, CR, CU, CZ, DE, DK, DM, DO, DZ, EC, EE, EG, ES, FI, GB, GR, GU, HK, HN, HR, HU, ID, IL, IN, IR, IS, JP, KE, KG, KN, KP, KR, KZ, LA, LC, LK, LR, LS, LU, LY, MA, MD, ME, MK, MN, MW, MX, MY, MZ, NA, NG, NI, NO, NZ, OM, PA, PE, PG, PH, PL, PT, QA, RO, RS, RU, RW, SA, SC, SD, SE, SG, SK, SL, SM, ST, SV, SY, TH, TJ, TM, TN, TR, TT, TZ, UA, UG, US, UZ, VC, VN, ZA, ZM, ZW.

(84) Designated States (unless otherwise indicated, for every kind of regional protection available): ARIPO (BW, GH, GM, KE, LR, LS, MW, MZ, NA, RW, SD, SL, ST, SZ, TZ, UG, ZM, ZW), Eurasian (AM, AZ, BY, KG, KZ, RU, TJ, TT), European (AL, AT, BE, BG, CH, CY, CZ, DE,

[Continued on next page]

(54) Title: SECURITY TAG WITH LASER-CUT PARTICLES OF BIOLOGICAL ORIGIN



(57) Abstract: The invention is directed to a security device individualized by permanently attaching present and arranged particles of biological origin, possessing large variability of optical effects and complexity of internal structure. The shape of present particles and their arrangement is chosen to maximize variability and complexity, while having durability, higher sensitivity, micron size thickness, and capability to store the information using additional processing. A security tag, comprising a transparent substrate (6); an arrangement of processed biological particles (9) in a specific pattern which is attached to the substrate (6); and a transparent superstrate (10), having a recess (7), and adhering to the substrate (6) and enclosing the biological particles (9), as well as a method to manufacture said tag suitable for visual, machine and forensic inspection, are disclosed.

DK, DE, ES, FI, FR, GB, GR, HR, HU, IL, IN, JP, KR,
LI, LV, MC, MK, MT, NL, NO, PL, PT, RO, RS, SE,
SI, SK, SM, TR, (EP) (RU), (U), (CN), (CA),
(AU), (NZ), (WO), (KM), (ML), (MR), (NE), (SN), (TD), (TG).

Published:

with international search report (Art. 21(3))

Security tag with laser-cut particles of biological origin

Field of Invention

The present invention relates to security tags for identification and authentication of goods, articles and documents.

5 Background of Invention

Optically variable devices (OVD) are a common protective element on various types of documents (e.g. identity cards, passports, visas, bank cards) – see the book “Optical Document Security”, ed. by R. L. Van Renesse, Artech House, (1998). Holograms and other diffractive elements are mainly used, because their protective value is based on complexity of micron and submicron structures. Manufacturing is a complicated and expensive process whose final result is a master hologram – a single, unique prototype. To make protection commercially acceptable, the master hologram is copied and multiplied, resulting in a replica shim used for embossing into a plastic foil, which is then integrated into a document using a hot tool. The final result is a series of documents possessing exactly the same protective OVD. This is a significant drawback, because, if the OVD is counterfeited, a large number of fake documents can be manufactured.

As a result, there is ongoing research for a simple and affordable, document individualization method. This makes counterfeit much harder, because each and every document has to be copied individually, i.e. large scale production of false documents becomes impossible. However, the trivial individualization by simply printing numbers will not work, because it is too simple and affordable, if using modern printing technologies (e.g. laser printing). Therefore the individualization-bearing features must possess a significant amount of complexity together with strong, unrepeatable, individual properties. They have to be comparable in its uniqueness with biometric characteristics, such as: fingerprints, iris and retina pattern, but significantly more complex and miniscule. Currently used OVD security methods are not well suited for individualization (fingerprinting), as this will significantly increase the production prices.

Attempts to obtain “fingerprint” documents are based on the idea of physical one-way functions (alternatively called physically unclonable functions, as in C. Boehm, M. Hofer,

"Physically unclonable functions in theory and practice", Springer, 2013) which are physical devices simple to manufacture, yet extremely difficult to reverse engineer and copy. Random structures can be highly significant for document security, because they offer simple and cheap production, almost impossible re-origination and unique features. It was proposed to tag documents with randomly dispersed objects such as metal, fluorescent or optical fibers (van Rensse book, and references therein)

Natural fibrous structure of paper-based substrates was used (i. D. R. Huchanan, R. P. Cowburn, A-V. Jausovec, D. Petit, P. Seem, G. Xiang, D. Atkinson, K. Lenton, D. A. Allwood, M. T. Bryan, "Fingerprinting documents and packaging", *Nature* **436**, (2005) 475). Laser beam was scattered from the paper surface and its statistics was observed and recorded. This however requires a large scale scanning of the document surface which is a slow process, and paper structure may be strongly affected by printing and everyday usage.

Yet another technique was described in R. Pappu, B. Recht, J. Taylor, N. Gershenfeld, "Physical One-Way Functions," *Science* **297**, (2002) 2026 -2030, where mesoscopic scattering from disordered array of plastic spheres embedded in a transparent substrate was used to construct physical one-way function. The response of the system strongly depends on the illumination direction, again producing unique individual characteristics. The proposed method is limited by the physical requirements for the mesoscopic scattering, resulting in a 10 mm x 10 mm sized tag, with 2.5 mm thickness, which is unsuitable for the modern plastic card technology. Furthermore, the dimension of scattering particles is rather large – 500 – 800 µm in diameter, with 100 µm average spacing – resulting in a bulky system which can be reverse engineered by techniques like micro-tomography.

In addition to randomization techniques, artificial aperiodic or quasiperiodic markings are used for document security purposes, with the aim to further increase the complexity of protective features making them less susceptible to counterfeiting. A method is described in US2015/0302677, 2015, F. Mueller, "Non-periodic tiling document security element", in which a macroscopic, two-dimensional quasi-crystalline tiling pattern is printed on a document.

It is a common knowledge that certain natural characteristic of living creatures are essentially complex and hard to reproduce. This was first realized by Benjamin Franklin who

used this for document protection (Earley Grubb, "Benjamin Franklin and the birth of the paper money economy", Essay based on March 30, 2006 lecture, published by Federal Reserve Bank of Philadelphia). He made casts of plant leaves (correctly recognizing the uniqueness of their venation) and used them to print the first dollar bills. Due to further technological advancements, Franklin's method became obsolete, and was replaced with different printing techniques, such as: intaglio, gilloche, watermark, holograms, etc

WO 2007/031077 (A1) 3/2007, C. Hamm-Dubschar, "Inorganic marking particles for characterizing products for proof of authenticity method for production and use thereof" and DE 10238506 A1, 3/2004, H. Rauche, "Producing information bearing micro particulate mixtures involves defining code that can be implemented using natural or subsequently applied particle characteristics selected from e.g. morphology", disclose an idea for document protection which uses natural complexity of inorganic shells of aquatic organism (like diatoms and radiolarians) according to characteristics of their surfaces. The practicing method is, however, not disclosed. Another problem is that the optical effects are not very pronounced, and the complexity can be observed only at the sub wavelength levels, using electron microscopy. Technique for estimating the degree of complexity was not described, either. Variation among the specimens of the same species is rather small. In that respect, the method can be used only for the forensic level of document authentication.

Recently, there was a significant amount of research aimed at using the principles of optics in nature for document protection (J. Sun, B. Bhushan and J. Tong, "Structural coloration in nature", *RSC Adv.* **3**, (2013) 14862–14889, and B. Yoon, J. Lee, I. S. Park, S. Jeon, J. Lee, J. M. Kim, "Recent functional material based approaches to prevent and detect counterfeiting", *J. Mater. Chem. C* **1**, (2013) 2368 - 2403). Variability of biological structures was also observed (J. P. Bire and J-P. Vigneron, "Photonic nanoarchitectures in butterflies and beetles: valuable sources for bioinspiration", *Laser Photonics Rev.* **5**, (2011) 27-51). Bi-templating was used to manufacture butterfly scale-like structures using metals (S. Sotiropoulou, Y. Sierra-Sastre, S. S. Mark, and C. A. Hut, "Bi-templated Nanostructured Materials", *Chem. Mater.* **20**, (2008) 821–831).

In addition to utilization of the unmodified biological particles, it is possible to use modified ones. The modification of the biological particles enable achievements of different

criteria in document security such as: improved security, facilitated forensic, more difficult counterfeiting, self advertising, logo imprint, aesthetics, etc. Biological particles of microscopic sizes can be modified in various manners in order to meet aforementioned criteria. Precise cutting the biological specimens at microscopic level using a laser beam is described in US 8535876 B2 (2013), Wesner, "Laser micro dissection method and device for laser micro dissection". It is possible to use other, for instance mechanical methods for micro cutting and shaping, but laser beams are in principle more convenient and especially ultrastart laser pulses due to precise cutting lines and lack of melted parts of the material. The biological particles can be modified in other manners except cutting, like photo damage or permanent photo bleaching.

10 Since chitin, the main building block of the arthropods, exhibits strong fluorescence when irradiated with blue or soft UV light, it is possible to bleach particles made of chitin. (M. Rabasovic et al. "Nonlinear microscopy of chitin and chitinous structures: a case study of two cave-dwelling insects". *J. Biomed. Opt.* **20**, (2015) 016010)

The randomized systems described above must be machine-inspected, based on radiation scattering with consequent optical or microwave detection (in the case of metal inclusions). Recorded pattern is encrypted and stored in a central repository or on the document itself. Public key encryption method is used, as described in the report: "Counterfeit deterrent features for the next generation currency design", Committee on Next-Generation Currency Design, National Materials Advisory Board, Commission on Engineering and Technical Systems, National Research Council, Publication NMAB-472, (1993), Section: Random Pattern/Encryption Counterfeit-Deterrence Concept, pg. 74 - 75, and Appendix E: "Methods for authentication of unique random patterns", pg. 117 - 119. The technique is based on two keys: a secret one, used for encryption, and a public one, used for decryption.

20

All the methods use a complexity of natural structures, but their variability remained completely unused in the context of document protection. Document variability was rather attained by randomly dispersing particle- or thread-like entities across the document.

Summary of the Invention

The problem solved by the present invention is individualization of security tags. This is done by permanently attaching an arrangement of biological particles with pronounced individuality that are modified in the manner of cutting, permanent bleaching, scribing and/or stacking.

5 The invention is directed to a security tag, comprising,

a transparent substrate;

an arrangement of processed biological particles in a specific pattern which is attached to the substrate; and

10 a transparent superstrate, having a recess, and adhering to the substrate and enclosing the biological particles

Preferably, the biological particles are obtained from dead, non-decomposable, tissues.

More preferably, the biological particles are selected from scales, hairs or bristles of Lepidoptera, Trichoptera, Coleoptera and Aranea or wings of Hymenoptera.

15 In a preferred embodiment of the invention, the processing of the biological particles is done by cutting them in predefined shapes, preferably by using a laser beam.

The arrangement of processed biological particles may preferably be further processed

20 In one embodiment of the present invention, the further processing of the arrangement of processed biological particles is done by permanently bleaching out the natural autofluorescence of the biological particles in a predefined pattern, bearing personal or other information, using actinic radiation. The actinic radiation may be laser or non-laser radiation.

In another embodiment of the invention, the further processing of the arrangement of processed biological particles is done by artificially dyeing the biological particles with fluorescent dyes, and permanently bleaching out the artificial fluorescence of the dyed particles

in a predefined pattern bearing personal or other information, using actinic radiation. The actinic radiation may again be laser or non-laser radiation.

More preferably, the arrangement of processed biological particles is defined according to a predetermined periodic, quasi-periodic, aperiodic or irregular pattern.

5 In one specific embodiment of the invention, the biological particles are cut in a gear shape, and positioned on cylindrically cut particles in a shaft shape, and the cylindrically shaped particles are strongly attached to the tag surface using a strong adhesive, while the gear shaped biological particles are not adhesively bonded to the tag surface, thus producing a freely moveable, interlocked, micromechanical iridescent system.

10 In one preferred embodiment, the arrangement of processed biological particles is defined by a bar-code pattern.

It is also preferred that the arrangement of processed biological particles is inscribed with additional information by laser ablation.

15 In one embodiment of the present invention, the transparent substrate comprises a transparent adhesive layer on its lower surface, which preferably is of the pressure-sensitive or hot printing type. In a preferred embodiment of the invention, the biological particles possess a grating-like diffracting structure.

Preferably, the inscribed information bears personal data, such as silhouette, fingerprint, retinal pattern image and/or numerical information such as a bar- or QR-code.

20 The invention preferably envisages that the arrangement of processed biological particles is inscribed with alternating bleached, ablated or untreated spots, in arbitrary order forming the numbers coded in ternary system.

Furthermore, the invention is directed to the use of a security tag according to the invention for identification and authentication of goods, articles and documents.

25 The invention is also directed to a method of manufacturing a security tag according to a preferred embodiment, wherein a laser beam with average intensity $0.002 - 2 \text{ kW/cm}^2$ at the focal area of the laser beam is used to bleach the biological particles.

Finally, the invention is directed to a method of manufacturing a security tag according to another preferred embodiment, wherein ultra-short laser pulses of a duration of less than 1ps and an average intensity in the range of 0.2 - 1000 kW/cm² at the focal area of the laser beam are used to cut the biological particles.

5 There are several criteria which must be simultaneously fulfilled in order to give a unique fingerprint, usable for document protection purposes. Biological particles are selected according to variability of optical effects (interference, diffraction, fluorescence, scattering), internal complexity of their structure, fragility, capability of being easily and reproducibly processed by a laser beam, non degradability and thinness.

10 A resulting tag containing biological nano- and microstructures is a unique and unrepeatable protective device. Organisms and tissues are chosen such that the observed optical effects are strongly localized, variable, and individual and the result of interference, diffraction, fluorescence and scattering from complicated three-dimensional structures. Additionally, tissues are chosen to be durable, with permanent optical properties and capable of being transferred and
15 processed before, during or after attachment to the substrate. Biological particles are permanently attached to the substrate, usually by using a strong adhesive. As a result, the tag cannot be disassembled without permanently destroying its optical properties.

Brief Description of Drawings

- 20 Fig. 1: Optical image of an individual butterfly scale, where the strong, local, variability of iridescence can be observed.
- Fig. 2: Scanning electron microscope image of the butterfly scale, where the complexity of its internal structure can be seen.
- Fig. 3: A natural biological particle is cut into predefined shapes, which are further
25 arranged in tiling (e.g. jigsaw and Penrose type) or non-repeating (e.g. tiling type) patterns.
- Fig. 4: A security tag presented in two orthogonal projections.

- Fig. 5: A security tag with an array of patches where pre-cut biological particles are arranged and attached.
- Fig. 6: A security tag with an array of patches where pre-cut biological particles are arranged, attached, and overtly and covertly inscribed.
- 5 Fig. 7: A security tag with an arrangement of pre-cut biological particles, which contain bits of information inscribed as bleached, ablated and untreated areas.
- Fig. 8: A security tag with an arrangement of pre-cut biological particles whose iridescence depends on the orientation of the light sources.
- Fig. 9: A security tag with an arrangement of pre-cut biological particles positioned in a
10 rectangular grid, defining a bar-code.
- Fig. 10: A security tag with biological particles pre-cut in a gear shape and attached to the surface, such that a moveable gear system is constructed.

Detailed Description of the Invention

15 In cooperation with the attached drawings, the technical contents and detailed embodiments of the present invention are described hereinafter, however, not limiting its scope of protection which is exclusively defined by the claims. Any equivalent variation and modification made according to the appended claims is to be covered by their scope of protection.

20 The tag manufacturing process starts with selecting appropriate biological particles according to several criteria, described in the following text.

The first criterion for biological particle selection is according to variability of optical properties across their surface (near-field) or in the far-field of the scattered radiation. Detected optical properties include optical field amplitude and phase, field vorticity, reflection and
25 transmission spectral distribution, overall biological particle shape, moiré pattern, polarization pattern, iridescence, diffraction, and fluorescence. The second selection criterion is the

underlying complexity of biological particle structure, which has to span the range from nano-meter to micron-size features, intricately distributed in three-dimensions. The third criterion is their fragility, necessary for tamper sensitivity. The fourth criterion is the non-degradability of the structure, at least within the validity period of the document. The fifth criterion is the thinness of the structures such that they can be easily used for security tag production or integrated within existing OVDs, whose thickness is of the order of several tens of microns. The selection process requires fulfillment of all five criteria.

Preferred biological particles, in the literature named scales, are those which can be found in or on the cuticle of various insects. There is a general ground plan of these particles, with the details significantly depending on the species. They are self-contained (Fig. 1), plate-like or cylindrical, having a wall of submicron thickness, which encloses the internal volume. Inside the particle, a number of features may exist, such as nano-pillars, photonic crystals, fluorescent nano-particles. One or both external surfaces are patterned with the grating-like ridges and cross-ridges (Fig. 2). Ridges have a lamellar structure, similar to the Bragg grating. The main constituent is chitin, a biological polysaccharide insoluble in water and many other solvents. They are permanent remnants of individual cells, and may endure without changing their optical properties for long periods – it is known that dried insects like butterflies may survive for decades in entomological collections. Iridescence, diffraction pattern or fluorescence of individual particles may strongly vary across the surface (of the order of $50 \times 150 \mu\text{m}^2$), as can be seen in Fig. 1. Thickness is of the order of few microns, resulting in fragility of the whole structure, which is stable enough to be transferred to the substrate during security tag production or transferred and adhered to the existing OVD's substrate.

More specifically, preferred biological particles are scales, hairs or bristles of Lepidoptera, Trichoptera, Coleoptera or Araneae. Preferred Lepidoptera species are those possessing silver spots or patches, but are not limited to them. Examples of species are: *Issoria lathonia*, *Argyrophorus argenteus*, *Dione moneta*, *Dione juno*, *Agrotis vanillae*. Other preferred Lepidoptera species are selected amongst Microlepidoptera, Rhopalocera (butterflies) or Heterocera (moths) exhibiting structural coloration, such as: *Dicobrytia chrysis*, *Macdunnoughia confusa*, *Autographa gamma*, *Lydaulita globulociae*, *Coltophrys rubi*, *Apatura iris*, *Apatura illis*, *Aglais io*. Preferred Coleoptera species are (but not limited to them): *Hoplia*

coemela, *Pseudomyzoxenus waterhousei*, *Lauprocoryphus angustus*, *Hypera diversipunctata*, *Prosopocera lactator*, *Cyphus hancocki*, *Eutimius imperialis*, *Sphingonotus mirabilis*, *Hoplia argentea*, some species of Curculionidae and Collembolae families. Preferred Trichoptera species, but not limited to them, are: *Pseudoleptocerus chinensis*, *Phylloncus abdominalis*,
 5 *Neotopsyba punctata*, *Banyalloga cecata*, *Hesperophylax designatus*, *Polycentropus flavomaculatus*, *Mystacides azurea*, *Mystacides longicornis*, *Anthropsodes albivitta*, *Limnephilus bicostatus*. Preferred Araneae species are those possessing scales on their cuticle, but not limited to them, such as: *Maratius volans*, *Maratius splendens*, *Phidippus audax*, *Pauphobetes autumnus*, *Cyriopagopus lividum*.

10 The tag manufacturing proceeds with precutting natural biological particles, described above, into required shapes. Preferably, referring to Fig. 3, an individual, unmodified, Lepidoptera scale 1 is removed from the wing and cut into a number of even smaller, shaped particles 2. As an alternative, hairs, scales or bristles of Coleoptera, Araneae and Trichoptera are used in the same manner. As another alternative, a Hymenoptera wing is precut into a number of
 15 even smaller, shaped, particles.

Particles are precut to enable tiled or irregular arrangements. Preferred tiling arrangements are periodic (e.g. jigsaw pattern 3 in Fig. 3) and quasi-periodic (e.g. Penrose tiling pattern 4 in Fig. 3), see the book B. Grünbaum, G. C. Shephard, Tilings and patterns, W.H. Freeman, 1990. Preferred non-tiled arrangements of precut particles are those which are not
 20 capable of tessellating (covering without gaps) a surface (e.g. tangram pattern 5 in Fig. 3).

The precut particles are transferred and attached to the surface of the tag substrate in a stack or in a predefined arrangement using micromanipulation techniques (as described in "Robotic microassembly", Ed. By M. Gauthier and S. Regnier, (2010) John Wiley and Sons).

25 The particles are cut in a predefined pattern by a laser beam. Preferably, a beam from an ultrafast laser is introduced in a system with a computer-controlled galvanometer-mirror scanner, which is used to angularly deflect the beam according to programmed trajectory. The beam is then expanded and focused to the tag with biological particles, using a microscope objective. The laser wavelength, scanning speed and power are chosen such that cutting or engraving or bleaching is enabled.

The obtained tag can be used independently, or it can be permanently attached to an existing QVD on the document. Only a subset of attached particles might be used for authentication purposes, while the rest is there as a distraction, which makes counterfeit harder, as a counterfeiter would not know which particles are used for authentication. Biological particles which possess different optical properties on their front and rear side are used to produce security features which can be read from both sides in perfect alignment (see-through register).

Reference is made to Fig. 4 which presents two orthogonal views of one embodiment of the security tag of the present invention. It is composed of a substrate 6, having an adhesive layer 7 at its lower surface, which can be activated either by heat, light or pressure in order to integrate the tag with the article, good or document. The upper surface of the substrate 6 comprises a small patch of adhesive 8, whose surface is just large enough to receive pre-cut biological particles 9. They are permanently attached onto the adhesive patch 8 in a predefined pattern (periodic, quasiperiodic, aperiodic or irregular).

The attached biological particles 9 are covered with a superstrate 10, having a recess 11 large enough to contain and enclose the attached biological particles 9, without touching their upper surfaces. The lower surface of the superstrate 10 is covered with a transparent layer of heat or pressure activated adhesive 12, such that the recess 11 is left without adhesive layer. Superstrate 10 and substrate 6 are attached to each other and sealed by an adhesive layer 12, such that they enclose the attached biological particles 9.

Additional marks 13, 14 and 15, whose dimensions are smaller than 200 μm , may be incorporated into the substrate 6. The marks are used as reference points and attached biological particles are put in pre-defined positions, with respect to said reference points.

In another embodiment (Fig. 5), the security tag of the present invention is designed and manufactured to have an unspecified number of small patches of adhesive 16, 17, 18, 19 and 20, whose surface is just large enough to each receive pre-cut biological particles 9 arranged in a pattern. The patches are placed in an orderly manner, corresponding to certain symmetry, as in Fig. 5. The width and height of the patches is preferably within the range of 150 μm - 1000 μm . Pre-cut biological particles of Lepidoptera, Trichoptera, Coleoptera, Araneae or Hymenoptera are

attached to each patch in a predefined arrangement. The patches are either filled with pre-cut biological particles from the single species, or from pre-cut biological particles from several different species. The substrate with pre-cut and arranged biological particles is covered with a transparent superstrate having recesses exactly matching the positions of the patches. A thin layer of a transparent adhesive is placed on the bottom side of a cover, without covering the recesses. This layer is used to seal the pre-cut biological particles between the substrate and the superstrate.

In a further embodiment, depicted in Fig. 6, a security tag is disclosed where the natural autofluorescence of pre-cut and arranged biological particles 9 is permanently bleached out in a predefined pattern. In this way the pre-cut and arranged biological particles are covertly inscribed with a secret code or personal information (e.g. text, numbers, image, barcode). The pattern is, for example, inscribed by a scanning sub-picosecond laser beam that induces two-photon absorption at the focal point. The laser wavelength is in the range 650-1050 nm, and its intensity is in the range $0.0002 - 2 \text{ kW/cm}^2$, at the focal area of the laser beam. Exact value of the intensity depends on the scanning speed and the size of the focal spot, too. The laser beam is focused using a high numerical aperture microscopic objective and scanned using galvo-scanning mirrors, as previously described.

In an alternative embodiment the pre-cut and arranged biological particles are dyed with fluorescent dye prior to the inscription. Information can be inscribed before or after the encapsulation of the pre-cut and arranged biological particles on the security tag.

In yet another embodiment of the present invention, portions of the pre-cut and arranged biological particles are ablated in a predefined pattern, as illustrated in Fig. 6. In this way the scales are overtly inscribed with a secret code or personal information (e.g. text, numbers, image, barcode). The pattern is, for example, inscribed by a scanning sub-picosecond laser beam that ablates material in the focal point. The laser wavelength is in the range 650-1050 nm and the intensity is in the range $0.2 - 1000 \text{ kW/cm}^2$. The laser beam is focused using a high numerical aperture microscopic objective and scanned using galvo-scanning mirrors, as previously described.

In yet another embodiment of the present invention (depicted in Fig. 7), a tag contains precut and arranged biological particles 21 which are inscribed with either bleached 22, ablated 23 or untreated 24 spots, in arbitrary order forming the numbers coded in the ternary system. This enables more data to be stored on the same area compared to the binary system.

5 In a further embodiment, biological particles, which possess diffraction grating-like structures, are selected. As a consequence, their iridescence depends on the illumination direction, with respect to the grating orientation. They are precut by taking care of mutual orientation between the cut shape and the grating. After arranging and attaching precut biological particles on the tag surface, iridescence pattern strongly depends on the illumination direction, as
10 shown in Fig. 8. If an arrangement of precut particles (e.g. tangram as in Fig. 8A) is illuminated from the lightsource 25, only particles *a*, *b*, *c* reflect light iridescently. If the same arrangement of precut particles (Fig. 8B) is illuminated from the light source 26, only precut particle *d* reflects light iridescently. Finally, if the same arrangement of precut particles (Fig. 8C) is illuminated from the lightsource 27, only particles *e*, *f*, *g* reflect light iridescently.

15 In yet another embodiment depicted in Fig. 9, precut biological particles are arranged and attached in a regular, rectangular grid within the adhesive patch 28 of a tag. Grid occupancy defines a binary encoding of information, where any occupied position, such as 29 in Fig. 9, designates binary 1, and any unoccupied position, such as 30 in Fig. 9, defines binary 0. In that sense, they represent a one- or two-dimensional iridescent bar-code.

20 In the next embodiment depicted in Fig. 10, iridescent biological particles are cut in a gear shape 31, 32. Shafts 33 and 34 (which can be made from biological particles, too, but can also be made from different material) are firmly attached to the tag surface 35 using, locally applied adhesive. Gears 31 and 32 are put on the shafts 33 and 34, respectively, without using any adhesive layer on the tag surface 35, and thus arranged in an interlocked position as to
25 produce a micromechanical moveable system.

Claims

1. A security tag, comprising:
 - a transparent substrate (6);
 - 5 an arrangement of processed biological particles (9) in a specific pattern which is attached to the substrate (6); and
 - a transparent superstrate (10), having a recess (11), and adhering to the substrate (6) and enclosing the biological particles (9).
2. The security tag according to claim 1, wherein the biological particles (9) are obtained from
10 dead, non-decomposable, tissues.
3. The security tag according to claim 2, wherein the biological particles (9) are selected from scales, hairs or bristles of Lepidoptera, Trichoptera, Coleoptera and Aranea or wings of Hymenoptera.
4. The security tag according to any of the preceding claims, wherein the processing of the
15 biological particles (9) is done by cutting them in predefined shapes.
5. The security tag according to claim 4, wherein the cutting is done by using a laser beam.
6. The security tag according to any of the preceding claims, wherein the arrangement of processed biological particles (9) is further processed.
7. The security tag according to claim 6, wherein the further processing of the arrangement of
20 processed biological particles (9) is done by permanently bleaching out the natural autofluorescence of the biological particles (9) in a predefined pattern, bearing personal or other information, using actinic radiation.
8. The security tag according to claim 6, wherein the further processing of the arrangement of
25 processed biological particles (9) is done by artificially dyeing the biological particles (9) with fluorescent dyes, and permanently bleaching out the artificial fluorescence of the dyed

particles (9), in a predefined pattern bearing personal or other information, using actinic radiation.

9. The security tag according to any of the preceding claims, where the arrangement of processed biological particles (9) is defined according to a predetermined periodic, quasi-periodic, aperiodic or irregular pattern.
10. The security tag according to claims 4 to 9, wherein the biological particles (9) are cut in a gear shape (31,32), and positioned on cylindrically cut particles in a shaft shape (33,34), and the cylindrically shaped particles (33,34) are strongly attached to the tag surface (35) using a strong adhesive, while the gear shaped biological particles (31, 32) are not adhesively bonded to the tag surface, thus producing a freely moveable, interlocked, micromechanical iridescent system.
11. The security tag according to any of the preceding claims, wherein the arrangement of processed biological particles (9) is defined by a bar-code pattern.
12. The security tag according to any of the preceding claims, wherein the arrangement of processed biological particles (9) is inscribed with additional information by laser ablation.
13. The security tag according to any of the preceding claims, wherein the transparent substrate (6) comprises a transparent adhesive layer (7) on its lower surface.
14. The security tag according to claim 13, wherein the transparent adhesive layer (7) is of the pressure-sensitive, hot printing or light activating type.
15. The security tag according to any of the preceding claims, wherein the biological particles (9) possess a grating-like diffracting structure.
16. The security tag according to any of claims 7 to 10, or 12 wherein the, covertly or overtly inscribed, information bears personal data, such as silhouette, fingerprint, retinal pattern image.
17. The security tag according to any of claims 7 to 10, or 12 wherein the, covertly or overtly, inscribed information bears numerical information such as a bar- or QR-code.

18. The security tag according to any of claims 7 to 10, or 12 wherein the arrangement of processed biological particles (9) is inscribed with alternating bleached, ablated or untreated spots, in arbitrary order forming the numbers coded in ternary system.
19. Use of a security tag according to any of the preceding claims for identification and authentication of goods, articles and documents.
- 5
20. A method of manufacturing a security tag according to claim 7 or 8, wherein a laser beam with average intensity $0.002 - 2 \text{ kW/cm}^2$ at the focal area of the laser beam is used to bleach the biological particles.
21. A method of manufacturing a security tag according to claim 5, wherein ultra-short laser pulses of a duration of less than 1ps and an average intensity in the range of $0.2 - 1000 \text{ kW/cm}^2$ at the focal area of the laser beam are used to cut the biological particles.
- 10

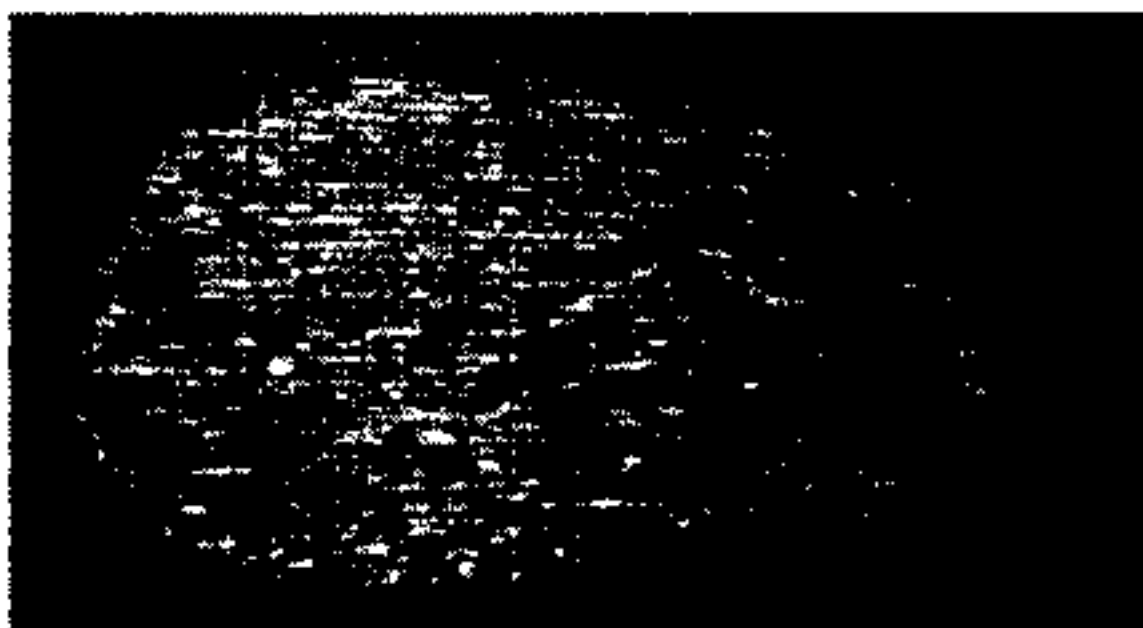


Fig. 1

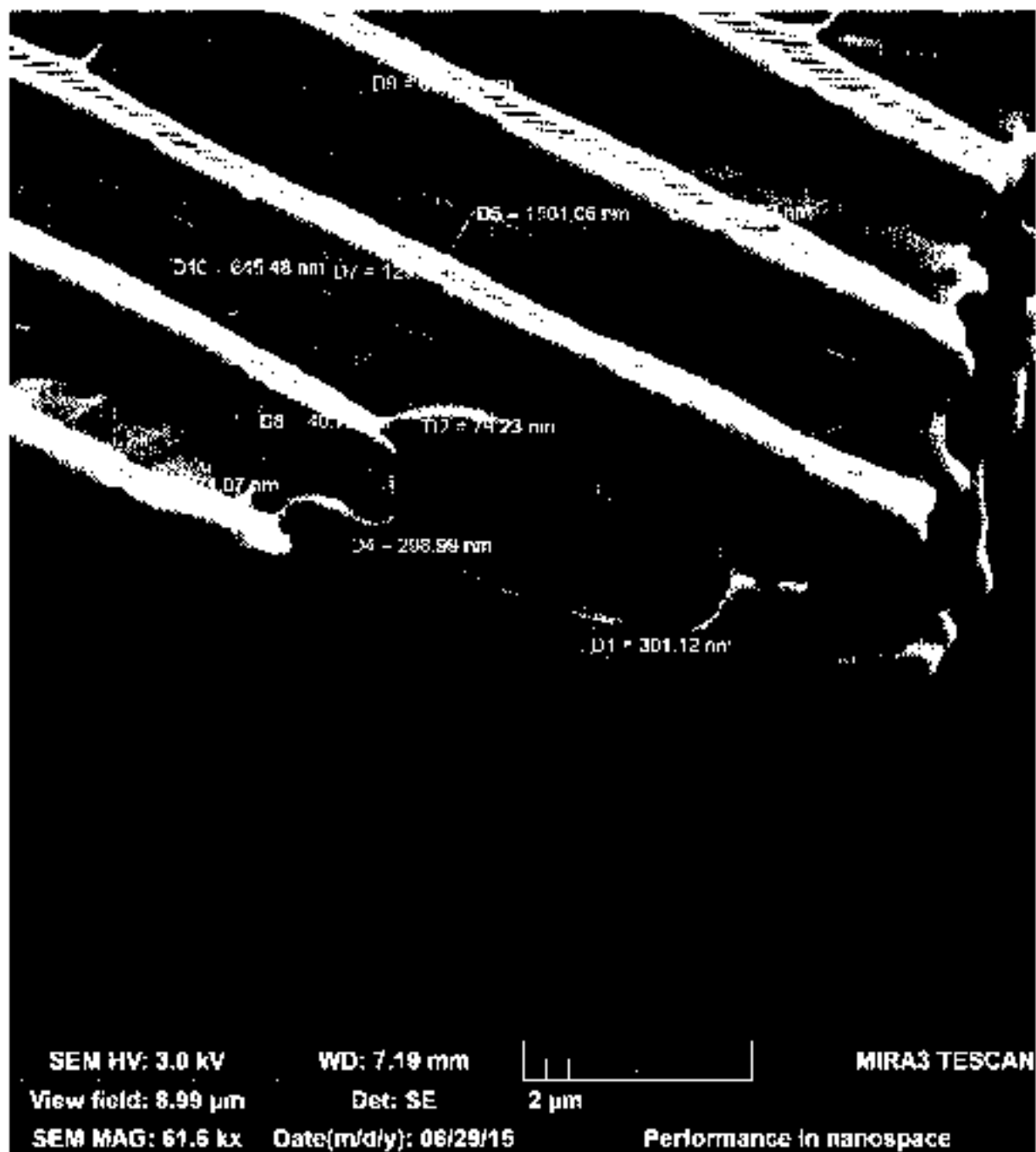


Fig. 2

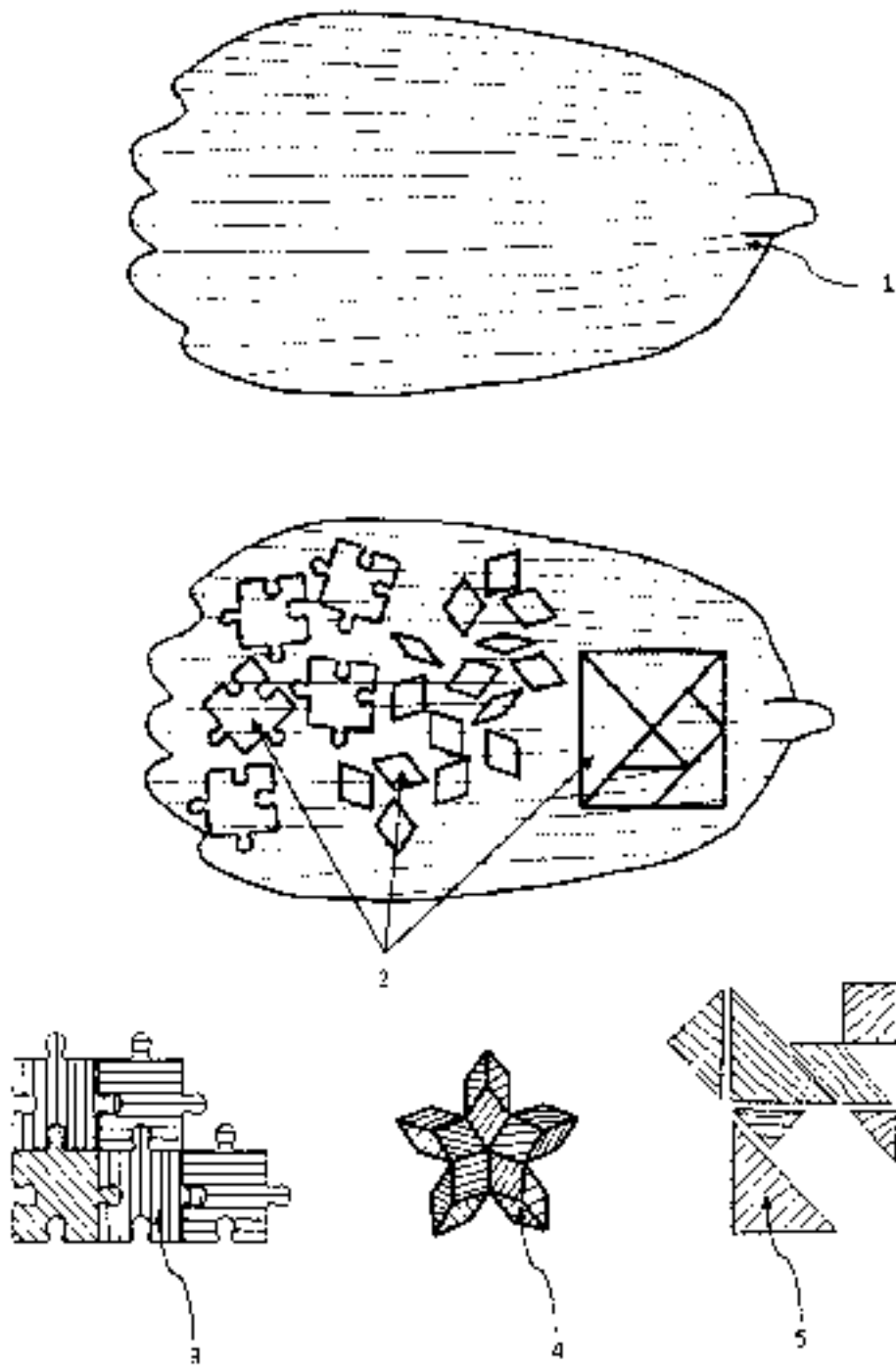


Fig. 3

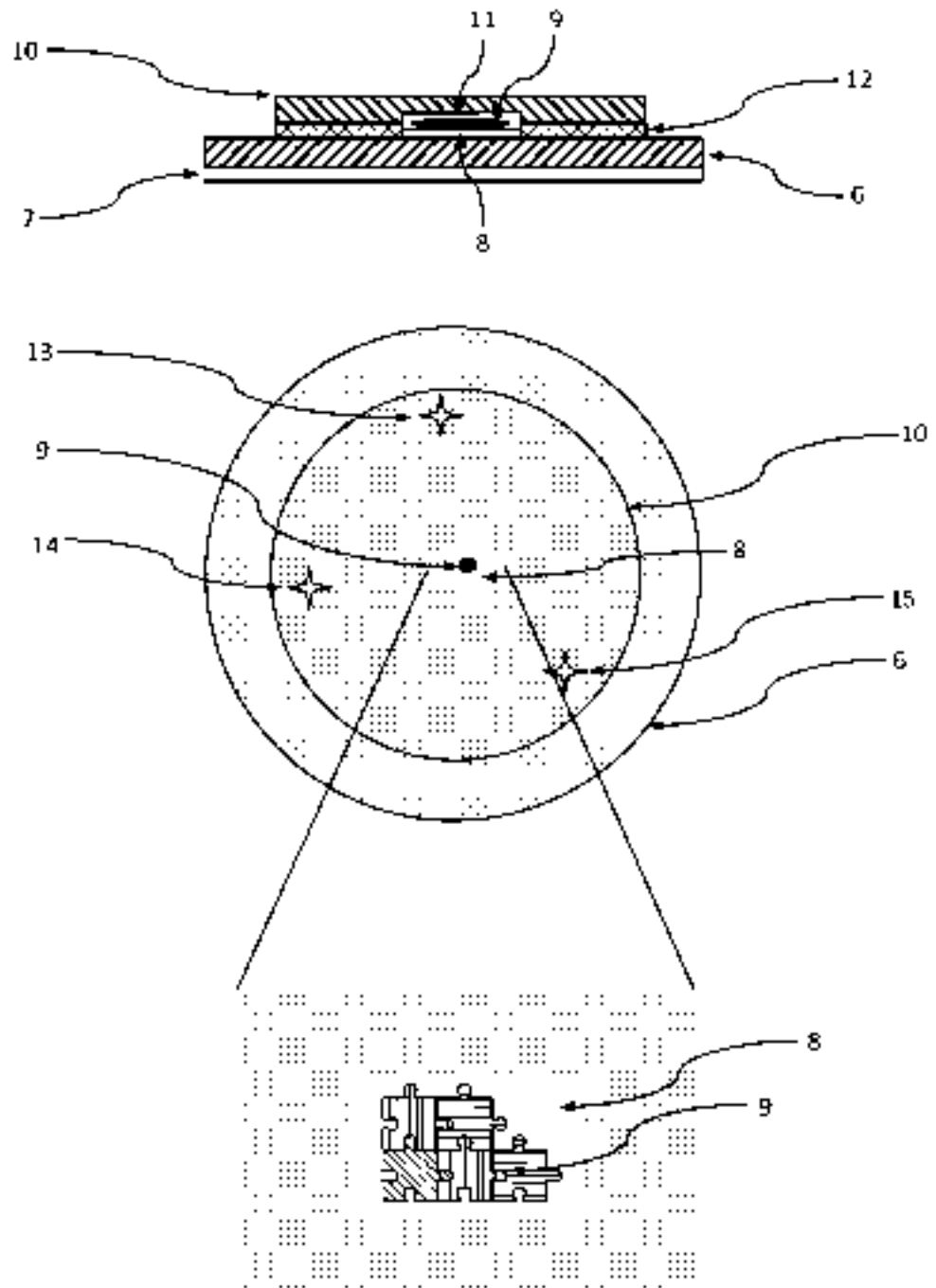


Fig. 4

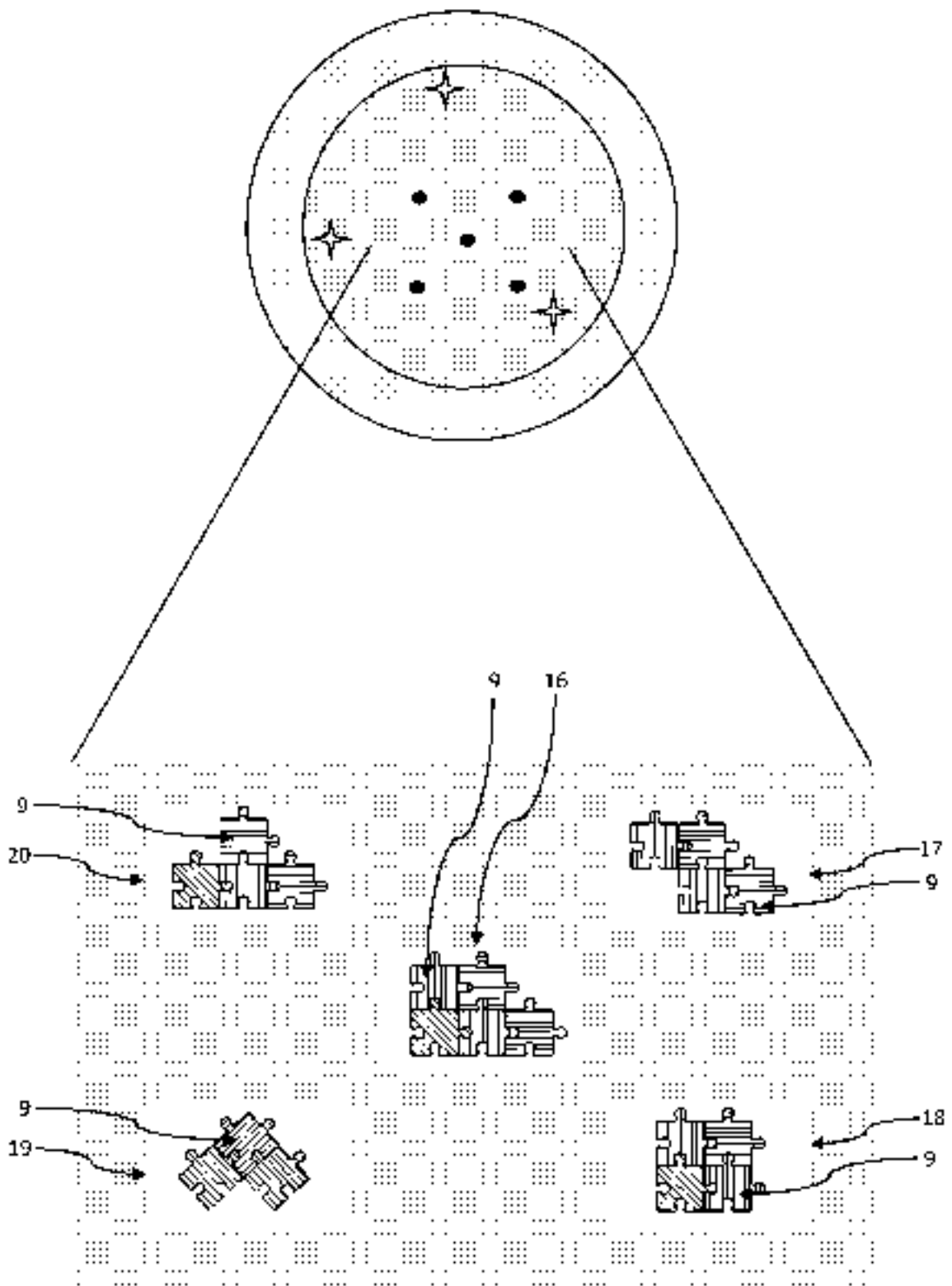


Fig. 5

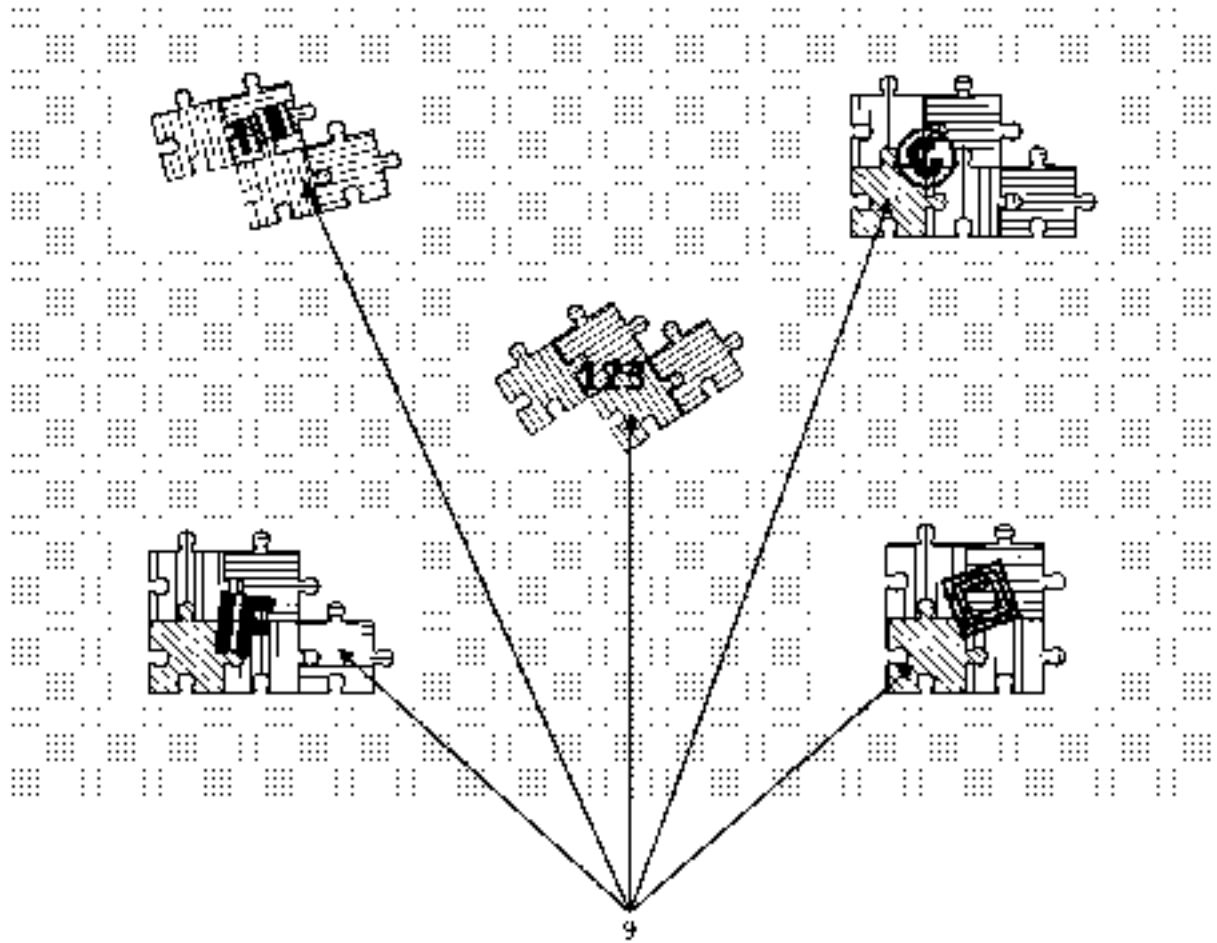


Fig. 6

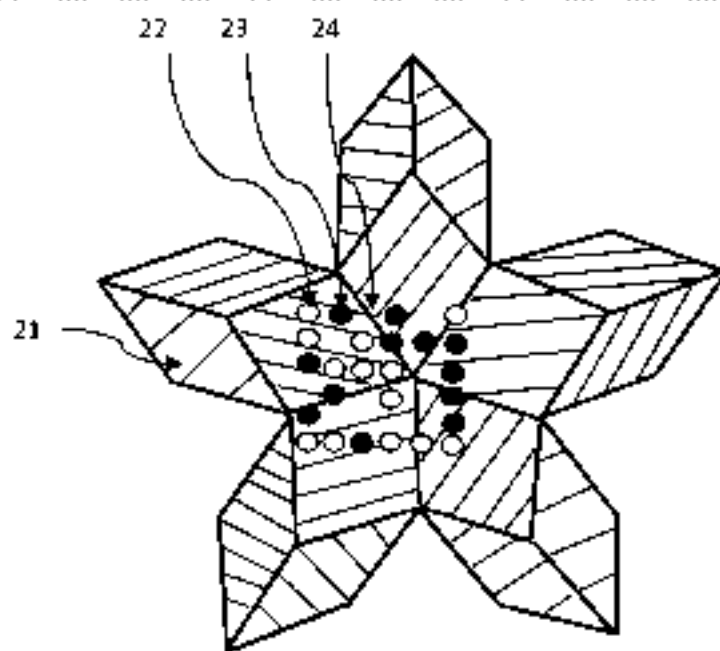
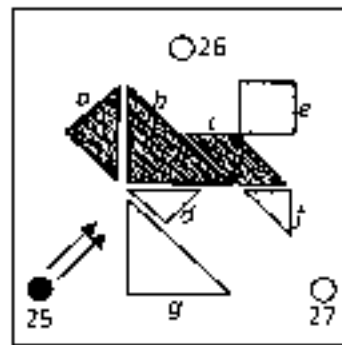


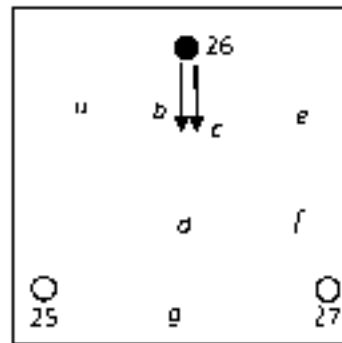
FIG. 7

5

A



B



C

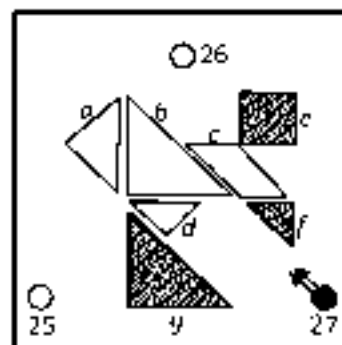


FIG. 8

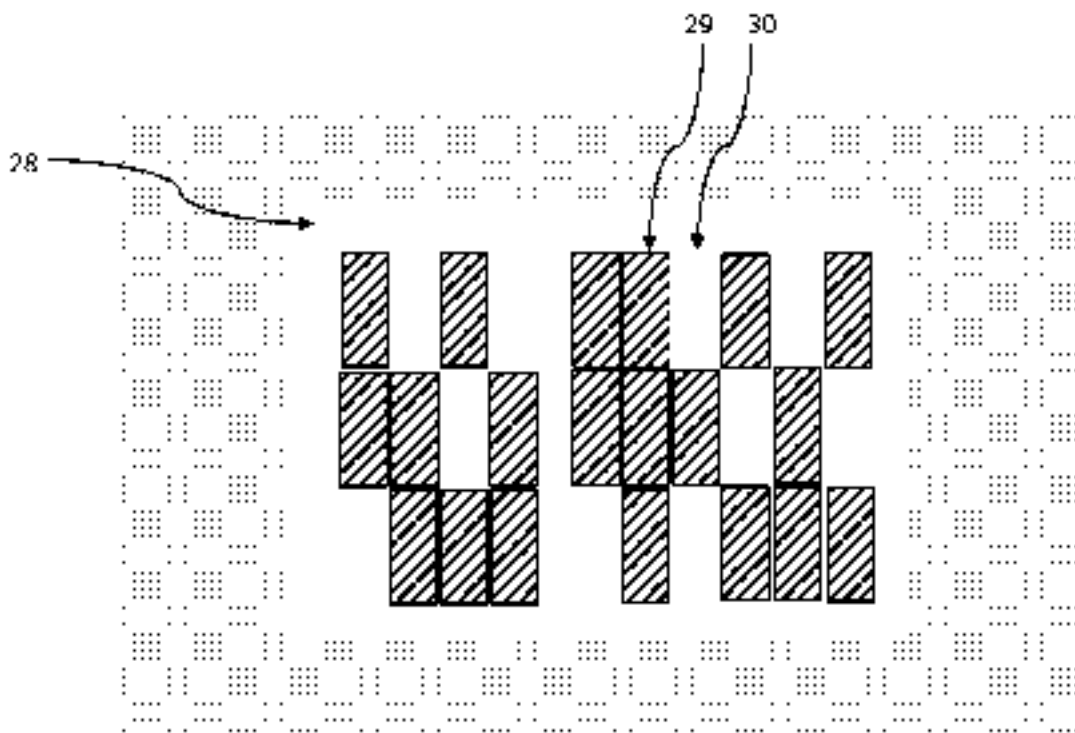


Fig. 9

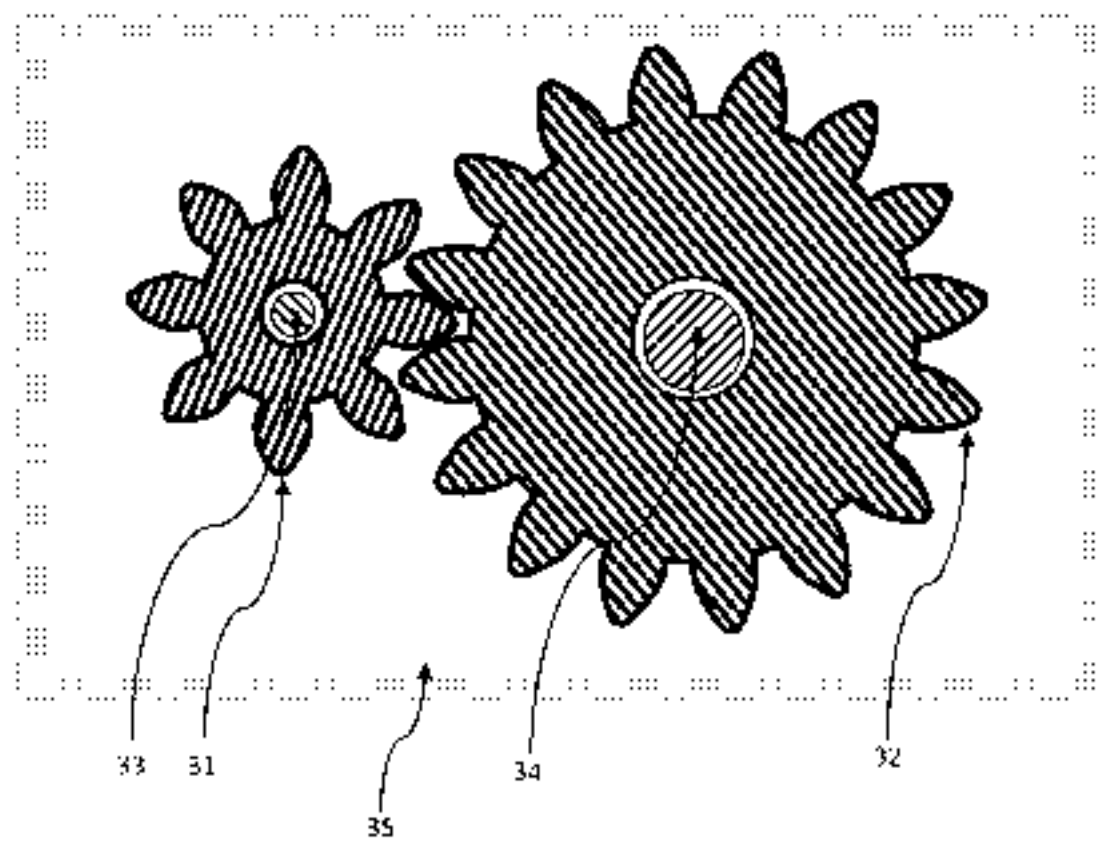


Fig. 10

INTERNATIONAL SEARCH REPORT

International application No.

PCT/EP2015/081407

A. CLASSIFICATION OF SUBJECT MATTER INV. B42D25/41 G09F3/02 B42D25/36 B42D25/45 ADD.		
According to International Patent Classification (IPC) or to both national classification and IPC		
B. FIELDS SEARCHED		
Minimum documentation searched (classification system followed by classification symbols) B42D G09F		
Documentation searched other than minimum documentation to the extent that such documents are included in the fields searched		
Electronic data base consulted during the international search (name of data base and, where practicable, search terms used) EP0-Internal, WPI Data		
C. DOCUMENTS CONSIDERED TO BE RELEVANT		
Category	Citation of document, with indication, where appropriate, of the relevant passages	Relevant to claim No.
X	WO 2007/031077 A1 (STIFTUNG A WEGENER INST POLAR [DE]; HAMM-DUBISCHAR CHRISTIAN [DE]) 22 March 2007 (2007-03-22) cited in the application	1,9,11
A	page 11, line 24 - page 12, line 1 page 14, line 13 - page 16, line 23 page 19, lines 5-32; figures 1,3	2-8, 12-21
A	DE 10 2007 052009 B3 (HOCHSCHULE BREMERHAVEN [DE]; STIFTUNG A WEGENER INST POLAR [DE]) 4 December 2008 (2008-12-04) paragraphs [0032] - [0035]; figures 1A,1B,2	1-21
<input type="checkbox"/> Further documents are listed in the continuation of Box C <input checked="" type="checkbox"/> See patent family annex.		
* Special categories of cited documents: "A" document defining the general state of the art which is not considered to be of particular relevance "E" earlier application or patent but published on or after the international filing date "L" document which may throw doubts on priority claim(s) or which is cited to establish the publication date of another citation or other special reason (as specified) "O" document referring to an oral disclosure, use, exhibition or other means "P" document published prior to the international filing date but later than the priority date claimed "T" later document published after the international filing date or priority date and not in conflict with the application but cited to understand the principle or theory underlying the invention "X" document of particular relevance: the claimed invention cannot be considered novel or cannot be considered to involve an inventive step when the document is taken alone "Y" document of particular relevance: the claimed invention cannot be considered to involve an inventive step when the document is combined with one or more other such documents, such combination being obvious to a person skilled in the art "B" document member of the same patent family		
Date of the actual completion of the international search		Date of mailing of the international search report
19 August 2016		14/09/2016
Name and mailing address of the ISA/ European Patent Office, P. B. 5518 Patentlaan 2 NL - 2280 HX Rijswijk Tel (+31-70) 340 2040, Fax (+31-70) 340 3016		Authorized officer O'Incecco, Raimondo

INTERNATIONAL SEARCH REPORT

Information on patent family members.

International application No
PCT/EP2015/081407

Patent document cited in search report	Publication date	Patent family member(s)	Publication date
WO 2007031077 A1	22-03-2007	DE 102005045642 A1	29-03-2007
		WO 2007031077 A1	22-03-2007

DE 102007052009 B3	04-12-2008	AT 510275 T	15-06-2011
		DE 102007052009 B3	04-12-2008
		EP 2227788 A2	15-09-2010
		WO 2009052811 A2	30-04-2009
